AD613053

This report may be released to OTS.

HANDBOOK OF SUPERSONIC AERODYNAMICS

SECTION 17

DUCTS, NOZZLES AND DIFFUSERS

DDC
RECEIVED
APR 5 19..
DDC-IRA B

COPY 1 OF 2
HARD COPY $. 3.25
MICROFICHE $. —
450P

PUBLISHED BY DIRECTION OF
THE CHIEF OF THE BUREAU OF NAVAL WEAPONS
DEPARTMENT OF THE NAVY

Best Available Copy

ARCHIVE COPY

NAVWEPS REPORT 1488 (VOLUME 6)

HANDBOOK OF SUPERSONIC AERODYNAMICS

SECTION 17

DUCTS, NOZZLES AND DIFFUSERS

Produced and edited by the Aerodynamics Handbook Staff of The Johns Hopkins University, Applied Physics Laboratory, Silver Spring, Maryland, operating under Contract NOw 62-0604-c, with the Bureau of Naval Weapons, Department of the Navy. The selection and technical review of this material were functions of a Laboratory Reviewing Committee consisting of Lester L. Cronvich and Ione D. V. Faro.

JANUARY 1964

For sale by the Superintendent of Documents
U.S. Government Printing Office
Washington, D.C., 20402 - Price: $3.25

SERIES CONTENTS

Section		Status
	Volume 1	
1	Symbols and Nomenclature	Published 1950
2	Fundamental Equations and Formulae	1950
3	General Atmospheric Data	1950
4	Mechanics and Thermodynamics of Steady One-Dimensional Gas Flow	1950
	Volume 2	
5	Compressible Flow Tables and Graphs	1953
	Volume 3	
6	Two-Dimensional Airfoils	1957
7	Three-Dimensional Airfoils	1958
8	Bodies of Revolution	1961
	Volume 4	
9	Mutual Interference Phenomena	In process
10	Stability and Control Analysis Techniques	In process
11	Stability and Control Parameters	In process
12	Aeroelastic Phenomena	1952
	Volume 5	
13	Viscosity Effects	In process
14	Heat Transfer Effects	In process
15	Properties of Gases	1953
16	Mechanics of Rarefied Gases	1959
	Volume 6	
17	Ducts, Nozzles and Diffusers	1964
18	Shock Tubes	1959
19	Wind Tunnel Design	In process
20	Wind Tunnel Instrumentation and Operation	1961

PREFACE

The preface appearing in Volume 1 of the Handbook of Supersonic Aerodynamics defines the Handbook's purpose and also traces the sequence of events leading to its undertaking. In accordance with the criteria established at that time, the subject matter of the Handbook is selected on the basis of anticipated usefulness to all who are actively concerned with the design and performance of supersonic vehicles. Essential to this subject matter are the properties of fluids in which a vehicle operates or is tested and the flight characteristics of the vehicle itself. Each section of the Handbook therefore presents appropriate theory and relevant data which are basic to supersonic aerodynamics and which conform to the above criteria.

A complete list of the Handbook sections and their status appears on the facing page. The unpublished sections, now being prepared by individual authors and the Handbook Staff, will be published separately as they become available.

It was intended that Volume 6 of the Handbook series should be devoted to the design, construction and operation of test facilities such as free jets, shock tubes and wind tunnels, from which facilities a great deal of aerodynamic data is obtained. Section 18, "Shock Tubes," was published in 1959; Section 20, "Wind Tunnel Instrumentation and Operation," in 1961. Section 17, "Ducts, Nozzles and Diffusers," is published herewith. Its scope is somewhat different from that originally intended as it now includes the design and operation of the inlets and exit nozzles of ramjet engines as well as those of wind-tunnel nozzles and diffusers which were the prime interest when the Handbook sections were first outlined.

Section 17 has been prepared for the most part by the Handbook Staff. Subsection 2.2 was written by George Rudinger (through the generosity of Cornell Aeronautical Laboratory, Inc.). Assistance was also given by C.L. Dailey of Space Technology Laboratories, Inc., and by G.V.R. Rao, National Engineering Science Co. The Handbook Staff is also grateful for constructive criticism and helpful advice from F.S. Billig, V.W. Brumbaugh, R.H. Cramer, G.L. Dugger, F.K. Hill, T.G. Konrad, R.A. Makofski, G.J. Pietrangeli, R.E. Walker (author of Subsec. 6.3.2), A.A. Westenberg (author of Subsec. 6.3.1), and H.W. Woolard, all staff members of the Applied Physics Laboratory.

The subject matter appearing in the Handbook is selected and reviewed by the Technical Reviewing Committee at the Applied Physics Laboratory, headed by L.L. Cronvich. Constructive criticism or recommendations relating to the inclusion of suitable material in the Handbook should be directed to:

Editor, Handbook of Supersonic Aerodynamics
Applied Physics Laboratory
The Johns Hopkins University
8621 Georgia Avenue
Silver Spring, Maryland

The Handbook is published and distributed by direction of the Bureau of Naval Weapons, Department of the Navy. It is available for public purchase (see Title Page) and is also distributed without charge to an approved list of facilities and institutions actively engaged in national defense research and development. Correspondence relating to the distribution of the Handbook should be directed to:

Chief, Bureau of Naval Weapons
Department of the Navy
Washington 25. D. C.

Although the format of this section follows in general that of the last three sections, more sketches have been included, the appearance has been improved by the adoption of justified typing, and a greater degree of consistency has been attained in the figures.

The Handbook of Supersonic Aerodynamics is edited and made ready for printing by the Handbook Staff, which includes Mrs. Doris McCeney who does the layout work and types the reproduction copy and Mrs. Carol Dick, mathematician, who draws all sketches and figures in addition to the manifold and sundry tasks associated with preparing the manuscript.

Ione D. V. Faro, Editor

CONTENTS

	Page
List of Tables	ix
List of Figures	ix
Symbols	xxiii
1. Introduction	1
1.1 Scope of Contents	1
2. Duct Flow Theory	3
2.1 One-Dimensional Steady Flow	3
2.1.1 Area Variation	3
2.1.2 Temperature Variation	5
2.1.3 Heat and Mass Addition	8
2.1.4 Steadily Moving Temperature Discontinuities	12
2.1.5 Heat Addition in a Channel of Varying Area	12
2.1.6 Adiabatic Normal Shock	12
2.1.7 Hypersonic and High-Temperature Flows in Ducts	13
2.1.8 One-Dimensional Treatment of Non-Uniform Flow	14
2.1.9 Flange Loads on Free-Jet Nozzles	18
2.1.10 Rocket Jet Thrust	19
2.1.11 Air-Breathing Engine Thrust	21
2.1.12 Viscous Effects and Heat Transfer in One-Dimensional Duct Flows	23
2.2 One-Dimensional Non-Steady Flow	24
2.2.1 Assumptions and Basic Equations	25
2.2.2 Construction of Wave Diagrams	29
2.2.2.1 Pressure Waves	30
2.2.2.2 Initial Conditions, Domain of Dependence and Range of Influence	31
2.2.3 Boundary Conditions	32
2.2.3.1 Closed End (No Discharge)	33
2.2.3.2 Subsonic Discharge	33
2.3.3.3 Supersonic Discharge	33
2.3.3.4 Inflow from an External Reservoir	34
2.2.4 Discontinuities	34
2.2.4.1 Contact Surfaces	34
2.2.4.2 Shock Waves	35
2.2.4.3 Flame Fronts	37
2.2.4.4 Discontinuous Area Changes	39

Page

2.2.5 Shock Interactions 40
2.2.5.1 Shock Reflection from an Open End 40
2.2.5.2 Interaction of Two Shock Waves 41
2.2.5.3 Shock Interaction with a Discontinuous Area Change 43
2.2.5.4 Interaction of a Shock with a Contact Surface . 43
2.2.5.5 Shock Interaction with a Flame Front . . . 44
2.2.6 Shock Passage Through a Duct of Gradually Varying Cross Section 45
2.2.7 Small Perturbation Approximations 45
2.2.7.1 Basic Flow of Infinite Extent 47
2.2.7.2 Uniform Basic Flow with a Moving Discontinuity 48
2.2.7.3 Transfer Functions for Wave Interactions . . 50
2.3 Two- and Three-Dimensional Flow 57
2.4 Boundary-Layer Correction 58
2.4.1 Boundary-Layer Thickness in Two-Dimensional Flow . 60
2.4.1.1 Zero Pressure Gradient 60
2.4.1.2 Positive or Negative Pressure Gradient . . 61
2.4.1.3 Estimated Test-Section Correction 61
2.4.2 Boundary-Layer Correction for Axially-Symmetric Flow 62
Table and Figures (See p. ix for list) 65

3. Supersonic Inlets 101
3.1 Diffuser Performance Parameters 102
3.1.1 Total Pressure Recovery 102
3.1.2 Capture-Area Ratio or Mass-Flow Ratio 103
3.1.3 Diffuser Drag 105
3.2 Internal-Compression Diffusers 108
3.2.1 Normal-Shock Diffusion 108
3.2.2 Variable-Area Diffusers 110
3.2.3 Perforated Convergent-Divergent Diffusers 113
3.3 Oblique-Shock Diffusers 114
3.3.1 Single-Cone Diffusers 116
3.3.1.1 Probe Diffusers 120
3.3.2 Double-Cone Diffusers 121
3.4 Isentropic-Spike Diffusers 125
3.4.1 Design Considerations 125
3.4.2 Off-Design Operation 132

Page

3.5 Comparative Evaluation 134
3.5.1 Mach Number Range of Basic Diffusers 134
3.5.2 Performance Comparison 135
3.6 Two-Dimensional Diffusers 136
3.7 Boundary-Layer Problems 137
3.7.1 Boundary Layer on the Compressing Surface 138
3.7.2 Boundary Layer in the Throat Region 138
3.7.3 Boundary Layer in the Subsonic Diffuser 141
3.7.4 Fuselage Boundary Layer 142
3.8 Diffuser Buzz 143
3.8.1 Theories of Buzz 143
3.8.2 Methods of Control 145
3.8.3 Engine-Inlet Stability 146

Tables and Figures (See pp. ix and xi for list) 149

4. Wind-Tunnel Nozzles 225
4.1 The Nozzle Throat 226
4.2 The Subsonic Contraction 229
4.3 Fixed Mach Number Nozzles 230
4.3.1 Nozzles with Continuous Curvature 232
4.3.2 Multi-Nozzles 233
4.4 Variable Mach Number Nozzles 234
4.4.1 Flexible Nozzles 234
4.4.2 Scissors-Type Nozzles 236
4.4.3 Asymmetric Sliding-Block Nozzles 237
4.4.4 The Tilting-Plate Nozzle Adapter 240
4.4.5 Plug-Type Nozzles 240
4.4.6 Slotted Nozzles 242
4.5 Hypersonic Nozzle Design 243
4.6 Nozzle Cooling 245
4.7 Nozzle Calibration 247
4.8 Boundary-Layer Correction of Nozzle Contours 248
4.8.1 Boundary-Layer Correction in Hypersonic Nozzles . . 249

Tables and Figures (See pp. ix and xvi for list) 253

5. Supersonic Wind-Tunnel Diffusers 269
5.1 Definitions of Diffuser Efficiency 269
5.2 Subsonic Diffusers 270
5.3 Diffusers Without Contraction 271
5.4 Diffusers With Contraction 272
5.4.1 Fixed-Area Second Throat 273
5.4.2 Variable-Area Second Throat 275

Page

5.5 Oblique-Shock Diffusers 276
5.6 Diffusers With Air Injection or Suction 277
5.6.1 Air Injection 277
5.6.2 Air Suction 278
5.6.3 Scavenger Scoop 279
5.7 Power Requirement and Diffuser Efficiency 279
5.8 Run Time and Diffuser Efficiency 280
5.9 Effect of a Model on Diffuser Efficiency 282
5.10 Hypersonic Diffusers 283

Figures (See p. xvii for list) 287

6. Propulsion Nozzles 307

6.1 Rocket Performance Relations for Ideal Nozzle Flows . . . 307
6.2 Nozzle Efficiency 310
6.2.1 Over-All Efficiency 310
6.2.2 Divergence Factor 313
6.2.3 Viscous Effects 314
6.2.4 Nozzle Throat Correction 318
6.2.5 Flow Separation in Over-Expanded Nozzles 321
6.3 Problems in Expansion Processes 325
6.3.1 Effect of Recombination in Exhaust Gases 325
6.3.1.1 Temperature Measurements 327
6.3.1.2 Acoustic Velocity in Real Gases 328
6.3.2 Gas-Particle Nozzle Flows 329
6.4 Design of Propulsion Nozzles 331
6.4.1 Conical Nozzles 332
6.4.2 Contoured Nozzles 332
6.4.3 Skewed Nozzles 335
6.4.4 Clustered Nozzles 337
6.4.5 Plug Nozzles 339
6.5 Thrust Vector Control 343
6.5.1 Movable Nozzles 343
6 5.2 Deflecting Surfaces 345
6.5.3 Shock-Induced Deflections 346

Figures (See p. xviii for list) 351

References 391

Appendix A 415

Index 419

LIST OF TABLES

Table		Page
2-1	Functions for Use in Turbulent Boundary-Layer Correction. Plane Flow and Axisymmetric Flow ($\gamma = 1.4$; n = 7)	65
3-1	Coefficients in the Equation of the Curved Shock of a Biconic Diffuser	149
3-2	Parameters at Point of Intersection of Curved and Conical Shocks of a Biconic Diffuser	150
4-1	Design of Two-Dimensional, Fixed Mach Number, Supersonic Nozzles. (Analysis of References)	253
4-2	Design of Variable Mach Number Nozzles. (Analysis of References).	255
4-3	Design of Axisymmetric Supersonic Nozzles. (Analysis of References)	256
4-4	Displacement Thickness Ratio and Momentum Thickness Ratio as a Function of Mach Number and Heat Transfer for n = 5, 7, 9, and 11	257

LIST OF FIGURES

Figure		
2-1	Mach numbers upstream and downstream of a temperature discontinuity, $\gamma = 1.4$	71
2-2	Temperature rise through a Chapman-Jouguet detonation as a function of initial Mach number; $\gamma = 1.4$	72
2-3	Initial temperature vs detonation Mach number; $f/a = 0.02, 0.04, 0.06$; $\gamma = 1.4$	73
2-4	Plot of f_1 for $M \leq 0.4$; $C_D = 0$ to 10; and $\gamma = 1.3$ and 1.4 . . .	74
2-5	Plot of f_2 for $M \leq 1.0$ and $\frac{\gamma}{1-K} = 1.0$ to 2.0	75
2-6	Plot of f_3 for $M \leq 1.0$; $K = 0$ to 0.3; and $\gamma = 1.15, 1.25$, and 1.35.	76
2-7	Plot of f_4 for $M \leq 0.5$; $C_D = 0$ to 10; and $\gamma = 1.3$ and 1.4 . . .	77
2-8	Plot of f_5 for $M \leq 0.6$; $C_D = 0$ to 10; and $\gamma = 1.3$ and 1.4 . . .	78

Figure		Page
2-9	Plot of f_5 for $M \leq 0.25$; $C_D = 0$ to 10; and $\gamma = 1.3$	79
2-10	Plot of f_5 for $M \leq 0.25$; $C_D = 0$ to 10; and $\gamma = 1.4$	80
2-11	Plot of f_6 for $M \leq 1.0$; $K \leq 0.3$; and $\gamma = 1.15$, 1.25 and 1.35	81
2-12	Temperature rise vs equivalence ratio for octene-1 and carbon; $T_i = 100$, 500, and 900°F	82
2-13	Temperature rise vs equivalence ratio for pentaborane, hydrogen, and magnesium; $T_i = 100$, 500, and 900°F	83
2-14	Ratio of specific heats vs temperature for octene-1 and carbon; equivalence ratio of 0 to 1.0	84
2-15	Ratio of specific heats vs temperature for hydrogen and pentaborane; equivalence ratio of 0 to 1.0	85
2-16	Ratio of specific heats vs temperature for magnesium; equivalence ratio of 0 to 0.6	86
2-17	Gas constant vs equivalence ratio for five fuels	87
2-18	Mass fraction of unburnt fuel vs equivalence ratio for magnesium and pentaborane	87
2-19	Effect of pressure on the flame temperature of propane; p = 0.1, 1.0, and 5.0 atm	88
2-20	Effect of pressure on the ratio of specific heats of propane-air combustion; p = 0.1, 1.0, and 5.0 atm	89
2-21	Y_o vs M'; parameter δ/r†	90
2-22	Y_1 vs M'; parameter δ/r	91
2-23	Y_2 vs M'; parameter δ/r	92
2-24	Y_3 vs M'; parameter δ/r	93
2-25	$\overline{M}/M'$ vs M'; parameter δ/r	94
2-26	$\overline{V}/V'$ vs M'; parameter δ/r	95
2-27	Average thrust per unit area as a function of M' and δ/r	96
2-28	$\bar{p}_t/p'_t$ vs M'; parameter δ/r†	97

†Parameters shown in Figs. 2-21 through 2-28 are defined in Subsec. 2.1.8.

Figure		Page
2-29	Change in the Riemann variables as a function of the shock Mach number; γ = 5/3, 7/5, and 4/3	98
2-30	Relationship between the shock Mach number and the function K	99
2-31	A parameter, h, as a function of M for use in Eq. 2-173 . . .	100
3-1	Typical flow distortion at diffuser exit; M = 3	151
3-2	Comparison of theoretical and experimental contraction ratio vs Mach number; M_∞ = 1 to 8; γ = 1.4	152
3-3	Comparison of theoretical and experimental total pressure recovery vs Mach number; all internal compression; M_∞ = 1 to 8; γ = 1.4	153
3-4	Theoretical total pressure recovery for a single-cone diffuser vs cone half-angle; M = 1.6, 2, 3, 4, 5, and 6; γ = 1.4 . . .	154
3-5	Maximum total pressure recovery and the cone angle at which it occurs as a function of Mach number (some experimental values); M_∞ = 1 to 6; γ = 1.4	155
3-6	Experimental total pressure recovery vs mass-flow ratio for single-cone inlets operating at design Mach number; M = 1.8, 2.0, 3.85, and 5.4; γ = 1.4	156
3-7	Experimental maximum total pressure recovery vs angle of attack for single-cone inlets; M_∞ = 1.8, 2.0, 3.85, and 5.4; γ = 1.4; α = 0 to 9°.	157
3-8	Effect of spike translation on the additive drag, cowl-pressure drag, and total pressure recovery as a function of mass-flow ratio for single-cone inlets; M_D = 2.0; γ = 1.4; Re/ft = 2.267×10^6.	158
3-9	Experimental total pressure recovery vs mass-flow ratio with and without boundary-layer bleed; M_D = 2.0; α = 0 and 6°; γ = 1.4; Re/ft = 2.267×10^5	159
3-10	Sketches of typical flow conditions with long and short probes on blunt-nosed diffusers; shock detached and swallowed; M = 1.8; γ = 1.4	160
3-11	Comparison of experimental total pressure recovery for two probe diffusers, a single-cone diffuser, and a normal-shock diffuser vs capture-area ratio; M_∞ = 1.8; α = 0°; γ = 1.4	161

Figure		Page
3-12	Comparison of the measured total pressure recovery vs capture-area ratio for a single-cone inlet and two probe diffusers; α = 0, 3, and 6°; M_∞ = 1.8; γ = 1.4	162
3-13	Effect of off-axis probe alignment for two probe diffusers at angle of attack; M_∞ = 1.8; α = 3 and 6°; γ = 1.4	163
3-14	Mach number behind point of shock intersection vs free-stream Mach number for biconic inlets; M_∞ = 2 to 5.6; θ_{S_1} = 20 and 25°; $\theta_{S_1} + \theta_{S_2}$ = 30, 35, 40, and 45°; γ = 1.4	164
3-15	Flow inclination behind point of shock intersection vs free-stream Mach number for biconic inlets; M_∞ = 2 to 5.6; θ_{S_1} = 20 and 25°; $\theta_{S_1} + \theta_{S_2}$ = 30, 35, 40, and 45°; γ = 1.4	165
3-16a	Calculated total pressure recoveries of biconic inlets as a function of cone angles and free-stream Mach number; external and internal compression; M_∞ = 2, 3, 4, and 6; γ = 1.4	166
3-16b	Calculated total pressure recoveries of biconic inlets as a function of cone angles and free-stream Mach number; all external compression; M_∞ = 2, 3, 4, and 6; γ = 1.4	167
3-17	Comparison of calculated and experimental maximum pressure recovery and associated cone half-angles for biconic inlets vs free-stream Mach number; M_∞ = 1 to 6; γ = 1.4	168
3-18	Experimental total pressure recovery vs mass-flow ratio for high- and low-drag cowls; biconic spike; M_∞ = 1.97, 2.44, 2.73, and 3.01; α = 0 and 10°; Re/ft = 2.5×10^6; γ = 1.4	169
3-19	Experimental values of thrust minus drag as a function of free-stream Mach number for high- and low-drag cowls; biconic spikes; γ = 1.4; Re/ft = 2.5×10^6	170
3-20	Critical total pressure recovery and associated supercritical mass-flow ratio as a function of angle of attack for high- and low-drag cowls; biconic spikes; M_∞ = 3.01, 2.73, 2.44, and 1.97; Re/ft = 2.5×10^6	171
3-21	Flow-distortion contours at the diffuser exit for two cowls at M_∞ = 3.01; α = 0 and 10°; γ = 1.4; Re/ft = 2.5×10^6	172
3-22	Measured total pressure recovery vs mass-flow ratio as a function of biconic spike position; $M_\infty = M_D$ = 3.01; γ = 1.4; α = 0°; Re/ft = 2.5×10^6	173
3-23	Off-design performance of translating biconic-spike inlets as a function of free-stream Mach number; γ = 1.4; Re/ft = 2.5×10^6	174

Figure		Page
3-24	Comparison of supercritical external-drag coefficient vs free-stream Mach number for various biconic spikes; $2 \leq M_\infty \leq 3$; Re/ft = 2.5×10^6	175
3-25	Effect of tip roughness and angle of attack on measured total pressure recovery vs mass-flow ratio for biconic inlets; $M_D = M_\infty = 3.85$; $\alpha = 0$, 3, 5.5, and 9°; $\gamma = 1.4$; Re/ft = 1.0×10^6	176
3-26	Calculated total pressure recovery through a conical shock as a function of free-stream Mach number and cone semi-angle; $2 \leq M_\infty \leq 10$; $5° \leq \theta_s \leq 35°$; $\gamma = 1.4$	177
3-27	Theoretical pressure-deflection polars; $\gamma = 1.4$; $M_\infty = 2$, 3, and 4	178
3-28a	Critical regions of shock polars showing compressive reflection waves; $M_\infty = 3$; $\gamma = 1.4$	179
3-28b	Critical regions of shock polars showing expansive reflection waves; $M_\infty = 6$; $\gamma = 1.4$	180
3-29	Limits imposed on flow parameters by the vortex-sheet criterion vs free-stream Mach number; isentropic spike, 15 and 25° tip; $\gamma = 1.4$; $2 \leq M_\infty \leq 8$	181
3-30	Maximum pressure recovery allowed by vortex-sheet criterion as a function of free-stream Mach number; isentropic spike, 15 and 25° tip; $\gamma = 1.4$; $2 \leq M_\infty \leq 8$	182
3-31a	Critical cowl-lip angles determined by vortex-sheet criterion and shock attachment for various free-stream Mach numbers; isentropic spike; M = 2 to 8; $\gamma = 1.4$	183
3-31b	Critical cowl-lip angles determined by vortex-sheet criterion and shock attachment for various free-stream Mach numbers; 15° cone tip; M = 2 to 8; $\gamma = 1.4$	184
3-31c	Critical cowl-lip angles determined by vortex-sheet criterion and shock attachment for various free-stream Mach numbers; 25° cone tip; M = 2 to 8; $\gamma = 1.4$	185
3-32	Maximum and minimum cowl-lip angles determined by vortex-sheet and shock-attachment criteria vs design Mach number; isentropic spike, 15 and 25° tip; $\gamma = 1.4$	186
3-33	Coordinates of isentropic spikes and ramps with 1% pressure loss due to nose shock; $M_D = 2$ to 4; $\gamma = 1.4$	187
3-34a	Surface flow angle vs axial-distance ratio; isentropic axisymmetric spike; $M_D = 2$ to 4; $\gamma = 1.4$	188

Figure		Page
3-34b	Surface Mach number vs axial-distance ratio; isentropic axisymmetric spike; M_D = 2 to 4; γ = 1.4	189
3-35a	Surface flow angle vs axial-distance ratio; isentropic ramp; M_D = 2 to 4; γ = 1.4	190
3-35b	Surface Mach number vs axial-distance ratio; isentropic ramp; M_D = 2 to 4; γ = 1.4	191
3-36	Coordinates of 15° tip isentropic spike; M_D = 2.5 to 6.5; γ = 1.4	192
3-37a	Surface flow angle vs axial-distance ratio; 15° tip isentropic spike; M_D = 2.5 to 6.5; γ = 1.4	193
3-37b	Surface Mach number vs axial-distance ratio; 15° tip isentropic spike; M_D = 2.5 to 6.5; γ = 1.4	194
3-38	Calculated additive-drag coefficient at off-design Mach numbers; cowl lip on design conical shock; 15° tip isentropic spikes; M_D = 3.5 and 5.0; 2.23 ≤ M_∞ ≤ 4.59	195
3-39	Calculated capture-area ratio at off-design Mach numbers; cowl lip on design conical shock; 15° tip isentropic spikes; M_D = 3.5 and 5.0; 2.23 ≤ M_∞ ≤ 4.59	196
3-40	Calculated Mach number at cowl lip at off-design Mach numbers; cowl lip on design conical shock; 15° tip isentropic spikes; M_D = 3.5 and 5.0; 2.23 ≤ M_∞ ≤ 4.59	197
3-41	Calculated flow angle at cowl lip at off-design Mach numbers; cowl lip on design conical shock; 15° tip isentropic spikes; M_D = 3.5 and 5.0; 2.23 ≤ M_∞ ≤ 4.59	198
3-42	Calculated additive-drag coefficient at off-design Mach numbers; cowl lip at constant radial distance; 15° tip isentropic spikes; M_D = 3.5 and 5.0; 2.23 ≤ M_∞ ≤ 4.59	199
3-43	Calculated capture-area ratio at off-design Mach numbers; cowl lip at constant radial distance; 15° tip isentropic spikes; M_D = 3.5 and 5.0; 2.23 ≤ M_∞ ≤ 4.59	200
3-44	Calculated Mach number at cowl lip at off-design Mach numbers; cowl lip at constant radial distance; 15° tip isentropic spikes; M_D = 3.5 and 5.0; 2.23 ≤ M_∞ ≤ 4.59	201
3-45	Calculated flow angle at cowl lip at off-design Mach numbers; cowl lip at constant radial distance; 15° tip isentropic spikes; M_D = 3.5 and 5.0; 2.23 ≤ M_∞ ≤ 4.59	202

Figure		Page
3-46	Calculated total pressure recovery and associated additive-drag coefficient at off-design Mach numbers; $M_D = 3.5$; 15° tip isentropic spikes; $\gamma = 1.4$	203
3-47	Theoretical additive-drag coefficient and capture-area ratio for 15° tip isentropic-spike diffusers at below-design Mach numbers; cowl lip at design focal point; $2.0 \leq M_D \leq 5.0$; $2.25 \leq M_\infty \leq 4.75$	204
3-48	Theoretical additive-drag coefficient and capture-area ratio for 15° tip isentropic-spike diffusers at below-design Mach numbers; cowl lip on design conical shock; $2.0 \leq M_D \leq 5.0$; $2.25 \leq M_\infty \leq 4.75$; radial-distance ratio = 0.98	205
3-49	Theoretical additive-drag coefficient and capture-area ratio for 15° tip isentropic-spike diffusers at below-design Mach numbers; cowl lip on design conical shock; $2.0 \leq M_D \leq 5.0$; $2.25 \leq M_\infty \leq 4.75$; radial-distance ratio = 0.96	206
3-50	Maximum theoretical total pressure recovery vs design Mach number for various basic diffusers; $M_D = 1$ to 8; $\gamma = 1.4$	207
3-51	Effect of tip roughness on total pressure recovery of an isentropic-spike inlet vs mass-flow ratio; $\alpha = 0$ to 9°; $M_\infty = 3.85$; $\gamma = 1.4$; Re/ft = 1.0×10^6	208
3-52	Theoretical total pressure recovery based on limits imposed on compression by the vortex-sheet criterion and shock attachment; isentropic wedge, $\theta_{S_1} = 0$ to 15°; shock attached to horizontal cowl; $M_\infty = 2$ to 8	209
3-53	Theoretical total pressure recovery vs free-stream Mach number for an isentropic-wedge diffuser operating at on-design Mach numbers; $\theta_{S_1} = 0$ to 15°, horizontal cowl; $M_\infty = 1$ to 8	210
3-54	Geometry of two isentropic wedges designed for Mach numbers from 3 to 7; $\gamma = 1.4$	211
3-55	Comparison of critical performance of double-cone diffusers utilizing various types of suction slots for boundary-layer control; $1.9 < M_\infty < 3.1$; Re/ft = 2.5×10^6	212
3-56	Effect of boundary-layer bleed on critical performance of double-cone diffusers at angle of attack; $\alpha = 0$ to 12°; $2.44 \leq M_\infty \leq 3.01$; $\gamma = 1.4$; Re/ft = 2.5×10^6	213
3-57	Effect of ram scoop on net-thrust ratio and cowl-plus-spillage drag coefficient; double-cone diffuser; $1.9 < M_\infty < 3.1$; Re/ft = 2.5×10^6; $\gamma = 1.4$	214

Figure		Page
3-58	Total pressure profile at various axial stations along a dump diffuser; $M_\infty = 3.85$; $Re/ft = 8.6 \times 10^4$	215
3-59a	Effect on total pressure loss of suction in subsonic ducting; suction = 5% of total mass flow; $1.41 < M_s < 1.46$	216
3-59b	Effect on total pressure loss of suction in subsonic ducting; suction = 10% of total mass flow; $1.41 < M_s < 1.46$	217
3-60	Minimum stable mass-flow ratio vs cowling parameter; single-cone diffuser; $M_\infty = 1.90$, 2.46, and 2.70; $\theta_s = 40°$; $2.3 \times 10^7 \leq Re/ft \leq 2.9 \times 10^7$.	218
3-61	Minimum stable mass-flow ratio vs free-stream Mach number; single-cone diffuser; $\theta_s = 27.5$, 30, 35, and 40°; $2.3 \times 10^7 \leq Re/ft \leq 2.9 \times 10^7$.	219
3-62	Frequency of pulsation and slope of diffuser pressure-recovery curve vs mass-flow ratio (experimental and calculated values); single-cone diffusers; $M_\infty = 1.8$ and 1.9	220
3-63	Effect of combustion-chamber volume on frequency of pulsation in various single-cone diffusers (experimental and theoretical values); $V_2 \approx 2.3V_1$; $M_\infty = 2.0$	221
3-64	Effect of dampers on frequency and amplitude of diffuser buzz; single-cone diffuser, $\theta_s = 22.75°$; $M_\infty = 1.73$	222
3-65	Performance of single-cone and step-nose diffusers; $M_D = 2.23$	223
4-1	Position of the sonic line for various values of r_w/r^*; axially-symmetric and two-dimensional nozzles; $\gamma = 1.4$	261
4-2	Mach number distribution in a sonic throat of axially-symmetric and two-dimensional nozzles; $r_w/r^* = 10$; $\gamma = 1.4$	262
4-3	Values of ψ^+, ψ^-, φ, and M as a function of distance from throat	263
4-4	Proposed flexible nozzle and working section for Mach number range of 1.6 to 3.5	264
4-5	Cross sections of a proposed nozzle section for Mach number range of 1.6 to 3.5	265
4-6	Variation of normalized recovery temperature with injection parameter for a water-cooled hypersonic nozzle; air and helium	266

Figure		Page
4-7	Comparison of reflection and displacement thickness ratios vs M for a velocity-profile parameter of 7; $\gamma = 1.4$	267
5-1	Comparison of calculated isentropic efficiency (η_σ) with calculated polytropic efficiency (η_D) for supersonic diffusers; M = 0 to 10; $\gamma = 1.40$.	287
5-2	Calculated and experimental isentropic efficiency of supersonic diffusers with full subsonic recovery as a function of Mach number; $\gamma = 1.4$; M = 1 to 10.	288
5-3	Effect of length of constant-area duct on diffuser efficiency; M = 2	289
5-4	Shock length as a function of Mach number in a constant-area duct	290
5-5	Calculated and experimental contraction ratio of supersonic diffusers as a function of Mach number; $\gamma = 1.4$; M = 1 to 8	291
5-6	Sketches of two-dimensional diffusers for high supersonic Mach number nozzles.	292
5-7	Experimentally determined polytropic efficiency as a function of area ratio for various Mach numbers	293
5-8	Theoretical isentropic efficiency of normal-shock and oblique-shock diffusers with sonic velocity behind the last shock wave and full subsonic recovery.	294
5-9	Experimentally determined effect of an oblique shock on the polytropic efficiency of a variable-geometry diffuser . . .	295
5-10	Layout of supersonic diffuser	296
5-11	Supersonic tunnel incidence gear	297
5-12	Effect of injection and suction on isentropic diffuser efficiency .	298
5-13	Experimentally determined effect of suction on isentropic diffuser efficiency as a function of shock-system length; M = 2	299
5-14	Comparison of theoretical and experimental compression ratios as a function of Mach number	300
5-15	Starting and running compression ratios as a function of contraction ratio for scoop diffusers; M = 2.86	301

Figure		Page
5-16	Theoretical and experimental values of run time as a function of diffuser efficiency; M = 1 to 10; γ = 1.4.	302
5-17	Effect of a model on the isentropic efficiency of variable geometry diffusers; optimum running conditions	303
5-18	Effect of models on starting and running compression ratios for scoop diffusers	304
5-19a	Compression ratio as a function of shock-duct length; α = 2.5°	305
5-19b	Compression ratio as a function of shock-duct length; α = 4°	305
5-19c	Minimum operating compression ratio as a function of convergence angle	305
6-1	Calculated ideal and vacuum thrust coefficients as a function of exit-area ratio; γ = 1.1, 1.2, 1.3, and 1.4	351
6-2	Calculated maximum thrust coefficient as a function of γ	352
6-3	Comparison of calculated and experimentally determined divergence factor in conical nozzles	353
6-4	Calculated performance of conical nozzles as a function of nozzle geometry; γ = 1.23	354
6-5	Calculated exit-area correction factor as a function of exit Mach number; γ = 1.2.	355
6-6	Calculated exit-area correction factor as a function of exit Mach number; γ = 1.3.	356
6-7	Calculated exit-area correction factor as a function of exit Mach number; γ = 1.4.	357
6-8	Calculated stagnation pressure loss due to friction as a function of exit Mach number; γ = 1.2	358
6-9	Calculated stagnation pressure loss due to friction as a function of exit Mach number; γ = 1.3	359
6-10	Calculated stagnation pressure loss due to friction as a function of exit Mach number; γ = 1.4	360
6-11	Nomograph for coefficients of friction and heat transfer of a turbulent boundary layer on a flat plate for air	361
6-12	Velocity boundary-layer thickness for nozzle shown on Fig. 6-15	362

Figure		Page
6-13	Momentum boundary-layer thickness for nozzle shown on Fig. 6-15	362
6-14	Displacement thickness for given nozzle	363
6-15	Heat-transfer coefficient for given nozzle	363
6-16	Calculated throat mass-flow correction factor as a function of throat radius and wall radius of curvature	364
6-17	Calculated non-isentropic throat Mach number as a function of nozzle efficiency; γ = 1.00, 1.20, 1.23, 1.40, and 1.67	365
6-18	Comparison of theoretical and experimental values of separation pressure ratio (p_s/p_c) vs nozzle pressure ratio (p_∞/p_c) for conical nozzles	366
6-19	Pressure ratios and related cone angles as a function of separation Mach number; separated turbulent boundary layer in conical nozzles; γ = 1.2 and 1.4	367
6-20	Comparison of theoretical and experimental values of separation pressure ratio (p_s/p_∞) vs nozzle pressure ratio (p_c/p_∞) for conical nozzles	368
6-21	Calculated thrust of 15° nozzle vs compression ratio; A_e/A^* = 6 and 25; γ = 1.20 and 1.26	369
6-22	Calculated exit Mach number and specific impulse as a function of expansion ratio for frozen and equilibrium composition	370
6-23	Static temperature as a function of nozzle length; frozen and equilibrium flow; p_c = 0.1 and 100 atmospheres	371
6-24	Comparison of theoretical and experimental gas temperatures at nozzle exit	371
6-25	Calculated relation between gas velocity and acoustic velocity for combustion products	372
6-26	Calculated net thrust coefficient of conical nozzles in terms of divergence angle, α, and expansion ratio; γ = 1.26	373
6-27	Chart for finding the angle at point of inflection of the contour in terms of exit radius and nozzle length; γ = 1.23	374
6-28	Chart for finding contour exit angle in terms of exit radius and nozzle length; γ = 1.23	375

Figure		Page
6-29	Stream-thrust coefficient vs nozzle pressure ratio for three oblique nozzles with nozzle flow at $M_e = 2$; $M_\infty = 0$, 1.69, 2.94, and 3.87; $\gamma = 1.4$	376
6-30	Stream-thrust coefficient vs nozzle pressure ratio for a half-contoured nozzle with nozzle flow at $M_e = 1$, 2, and 3; $M_\infty = 0$, 1.69, 2.94, and 3.87; $\gamma = 1.4$	377
6-31	Regions of exhaust patterns for four-nozzle cluster as a function of rocket chamber pressure; $\gamma = 1.20$, $\alpha = 15°$; $d_c/d_e = 2.4$; $A_e/A^* = 10$; $A_V/A_R = 0.50$	378
6-32	Regions of exhaust patterns for four-nozzle cluster as a function of nozzle exit angle; $p_c = 500$ psi; $\gamma = 1.20$; $d_c/d_e = 2.4$; $A_e/A^* = 10$; $A_V/A_R = 0.50$	378
6-33	Regions of exhaust patterns for four-nozzle cluster as a function of nozzle area ratio; $p_c = 500$ psi, $\gamma = 1.20$; $\alpha = 15°$, $d_c/d_e = 2.4$; $A_V/A_R = 0.50$	379
6-34	Regions of exhaust patterns for four-nozzle cluster as a function of rocket spacing; $A_e/A^* = 10$; $\alpha = 15°$; $\gamma = 1.20$; $p_c = 500$ psi, $A_V/A_R = 0.50$	379
6-35	Base thrust increment for four-nozzle cluster in vacuum as a function of nozzle area ratio and rocket spacing	380
6-36	Base thrust increment for four-nozzle cluster in vacuum as a function of base vent area and nozzle exit angle	381
6-37	Shroud-thrust increment for four-nozzle cluster as a function of nozzle area ratio and rocket spacing (in vacuum); $\gamma = 1.20$; $\alpha = 15°$	382
6-38	Comparison of theoretical and experimental performances of plug and conventional nozzles; $\gamma = 1.4$	382
6-39	Profiles obtained by shortening an isentropic plug using tangent cones	383
6-40	Theoretical loss in performance caused by shortening an isentropic plug; $\gamma = 1.26$; $p_c/p_\infty = 61.5$	383
6-41	Radial length vs contour angle for a plug nozzle; $\gamma = 1.17$; $A_e/A^* = 5$, 10, 15, 20, and 25	384
6-42	Specific impulse vs area ratio for a two-dimensional plug nozzle; $M_\infty = 7$, $\eta_D = 0.1$, ER = 0.5	385

Figure		Page
6-43	Thrust and lift coefficients as a function of area ratio for a two-dimensional plug nozzle; $M_\infty = 7$; $\eta_D = 0.1$; ER = 0.5	386
6-44	Variation in I with C_F and nozzle efficiency for a two-dimensional plug nozzle; $M_\infty = 7$; $A_e/A_i = 1.0$	387
6-45	Specific impulse as a function of jet stagnation pressure for various injectants	388
6-46	Specific impulse ratio as a function of injectant weight-flow ratio; M = 1.86; H_2/O_2 propellant; $\ell = 0.50$ in.; $d_i = 0.0625$ in.	389

Intentionally Blank

SYMBOLS

Only those symbols which are frequently used are defined here; all others are defined where they are used.

A	cross-sectional area
a	local velocity of sound
C_{AD}	additive drag coefficient
C_D	supercritical external drag coefficient; drag coefficient
C_{DC}	cowl-drag coefficient
C_F	thrust coefficient
C_{FG}	gross thrust coefficient
C_f	skin-friction coefficient
C*	characteristic velocity
C-J	Chapman-Jouguet condition
c_p	specific heat at constant pressure
c_v	specific heat at constant volume
D	drag; flow distortion parameter; diffuser characteristic slope
D_A	additive drag
D_C	cowl drag
d	diameter
ER	equivalence ratio = $(f/a)_{actual}/(f/a)_{stoich}$
F	thrust; force
F_G	gross thrust
F_N	net thrust = F_G - D
f	force per unit mass; frequency of pulsation, cps
f/a	fuel-air ratio
g	acceleration due to gravity

h	height; enthalpy; heat-transfer coefficient
I	thrust specific impulse or fuel specific impulse
K	mass-fraction of unburnt fuel
L	lift
ℓ	length
ℓ_s	length of shock system
ℓ^*	characteristic length
M	Mach number = V/a
M_{CL}	Mach number at cowl lip
M_D	design Mach number; detonation Mach number
M_s	shock Mach number; separation Mach number
m	mass; mass flow
P	Riemann variable = $\frac{2}{\gamma-1}$ a + u
Pr	Prandtl number
p	pressure
Q	Riemann variable = $\frac{2}{\gamma-1}$ a - u; quantity of heat transferred
q	quantity of heat added per unit mass and unit time
R	universal gas constant = 1715 $ft^2/sec^2°F$
Re	Reynolds number = $\frac{V \rho \ell}{\mu}$
r	radius of curvature
s	specific entropy
T	temperature
T_{aw}	adiabatic wall temperature
t	time
U	axial component of velocity
V	radial component of velocity; volume; velocity
W	molecular weight

x	axial distance
y	injectant velocity ratio; radial distance
Z	impedance
α	angle of attack; divergence angle; flow acceleration along nozzle axis
γ	ratio of specific heats = c_p/c_v
δ	boundary-layer thickness; cowl lip angle
δ^*	boundary-layer displacement thickness
δ_e	external cowl lip angle
δ_i	internal cowl lip angle
η	efficiency
η_d	discharge correction factor
η_D	polytropic diffuser efficiency
η_{KE}	kinetic energy efficiency
η_V	velocity coefficient
η_σ	isentropic diffuser efficiency
η^*	throat efficiency factor
θ	boundary-layer momentum thickness; slope
θ_ℓ	cowling parameter
θ_s	cone semi-angle
θ_w	shock-wave angle
λ	boundary-layer reflection thickness; divergence factor
μ	coefficient of viscosity; Mach angle
ρ	density
τ	local viscous stress; time
φ	flow angle; energy boundary-layer thickness
φ_{CL}	flow angle at cowl lip

Subscripts

o, 1, 2, . . .	designated stations
∞	free-stream
c	combustion chamber
e	exit station
g	gas
i	inlet; injectant
p	particle
s	innerbody surface; shock; separation
t	stagnation or total; throat
w	wall

Superscripts

*	sonic or critical conditions
–	average value of parameter

DUCTS, NOZZLES AND DIFFUSERS

1. Introduction

A duct is commonly used for two functions: either to conduct a fluid from one point to another, as in heating and ventilating systems, or to produce some desired change in the properties of the fluid, as in a wind tunnel. These separate functions are sometimes combined in such applications as the air intake of an aircraft propulsion system.

When applied to the simple transfer of a fluid, duct theory is concerned chiefly with methods of assessing the penalties incurred in fluid transfer (i.e., viscous and heat-transfer effects) and the means for minimizing these penalties by using such devices as turning vanes and heat insulators. The field of fluid transfer is relatively simple, well-developed, and adequately documented in engineering texts and handbooks. In this Handbook section, therefore, fluid transfer as such is treated only briefly and in close association with the more complex problems of the flow properties in a duct system.

For practical purposes the use of ducts to control flow properties is limited to propulsion devices, flow generators for experimental work (such as wind tunnels and shock tubes), and various components for these systems.

1.1 Scope or Contents

This Handbook section presents the basic techniques and related information needed for the control of duct flow in high-speed propulsion devices and in supersonic and hypersonic wind tunnels. No discussion of shock tubes is included since they have been treated fully in Section 18. The design of the complete wind tunnel system will be given in Section 19 of the Handbook.

The general mechanical and thermodynamic theory of steady flow in a duct is simplified as much as possible and is concisely reviewed. The effects of many flow parameters are analyzed by considering simple one-dimensional flows in which all but one of the independent variables are held constant. Although such assumptions are somewhat restrictive, it has been shown that their use in many practical problems provides reasonably accurate results.

Non-steady, one-dimensional flows are discussed next and methods of solution for a great number of practical problems are outlined. Two- and three-dimensional flows are touched upon briefly. Generalized techniques are presented for the inclusion of viscous and heat-transfer effects by means of which boundary-layer correction may be made to profiles designed for potential flow.

The general solutions of duct flow are subsequently applied to specific problems concerning the air intakes of jet engines, various propulsion nozzles, as well as nozzles and diffusers for typical supersonic and hypersonic wind tunnels. The performance characteristics and efficiency factors associated with these systems are included in the discussion and are amply supplemented by experimental data. Also presented are many practical geometric modifications and design techniques.

It is intended that this volume may give a reasonably comprehensive, and yet at the same time, a concise outline of each phase of the subject, from simple definitions to the current research of the specialist in each area. The conciseness has been achieved by omitting those theoretical developments which are readily available in textbooks and by bearing heavily on reference material. In this way the reader is not only given an insight into the present state-of-the-art but is also directed to the individuals and organizations currently working on the specialized problem in which he may be interested.

2. Duct Flow Theory

The theories of internal aerodynamics have been applied to the solution of many practical problems which involve neither separated flow nor wake effects. Experimental data have been utilized to supplement existing theory and to establish empirical equations for channel flows with heat addition and in the presence of viscous effects and flow separation. Simple duct flow theory has been used extensively to compile working charts and tables.

The material presented in this subsection is arranged in the order of increasing complexity. One-dimensional steady flow is treated first, one-dimensional transient flow is discussed next, and the theory of two-dimensional steady supersonic flow is presented last. The only theoretical developments to be included are those not readily available either in aerodynamic textbooks or scientific journals.

2.1 One-Dimensional Steady Flow

The fundamental differential equations of compressible flow have been derived in Section 2 of the Handbook (Ref. 1), and expressed in Cartesian, cylindrical, and spherical coordinates. Nearly a hundred valuable relations connecting the flow parameters have been obtained by using one or more of a number of simplifying assumptions. These are listed in Section 2, and many of the relevant ones will be repeated as the present section progresses.

In Section 4 (Ref. 1), general equations for one-dimensional flow have been derived. These include the effects of a continuous variation of molecular weight and specific heat, as well as heat and mass addition, change of state, and the presence of drag and frictional forces. Tables of Influence Coefficients are included to assist in the numerical integration of the equations and enable one to proceed from a known set of conditions to an unknown set. Since one-dimensional flow assumes constant properties across any section perpendicular to the flow direction, it is only an approximation to realistic flow in which viscous effects produce velocity gradients normal to the surface. It has, however, been shown experimentally that the equations of one-dimensional flow introduce no significant errors into many practical problems. The specific conditions under which the errors are negligible are listed in Section 4, Subsec. 2 (Ref. 1). Methods have been developed by means of which the isentropic flow equations may be corrected to include viscous effects (Subsec. 2.4) and to account for the presence of normal and oblique shocks (Subsec. 2.1.6).

After the basic characteristics of the flow patterns described by the general equations of Section 4 have been outlined, the equations are simplified by the introduction of constant values for the molecular weight and the specific heat. When all independent variables but one are held constant, simple types of flow may be analyzed.

2.1.1 Area Variation

A useful model of simple isentropic flow for most practical problems is that in which only the duct cross-sectional area varies. Although such flow is discussed fully in Section 4, many of the basic equations are repeated

in this section where they will be used frequently.

The most fruitful are the relationships between the flow properties at any cross section and those in either the stilling chamber or the throat. In the stagnation or stilling chamber, the velocity is assumed to be zero and the gas properties are designated by subscript t. In the throat the velocity is assumed to be equal to the local speed of sound and the gas properties are designated by an asterisk. The most useful forms of these relationships are:

$$\frac{T}{T_t} = \left(1 + \frac{\gamma - 1}{2} M^2\right)^{-1} \tag{2-1}$$

$$\frac{p}{p_t} = \left(1 + \frac{\gamma - 1}{2} M^2\right)^{\frac{-\gamma}{\gamma-1}} \tag{2-2}$$

$$\frac{\rho}{\rho_t} = \left(1 + \frac{\gamma - 1}{2} M^2\right)^{\frac{-1}{\gamma-1}} \tag{2-3}$$

and

$$\left(\frac{A}{A^*}\right)^2 = \frac{1}{M^2}\left[\frac{2}{\gamma + 1}\left(1 + \frac{\gamma - 1}{2} M^2\right)\right]^{\frac{\gamma+1}{\gamma-1}} \tag{2-4}$$

Properties without any subscripts are free-stream (static) values and often carry the subscript ∞ to distinguish them from local properties.

Another relationship much used in the analysis of duct flows is

$$m = \rho VA = Ap\mathring{m}\left[T_t\right]^{-1/2} \tag{2-5}$$

where

$$\mathring{m} = g(\gamma/R)^{1/2} M\left(1 + \frac{\gamma - 1}{2} M^2\right)^{1/2} \tag{2-6}$$

Tabulations and graphs of the variables of Eqs. 2-1 to 2-6 are to be found in Refs. 1 and 21 to 34. The range and frequency of the dependent variables in the referenced tables are listed in Appendix A. Shorter forms of isentropic flow tables are found in many textbooks.

The effect of the viscous forces (neglected in the above equations) may be accounted for by means of the boundary-layer corrections which are discussed in Subsec. 2.4. Discontinuous entropy changes may be included by use of normal-shock theory.

For non-isentropic or non-adiabatic flows, Eq. 2-4 can be generalized the same way as Eqs. 2-1, 2-2, and 2-3 by introducing the concept of

local stagnation and sonic conditions. The local stagnation pressure is defined as that which would be attained if the local flow were brought isentropically to rest; the local sonic throat is the area which the local stream tube would have if the flow were conducted isentropically to a sonic speed. In adiabatic dissipative flows, it can be shown that for two stations, 1 and 2, in the same channel

$$\frac{A^*_2}{A^*_1} = \frac{p_{t_1}}{p_{t_2}} \tag{2-7}$$

i.e., the local sonic area for this case is defined in terms of the local stagnation pressure.

2.1.2 Temperature Variation

The continuous change of temperature in a constant-area duct is treated fully in Section 4, Subsec. 5g (Ref. 1). From the differential equations given therein, the following useful equations are derived:

$$\frac{T_t}{T^*_t} = \frac{2(\gamma + 1)\ M^2 \left(1 + \frac{\gamma - 1}{2} M^2\right)}{(1 + \gamma M^2)^2} \tag{2-8}$$

$$\frac{V}{V^*} = \frac{(\gamma + 1)\ M^2}{1 + \gamma M^2} \tag{2-9}$$

$$\frac{p_t}{p^*_t} = \frac{\gamma + 1}{1 + \gamma M^2} \left[\frac{2\left(1 + \frac{\gamma - 1}{2} M^2\right)}{\gamma + 1}\right]^{\frac{\gamma}{\gamma - 1}} \tag{2-10}$$

and

$$\frac{T}{T^*} = \frac{(\gamma + 1)^2\ M^2}{(1 + \gamma M^2)^2} \tag{2-11}$$

where the starred symbols, as usual, represent a condition in the uniform duct where the flow is sonic. Values of T_t/T^*_t, T/T^*, p_t/p^*_t, p/p^*, and V/V^* are tabulated in Refs. 1 and 29 for a wide range of values of M and γ (see Appendix A).

The above equations and the tables derived from them may be used to compare the flow properties at any two stations, 1 and 2, along the duct. One such comparison is shown in Fig. 2-1 where the relationship between M_1 and M_2 for various values of the ratio T_{t_2}/T_{t_1} is plotted. From this graph it may be seen that for each value of M_1 there are two theoretical values of M_2, the physical meaning of which will be discussed later.

Although the assumption of a continuously changing temperature lends itself to analytical treatment it has limited practical application. It may, for instance, be used where the working fluid of a wind tunnel is heated by means of radiation either from the tunnel walls or from a heater inserted in the flow. In ramjets and most wind tunnels, the heat addition is not continuous

along the duct but takes place within a finite length. Furthermore, in the ramjet, heat addition is associated with mass addition and changes in the thermodynamic properties. However, an adequate theory for a simple discontinuous heat addition may be developed by assuming that the heat is added instantaneously at some station along the duct, or else that it is added continuously between two stations of equal area in a channel whose area is varying slowly.

Whenever the station at which heat addition begins is equal in area to the station at which heat addition terminates, the flow characteristics before and after heat addition are independent of the channel configuration between the two stations. The relationship between the Mach numbers at the two stations is thus also represented by the curves of Fig. 2-1. In simple subsonic combustion or deflagration, i.e., $M_1 < 1$ and $T_{t_2} > T_{t_1}$, the value of M_2 is always subsonic but greater than M_1. When M_2 reaches the sonic value, the flow is choked and the mass flow reduced to a level at which it can support the given temperature rise, and hence in Fig. 2-1 the curves extending beyond $M_2 = 1$ are imaginary. Heat addition in supersonic flow may be accompanied either by a weak detonation (solid lines) or a strong detonation (dashed lines). In the first case, the flow downstream of the heat addition is supersonic; in the second, the downstream flow is subsonic.

The strong detonation apparently combines the effects of combustion with those of a normal shock. Considering any two points such as A and B for which both M_1 and T_{t_2}/T_{t_1} are the same, it will be seen that the subsonic Mach number, M_B, is always that which would occur downstream of a normal shock at the supersonic Mach number, M_A, showing that a strong detonation has the same effect on the Mach number as a thermal discontinuity followed by an adiabatic normal shock. The maximum temperature rise that can be sustained in a flow is that which produces a downstream sonic flow. Such a detonation is known as a Chapman-Jouguet detonation. Typical C-J points are noted on Fig. 2-1.

The value of the temperature rise at the C-J point has been plotted against M_1 in Fig. 2-2. By comparison with Fig. 2-1 it may be seen that in Fig. 2-2 the supersonic Mach numbers, M_1, are the minimum values that will support the given temperature rise, whereas the subsonic values are maximum ones.

The phenomenon of detonation was observed independently by Chapman (Ref. 45) and Jouguet (Ref. 46) while measuring the rate of propagation of a deflagration flame front in a coiled glass tube filled with hydrogen and oxygen. Under certain conditions the rate was observed to increase suddenly by several orders of magnitude. Since this early work, extensive measurements have been made of detonation wave velocity in various gas mixtures using the shock-tube technique (e.g., Ref. 47), and numerous calculations have also been made, the most recent and extensive being those of Eisen, Gross, and Rivlin (Ref. 48). An excellent summary of the recent work in gaseous detonation is presented in Ref. 49 which also includes an extensive bibliography.

Zeleznik and Gordon in Ref. 50 present a general iterative method by which detonation parameters may be obtained for any chemical reactants. A

procedure is also described for obtaining initial estimates of the detonation temperature and pressure. Results of calculations for a hydrogen-oxygen system show:

1) Increasing the initial pressure increases the detonation velocity, pressure ratio, and temperature ratio.

2) Increasing the initial temperature decreases the detonation velocity, pressure ratio, and temperature ratio, and

3) Increasing the initial enthalpy increases the detonation velocity, pressure ratio, and temperature ratio.

Although the detailed chemical kinetics of detonation are obscure the macroscopic phenomenon is easy to picture. In normal deflagration, heat addition is accompanied by a slight pressure drop. Disturbances superimposed on the steady phenomenon result in a divergent coupling of pressure rise, which climaxes in detonation.

From an intuitive standpoint, the downstream sonic condition seems reasonable. If the flow were locally subsonic the pressure-combustion coupling mechanism which initiated detonation would continue to communicate through the subsonic flow to the shock wave and generate an increased pressure rise. If the flow were supersonic the combustion zone would be isolated from the wave front and would be attenuated to the C-J condition.

It may also be seen from Fig. 2-1 that increasing the value of T_{t_2}/T_{t_1} increases the Mach number at which detonation occurs. The temperature rise may be expressed by

$$T_{t_2}/T_{t_1} = 1 + \frac{Q}{c_p T_{t_1}} \qquad (2\text{-}12)$$

where Q is the heat addition.

From Eq. 2-12 it follows that the detonation Mach number must increase as the ratio of combustion heat release to the initial stagnation enthalpy increases. For example, the detonation Mach number in a fuel-air mixture of constant ratio must increase as the initial temperature of the mixture decreases; for a mixture at a constant temperature the detonation Mach number must increase with increasing fuel-air ratio.

It is sometimes helpful to express the dependence of the detonation Mach number on the initial static temperature and fuel-air ratio. The nomenclature is shown by the sketch below.

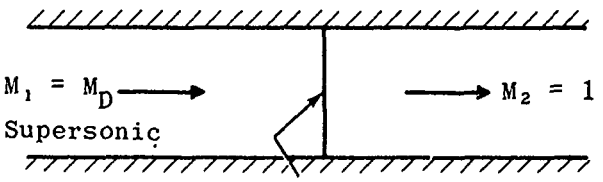

C-J Detonation

From Eq. 2-11 one may easily obtain

$$\frac{1 + \gamma M_D^2}{M_D} = (1 + \gamma) \sqrt{T_2/T_1} \qquad (2\text{-}13)$$

Combining Eqs. 2-1, 2-12, and 2-13 one obtains the following expression relating detonation Mach number and upstream temperature:

$$T_1 = \frac{Q/c_p}{\frac{(1 + \gamma M_D^2)^2}{2(\gamma + 1) M_D^2} - \left(1 + \frac{\gamma - 1}{2} M_D^2\right)} \qquad (2\text{-}14)$$

As an illustrative example, consider a hydrocarbon fuel having a heat release of 18,000 BTU/lb. Thus,

$$\frac{Q}{c_p} = \frac{18{,}000 \ f/a}{0.24 \ (1 + f/a)} = \frac{7.5 \times 10^4 \ f/a}{1 + f/a}$$

where

$c_p = 0.24$ BTU/lb°F

f/a = fuel-air ratio.

A plot of Eq. 2-14 using this value of Q is shown in Fig. 2-3 for $f/a = 0.02$, 0.04, and 0.06, and $\gamma = 1.4$. It is seen that the upstream temperature required for detonation increases rapidly with decreasing Mach number in the low supersonic regime but more gradually as the Mach number increases. The temperature at any Mach number is approximately proportional to f/a when f/a is small compared to unity. Although this analysis neglects real-gas effects and therefore is oversimplified, it nevertheless serves to demonstrate the principal features of C-J detonation. For more precise calculations see Ref. 48, and for experimental data see Ref. 47.

2.1.3 Heat and Mass Addition

In the preceding subsection the temperature was assumed to vary without the addition of fuel and without any subsequent effect on the chemical properties of the gas. The more realistic case of both heat and mass addition within a limited region of a constant-area duct is analyzed in Section 4, Subsec. 6 (Ref. 1). Several simplifications are made to the general equations. It is assumed that all changes take place between control stations which are of equal cross section. It is also assumed that the specific heat, c_p, of the initial fluid does not vary with temperature but is dependent only upon the chemical composition. Errors may be minimized by choosing c_p at a mean flow temperature.

In the sketch below, the equal-area control stations are designated as 1 and 2.

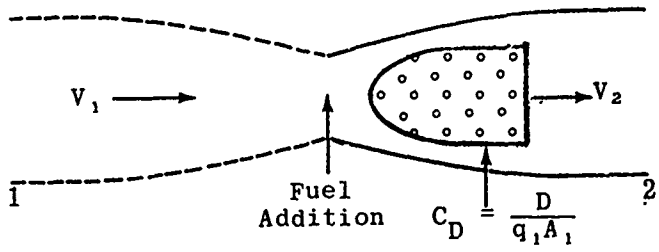

The added fuel may be partly gaseous and partly liquid and may be injected at a velocity different from that of the initial stream. The following summary equations are taken from Ref. 1.

$$\frac{p_2}{p_1} = \frac{1 + \left[1 + \left(\frac{m_2}{m_1} - 1\right) y - \frac{C_D}{2}\right] \gamma_1 M_1^2}{1 + \gamma_2 M_2^2} \tag{2-15}$$

$$\frac{p_{t_2}}{p_{t_1}} = \frac{p_2}{p_1} \cdot \frac{\left[1 + \frac{\gamma_2 - 1}{2} M_2^2\right]^{\gamma_2/(\gamma_2-1)}}{\left[1 + \frac{\gamma_1 - 1}{2} M_1^2\right]^{\gamma_1/(\gamma_1-1)}} \tag{2-16}$$

$$\frac{T_{t_2}}{T_{t_1}} = \frac{\gamma_2 M_2^2}{\gamma_1 M_1^2} \cdot (p_2/p_1)^2 \cdot \frac{\left(1 + \frac{\gamma_2 - 1}{2} M_2^2\right)}{\left(1 + \frac{\gamma_1 - 1}{2} M_1^2\right)} \left(\frac{W_2}{W_1}\right) \left(\frac{m_1}{m_2}\right)^2 \tag{2-17}$$

where

W = molecular weight

C_D = drag coefficient (based on cross section of the duct) of bodies immersed in the flow

m = mass flow rate

$m_2 = m_1 + \overbrace{m_{gas} + m_{liq}}^{\text{fuel}}$

y = velocity ratio of injected fuel to primary stream (V_1)

$= \frac{V_g m_g + V_\ell m_\ell}{V_1 (m_g + m_\ell)}$ (V = streamwise component of velocity).

The quantities relating M and γ which appear in Eqs. 2-15 to 2-17 may be found in Ref. 1 for γ = 1.0, 1.1, 1.2, 1.4, and 1.67. Many calculations have been made for the special cases of y = 0 and y = 1, i.e., where the fuel is injected with zero velocity and where its forward velocity is equal to that of the primary stream. Tabulated values are given in Refs. 31 and 32 (see Appendix A).

Equations 2-15 to 2-17 assume that the flow downstream of Station 2 is homogeneous. A further parameter, K, may be introduced to represent the mass-fraction of the total exhaust products which are non-gaseous, but which move with the same velocity as the exhaust gases and have the same temperature. For the case of fuel addition (zero momentum) Eq. 2-15 becomes

$$\frac{p_2}{p_1} = \frac{1 + \left(1 - \frac{C_D}{2}\right) \gamma_1 M_1^2}{1 + \frac{\gamma_2}{1 - K} M_2^2} = \frac{f_1(M, \gamma, C_D)}{f_2(M, \gamma, K)} \qquad (2\text{-}18)$$

where

$$f_1(M, \gamma, C_D) = 1 + \left(1 - \frac{C_D}{2}\right) \gamma M^2$$

and

$$f_2(M, \gamma, K) = 1 + \frac{\gamma}{1 - K} M^2$$

Equation 2-16 becomes

$$p_{t_2}/p_{t_1} = p_2/p_1 \cdot \frac{\left(1 + \frac{\gamma_2 - 1}{2} M_2^2\right)^{\gamma_2/(\gamma_2 - 1)}}{\left(1 + \frac{\gamma_1 - 1}{2} M_1^2\right)^{\gamma_1/(\gamma_1 - 1)}} \qquad (2\text{-}19)$$

or

$$p_{t_2}/p_{t_1} = \frac{f_3(M, \gamma, K)}{f_4(M, \gamma, C_D)}$$

where

$$f_3(M, \gamma, K) = \frac{\left(1 + \frac{\gamma - 1}{2} M^2\right)^{\gamma/(\gamma - 1)}}{1 + \frac{\gamma}{1 - K} M^2}$$

and

$$f_4(M, \gamma, C_D) = \frac{\left(1 + \frac{\gamma - 1}{2} M^2\right)^{\gamma/(\gamma - 1)}}{1 + \left(1 - \frac{C_D}{2}\right) \gamma M^2}$$

Equation 2-17 becomes

$$T_{t_2}/T_{t_1} = \frac{\gamma_2 M_2^2}{\gamma_1 M_1^2} \cdot (p_2/p_1)^2 \frac{\left(1 + \frac{\gamma_2 - 1}{2} M_2^2\right)}{\left(1 + \frac{\gamma_1 - 1}{2} M_1^2\right)} \cdot \frac{W_2}{W_1} \frac{(1 - K)^{-2}}{(1 + f/a)^2} \qquad (2\text{-}20)$$

where

f/a = fuel-air ratio = $\frac{m_2 - m_1}{m_1}$ in previous notation.

Equation 2-20 may be rewritten as:

$$(1 + f/a) \left(W_1/W_2 \cdot T_{t_2}/T_{t_1}\right)^{1/2} f_5(M, \gamma, C_D) = f_6(M, \gamma, K)$$

where

$$f_5(M,\ \gamma,\ C_D) = \frac{\sqrt{\gamma}\ M\left(1 + \frac{\gamma - 1}{2}\ M^2\right)^{1/2}}{1 + \left(1 - \frac{C_D}{2}\right)\gamma\ M^2}$$

and

$$f_6(M,\ \gamma,\ K) = \frac{\sqrt{\gamma}\ M\left(1 + \frac{\gamma - 1}{2}\ M^2\right)^{1/2}}{1 - K + \gamma\ M^2}$$

The functions f_1, f_2, f_3, f_4, f_5, and f_6 are presented in Figs. 2-4 to 2-11. The solution of Eqs. 2-18 to 2-20 require that the following be known:

1. The characteristics of gas entering Station 1, i.e., M, T, γ, and R. These are assumed to be known functions of the channel geometry, stagnation conditions and the gas employed (usually air).

2. The characteristics of the exhaust gases, T, γ, and R at Station 2. These are given in Figs. 2-12 through 2-17 as a function of inlet temperature, T, and the equivalence ratio, ER. The equivalence ratio is the ratio between the actual value of the fuel-air ratio, $(f/a)_{actual}$, and the stoichiometric value, $(f/a)_{stoich}$†. The inlet temperatures shown in Figs. 2-12 to 2-17 are static temperatures as used in Eqs. 2-13 and 2-14. However, since combustion usually takes place at low flow velocity, there is very little difference between the inlet stagnation temperature required in Eq. 2-20 and the inlet static temperature.

3. The mass fraction, K, of unburnt fuel in liquid or solid form in the exhaust gases. This is shown as a function of the equivalence ratio in Fig. 2-18. Values of ER have to be assumed at this time.

Figures 2-12 to 2-18 were prepared from data taken from Refs. 39, 51, and 52.

In the above discussion it was assumed that the relationships between the flame temperature, the ratio of specific heats, and the equivalence ratio are independent of pressure. Figures 2-19 and 2-20 (derived from Ref. 53) show the variation of flame temperature and of γ with ER at pressures of 0.1, 1, and 5 atm and thus indicate the extent of error incurred by assuming that these parameters are independent of pressure. For propane gas with an inlet temperature of 540°R the maximum variation (at ER = 1) of the ratio of the specific heats is about 0.4%; for the flame temperature the maximum variation is 5% in the pressure range of 0.1 to 5 atm Except for the values in the region of ER = 1.0 the effect is negligible.

†Ratio giving complete oxidation and reduction.

2.1.4 Steadily Moving Temperature Discontinuities

In the preceding subsections it has been assumed that the heat and mass additions take place between two fixed stations in a duct. The problem of a flame front (or pressure wave) which moves at a uniform rate is analyzed and discussed in Section 4, Subsecs. 6 and 7 (Ref. 1).

2.1.5 Heat Addition in a Channel of Varying Area

The case of heat addition between unequal areas may be treated by assuming that the upstream flow passes a fictitious station having the same area as the exit station. To determine the flow characteristics after heat addition, the momentum equation is applied between the fictitious station and the actual exit station. The flow conditions at the fictitious station and the drag force between the fictitious and actual inlet stations, which must be included in the total drag, are obtained from the isentropic flow equations.

Waiter (Ref. 54) has analyzed the flow properties of heat addition in a supersonic nozzle as illustrated below.

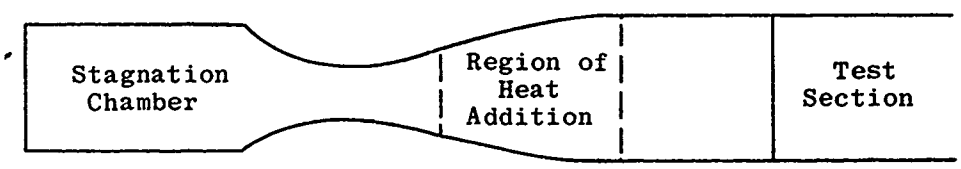

His technique employs a Mollier diagram of the working gas and is based on the assumptions of the one-dimensional steady frictionless flow of a gas which is always in thermodynamic equilibrium. The heat source input is constant with time and with distance along the nozzle axis. In addition to heating in a constant-area section (as in Subsecs. 2.1.2 and 2.1.3), Waiter considered constant Mach number and constant-pressure regimes. These three correspond to decelerating, accelerating, and constant-speed flow. His solutions were obtained for a test section of $M = 15.65$, $p_t = 100$ atm, and $T_{t_1} = 2000°K$, but the method may be applied directly for other flow parameters with nitrogen as the working fluid and easily modified for any other gas whose thermodynamic properties are known.

2.1.6 Adiabatic Normal Shock

Equations 2-15 to 2-17 may be much simplified for the case of an adiabatic normal shock, i.e., one in which T_t, W, m, and γ are not changed through the shock, and $C_D = 0$. The most useful forms of the shock equations, derived from the above considerations, are as follows:

$$M_2^2 = \frac{1 + \frac{\gamma - 1}{2} M_1^2}{\gamma M_1^2 - \frac{\gamma - 1}{2}} \qquad (2\text{-}21)$$

$$\frac{p_2}{p_1} = \frac{2\gamma}{\gamma + 1} M_1^2 - \frac{\gamma - 1}{\gamma + 1} \tag{2-22}$$

$$\frac{p_2 - p_1}{p_1} = \frac{2\gamma}{\gamma + 1} (M_1^2 - 1) \tag{2-23}$$

$$\frac{p_{t_1}}{p_{t_2}} = \left[\frac{2\gamma}{\gamma + 1} M_1^2 - \frac{\gamma - 1}{\gamma + 1}\right]^{\frac{1}{\gamma-1}} \left[\frac{(\gamma - 1) M_1^2 + 2}{(\gamma + 1) M_1^2}\right]^{\frac{\gamma}{\gamma-1}} \tag{2-24}$$

Tables of normal-shock relations are found in Refs. 1, 21, 22, 25, and 27, and the data are shown graphically in Ref. 23 (see Appendix A).

2.1.7 Hypersonic and High-Temperature Flows in Ducts

The above treatment of one-dimensional theory for adiabatic and non-adiabatic flows is limited to the range of temperature within which the assumption of a perfect gas is not violated, i.e., the gas obeys the thermal equation of state, $p = \rho RT$, and has constant values of the specific heats, c_p and c_v. Although most supersonic applications remain within this regime, at hypersonic speeds the gas imperfections may no longer be ignored.

Gas imperfections may be either thermal or caloric. The effects of thermal imperfection in wind tunnels appear primarily when a gas is at or near the condensation point and are usually negligible except at the low densities and temperatures encountered in a hypersonic wind tunnel. When the working fluid of a wind tunnel is heated enough to avoid actual condensation of any or all of the gas elements at every point along the nozzle, then the fluid, even near the critical point, behaves essentially as a perfect gas. For most practical purposes, all gases may be regarded as thermally perfect.

Caloric imperfections appear when the temperature is high enough (about 1000°R for air) to excite the intra-molecular modes of energy absorption. In the order of increasing critical temperature these modes are vibration, dissociation, and ionization. The temperatures encountered in aerodynamic calculations are rarely high enough to involve excitation of the higher energy modes associated with the nuclei.

In the temperature range for which vibration is the only mode of caloric imperfection, representation of the molecule as a simple harmonic oscillator adequately accounts for the temperature dependence of specific heats. Although the theory becomes unwieldy, the resulting analytical expressions can be incorporated in the one-dimensional theory and the results presented as corrections to the perfect-gas curves.

Reference 22 gives all the equations necessary for calculating the flow properties of a calorically and thermally imperfect gas and a calorically imperfect, thermally perfect gas at temperatures up to 5000°R. For the calorically imperfect, thermally perfect gas, charts are given which give a correction factor as a function of Mach number for the following properties: V/a^*, T/T_t, ρ/ρ_t, p/p_t, q/p_t, and A/A^*. Correction factors are also given for the flow properties associated with a normal and an oblique shock.

For the temperature range above that for excitation of vibration only, no analytical representation of these functions is possible, and it becomes necessary to resort to iterative methods of calculation. For further discussion of this subject, see Refs. 7, 55, and 56. Effects of dissociation and recombination are treated briefly in Subsec. 6.3.

2.1.8 One-Dimensional Treatment of Non-Uniform Flow

In most practical cases of steady duct flow, a well-developed boundary layer will produce a velocity distribution which is far from uniform at any cross section. Even under these conditions it is possible to adapt one-dimensional theory to predict flow characteristics at various sections. To do so the constant values of the fluid properties at each station are replaced by some form of average values. Simple arithmetical averages of p, T, and V over the area, although often used, are not realistic since they give equal emphasis to the midstream, high-velocity unit of area and to the unit of area near the wall, where the velocity is approaching zero.

Two questions need to be answered. How does one define the average value of any flow property at the required cross section? What is the magnitude of the difference between such average values and those determined from the simple, uniform, one-dimensional flow equations?

Mean values of the flow properties at the station in question may be derived from the assumption of continuity of mass flow, of momentum, or of energy. It may be shown that no definition can satisfy all continuity conditions simultaneously. In each case the mean values will be somewhat different. The choice of a basic assumption will depend on the type of problem. For flow in the ducts of a ramjet, where a knowledge of the mass flow is of importance, a good choice would be to define the averages in such a way as to preserve a realistic mass flow.

Tyler in Ref. 57 has assumed a constant mass flow and derived a set of average values of the flow properties in a duct of circular cross section (radius r) in which the isentropic flow model is modified only by the assumption of a friction boundary layer. The velocity distribution in the boundary layer of thickness δ is given by

$$\left.\begin{aligned} \frac{V}{V'} &= (y/\delta)^{1/n} \qquad \text{for} \quad 0 \le y \le \delta \\ \text{and} \\ \frac{V}{V'} &= 1 \qquad\qquad \text{for} \quad y > \delta \end{aligned}\right\} \tag{2-25}$$

where

V' = free-stream velocity (usually designated V_∞) at the station in question

y = distance from the duct wall.

The value of the exponent, n, is discussed in Subsec. 2.4. Although Eq. 2-166 relates n to the Reynolds number, a value of n = 7 is frequently used (as in these calculations) over a wide range of Reynolds numbers.

The static pressure and the total temperature are assumed to be constant over each cross section. The correction factors are defined by the following equations:

$$\Sigma\, V\delta A = \eta \bar{V} A \qquad \text{i.e., } \eta = \text{volume flux correction factor}$$

$$\Sigma\, \rho V^2 \delta A = \xi_2 \bar{\rho} \bar{V}^2 A \qquad \text{i.e., } \xi_2 = \text{momentum flux correction factor}$$

$$\Sigma\, \rho V^3 \delta A = \xi_3 \bar{\rho} \bar{V}^3 A \qquad \text{i.e., } \xi_3 = \text{kinetic energy flux correction factor}$$

and

$$\Sigma\, \rho V \delta A = \bar{\rho} \bar{V} A \qquad \text{since the mass flow is constant.}$$

The correction factors are obtained in terms of δ/r from the following equations:

$$\eta = Y_0/Y_1 \left[\frac{1}{2n+1} (\delta/r)^2 - \frac{2}{n+1} (\delta/r) + 1 \right] \qquad (2\text{-}26)$$

and

$$\xi_i = (Y_0/Y_1)^i \, (Y_i/Y_0) \qquad (2\text{-}27)$$

where

$$Y_i = Z_i - (\delta/r)\, Z_{i+n} + (1 - \delta/r)^2 \qquad (2\text{-}28)$$

and

$$Z_i = \frac{2(\delta/r)}{1 + \frac{\gamma - 1}{2} M'^2} \sum_{j=c}^{j=\infty} \left(\frac{\frac{\gamma - 1}{2} M'^2}{1 + \frac{\gamma - 1}{2} M'^2} \right)^j \frac{n}{2j + i + n} \qquad (2\text{-}29)$$

Values of Y_0, Y_1, Y_2, and Y_3 are given in terms of M' and δ/r in Figs. 2-21 to 2-24. From these all other parameters may be derived. The Y's have been calculated for values of δ/r from 0 to 1.0, i.e., to fully-developed, turbulent, pipe flow. However, for the Reynolds number range of most supersonic applications the value of δ/r varies from about 0.01 to 0.1. Therefore, enlarged-scale graphs of the Y's are included for this range of boundary-layer thickness.

The flow properties in the free stream (i.e., outside the boundary layer) are designated by primed symbols. In most practical cases, p' and p'_t are measured and M' is then derived from isentropic flow equations (see Appendix A). The average flow functions are given by the following equations:

$$\bar{p} = p' = \sqrt{R/\gamma} \cdot m/A \cdot \sqrt{T_t}/(Y_1 M') \left(1 + \frac{\gamma - 1}{2} M'^2\right)^{-1/2} \quad (2\text{-}30)$$

$$\bar{T} = \frac{T_t}{Y_0 \left(1 + \frac{\gamma - 1}{2} M'^2\right)} \quad (2\text{-}31)$$

$$\bar{\rho} = 1/\sqrt{\gamma R} \cdot m/(A\sqrt{T_t}) \cdot \frac{Y_0 \left(1 + \frac{\gamma - 1}{2} M'^2\right)^{1/2}}{Y_1 M'} \quad (2\text{-}32)$$

$$\bar{V} = \sqrt{\gamma R}\sqrt{T_t} \frac{Y_1 M'}{Y_0 \left(1 + \frac{\gamma - 1}{2} M'^2\right)^{1/2}} \quad (2\text{-}33)$$

$$\bar{F} = \sqrt{R/\gamma} \frac{m\sqrt{T_t}}{Y_1 M'} \frac{(1 + \gamma Y_2 M'^2)}{\left(1 + \frac{\gamma - 1}{2} M'^2\right)^{1/2}} \quad (2\text{-}34)$$

$$\bar{M}^2 = \frac{\xi_3 \bar{V}^2}{\gamma R \eta \bar{T}} = \frac{\xi_3 Y_2 M'^2}{\xi_2 \eta} = \frac{Y_3 Y_0}{Y_1 \eta} \cdot M'^2 \quad (2\text{-}35)$$

A further useful relationship derived from the expression for mass flow is

$$m/A \cdot \sqrt{T_t} \cdot \sqrt{R/\gamma} = Y_1 p'_t M' \left(1 + \frac{\gamma - 1}{2} M'^2\right)^{-\frac{(\gamma+1)}{2(\gamma-1)}} \quad (2\text{-}36)$$

An indication of the magnitude of the correction factors is best seen by a comparison of the average quantities with those measured in the isentropic core. By assumption $\bar{p}/p' = 1$. Values of $\bar{M}/M'$ calculated from Eq. 2-35 are shown in Fig. 2-25. The density ratio, $\bar{\rho}/\rho' = Y_0$, may therefore be found as a function of M' and δ/r in Fig. 2-21. Since $\bar{T}/T' = 1/Y_0$, it may also be readily obtained from the same figure. The velocity ratio, $\bar{V}/V' = Y_1/Y_0$, is shown in Fig. 2-26.

A comparative measure of the thrust is found by taking the thrust per unit of effective area, i.e., $(\bar{F}/A)(A'/F')$ where A' is the area of the core

of isentropic flow $[\pi(r - \delta)^2]$. The thrust, F', is given by

$$F' = A' \; p'(1 + \gamma \; M'^2) \tag{2-37}$$

and hence, by use of Eqs. 2-34 and 2-37

$$(\bar{F}/A) \; (A'/F') = \frac{\left(1 + \gamma \; Y_2 \; M'^2\right)}{1 + \gamma \; M'^2} \tag{2-38}$$

This relationship is shown graphically in Fig. 2-27. A mean total pressure is defined by Tyler (Ref. 57) as the total pressure of a uniform stream having the same total temperature (considered uniform) and mass flux as the non-uniform stream and possessing the same value of the availability flux. The ratio of the average total pressure to that measured in the free stream is given by

$$\log_e \left(\bar{p}_t/p'_t\right) = \left\{ r/\delta \sum_{j=1}^{j=\infty} \frac{n}{2j + 1 + n} \; a_j \left[\frac{(\gamma - 1) \; M'^2}{2 + (\gamma - 1) \; M'^2}\right]^j \right.$$

$$\left. - \sum_{j=1}^{j=\infty} \frac{n}{2j + 1 + 2n} \; a_j \left[\frac{(\gamma - 1) \; M'^2}{2 + (\gamma - 1) \; M'^2}\right]^j \right\} \frac{\frac{2}{\gamma - 1} \; (\delta/r)^2}{Y_1 \left(1 + \frac{\gamma - 1}{2} \; M'^2\right)}$$

$$- \left(\frac{\gamma}{\gamma - 1}\right) \frac{Y_1 - (1 - \delta/r)^2}{Y_1} \log_e \left(1 + \frac{\gamma - 1}{2} \; M'^2\right) \tag{2-39}$$

where

$$a_j = \sum_{j=1}^{j=j} 1/j$$

Figure 2-28 gives values of $\bar{p}_t/p'_t$ as a function of M' and δ/r for $\gamma = 1.4$ and $n = 7$.

The problem of non-uniform flows has also been treated by Crocco in Ref. 17 (pp. 293-348). He defines the average temperature in terms of the stagnation enthalpy flux and the average velocity in terms of the kinetic energy flux. Average values of the gas constant and the ratio of specific heats are included, whereas in the work of Tyler these are assumed to be constant. The effect of cross-sectional variation of the pressure is considered as well as the effect of entropy flux variation. Examples are included for laminar pipe flow, vortex flow in a two-dimensional annular duct, and choked flow in an axially-symmetric throat.

McLafferty in Ref. 58 shows how several forms of average total pressure and velocity may be used to describe the integrated properties of ducted, non-uniform flow of both compressible and incompressible fluids. His ultimate analyses are, however, limited to fully-developed flow, i.e., with the boundary layer extending across the axially-symmetric duct. Both laminar and turbulent flows are considered.

2.1.9 Flange Loads on Free-Jet Nozzles

The general subject of reaction forces on ducts arising from momentum changes of the internal flow represents one useful area of application of the one-dimensional theory. Use of the momentum theorem permits determination of over-all forces in terms of end conditions which are often essentially steady, one-dimensional, and easy to calculate, although flow between the end stations, as in a turbojet engine, is neither steady nor one-dimensional.

For ducts in which there is no obstruction, the steady flow form of the momentum theorem asserts that the total force acting on the nozzle walls is equal to the total rate of momentum flux out of the region. It is necessary only that flow conditions be steady at every point of the surface, and that within the surface the volume integral of the partial derivative of local momentum with respect to time be zero. The class of objects satisfying these general requirements includes not only propulsion systems of all kinds, but such components as nozzles and diffusers as well.

Steady one-dimensional flow through a duct is illustrated below.

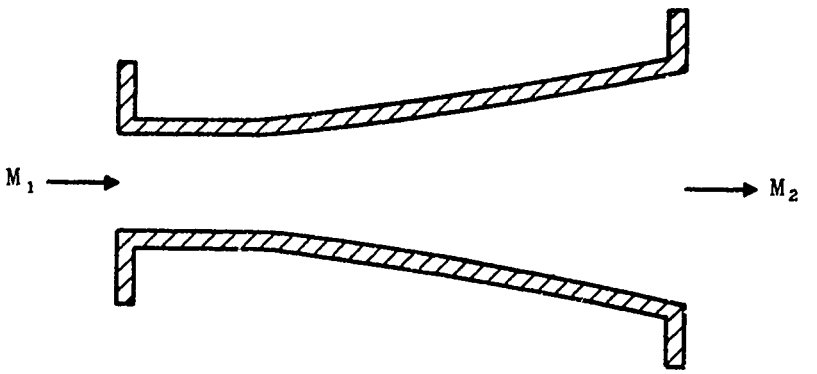

From Eq. 2-34 the accelerating force exerted on the fluid by the duct walls can be written as

$$\bar{F}_2 - \bar{F}_1 = \sqrt{(R/\gamma)\,T_t}\; m[f(\bar{M}_2) - f(\bar{M}_1)] \qquad (2\text{-}40)$$

Thus if the incoming Mach number, stagnation pressure, and inlet duct area, A_1, are known, the force exerted by the fluid against the duct walls and opposite to the flow direction is determined by the exit Mach number. Actually, because of the various relations existing in the one-dimensional theory, the inlet conditions for a given duct are defined by any two of the following local inlet variables: Mach number (or sonic area), the local pressure, and the stagnation pressure.

If the flow is isentropic the exit Mach number, M_2, is calculated from the ratio A_2/A_1 and M_1. For one-dimensional steady flow with heat addition, the exit Mach number is found according to the method presented in Subsecs. 2.1.2 and 2.1.3.

In most cases of practical importance the exit flow has a significant profile, and the proper procedure would be to determine an equivalent exit Mach number by the method described in Subsec. 2.1.8. However, when errors on the order of several per cent are considered unimportant, this degree of refinement need not be resorted to. Adiabatic flows are usually assumed to be isentropic, or the friction losses may be estimated as a function of flow velocity and Reynolds number by the methods given in Ref. 8.

2.1.10 Rocket Jet Thrust

The thrust force of a rocket motor can be expressed quite simply by use of the one-dimensional theory. The net thrust force, F, acting along the axis of a motor is simply the complete surface integral over the internal and external areas of the local surface multiplied by the axial components of the local pressure, p, and local viscous stress, τ, as shown below.

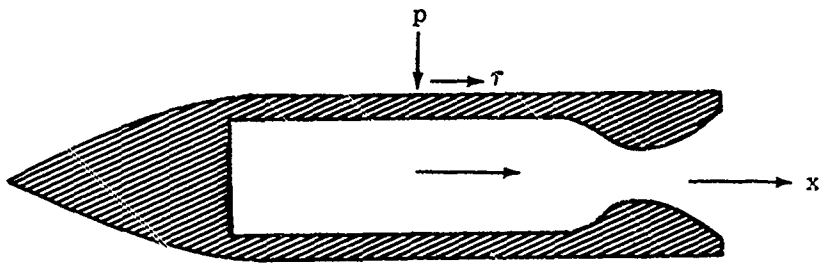

Thus the net thrust force, positive upstream, is

$$F_N = F_i - \int_{ext} (p_x + \tau_x)\, dA \qquad (2\text{-}41)$$

where

F_i = net thrust force acting on the inner surface of the motor

and p_x and τ_x are the x-components of p and τ. Since the gaseous combustion products are generated with zero net momentum relative to the rocket, the only momentum flux is that across the exit plane. Therefore,

$$F_i - p_e A_e = \rho_e A_e V_e^2 \qquad (2\text{-}42)$$

Eliminating F_i from Eqs. 2-41 and 2-42 gives

$$F_N = p_e A_e + \rho_e A_e V_e^2 - \int_{ext} (p_x + \tau_x)\, dA \qquad (2\text{-}43)$$

It is common practice to represent the pressures as gauge values, relative to the free-stream pressure, p_∞ (or p_0 since it is the pressure at station o; see sketch in Subsec. 2.1.11). The net force then becomes

$$F_N = (p_e - p_\infty)\, A_e + \rho_e\, A_e\, V_e^2 - \int_{ext} \left[(p - p_\infty)_x + \tau_x\right] dA \tag{2-44}$$

since

$$p_\infty\, A_e = - \int_{ext} (p_\infty)_x\, dA$$

The sum of the exit momentum and gauge pressure terms is customarily regarded as gross thrust, F_G, and the external surface stress integral as drag, i.e.,

$$F_G = (p_e - p_\infty)\, A_e + \rho_e\, A_e\, V_e^2 \tag{2-45}$$

and

$$D = \int_{ext} \left[(p - p_\infty)_x + \tau_x\right] dA \tag{2-46}$$

i.e.,

$$F_N = F_G - D$$

In most practical cases the rocket motor is buried within the airframe, and the shape of the external surface over which the drag integral is calculated therefore is that of the total missile configuration. The net thrust is seldom used as a motor parameter, but is used for determining the acceleration or performance of the vehicle in which the motor is installed. From the practical point of view, therefore, the performance of the rocket motor is usually defined in terms of the gross thrust.

Another useful parameter is the thrust specific impulse or fuel specific impulse. This is defined as the ratio of the thrust force to the weight of fuel-plus-oxidizer which flows through the motor in producing the thrust. Thus,

$$I = F_G/mg \text{ sec} \tag{2-47}$$

where

mg = weight of fuel-plus-oxidizer flowing per sec.

Since the performance of a given rocket motor depends only on the flow-rates of fuel and oxidizer into the combustion chamber and is relatively independent of the altitude and flight speed at which it is operated, dimensionless coefficients are not customarily used. The only parameters of interest are the size of the motor in terms of its maximum gross-thrust capability and the thrust specific impulse. In dealing with solid-fuel rockets, it is also important to know the burning time and the variation of the gross thrust during the burning period.

2.1.11 Air-Breathing Engine Thrust

The general formulation of the thrust expression for an air-breathing engine in its basic form is similar to that of the rocket motor, except that the momentum of the entering air must be accounted for.

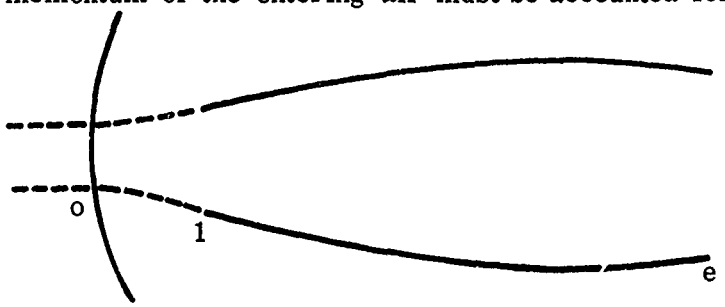

Station o in the above sketch is taken in the undisturbed free stream, and station e at the engine exit. The net thrust can then be written

$$F_N = p_e A_e + \rho_e A_e V_e^2 - (p_o A_o + \rho_o A_o V_o^2) - \int_{ext} (p_x + \tau_x)\, dA \tag{2-48}$$

If the absolute pressure is now replaced by gauge pressure, this expression becomes

$$F_N = \rho_e A_e V_e^2 - \rho_o A_o V_o^2 + (p_e - p_o) A_e - \int_{ext} \left[(p - p_o)_x + \tau_x\right] dA \tag{2-49}$$

As before, the momentum terms plus the exit gauge pressure term in this expression are referred to as gross thrust and the remaining term as drag. Thus,

$$F_G = \rho_e A_e V_e^2 - \rho_o A_o V_o^2 + (p_e - p_o) A_e \tag{2-50}$$

and since

$$D = \int_{ext} \left[(p - p_o)_x + \tau_x\right] dA$$

as before

$$F_N = F_G - D$$

When $A_o \neq A_1$ (i.e., when the shock is expelled), there is a further drag component, known as the additive drag, which is the integrated pressure along the surface of the last streamlines from the shock intersection to the duct entrance (see Subsec. 3.1.3).

An air-breathing engine, unlike the rocket motor, derives its oxidizer from the atmosphere and by decelerating the incoming air it incurs a

penalty in terms of internal drag. Thus its performance is dependent upon altitude and flight speed, and it becomes useful to define the performance of an air-breathing engine in terms of dimensionless parameters.

Equation 2-50, for gross thrust, is usually written as a dimensionless coefficient in terms of some characteristic reference area, A_R, the free-stream dynamic pressure, and the Mach number rather than the velocity. In these terms the gross-thrust coefficient becomes

$$C_{FG} = 2\, A_o/A_R \left[\frac{\gamma_e}{\gamma_o} \frac{A_e}{A_o} \left(\frac{p_{te}}{p_{t_o}}\right) \left(\frac{M_e}{M_o}\right)^2 \frac{(p_t/p)}{(p_t/p)_e^o} - 1 \right] + \frac{2}{\gamma M_o^2} \left(\frac{p_e}{p_o} - 1\right) \frac{A_e}{A_R} \tag{2-51}$$

This equation is valid for ramjets, turbojets, and turbo-rockets.

When it is expressed in this form, the gross-thrust coefficient depends on the following factors: Mach number change across the engine, M_e/M_o; ratio of stagnation pressures across the complete engine, p_{te}/p_{t_o}; and exit area, A_e, required to pass the low-density, hot, exhaust gas at the required exit pressure (usually ambient).

In the special case of an ideal exhaust nozzle with the exit pressure, p_e, equal to the free-stream pressure, p_o, and the free-stream capture area, A_o, used as a reference area, A_R, and no mass-flow addition to provide the energy input, Eq. 2-51 may be reduced to

$$C_{FG} = 2(V_e/V_o - 1) \tag{2-52}$$

Thus Eq. 2-52 clearly shows the basic dependence of the gross-thrust coefficient on the exit-to-free-stream velocity ratio.

In order to calculate the thrust, it is necessary to determine the characteristics of the flow at each station (or component section) from inlet to exit. The first component of the system is always a diffuser. (The design and operation of the diffuser will be discussed in detail in Subsec. 3.) Its function is to decelerate the incoming air, usually to a low subsonic Mach number. However, in the case of a hypersonic ramjet, combustion at supersonic Mach numbers will be more efficient. The compression is usually a non-isentropic process (in its simplest form, it is a normal shock) and therefore is characterized by a loss in stagnation pressure.

The relationship between the flow properties at the inlet station o and the exit station 2 of the diffuser may be found by equating the mass flow at the two stations in terms of the stagnation pressures, temperatures and the area ratios.

Thus,

$$\sqrt{\gamma_1/R_1}\,\frac{p_{t_o}}{\sqrt{T_{t_o}}}\,\frac{A_o}{A_1}\,f(M_o) = \frac{p_{t_2}}{\sqrt{T_{t_2}}}\,\frac{A_2}{A_1}\,f(M_2)\,\sqrt{\gamma_2/R_2} \qquad (2\text{-}53)$$

where

$$f(M) = M\left(1 + \frac{\gamma - 1}{2}\,M^2\right)^{\frac{-(\gamma+1)}{2(\gamma-1)}}$$

The change in stagnation temperature is usually negligible when there is no combustion ($\gamma_1 = \gamma_2$ and $R_1 = R_2$); hence M_2 is dependent only upon the known value of M_o, the measured value of A_o/A_1, the known value of A_2/A_1, and the stagnation pressure loss in the diffuser. As will be shown in Subsec. 3, the geometry may be optimized for any given free-stream Mach number and an empirically determined, realistic, pressure loss.

The flow calculations for the next component of the system will vary according to the type of engine employed. For the ramjet they will consist of the addition of terms to represent the drag and the heat addition as exemplified in Subsecs. 2.1.2 to 2.1.5. The details of compressor turbine performance lie outside the scope of this volume.

The hot products of combustion pass through the exhaust nozzle, the last component of the system. This is usually assumed to be an isentropic process (see Subsec. 2.1.1); however, a nozzle efficiency factor of the order of 0.97 is usually included to account for the effect of viscosity in the nozzle (see Subsec. 6).

2.1.12 Viscous Effects and Heat Transfer in One-Dimensional Duct Flows

Simple one-dimensional theory may be modified in several different ways to include the effects of viscosity. Since moderate heat transfer at the duct walls is reflected chiefly by changes in the skin friction, it may generally be treated as a viscous force. Three methods of including viscosity are noted below.

1. Following the general equations given in Section 4 (Ref. 1) or a similar method to that used in Subsecs. 2.1.2 and 2.1.3, viscous forces may be included with the internal pressure forces on the duct walls and objects immersed in the flow. Values of the skin friction may be computed as a function of the Reynolds number and wetted area from laminar and turbulent skin-friction coefficients given in many textbooks or in Refs. 9 and 10.

2. Since viscous effects are manifested chiefly in the velocity profile, they may be included in two-dimensional flow calculations by the use of integrated values of the parameters across any area section (see Subsec. 2.1.8). The velocity profile may be determined from boundary-layer theory (Ref. 11).

732-339 O - 64 - 4

3. Viscous effects may be included by the assumption of constant-flow parameters in a cross section whose area has been adjusted to take into account the displacement thickness of the boundary layer. This will be discussed further in Subsec. 2.4.

2.2 One-Dimensional Non-Steady Flow

This subsection is concerned with the propagation of pressure waves in ducts. Such waves may produce a nonsteady flow or they may modify an initially steady flow. In general, whenever a wave passes through a region of continuously or discontinuously changing flow conditions, it is modified and also generates reflected waves. Wave interactions and repeated reflections, as well as reflections from the ends of the duct, build up a complex flow pattern for which analytical solutions usually cannot be obtained.

In the problems under consideration here, the cross-sectional dimensions of the duct may be considered small compared with the length of the duct. In such quasi-one-dimensional flow, all flow variables may be assumed to be uniform across any section of the duct, with the consequence that time and one space coordinate are the only independent variables. In a coordinate system of these variables, one may follow the propagation of gas particles and pressure waves graphically. Such plots are usually called wave diagrams, and the following subsections include a summary of the computing procedures that may be used in their preparation. The procedures given herein are not unique, but have been expressed by Rudinger (Ref. 59) in a form convenient for both simple and complex problems. Alternative procedures may be found in Refs. 15 and 60 to 65.

A wave diagram yields all the flow variables at any location in the duct and at any time. It will be evident, however, that the preparation of wave diagrams is time consuming even for relatively simple problems. A specific problem may be programmed for a high-speed digital computer if the number of cases is sufficient to warrant the investment of the programming time. The main programming difficulties arise from the necessity of treating flow discontinuities, such as shock waves or contact surfaces, which may appear at times or locations that are unknown at the beginning of the calculation. These and other problems of machine programming have been discussed by Fox in Ref. 65.

A complete wave diagram must be prepared even when not all the information it provides is needed. This aspect, or the uncertainties imposed by the need to make simplifying assumptions, may make it preferable to deal occasionally with the problems in a more approximate manner. A discussion of several such techniques is included in Subsec. 2.2.4.4, 2.2.5.5, 2.2.6, and 2.2.7. The last two of these consider solutions for the linearized basic differential equations. Subsection 2.2.6 is concerned with the approximate solution of shock passage through a duct of variable cross section. Although a number of such solutions have been published (e.g., Refs. 66 to 72), the discussion given herein follows that of Chester (Ref. 66), since his solutions are obtained in a particularly convenient form.

In a more general solution of the linearized partial differential equations, the perturbations represent small-amplitude waves which are superposed

on a basic steady flow. A variety of alternative methods of solution are available in Refs. 69, 71, and 73 to 76; the discussion in Subsec. 2.2.7 essentially follows and extends the approach of Mirels (Ref. 74).

To present material from different sources in a consistent manner, it was necessary to change the meaning of some of the symbols. This point should be kept in mind when referring to the original publications for further details.

2.2.1 Assumptions and Basic Equations

It will be assumed that the gas follows the ideal-gas law and that the specific heats are constant. Although it is possible to assume other equations of state, or variable specific heats as done by Benson (Ref. 77), the complications introduced by such refinements do not seem warranted in general. Furthermore, as pointed out by Kantrowitz (Ref. 62), the temperature-sensitive part of the heat capacity usually is unable to follow the rapid changes of state, and consequently these lags should be considered simultaneously with the variations of the specific heats. At the present time, procedures for nonsteady, nonequilibrium flows are still in an early state of development and will not be considered here. The assumption of constant specific heats does not exclude the possibility that two or more different gases are involved in a problem. The thermodynamic properties are assumed to be constant in any one regime and to change only across a contact surface where the change will be a discontinuous one. Mixing of the gases at such an interface will be neglected. In the case of flame fronts, the large temperature change may make it desirable to allow for a discontinuous change of the thermodynamic properties across the front.

The flow conditions at any location and time are completely determined by any three flow variables, so that the problem becomes one of solving a system of three partial differential equations. The choice of the dependent variables is arbitrary and is influenced only by the convenience of the resulting computing procedures (compare Subsec. 2.2.2 and 2.2.7). Since additional variables are readily obtained with the aid of the appropriate thermodynamic equations, the relationships can be expressed in the most concise form by retaining more than three variables in the equations.

It is convenient to base all numerical calculations on dimensionless variables and to use a prime (') to indicate dimensional variables. The state of the gas is then expressed in terms of:

$$\text{pressure} = p = p'/p'_0$$

$$\text{density} = \rho = \rho'/\rho'_0$$

$$\text{temperature} = T = T'/T'_0$$

and

$$\text{speed of sound} = a = a'/a'_0$$

where the subscript zero signifies a suitable reference state. A dimensionless

specific entropy will be used in the form $s = s'/\gamma R'$, where $\gamma = c_p'/c_v'$ is the ratio of the specific heats at constant pressure and constant volume, and R' is the individual gas constant. The gas velocity relative to the duct will be denoted by $u = u'/a_o'$. As pointed out in the preceding subsection, the flow will be treated as one-dimensional; the independent variables are thus the position along the duct $x = x'/\ell_o'$ and the time $t = a_o' t'/\ell_o'$, where ℓ_o' is a suitable reference length.

Within the limitation of the stated assumptions, the formulation of any nonsteady-flow problem requires that the following be known:

1. Variations of the cross-sectional area of the duct, A'. Ordinarily only rigid ducts need to be considered, but changes of duct shape as a function of time or of the instantaneous flow conditions may be prescribed.

2. Conditions which control the flow at the ends of the duct.

3. Initial flow conditions in the duct. Usually, but not necessarily, they are represented by a steady flow or by a gas at rest.

4. The amount of heat, q', added per unit mass and unit time as a function of x, t, and of the flow conditions.

5. Dissipative or body forces, f', per unit mass. It should be noted that the work done by dissipative forces, for instance wall friction, is converted into heat and must be included in the amount of heat added to the flow. Since the flow is treated as one-dimensional, those forces must act, or must be assumed to act, over the entire cross section of the duct. On the basis of such assumptions, one may include effects of wall friction.

6. The amount of mass, m', added to the flow per unit volume and per unit time as a function of x, t, and of the flow conditions. The velocity and temperature of the added mass may be different from that of the main flow, in which case instantaneous mixing is assumed; however, the resultant heat addition must be included in q' and the momentum change in f'. No such difficulties arise in the case of mass removal ($m' < 0$). Flow through porous walls is included in this category.

The foregoing requirements are not always easily formulated explicitly without the aid of simplifying assumptions.

The three partial differential equations which must be solved are those which express the conservation of mass, momentum, and energy. The continuity equation may be written

$$\frac{\partial \rho' A'}{\partial t'} + \frac{\partial \rho' u' A'}{\partial x'} - m' A' = 0 \qquad (2\text{-}54)$$

and the equation of motion is given by

$$\frac{\partial u'}{\partial t'} + u' \frac{\partial u'}{\partial x'} = -\frac{1}{\rho'} \frac{\partial p'}{\partial x'} + f' \qquad (2\text{-}55)$$

Instead of writing the energy equation in one of its usual forms, it is more convenient here to use the entropy condition

$$\frac{Ds'}{Dt'} = \frac{q'}{T'} \tag{2-56}$$

where $q' = q'(x', t', T', u', \ldots.)$ must be specified for each problem to be investigated. The substantial derivative

$$\frac{D}{Dt} = \frac{\partial}{\partial t} + u \frac{\partial}{\partial x} \tag{2-57}$$

signifies differentiation along the path of a gas particle.

The necessary thermodynamic equations are the equation of state,

$$p' = \rho' R' T' \tag{2-58}$$

the equation for the speed of sound,

$$a'^2 = \gamma \frac{p'}{\rho'} = \gamma R' T' \tag{2-59}$$

and the relationships between entropy, speed of sound, and pressure or density which may be written in the dimensionless form

$$p = a^{\frac{2\gamma}{\gamma-1}} e^{-\gamma(s-s_o)} \tag{2-60}$$

$$\rho = a^{\frac{2}{\gamma-1}} e^{-\gamma(s-s_o)} \tag{2-61}$$

Since only entropy differences appear in the calculations, it usually will be possible to set the entropy of the reference state, s_o, equal to zero.

Since all terms of Eq. 2-54 contain the cross-sectional area, A' may be replaced by $A = A'/A'_o$, where the reference value A'_o need not be specified. With the aid of the dimensionless variables

$$q = \frac{\ell'_o}{a'^3_o} q' \quad , \tag{2-62}$$

$$f = \frac{\ell'_o}{a'^2_o} f' \quad , \tag{2-63}$$

and

$$m = \frac{\ell'_o \, a'_o}{\gamma p'_o} m' \quad , \tag{2-64}$$

the preceding equations may be combined to yield

$$\frac{\delta^+ P}{\delta t} = -\frac{au}{A}\frac{\partial A}{\partial x} - \frac{a}{A}\frac{\partial A}{\partial t} + a\frac{\delta^+ s}{\delta t} + (\gamma - 1)\frac{q}{a} + f + \frac{a^3}{p}m \qquad (2\text{-}65)$$

$$\frac{\delta^- Q}{\delta t} = -\frac{au}{A}\frac{\partial A}{\partial x} - \frac{a}{A}\frac{\partial A}{\partial t} + a\frac{\delta^- s}{\delta t} + (\gamma - 1)\frac{q}{a} - f + \frac{a^3}{p}m \qquad (2\text{-}66)$$

and

$$\frac{Ds}{Dt} = \frac{q}{a^2} \qquad (2\text{-}67)$$

where

$$\frac{\delta^\pm}{\delta t} = \frac{\partial}{\partial t} + (u \pm a)\frac{\partial}{\partial x} \qquad (2\text{-}68)$$

and the "Riemann variables" P and Q are defined (Ref. 78) by

$$P = \frac{2}{\gamma - 1}a + u \qquad (2\text{-}69)$$

and

$$Q = \frac{2}{\gamma - 1}a - u \quad . \qquad (2\text{-}70)$$

Thus, Eqs. 2-65 to 2-67 indicate how the variables P, Q, and s vary along those lines in the x, t-plane which have the slope

$$\frac{dx}{dt} = u + a \text{ for } P$$

$$\frac{dx}{dt} = u - a \text{ for } Q \qquad (2\text{-}71)$$

and

$$\frac{dx}{dt} = u \qquad \text{for } s \quad .$$

In accordance with the theory of partial differential equations (e.g., Refs. 60 and 64), these lines are called the characteristics of the equations, and Eqs. 2-65 to 2-67 are called compatibility equations.

Small disturbances in a flow travel through the gas with the local speed of sound and, at the same time, are carried along by the gas with its own velocity. It is therefore appropriate to call the lines defined by Eq. 2-71 P-waves, Q-waves, and entropy waves (or particle paths) and to refer to a plot of such lines as a wave diagram.

2.2.2 Construction of Wave Diagrams

Equations 2-65 to 2-67 suggest a graphical-numerical technique for solving nonsteady-flow problems. Let the derivatives of P, Q, and s with respect to time in the characteristic directions be approximated by the ratios of finite differences, $\frac{\Delta P}{\Delta t}$, $\frac{\Delta Q}{\Delta t}$, and $\frac{\Delta s}{\Delta t}$. Construction of a wave diagram proceeds then as illustrated in the sketch below.

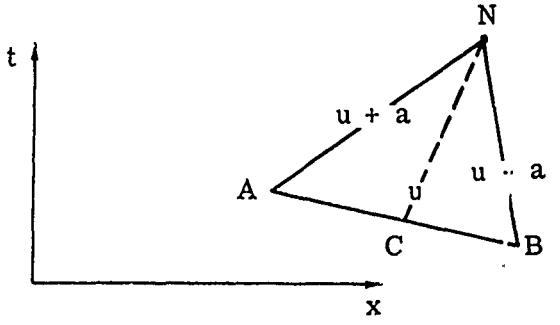

Let A and B represent two points at which all flow conditions are either prescribed or obtained from preceding computations. Draw the lines having slopes u + a and u - a through points A and B respectively; their intersection defines a new point, N. Then, find point C on the line through A and B so that the interpolated value of u_C agrees with the slope of the line which connects C with N. All other flow conditions at C also can be found by interpolation between A and B. The finite differences must obey the following equations:

$$s_N = s_C + \left(\frac{Ds}{Dt}\right)_C (t_N - t_C) , \tag{2-72}$$

$$P_N = P_A + \left(\frac{\delta^+ P}{\delta t}\right)_A (t_N - t_A) , \tag{2-73}$$

and

$$Q_N = Q_B + \left(\frac{\delta^- Q}{\delta t}\right)_B (t_N - t_B) , \tag{2-74}$$

where the derivatives are evaluated with the aid of Eqs. 2-65 to 2-67, and the values of the time coordinates are taken from the wave diagram. Finally, one obtains from Eqs. 2-68 and 2-69 that

$$u_N = \frac{P_N - Q_N}{2} \tag{2-75}$$

and

$$a_N = \frac{\gamma - 1}{4} (P_N + Q_N) \tag{2-76}$$

If desired, p_N and ρ_N may be found from Eqs. 2-60 and 2-61.

The accuracy may be improved by iteration. The characteristics through A and B are redrawn with the slopes

$$\left[(u + a)_A + (u + a)_N\right]/2 \quad \text{and} \quad \left[(u - a)_B + (u - a)_N\right]/2$$

respectively, giving an improved location of N. Similarly, an improved location for C is found, and the derivatives in Eqs. 2-72 to 2-74 are evaluated by taking the appropriate mean values for all terms involved. The procedure may be repeated until the conditions at N remain unchanged. In many cases it is entirely satisfactory to accept the first set of values for N.

The terms on the right-hand side of Eqs. 2-65 and 2-66 represent distinct features of the flow. In the order written, they represent

1) Changes of the cross-sectional area along the duct
2) Variation of the cross-sectional duct area with time
3) Adjacent particles having different entropy levels
4) Heat addition
5) External forces
6) Mass addition.

Usually, only a few of these terms will be needed in a particular problem, and the calculations are then correspondingly simplified.

2.2.2.1 Pressure Waves

Consider a flow for which A = constant and q = f = m = 0. If there are no initial entropy gradients, Eqs. 2-72 to 2-74 simplify to

$$\frac{Ds}{Dt} = \frac{\delta^+ P}{\delta t} = \frac{\delta^- Q}{\delta t} = 0 \tag{2-77}$$

with the solution

$$s = \text{constant} \tag{2-78}$$

$$P = \text{constant} \quad \text{for} \quad \frac{dx}{dt} = u + a \ , \tag{2-79}$$

and

$$Q = \text{constant} \quad \text{for} \quad \frac{dx}{dt} = u - a \ . \tag{2-80}$$

This result clearly shows the advantage of the choice of P, Q, and s for the dependent variables.

It is evident from the manner in which a wave diagram is constructed that any local disturbance of the flow can be felt at any other point of the duct only after the arrival of the P- and Q-waves at that point. The characteristics are thus signals which carry information about local flow disturbances to other parts of the duct. Pressure waves are spread out over a certain time and are therefore composed of an entire family of characteristics. If P or Q is constant for such a family, the wave is called a simple wave. In regions of a steady flow, the P- and Q-waves are families of parallel curves, while in a non-steady flow they will either diverge or converge. Equations 2-78 and 2-60 imply that an increase in the speed of sound is accompanied by an increase in pressure, and it is readily seen from Eqs. 2-79 and 2-80 that the characteristics converge for compression waves and diverge for expansion waves.

Since the characteristics of a compression wave converge, they eventually coalesce and form a discontinuity in the flow known as a shock wave which requires special treatment in the wave diagram (see Subsec. 2.2.4). A shock wave is also produced by any imposed instantaneous pressure rise. In contrast, an imposed instantaneous pressure drop leads to a fan of characteristics which diverge from a singular point. Such a wave is called a centered expansion wave. Centered expansion waves may appear in a wave diagram also as the result of interaction of discontinuous disturbances (see Subsec. 2.2.5). Changes of state in an expansion wave are isentropic, whereas a shock wave gives rise to an entropy increase whose magnitude depends on the strength of the wave (see Subsec. 2.2.4.2).

2.2.2.2 Initial Conditions, Domain of Dependence, and Range of Influence

To start a wave diagram according to the basic procedure previously described in this subsection, flow conditions must be prescribed along a line in the x, t-plane which nowhere coincides with a characteristic. In the vast majority of problems, this line will represent the initial conditions. These conditions may be given at discrete points or they may be expressed as a continuous distribution. In the latter case, a number of points must be selected at intervals small enough to give the required accuracy. Values of ΔP and ΔQ between 0.2 and 0.4 are usually satisfactory. Smaller values may be chosen if the greater degree of accuracy required justifies the additional labor.

The flow at any point depends only on the initial conditions between the P- and Q-waves that intersect at the point. This is shown clearly by the sketch on the following page in which points 1 to 6 represent a prescribed set of initial conditions. Applying the basic procedure, one may find the flow characteristics at point 7 from those at points 1 and 2, at 8 from 2 and 3, and so on. As indicated by the sketch, the conditions at point 17 depend only on the initial conditions between 2 and 5. The region bounded by these characteristics is called the domain of dependence for the conditions between points 2 and 5. Similarly, one may speak of a range of influence; any change of the initial conditions, say at point 3, can influence the flow only within the region bounded by the P- and Q-wave starting from this point, e.g., the region bounded by lines 3 to 12 and 3 to 18.

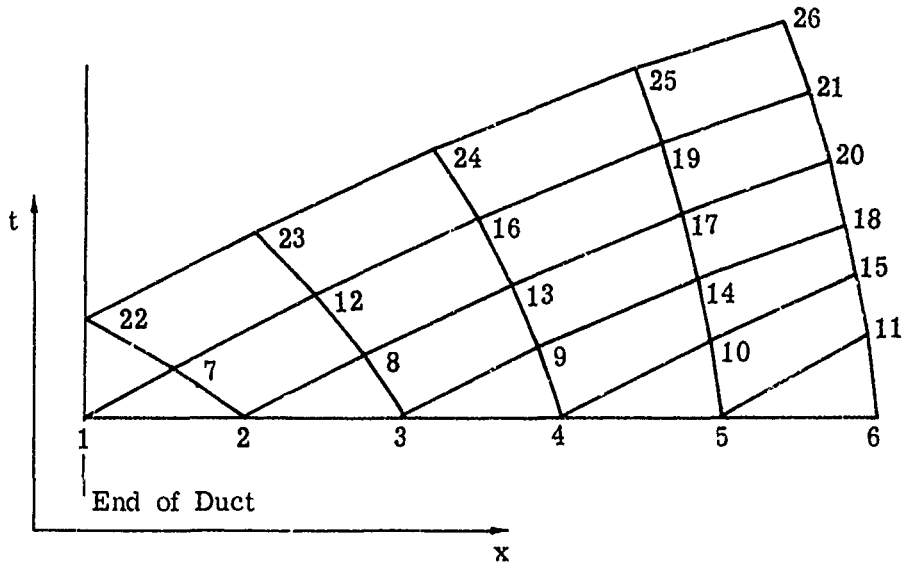

2.2.3 Boundary Conditions

Wave-diagram construction, as outlined in Subsec. 2.2.2.2, can be continued over the entire domain of dependence of the given initial conditions, that is, the region bounded by the lines 1 to 6, 1 to 21, and 6 to 21 in the above sketch. Suppose that point 1 is located at the end of the duct. The flow conditions there at later times cannot be obtained by means of the described procedure. For instance, one can draw the Q-wave through point 7 to find point 22 on the boundary, but the P-wave, which would come from outside the duct, cannot be drawn. The conditions at a boundary point must therefore be computed with the aid of an appropriate boundary condition. A number of these will be discussed in this subsection. Once the conditions at a boundary point, say 22, have been determined, the domain of dependence has been increased, and one can extend the wave-diagram to points 23 to 26. This procedure may be continued as long as it is pertinent to the problem under consideration. Boundary points will be indicated by subscript E. The procedures will be described for the left end of the duct where Q_E will be known. Analogous procedures apply at the right end where P_E would be known.

In a steady-flow discharge, the pressure at the end of the duct is well defined. In a nonsteady flow, the wave processes modify the end pressure. Although the pressure tends to reestablish its steady-flow level at a finite rate, it is also continually disturbed by further waves. As a result of this lag in establishing the steady-flow pressure level, the instantaneous pressure depends on the flow history (Refs. 79-83). The magnitude of the lag is of the order of the time in which a sound wave travels a few exit diameters. This effect can usually be neglected unless extreme accuracy of the wave diagram is required. All boundary conditions in the following discussion are based on the assumption that the end pressure adjusts instantaneously to its steady-flow level.

The different boundary conditions that apply for no discharge (closed end), subsonic outflow, supersonic outflow, or inflow at the end of a duct are given next. When the end conditions are not known, one must verify that the results of the calculations are compatible with the assumed boundary condition.

2.2.3.1 Closed End (No Discharge)

The boundary condition is clearly given by $u_E = 0$, and the relevant part of the wave diagram is shown in the sketch below. One computes s_E from the data at the preceding point, D, with the aid of Eq. 2-72. Equations 2-69 and 70 together with the boundary condition then yield $P_E = Q_E$.

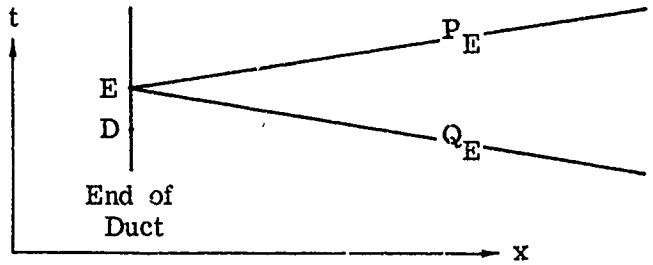

2.2.3.2 Subsonic Discharge

The wave diagram is shown in the following sketch, and the boundary condition is given by the fact that p_E must be equal to the pressure in the external region into which the discharge takes place. One computes first s_E from s_D and Eq. 2-72. From p_E and s_E, one finds a_E with the aid of Eq. 2-60 and, finally, u_E and P_E from the known value of Q_E and Eqs. 2-69 and 2-70.

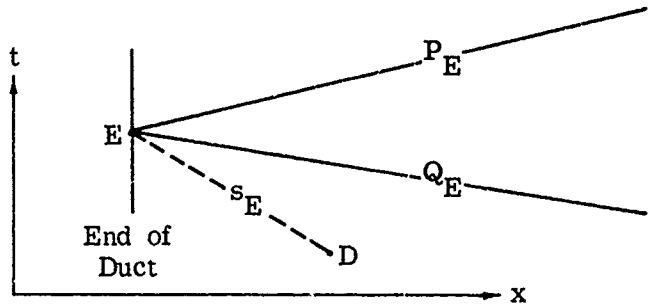

2.2.3.3 Supersonic Discharge

In the case of a supersonic discharge, both the P- and Q-waves through E come from inside the duct, and in consequence the conditions at E may be found by means of the basic procedure (Subsec. 2.2.2). No special boundary condition is needed. The wave diagram is shown below.

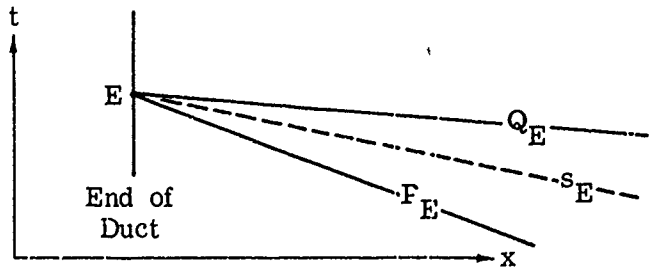

This non-steady flow case corresponds to the similar case in steady, supersonic outflow which is also unaffected by the conditions in the outside region.

2.2.3.4 Inflow from an External Reservoir

The state of the gas in the external reservoir represents the stagnation conditions for the inflowing gas, indicated by subscript s. From the stagnation speed of sound a_{Es} and the known value of Q_E, one can compute a_E according to the equation

$$a_E = \frac{\gamma - 1}{\gamma + 1}\left(Q_E + \sqrt{\frac{\gamma + 1}{\gamma - 1}a_{Es}^2 - \frac{\gamma - 1}{2}Q_E^2}\right). \qquad (2\text{-}81)$$

Equation 2-81 applies at the left end of the duct; at the right end, Q_E would be replaced by the known value of P_E. The values of u_E and P_E (or Q_E) follow from Eqs. 2-69 and 2-70.

If the inflow is assumed to be isentropic, then s_E is equal to the entropy of the gas in the external reservoir. If losses at the inlet are to be included, Eq. 2-81 still applies, but appropriate assumptions for the entropy rise as a function of the flow velocity must be made.

2.2.4 Discontinuities

Problems frequently arise in which discontinuous changes of the flow variables (contact surfaces, shock waves, flame fronts, or area changes) must be considered. The basic differential equations apply only in regions where all changes of the variables are continuous, and hence flow fields on both sides of a discontinuity surface must be matched to satisfy the appropriate conditions. These conditions of matching depend on the particular discontinuity, and each type requires its own treatment.

2.2.4.1 Contact Surfaces

A contact surface, as shown in the sketch below, represents the interface between two gases adjacent to each other. The two regions may be occupied by two different gases or they may have the same gas but at two different temperatures.

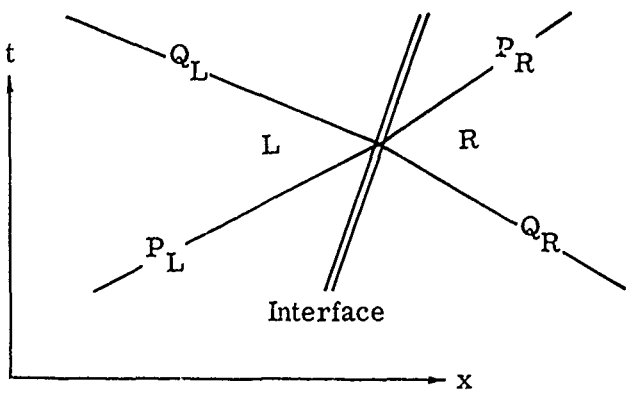

A plane interface, normal to the axis of the duct will be assumed, and diffusion, or mixing, as a result of interface instability during accelerations will be ignored (see Refs. 84 to 86). Let subscripts L and R indicate the flow conditions on the left and right sides of the contact surface, respectively. The problem then consists in finding Q_L and P_R from the known, or previously determined, values of P_L, Q_R, s_L, and s_R, and from the condition that the pressure and velocity must have equal values on both sides of the interface.

It is convenient to assume the same reference pressure and speed of sound on both sides of the contact surface and to allow the entropy for both reference states to be zero. The conditions to be satisfied are then that $P_L = P_R$ which, from Eq. 2-60, gives

$$a_L^{\frac{2\gamma_L}{\gamma_L - 1}} e^{-\gamma_L s_L} = a_R^{\frac{2\gamma_R}{\gamma_R - 1}} e^{-\gamma_R s_R} \tag{2-82}$$

and that $u_L = u_R$ which, from Eqs. 2-69 and 2-70, gives

$$\frac{2}{\gamma_L - 1} a_L + \frac{2}{\gamma_R - 1} a_R = P_L + Q_R \tag{2-83}$$

Equations 2-82 and 2-83 are solved best by a trial-and-error procedure based on an estimated value of one of the unknowns. When $\gamma_L = \gamma_R = \gamma$, the calculations reduce to

$$Q_L - Q_R = -\left(P_R - P_L\right) = \left(P_L + Q_R\right) \tanh\left[\frac{\gamma - 1}{4}\left(s_L - s_R\right)\right]. \tag{2-84}$$

2.2.4.2 Shock Waves

As pointed out in Subsec. 2.2.2.1, shock waves form when the characteristics of a compression wave merge. Depending on whether P-waves or Q-waves merge, one may speak of a P-shock or a Q-shock. The following sketch shows a P-shock in a wave diagram.

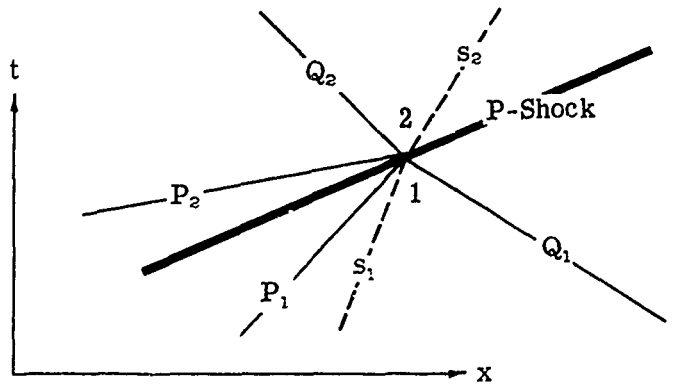

Variables of the low-pressure and high-pressure sides of the shock are distinguished by subscripts $_1$ and $_2$, respectively.

The velocity of a shock wave relative to the duct is given by

$$w_S = u_1 \pm a_1 M_S \quad . \tag{2-85}$$

Here, and in the following equations, the upper sign applies to a P-shock and the lower to a Q-shock. The strength of the shock may be characterized by the shock Mach number, M_S (always treated as a positive number), or any function of M_S such as the pressure ratio,

$$\frac{p_2}{p_1} = \frac{2\gamma}{\gamma + 1} M_S^2 - \frac{\gamma - 1}{\gamma + 1} \tag{2-86}$$

the density ratio,

$$\frac{\rho_2}{\rho_1} = \frac{(\gamma + 1) M_S^2}{2 + (\gamma - 1) M_S^2} \tag{2-87}$$

the velocity change,

$$\frac{u_2 - u_1}{a_1} = \pm \frac{2}{\gamma + 1} \left(M_S - \frac{1}{M_S} \right) \tag{2-88}$$

the speed-of-sound ratio,

$$\frac{a_2}{a_1} = \sqrt{\frac{p_2/p_1}{\rho_2/\rho_1}} \tag{2-89}$$

or entropy rise,

$$s_2 - s_1 = \frac{1}{\gamma(\gamma - 1)} \ln \left[\frac{p_2}{p_1} \left(\frac{\rho_2}{\rho_1} \right)^{-\gamma} \right] \tag{2-90}$$

It is assumed that the shock path in the wave diagram has been plotted as far as point 1 (see sketch on preceding page), where P_1, Q_1, and s_1, and therefore all other flow variables, are known. The value of P_2 for a P-shock (or Q_2 for a Q-shock) is also known from preceding work. The problem is to find the continuation of the shock path and the flow conditions at point 2. The solution is given in terms of Eqs. 2-86 to 2-89. For a P-shock, the solution is:

$$\frac{P_2 - P_1}{a_1} = \frac{2}{\gamma - 1} \left(\frac{a_2}{a_1} - 1 \right) + \frac{u_2 - u_1}{a_1} \tag{2-91}$$

and for a Q-shock, it is

$$\frac{Q_2 - Q_1}{a_1} = \frac{2}{\gamma - 1}\left(\frac{a_2}{a_1} - 1\right) - \frac{u_2 - u_1}{a_1} \qquad (2\text{-}92)$$

Because of the ± sign in Eq. 2-88, the right-hand sides of Eqs. 2-91 and 2-92 represent the same function of M_S. The left-hand side of one of these equations is known, and the right-hand side can thus be used to find M_S. Fig. 2-29 shows this relationship for $\gamma = 1.4$, 5/3, and 4/3. Tabulated values of M_S for $\frac{\Delta P}{a}$ and $\frac{\Delta Q}{a}$ from 0.01 to 10.0 with increments of 0.01 may be found in Ref. 59. Once M_S is determined, the shock path in the wave diagram can be continued according to Eq. 2-85. The remaining variables at point 2 may be computed with the aid of Eqs. 2-86 to 2-90 or taken from one of the many available shock tables (e.g., Refs. 1, 21 to 28, 33, and 34, see Appendix A).

For weak shock waves, the entropy rise across the shock often may be neglected. Under this condition, Q does not change across a P-shock, or P across a Q-shock. The flow at point 2 in the sketch on page 35 is then given by $s_2 = s_1$, $Q_2 = Q_1$, and the known value of P_2. Equation 2-85 can be reduced to

$$w_S = \frac{(u_1 \pm a_1) + (u_2 \pm a_2)}{2} \qquad (2\text{-}93)$$

so that the propagation velocity of weak shocks is the mean of the velocities of the merging characteristics.

2.2.4.3 Flame Fronts

Problems involving heat addition by burning may have to be considered. If the combustion region extends over some length of the duct, the wave diagram must be prepared according to the general procedure given in Subsec. 2.2.2, but if the region is sufficiently narrow, it may be approximated by a discontinuous flame front. The latter advances into the unburned gas with a flame speed, v'_f, which will be treated as a positive quantity. Let h' be the heat released per unit mass of the gas. Both v'_f and h' must be prescribed in the form of some functions of the flow conditions in the unburned gas; they may be chosen independently of each other except for the limitation stated at the end of this subsection.

A general solution for the interaction of characteristics with a flame front, based on conservation of mass, momentum, and energy, involves lengthy calculations which are discussed by Rudinger in Ref. 59. Considerable simplifications are possible for moderate flame speeds (less than about 15% of the speed of sound in the unburned gas), because the pressure change across the flame then becomes insignificant. The flame speed increases with the temperature of the unburned gas, T'_u. It is convenient to assume

$$v'_f = k' T'_u \quad ; \quad \text{where } k' = \text{constant.} \qquad (2\text{-}94)$$

When the thermodynamic properties of the gas are constant across the flame, a solution in closed form becomes possible.

The left and right sides of the flame front are indicated by subscripts L and R, respectively, and the unburned gas may be on either side. To distinguish between properties of the unburned and burned gas, subscripts u and b are used. The known quantities are thus P_L, Q_R, and s_u. The nomenclature is shown in the sketch below.

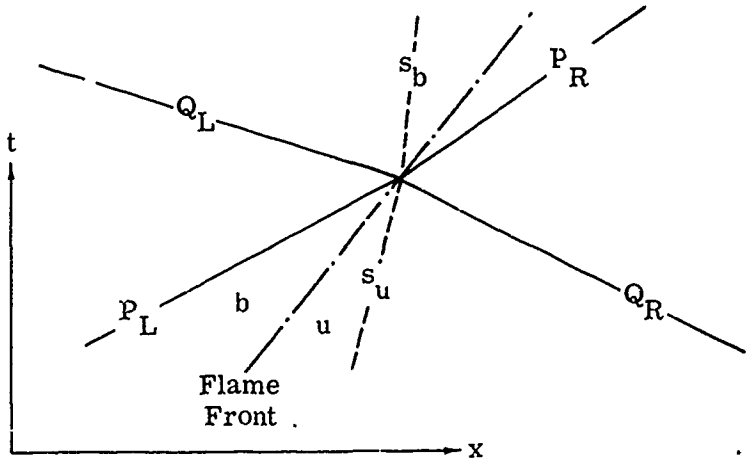

The following dimensionless variables may be used:

$$v_f = v_f'/a_o' = k\, a_u^2 \tag{2-95}$$

where

$$k = \frac{a_o'}{\gamma R'}\, k'$$

and

$$h = \frac{h'}{c_p'\, T_o'} \,. \tag{2-96}$$

The solution of the problem is then given by

$$a_b = 0.5(\nu + h/\nu) \quad , \tag{2-97}$$

$$a_u = 0.5(\nu - h/\nu) \quad , \tag{2-98}$$

and

$$s_b = s_u + \frac{2}{\gamma - 1} \ln \frac{a_b}{a_u} \tag{2-99}$$

where

$$\nu = \frac{\gamma - 1}{2} (P_L + Q_R + kh) \,. \tag{2-100}$$

Equations 2-97 and 2-98 together with the appropriate Riemann variables, P_L and Q_R, determine u_u and u_b according to Eqs. 2-69 and 2-70. Finally, the propagation velocity of the flame front relative to the duct is given by

$$w_f = w_f'/a_o' = u_u \pm v_f \tag{2-101}$$

where v_f follows from Eq. 2-95 and the upper sign must be used if the unburned gas is on the right side of the flame front.

Since heat addition cannot accelerate the burned gas relative to the flame front to more than the speed of sound in the burned gas (see Refs. 15, 64 and 87, and Subsec. 2.1.2), the inequality

$$\frac{|u_b - w_f|}{a_b} \leq 1 \tag{2-102}$$

must be satisfied. This condition points out the restriction, referred to earlier, on the extent to which the flame speed and the amount of heat released can be chosen independently. Rudinger (Ref. 88) stresses the fact that Eq. 2-102 should not be interpreted as implying an upper limit to the amount of heat that can be added, but rather as indicating a limit on the flame speed that can be assumed.

2.2.4.4 Discontinuous Area Changes

Gradual changes of the duct area can be handled according to the basic procedure described in Subsec. 2.2.2. Sometimes it is not necessary to have detailed knowledge of the flow during transition from one area to another but only of the over-all changes. It is then possible to approximate the variable-area duct by a discontinuous change between two sections of constant area. On the basis of steady-flow relationships the flow transition across the discontinuity is assumed to take place instantaneously.

The problem is then to find the flow conditions on the left and right sides of the area discontinuity by using the given areas, A_L and A_R, and the values of P_L and Q_R. For steady-flow calculations, it is preferable to use the flow Mach number, $M = u/a$, instead of u, and the equations to be solved are

$$a_L\left(\frac{2}{\gamma - 1} + M_L\right) = P_L \ , \tag{2-103}$$

$$a_R\left(\frac{2}{\gamma - 1} - M_R\right) = Q_R \ , \tag{2-104}$$

$$a_L^2\left(\frac{2}{\gamma - 1} + M_L^2\right) = a_R^2\left(\frac{2}{\gamma - 1} + M_R^2\right) , \tag{2-105}$$

and

$$\frac{\varphi(M_L)}{A_L} = \frac{\varphi(M_R)}{A_R} \tag{2-106}$$

where

$$\varphi(M) = \frac{1}{M}\left(\frac{2}{\gamma+1} + \frac{\gamma-1}{\gamma+1} M^2\right)^{\frac{\gamma+1}{2(\gamma-1)}} \tag{2-107}$$

i.e., $\varphi(M) = (A/A^*)$ as given in Eq. 2-4. It is tabulated in Refs. 1, 21 to 28, 33, and 34 (see Appendix A). Equations 2-103 to 2-106 are conveniently solved by iteration based on an initial estimate for one of the variables.

If the flow is entirely subsonic or entirely supersonic, there is no entropy change across the area discontinuity, and $s_L = s_R$. However, if the duct represents the diverging part of a supersonic diffuser, a normal shock may be located within the region that is approximated by a discontinuous area change. The flow then enters the discontinuity at known conditions of supersonic flow and one must find the conditions in the subsonic flow leaving the discontinuity. Suppose the flow direction is from left to right. Since the flow is supersonic, P_L, Q_L, and s_L, and therefore all conditions on the left side of the discontinuity, are known. Equations 2-104 and 2-105 can then be solved for a_R and M_R. Equation 2-106 must not be used since it applies only in isentropic flow. The entropy rise is finally computed from

$$s_R - s_L = \frac{1}{\gamma} \ln \frac{A_R\, \varphi(M_L)}{A_L\, \varphi(M_R)} \tag{2-108}$$

2.2.5 Shock Interactions

When two shock waves interact or when a shock wave meets a surface of discontinuity, the wave diagram in the vicinity of the interaction point is divided by the newly created waves into several regions. The flow conditions must be found for each region and matched to the flow in the adjoining regions by the methods discussed in the preceding subsections. It is often possible to write the solutions in closed form (see Ref. 63), but the resulting formulas are rather complicated, and it usually is easier to solve the equations by trial and error.

2.2.5.1 Shock Reflection from an Open End

The reflected wave is an expansion wave which is determined by the condition that either the discharge is subsonic at ambient pressure or it is sonic at greater than ambient pressure. If the flow behind the incident shock is supersonic, no reflected wave is formed. The first two cases are illustrated

for a P-shock in the following two sketches:

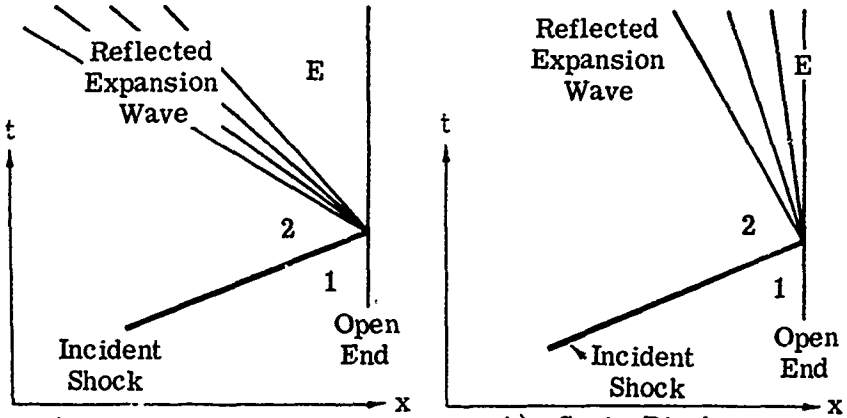

a) Subsonic Discharge b) Sonic Discharge

Regions 1 and 2 are determined by the prescribed problem. The discharge conditions are then given by

$$\begin{array}{lll} \text{Case a)} & u_E < a_E & \text{Case b)} \quad u_E = a_E \\ & a_E = a_2 (p_1/p_2)^{\frac{\gamma-1}{2\gamma}} & a_E = \frac{\gamma-1}{\gamma+1} P_2 \\ & u_E = P_2 - \frac{2}{\gamma-1} a_E & u_E = \frac{\gamma-1}{\gamma+1} P_2 \\ & s_E = s_2 & s_E = s_2 \end{array} \qquad (2\text{-}109)$$

For an incident Q-shock, replace P_2 by Q_2.

It is assumed here that the reflection process is instantaneous. All characteristics of the reflected expansion wave then originate from the same point so that a centered expansion wave is formed. The small lag in the actual establishment of the required exit pressure (see Ref. 79 and Subsec. 2.2.3) usually can be neglected in engineering applications.

2.2.5.2 Interaction of Two Shock Waves

Two shock waves interact when one overtakes the other (merging) or when one crosses the other. These two cases are illustrated in the following sketches.

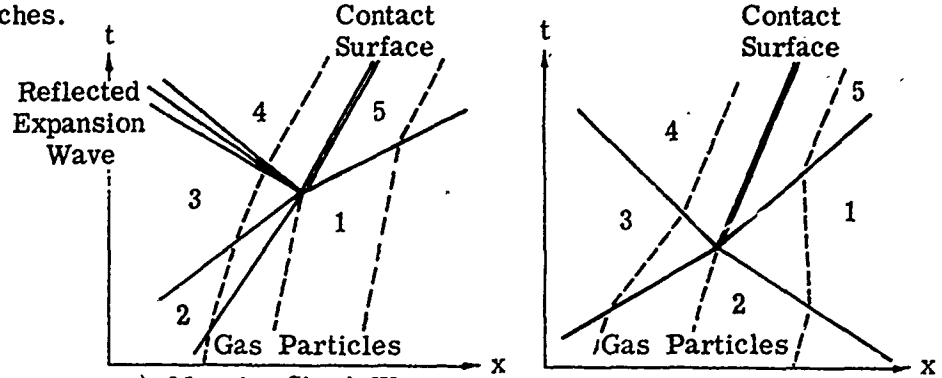

a) Merging Shock Waves b) Crossing Shock Waves

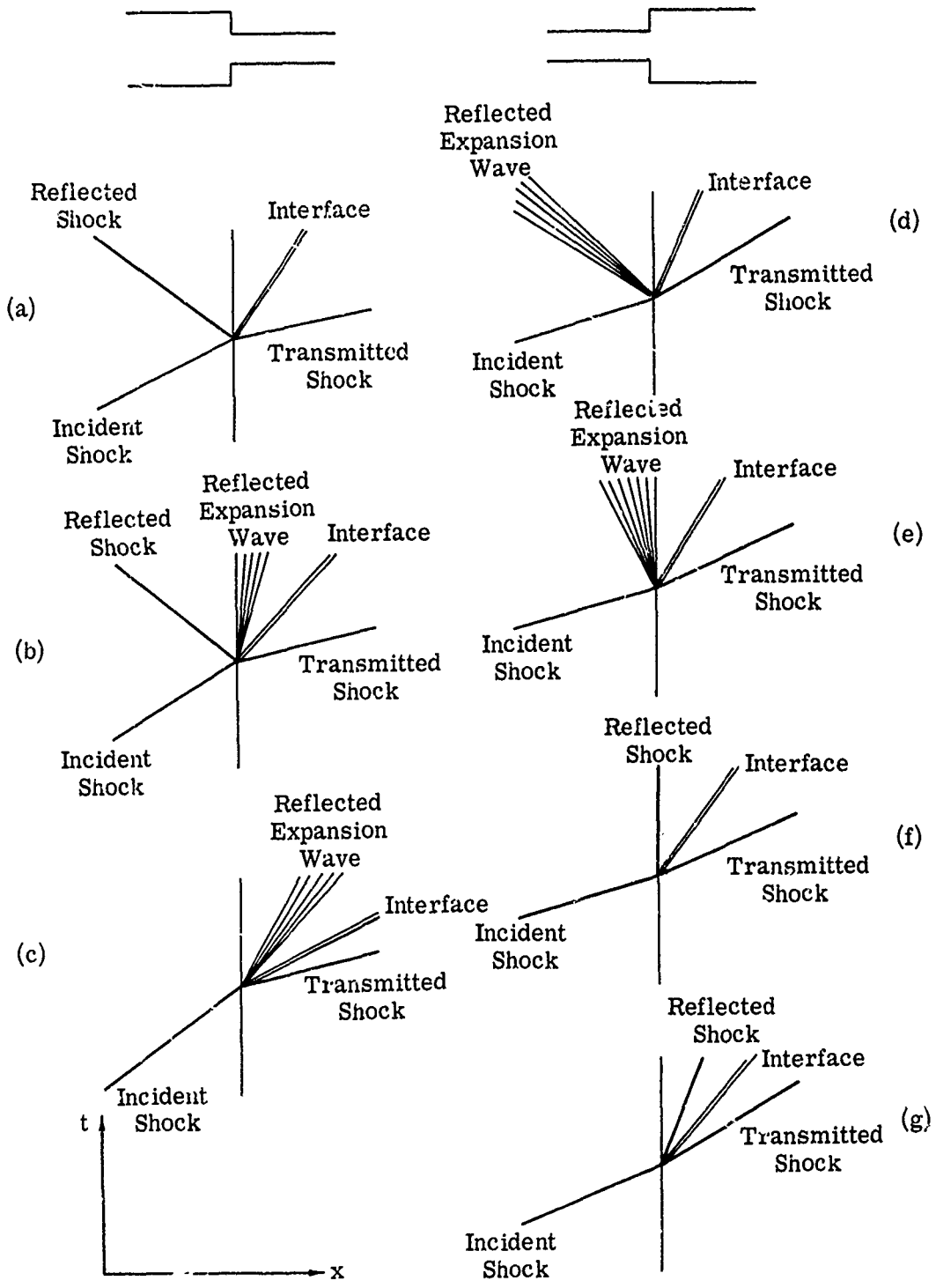
(a)
Reflected Shock
Interface
Transmitted Shock
Incident Shock
(b)
Reflected Shock
Reflected Expansion Wave
Interface
Transmitted Shock
Incident Shock
(c)
Reflected Expansion Wave
Interface
Transmitted Shock
Incident Shock
t
x
(d)
Reflected Expansion Wave
Interface
Transmitted Shock
Incident Shock
(e)
Reflected Expansion Wave
Interface
Transmitted Shock
Incident Shock
(f)
Reflected Shock
Interface
Transmitted Shock
Incident Shock
(g)
Reflected Shock
Interface
Transmitted Shock
Incident Shock

Regions 1, 2, and 3 are determined by the prescribed conditions, but 4 and 5 are unknown. An estimate for any of the unknown variables, say a_4, yields all conditions in region 4. The interface conditions then give $u_5 = u_4$ and $p_5 = p_4$. One of these variables is sufficient to compute all conditions in region 5, and the other serves as a check on the correctness of the original estimate.

The particle path through the interaction point becomes a contact surface after the interaction because the gases on either side of this surface experience different entropy rises.

2.2.5.3 Shock Interaction with a Discontinuous Area Change

An area discontinuity usually represents the net result of a gradual area change (see Subsec. 2.2.4.4), in which case the results of the calculations apply only at distances far enough removed from the discontinuity for steady flow to be re-established.

This interaction may lead to a considerable variety of wave patterns which depend on: 1) the direction of area increase with respect to the flow direction, 2) the direction in which the incident shock travels, and 3) whether the flow is entirely subsonic, entirely supersonic, or partly subsonic and partly supersonic. No general rules can be given and the actual wave pattern will have to be found in each case by trial and error. A number of possible wave patterns are shown in the sketches on the opposite page. Sometimes the reflected wave cannot travel upstream and is swept downstream (cases c and g), or it may split into two waves, one of which travels upstream while the other is swept downstream (case). A reflected shock may also be stationary in the divergent portion of the duct. Since this portion is approximated by a discontinuous area change, the wave pattern is that of case f.

In general, all matching conditions can be satisfied by only one wave pattern. However, if a shock which is strong enough to produce supersonic flow enters a contraction, it has been shown by Oppenheim, et al (Ref. 89) that there exists a narrow range of the contraction ratio for which all conditions can be satisfied by both type (b) and type (c) patterns. For the case without initial flow, Rudinger (Ref. 90), shows that this ambiguity is resolved in the sense that pattern (c) would be obtained if the problem were solved by a wave diagram for a gradual area change. If there is an initial flow the same result presumably holds, but this case has apparently not yet been investigated.

2.2.5.4 Interaction of a Shock with a Contact Surface

The interaction of an incident shock with a contact surface results in a transmitted shock and, in general, a reflected wave. In the illustrative sketch on the next page, the gas properties are known in the regions 1, 2, and 3 and may be found in regions 4 and 5 by trial and error as in Subsec. 2.2.5.2. Depending on the strength of the incident shock and on the specific-heat ratio and the speed of sound of the gases that form the interface, the transmitted shock may be stronger or weaker than the incident shock. Correspondingly, the reflected wave, indicated in the sketch as a single line, is either a shock or a centered expansion wave. These two cases are separated by the special

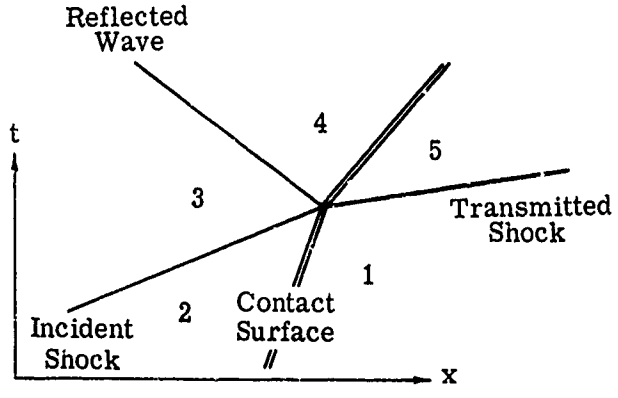

condition of no reflected wave. If the specific-heat ratio on the two sides of the interface is the same, the condition for no reflection is $a_2 = a_1$. If the incident wave travels in the gas with the higher (lower) speed of sound, the reflected wave is a shock (expansion) wave. In a general case there is no simple rule for predicting the type of the reflected wave.

2.2.5.5 Shock Interaction with a Flame Front

There are two possible shock interactions since the incident shock wave may travel either in the unburned gas or in the burned gas. These cases are illustrated in the sketches below where regions 1 to 3 are again known from the prescribed information.

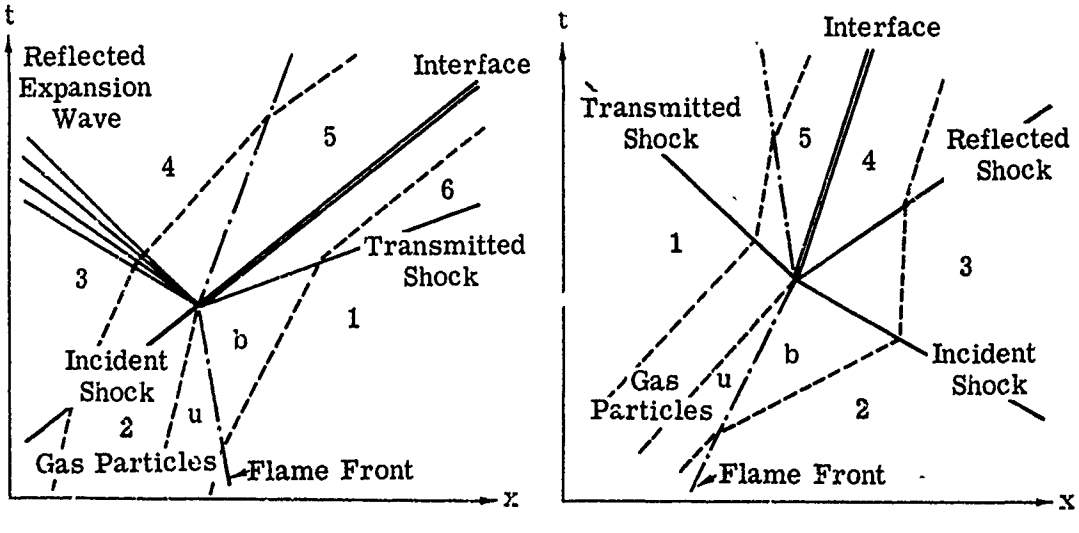

There are now three unknown regions, but the same trial and error method as before can be applied. Since the flame speed and heat release are normally given in terms of the state of the unburned gas, the estimate should be made for one of the variables on the unburned side of the flame front. The remaining procedure is the same as in the preceding cases. The limitations on the assumptions for the flame speed which were discussed in Subsec. 2.2.4.3 also apply in this case.

2.2.6 Shock Passage Through a Duct of Gradually Varying Cross Section

As a shock wave travels through a duct of variable cross section, its strength changes and a complicated nonsteady flow field of reflected and re-reflected waves is created. The entire flow may be obtained by means of the general procedures of Subsecs. 2.2.2 and 2.2.4.2. Several analytical approximations have been published which yield the shock strength as an explicit function of the duct area (Refs. 66-72). If the gas ahead of the shock wave is at rest, and the shock is of only moderate strength, (shock Mach number up to about 2.0), the relationship between shock Mach number and duct area is well approximated by the following simple formula given by Chester (Refs. 66 and 70).

$$A^K \left(M_S^2 - 1 \right) = \text{constant} \tag{2-110}$$

The exponent K is a slowly varying function of γ and M_S given by

$$K = 2 \left[\left(1 + \frac{2}{\gamma + 1} \frac{1 - \alpha^2}{\alpha} \right) \left(2\alpha + 1 + \frac{1}{M_S^2} \right) \right]^{-1} \tag{2-111}$$

where

$$\alpha^2 = \frac{(\gamma - 1) M_S^2 + 2}{2\gamma M_S^2 - \gamma + 1}$$

This function is plotted in Fig. 2-30 for $\gamma = 1.4$. Chisnell (Ref. 67) recommended the use of an estimated mean value of K derived from the shock strengths at both ends of the variable-area section. More elaborate expressions that may be applied to shock waves of arbitrary strength may be found in Refs. 67, 70, and 72.

2.2.7 Small Perturbation Approximations

If external forces, heat and mass addition, or variations of the duct area produce only small disturbances in an otherwise uniform or locally uniform flow, the basic differential equations (Eqs. 2-54 to 2-56) can be linearized. Numerous methods of finding solutions for general non-steady flows as well as for specific problems have been published (e.g., Refs. 69, 71, 73 to 76, 88, 91 and 92). The approach described here follows essentially the source distribution method of Mirels (Ref. 76), although a few of the results may also be found in some of the other references.

Consider a steady flow through a duct of constant cross section with the flow properties u, p, ρ, ... When this basic flow is only locally uniform, appropriate subscripts will be used to identify the different regions. Under the influence of disturbances, the flow is modified and the actual conditions are given by $u + \Delta u$, $p + \Delta p$, ..., where the small perturbations Δu, Δp, ... are the unknown functions of x and t. The linearized Equations (Eqs. 2-54 to 2-56), in terms of dimensionless variables, then become

$$\frac{\partial \Delta\rho}{\partial t} + u \frac{\partial \Delta\rho}{\partial x} + \rho \frac{\partial \Delta u}{\partial x} = \mu(x, t) \tag{2-112}$$

$$\frac{\partial \Delta u}{\partial t} + u \frac{\partial \Delta u}{\partial x} + \frac{1}{\rho} \frac{\partial \Delta p}{\partial x} = f(x, t) \tag{2-113}$$

$$\frac{\partial \Delta s}{\partial t} + u \frac{\partial \Delta s}{\partial x} = \frac{q(x, t)}{T} \tag{2-114}$$

where

$$\mu(x, t) = m(x, t) - \frac{\rho}{A} \left(\frac{\partial \Delta A}{\partial t} + u \frac{\partial \Delta A}{\partial x} \right) \tag{2-115}$$

The quantities μ, f, and q represent the sources of the disturbances whose distribution along the duct must be prescribed as a function of time.

As in the case of complete wave diagrams, the perturbations propagate along the characteristic directions u ± a and u and change in a manner that can be derived from Eqs. 2-112 to 2-114. In a wave diagram, the most convenient variables to describe the flow are the entropy, s, and the Riemann variables, P and Q, (see Subsec. 2.2.2). In the present approach, it is more convenient to replace the perturbations ΔP and ΔQ by the pressure perturbations, $\Delta p^{\pm}$, which are associated with the characteristic directions, u ± a. The net pressure perturbation at any point is then given by

$$\Delta p(x, t) = \Delta p^{+}(x, t) + \Delta p^{-}(x, t) \tag{2-116}$$

These perturbations are related to the perturbations of the Riemann variables, ΔP and ΔQ, and of the entropy, Δs, by the equations

$$\frac{\gamma}{2} \left(\frac{\Delta P}{a} - \Delta s \right) = \frac{\Delta p^{+}}{p} \tag{2-117}$$

and

$$\frac{\gamma}{2} \left(\frac{\Delta Q}{a} - \Delta s \right) = \frac{\Delta p^{-}}{p} \tag{2-118}$$

The perturbations Δp^{+}, Δp^{-}, and Δs can be obtained by integrating along the appropriate characteristics as outlined in the following section. Once they have been determined, the velocity perturbations may be found with the aid of the relationship

$$\begin{aligned} \Delta u(x, t) &= \frac{1}{\rho a} \left[\Delta p^{+}(x, t) - \Delta p^{-}(x, t) \right] \\ &= \frac{a}{\gamma} \left[\frac{\Delta p^{+}(x, t)}{p} - \frac{\Delta p^{-}(x, t)}{p} \right] \end{aligned} \tag{2-119}$$

The quantity $\rho a = \gamma p/a$ represents the characteristic acoustic resistance of the medium and is of great importance in all problems involving transmission or reflection of acoustic waves (see Ref. 93). In Eq. 2-119, the difference between the pressure perturbations must be used because a compression wave Δp^+ increases both the pressure and the velocity, while a compression wave Δp^- increases the pressure but decreases the velocity. Density and temperature perturbations are determined by the equations

$$\frac{\Delta\rho(x,t)}{\rho} = \frac{\Delta p(x,t)}{\gamma p} - (\gamma - 1)\,\Delta s(x,t) \tag{2-120}$$

and

$$\frac{\Delta T(x,t)}{T} = \frac{\Delta p(x,t)}{p} - \frac{\Delta\rho(x,t)}{\rho} \tag{2-121}$$

2.2.7.1 Basic Flow of Infinite Extent

Consider a steady flow in an infinitely long duct of constant cross section, and assume that certain sources of disturbances, μ, f, and q, are prescribed which are also functions of time and space, i.e., expressed in a coordinate system (ξ,τ) which is coincident with the (x, t) coordinate system. The problem is then to find the flow conditions at any point in the duct characterized by the coordinates x and t. These conditions can be influenced only by disturbances which propagate along the characteristics through this point (see the following sketch and also Subsec. 2.2.2.2).

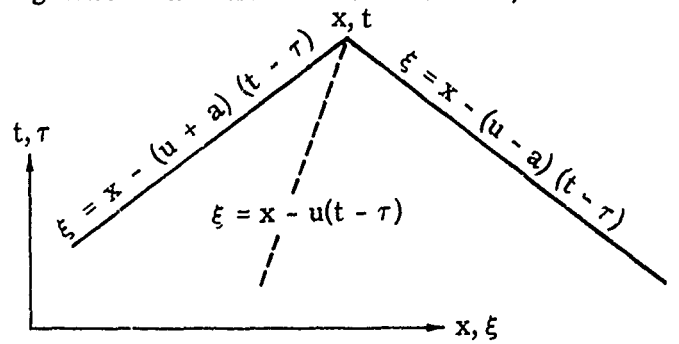

The equations of the characteristic lines through point (x, t) are given by

$$\begin{aligned} \xi &= x - (u + a)(t - \tau) \\ \xi &= x - (u - a)(t - \tau) \\ \xi &= x - u(t - \tau) \end{aligned} \tag{2-122}$$

The perturbations at point (x, t) can then be obtained by evaluating the following integrals along the appropriate characteristics:

$$\frac{\Delta p^+(x,t)}{p} = \frac{\gamma}{2}\int_{-\infty}^{t}\left\{\left[\frac{\mu(\xi,\tau)}{\rho} + (\gamma - 1)\,\frac{q(\xi,\tau)}{T} + \frac{f(\xi,\tau)}{a}\right]_{\xi = x-(u+a)(t-\tau)}\right\}d\tau \tag{2-123}$$

$$\frac{\Delta p^{-}(x,t)}{p} = \frac{\gamma}{2}\int_{-\infty}^{t}\left\{\left[\frac{\mu(\xi,\tau)}{\rho} + (\gamma - 1)\frac{q(\xi,\tau)}{T} - \frac{f(\xi,\tau)}{a}\right]_{\xi=x-(u-a)(t-\tau)}\right\} d\tau \tag{2-124}$$

$$\Delta s(x,t) = \frac{1}{T}\int_{-\infty}^{t}\left\{\left[q(\xi,\tau)\right]_{\xi=x-u(t-\tau)}\right\} d\tau \tag{2-125}$$

The remaining perturbations are given by Eqs. 2-116, and 2-119 to 2-121. In this manner, the flow conditions may be determined at any point of interest.

2.2.7.2 Uniform Basic Flow with a Moving Discontinuity

Consider a basic flow in which two regions, 1 and 2, are separated by a discontinuity which propagates along the duct with the velocity w. This discontinuity may be a shock wave, a contact surface, a flame front or an end of the duct, and the flow changes at the discontinuity need not be small. The disturbance waves which pass through point (x, t) are shown as lines a, b, and c in the following sketch.

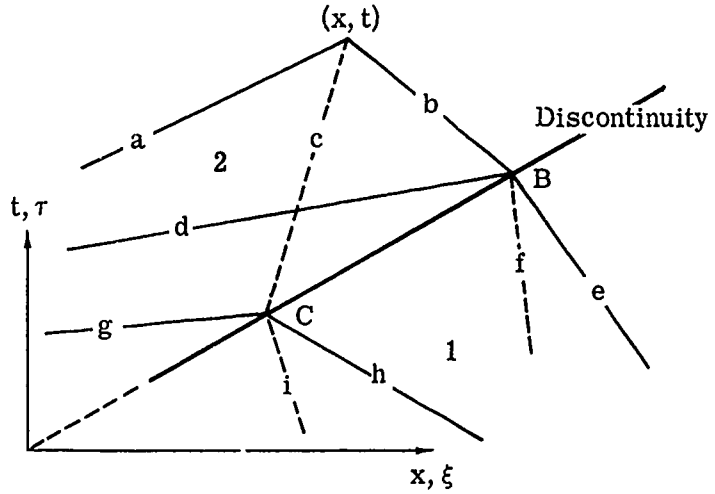

The sources along lines a, b, and c contribute directly to the conditions at point (x, t). Suppose lines b and c intersect the path of the discontinuity at points B and C respectively. The disturbance waves, d, e, and f, which arrive at point B interact with the discontinuity and generate further disturbances which also pass along b to the point (x, t). Similarly, disturbances from g, h, and i pass along the line c. The disturbance wave that arrives at B along line d in region 2 is symbolized by $\Delta p^{+}_{2,B,}$ and its reflected disturbance wave by $\Delta p^{-}_{2,B}$. Similarly the disturbance wave that arrives at C along line h in region 1, $\Delta p^{-}_{1,C}$, interacts with the discontinuity to produce the wave $\Delta s_{2,C}$ along line c. The ratio of the perturbation wave generated by interaction with the "incident" wave is called the transfer function for the particular interaction. Examples of transfer functions are $\Delta p^{-}_{2,B}/\Delta p^{+}_{2,B}$ and $\Delta s_{2,C}/\Delta p^{-}_{1,C}$. Several important transfer functions are given in the following subsection.

The solution for point (x, t) for the example of the preceding sketch is given by

$$\frac{\Delta p_2^+(x,t)}{p_2} = \left(I^+_{2,\xi_a}\right)^t_{-\infty} \tag{2-126}$$

$$\frac{\Delta p_2^-(x,t)}{p_2} = \left(I^-_{2,\xi_b}\right)^t_{\tau_B} + \frac{\Delta p^-_{2,B}/p_2}{\Delta p^+_{2,B}/p_2}\left(I^+_{2,\xi_d}\right)^{\tau_B}_{-\infty} + \frac{\Delta p^-_{2,B}/p_2}{\Delta p^-_{1,B}/p_1}\left(I^-_{1,\xi_e}\right)^{\tau_B}_{-\infty} + \frac{\Delta p^-_{2,B}/p_2}{\Delta s_{1,B}}\left(I_{1,\xi_f}\right)^{\tau_B}_{-\infty} \tag{2-127}$$

$$\Delta s_2(x,t) = \left(I_{2,\xi_c}\right)^t_{\tau_C} + \frac{\Delta s_{2,C}}{\Delta p^+_{2,C}/p_2}\left(I^+_{2,\xi_g}\right)^{\tau_C}_{-\infty} + \frac{\Delta s_{2,C}}{\Delta p^-_{1,C}/p_1}\left(I^-_{1,\xi_h}\right)^{\tau_C}_{-\infty} + \frac{\Delta s_{2,C}}{\Delta s_{1,C}}\left(I_{1,\xi_i}\right)^{\tau_C}_{-\infty} \tag{2-128}$$

where

$$\left(I^\pm_{j,\xi_n}\right)^t_{\tau_A} = \frac{\gamma_j}{2}\int_{\tau_A}^{t}\left[\frac{u_j(\xi,\tau)}{\rho_j} + (\gamma - 1)\frac{q_j(\xi,\tau)}{T_j} \pm \frac{f_j(\xi,\tau)}{a_j}\right]_{\xi_n} d\tau \tag{2-129}$$

and

$$\left(I_{j,\xi_n}\right)^t_{\tau_A} = \frac{1}{T_j}\int_{\tau_A}^{t}\left[q_j(\xi,\tau)\right]_{\xi_n} d\tau \tag{2-130}$$

Where subscript j denotes the flow region (1 or 2), ξ_n indicates the integration path (lines a, b, c...), and each integration must be carried out from its appropriate starting point, τ_A to $\tau = t$.

The integration paths in these equations are given by Eq. 2-122 and the coordinates of points B and C can be computed for a prescribed path

of the discontinuity. For example, if the discontinuity passes through the origin of the coordinate system, the coordinates of point C are given by

$$\tau_C = \frac{x - u_2 t}{w - u_2} \tag{2-131}$$

and

$$\xi_C = w\tau_C \tag{2-132}$$

Once Eqs. 2-126 to 2-128 have been evaluated, the flow conditions at point (x, t) follow from Eqs. 2-116, and 2-119 to 2-121.

Only the case of a single discontinuity has been described here; however, it is easy to extend the method to include additional discontinuities.

2.2.7.3 Transfer Functions for Wave Interactions

If a disturbance wave interacts with a discontinuity surface, its amplitude is, in general, modified and new waves are generated. Since the transfer function is the ratio of the amplitude of the modified or newly generated wave to that of the incident wave, it depends on the nature of the incident wave and of the discontinuity. A transfer function is usually derived by linearizing the equations of the steady-flow boundary conditions associated with the particular discontinuity (see Subsec. 2.2.3) for small perturbations Δp^+, Δp^-, and Δs of the flow on both sides of the discontinuity. The transfer function is then obtained from these equations as the ratio of the appropriate perturbations. Out of a great number of possible transfer functions, some of the more important ones are given below, the nomenclature being given by means of appropriate sketches. For the sake of consistency, the relative amplitudes of the pressure perturbations, $\Delta p^{\pm}/p$, are written in the transfer functions although the denominator could be omitted in some of the cases. Most of the following transfer functions were derived in their stated form by Mirels (Ref. 76); a number of them may also be found in the literature in different but equivalent forms (Refs. 75, 91 and 93).

Contact Surface

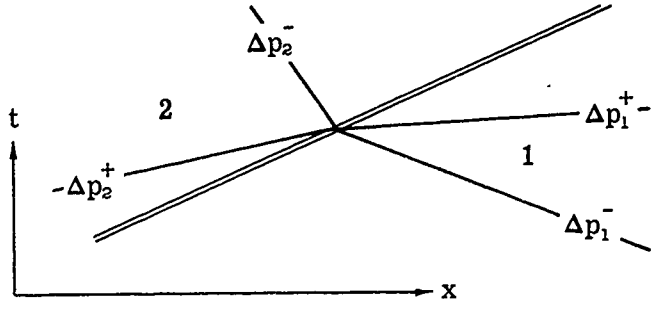

Pressure and velocity must be continuous across the surface.

Incident Wave Δp_1^-

$$\frac{\Delta p_1^+/p_1}{\Delta p_1^-/p_1} = \frac{\frac{\gamma_2 a_1}{\gamma_1 a_2} - 1}{\frac{\gamma_2 a_1}{\gamma_1 a_2} + 1} \qquad (2\text{-}133)$$

$$\frac{\Delta p_2^-/p_2}{\Delta p_1^-/p_1} = \frac{2}{\frac{\gamma_1 a_2}{\gamma_2 a_1} + 1} \qquad (2\text{-}134)$$

Incident Wave Δp_2^+

$$\frac{\Delta p_1^+/p_1}{\Delta p_2^+/p_2} = \frac{2}{\frac{\gamma_2 a_1}{\gamma_1 a_2} + 1} \qquad (2\text{-}135)$$

$$\frac{\Delta p_2^-/p_2}{\Delta p_2^+/p_2} = \frac{\frac{\gamma_1 a_2}{\gamma_2 a_1} - 1}{\frac{\gamma_1 a_2}{\gamma_2 a_1} + 1} \qquad (2\text{-}136)$$

Constant Velocity Discontinuity

This case corresponds to a duct terminated by a moving piston or a duct with a closed end.

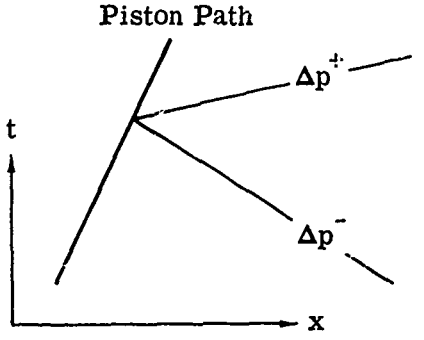

To the right of the piston $\dfrac{\Delta p^+/p}{\Delta p^-/p} = 1$

To the left of the piston $\dfrac{\Delta p^-/p}{\Delta p^+/p} = 1$ (2-137)

Subsonic Discharge

Constant-Pressure Discontinuity

This case corresponds to a tube with an open end.

For the left end

$$\frac{\Delta p^+/p}{\Delta p^-/p} = -1$$

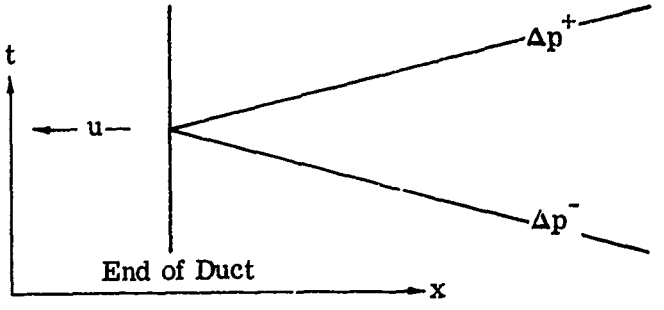

For the right end

$$\frac{\Delta p^-/p}{\Delta p^+/p} = -1 \qquad (2\text{-}138)$$

Subsonic Diffuser

Constant Stagnation Pressure and Stagnation Temperature

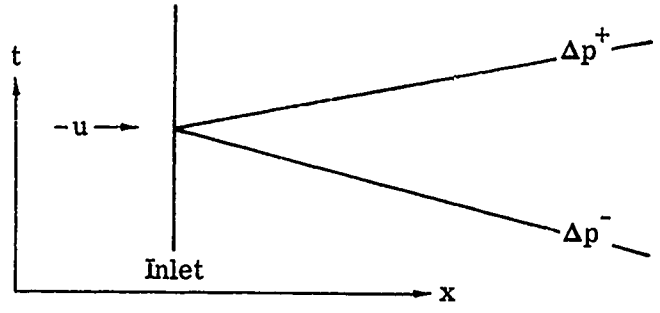

$$\text{For a left inlet} \quad \frac{\Delta p^+/p}{\Delta p^-/p} = -\frac{1 - M^2}{1 + M^2} \qquad (2\text{-}139)$$

$$\text{For a right inlet} \quad \frac{\Delta p^-/p}{\Delta p^+/p} = -\frac{1 - M^2}{1 + M^2}$$

where M is the Mach number of the unperturbed basic flow.

Supersonic Diffuser

Constant mass flow and stagnation temperature

The boundary is located at the shock in the diffuser.

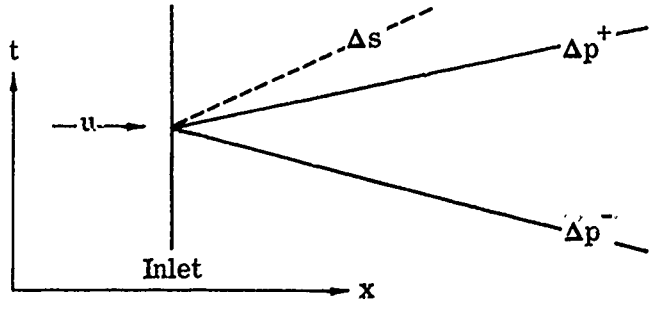

$$\text{For a left inlet} \quad \frac{\Delta p^+/p}{\Delta p^-/p} = \frac{1 - \gamma M + (\gamma - 1) M^2}{1 + \gamma M + (\gamma - 1) M^2} \qquad (2\text{-}140)$$

and

$$\frac{\Delta s}{\Delta p^-/p} = \frac{2(M - 1)}{\gamma[1 + (\gamma - 1) M]} \qquad (2\text{-}141)$$

For a right-end inlet, one must interchange the superscripts + and -; the Mach number of the unperturbed flow, M, is always taken as a positive quantity.

Shock Wave

Let regions 1 and 2 represent the low-pressure and high-pressure sides of the shock, respectively. The following relationships then apply to P-shocks.

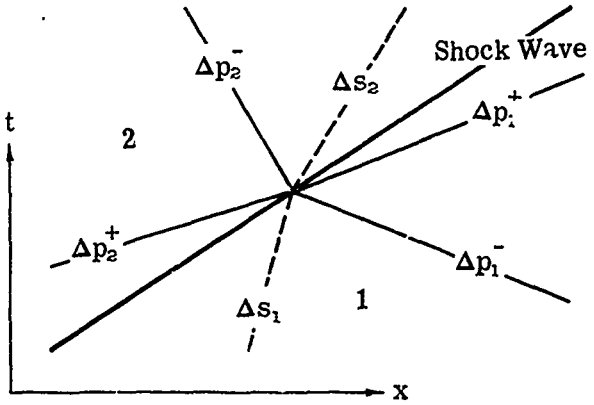

The corresponding equations for Q-shocks are obtained by interchanging the superscripts + and -, provided the shock Mach number, M_S, is always taken as a positive quantity. The following functions of M_S are used in order to allow the transfer functions to be written in a concise form.

$$y = \frac{(M_S^2 - 1)^2}{\gamma M_S^2 [(\gamma - 1) M_S^2 + 2]} \tag{2-142}$$

and

$$z = \frac{2(\gamma + 1) M_S^2}{(2\gamma M_S^2 - \gamma + 1)(M_S^2 + 1)} \tag{2-143}$$

Incident Wave Δp_2^+

$$\frac{\Delta p_2^-/p_2}{\Delta p_2^+/p_2} = \frac{z \frac{a_2}{a_1} - 1}{z \frac{a_2}{a_1} + 1} \tag{2-144}$$

$$\frac{\Delta s_2}{\Delta p_2^+/p_2} = y \left(\frac{\Delta p_2^-/p_2}{\Delta p_2^+/p_2} + 1 \right) \tag{2-145}$$

Incident Wave Δp_1^-

$$\frac{\Delta p_2^-/p_2}{\Delta p_1^-/p_1} = \frac{1 + z \left(1 - \frac{\gamma - 1}{\gamma + 1} \frac{M_S^2 - 1}{M_S} \right)}{1 + z \frac{a_2}{a_1}} \tag{2-146}$$

$$\frac{\Delta s_2}{\Delta p_1^-/p_1} = y \left(\frac{\Delta p_2^-/p_2}{\Delta p_1^-/p_1} - 1 \right) \tag{2-147}$$

Incident Wave Δp_1^+

$$\frac{\Delta p_2^-/p_2}{\Delta p_1^+/p_1} = \frac{1 - z\left(1 + \frac{\gamma - 1}{\gamma + 1}\frac{M_S^2 - 1}{M_S}\right)}{1 + z\,\frac{a_2}{a_1}} \tag{2-148}$$

$$\frac{\Delta s_2}{\Delta p_1^+/p_1} = y\left(\frac{\Delta p_2^-/p_2}{\Delta p_1^+/p_1} - 1\right) \tag{2-149}$$

Incident Wave Δs_1

$$\frac{\Delta p_2^-/p_2}{\Delta s_1} = -\frac{\gamma(\gamma - 1)\,(M_S^2 - 1)\,z}{(\gamma + 1)\,M_S\left(1 + z\,\frac{a_2}{a_1}\right)} \tag{2-150}$$

$$\frac{\Delta s_2}{\Delta s_1} = 1 + y\,\frac{\Delta p_2^-/p_2}{\Delta s_1} \tag{2-151}$$

Flame Front

The transfer functions associated with a flame front given here are derived with the assumption that:

1) $[(w_f - u_u)/a_u]^2 \ll 1$ and $[(w_f - u_b)/a_b]^2 \ll 1$

2) $v_f = \left|w_f - u_u\right| = \text{constant}$

3) $h' = \text{constant}$

As a consequence of the first assumption, the pressure in the burned gas is approximately equal to that in the unburned gas. Furthermore, in both the burned and the unburned gases, the stagnation temperature in a coordinate system fixed with respect to the flame front is approximately equal to the static temperature. The temperatures on the two sides of the flame are then related through the energy equation

$$(c_p'\,T')_u + h' = (c_p'\,T')_b \quad . \tag{2-152}$$

Since the thermodynamic properties of the gas are allowed to change across the flame front, the dimensionless entropies by definition (see Subsec. 2.2.1), are $\Delta s_u = \Delta s_u'/\gamma_u\,R_u'$ and $\Delta s_b = \Delta s_b'/\gamma_b\,R_b'$.

The entropy levels in the burned and unburned gases are specified as part of the unperturbed basic flow.

Let

$$\lambda = \frac{(c_p' T')_b}{(c_p' T')_u} \tag{2-153}$$

and also let

$$Y = \frac{1}{\gamma_b}\left(\frac{\gamma_u - 1}{\gamma_b - 1}\frac{\gamma_b}{\gamma_u}\frac{1}{\lambda} - 1\right) \tag{2-154}$$

and

$$Z = \frac{\gamma_u}{\gamma_b}(\gamma_b - 1)(\lambda - 1)\frac{v_f}{a_u} \quad . \tag{2-155}$$

The transfer functions are then given by the following equations which apply if the unburned gas is to the right of the flame front as shown in the sketch below. If the unburned gas is on the left side, the same equations apply provided that the superscripts + and - are interchanged, and that v_f is always taken as a positive quantity.

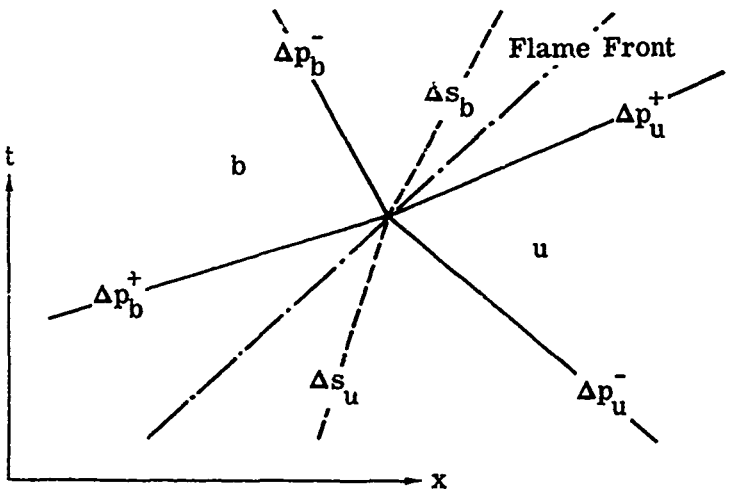

Incident Wave Δp_u^-

$$\frac{\Delta p_u^+/p_u}{\Delta p_u^-/p_u} = \frac{1 - Z - \frac{\gamma_u}{\gamma_b}\frac{a_b}{a_u}}{1 + Z + \frac{\gamma_u}{\gamma_b}\frac{a_b}{a_u}} \tag{2-156}$$

$$\frac{\Delta p_b^-/p_b}{\Delta p_u^-/p_u} = 1 + \frac{\Delta p_u^+/p_u}{\Delta p_u^-/p_u} \tag{2-157}$$

$$\frac{\Delta s_b}{\Delta p_u^-/p_u} = Y \frac{\Delta p_b^-/p_b}{\Delta p_u^-/p_u} \tag{2-158}$$

Incident Wave Δp_b^+

$$\frac{\Delta p_b^-/p_b}{\Delta p_b^+/p_b} = - \frac{1 + Z - \dfrac{\gamma_u\, a_b}{\gamma_b\, a_u}}{1 + Z + \dfrac{\gamma_u\, a_b}{\gamma_b\, a_u}} \tag{2-159}$$

$$\frac{\Delta p_u^+/p_u}{\Delta p_b^+/p_b} = 1 + \frac{\Delta p_b^-/p_b}{\Delta p_b^+/p_b} \tag{2-160}$$

$$\frac{\Delta s_b}{\Delta p_b^+/p_b} = Y \frac{\Delta p_u^+/p_u}{\Delta p_b^+/p_b} \tag{2-161}$$

Incident Wave Δs_u

$$\frac{\Delta p_u^+/p_u}{\Delta s_u} = \frac{\Delta p_b^-/p_b}{\Delta s_u} = - \frac{\gamma_u\, Z}{1 + Z + \dfrac{\gamma_u\, a_b}{\gamma_b\, a_u}} \tag{2-162}$$

$$\frac{\Delta s_b}{\Delta s_u} = \frac{1}{\lambda} \frac{\gamma_u - 1}{\gamma_b - 1} + Y \frac{\Delta p_u^+/p_u}{\Delta s_u} \tag{2-163}$$

2.3 Two- and Three-Dimensional Flow

The one-dimensional theory and methods outlined in Subsecs. 2.1 and 2.2 are adequate for determining the properties of flows in ducts which have neither rapidly changing cross sections nor rapidly changing flow direction. Since the pattern of the streamlines may be determined, one is able to deal with simple shock waves. This simplified approach has also been shown to be applicable to cowl-lip studies, where the duct radius is sufficiently large compared with the leading edge radius to give an approximation to infinite plane flow. In many problems, satisfactory solutions may be obtained by considering the duct flow as composed of two more-or-less independent components, i.e., a potential flow and a boundary-layer flow. The presence of shock waves not only produces rotational flow, but may set up iterated interactions between the shock regions in the boundary layer and in the so-called potential flow.

In three-dimensional flow the streamline pattern is not usually known. The equations may be formulated but solutions are obtainable only for a few special cases or under certain simplifying assumptions. Solutions are usually obtained by assuming that the flow is frictionless and isentropic, and subsequent corrections are made to account for the effects of viscosity and the presence of shock waves. In regions where the changes in entropy are small the solutions of the simplified equations give very good predictions of the flow properties.

The equations of three-dimensional flow, taking into account viscosity and heat transfer, have been expressed in varying degrees of complexity in such texts as Refs. 2, 3, 7, and 11 together with methods of solution for certain simplifying assumptions.

Solutions are obtained by approximations which linearize the equations, by transformations of the variables, or by numerical and graphical integration. Assumptions made to linearize or otherwise simplify the equations often limit the applicability of the solutions as well as the accuracy of the results. Numerical solutions, although tedious to obtain, may be made as accurate as one desires. However, the form of the solution or of the analysis as it proceeds does not usually indicate general trends or rules.

Many methods of solution and their application to bodies of various shapes are given in some detail in Section 8 of the Handbook (Ref. 10). In the current section, however, the emphasis is on flow in channels rather than around objects. For the analysis of this type of flow the method of characteristics is most suitable. This method requires a carefully detailed step-by-step procedure if it is to be used under any but the most simple conditions. The method may be applied to two-dimensional, general three-dimensional, and axially-symmetric flows. The underlying theory and the details of its practice can be found in aerodynamics textbooks, such as Refs. 2, 3, 7, and 15. One of the most complete treatments of the method is given by Ferri (Refs. 2, 18, and 94) who not only deals with two- and three-dimensional flows, but also includes the effects of rotationality in the flow. Various aspects of the method are dealt with in Refs. 95 to 99. Pietrangeli, et al (Ref. 95) applies the method to rotational flow through a circular conical inlet.

2.4 Boundary-Layer Correction

For calculations involving two-dimensional, three-dimensional, and axially-symmetric flows, it is customary to use the equations for frictionless flow and then adjust the solutions to account for viscous and heat-transfer effects. At moderate supersonic velocities these effects may be considered as concentrated in a viscous layer over all surfaces presented to the flow. The stream velocity is reduced to zero at the wall (no slip) and, by definition, reaches its free-stream value at a distance, δ, from the wall. (Where the velocity is found by measurement, δ is often taken to be the distance from the wall where the velocity has reached 99% of its free-stream value.)

In laminar flow, the velocity distribution is usually assumed to bear a linear relation to the boundary-layer thickness, δ, i.e.,

$$\left.\begin{aligned} \frac{V}{V_\infty} &= \left(\frac{y}{\delta}\right) \quad 0 < y < \delta \\ V &= V_\infty \quad \text{at} \quad y \geq \delta \end{aligned}\right\} \tag{2-164}$$

where

V = stream velocity at any distance, y, from the wall

V_∞ = free-stream velocity

In turbulent flows the velocity distribution is usually given by

$$\frac{V}{V_\infty} = \left(\frac{y}{\delta}\right)^{1/n} \quad 0 < y < \delta \tag{2-165}$$

where

n = a numerical parameter

and as before

$$V = V_\infty \quad \text{at} \quad y \geq \delta$$

Reference 100 gives the empirical relation between n and the Reynolds number as

$$n = 2.6\ \mathrm{Re}^{1/14} \tag{2-166}$$

The Reynolds number may be given in terms of the density and the viscosity, either of the free stream or of the flow adjacent to the wall, i.e.,

$$\mathrm{Re} = \frac{V_\infty \rho_\infty x}{\mu_\infty} \quad \text{or} \quad \frac{V_\infty \rho_w x}{\mu_w}$$

When Re is 10^6, Eq. 2-166 gives $n \sim 7$. This value has been verified experimentally and is often used in calculations over a much wider range of Reynolds numbers than Eq. 2-166 would allow.

The boundary-layer displacement thickness, δ^*, indicates the displacement distance of the streamlines due to the boundary layer and is given by

$$\delta^* = \int_{y=0}^{y=\delta} \left(1 - \frac{\rho V}{\rho_\infty V_\infty}\right) dy \qquad (2\text{-}167)$$

A third useful form of boundary-layer thickness is known as the momentum thickness, θ, or the thickness which will account for the loss of momentum due to the boundary layer. It is given by

$$\theta = \int_{y=0}^{y=\delta} \frac{\rho V}{\rho_\infty V_\infty} \left(1 - \frac{V}{V_\infty}\right) dy \qquad (2\text{-}168)$$

Numerical values of the ratios, θ/δ, δ^*/δ, and δ^*/θ are tabulated to five decimal places in Ref. 100 for $0.1 < M < 1.0$ ($\Delta M = 0.1$) and $1.0 < M < 10.0$ ($\Delta M = 0.04$) with $n = 5$, 7, 9, and 11. The values of δ^*/δ and δ^*/θ for $n = 7$ are repeated here in Table 2-1 to four significant figures.

In calculating duct flow characteristics, viscous corrections are usually made by considering the "effective" area, i.e., the geometric area reduced by the boundary-layer displacement thickness. The displacement thickness, δ^*, is generally taken as the appropriate correction in order to maintain the continuity of mass flow.

In the design of a new nozzle or duct, the contour is first determined by applying the characteristics method to potential flow. The actual or design contour is displaced from the potential contour (as shown in the sketch below) by the calculated values of δ^* at all points along the surface.

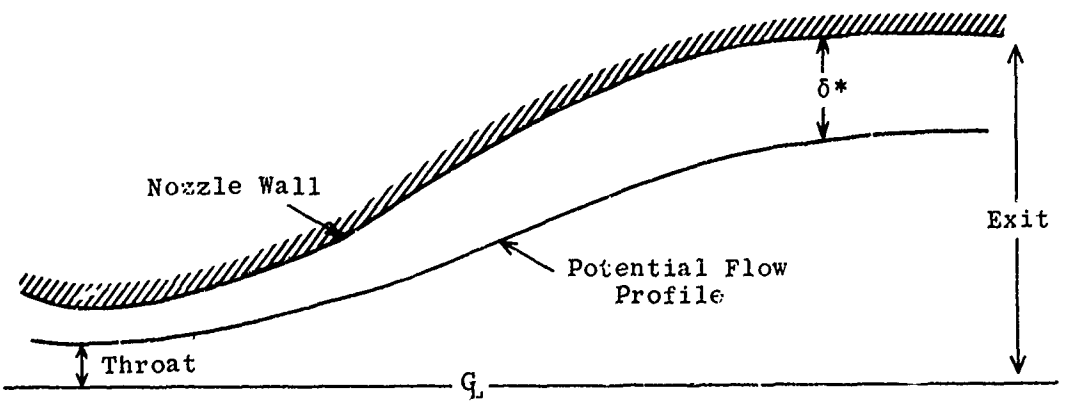

It will be shown that δ^* is dependent upon the Reynolds number of the flow and that the geometric correction therefore will be accurate for only a limited range of pressures and temperatures at the design Mach number. However, when a nozzle with a potential flow profile or a nozzle corrected for a specific Reynolds number is used for off-design Reynolds numbers, a further correction may be made by calculating the difference between the actual and initial boundary-layer thickness on the test-section walls. The "effective" area ratio of the nozzle may be used to determine the Mach number and pressure ratio of the test section (see Subsec. 2.1.8).

2.4.1 Boundary-Layer Thickness in Two-Dimensional Flow

Some of the most easily applied formulas derived by Tucker (Ref. 100) for the calculation of boundary-layer thickness along a surface are summarized below.

2.4.1.1 Zero Pressure Gradient

In a duct of uniform cross section and moderate length, the Mach number and static pressure are not changed appreciably by the growth of boundary layer. In this case the change in momentum thickness between two points, a and b, may be expressed as

$$\theta_b - \theta_a = 0.0254 \left[\frac{\mu_t \sqrt{T_t}}{p_t M\left(1 + \frac{\gamma - 1}{2} M^2\right)^3} \right]^{1/7} \left(x_b^{6/7} - x_a^{6/7}\right) \qquad (2\text{-}169)$$

for $\gamma = 1.4$ and "wall" values of density and the coefficient of viscosity, μ

or

$$\theta_b - \theta_a = 0.0254 \left[\frac{\mu_t \sqrt{T_t}}{p_t} \cdot \frac{\left(1 + \frac{\gamma - 1}{2} M^2\right)^2}{M} \right]^{1/7} \left(x_b^{6/7} - x_a^{6/7}\right) \qquad (2\text{-}170)$$

for free-stream values of the parameters,

where

x = distance measured from effective origin of boundary-layer development

M = average free-stream Mach number in the interval a to b.

Since the numerical coefficient in the above equations is dimensional, the method requires careful use of consistent units (i.e., the slug-foot-second system with temperature in degrees Rankine). The required boundary-layer displacement thickness, δ^*, is found from δ^*/θ, which is given as a function of M in Ref. 100 and also in the last column of Table 2-1.

Since the Mach number is assumed to be constant along a duct in which there is no pressure gradient, point a may be chosen as the beginning of the duct and b as the point at which boundary-layer corrections are required.

2.4.1.2 Positive or Negative Pressure Gradient

Where a negative pressure gradient exists, i.e., where dM/dx is positive, one has

$$\delta_b = 0.0218 \left(\frac{\mu_t \sqrt{T_t}}{\bar{x}\, p_t} \right)^{1/7} B_b \frac{dx}{dM} (D_b - D_a) + \delta_a A_a B_b \qquad (2\text{-}171)$$

For a positive pressure gradient

$$\delta_b = 0.0218 \left(\frac{\mu_t \sqrt{T_t}}{\bar{x}\, p_t} \right)^{1/7} A_b \frac{dx}{dM} (C_b - C_a) + \delta_a A_b B_a \qquad (2\text{-}172)$$

where δ is given in wall values of the parameters. The values of A, B, C, and D are given in Ref. 100 for the same range of parameters as θ/δ, etc., (see p. 59), and are presented in Table 2-1 for n = 7. According to Eq. 2-166 these values should be restricted to regimes where the Reynolds number is in the neighborhood of 10^6 (based on free-stream characteristics).

In Eqs. 2-171 and 2-172, $\bar{x}$ is the average distance of all points in the interval a to b from the origin of the boundary layer, and M is an average Mach number in the interval. The accuracy required and the value of dM/dx will dictate the length of the interval to be chosen.

In many cases the nozzle throat is assumed to be the region of zero boundary layer, and hence the origin for calculations. The error incurred by such a simplification may easily be estimated by a calculation of the boundary-layer growth in the subsonic portion of the nozzle (see Subsec. 6.2.3).

The foregoing step-by-step correction is applied to the contoured walls of a two-dimensional supersonic nozzle. The two plane walls are usually left uncorrected or else diverged to allow for the calculated displacement thickness at the entrance to the test section.

2.4.1.3 Estimated Test-Section Correction

The preceding subsection presents a method of calculating the boundary-layer correction along the length of a nozzle. If dM/dx is large, this method may require several calculations before the nozzle exit values are obtained. Kuethe and Epstein (Ref. 101) give a method of estimating the boundary-layer correction in a two-dimensional nozzle.

For turbulent boundary layer originating at a sonic throat and having a one-seventh power velocity profile in the test section,

$$\delta_\ell = 0.0677 \left(\frac{\mu_t \sqrt{T_t}}{p_t} \right)^{1/5} \ell^{4/5} \, h \qquad (2\text{-}173)$$

where

ℓ = axial length from throat to test section

h = a function of test-section Mach number (shown in Fig. 2-31)

The displacement thickness δ^* is given by

$$\delta^* = \delta_\ell \left\{ 1 - \frac{17.32}{M^2} \left[d^3 \log_e \left(\frac{d}{d - \cdot} \right) - \left(d^2 + \frac{d}{2} + \frac{1}{3} \right) \right] \right\} \qquad (2\text{-}174)$$

where

$$d = 1 + 5/M^2$$

The value of $\gamma = 1.4$ is implicit in these equations.

Maxwell and Jacocks (Ref. 102) have derived a method of boundary-layer correction for two-dimensional supersonic nozzles which does not require integrating the rate of boundary-layer growth. Their work is based on that of Tucker (Ref. 100) but differs from it in several ways. In the first place the boundary-layer thickness is non-dimensionalized by means of a factor based on the stagnation conditions. In this way the equations may be integrated with respect to distance and a boundary-layer thickness parameter obtained which may later be corrected for any stagnation conditions. A second feature of the method of Ref. 102 is that the x-coordinate is always taken in terms of the total nozzle length in order that the corrected nozzle may always be a scaled version of the original contour. In most methods, corrections are applied to transverse measurements while the length remains unchanged. The displacement thickness at the nozzle throat is calculated by Maxwell and Jacocks as a function of the nozzle geometry and the exit Mach number; in most methods it is assumed that the boundary-layer growth starts from zero at the throat. Reference 102 not only gives all necessary equations, but includes tables of Mach number and the boundary-layer parameter as a function of distance from throat to exit for Mach numbers from 1.5 to 8.0 with $\gamma = 1.4$ and a one-seventh velocity profile. An experimental verification of the accuracy of the method is given in the range of M from 1.5 to 5.

2.4.2 Boundary-Layer Correction for Axially-Symmetric Flow

Tucker (Ref. 100) also describes an iterative method for boundary-layer calculation in an axially-symmetric nozzle. The nozzle is divided into a number of segments, each of which is replaced by a conical section passing

between the end points of the segment as shown in the sketch below.

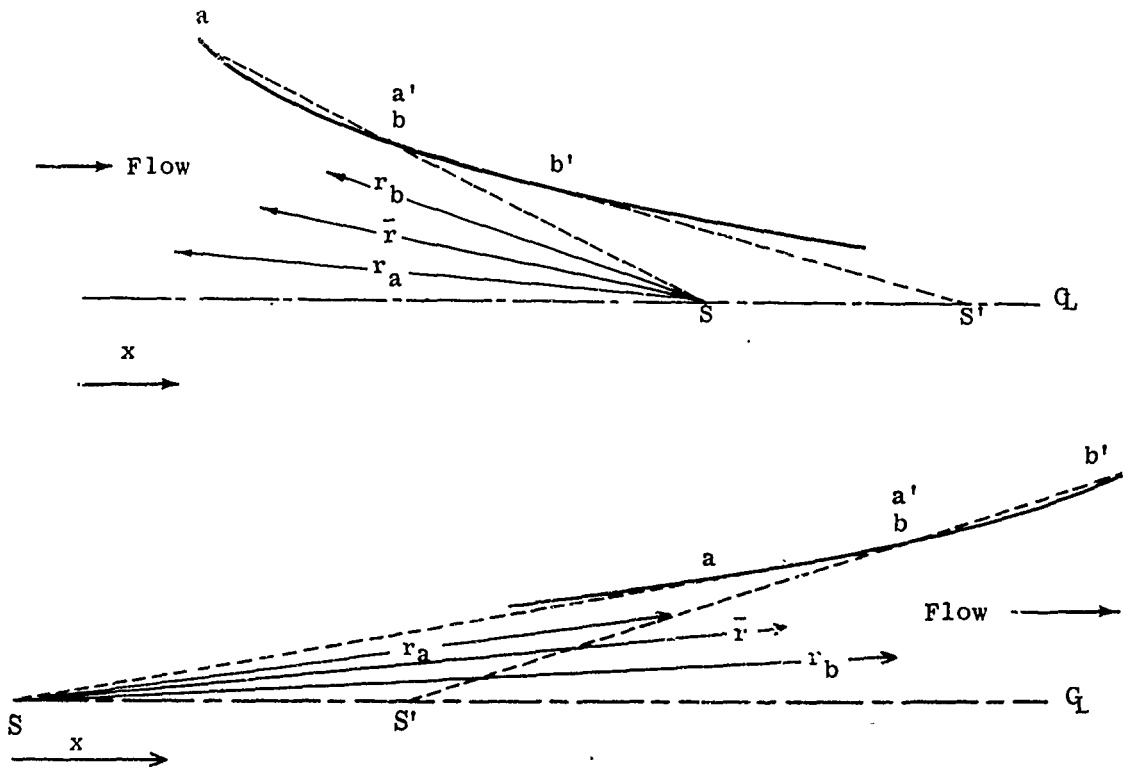

S and S' are apparent sink or source points for the first two segments, ab and a'b'. For each segment it is necessary to know the Mach number at a and b, i.e., M_a and M_b; the average distance, $\bar{x}$, from the effective origin of the boundary layer; and the average distance, $\bar{r}$, from the source or sink. When the pressure gradient is positive in the flow direction (i.e., subsonic divergent flow or supersonic convergent flow with dM/dr negative), then

$$\delta_b = 0.0218\left(\frac{\mu_t \sqrt{T_t}}{\bar{x}\, p_t}\right)^{1/7} A_b \frac{dr}{dM}\frac{\bar{r}}{r_b}(C_b - C_a) + \delta_a A_b B_a \frac{r_a}{r_b} \qquad (2\text{-}175)$$

For a negative pressure gradient in the flow direction (i.e., subsonic convergent flow or supersonic divergent flow with dM/dr positive)

$$\delta_b = 0.0218\left(\frac{\mu_t \sqrt{T_t}}{\bar{x}\, p_t}\right)^{1/7} B_b \frac{dr}{dM}\frac{\bar{r}}{r_b}(D_b - D_a) + \delta_a A_a B_b \frac{r_a}{r_b} \qquad (2\text{-}176)$$

Values of the constants A, B, C, and D are given in Table 2-1 and the conditions appertaining to them are listed in Subsec. 2.4.1.2. The value of δ^* required for correcting a nozzle contour is obtained from calculated values of δ and the value of δ^*/δ given in Table 2-1. The constants in the equations imply the use of the slug-foot-second system of units.

Intentionally Blank

Table 2-1

Functions for Use in Turbulent Boundary-Layer Correction.
Plane Flow (Subsec. 2.4.1) and Axisymmetric Flow (Subsec. 2.4.2)
(γ = 1.4 and n = 7)

(a) Subsonic Flow

M	A	B	C	D	δ^*/δ	δ^*/θ
0.10	1.000	1.000	0	0	0.1253	1.290
0.20	9.5605	0.1046	0.4999	5.6783	0.1264	1.304
0.30	35.0436	0.02854	0.5708	31.2372	0.1281	1.326
0.40	86.1217	0.01161	0.5929	100.4080	0.1305	1.357
0.50	109.1174	0.005913	0.6025	243.5969	0.1336	1.398
0.60	287.0373	0.003484	0.6075	494.4231	0.1373	1.447
0.70	439.2610	0.002277	0.6106	885.9813	0.1416	1.505
0.80	621.7789	0.001608	0.6126	1447.3937	0.1465	1.572
0.90	827.9143	0.001208	0.6141	2201.1412	0.1519	1.649
1.00	1049.2641	0.000953	0.6152	3161.3698	0.1578	1.734

Table 2-1 (Cont)

(b) Supersonic Flow

M	A	B	C	D	δ^*/δ	δ^*/θ
1.00	1.0000	1.0000	0	0	0.1578	1.7336
1.04	1.0865	0.9204	0.3886	0.4226	0.1603	1.7701
1.08	1.1733	0.8523	0.7450	0.8774	0.1629	1.8080
1.12	1.2600	0.7937	1.0741	1.3643	0.1656	1.8474
1.16	1.3459	0.7430	1.3795	1.8827	0.1683	1.8882
1.20	1.4307	0.6990	1.6646	2.4320	0.1711	1.9303
1.24	1.5137	0.6606	1.9319	3.0114	0.1739	1.9739
1.28	1.5946	0.6271	2.1838	3.6199	0.1768	2.0190
1.32	1.6730	0.5977	2.4223	4.2564	0.1798	2.0654
1.36	1.7485	0.5719	2.6488	4.9196	0.1828	2.1132
1.40	1.8208	0.5492	2.8650	5.6082	0.1859	2.1625
1.44	1.8897	0.5292	3.0720	6.3208	0.1890	2.2132
1.48	1.9548	0.5116	3.2709	7.0559	0.1922	2.2653
1.52	2.0160	0.4960	3.4626	7.8120	0.1954	2.3188
1.56	2.0732	0.4824	3.6481	8.5873	0.1987	2.3737
1.60	2.1261	0.4703	3.8279	9.3805	0.2020	2.4300
1.64	2.1749	0.4598	4.0028	10.1897	0.2053	2.4877
1.68	2.2193	0.4506	4.1734	11.0134	0.2087	2.5469
1.72	2.2594	0.4426	4.3402	11.8499	0.2121	2.6074
1.76	2.2952	0.4357	4.5036	12.6977	0.2156	2.6694
1.80	2.3268	0.4298	4.6641	13.5552	0.2191	2.7328
1.84	2.3541	0.4248	4.8221	14.4209	0.2226	2.7975
1.88	2.3774	0.4206	4.9780	15.2932	0.2261	2.8637
1.92	2.3966	0.4173	5.1319	16.1708	0.2297	2.9313
1.96	2.4120	0.4146	5.2844	17.0522	0.2333	3.0003
2.00	2.4236	0.4126	5.4355	17.9362	0.2369	3.0706
2.04	2.4316	0.4113	5.5857	18.8214	0.2405	3.1424
2.08	2.4361	0.4105	5.7351	19.7067	0.2441	3.2156
2.12	2.4373	0.4103	5.8840	20.5908	0.2478	3.2902
2.16	2.4354	0.4106	6.0326	21.4729	0.2515	3.3662
2.20	2.4304	0.4115	6.1810	22.3518	0.2552	3.4436
2.24	2.4227	0.4128	6.3295	23.2265	0.2589	3.5223
2.28	2.4124	0.4145	6.4783	24.0963	0.2626	3.6025
2.32	2.3996	0.4167	6.6276	24.9603	0.2663	3.6841
2.36	2.3844	0.4194	6.7774	25.8178	0.2700	3.7671
2.40	2.3672	0.4225	6.9280	26.6679	0.2738	3.8514
2.44	2.3479	0.4259	7.0795	27.5102	0.2775	3.9372
2.48	2.3268	0.4298	7.2321	28.3441	0.2813	4.0243
2.52	2.3041	0.4340	7.3859	29.1689	0.2850	4.1129
2.56	2.2798	0.4386	7.5411	29.9843	0.2888	4.2028
2.60	2.2541	0.4436	7.6979	30.7898	0.2925	4.2942
2.64	2.2272	0.4490	7.8563	31.5851	0.2962	4.3869
2.68	2.1992	0.4547	8.0164	32.3698	0.3000	4.4810
2.72	2.1702	0.4608	8.1786	33.1435	0.3037	4.5765
2.76	2.1403	0.4672	8.3427	33.9061	0.3075	4.6734

Table 2-1 (Cont)

M	A	B	C	D	δ^*/δ	δ^*/θ
2.80	2.1096	0.4740	8.5091	34.6574	0.3112	4.7717
2.84	2.0782	0.4812	8.6778	35.3972	0.3149	4.8714
2.88	2.0463	0.4887	8.8490	36.1253	0.3186	4.9724
2.92	2.0139	0.4965	9.0228	36.8416	0.3223	5.0749
2.96	1.9812	0.5048	9.1994	37.5461	0.3261	5.1787
3.00	1.9481	0.5133	9.3788	38.2386	0.3297	5.2840
3.04	1.9149	0.5222	9.5612	38.9191	0.3334	5.3906
3.08	1.8814	0.5315	9.7468	39.5877	0.3371	5.4986
3.12	1.8479	0.5412	9.9357	40.2444	0.3408	5.6080
3.16	1.8143	0.5512	10.1280	40.8890	0.3444	5.7188
3.20	1.7808	0.5615	10.3238	41.5219	0.3480	5.8309
3.24	1.7474	0.5723	10.5233	42.1428	0.3517	5.9445
3.28	1.7141	0.5834	10.7267	42.7521	0.3553	6.0594
3.32	1.6810	0.5949	10.9341	43.3496	0.3589	6.1757
3.36	1.6481	0.6068	11.1456	43.9357	0.3625	6.2934
3.40	1.6154	0.6190	11.3614	44.5102	0.3660	6.4125
3.44	1.5830	0.6317	11.5817	45.0735	0.3696	6.5330
3.48	1.5510	0.6448	11.8065	45.6236	0.3731	6.6548
3.52	1.5193	0.6582	12.0361	46.1666	0.3766	6.7780
3.56	1.4879	0.6721	12.2706	46.6967	0.3802	6.9027
3.60	1.4570	0.6864	12.5102	47.2161	0.3836	7.0287
3.64	1.4264	0.7011	12.7550	47.7248	0.3871	7.1560
3.68	1.3963	0.7162	13.0052	48.2231	0.3906	7.2848
3.72	1.3666	0.7318	13.2610	48.7112	0.3940	7.4150
3.76	1.3373	0.7478	13.5224	49.1891	0.3974	7.5465
3.80	1.3086	0.7642	13.7899	49.6571	0.4008	7.6794
3.84	1.2802	0.7811	14.0634	50.1153	0.4042	7.8137
3.88	1.2524	0.7985	14.3432	50.5640	0.4076	7.9493
3.92	1.2250	0.8163	14.6295	51.0032	0.4109	8.0864
3.96	1.1982	0.8346	14.9224	51.4331	0.4143	8.2248
4.00	1.1718	0.8534	15.2222	51.8540	0.4176	8.3646
4.04	1.1459	0.8727	15.5290	52.2660	0.4209	8.5058
4.08	1.1205	0.8925	15.8431	52.6692	0.4241	8.6484
4.12	1.0955	0.9128	16.1647	53.0639	0.4274	8.7923
4.16	1.0711	0.9336	16.4939	53.4502	0.4306	8.9377
4.20	1.0472	0.9550	16.8310	53.8283	0.4338	9.0844
4.24	1.0237	0.9768	17.1762	54.1984	0.4370	9.2325
4.28	1.0007	0.9993	17.5297	54.5606	0.4402	9.3819
4.32	0.9782	1.0222	17.8918	54.9150	0.4433	9.5328
4.36	0.9562	1.0458	18.2626	55.2620	0.4465	9.6850
4.40	0.9347	1.0699	18.6425	55.6015	0.4496	9.8386
4.44	0.9136	1.0946	19.0317	55.9338	0.4527	9.9936
4.48	0.8929	1.1199	19.4303	56.2590	0.4558	10.1499
4.52	0.8728	1.1458	19.8388	56.5773	0.4588	10.3077
4.56	0.8530	1.1723	20.2572	56.8880	0.4618	10.4668

Table 2-1 (Cont)

M	A	B	C	D	δ*/δ	δ*/θ
4.60	0.8337	1.1994	20.6859	57.1937	0.4649	10.6273
4.64	0.8149	1.2272	21.1252	57.4922	0.4679	10.7891
4.68	0.7964	1.2556	21.5753	57.7843	0.4708	10.9524
4.72	0.7784	1.2847	22.0366	58.0702	0.4738	11.1170
4.76	0.7608	1.3144	22.5091	58.3501	0.4767	11.2830
4.80	0.7436	1.3448	22.9934	58.6241	0.4796	11.4504
4.84	0.7268	1.3759	23.4897	58.8923	0.4825	11.6192
4.88	0.7104	1.4077	23.9982	59.1548	0.4854	11.7893
4.92	0.6943	1.4402	24.5193	59.4118	0.4883	11.9608
4.96	0.6787	1.4735	25.0533	59.6635	0.4911	12.1337
5.00	0.6634	1.5075	25.6005	59.9098	0.4939	12.3079
5.04	0.6484	1.5422	26.1613	60.1511	0.4967	12.4836
5.08	0.6339	1.5777	26.7360	60.3873	0.4995	12.6606
5.12	0.6196	1.6139	27.3249	60.6186	0.5023	12.8390
5.16	0.6057	1.6510	27.9283	60.8450	0.5050	13.0187
5.20	0.5921	1.6888	28.5467	61.0668	0.5077	13.1999
5.24	0.5789	1.7275	29.1804	61.2840	0.5104	13.3824
5.28	0.5660	1.7670	29.8297	61.4968	0.5131	13.5663
5.32	0.5533	1.8073	30.4951	61.7051	0.5158	13.7516
5.36	0.5410	1.8485	31.1769	61.9092	0.5184	13.9382
5.40	0.5290	1.8905	31.8754	62.1091	0.5210	14.1262
5.44	0.5172	1.9334	32.5912	62.3050	0.5236	14.3156
5.48	0.5058	1.9772	33.3246	62.4968	0.5263	14.5064
5.52	0.4946	2.0219	34.0760	62.6848	0.5288	14.6986
5.56	0.4837	2.0676	34.8459	62.8689	0.5314	14.8921
5.60	0.4730	2.1142	35.6346	63.0494	0.5339	15.0870
5.64	0.4626	2.1617	36.4427	63.2262	0.5364	15.2833
5.68	0.4525	2.2102	37.2705	63.3994	0.5389	15.4809
5.72	0.4425	2.2597	38.1186	63.5692	0.5414	15.6800
5.76	0.4329	2.3102	38.9873	63.7357	0.5438	15.8804
5.80	0.4234	2.3617	39.8772	63.8988	0.5463	16.0822
5.84	0.4142	2.4142	40.7887	64.0586	0.5487	16.2853
5.88	0.4052	2.4677	41.7224	64.2153	0.5511	16.4898
5.92	0.3965	2.5224	42.6787	64.3690	0.5535	16.6957
5.96	0.3879	2.5781	43.6580	64.5196	0.5559	16.9030
6.00	0.3795	2.6348	44.6611	64.6673	0.5582	17.1117
6.04	0.3714	2.6927	45.6884	64.8120	0.5606	17.3217
6.08	0.3634	2.7518	46.7403	64.9540	0.5629	17.5331
6.12	0.3556	2.8119	47.8175	65.0932	0.5652	17.7459
6.16	0.3480	2.8732	48.9206	65.2298	0.5675	17.9601
6.20	0.3406	2.9357	50.0500	65.3636	0.5698	18.1755
6.24	0.3334	2.9994	51.2064	65.4950	0.5720	18.3925
6.28	0.3263	3.0643	52.3903	65.6238	0.5742	18.6107
6.32	0.3195	3.1304	53.6025	65.7502	0.5765	18.8304
6.36	0.3127	3.1978	54.8434	65.8741	0.5787	19.0514

Table 2-1 (Cont)

M	A	B	C	D	δ^*/δ	δ^*/θ
6.40	0.3062	3.2664	56.1137	65.9957	0.5809	19.2739
6.44	0.2997	3.3363	57.4140	66.1150	0.5830	19.4976
6.48	0.2935	3.4076	58.7450	66.2321	0.5852	19.7228
6.52	0.2874	3.4801	60.1073	66.3470	0.5873	19.9493
6.56	0.2814	3.5540	61.5016	66.4597	0.5894	20.1772
6.60	0.2755	3.6292	62.9287	66.5704	0.5916	20.4065
6.64	0.2699	3.7058	64.3890	66.6790	0.5937	20.6371
6.68	0.2643	3.7838	65.8834	66.7855	0.5957	20.8692
6.72	0.2589	3.8632	67.4126	66.8901	0.5978	21.1026
6.76	0.2536	3.9441	68.9773	66.9928	0.5998	21.3374
6.80	0.2484	4.0264	70.5782	67.0936	0.6019	21.5736
6.84	0.2433	4.1101	72.2161	67.1926	0.6039	21.8111
6.88	0.2384	4.1954	73.8918	67.2898	0.6059	22.0500
6.92	0.2335	4.2822	75.6060	67.3852	0.6079	22.2903
6.96	0.2288	4.3705	77.3595	67.4789	0.6099	22.5319
7.00	0.2242	4.4604	79.1532	67.5709	0.6118	22.7749
7.04	0.2197	4.5519	80.9879	67.6613	0.6138	23.0193
7.08	0.2153	4.6449	82.8643	67.7500	0.6157	23.2651
7.12	0.2110	4.7396	84.7834	67.8372	0.6176	23.5122
7.16	0.2068	4.8359	86.7460	67.9228	0.6195	23.7608
7.20	0.2027	4.9339	88.7530	68.0069	0.6214	24.0107
7.24	0.1987	5.0336	90.8052	68.0896	0.6233	24.2619
7.28	0.1947	5.1350	92.9035	68.1707	0.6251	24.5146
7.32	0.1909	5.2381	95.0490	68.2505	0.6270	24.7687
7.36	0.1872	5.3430	97.2425	68.3289	0.6288	25.0240
7.40	0.1835	5.4496	99.4849	68.4059	0.6306	25.2808
7.44	0.1799	5.5581	101.7773	68.4816	0.6325	25.5390
7.48	0.1764	5.6684	104.1207	68.5560	0.6342	25.7985
7.52	0.1730	5.7805	106.5159	68.6291	0.6360	26.0594
7.56	0.1697	5.8945	108.9640	68.7009	0.6378	26.3217
7.60	0.1664	6.0104	111.4660	68.7715	0.6396	26.5853
7.64	0.1632	6.1282	114.0231	68.8410	0.6413	26.8503
7.68	0.1601	6.2479	116.6362	68.9092	0.6430	27.1167
7.72	0.1570	6.3696	119.3064	68.9763	0.6447	27.3846
7.76	0.1540	6.4933	122.0349	69.0423	0.6465	27.6536
7.80	0.1511	6.6191	124.8227	69.1071	0.6481	27.9243
7.84	0.1482	6.7468	127.6710	69.1709	0.6498	28.1962
7.88	0.1454	6.8767	130.5810	69.2336	0.6515	28.4693
7.92	0.1427	7.0086	133.5537	69.2953	0.6532	28.7440
7.96	0.1400	7.1427	136.5904	69.3560	0.6548	29.0201
8.00	0.1374	7.2789	139.6924	69.4156	0.6564	29.2975
8.04	0.1348	7.4173	142.8609	69.4743	0.6581	29.5762
8.08	0.1323	7.5579	146.0970	69.5320	0.6597	29.8564
8.12	0.1299	7.7007	149.4019	69.5888	0.6613	30.1379
8.16	0.1275	7.8457	152.7771	69.6447	0.6628	30.4208

Table 2-1 (Cont)

M	A	B	C	D	δ^*/δ	δ^*/θ
8.20	0.1251	7.9931	156.2238	69.6997	0.6644	30.7051
8.24	0.1228	8.1427	159.7433	69.7537	0.6660	30.9908
8.28	0.1206	8.2947	163.3368	69.8069	0.6675	31.2778
8.32	0.1184	8.4490	167.0059	69.8593	0.6691	31.5661
8.36	0.1162	8.6058	170.7520	69.9108	0.6706	31.8560
8.40	0.1141	8.7649	174.5762	69.9615	0.6721	32.1471
8.44	0.1120	8.9266	178.4802	70.0114	0.6736	32.4396
8.48	0.1100	9.0906	182.4654	70.0605	0.6751	32.7336
8.52	0.1080	9.2572	186.5332	70.1088	0.6766	33.0288
8.56	0.1061	9.4264	190.6851	70.1564	0.6781	33.3254
8.60	0.1042	9.5981	194.9227	70.2033	0.6796	33.6234
8.64	0.1023	9.7724	199.2475	70.2494	0.6810	33.9230
8.68	0.1005	9.9493	203.6609	70.2948	0.6825	34.2236
8.72	0.09873	10.1289	208.1646	70.3395	0.6839	34.5258
8.76	0.09698	10.3111	212.7601	70.3835	0.6853	34.8293
8.80	0.09527	10.4961	217.4492	70.4268	0.6868	35.1343
8.84	0.09360	10.6838	222.2333	70.4694	0.6882	35.4406
8.88	0.09196	10.8743	227.1143	70.5115	0.6896	35.7481
8.92	0.09035	11.0677	232.0936	70.5528	0.6910	36.0573
8.96	0.08878	11.2638	237.1735	70.5936	0.6923	36.3677
9.00	0.08724	11.4629	242.3552	70.6337	0.6937	36.6794
9.04	0.08573	11.6648	247.6406	70.6732	0.6951	36.9926
9.08	0.08425	11.8697	253.0316	70.7122	0.6964	37.3072
9.12	0.08280	12.0775	258.5299	70.7505	0.6977	37.6230
9.16	0.08138	12.2884	264.1373	70.7883	0.6991	37.9402
9.20	0.07999	12.5023	269.8559	70.8255	0.7004	38.2590
9.24	0.07862	12.7193	275.6873	70.8622	0.7017	38.5789
9.28	0.07728	12.9393	281.6337	70.8983	0.7030	38.9003
9.32	0.07597	13.1626	287.6968	70.9339	0.7043	39.2232
9.36	0.07469	13.3889	293.8788	70.9690	0.7056	39.5474
9.40	0.07343	13.6185	300.1817	71.0036	0.7069	39.8730
9.44	0.07220	13.8514	306.6073	71.0376	0.7081	40.1998
9.48	0.07099	14.0875	313.1579	71.0712	0.7094	40.5280
9.52	0.06980	14.3269	319.8352	71.1043	0.7106	40.8578
9.56	0.06864	14.5697	326.6417	71.1369	0.7119	41.1887
9.60	0.06750	14.8158	333.5795	71.1690	0.7131	41.5212
9.64	0.06638	15.0654	340.6508	71.2007	0.7143	41.8552
9.68	0.06528	15.3184	347.8575	71.2319	0.7156	42.1902
9.72	0.06421	15.5750	355.2020	71.2627	0.7168	42.5267
9.76	0.06315	15.8350	362.6866	71.2931	0.7180	42.8646
9.80	0.06212	16.0986	370.3136	71.3230	0.7191	43.2040
9.84	0.06110	16.3658	378.0854	71.3525	0.7203	43.5448
9.88	0.06011	16.6367	386.0043	71.3816	0.7215	43.8867
9.92	0.05913	16.9112	394.0728	71.4103	0.7227	44.2302
9.96	0.05818	17.1895	402.2931	71.4385	0.7238	44.5750
10.00	0.05724	17.4715	410.6677	71.4664	0.7250	44.9212

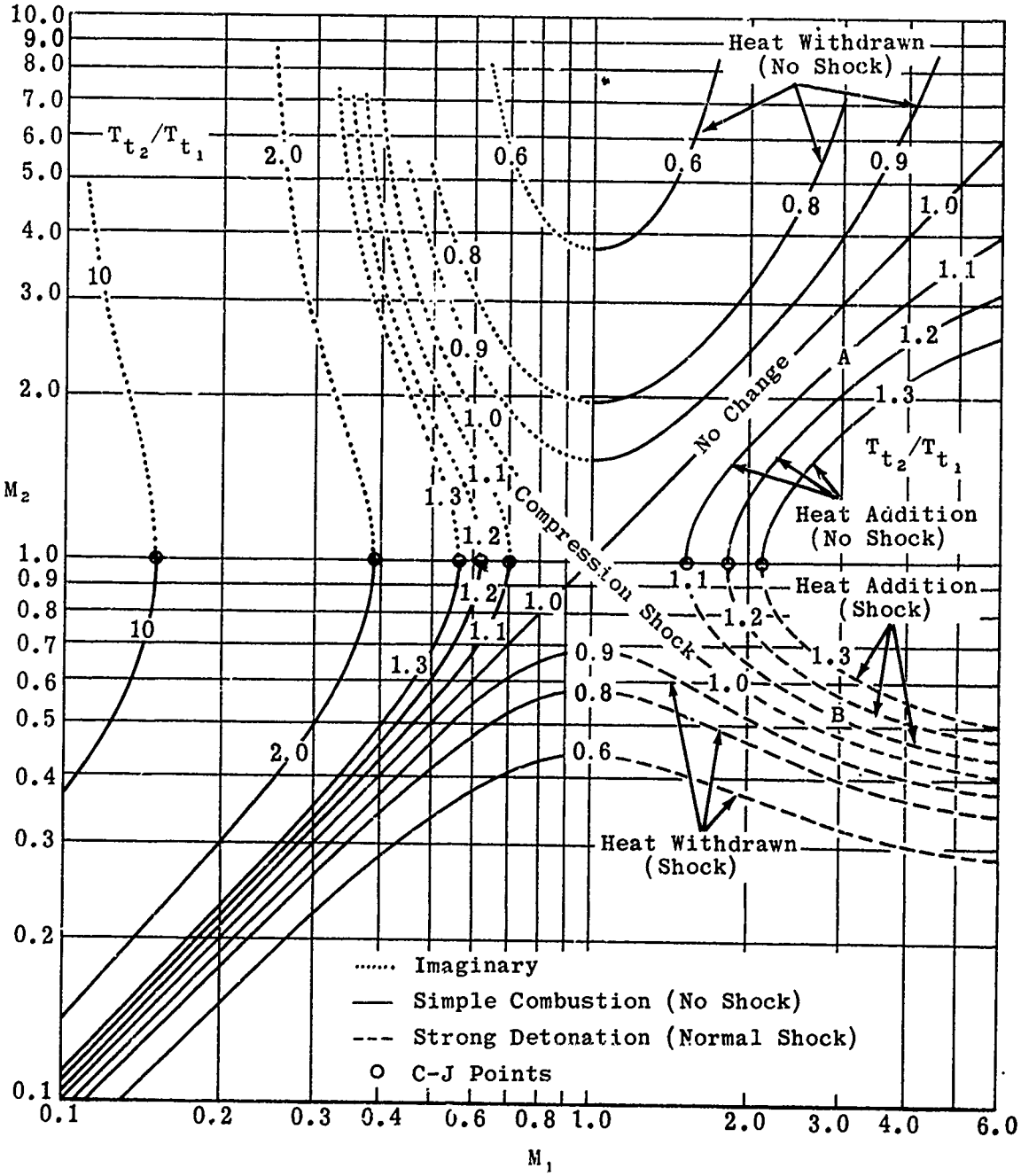

Fig. 2-1. Mach numbers upstream and downstream of a temperature discontinuity; $\gamma = 1.4$ (see Subsec. 2.1.2).

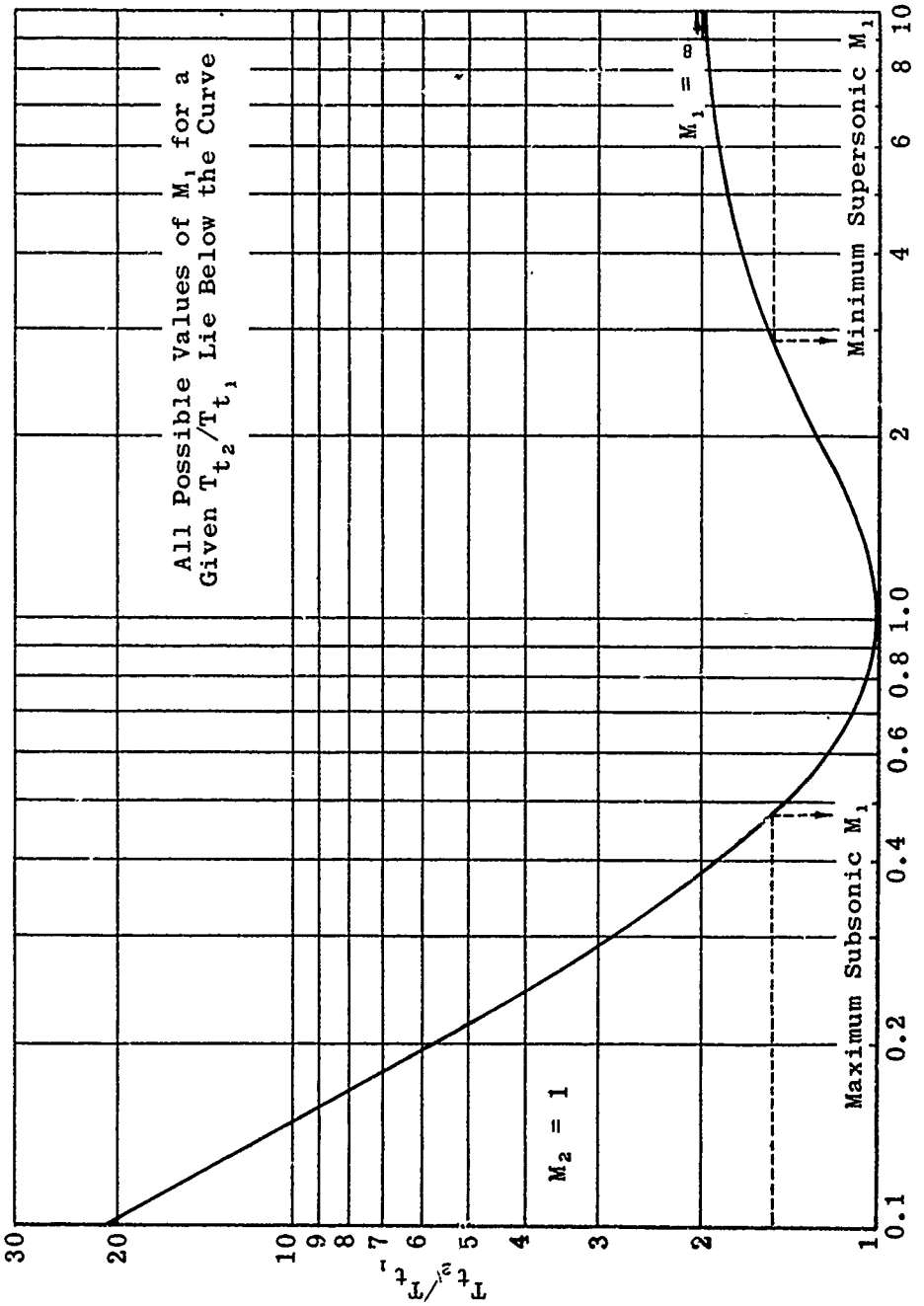

Fig. 2-2. Temperature rise through a Chapman-Jouguet detonation as a function of initial Mach number; $\gamma = 1.4$.

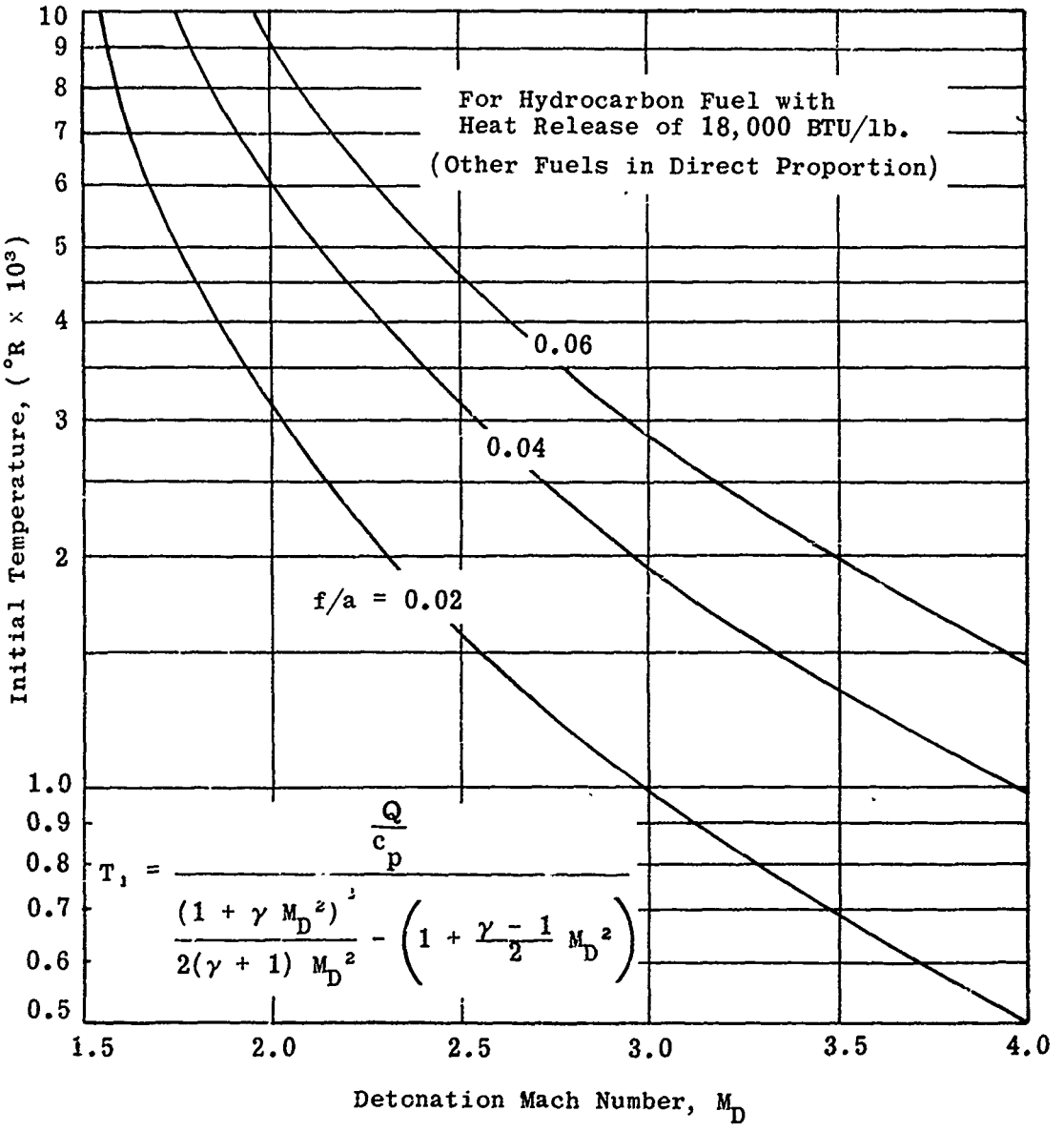

Fig. 2-3. Initial temperature vs detonation Mach number; f/a = 0.02, 0.04, 0.06; γ = 1.4.

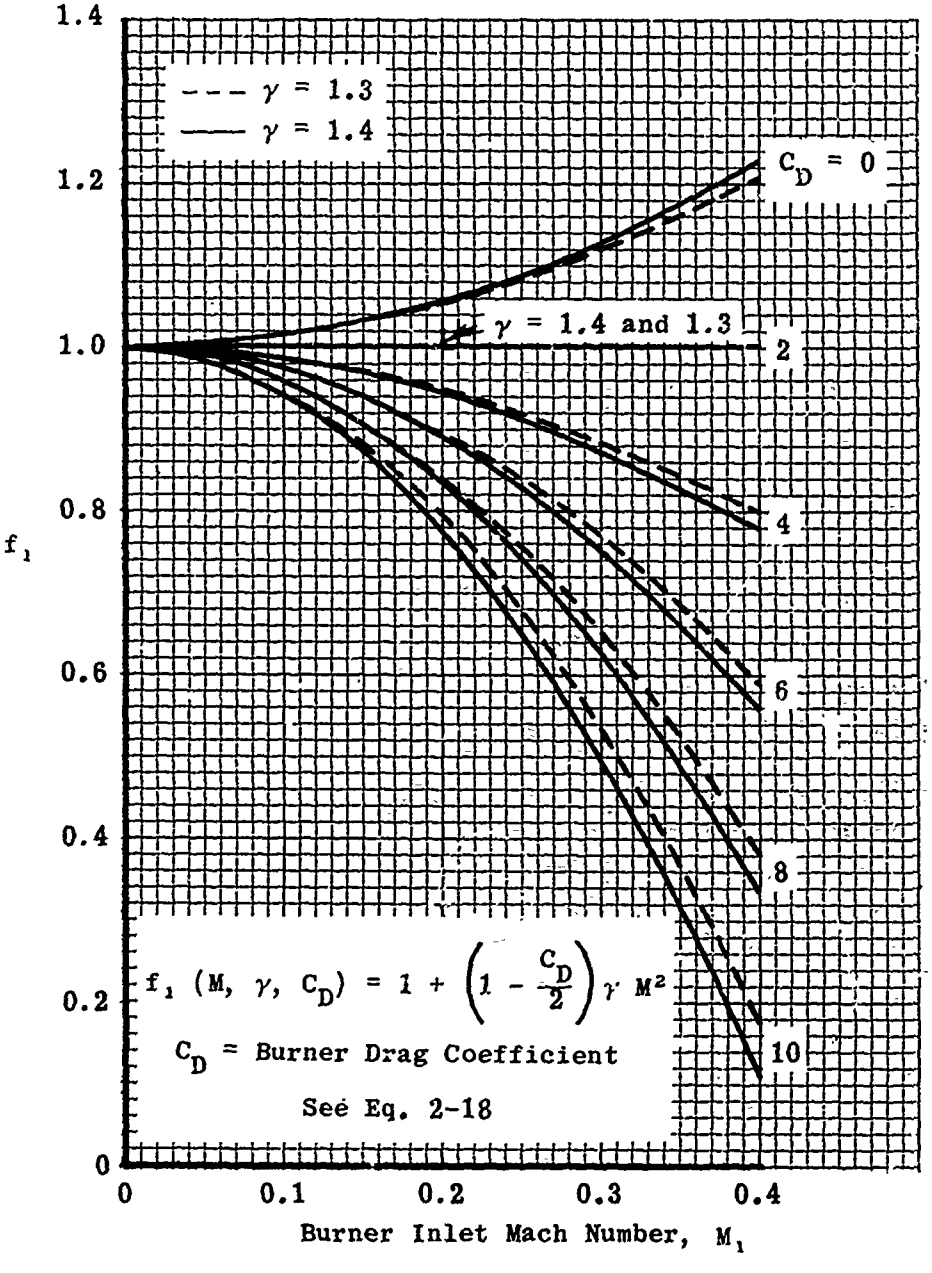

Fig. 2-4. Plot of f_1 for $M \leq 0.4$; C_D = 0 to 10; and γ = 1.3 and 1.4.

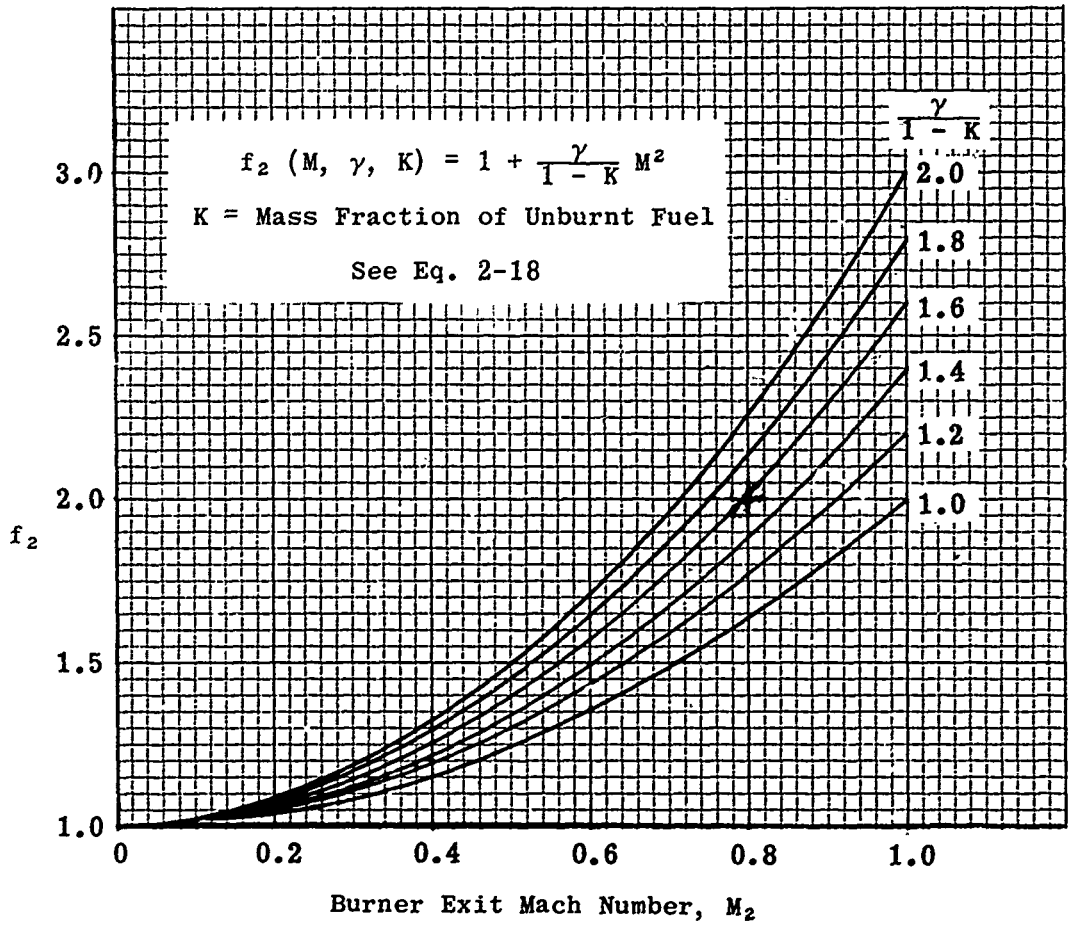

Fig. 2-5. Plot of f_2 for $M \leq 1.0$ and $\frac{\gamma}{1-K}$ = 1.0 to 2.0.

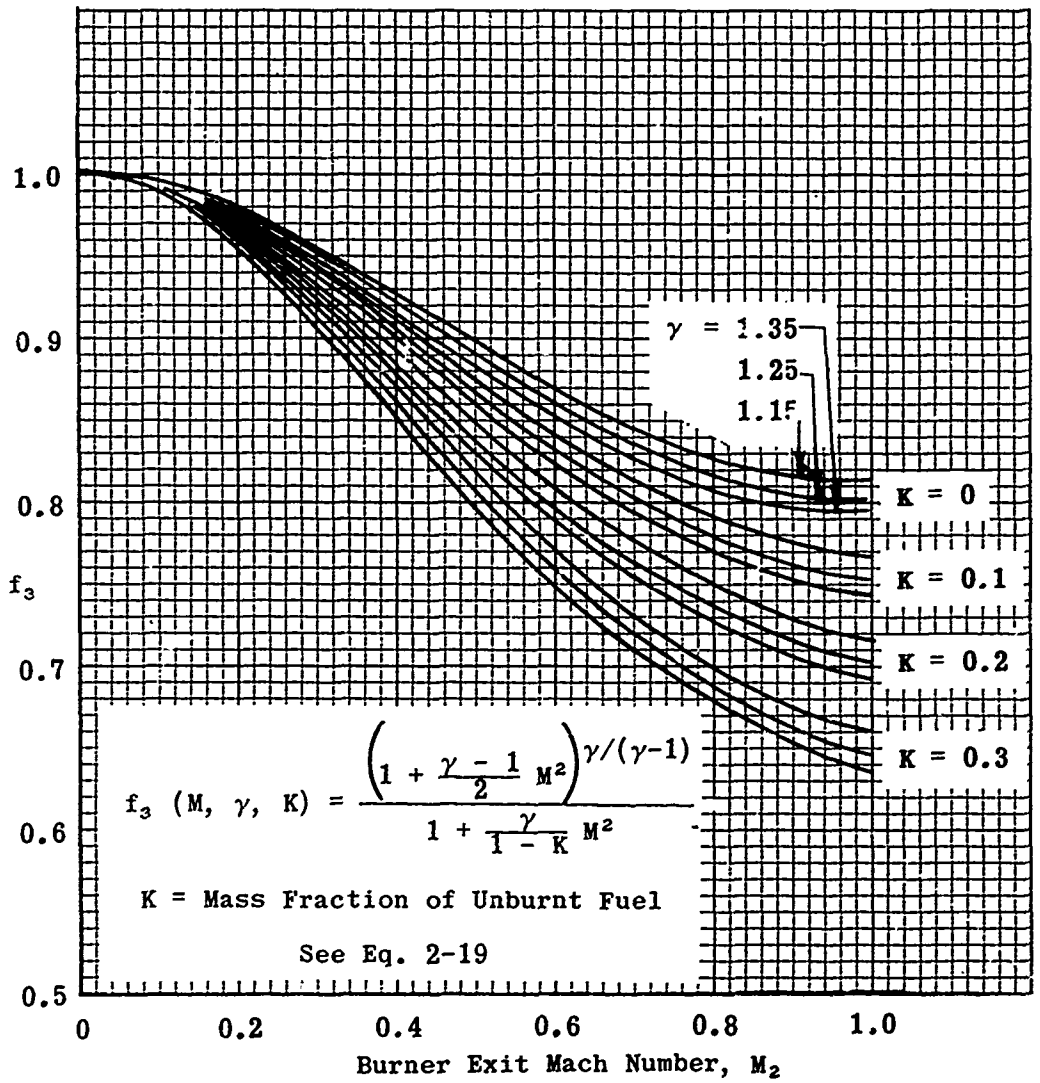

Fig. 2-6. Plot of f_3 for $M \leq 1.0$; K = 0 to 0.3; and γ = 1.15, 1.25, and 1.35.

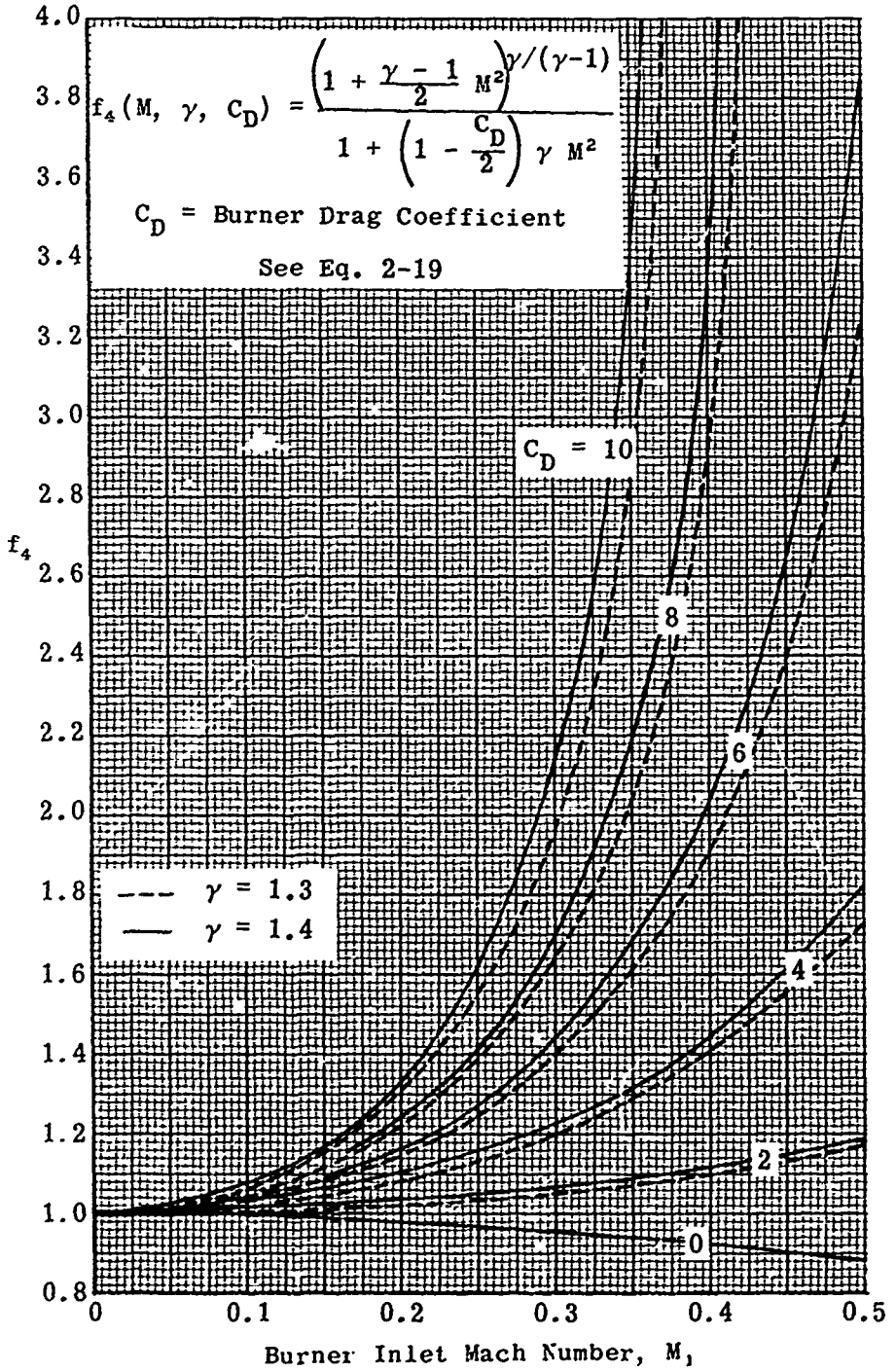

Fig. 2-7. Plot of f_4 for $M < 0.5$; C_D = 0 to 10; and γ = 1.3 and 1.4.

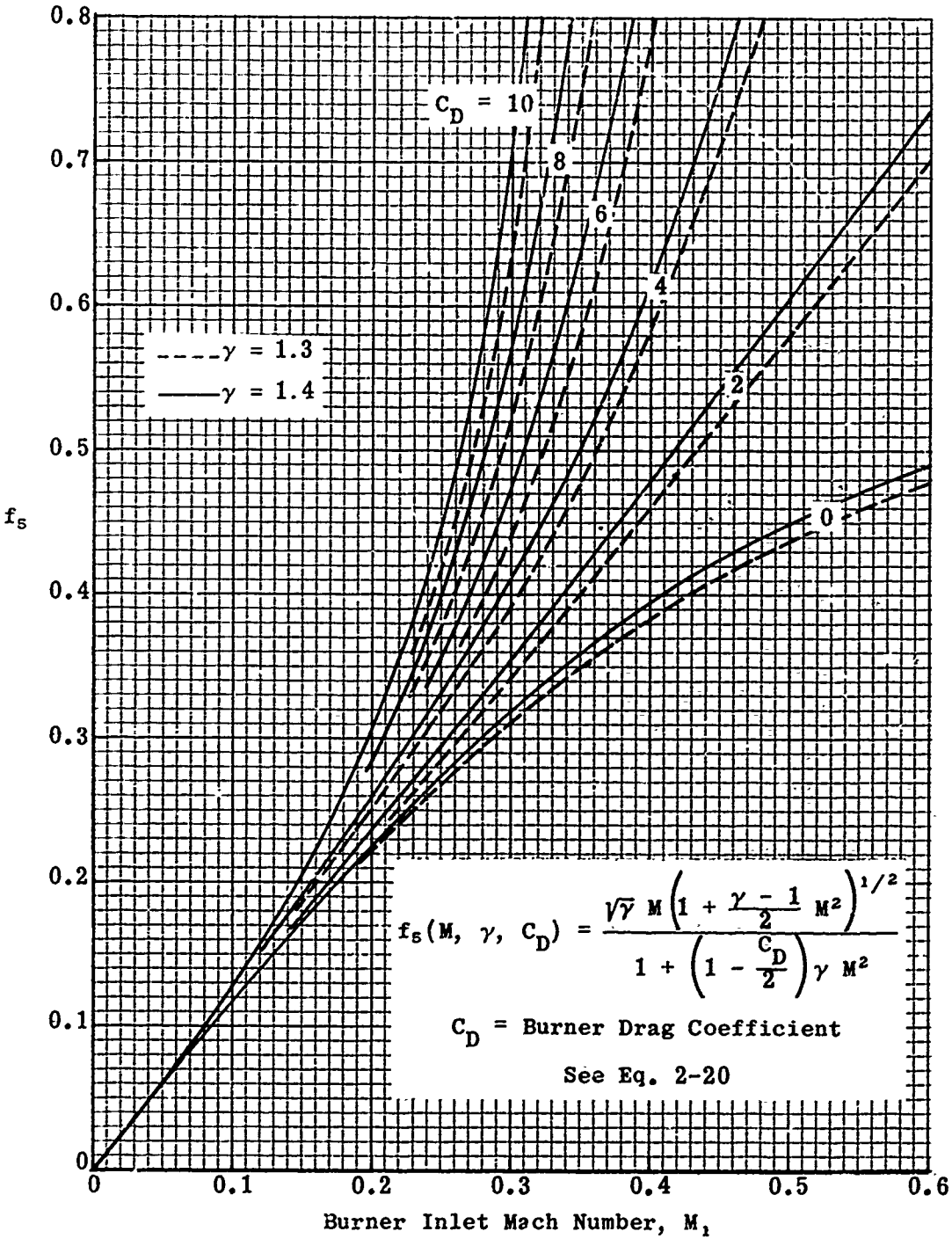

Fig. 2-8. Plot of f_s for $M \leq 0.6$; C_D = 0 to 10; and γ = 1.3 and 1.4

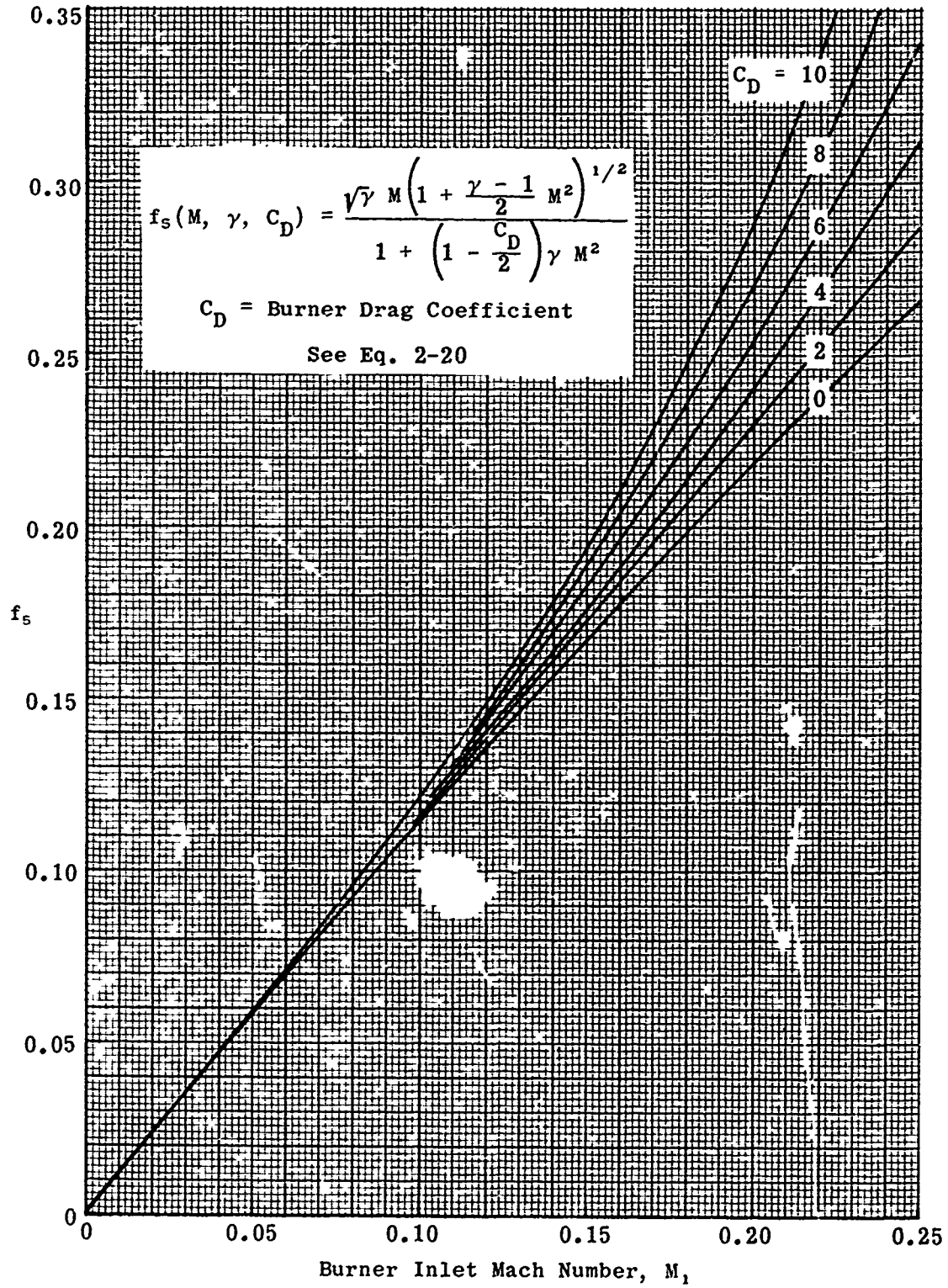

Fig. 2-9. Plot of f_s for $M \leq 0.25$; $C_D = 0$ to 10; and $\gamma = 1.3$.

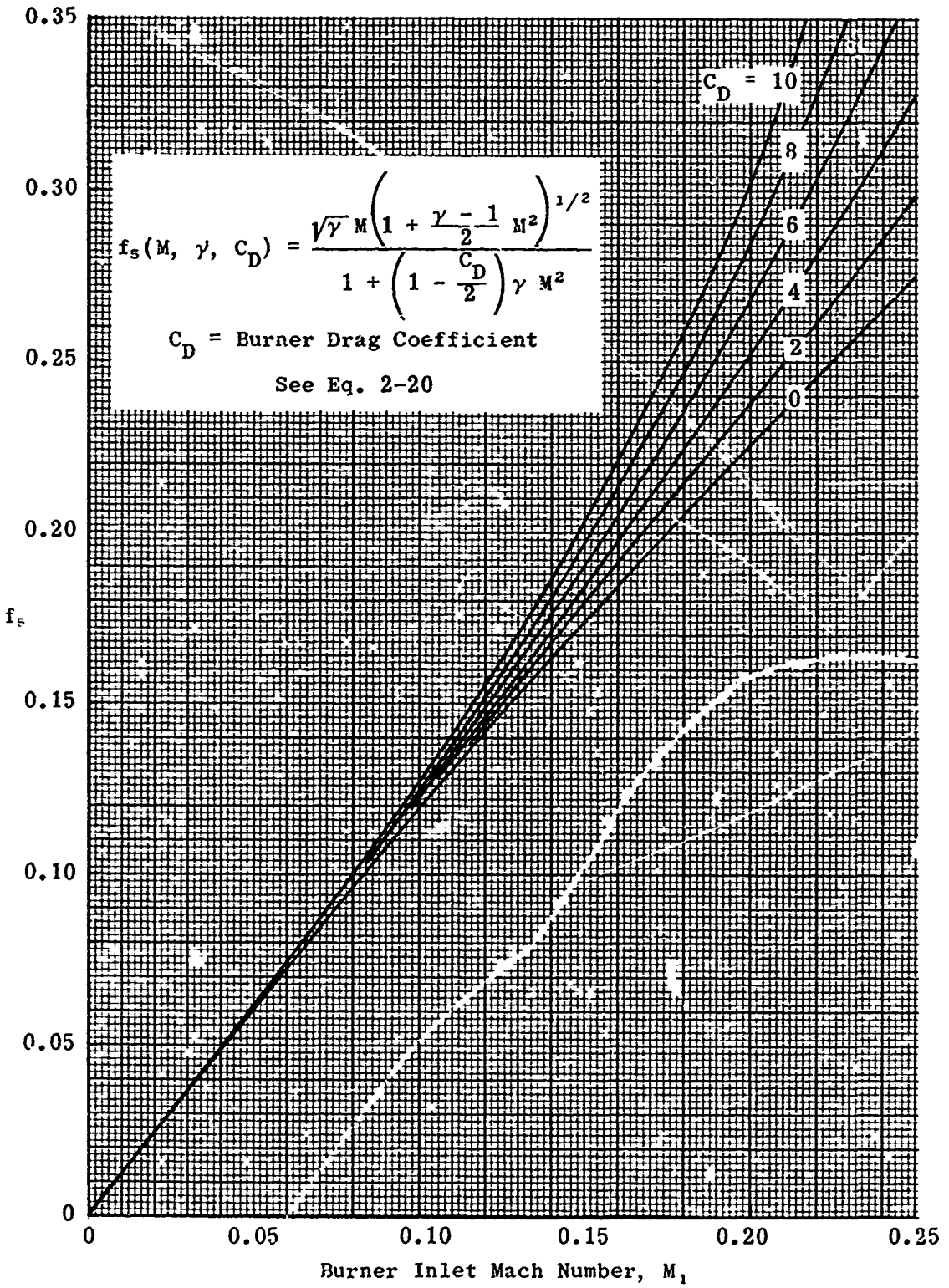

Fig. 2-10. Plot of f_s for $M \leq 0.25$; C_D = 0 to 10; and γ = 1.4.

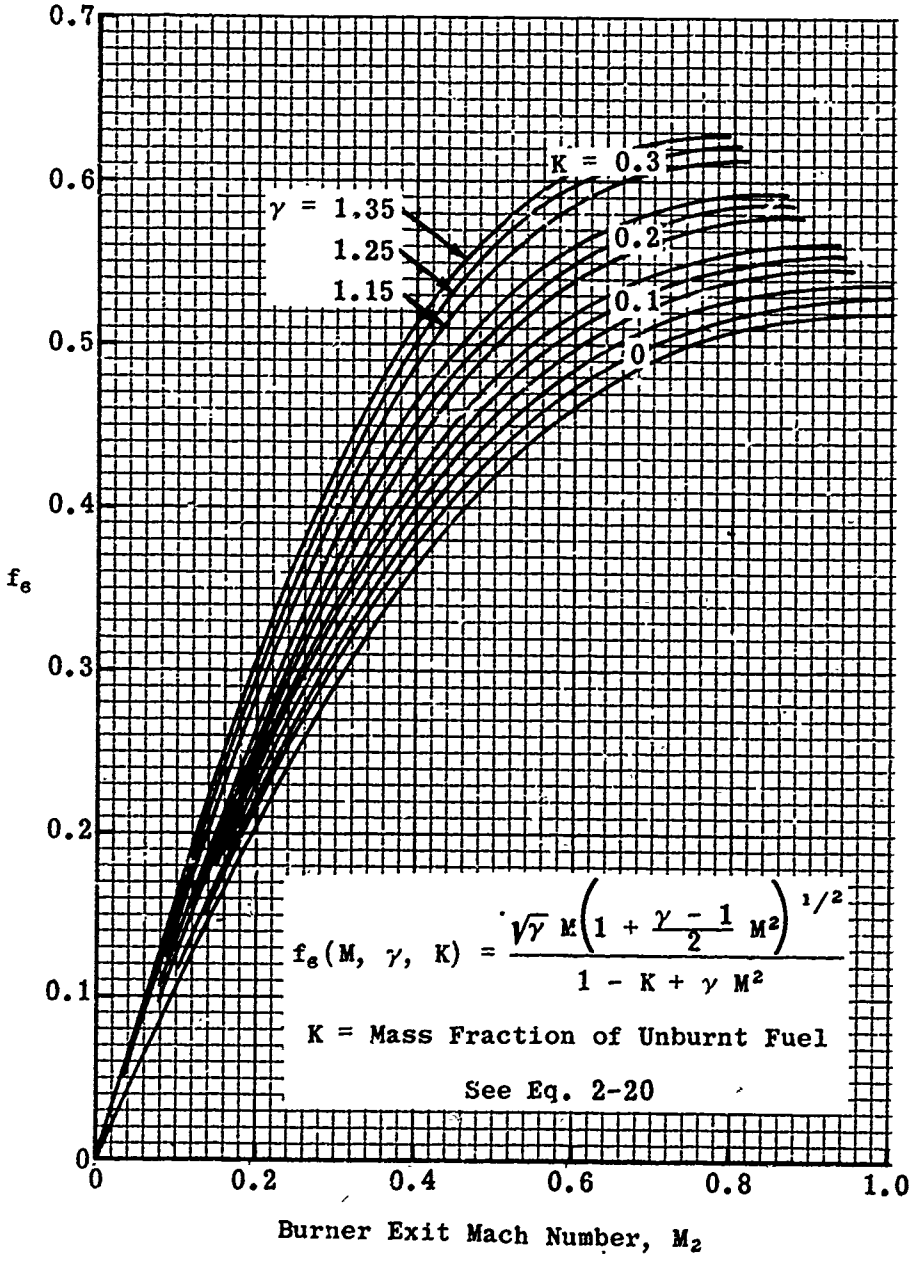

Fig. 2-11. Plot of f_e for $M \leq 1.0$; $K \leq 0.3$; and $\gamma = 1.15$, 1.25, and 1.35.

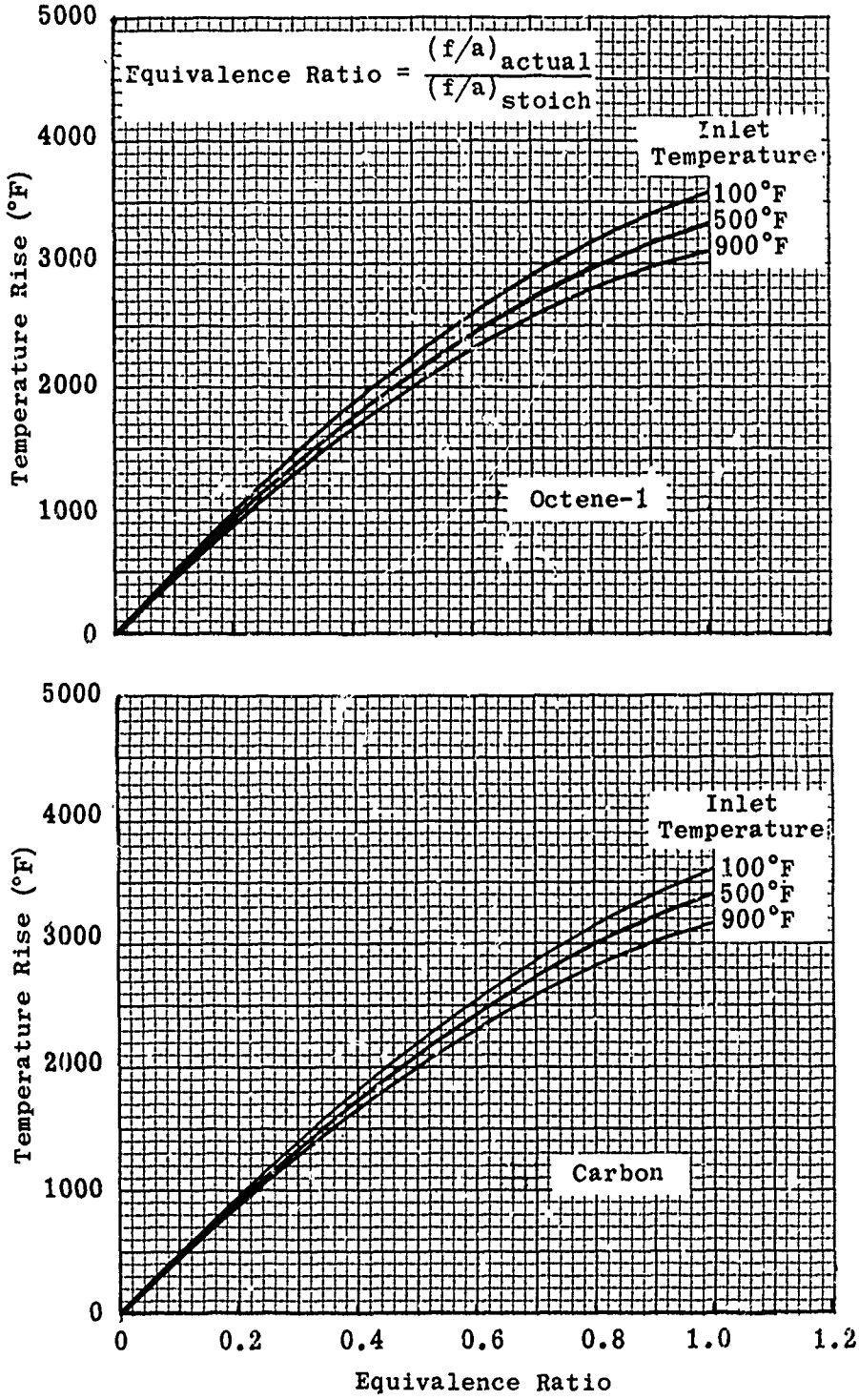

Fig. 2-12. Temperature rise vs equivalence ratio for octene-1 and carbon; T_i = 100, 500, and 900°F.

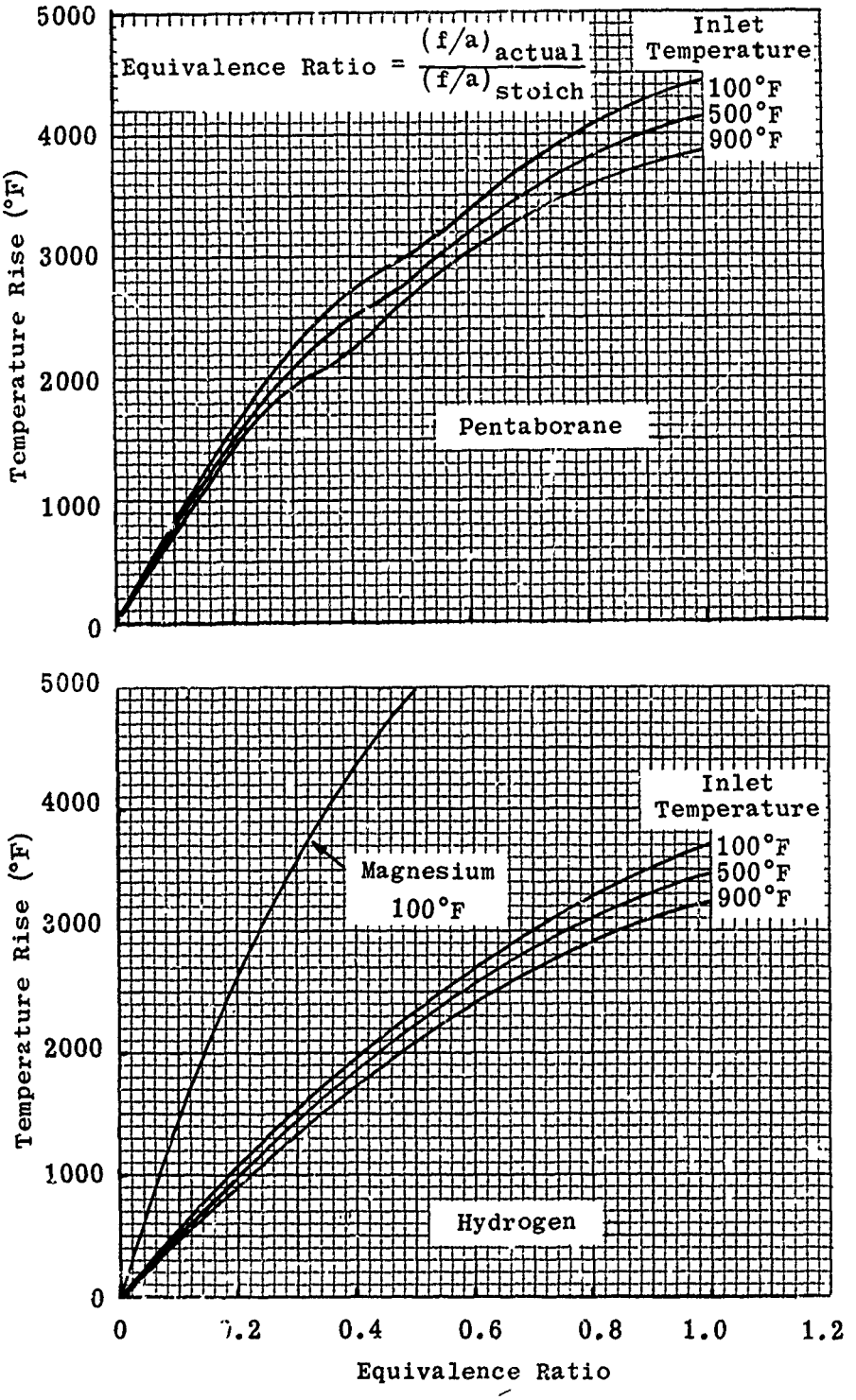

Fig. 2-13. Temperature rise vs equivalence ratio for pentaborane, hydrogen, and magnesium; T_i = 100, 500, and 900°F.

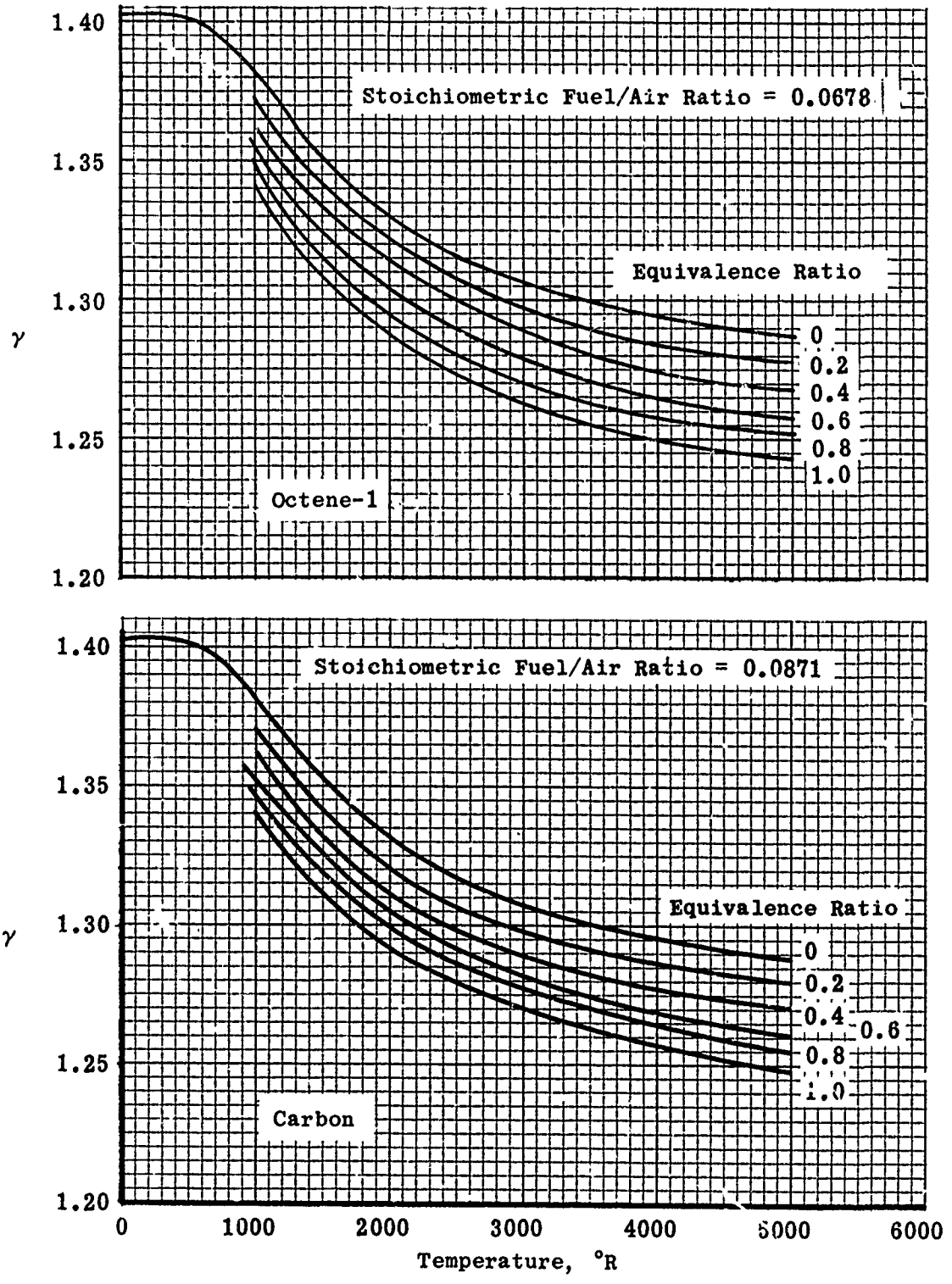

Fig. 2-14. Ratio of specific heats vs temperature for octene-1 and carbon; equivalence ratio of 0 to 1.0.

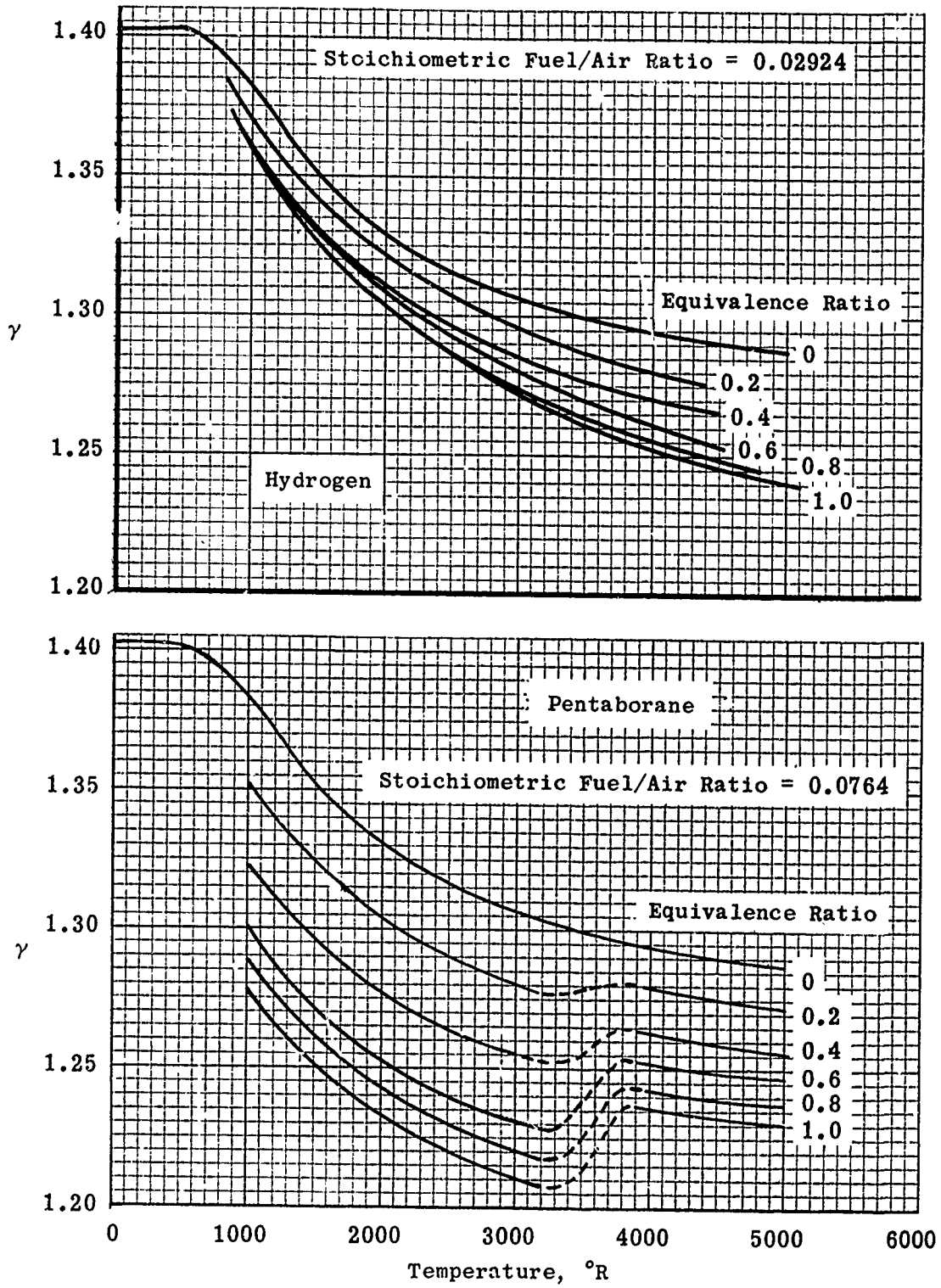

Fig. 2-15. Ratio of specific heats vs temperature for hydrogen and pentaborane; equivalence ratio of 0 to 1.0.

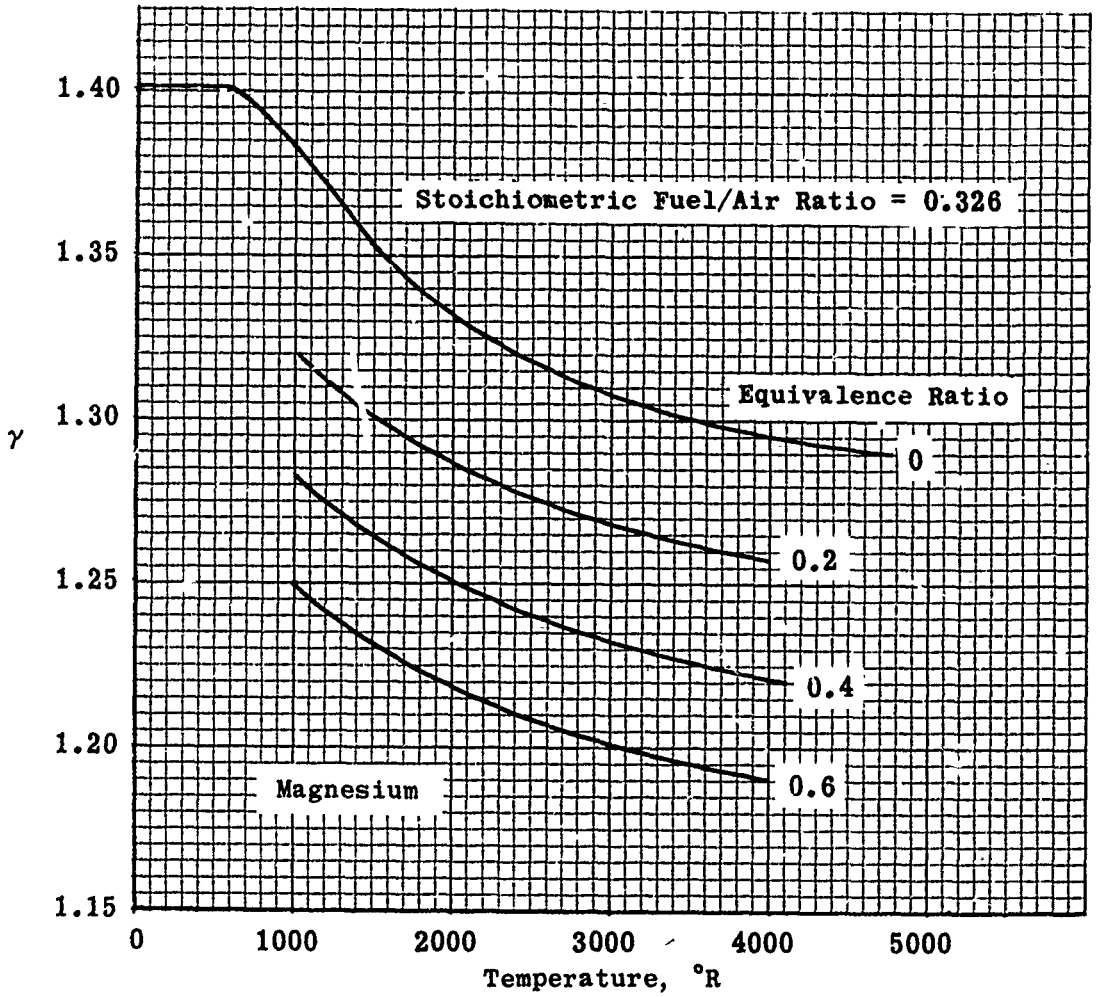

Fig. 2-16. Ratio of specific heats vs temperature for magnesium; equivalence ratio of 0 to 0.6.

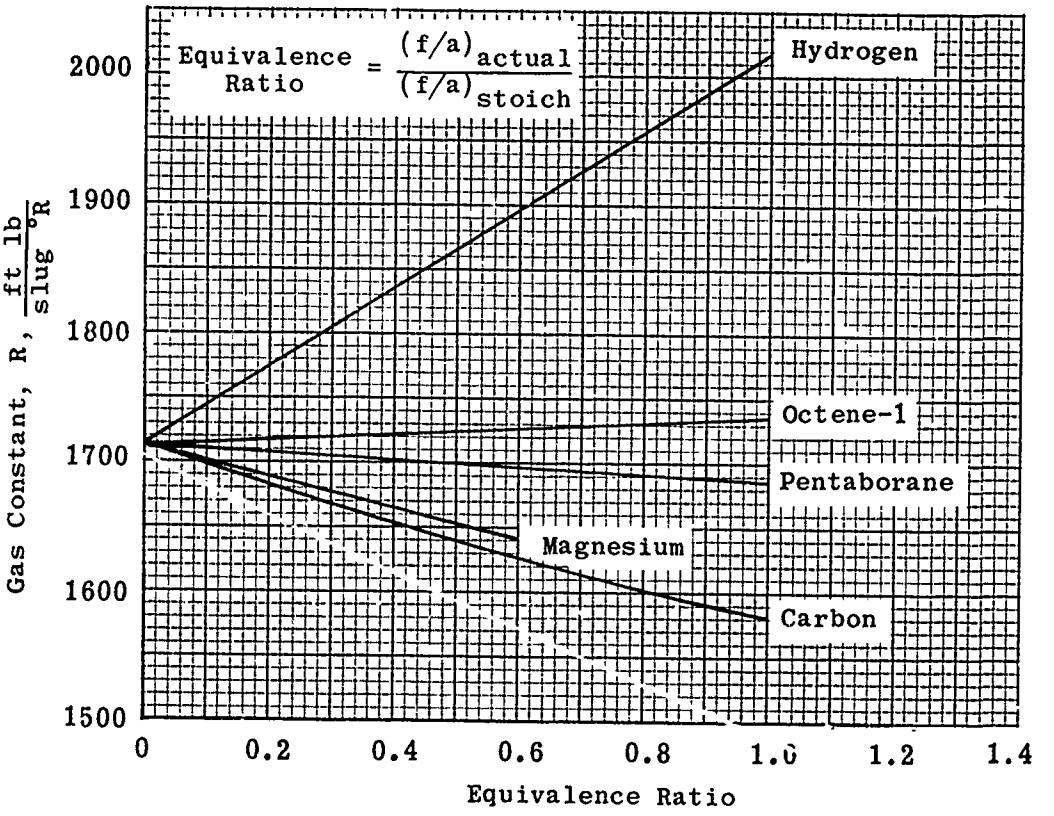

Fig. 2-17. Gas constant vs equivalence ratio for five fuels.

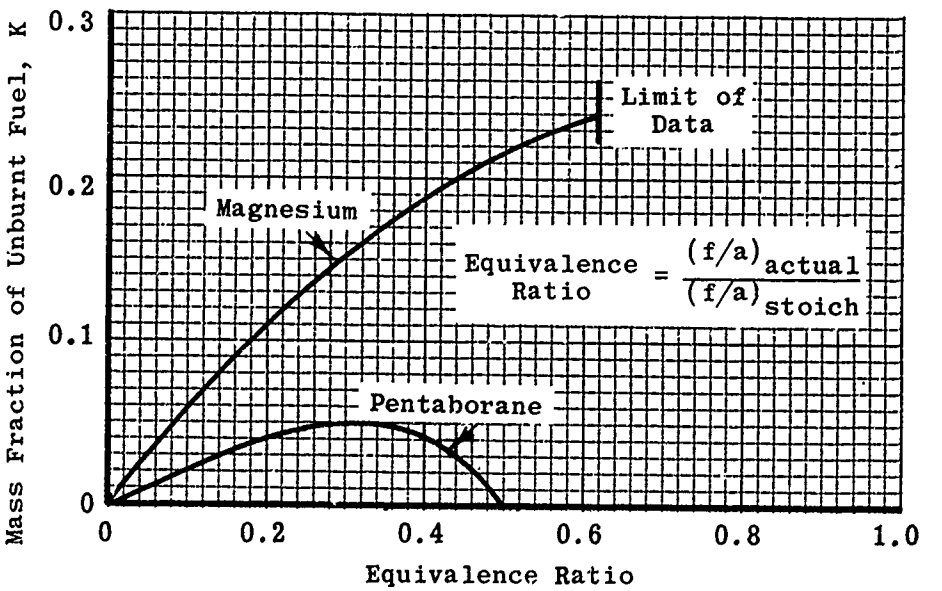

Fig. 2-18. Mass fraction of unburnt fuel vs equivalence ratio for magnesium and pentaborane.

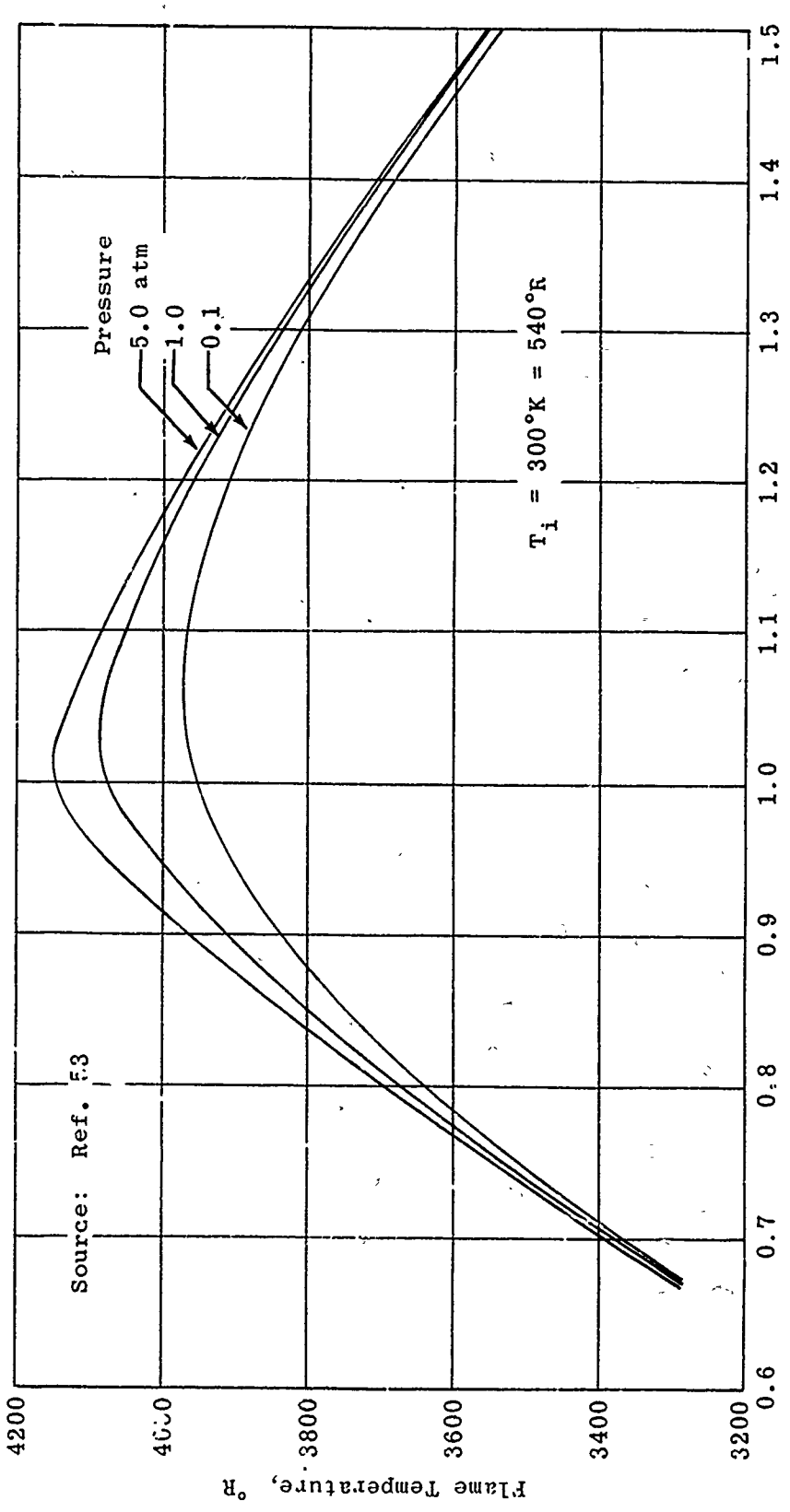

Fig. 2-19. Effect of pressure on the flame temperature of propane; p = 0.1, 1.0, and 5.0 atm.

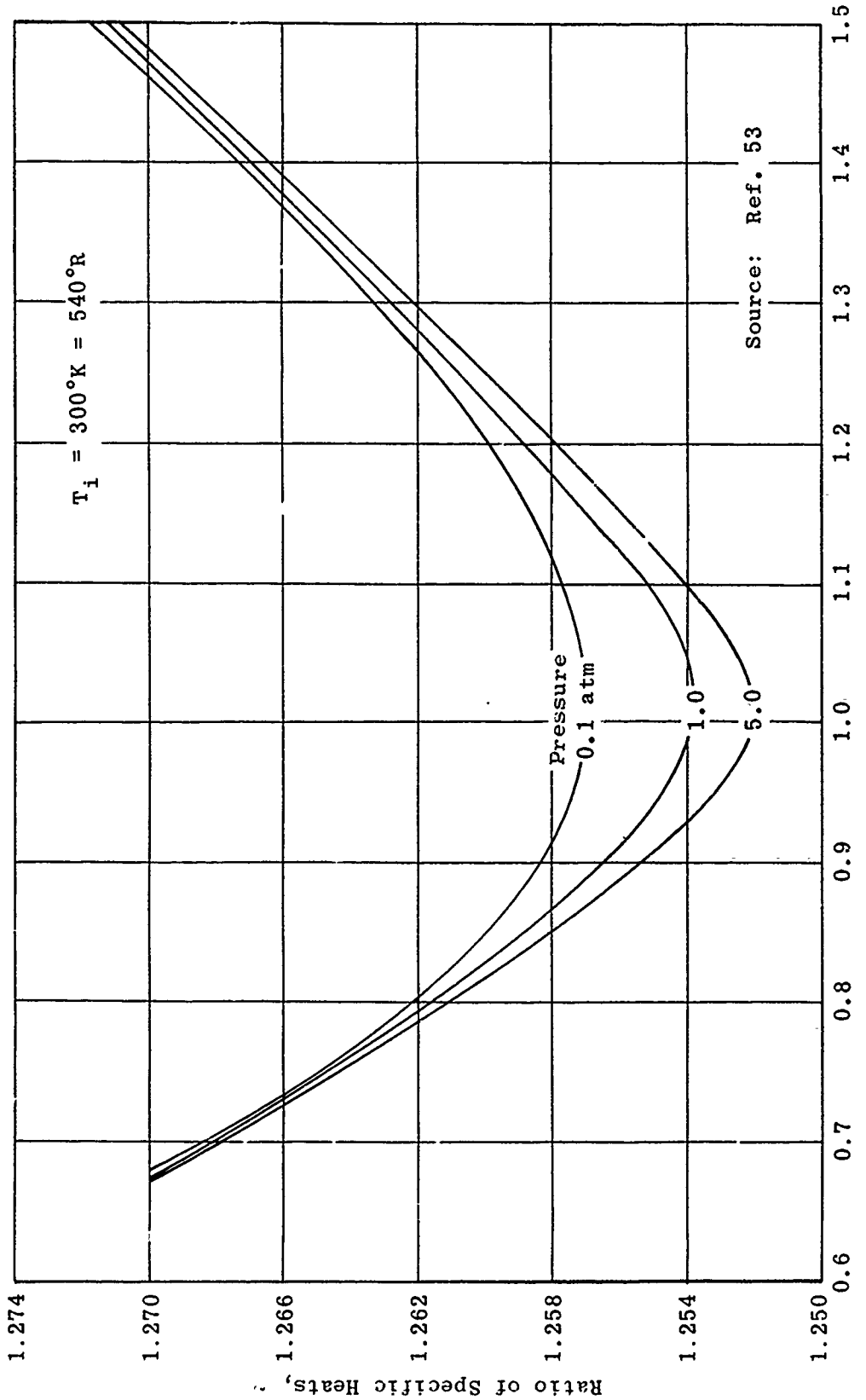

Fig. 2-20. Effect of pressure on the ratio of specific heats of propane-air combustion; p = 0.1, 1.0, and 5.0 atm.

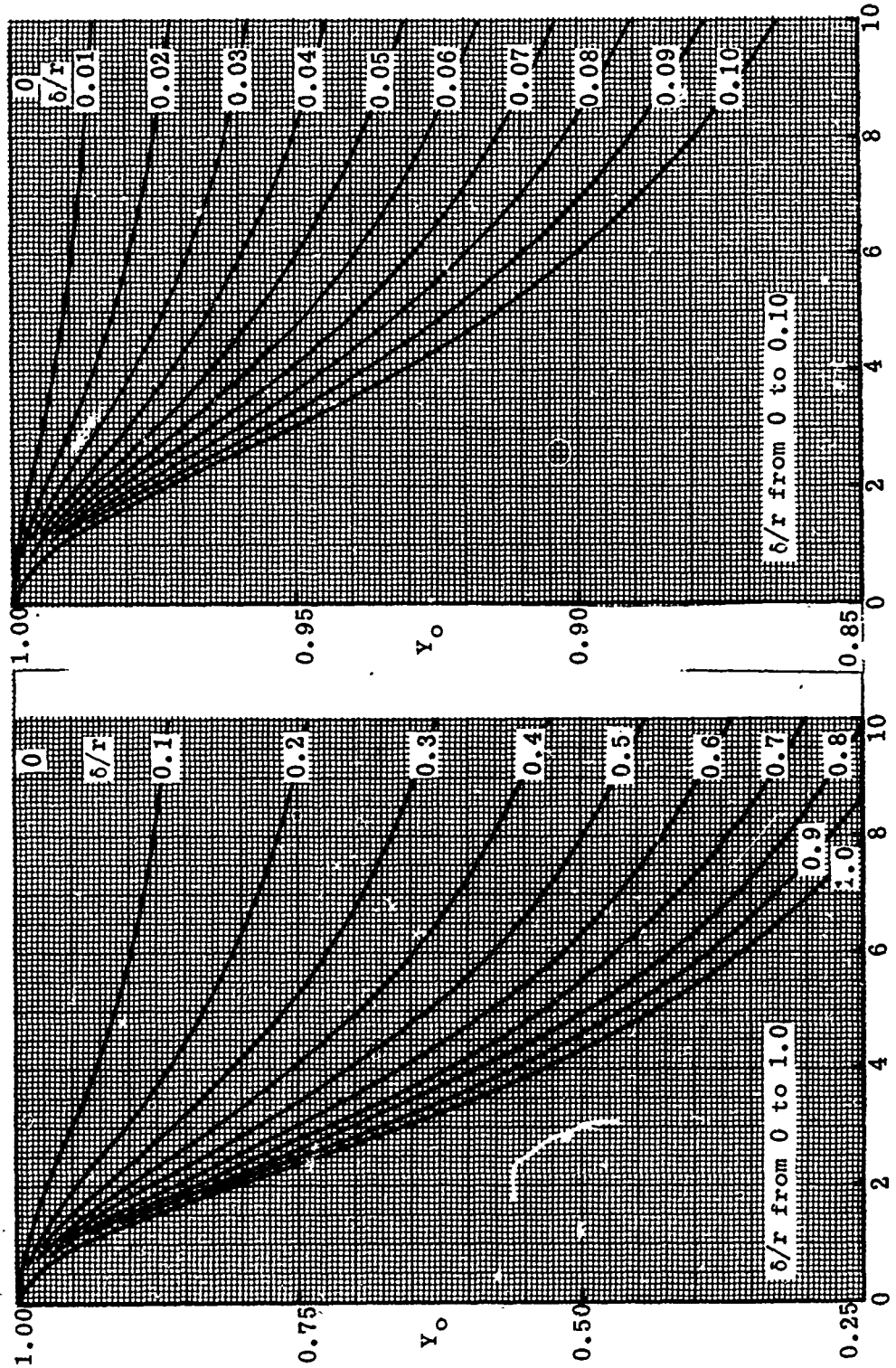

Fig. 2-21. Y_o vs M'; parameter δ/r (see Subsec. 2.1.8).

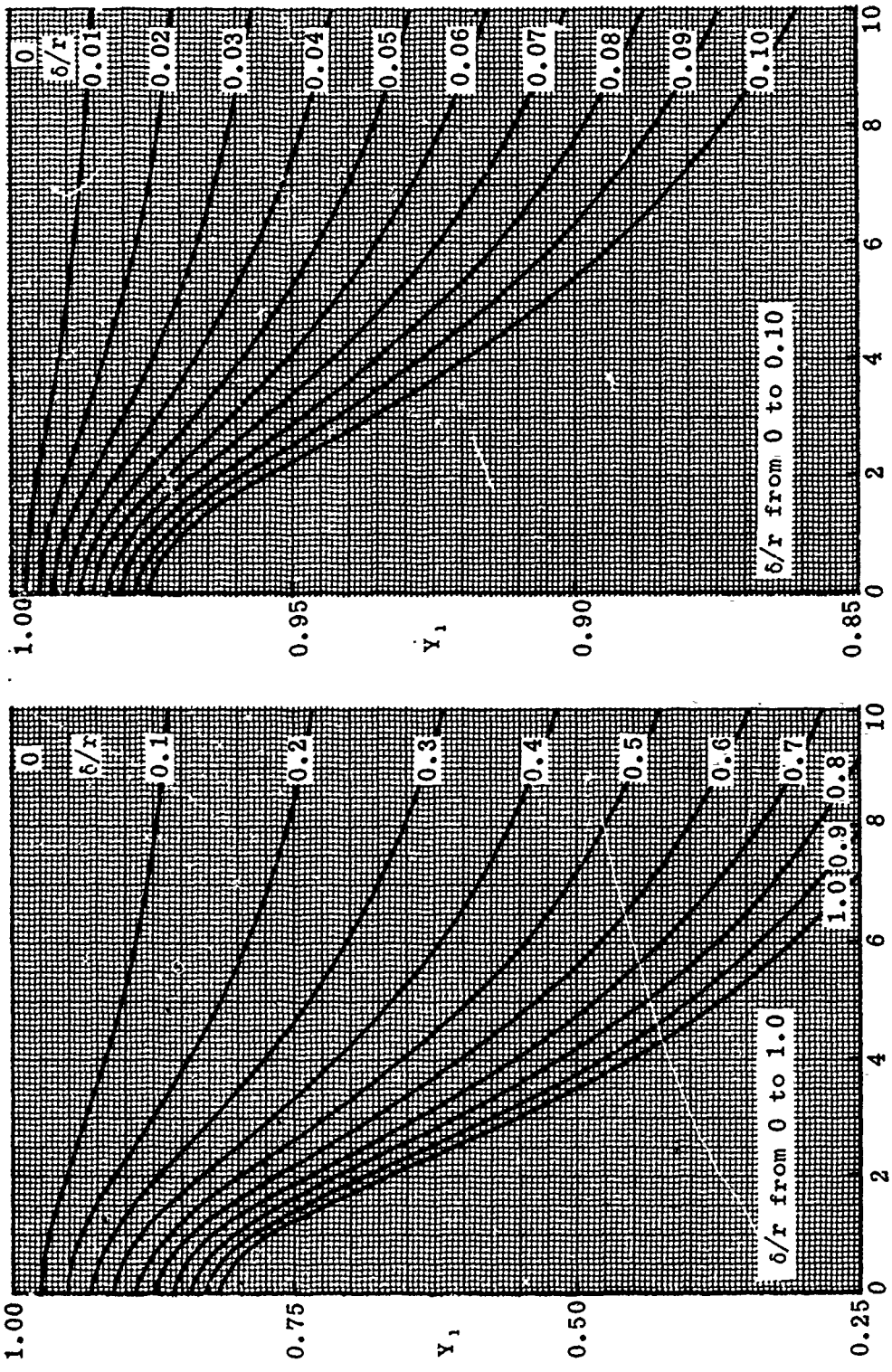

Fig. 2-22. Y_1 vs M'; parameter δ/r (see Subsec. 2.1.8).

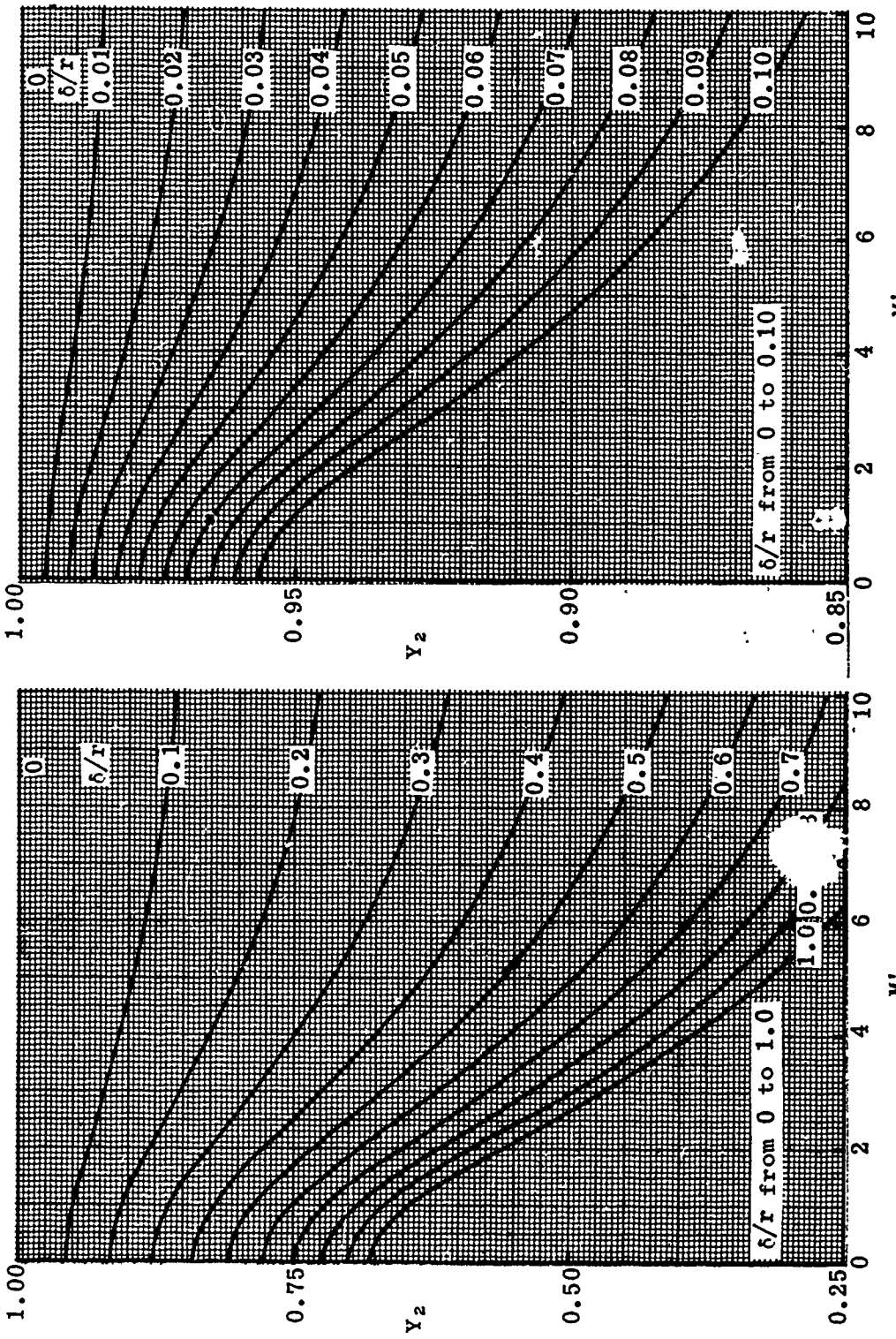

Fig. 2-23. Y_2 vs M'; parameter δ/r (see Subsec. 2.1.8).

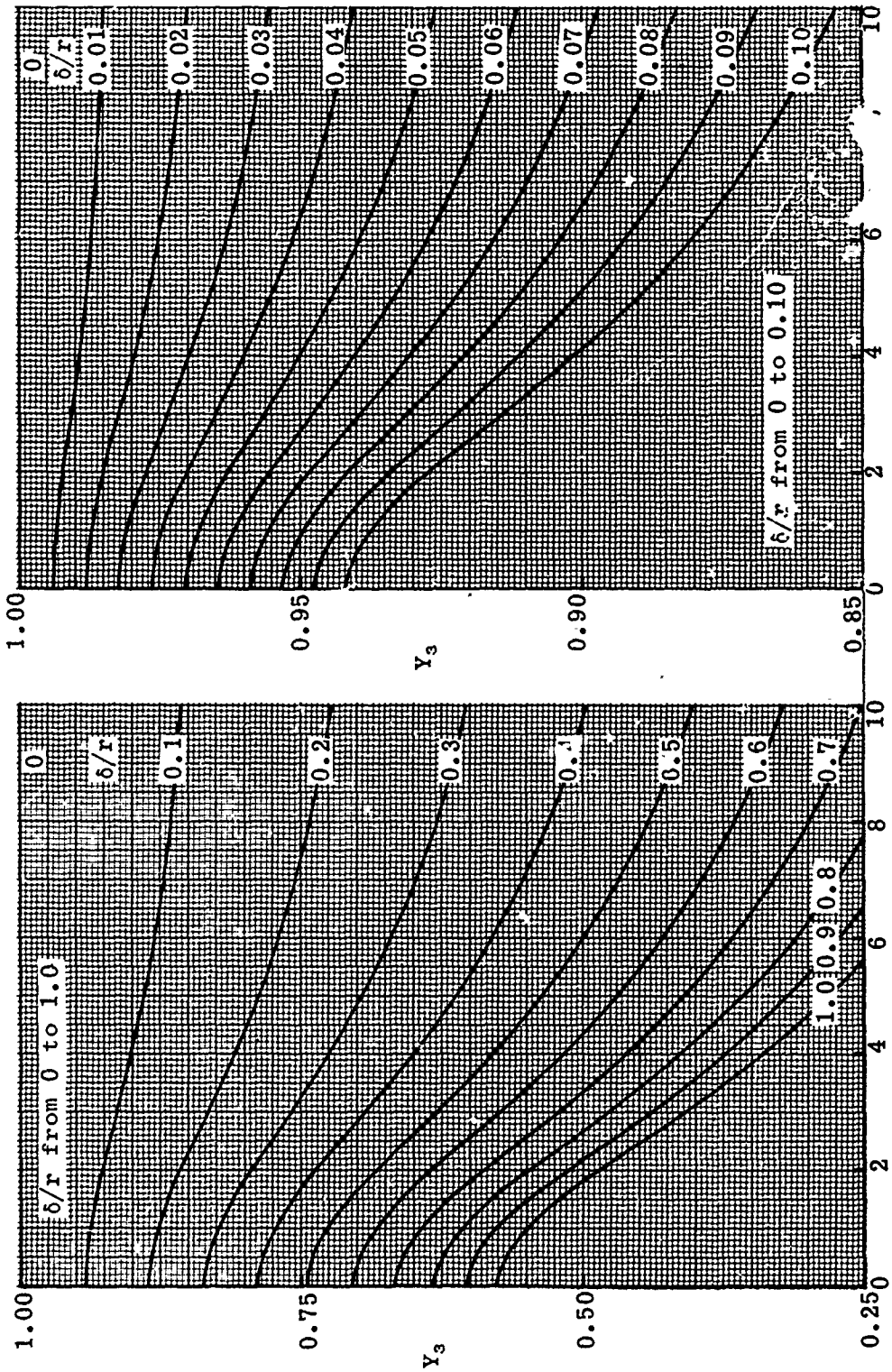

Fig. 2-24. Y_3 vs M'; parameter δ/r (see Subsec. 2.i.d).

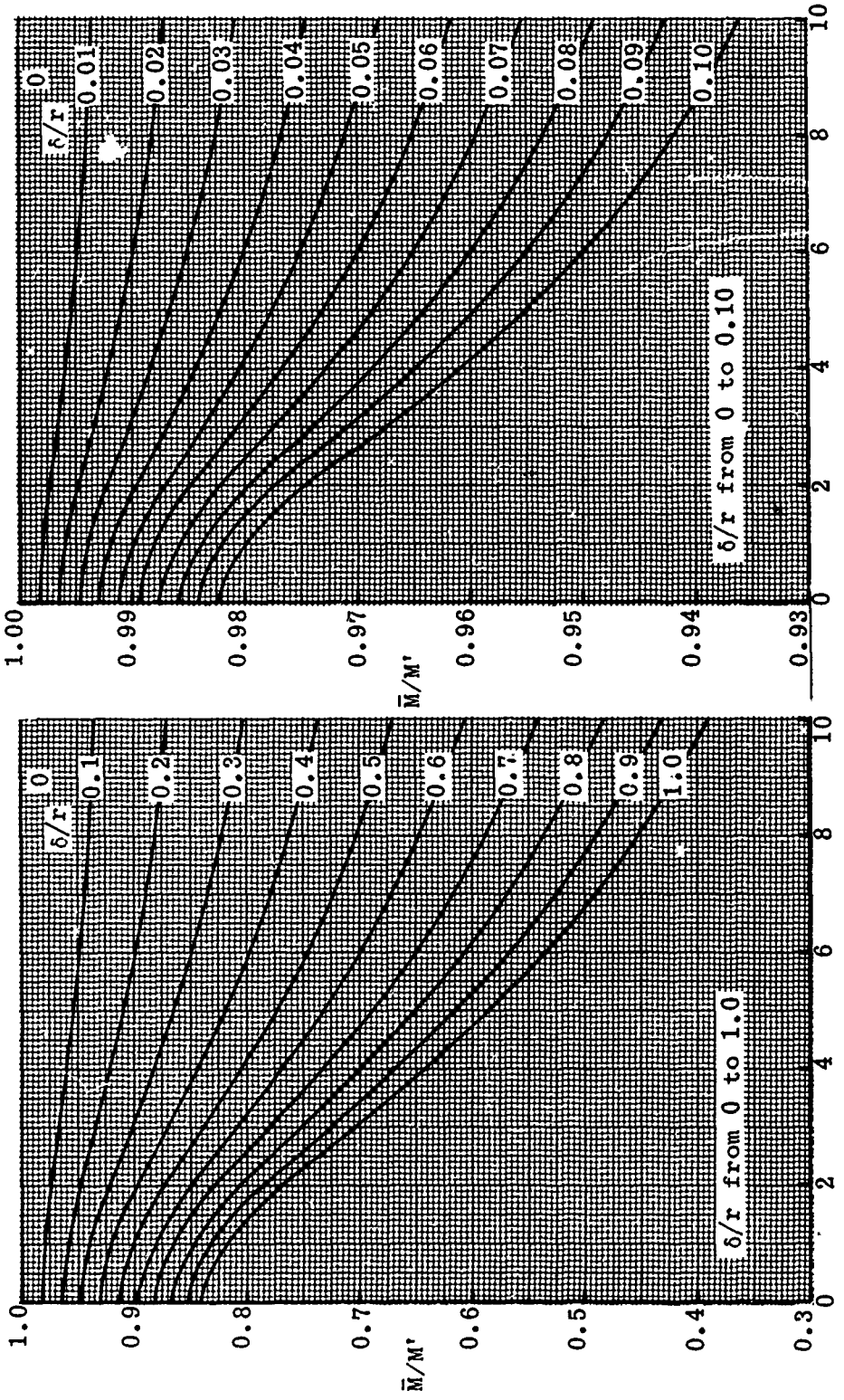

Fig. 2-25. $\bar{M}/M'$ vs M'; parameter δ/r (see Subsec. 2.1.8).

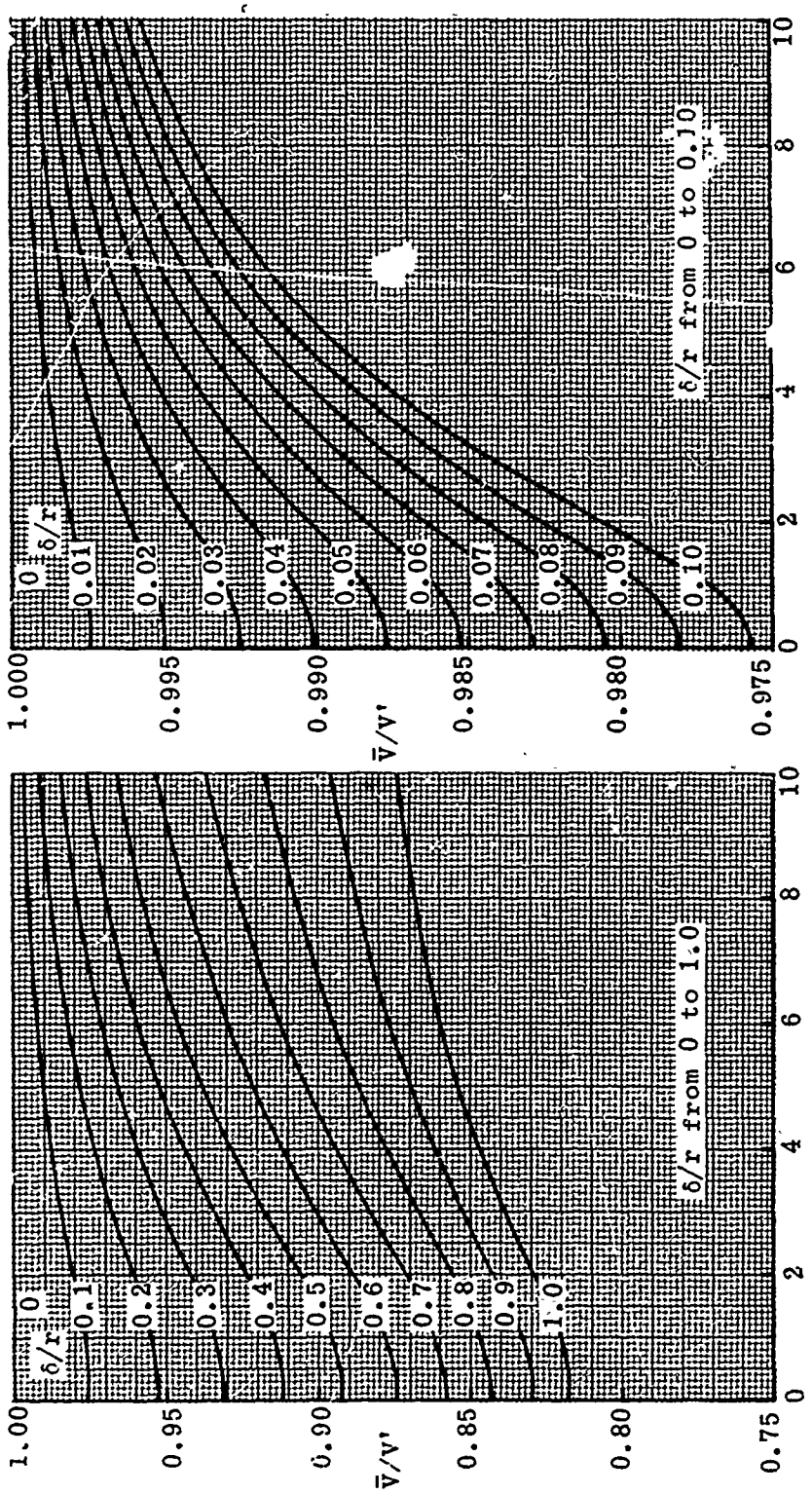

Fig. 2-26. $\bar{V}/V'$ vs M'; parameter δ/r (see Subsec. 2.1.8).

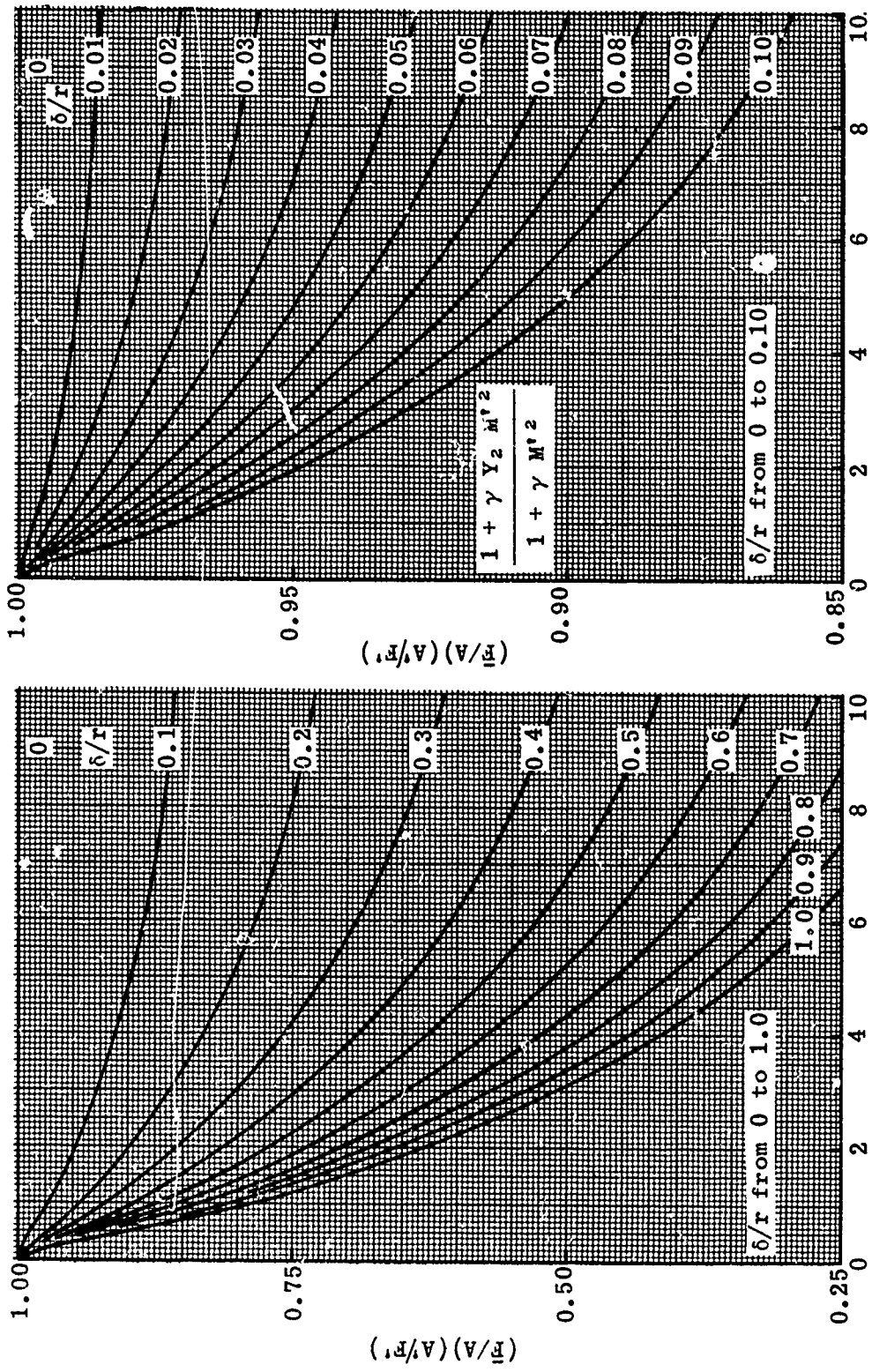

Fig. 2-27. Average thrust per unit area as a function of M' and δ/r (see Subsec. 2.1.8).

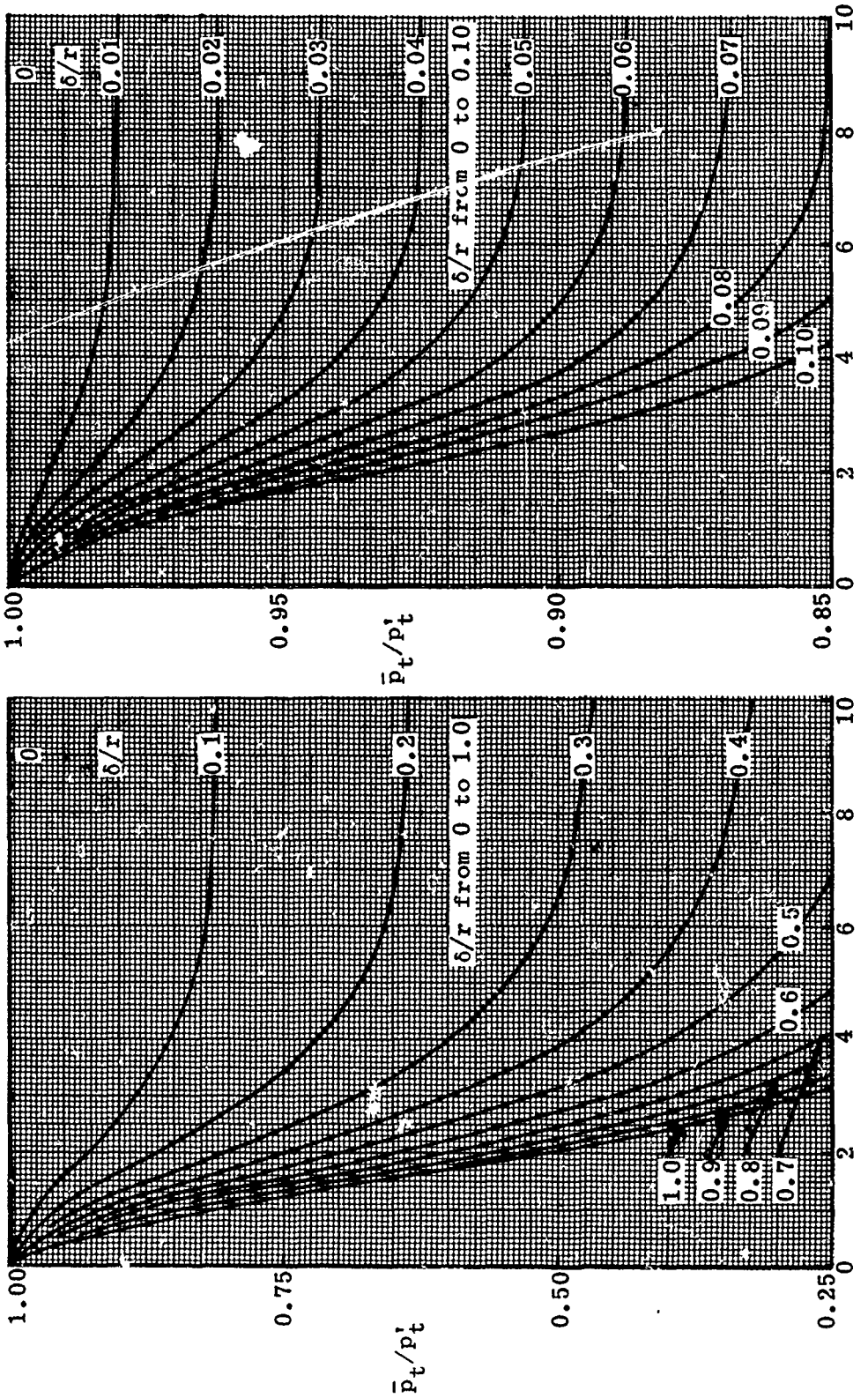

Fig. 2-28. $\bar{p}_t/p'_t$ vs M'; parameter δ/r (see Subsec. 2.1.8)

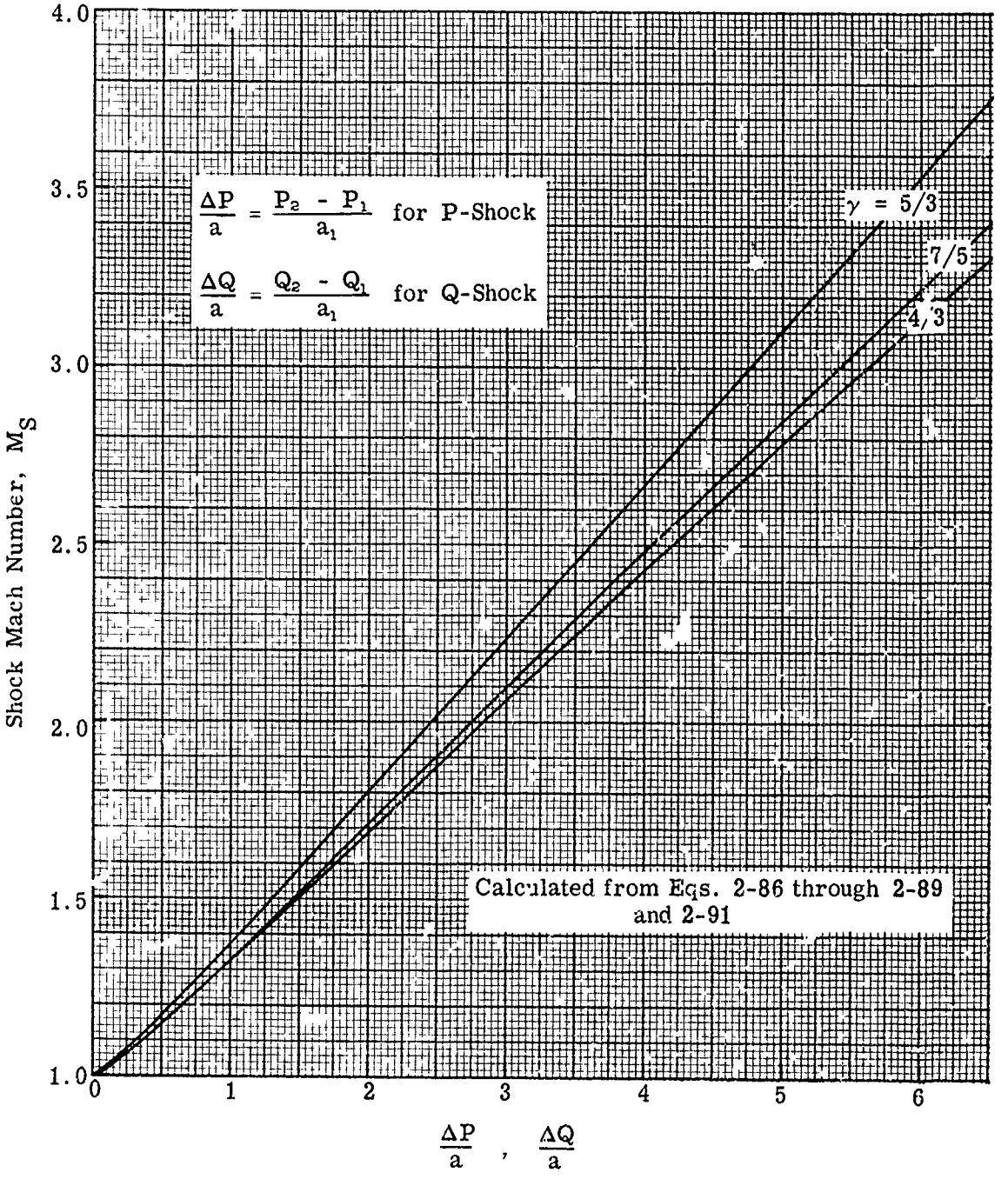

Fig. 2-29. Change in the Riemann variables as a function of the shock Mach number; γ = 5/3, 7/5, and 4/3.

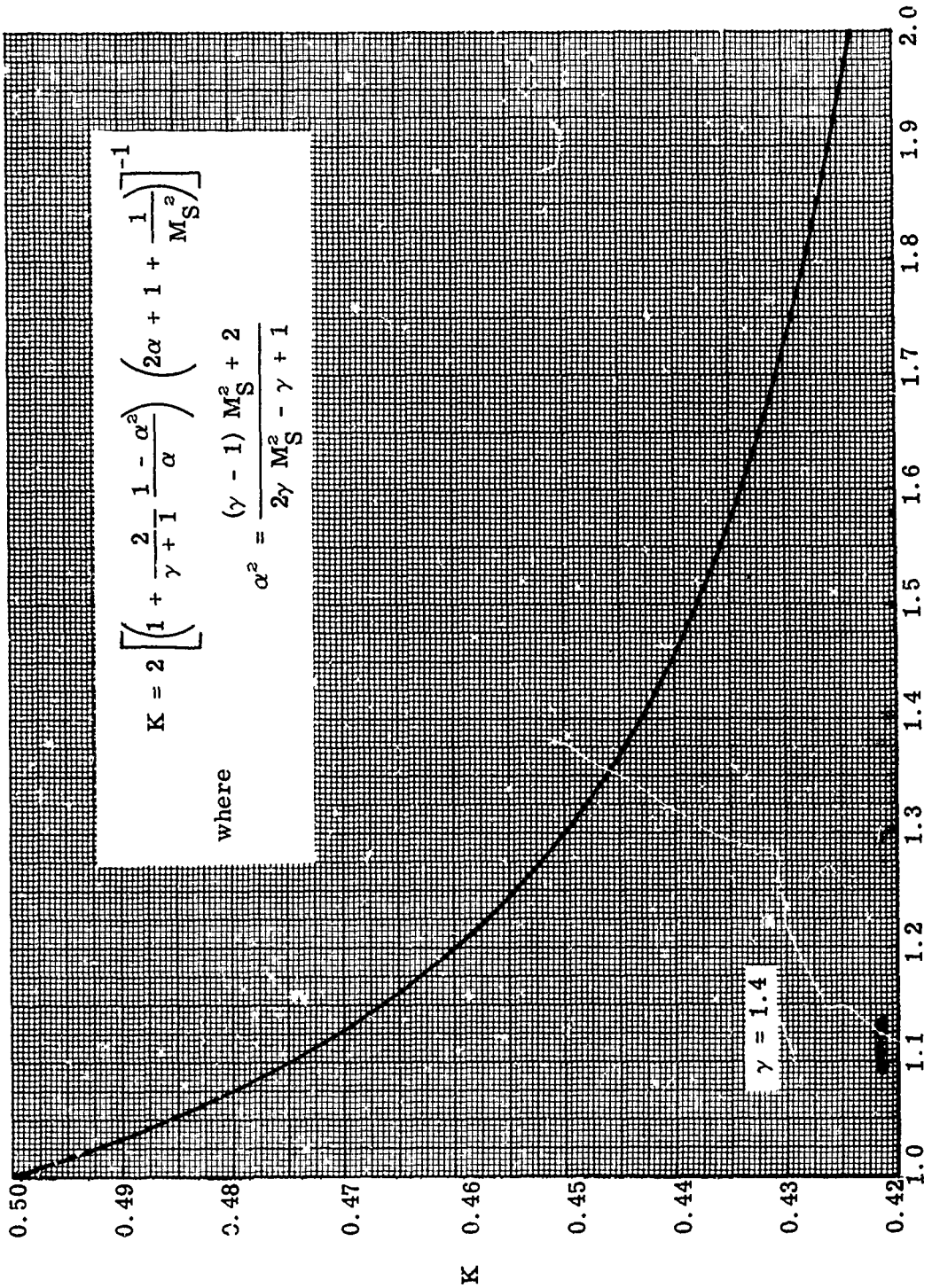

Fig. 2-30. Relationship between the shock Mach number and the function K.
(See Subsec. 2.2.6)

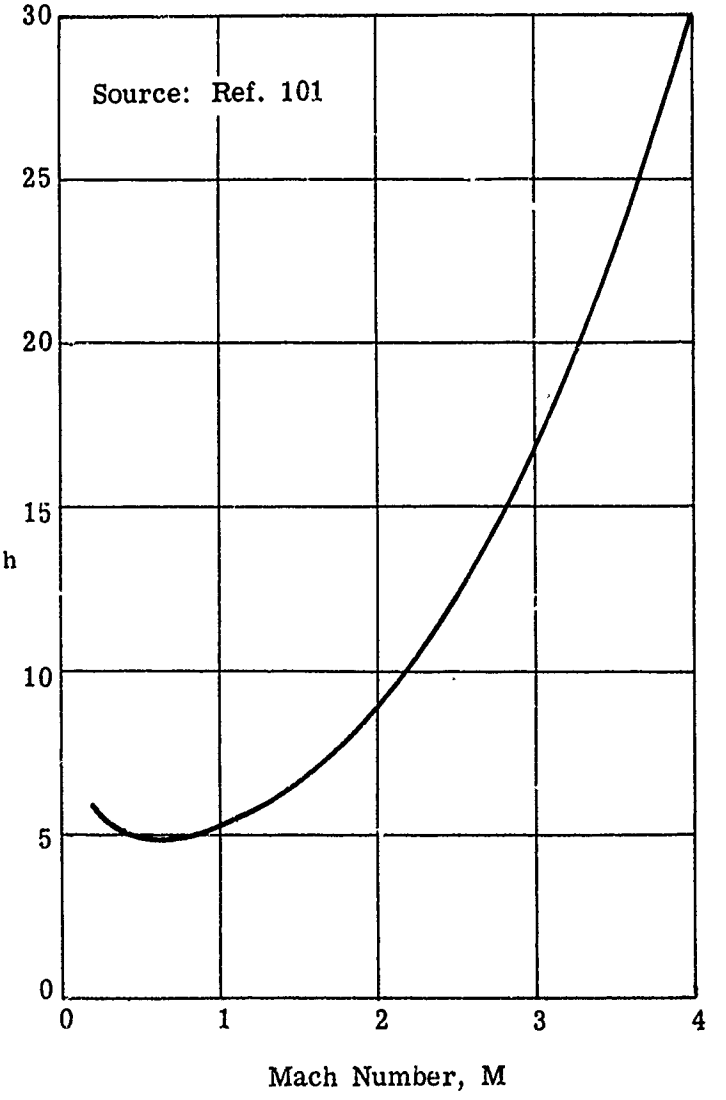

Fig. 2-31. A parameter, h, as a function of M for use in Eq. 2-173.

3. Supersonic Inlets

The function of a ramjet diffuser is to decelerate the air from its free-stream velocity at the intake to a velocity at the combustor which is compatible with the available flame velocity. Because the latter is usually a low velocity, the diffuser also helps to minimize the drag across the combustor itself. Efficient diffusion results in a static pressure as high as possible in order to support the maximum momentum that can be imparted to the air by heating.

It is usual to define a supersonic diffuser as one which decelerates a supersonic stream to approximately sonic speed and a subsonic diffuser as one which completely converts the kinetic energy in a subsonic stream into pressure energy. However, a complete ramjet diffuser is often called a supersonic diffuser although it is generally composed of both a supersonic and a subsonic diffuser, i.e., the inlet speed is usually supersonic and the combustor Mach number has a low subsonic value. Although a ramjet diffuser designed for a supersonic missile is usually axisymmetric, a two-dimensional design is often used when the ramjet is incorporated into a more complex vehicle. For hypersonic speeds the two-dimensional diffuser may even be preferred. Although the discussions that appear in this subsection usually refer to axisymmetric configurations, they may be applied in general with equal validity to the two-dimensional configurations.

Diffusion may be effected either inside the diffuser itself or external to it, or it may be effected by a combination of external and internal compression. Diffusers may also be classified according to their shape or according to the type and number of shocks effecting the compression.

The basic design of a highly efficient diffuser for the flow of an ideal non-viscous gas at a constant free-stream Mach number presents relatively few problems. However, viscous forces cannot be ignored since they cause complex shock patterns, shock instability, and separated flow in the duct as well as vortex sheets in the spilled flow. Some of these effects may be accounted for by semi-empirical theories but many can be assessed only by experimental means. The wide variations in Mach number that a vehicle experiences in accelerating to a steady flight speed, as well as the variations in angle of attack often required in climb and maneuver, increase many fold the problems in the design of an optimum diffuser.

Test data will be given for operation at both the design Mach number and also under off-design conditions. Such data will serve to indicate the performance levels attainable with certain basic and conventional designs. They will also show the effect of many modifications made to specific models tested under limited conditions. Many of the problems and alternatives will be discussed, but the ultimate solutions and the choice of a diffuser design will also be dependent upon the propulsion system and the flight characteristics of the missions of the vehicle in which it is to be housed.

The simplified theory of the basic designs will be given with a discussion of the relevant parameters upon which the performance depends. Adjustments and improvements that have been incorporated into the basic designs will be presented and supplemented by test data for both design and off-design operation.

3.1 Diffuser Performance Parameters

Before discussing the various diffuser designs it is necessary to establish some standards by which their usefulness and efficiency may be assessed. The performance of an inlet diffuser is related to three basic characteristics. They are, the magnitude and quality of the pressure recovery, the capture-area ratio (or mass-flow ratio), and the total drag of the diffuser. These characteristics are discussed briefly in this subsection. They will be treated in more detail in relation to the various types of diffusers to be discussed in the following subsections. Quantitative values derived from simple theory will be compared with those obtained experimentally. The over-all worth of a diffuser must always be arrived at by simultaneously assessing all three characteristics since the gain in one is often achieved at the expense of another. It should also be borne in mind that the most serious aspect of the engine-inlet problem is concerned with off-design operation; none of the characteristics should deteriorate rapidly under conditions of overspeed or underspeed or at angles of attack. Experimentally determined performance data will be presented in subsequent subsections for each diffuser type and modification.

In actual vehicles many compromises have to be made in order to achieve an acceptable performance throughout the variations of flight Mach number, angles of attack, and sideslip as well as variations in the properties of the atmosphere. Variations of the inlet geometry often achieve a better compromise than may be possible with a fixed-geometry diffuser.

3.1.1 Total Pressure Recovery

Although efficient diffusion prescribes that the final static pressure be as high as possible, it is more usual to measure the efficiency in terms of the total pressure recovery. Since at any Mach number the ratio between the static and total pressures is a constant, there is no loss of generality in using one form of pressure rather than the other. Diffuser efficiency, η_D, is then defined as

$$\eta_D = p_{t_2}/p_{t_1} \tag{3-1}$$

where subscripts $_1$ and $_2$ refer to the inlet and exit (combustor) stations respectively.

The total pressure loss is composed of the viscous losses and the shock losses, neither of which are amenable to exact calculation. The shock loss may be estimated by a knowledge of some of the properties of the shock, i.e., whether normal or oblique, the Mach number at which it occurs, or the position at which it occurs. In actual practice only the losses through attached bow shocks may be known with any degree of accuracy. The nature of most other shocks is complicated by the interaction of the shock and the boundary layer. What is usually considered as a simple normal shock in the throat of a diffuser channel is actually a complex shock system occupying a length many times the equivalent diameter of the duct (see Subsec. 5.3). Total pressure losses, calculated for basic diffuser configurations with the assumption of simple, normal shocks at known stations, will be included in each section and will be compared with experimental data.

One of the important features of the total pressure recovery that is sometimes ignored when assessing diffuser performance is the quality of the flow at the exit, i.e., the pressure (or velocity) distribution over the exit area. This is most critically affected during angle-of-attack operation, at which time, large, separated areas may occur in the subsonic ducting. Unevenly distributed mass flow may cause less efficient burning than a lower but evenly distributed pressure recovery over the combustor region. An often-used measure of the flow quality or flow distortion, D, is given by

$$D = (p_{t\ max} - p_{t\ min})/p_{t\ av} \tag{3-2}$$

However, such an expression should also be supplemented by a pressure contour in order to make it of real value. Examples of such contours and distortion factors are shown in Fig. 3-1, taken from Ref. 103.

3.1.2 Capture-Area Ratio or Mass-Flow Ratio

The second characteristic of a diffuser that is used in rating its effectiveness is its capture-area ratio or its mass-flow ratio.

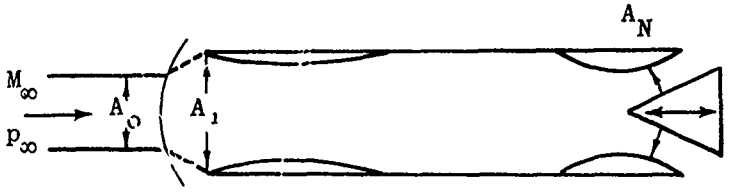

In the sketch above

A_o = cross-sectional area of the entering stream tube

A_1 = cross-sectional area of the diffuser entrance.

The capture-area ratio is defined as A_o/A_1. When the shock is swallowed, $A_o = A_1$. When the shock is expelled some of the air that would have entered the diffuser is spilled around the lips. The ratio of the mass that enters to the maximum mass that could enter is

$$\frac{m_\infty}{m_1} = \frac{m_o}{m_1} = \frac{\rho_o V_o A_o}{\rho_o V_o A_1}$$

which reduces to the capture-area ratio, A_o/A_1. It may be noted that here, and in cases where the diffuser entrance is in the free stream, the subscripts o and ∞ are used interchangeably for the flow characteristics at station o.

The capture-area ratio may be measured in a wind tunnel by the use of a throttling plug (as shown above) which is adjusted to produce a sonic throat of "effective" area A_N. Continuity of mass flow gives

$$A_o \rho_o V_o = A_N \rho_N V_N \tag{3-3}$$

which by means of Eqs. 2-1, 2-2, 2-5, and 3-1, and the assumption that the total temperature remains constant down the duct, may be transformed into

$$\frac{A_o}{A_1} = \frac{p_{t_N}}{p_{t_o}} \cdot \frac{A_N}{A_1} \cdot \left(\frac{A}{A^*}\right)_{M_o} = \eta_D \frac{A_N}{A_1} \cdot \left(\frac{A}{A^*}\right)_{M_o} \qquad (3\text{-}4)$$

where the total pressure, p_{t_N}, is assumed to be the same as p_{t_r}, the recovery pressure actually measured by a rake upstream of the throttle. The value of A_N is usually determined beforehand as a function of the throttle setting by using a simple normal-shock diffuser with swallowed shock. As the area A_N is decreased, the normal shock is forced further upstream in the diffuser until, at the critical condition, the shock rests on the rim. Since $A_o = A_1$ as long as the shock remains in the duct (i.e., during supercritical operation) and since η_D may be measured, the effective value of A_N can be calculated from Eq. 3-4 for each position of the throttle setting.

A few typical curves of pressure recovery as a function of capture-area ratio are shown in the sketch below. Such curves will be discussed fully under the headings of the various types of diffusers (Subsecs. 3.2 to 3.4).

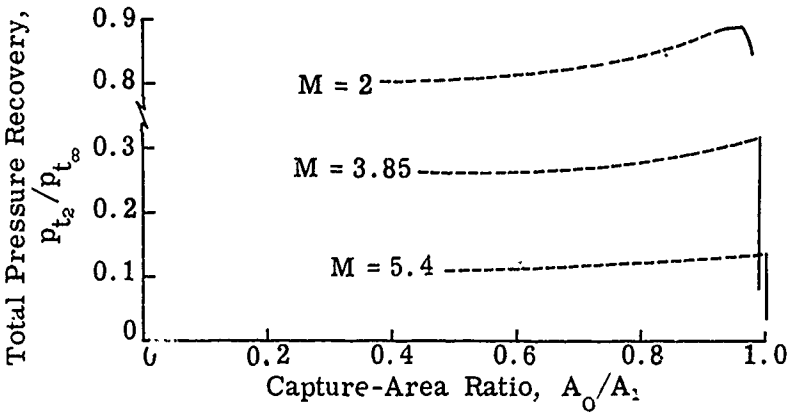

In general the pressure recovery rises rapidly to a peak value as A_N is decreased. The peak pressure recovery may or may not coincide with the critical point. As the shock is expelled, the pressure recovery drops with varying degrees of rapidity. While it is usually desirable to have complete flow capture at the design Mach number, it is, however, sometimes advisable to accept some spill-over at the design condition in order to give improved engine performance at angles of attack (see Subsec. 3.1.3). If the vehicle is to operate over a wide range of high Mach numbers, variable geometry becomes imperative. Plots of η_D vs A_o/A_1 with Mach number and angle of attack as parameters are usually obtained by means of wind-tunnel testing for each specific diffuser. Examples will be given in conjunction with the discussion of particular diffuser designs in Subsecs. 3.2, 3.3, and 3.4.

3.1.3 Diffuser Drag

The third parameter by which the merit of a diffuser is assessed is the total drag of the diffuser. The first component of the total drag is that of the cowl itself and is made up of the wave drag and skin-friction drag. At small angles of attack with no spill-over, the cowl wave drag is amenable to calculation by the methods discussed in Subsec. 6.3 of Section 8 of the Handbook (Ref. 10). The skin friction is discussed in the same volume (Subsec. 6.10) and will be treated more fully in Sections 13 and 14. When the drag of the diffuser is to be considered separately from that of the whole missile, it is necessary to take the reference station far enough downstream of the cowl shoulder for the ambient pressure to have recovered from the effect of the bow shock wave. The theoretical cowl drag is based on a sharp lip and must be corrected for the presence of a blunt lip where one is used. The change in cowl drag due to spill-over at various angles of attack is usually found experimentally.

Another component of the spill-over drag is known as the additive drag, D_A, and is the sum of the pressure forces acting parallel to the axis along the streamlines AB. When $A_o = A_1$, i.e., when there is no spill-over, there is no additive drag. The additive drag is usually kept relatively small in the supercritical regime, i.e., swallowed shock, by suitable diffuser design, but in the subcritical regime of operation, i.e., expelled shock, it rises rapidly with increased spill-over and accounts for a large part of the subcritical drag.

An internal-compression diffuser operating with a detached normal shock is not only a good illustration of how the additive drag arises, but is one in which the value may be calculated in a simple manner.

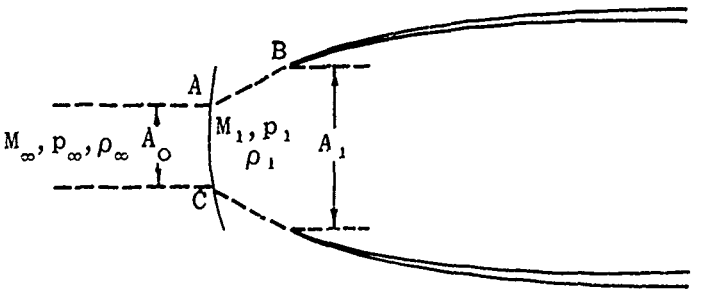

Application of Newton's second law of motion to the flow shown in the above sketch gives

$$A_o\, p_\infty + D_A - A_1\, p_1 = \rho_1\, A_1\, V_1^2 - \rho_o\, A_o\, V_o^2 . \qquad (3\text{-}5)$$

Since the additive drag will ultimately be combined with the cowl drag it is necessary that the pressures for both are considered on the same basis, i.e.,

as differences between the measured pressure and the free-stream static pressure, p_∞. Using this fact, Eq. 3-5 may be written as

$$D_A = p_\infty A_1 \left[\frac{p_1}{p_\infty} (1 + \gamma M_1^2) - 1 - \gamma \frac{A_0}{A_1} M_\infty^2 \right] \qquad (3\text{-}6)$$

Assuming that the shock is normal to the free-stream direction over the cross section, AC, it is possible by means of normal-shock and isentropic-flow tables to calculate D_A from Eq. 3-6 in terms of A_0/A_1, the known free-stream conditions and the known value of A_1.

Moeckel (Ref. 104) considers a more realistic shape for the detached shock and obtains an expression for the additive drag for two-dimensional and axisymmetric diffusers which have the sonic point at the cowl lip. However, since in all practical considerations a diffuser with a detached shock would be avoided, both of the above methods are of somewhat academic interest.

The additive drag of paramount importance to the ramjet designer is that due to spill-over caused by operation at below-design Mach numbers. Such spill-over for an isentropic-spike diffuser is shown in the sketch below.

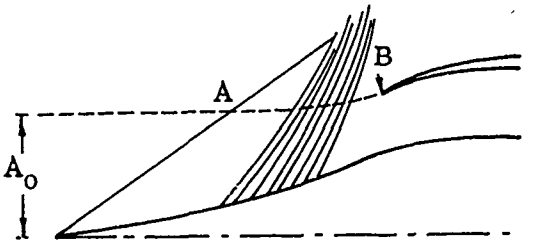

The additive drag is found by integrating the pressure over the surface AB. This demands a detailed knowledge of the properties of the flow field in the vicinity of AB. For two-dimensional diffusers the flow field is readily amenable to calculation as the compression waves are linear. For axially-symmetric diffusers, the flow field must be analyzed by means of a characteristics calculation (Refs. 95, 97, and 98). A detailed example of such a calculation is given in Ref. 105. The calculated additive drag for isentropic spike diffusers designed for M = 3.5 and M = 5 is shown in Figs. 3-38, 3-42, and 3-46 as a function of the cowl-lip position and the free-stream Mach number. Figures 3-47, 3-48, and 3-49 give similar information as a function of design Mach number in the range of $2 \leq M_D \leq 5$.

It has been shown experimentally that better angle-of-attack performance may be obtained if about 4% flow spillage is allowed for at the design Mach number and zero angle of attack. It is fortunate that under such conditions the total external drag is not always increased. When the normal shock is expelled, the spilled flow is subsonic, and thus the cowl-lip pressure drag may decrease significantly and compensate for the additive drag due to spill-over. However, where a conical shock from an innerbody falls outside the cowl lip and causes supersonic spill-over, the cowl-lip drag will increase unless the Mach number behind the shock is less than about 1.4.

Sometimes the diffuser performance is improved by bleeding off some or all of the boundary layer on the innerbody or inner cowl surfaces (see Subsec. 3.7). In such cases the drag must take into account the introduction of the bleed air into the free stream.

The following sketch shows how the total external drag at zero angle of attack and at a constant Mach number is made up and particularly how rapidly the additive drag increases with increased spill-over.

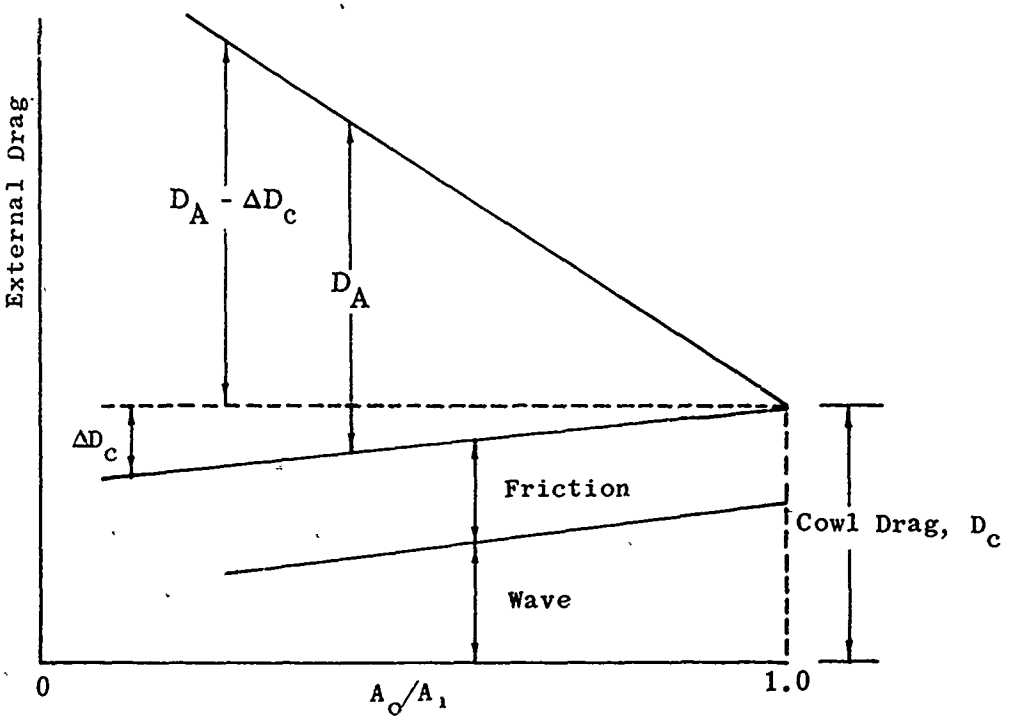

The following sketch from Ref. 103 shows the typical variation of the drag components for supercritical flow as a function of Mach number for a diffuser designed to operate at M = 3.

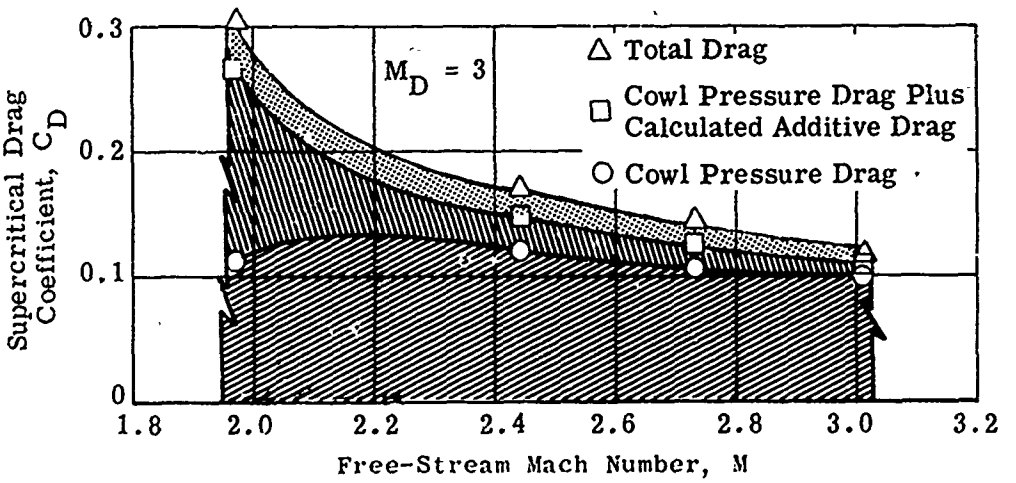

Diffusers designed to optimize the pressure recovery, capture-area ratio, and external drag are discussed in the next three subsections, together with experimental data. The analysis of experimental results has shown that the diffuser drag is of such importance in the design of long-range cruise missiles that it is often desirable to compromise the external compression in order to minimize the cowl drag. For a maximum-thrust missile, the pressure recovery is of paramount importance, and hence design emphasis is laid on the inlet rather than the cowl.

3.2 Internal-Compression Diffusers

Theoretically it is possible to compress the flow isentropically from supersonic speed to sonic speed by duct contraction and then by duct expansion to decelerate the subsonic flow to the required terminal velocity. A reverse Laval nozzle, as shown in the sketch below, is such a diffuser.

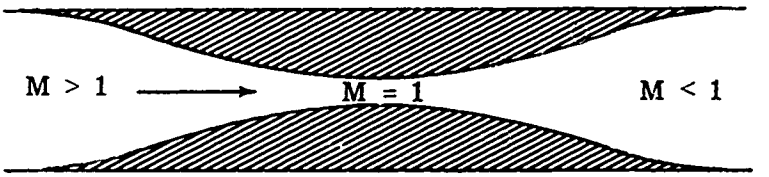

In the absence of viscous forces the required compression would involve no losses. However, even under such ideal flow conditions the diffuser would be impractical for a ramjet inlet because it would operate only at precisely the design inlet Mach number. If the throat area were too small (in terms of the inlet Mach number and area ratio) the flow would choke, and if it were too large the flow would not reach the sonic critical speed and hence would reaccelerate downstream of the throat. It is, however, readily adaptable to wind-tunnel diffusion (see Subsec. 5.4). In real flows, viscous forces may not be neglected and furthermore the viscous losses in a reverse Laval nozzle employed as a diffuser may be much greater than when the same nozzle is used as an effusor, because when the boundary layer undergoes compression it is more likely to separate than when it is undergoing expansion. Because of this, a reverse Laval nozzle, in practice, is never free from shocks.

3.2.1 Normal-Shock Diffusion

The next most simple theoretical approach to an internal-compression type of diffuser is one in which all the supersonic compression is achieved by means of a single normal shock. In this case the losses, apart from those due to viscosity, are dependent upon the Mach number at which the shock occurs. They are zero at M = 1 and increase with increasing Mach number. The ideal normal-shock diffuser then would be a Laval nozzle with the normal shock occurring at the throat. It has been shown (Ref. 3) that the shock is not stable when it occurs upstream of the throat, or even at the throat, but must stabilize itself in some position downstream of the throat and consequently at a velocity in excess of sonic. A stable shock then implies supersonic flow downstream of the throat which in turn implies a throat somewhat larger than a sonic throat, i.e., $A_t \neq A^*$. It also involves a pressure loss since the shock

no longer actually occurs at M = 1. If the back pressure is such that the shock occurs upstream of the throat, it will emerge from the duct and stand in front of the opening as shown below.

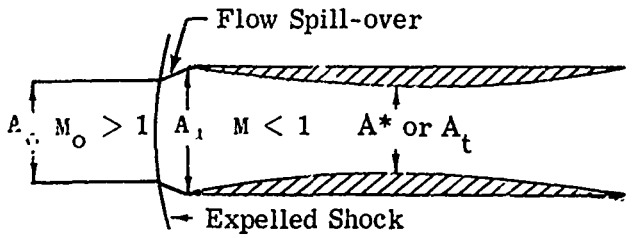

The diffuser cannot be started, or the shock re-swallowed once it has been expelled, unless the throat-to-inlet area ratio is equal to or greater than that shown in curve B of Fig. 3-2. This limiting area ratio is found by assuming that the normal shock is on the lip, i.e., in the critical position. The area ratio, A_t/A_1, is that found from Eq. 2-4 for M_2 which is the Mach number behind a normal shock at M_o, i.e., given by Eq. 2-21. Combining these two equations gives

$$\left(\frac{A_t}{A_1}\right)_B = (A^*/A)_{M_2} = \left[\frac{\gamma+1}{2}\right]^{\frac{-(\gamma+1)}{2(\gamma-1)}} \frac{\left(1+\frac{\gamma-1}{2}M_o^2\right)^{1/2}\left(\gamma M_o^2 - \frac{\gamma-1}{2}\right)^{\frac{1}{\gamma-1}}}{\frac{\gamma+1}{M_o^{\gamma-1}}} \qquad (3\text{-}7)$$

The values shown in Fig. 3-2 are based on $\gamma = 1.4$. Once the flow is started, i.e., the shock swallowed, the area may be reduced to the value shown in curve A (calculated from Eq. 2-4).

Actual area ratios at which such diffusers have operated are shown for comparison in Fig. 3-2. The difference between the theoretical curve A and experimental data gives a good estimate of the viscous losses. It may be seen that the curve of experimental values follows curve A quite closely, although the increase in actual throat area varies from about 16% of the isentropic value at M = 2 to 100% at M = 5.

If a ramjet having such a diffuser with fixed area ratio, (A^*/A_1 or A_t/A_i), is accelerating as shown by the arrow in Fig. 3-2, the shock will not be expelled at the point P but will remain swallowed until the Mach number of point Q is reached. However, if the same missile is decelerating, the shock will not be expelled at Q but will remain swallowed until point P is reached. Thus the position of the shock for conditions between curves A and B will depend on its previous history. To offset this "hysteresis" effect, the diffuser will require a "starting" value of A_t/A_i (curve B), or else the missile will have to overspeed until the shock is swallowed.

This type of diffusion is discussed more fully in Ref. 2 and in Subsec. 5.4 since it is applied to wind tunnels more successfully than to ramjets.

The total pressure recovery for a single-shock internal-compression diffuser, assuming non-viscous flow is shown in Fig. 3-3. In the optimum case, i.e., with area ratios of curve A in Fig. 3-2, the shock would occur at a sonic throat giving a shock pressure recovery of 1.0. If the throat has the minimum area required for starting (curve B of Fig. 3-2), the highest pressure recovery is achieved when the normal shock occurs at the throat. The Mach number at which this shock occurs is found by compressing isentropically from M_∞ at the inlet area, A_1, to M_t at the given throat area, A_t. The pressure recovery in this case is given by curve B in Fig. 3-3. When the shock of this diffuser is at the point of being expelled, i.e., at the entrance, the pressure recovery is shown by curve B' which is the normal-shock recovery at the free-stream Mach number. In actual practice, the pressure losses due to viscous effects will have to be included. They will depend on the Reynolds number of the flow, i.e., on the temperature, pressure, and velocity of the air flow and the length of the duct.

The outstanding advantages of the simple, fixed-throat, normal-shock diffuser are the low external drag that may be associated with it and the simplicity of construction. The main disadvantage is that the large area ratio required for starting such a diffuser gives rise to low efficiency once the shock is swallowed. The efficiency may be much improved by opening up the throat after shock-swallow; however, the mechanical complexity of such an operation and the additional weight required do much to counter its usefulness in a ramjet. A second disadvantage of the normal-shock diffuser is that the length of the convergent section required to compress to sonic conditions without flow disturbance gives rise to a thick boundary layer at the throat. Thirdly, the duct requires an extended throat region for the complex normal-shock system (see Subsec. 5.4). At moderate Mach numbers, it has been shown that a throat length of about four times the throat diameter gives the most satisfactory results. The throat length may, however, be reduced by the insertion of a vortex trap or subsonic dump as described in Subsec. 3.7.2. The above features of the simple inlet are increasingly detrimental as the free-stream Mach number increases.

For these reasons, this type of diffuser is usually limited to flight Mach numbers less than about 1.6 where the pressure recovery is high and the hysteresis effect small. This type of diffusion is applied to wind tunnels more successfully than to ramjets and is discussed further in Subsec. 5.4. It is also treated fully in Ref. 2. However, because of its inherent simplicity and low drag, a good deal of effort has been exerted toward finding methods of overcoming its disadvantages. Methods of varying the inlet-to-throat area ratio will be discussed in the next two subsections. Methods of controlling the boundary layer and minimizing flow distortion will be treated in Subsec. 3.7.

3.2.2 Variable-Area Diffusers

Performance of a fixed-geometry diffuser deteriorates rapidly at Mach numbers other than the design Mach number. Above the optimum Mach number, the throat area is larger than necessary and the efficiency drops off due to increasing throat shock losses. Below the optimum Mach number, the throat is not large enough and the inlet flow breaks down giving a strong shock

in front of the diffuser with attendant high drag and low efficiency. It is therefore imperative to employ variable geometry devices to alleviate these adverse effects as well as to overcome the heavy penalty of the starting area ratio. Many ways of varying the throat area have been devised. One of the most direct methods is by employing flexible plates to form two opposite walls of a two-dimensional diffuser. Investigation of such a diffuser for flows in the Mach number range from 2.5 to 4.0 is described by Gunther in Ref. 106. Flexible plates of constant thickness were deflected by two sets of levers as shown in the following sketch.

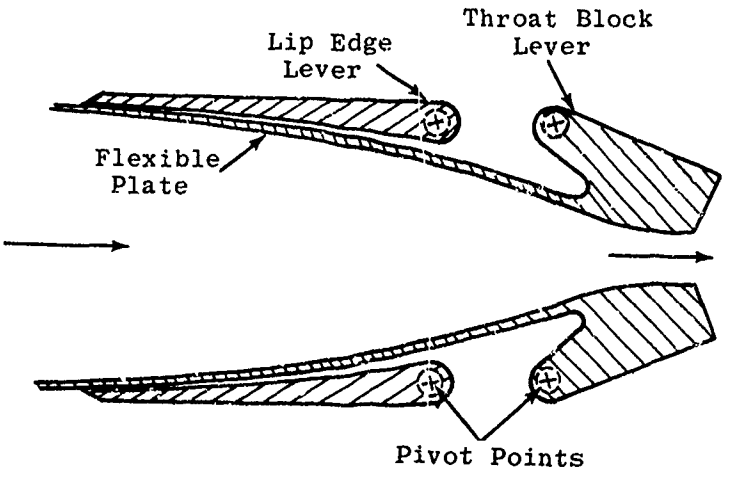

The mechanism functioned satisfactorily but the resulting pressure recoveries were limited by the thick boundary layers which developed in the throat region especially on the side walls. Substantial improvement in the diffuser efficiency was achieved by several methods of bleeding off the boundary layer. The plate surfaces were designed to give isentropic compression to sonic velocity at the throat. Actually, because of the effective area change due to the boundary layer, the lowest Mach number at which the normal shock occurred was about 1.4. Since the boundary-layer problem, in varying degrees, is common to most diffusers, a general discussion of it will be found in Subsec. 3.7.

A second method of varying the contraction ratio is by means of a translating centerbody in an axisymmetric duct. A typical configuration is shown in the sketch below

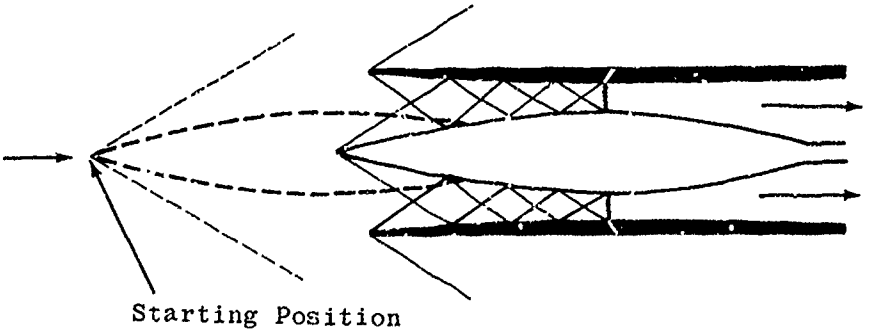

In an arrangement of this type, the duct entry area and the minimum area are varied simultaneously giving rise to quite rapid changes in the contraction ratio. A typical plot of the contraction ratio as a function of the translation of the centerbody is shown in the following sketch. The diffuser with which this ratio is associated was designed for operation at Mach numbers from 2 to 3.

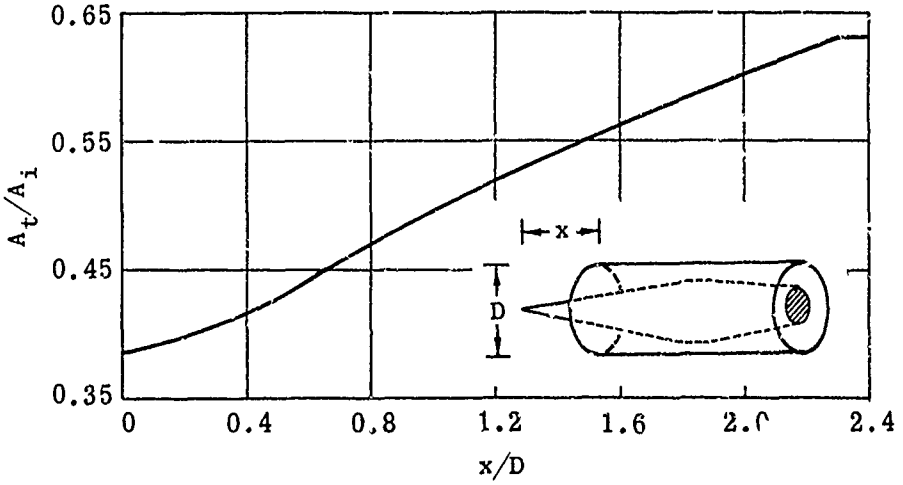

The most stringent requirements of the starting contraction ratio are further ameliorated by the presence of the oblique shock caused by the centerbody tip. For completely internal compression this shock must lie within the duct. (Operation with the shock outside the duct is discussed in Subsec. 3.3.) The shock and its reflections from the duct walls reduce the Mach number at which the normal shock occurs. Mossman and Pfyl in Ref. 107 describe an experimental investigation of axisymmetric diffusers with translating innerbodies. Their first model had a conical-tipped innerbody and a small-angle conical frustum as the annulus. In the second model, the two surfaces were designed to give a uniform longitudinal pressure gradient from entry to throat. A third model was designed by the method of characteristics to eliminate all strong shocks from entry to throat. They concluded that the first model gave the best pressure recovery in the range $2.1 \leq M \leq 2.7$ and the second in the range $2.7 \leq M \leq 3.0$. In all models, even the third one, there is a small inclination between the free stream and the inner cowl surface. This virtual wedge angle produces an oblique shock (and reflections) that further reduces the Mach number at which the normal shock occurs. The values of the pressure recovery for several internal compression diffusers are shown in Fig. 3-3.

Similar oblique shocks, of course, also occur in a practical reverse Laval nozzle in which the purely isentropic nozzle is shortened to prevent undue boundary-layer growth. The necessary finite lip thickness also gives rise to a shock and pressure loss on the outer surface, or the inner surface or both. For the innerbody diffusers of Ref. 107 the flow distortion, as computed from Eq. 3-2, is about 0.035 for Mach numbers from 2.1 to 2.5. At the higher test Mach numbers there is some evidence of an effective angle of attack of 1.0 to 1.5 deg which distorts the total pressure profile at the diffuser exit. For the two profiles (at these small angles of attack) the flow distortion jumps from 0.035 to 0.18. The evidence is too slim to be taken as more than an indication of typical performance at angles of attack. It has been shown that the performance has been much improved by the use of boundary-layer bleeds (see Subsec. 3.7).

3.2.3 Perforated Convergent-Divergent Diffusers

Varying the physical contraction ratio of a diffuser by means of flexible plates or a translating spike, as discussed in the preceding subsection, is readily applicable to wind-tunnel diffusion (see Subsec. 5). As an inlet diffuser for ramjet vehicles its beneficial effect is somewhat cancelled by the added weight of the required mechanisms. In addition, the rapid velocity fluctuations that may occur in flight would necessitate a very sensitive and rapid throat control. It must also be remembered that if the shock is ever regurgitated during flight, an extreme change of contraction ratio would be required for restarting the diffuser.

As an alternative to controlling the area ratio, one may control the mass flow passing through the throat. This control may be achieved by perforating the convergent section of the diffuser. Evvard and Blakey (Ref. 108) calculated the required size and spacing of such perforations as a function of the local Mach number and inlet geometry and estimated the subsonic flow coefficient through the holes. Tests were made at M = 1.85. At zero angle of attack, the total pressure recovery was increased from 0.838 to 0.931 by means of the perforations. It dropped back to 0.920 at three degrees angle of attack and to 0.906 at five degrees.

One of the attractive features of such a diffuser is its "self-adjusting" capability. If the shock is detached and the flow in the converging section is subsonic, the pressure differential (assuming a free-stream static pressure on the outer surface) causes flow through the perforations, thereby reducing the spill-over and moving the shock closer to the inlet. If the perforated area is large enough the shock is ultimately swallowed. When the flow in the convergent section is supersonic, the mass flow is greatly reduced, due to the combined effect of the reduced pressure differential and the increased speed of the flow past the holes. The relationship between free-stream speed, mass flow through the perforations, and the shock position is shown in the following sketch taken from Ref. 108.

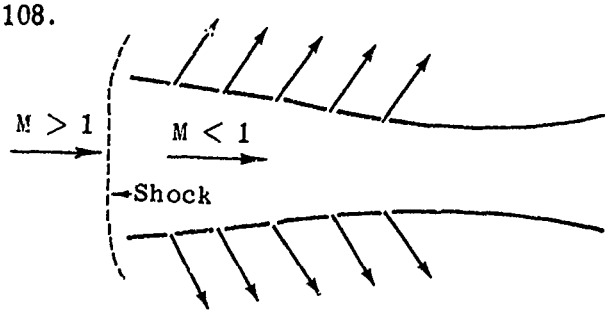

(a) Normal Shock Ahead of Inlet

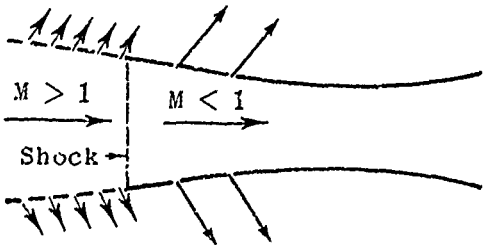

(b) Normal Shock Partly Swallowed

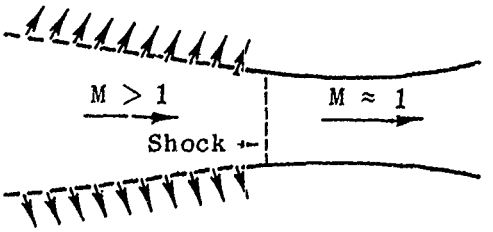

(c) Normal Shock Near Throat

Further tests were made by Hunczak and Kremzier (Ref. 109) for similar inlets at M = 1.9. The average diameter of the sharp-edged (i.e., countersunk) holes was of the order of 0.1 in. Under these test conditions the subsonic flow coefficient was determined to be 0.5. A maximum total pressure recovery of 9[illegible]% was obtained with 18% of the mass flow being spilled through the perforations of a diffuser with a contraction ratio of 1.63. A maximum relative mass flow of 98% was obtained with a peak pressure recovery of 90% in an inlet with a contraction ratio of 1.40. During supercritical operation the theoretical and measured values of the mass-flow ratios agreed within about 1%.

Although these results appear very promising, they have never been assessed in terms of the external-drag increment due to the escaping air. The effect of perforations at higher Mach numbers has not been tested. Perhaps the continuation of this study has been limited by the fact that the interest is now focussed on high flight Mach numbers and isentropic-spike diffusers.

3.3 Oblique-Shock Diffusers

The use of an internal oblique shock as a means of reducing the Mach number at which the normal shock occurs has been described in the preceding subsection. Greater flexibility of operation is achieved if the compression through the oblique shock takes place externally. The shock attached to the tip of a central body eliminates the starting problem and the hysteresis effect associated with the internal-compression diffuser.

Since this idea was put forward by Oswatitsch, such diffusers usually bear his name. The basic principles are illustrated in the following sketch.

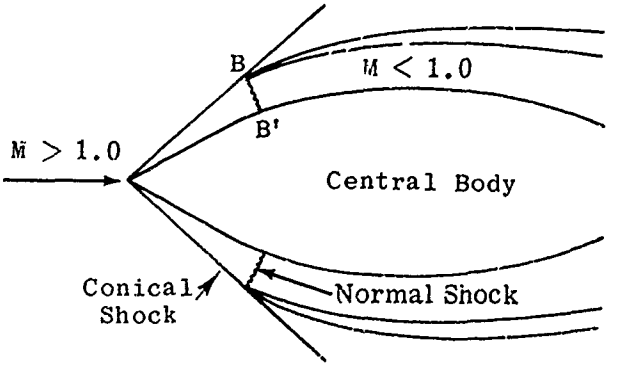

The diffuser is said to be operating critically when the heat released by the burner is of such magnitude that the back pressure maintains the normal shock at the cowl lip. If the back pressure is less than its critical value, the shock is in a stable position downstream of the cowl lip. Such operation is said to be supercritical. When the back pressure exceeds its critical value, the normal shock is detached from the cowl lip giving subcritical flow. These three flow regimes are shown in the sketch below.

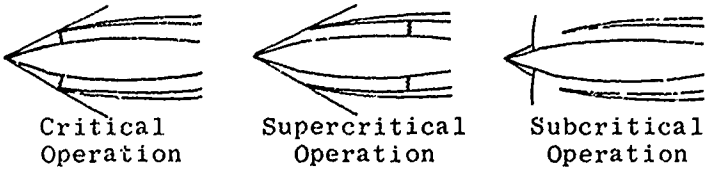

At the design Mach number the conical shock is usually assumed to graze the cowl lip, i.e., there is no supersonic flow spill-over. The relationship between the pressure recovery and the capture-area ratio during the three types of operation may be seen in the sketch on page 104. During supercritical operation the mass capture is a maximum and the pressure recovery increases as the shock moves toward the cowl lip. If there is 100% mass capture, the pressure recovery reaches its peak as the shock reaches the cowl lip, i.e., the critical point, and drops as soon as the normal shock is expelled. If the conical shock does not impinge upon the lip, supersonic flow is spilled even in the supercritical regime, and the mass-flow ratio is less than one. The peak pressure recovery does not always occur at the maximum mass-flow ratio, but is dependent on the cowl geometry and the relative position of the innerbody and the cowling. By a judicious combination of external compression and variation of the duct area, a diffuser may be designed to operate over a wide range of flight conditions.

In the absence of boundary-layer effects, the recovered stagnation pressure increases as the number of oblique shocks increases, since the sum of the total pressure losses across a series of weak shocks is less than the loss across a single oblique shock leading to the same terminal Mach number (see Fig. 5-8). The same principle may be carried to its limit and a continuous curve designed which will give rise to an infinite number of very weak waves. By means of such an "isentropic surface" the flow velocity may be reduced, in theory, to the sonic value without incurring any shock losses. The limitations which are imposed upon such an isentropic compression will be discussed in Subsec. 3.4.1.

The primary design variables which affect the performance of an oblique-shock diffuser are:

1. The shape of the external compressing surface, i.e., a single cone or wedge (Subsec. 3.3.1), a double cone or double wedge (Subsec. 3.3.2), or an isentropic spike or ramp (Subsec. 3.4).

2. The position of the cowl lip with respect to the innerbody tip.

3. The position and shape of the "shoulder" of the innerbody with respect to the cowl lip.

4. The geometry of the cowl lip.

5. The cross-sectional area distribution of the annular diffuser downstream of the inlet, as determined by the inner surface of the cowl and the aft portion of the innerbody.

The last named is often considered a secondary design variable since its effect on the pressure recovery is usually small in comparison with the external compression. However, it does have far-reaching effects on the flow stability (Subsec. 3.8) and on the boundary-layer development in the duct (Subsec. 3.7).

3.3.1 Single-Cone Diffusers

The simplest oblique-shock diffuser employs an innerbody with a conical nose.

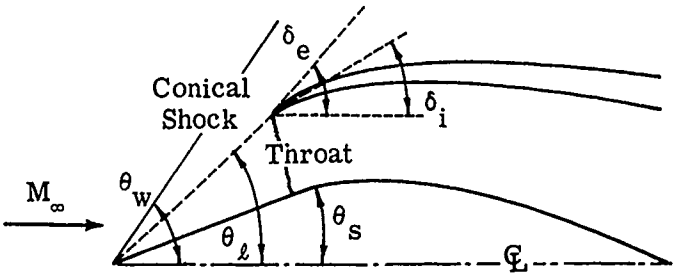

The basic design parameters are:

θ_s = semi-angle of the nose cone

θ_ℓ = angle between the axis and the line joining cone tip and cowl lip

δ_i = interior cowl lip angle

δ_e = exterior cowl lip angle

The maximum diameter of the innerbody, its shape at the maximum diameter, and the shape of the inner and outer cowl walls also must be chosen to give stable, unseparated flow in the duct as well as minimum external drag.

The nose angle, θ_s, should be chosen small enough to prevent shock detachment at the lowest Mach number it will encounter and yet sufficiently large to minimize the length of the conical tip and the boundary-layer growth thereon. Angles between 25 and 30 deg have been found satisfactory at Mach numbers from 1.8 to 5.4 (Refs. 110, 111, and 112).

The theoretical pressure recovery for inviscid flow has been calculated as a function of the Mach number and the cone angle. The calculations assume that the cowl lip is situated on the conical shock. A first case assumes that the normal shock occurs at the duct entrance. A second case incorporates the maximum contraction ratio (from curve B of Fig. 3-3) for shock-swallow associated with the average Mach number, M_2, at the duct entrance. The different flow regions are shown in the sketch below.

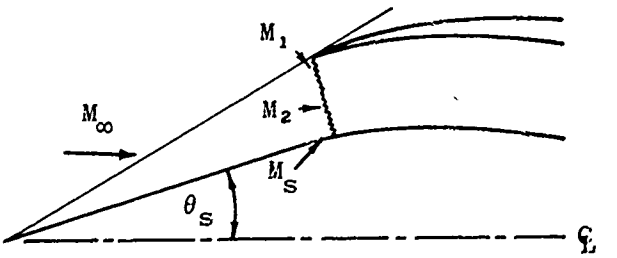

The values of the Mach number behind the conical shock, M_1, and the Mach number on the cone surface, M_s, may be found as a function of M_∞ and θ_s in Kennedy's tables of supersonic conical flow (Ref. 36). The average Mach number, M_2, before the normal shock is taken as $(M_1 + M_s)/2$, although this value is only approximately true in axisymmetric flow. The calculated pressure recovery for both the above cases is shown in Fig. 3-4 as a function of M_∞ and θ_s. From this figure the advantage of a combination of external and internal compression may be seen. Although there is definitely an optimum cone angle for each Mach number, its value is not critical. The spread of cone angles within which the pressure recovery drops by 2% from the maximum is indicated by the bars on the curves of Fig. 3-4. Figure 3-5 gives the optimum cone angle as a function of Mach number and also shows the pressure recovery associated with that optimum value for both cases. Experimental data from several sources are included for purposes of comparison with the theoretical values. The difference between the calculated and the experimental values consists largely of the viscous losses which are ignored in these calculations.

The internal cowl-lip angle, δ_i, may be made equal to the flow inclination behind the bow shock in the neighborhood of the lip, i.e., the inner cowl surface will then be coincident with a streamline of the entering flow. Sometimes δ_i is made slightly less than this value in order to produce a weak "wedge" shock by means of which further compression may be effected. The external cowl-lip angle, δ_e, is usually determined by the value of δ_i, the degree of sharpness of the lip, and the cowl thickness dictated by structural requirements. Although a sharp lip is usually preferred in order to minimize the pressure drag, a blunt lip may reduce the additive drag by delaying the expulsion of the normal shock. It does this by virtue of the fact that the stagnation point moves inside the cowl as the inlet mass-flow ratio diminishes. Such an effect is illustrated below.

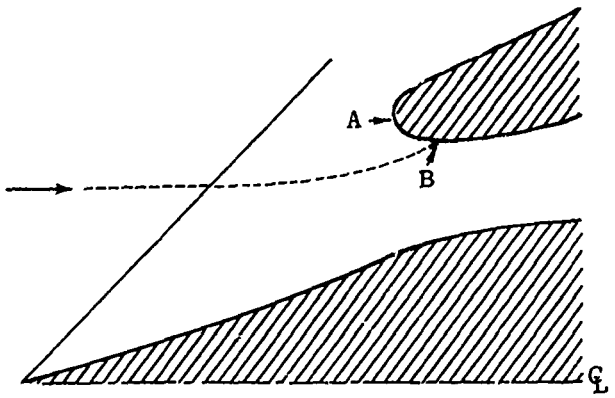

With no spill-over the stagnation point is at A, but it moves around to B as the capture-area ratio diminishes.

For optimum performance at the design Mach number the bow shock from the conical nose should impinge on the cowl lip. In this position there

is no additive drag, i.e., $A_o/A_i = 1$. At the same time the internal ducting should be designed to give a slightly increasing area behind the lip in order to stabilize the shock on the rim. Such a design was first suggested by Ferri and such a diffuser often bears his name. More often the duct is of the convergent-divergent type with the throat area optimized for starting the diffuser. The area variation of the internal ducting is usually the result of a compromise between the desire for a flat, low-drag cowl and the need for a gradual turning of the innerbody to prevent flow separation.

For off-design operation the position of the innerbody in relation to the cowl and the distribution of the duct cross-sectional area must be optimized with respect to each other. As the centerbody is translated along the axis the longitudinal distribution of the duct cross-sectional area varies. In the ultimate design of a ramjet vehicle many compromises must be made. The operating characteristics at all required Mach numbers and angles of attack must be known in order to calculate the performance throughout the whole range of a flight. Even when the geometry may be varied in flight, it may be necessary to take less than optimum conditions at the design Mach number in order to provide sufficient thrust during climb-out or to assure stable operation during the high angles of attack demanded by prescribed maneuvers.

Tests at $M = 5.4$ which are described in Ref. 112 show how critical the relative position of nose and cowl lip may be. The design model operated supercritically at a mass-flow ratio, m_2/m_∞, of 0.96. Retraction of the cone by 0.01 in., i.e., an increase of θ_ℓ (~32 deg) by 0.2 deg allowed 100% mass capture for all supercritical operation. How critical this improved flow capture may be is ultimately dependent on the tactical requirements of the vehicle. Perhaps more significant is the fact that when the bow shock was slightly within the cowl, the inlet operated with high mass-flow ratios for angles of attack of 3 and 4 deg whereas with shock-on-rim, there was a large amount of flow spillage even at 2 deg angle of attack.

The most suitable position of the throat in the duct is dependent on the nose and inlet geometry and on the flow parameters. When the spike is translated to give the maximum mass-flow ratio at several Mach numbers, the optimum rate of internal expansion is strongly dependent on the Mach number range within which the diffuser must operate. The shape that gives a gradual rate of internal expansion for the highest Mach number may give a too-rapid internal contraction when operating at the lowest Mach number.

It is also important that the rate of change of the duct area be very small in the region of the throat. It has been shown to be even better to have a constant-area section at the throat. The optimum length of this section varies with Mach number (see Subsec. 5.4). However, in a diffuser with internal as well as external compression, the normal shock occurs at an almost constant Mach number not much greater than one and hence the throat length need not vary. At moderate free-stream Mach numbers it has been shown that a throat length of about four times the throat height gives the most satisfactory results.

Typical total pressure recoveries for single-cone inlets are shown in Fig. 3-6 as a function of mass-flow ratio for $M_\infty = M_D = 1.8, 2.0, 3.85,$

and 5.4. The effect of small angles of attack (under slightly different test conditions) is shown in Fig. 3-7. The systematic degradation of pressure recovery with increasing angle of attack may be seen for all Mach numbers.

The effect of translating the spike was tested at M = 1.8 and 2.0 and reported in Ref. 110; some of these results are shown in Fig. 3-8. As the spike was moved out of the inlet to reduce θ_ℓ from 41.6 deg to 37.4 deg, the effect on the additive drag and the drag of the cowl was quite marked, whereas the pressure recovery showed relatively little change.

Two basic modifications were made in the test models of Ref. 111. The first was concerned with reducing the cowl drag and the second with improving the pressure recovery by bleeding off the low-energy boundary layer. By going from a relatively steep cowl (δ_e = 38.3 deg and δ_i = 29.2 deg) to a flat cowl (δ_e = 4 deg and δ_i = 0 deg), the pressure-drag coefficient at M = 3.85 was reduced from 0.112 to 0.007. However, at the same time the maximum inlet mass-flow ratio was reduced from 0.95 to 0.81 and the total pressure recovery from 0.32 to 0.285. The pressure loss is due primarily to separated flow in the vicinity of the sharp shoulder of the innerbody dictated by the shape of the low-drag cowl as shown in the sketch below.

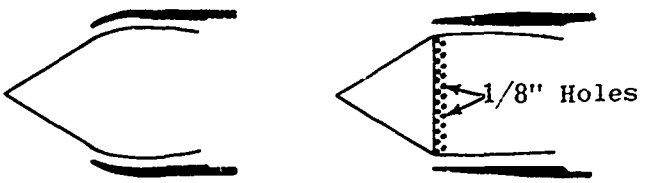

High-Angle Cowl Low-Angle Cowl

The reduced value of the pressure recovery was later restored to the original value and the inlet mass-flow rate increased to 0.925 by bleeding off the boundary layer through a double row of staggered 1/8 in.-diameter holes immediately downstream of the shoulder of the conical innerbody (Ref. 111). In the tests at M = 1.8 and 2.0, the boundary layer was bled off through three subinlets which consisted of slots in the inner wall of the cowl downstream of the narrowest section as shown in the sketch below.

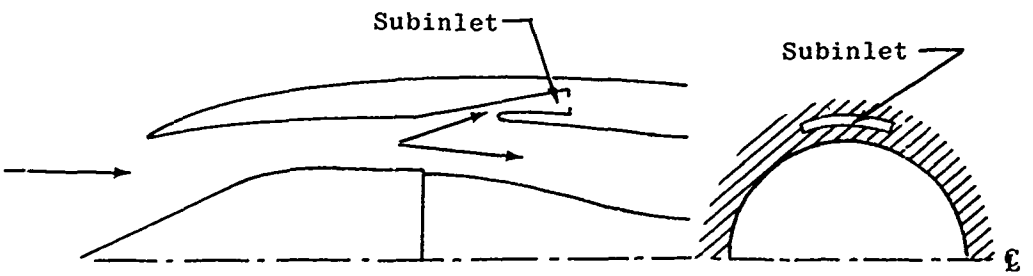

Each inlet carried about 3% of the total mass flow. The inlets not only improved the pressure recovery by two or three per cent, but also resulted in a better pressure distribution at the diffuser outlet as shown in Fig. 3-9. This

latter improvement was most marked at 6 deg angle of attack. It may be noted that these inlets had no significant effect on the mass-flow ratio. With the inlets closed there was a considerable region of separated flow in the duct which did not appear when the boundary layer was removed.

3.3.1.1 Probe Diffusers

Occasionally a bluff surface, in which a dish homing system may be installed, is required in the centerbody of a diffuser. The consequent detached shock, with its high pressure losses and high drag, demands heavy penalties from both the aerodynamic and propulsive viewpoints. A simple probe protruding from the nose cap may produce a flow regime comparable to that of a conical tip and thus it may satisfy the aerodynamic requirements without jeopardizing the guidance system. The performance of such a probe on a hemispherical and on a flat-capped central body of a diffuser is described by Dean in Ref. 113. Sketches of the two models are shown below.

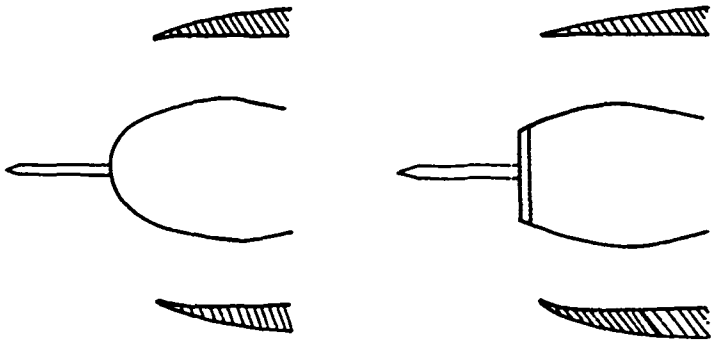

Tests in which the probe length was varied were run in a free jet at M = 1.8. When equilibrium is established the flow field resembles that due to a conical spike. In order to facilitate comparison, a 22.75 deg cone diffuser was run under the same test conditions. Typical flow sketches of the two models, with different probe lengths, are shown in Fig. 3-10 for both swallowed-shock and detached-shock conditions. The flow was unstable for detached-shock conditions with the greater probe length. The measured total pressure recovery at zero angle of attack is shown as a function of the capture-area ratio in Fig. 3-11 where it is compared with that of a single-cone diffuser. It may be seen that the pressure recovery of the probe attached to a spherical head is as high ($\sim$ 0.875) as that of the single-cone diffuser. However, since there is more spill-over in the probe configuration the additive drag will also be higher. It may also be seen from this figure that the flow field due to the probe becomes unstable as the spill-over increases and that the diffuser is inoperable for capture-area ratios between about 0.73 and 0.87. The effect on the pressure recovery of angles of attack of 3 and 6 deg is shown in a similar manner in Fig. 3-12. The formation of a strong shock on one side of the diffuser and the loss of a large part of the separation cone on the other side results in lower pressure recoveries. However, if the probe is aligned with the freestream when the diffuser is at an angle of attack, the losses are reduced as shown in Fig. 3-13.

The length of the probe was shown to be an important parameter in determining the stability of the diffuser operation. At the test Mach number

the maximum probe length for stable operation was found to be about three times the radius of the base of the separation cone. The position of the bluff body with respect to the cowl inlet was also found to be a critical function of probe length.

Similar tests at Mach numbers of 1.76, 1.93, and 2.10 are reported by Moeckel and Evans in Ref. 114. They also found that at zero angle of attack the pressure recovery and mass-flow ratio are comparable to those of a solid conical-nosed innerbody. However, even at small angles of attack the diffuser efficiency is greatly reduced.

3.3.2 Double-Cone Diffusers

Theoretically, a diffuser with two oblique shocks will give a better pressure recovery than one with a single shock (see Fig. 5-8). The addition of some internal compression not only improves the pressure recovery but may also assist in stabilizing the normal shock.

The double-cone diffuser is usually designed to allow the two oblique shocks to coalesce at the cowl lip as shown in the sketch below.

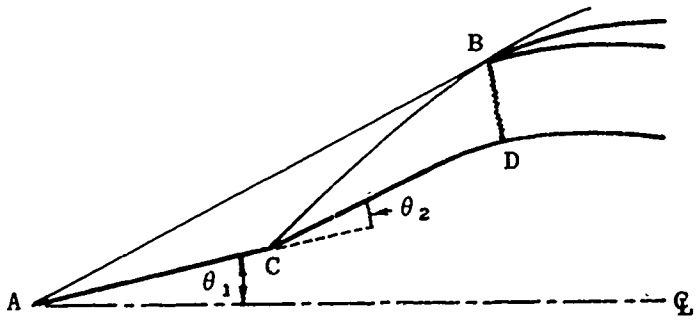

In the region behind the bow shock, AB, the flow is conical and isentropic. When this flow strikes the second cone a curved shock, BC, is produced, the curvature being due to the variation of flow angle and Mach number in the conical region. In the region downstream of the curved second shock the flow is rotational. A normal shock, BD, may occur at the lip or it may occur near a throat in the annular duct, i.e., the double-cone diffuser may employ all external compression or a combination of external and internal compression.

By means of the method of characteristics, Kennedy (Ref. 37) has analyzed the flow field around several biconic bodies for a wide range of Mach numbers. Calculations which include the effect of the rotationality show that even at the highest Mach numbers used (~ 5) the accuracy of the results is not appreciably impaired ($\leq 1.5\%$ change in M) when this entropy variation is neglected. Included in Ref. 37 are the cartesian coordinates, the Mach number, and the flow orientation for all mesh points, as well as the flow variables on both sides of the curved shock and along the cone surfaces. Equations for the curved shocks and for the loci of the point of intersection of the conical and curved shocks are also included. Table 3-1, derived from this material, permits the reader to reconstruct the curved shock front for many

different biconic inlets over a wide range of Mach numbers. Table 3-2 and Figs. 3-14 and 3-15 give the position of the point of intersection of the two shocks as well as the flow characteristics immediately behind it as a function of the free-stream Mach number and the cone angles.

The total pressure recovery may be obtained from the data in Ref. 37 by using

$$\frac{p_{t_5}}{p_{t_\infty}} = \frac{p_{t_1}}{p_{t_\infty}} \cdot \frac{p_{t_3}}{p_{t_2}} \cdot \frac{p_{t_5}}{p_{t_4}}$$

where the total pressure is assumed constant in any region between shocks, i.e., $p_{t_1} = p_{t_2}$ and $p_{t_3} = p_{t_4}$ (see sketch below).

p_{t_1}/p_{t_∞} is obtained from either oblique or normal-shock tables using any pair of values from among M_∞, M_1, ϑ_{w_1}, and φ_1.

p_{t_3}/p_{t_2} is found in a similar manner for each mesh point along the shock and averaged.

p_{t_5}/p_{t_4} is the normal-shock recovery found by using the mesh point values of M_4 averaging the pressure ratio.

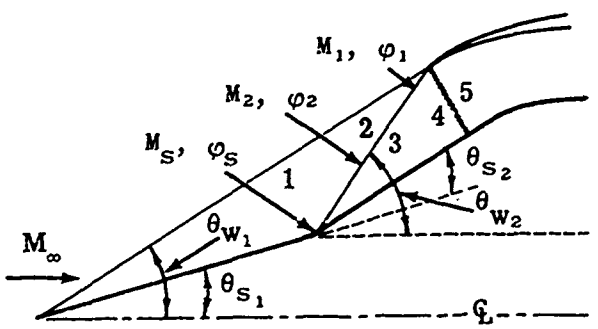

If the normal shock occurs within the duct rather than at the entrance, it may be assumed to occur at the station of least cross-sectional area. The Mach number at that station is found by comparing A_t with A_i. In order to avoid time consuming averaging of the values at the curved shock and at the diffuser entrance, a short-cut method has been based on that of Connors and Meyer (Ref. 115). In it the average Mach number, M_2, is taken as $(M_1 + M_S)/2$ and the average flow deflection in front of the second shock as $(\varphi_S + \varphi_1)/2$. The flow direction behind the second shock is taken as $(\theta_{S_1} + \theta_{S_2})$ (see above sketch) throughout its length.

This method has been used to construct the curves of Fig. 3-16 which give the pressure recovery of double cones for Mach numbers from 2 to 6 and a wide range of cone angles. Two limiting cases have been considered. The first case deals with both external and internal compression, the internal contraction being the "starting throat" for the average entering Mach number. In

the second, the compression is completely external with the terminal normal shock occurring at the cowl lip. Figure 3-17 gives the maximum pressure recovery as a function of Mach number and shows the values of the first and second cone angles that are associated with maximum pressure recovery. It may be seen from this figure that the optimum first cone angle is relatively insensitive to Mach number, but that the optimum second cone angle varies rapidly with Mach number, particularly in the Mach number range below four.

Calculations using average values from the Kennedy data and those using the simplified method of Ref. 115 were compared for 25-40 deg biconic noses at Mach numbers of 2.3604, 3.9260, and 5.1233. In spite of the unrealistic assumptions, the short method underestimated the total pressure recovery by only about one-half of one per cent at the lowest Mach number and by two per cent at the highest Mach number. The simpler method does not, of course, give any information about the flow field as does the Kennedy method.

The calculation of the internal compression contains two known areas of over-simplification. In the first place, it is assumed that the ultimate compression is achieved by a single, simple normal shock at the throat. In reality the shock is usually a complex shock system (see Subsec. 5.4) and is stable only when it occurs downstream of the throat. This shock system does, however, allow a somewhat smaller throat than the one calculated under the simple assumptions and thus provides a compensating error.

The second over-simplification is that the internal compression before the normal shock is assumed to be isentropic, i.e., that δ_i is equal to the flow angle and creates no oblique shocks. If the entering flow angle is large, a high cowl drag would be associated with the maximum pressure recoveries shown in Fig. 3-17.

Representative measured pressure recoveries for double-cone diffusers are taken from Refs. 111 and 116. When the inlets were operated at below-design Mach numbers, the spike was translated to allow the second shock to touch the cowl lip. The measured maximum pressure recoveries are shown in Fig. 3-17. The difference between the actual pressure loss and the theoretical one increases as the Mach number increases and is due mainly to the viscous forces that are neglected in the calculations.

Tests designed to assess the relative merits of optimizing the internal flow and minimizing the external cowl drag are reported in Ref. 103. Two versions of the 20-35 deg biconic spike were made. In one the internal flow was turned very gradually and in the other, much more sharply. The projected areas of the cowl were 20% and 40% of the maximum cross-sectional area. The pressure recovery as a function of the mass-flow ratio and angle of attack is shown for the two models at four Mach numbers in Fig. 3-18.

The total-drag coefficient for the same models was obtained by force measurements and the cowl drag from integrated pressure measurements. The skin friction was computed and the additive drag determined by subtracting the last two components from the total drag. The values of thrust-minus-drag are shown as a function of Mach number in Fig. 3-19. They are normalized

with respect to the ideal thrust coefficient, i.e., that with no pressure losses. It may be seen that the drag penalty of the deeper cowl more than outweighs the improved flow due to the more gradual turning at the shoulder of the innerbody.

The critical total pressure recovery at angle of attack is shown in Fig. 3-20 together with the associated supercritical mass-flow ratio. For a valid assessment of the worth of such a diffuser at angles of attack, these graphs should be considered in conjunction with those of Fig. 3-21 which gives the flow-distortion contours at the diffuser exit. Large areas of separated flow or an unbalanced pressure distribution at the exit due to angles of attack would be unsatisfactory for the propulsion requirements. In the particular diffuser of these tests, the flow-distortion parameter (Ref. 103) was, as would be expected, greater with the low-drag cowl than with the high-drag one.

The external and internal cowl-lip angles for these models were 32.6 deg and 27.6 deg. The latter angle is smaller than the flow angle of the entering stream at that point and therefore causes another oblique shock from the lip. It is often advantageous to position the spike so that the second oblique shock strikes the inner surface of the cowl rather than grazing the lip. This ensures an internal oblique shock and consequent improved pressure recovery.

The effect of translating the spike at the design Mach number is shown in Fig. 3-22. When the spike is moved further from the cowl lip both the mass-flow ratio and the pressure recovery deteriorate. With spike retraction, 100% mass flow is achieved at the expense of an 8 to 10% loss in critical total pressure recovery. Furthermore, the retracted spike in conjunction with the gradually curved shoulder of the innerbody gives stable subcritical flow down to a mass-flow ratio of 0.6. The same effect was obtained at $M_D = 3.85$ (Ref. 111) by a slight extension of the cowl.

The effect of translating the spike to give the optimum shock configuration at Mach numbers less than the design Mach number is shown in Fig. 3-23. The critical pressure recovery of the model with the translating spike shows a slight improvement over that of a fixed-geometry model for Mach numbers between 2 and the design Mach number of 3. The improvement of the mass-flow ratio is much more marked. The same figure shows the slight further improvement in both critical pressure recovery and mass-flow ratio due to a more gradual expansion of the subsonic duct (see tests of Ref. 116).

Figure 3-24 (from Ref. 116) shows a comparison of the supercritical external-drag coefficient for the fixed-geometry model and for the two versions of the translating-spike diffuser. A significant decrease in drag is obtained by the variable geometry at Mach numbers less than 3.0. This improvement, however, will ultimately have to be assessed in terms of the additional weight required for the translating mechanism.

Boundary-layer effects show up very strongly in the operation of the two-cone diffuser. The advantage due to the double cone is often offset by the

"bridging" effect of the boundary layer at the junction of the two conical surfaces, as shown in the sketch below.

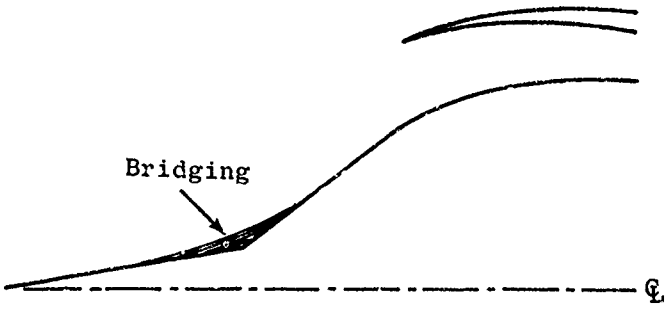

This flow separation and subsequent re-attachment not only changes the effective spike geometry but also may induce a greatly modified shock pattern. It is generally agreed that such separation takes place only in laminar flow and thus may be alleviated or entirely eliminated by roughening the spike tip to ensure boundary-layer transition before the juncture of the two surfaces. (This phenomenon has been discussed in Section 8 of the Handbook, Subsec. 4.1.4.) Figure 3-25 shows the effect of tip roughness on the pressure recovery at M = 3.85 for a biconic inlet; both pressure recovery and mass-flow ratio are much improved at all angles of attack included in the test except the highest (9 deg). Almost identical results were obtained by applying suction to a ring of holes just upstream of the juncture between the surfaces. This latter method allowed the diffuser to operate up to an angle of attack of 11 deg. Off-setting this improvement is the fact that the mass flow is reduced by the amount of the bleed flow. Bridging has also been alleviated by the use of a porous inner-body through which passed about 1-1/2 to 2% of the total mass flow (Ref. 111).

The presence of a thickened boundary layer may cause poor quality flow at the diffuser exit and, under critical conditions, may be responsible for premature choking of the subsonic duct. Methods of boundary-layer control which provide improved duct flow are discussed in Subsec. 3.7.

The interaction of the shock system with the boundary layer initiates flow instability or "buzz". This will be discussed in Subsec. 3.8.

3.4 Isentropic-Spike Diffusers

If the external compression is achieved by means of multiple shocks rather than by just one or two shocks as described in preceding subsections, the pressure recovery will improve as the shock strength diminishes. Carrying this concept to its limit, the spike may be designed so that the flow is isentropic, i.e., all shocks are reduced to Mach shocks and may be made to coalesce at a single point. Such compression, if continued to the sonic velocity, theoretically involves no total pressure loss. Viscous effects and practical design considerations preclude such ideal isentropic compression.

3.4.1 Design Considerations

The length of a true isentropic spike would be impractical. Not only would the needle-like tip be structurally unstable but the long spike would

give rise to a boundary layer which would be very thick by the time the flow entered the subsonic duct. When a conical tip is used in conjunction with an otherwise isentropic spike, the value of the pressure recovery associated with a conical tip may be found from

$$\frac{p_{t_2}}{p_{t_1}} = \left[\frac{(\gamma+1)\ M^2\ \sin^2\ \theta_w}{(\gamma-1)\ M^2\ \sin^2\ \theta_w + 2}\right]^{\frac{\gamma}{\gamma-1}} \left[\frac{(\gamma+1)}{2\gamma\ M^2\ \sin^2\ \theta_w - (\gamma-1)}\right]^{\frac{1}{\gamma-1}} \qquad (3\text{-}8)$$

where

M = free-stream Mach number

θ_w = shock-wave angle.

The bow shock may be considered as a plane shock everywhere except in the vicinity of the nose itself.

Associated values of M, θ_w, and the cone semi-angle, θ_s, may be found from such tables as Refs. 21, 22, 23, and 26. Calculated values of the pressure recovery are shown in Fig. 3-26 as a function of the Mach number for various values of θ_s. The compromise between pressure recovery and boundary-layer build-up, or between pressure recovery and satisfactory performance over a range of angles of attack, will have to be made in the light of the anticipated flight and maneuver conditions. Connors and Meyer (Ref. 115) suggest the use of a conical tip whose attached shock has a total pressure recovery of 99%. Brumbaugh and Konrad, in unpublished studies on diffuser design for Mach numbers from 3 to 7, use a constant tip angle of 15 deg in order to maintain a spike of short length.

The ideal isentropic compression is limited in extent. There are two entirely separate and distinct design criteria to be observed for satisfactory performance of an isentropic spike; one dependent on the shock waves associated with the innerbody, and the other on the shock waves associated with the cowl lip.

From the point of intersection of the shock wave and the compression fan there arises a vortex sheet and also there is usually a reflected wave as shown in the sketch opposite. The vortex sheet adjusts itself until the pressure and the flow direction are the same on either side of it, i.e., $p_a = p_b$ in the terminology of the sketch. The pressure ratio, p_a/p_∞, as a function of M_∞, and the flow deflection, φ, is most easily obtained from graphs (Ref. 22 or 23) since there is no convenient explicit function by which it may be calculated. The curves of p_a/p_∞ vs φ for various values of M_∞ are shown in Fig. 3-27. The same figure shows the value of p_c/p_∞ for an isentropic compression. They are obtained by the use of reverse Prandtl-Meyer expansions. These calculations are valid only in the immediate vicinity of the point P. When a conical tip is used the expansion begins at the Mach number behind the

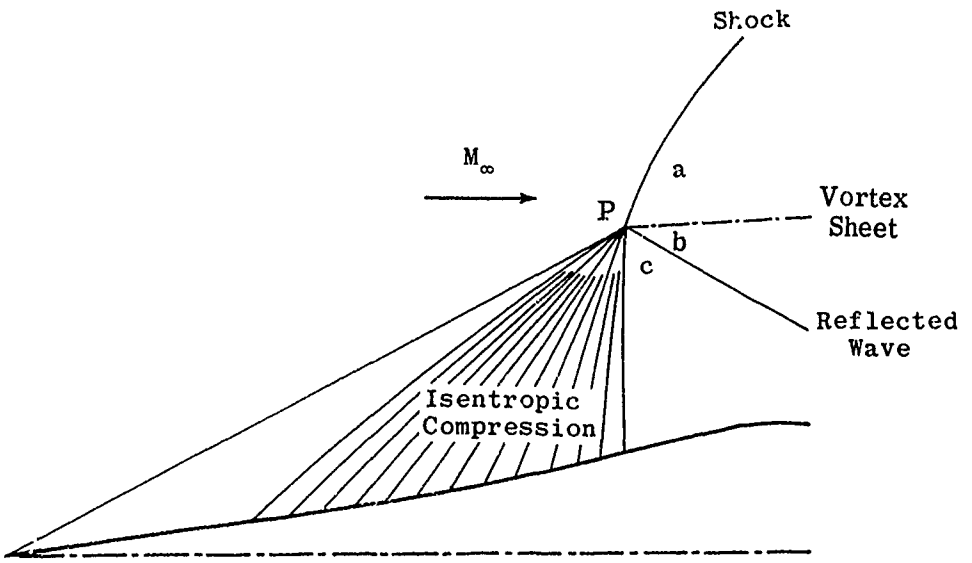

bow shock and the static pressure recovery is the product of that through the bow shock and that due to the flow deflection along the "isentropic" part of the spike surface.

If there is no reflected wave the pressures p_a and p_c will be equal, and the only possible flow deflection angle at each Mach number will be that given by the intersection of the p_a/p_∞ and p_c/p_∞ curves. Where there is a reflected wave its deflection will be equal in value but opposite in sign to that of the isentrope. Possible values of the flow deflection will be found where lines of such slope intersect the shock polars. The limiting condition occurs at a point on the isentrope, e.g., A, B, or C from which the reflected wave will be tangent to the polar. The tangent points, T_A, T_B, and T_C are shown in Fig. 3-27. Enlargements of the critical regions at Mach numbers of 3 and 6 are shown in Fig. 3-28, since they exemplify, respectively, a compressive and an expansive reflection wave. In these enlargements the local pressures have been related to the stagnation rather than the static pressure. The values of the limiting expansion Mach number, M_P, and the limiting flow angle, φ_P, are shown as a function of the free-stream Mach number and the cone tip angle in Fig. 3-29. The maximum pressure recovery associated with these conditions is shown in Fig. 3-30 for the cases of a normal shock occurring either just inside the lip or at the minimum "starting" throat. In a practical design, the cowl lip is often placed slightly below the point of intersection of the compression waves and on the conical shock of the design Mach number. This ensures that the vortex sheet does not enter the diffuser where it could cause serious flow separation.

The second criterion for the limiting value of the isentropic expansion is derived from a consideration of the flow characteristics at the cowl lip. Experimental investigation has shown the cowl-lip angle to be one of the most

critical design parameters. The nomenclature used in connection with the cowl lip is shown in the sketch below.

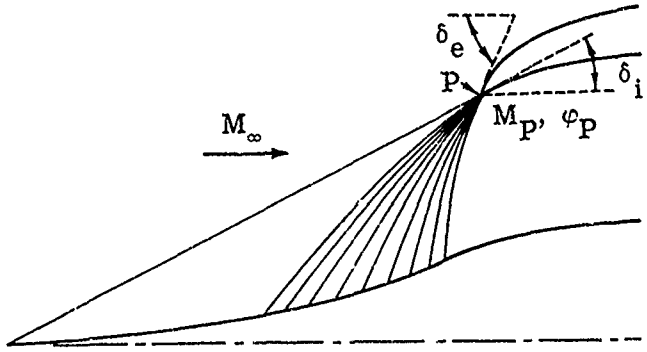

It is required that the shock caused by the incoming flow will not detach from the internal or external cowl-lip surfaces. The critical incidence δ_i, of the inner cowl surface must be evaluated at the lowest Mach number anticipated, and hence may be defined by

$$\delta_i = \varphi_P - (\delta)_{M_P}$$

where φ_P and M_P are the flow direction and Mach number after the last permissible compression wave, and $(\delta)_{M_P}$ is the limiting wedge angle for shock attachment at M_P. For a given free-stream Mach number and flow direction, each value of M_P uniquely determines a value of φ_P and $(\delta)_{M_P}$ and hence of δ_i. Critical values, i.e., lower limits, of δ_i vs M_P for free-stream Mach numbers from 2 to 8 and various tip configurations are shown as curves A in Figs. 3-31a, b, and c. An upper limit (shown by curve B) is placed on δ_e by the requirement of an attached shock at the free-stream Mach number. The value of $(\delta_e - \delta_i)$ is usually defined by structural requirements as about 3 or 4 deg and hence an upper limit may be placed on δ_i. This limit for a lip angle of 4 deg is shown as curve C in Figs. 3-31. Also shown on the same set of figures by curve D is the limiting value of M_P determined from the vortex-sheet criterion. The values of δ_i that lie to the left of curve D and above curve C are those that fulfull the requirements of both the vortex sheet and the attached lip-shock criteria. The limiting values taken from Figs. 3-31 are shown as a function of Mach number in Fig. 3-32. The difference between δ_e and δ_i should include not only the lip thickness but also a safety factor of about 4 deg in order to allow for viscous effects and ensure only supersonic spillage and hence minimum additive drag during all critical and supercritical operation. An analysis also should be made of the effect of the proposed cowl lip on the flow characteristics at all anticipated off-design Mach numbers and angles of attack (see Subsec. 3.4.2). It may be necessary to sacrifice efficiency at the design Mach number in order to increase the range of operable conditions.

The pressure recovery will increase as M_P decreases, and as M_P decreases, the critical value of δ_i increases. Thus, high pressure recovery may be indirectly associated with higher values of δ_i. On the other hand, high values of δ_i mean still higher values of δ_e and a consequent increase in the external wave drag. The fact that δ_i has a lower limit means that there is always at least a minimum cowl drag for this type of diffuser whereas an all-internal-compression diffuser may be designed to have zero cowl drag. The optimum value will be determined not only by consideration of δ_e and δ_i but will also have to take into account the allowable contraction ratios given by the geometry of the innerbody and the annular ducting.

After having decided on the tip angle of the isentropic spike and the extent of external compression (i.e., M_P), the next step is to design the isentropic surface of the spike.

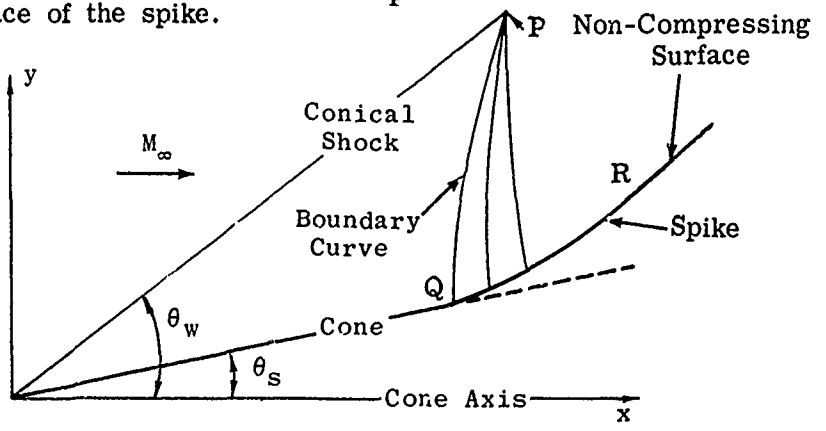

The calculations start at P, a point on the conical nose shock which is a specified distance from the cone axis. Values of M and φ (flow direction) at P, as well as along all rays emanating from the cone tip, may be determined from cone-flow tables such as Refs. 35 and 36. The left running characteristic from P has an inclination of $\varphi_P + \alpha_P + 180$ deg, where α_P is the Mach angle at P. The boundary curve, PQ, of the characteristics net is constructed in short segments whose end points lie on adjacent rays. The inclination of each segment is made equal to the average of the inclinations of the two ends. This construction is continued until the characteristics line meets the cone surface at Q. Each subsequent characteristics line starts from P, has an arbitrary increment of turning, and is continued until it meets the streamline passing through Q. This streamline forms the isentropic surface and is developed incrementally until the flow inclination behind the last characteristics line from P is equal to some predetermined value (equal to or less than that given in Fig. 3-29). The non-compressing surface is generated by a straight line which is drawn tangent to the compressing surface at the terminal point R. The Mach number increase along this surface, and along all the streamlines of the non-compressing flow, results in an approximately constant Mach number along a line normal to the flow drawn from the point of shock intersection.

An example of the calculation of an axially-symmetric isentropic spike is given by Kennedy in Ref. 117. A more detailed method for the use of characteristics in axially-symmetric flow may be found in Refs. 96 and 98.

Contours have been calculated by Connors and Meyer (Ref. 115) for isentropic spikes with conical tips whose shocks cause a 1% loss in total pressure. The coordinates of the surfaces are given in Fig. 3-33 and the surface Mach number and flow direction in Fig. 3-34, both for design Mach numbers from 2 to 4. Similar information from the same source is given for two-dimensional wedge-type inlets in Figs. 3-33 and 3-35. The position of the focal point is indicated in the figures. The Mach number at the focal point is that given by the compression limitations in Fig. 3-29. Figure 3-36 gives the surface coordinates for an axisymmetric isentropic spike with a 15 deg tip and Fig. 3-37 gives the surface Mach number and flow inclination.

For operation with the normal shock at the cowl lip, or just inside it, the turning surface of the spike and the inner surface of the cowl must be adjusted as shown in the following sketch. Both the inner and outer cowl surfaces in this case are composed of two straight sections extended by tangent arcs.

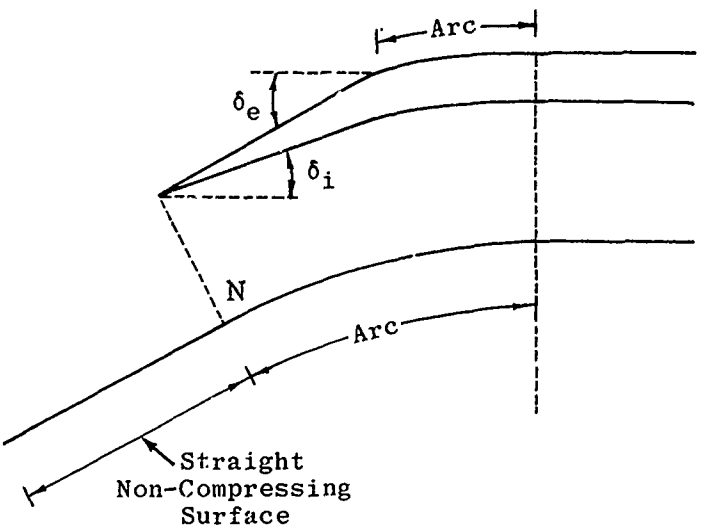

A line from the cowl lip, normal to the flow, intersects the non-compressing surface at N. From this point the turning surface begins. The shape of the arc is determined by the required area variation in the entrance of the annulus.

If the required cowl-lip angles and the flow direction allowed by the limiting compression result in too great a contraction ratio, it may be necessary to undercut the turning surface as shown below.

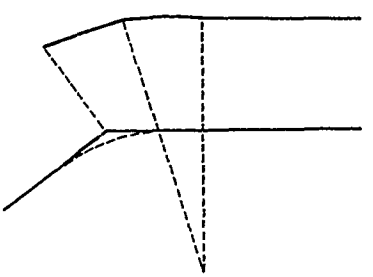

Where the cowl angles are critical, i.e., the drag or the structural load is critical, it may be necessary to sacrifice some of the allowable external compression (see Fig. 3-29) in order to stay within the possible range of flow turning.

It is often desirable to incorporate some internal compression by means of area variation in the ducting. In a typical long range missile, an area reduction of 0.09 A_i slightly downstream of the cowl lip was found to give the lowest shock loss and highest pressure recovery in the turning region. In this case it is necessary to place a further limitation on the turning surface to prevent the normal shock occurring at the lip. The required geometry is shown in the sketch below.

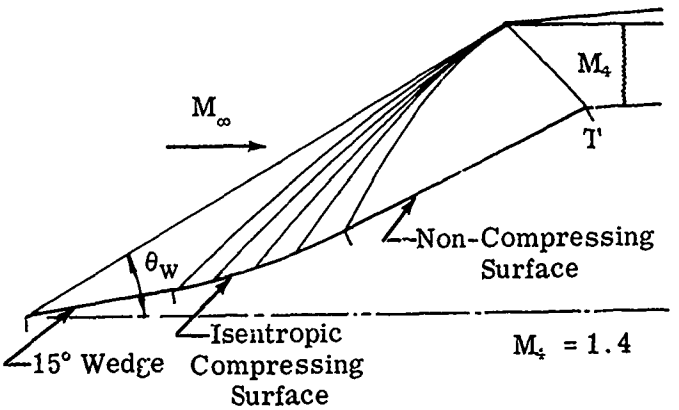

The point of critical importance is the intersection, T, of the non-compressing surface and the oblique shock from the cowl lip. If the turning of the surface is delayed beyond the point T the flow deflection will be too great, causing the reflected shock to detach from the surface and form either a Mach reflection or a lambda shock. On the other hand, if the surface turns before T an expansion fan will occur upstream of the oblique shock causing an increase in the total pressure loss. Careful choice of the point T with respect to the flow field is of increasing importance as the free-stream Mach number increases.

The desired rate of change of the cross-sectional area along the annular duct will depend on the type of operation for which the diffuser is intended. The same considerations that were discussed in relation to conical innerbodies will apply to isentropic tips also. Experience has shown that for an all-external-compression inlet it is desirable to have the surfaces of the cowl lip generated by straight lines which lead tangentially into the arcs which generate the remaining cowl surfaces. In addition, a short constant-area section downstream of the lip is necessary to stabilize the normal-shock system.

At Mach numbers in excess of about three, the inlet duct area is affected by the differential heating rates of the innerbody and the cowl structures. The materials from which they are constructed and the position and thickness of the struts which join them are among the factors that disturb the matching between diffuser and combustor as a function of time. Buzz (see Subsec. 3.8) or thrust degradation may result.

3.4.2 Off-Design Operation

The determination of the performance of a supersonic diffuser at Mach numbers below the design value is a factor of paramount importance in the ultimate assessment of the total worth of a vehicle in terms of its prescribed mission.

A diffuser designed to give a maximum total pressure recovery at the design Mach number may be severely limited in its climb-out capabilities due to excessive spillage and consequent additive drag at below-design Mach numbers. However, it must be remembered that a reduced mass flow may allow the engine to burn a richer fuel mixture and hence produce a greater gross thrust. At the same time the net thrust may be reduced by the associated additive drag. The optimum mass-capture ratio will depend on the vehicle configuration and the combustion characteristics. One means of increasing the capture-area ratio without excessive additive drag at below-design Mach numbers is to locate the cowl lip on the conical shock of the design Mach number but at a radial position less than that of the intersection of the conical shock and compression fan. In this case the reduction of additive drag is accompanied by a reduction in the total pressure recovery at the design Mach number. A second method of reducing the additive drag is by means of a translating spike. Not only does this involve extra weight but may require extensive modification of the design of the internal ducting to prevent choking when the innerbody is in its retracted position.

The extreme angles of attack sometimes encountered during vehicle maneuvers may cause complete and sudden separation of the flow from the leeward side of the spike and missile body with consequent large reduction in pressure recovery leading to combustion failure. It has been shown that this can be forestalled by means of spike translation with, however, its attendant disadvantages.

For an isentropic-spike diffuser, the off-design flow analysis is almost the reverse of the design analysis. In the latter the shock intersection and consequent characteristics network determines the surface variables whereas in the off-design analysis the surface variables and the free-stream Mach number start the network and determine the flow variables near the cowl. In particular, one is able to determine the capture-area ratio, the additive-drag coefficient and the flow parameters at the cowl lip for any free-stream Mach number and prescribed surface. The characteristics curves do not coalesce in the off-design network as they do in the on-design analysis.

A below-design Mach number flow analysis has been carried out by Kennedy (Ref. 105) for 15 deg conical-tipped isentropic spikes designed for $M = 3.5$ and $M = 5$. The cowl was translated first along the design conical shock and then in an axial direction as illustrated in the sketch on the opposite page.

The following parameters were considered: 1) maximum allowable compression (see Fig. 3-29) and compression less than maximum; 2) three free-stream Mach numbers less than the design Mach number; 3) five to eight positions of the cowl at each free-stream Mach number. The values of these

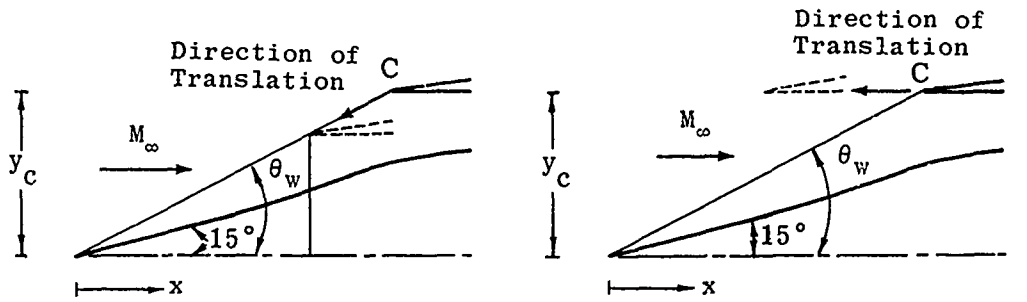

parameters may be seen in Figs. 3-38 to 3-45 which show the calculated values of the additive drag, the capture-area ratio, the Mach number, and the flow inclination at the cowl lip as functions of the cowl-lip position, free-stream Mach number, and design Mach number. To estimate the pressure recovery for any of these cases it is necessary to set the mass flow of the entering stream tube (station o) equal to that in front of the normal shock at the cowl lip, i.e.,

$$\frac{A_o\, p_{t_o}}{(A/A^*)_o} = \frac{A_t\, p_{t_t}}{(A/A^*)_t}$$

or

$$(A/A^*)_t = \frac{A_1}{A_o} \cdot \frac{A_t}{A_1} \cdot \frac{p_{t_t}}{p_{t_o}} (A/A^*)_o \qquad (3\text{-}9)$$

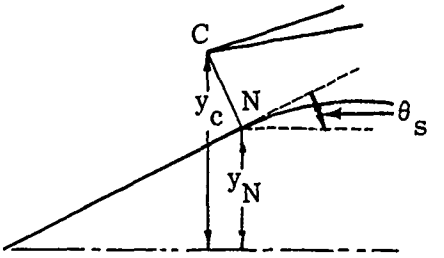

A_o/A_1 is given in Figs. 3-39 and 3-43; p_{t_t}/p_{t_o} is the pressure recovery through the bow shock; $(A/A^*)_o$ is found from tables. The throat area, A_t, generated by CN, is a cone frustum whose radii are y_c (known) and y_N (to be found either graphically or by computation). $(A/A^*)_t$ derived from Eq. 3-9 allows the evaluation of M_t and the ratio p_{t_2}/p_{t_t} from tables. The pressure recovery of the inlet is then $p_{t_2}/p_{t_t} \cdot p_{t_t}/p_{t_o}$. Figure 3-46 shows the shock pressure recovery calculated by this method for a few representative cases for the $M_D = 3.5$ diffuser. The associated additive drag is also shown in this figure.

Cross-plots of the additive-drag and capture-area ratio as a function of both design and free-stream Mach numbers from 2.25 to 5 are given in Figs. 3-47 to 3-49 for y/y_p of 1.0, 0.98, and 0.96 and the cowl lip on the

design conical shock where y_p is the ordinate of the focal point of the compression waves at the design Mach number. These figures (from Konrad) show the effect of operating at below-design Mach numbers. The vertical scales on Figs. 3-48 and 3-49 have been exaggerated to facilitate the reading of the data.

3.5 Comparative Evaluation

Throughout this subsection, stress has been laid upon the fact that the ultimate evaluation of a ramjet diffuser can only be made in terms of the associated engine characteristics and of its prescribed range or mission. However, a few generalized comparisons may be made which will assist the designer to limit the field of choice for a given range of desired operating conditions.

3.5.1 Mach Number Range of Basic Diffusers

The maximum theoretical pressure recovery for the basic diffuser types operating in frictionless flow is shown in Fig. 3-50. Two extreme cases are shown. The first assumes a simple normal shock at the lip and the second has the maximum internal contraction allowed by the entering Mach number and a simple normal shock at the associated minimum throat. These values must be considered in conjunction with the diffuser drag and off-design performance.

It has been shown that not only does the performance of the normal-shock diffuser deteriorate rapidly with increasing Mach number but at the same time the hysteresis effect increases. Its drag, however, may be kept very small. The single- and double-cone innerbodies give high pressure recoveries in the low Mach number range, but as the number of oblique shocks is increased the drag is also increased, and hence there may be but little gain in the net thrust.

3.5.2 Performance Comparison

Connors and Woollett (Ref. 111) have combined the experimentally determined characteristics of a single-cone, a double-cone, and an isentropic-spike diffuser with the performance of a hypothetical ramjet engine operating at zero angle of attack. The pressure recovery and the mass-flow ratio of the diffusers which were designed for a Mach number of 3.85 are given in Figs. 3-6, 3-25, and 3-51 for the three innerbody noses. They are compared in the next two sketches.

Maximum Total Pressure Recovery

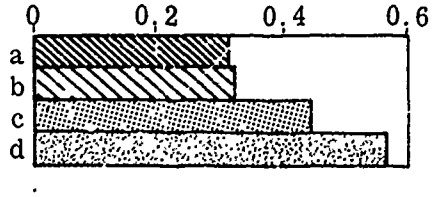

Mass-Flow Ratio

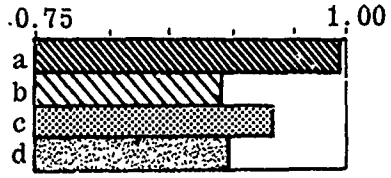

where

a Single Cone

b Single Cone (Low-Angle Cowl)

c Double Cone (Tip Roughness)

d Isentropic Spike

The external drag coefficient comprises three parts. The cowl pressure drag was determined experimentally. The friction drag was computed with the assumption of an average skin friction coefficient of 0.0013. The additive drag was also calculated. In the case of the isentropic spike, since the character of the flow spillage may vary, two extreme possibilities were considered. Supersonic flow spillage was assumed to give a minimum additive drag, and a complete loss of momentum in the spilled flow resulted in a maximum additive drag. The comparison of the external drag coefficients for the three diffusers is shown in the next sketch.

External-Drag Coefficient

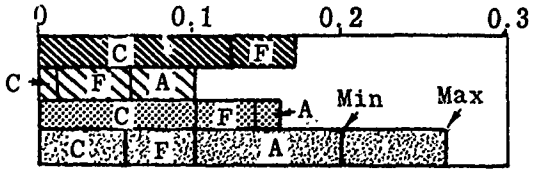

A = Additive
C = Cowl
F = Friction

The missile is assumed to cruise at 80,000 ft; the fuel-to-air ratio is 0.024 and the combustion efficiency is 90%. A comparison of the specific fuel consumption for each missile is shown in the next sketch.

Specific Fuel Consumption

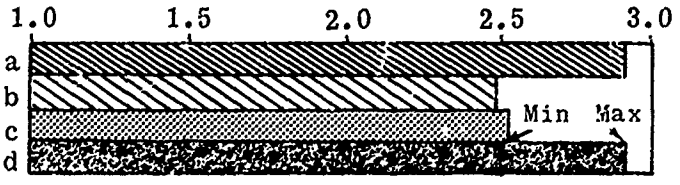

The single cone with the low-drag cowl, the double cone and the isentropic spike (with minimum additive drag) have approximately equal fuel consumption which is about 14% lower than that of the single cone with high-drag cowl.

If the hypothetical engine in each case is to produce the same net thrust, the relative engine size may be considered an index of efficiency. The following sketch relates the engine diameters to that of the single-cone engine.

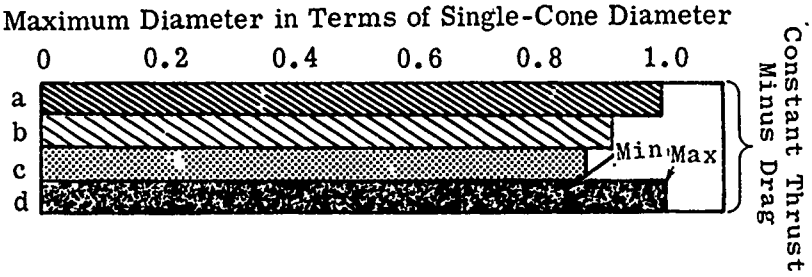

This criterion indicates that smaller engine sizes are linked to high pressure-recovery inlets.

Within the scope of their investigation, i.e., angles of attack up to 9 deg at M = 3.85, Connors and Woollett (Ref. 111) found that the isentropic inlets which gave the highest pressure recoveries at zero angle of attack were more sensitive to angle-of-attack effects than either the single- or double-cone inlets. However, by accepting a decrease in the mass-flow ratio at zero angle of attack, i.e., by retracting the cowl, the range of angle-of-attack operation could be extended without flow separation from the upper portion of the spike surface.

3.6 Two-Dimensional Diffusers

Feasibility studies concerned with a hypersonic transport (Ref. 118) have indicated a preference for two-dimensional engine configurations for very high Mach number flight applications. Such a design offers a number of aerodynamic as well as mechanical advantages over an axisymmetric design. Aerodynamically, the two-dimensional design allows additive lift to be associated with diffuser additive drag and by using a plug exit nozzle (see Subsec. 6.4.5) lift is obtained as a result of the under-expanded exit flow from the nozzle. Mechanically, the two-dimensional design permits simpler geometric variations in both the diffuser and the exit nozzle. Furthermore, the plug exit nozzle allows the supersonic portion of the nozzle to be cooled by radiation.

The theoretical limitations imposed on the compression produced by the isentropic wedge may be computed in a manner similar to that of the axisymmetric case (Subsec. 3.4.1). The results of such calculations for initial-wedge angles from 0 to 15 deg for Mach numbers from 2 to 8 are shown in Fig. 3-52 which also shows the maximum pressure recovery for the case of a horizontal cowl with no internal compression, i.e., with normal shock on the cowl lip. It may be seen from this figure that the requirement of a horizontal cowl causes a significant reduction in the pressure recovery over that allowed by the vortex-sheet criterion. However, the pressure recovery may be improved by including some internal contraction. For the near-optimum case of M = 1.4 behind the wedge shock from the cowl lip, the pressure recovery is shown in Fig. 3-53.

In order to meet the requirements of all the criteria of Subsec. 3.4.1 in a diffuser to operate over a range of high Mach numbers, it is essential that both the shape of the innerbody and its position with respect to the cowl lip be readily varied. Calculations in the range of M = 3 to M = 7 for such two-dimensional inlets with initial wedges of 9 deg and 15 deg have been carried out by Konrad (unpublished APL study). Figure 3-54 illustrates the flexibility required in the isentropic surface as well as the cowl position and throat area. It may be noted that the axial motion of the throat position associated with the 15 deg wedge is about half of that for the 9 deg case. The 15 deg initial wedge results in greater throat heights and is thus less sensitive to inaccuracies of positioning the throat normal to the inner cowl surface. These mechanical advantages associated with the larger wedge angle may well outweigh the decrease in pressure recovery in comparison with the smaller wedge angle.

A two-dimensional internal-compression inlet for Mach numbers from 2.5 to 4.0 has been discussed briefly in Subsec. 3.2.2 and will be discussed more fully in the next subsection, since boundary-layer bleed and the consequent drag penalty are critical.

3.7 Boundary-Layer Problems

The growth of boundary layer on the surfaces of a ramjet inlet may cause problems in many areas of the diffuser. The boundary-layer displacement thickness effectively changes the surface contours, often critically affecting nose shapes and minimum area regions. Not only does the boundary layer vary with altitude and missile velocity, but it is also affected by the pressure gradient and heat transfer associated with each surface. Contour corrections may be made to include (at a particular Reynolds number), the effects of the first two parameters but at present, quantitative effects of pressure gradient and heat transfer cannot be determined with accuracy.

Under the effect of adverse pressure gradients caused by either the surface slope or shock interactions, the boundary layer may cause flow separation from the diffuser walls. Under certain conditions, as shown below, the pressure recovery may be improved by boundary-layer effects but this improvement is at the expense of air capture.

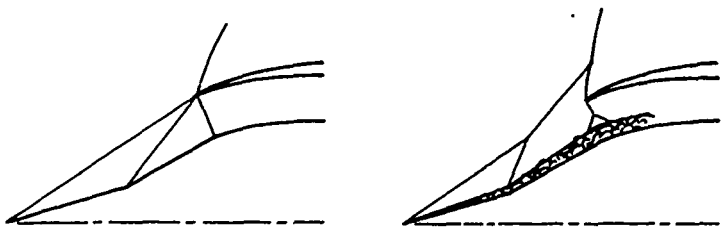

The sketch also illustrates the effect of boundary-layer growth on the shape of the surface. In this case the biconic inlet has virtually been changed to a multiconic inlet at off-design conditions.

Boundary-layer problems in diffusers may be divided into two groups: growth and separation on the compressing surface and shock-interaction effects in the throat region with subsequent separation in the subsonic regime. It will be seen that this division is somewhat arbitrary. When the minimum section occurs at the cowl lip its boundary-layer problems are closely related to those of the compressing surface, i.e., are due more to boundary-layer buildup than to the shock interactions that complicate the flow at a minimum section in the annulus. In this subsection the problems will be discussed briefly and a description given of some corrective measures that have been suggested.

3.7.1 Boundary Layer on the Compressing Surface

The sensitive relation between the positions of the cowl lip and the spike surface of an isentropic inlet and their effect on the pressure recovery, flow spillage and even flow stability has been mentioned (Subsec. 3.3.1).

Any correction to the spike contour for the boundary-layer thickness will of necessity be associated with a specific altitude and Mach number. Before a decision can be reached for the optimum conditions of boundary-layer correction, the performance of the corrected diffuser will have to be calculated for other Mach numbers and altitude conditions. Where the performance is critical, the process may require iteration. The diffuser performance will have to be matched with the engine characteristics over the expected requirements of the climb-out, cruise, and maneuver phases of flight.

The separation of the boundary layer from the compression surface is particularly critical in two regions, both of which contain a rapid change in the slope of the contour. It has already been noted (Subsec. 3.3.2) that separation or bridging occurs at the juncture of the two cone surfaces in the biconic spike and at the beginning of the curved section of the isentropic spike. It has been shown that this phenomenon occurs only in laminar flow and hence one simple remedy is to apply sufficient roughness to create boundary-layer transition upstream of the discontinuity in the slope. Tests on biconic inlets at M = 3.85 show not only an increased supercritical mass-flow ratio due to a roughened tip but also show that the flow detachment at the engine face was delayed from 6 deg angle of attack to nearly 9 deg by the roughness (Ref. 111).

A second method of alleviating bridging is by means of boundary-layer suction. Bridging did not occur and the total pressure recovery increased from 0.56 to 0.62 when about 2% of the air mass-flow was withdrawn through a porous isentropic spike made of sintered bronze (Ref. 111). Angle-of-attack performance was also improved by this technique. However, in comparison tests it was shown that the roughened tip gave better results than in the case of the porous spike.

3.7.2 Boundary Layer in the Throat Region

The boundary layer in the throat region may give rise to many problems. Even under the simplified assumption of a single normal shock in the minimum-area section the boundary-layer displacement thickness is critical. High pressure recovery through the nose shock demands a long slender spike which produces a thick boundary layer by the time the flow reaches the inlet.

The lower the Mach number at the throat the less the shock loss but also the thicker the boundary layer that may easily occupy a large percentage of the area, which is a minimum at this point. Problems also arise from the complex interactions of the boundary layer with the oblique or normal shock of the diffuser.

If the throat is at or very near the cowl lip, boundary-layer separation is apt to occur when the flow is turned too rapidly over the innerbody near the diffuser throat. The most obvious remedy, that of turning the flow more gradually, implies an increased cowl-lip angle and hence an increased external-drag penalty. Boundary-layer bleed immediately downstream of the sharp turn has been found effective provided there is no internal compression. Both circular perforations and slots have proved satisfactory for about a 1% bleed flow. The sketches below are of two configurations that have prevented flow separation.

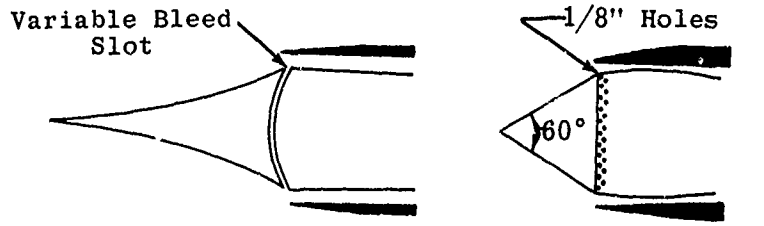

Isentropic Spike

Single Cone (Low-Angle Cowl)

Ferri (Ref. 119) used boundary-layer suction slots on the tips of both 25 and 30 deg conical noses; however, they were too close to the tip and allowed the boundary layer to separate further downstream. Three variations of boundary-layer bleed at the diffuser entrance are described in Ref. 116 and are shown in the sketch below.

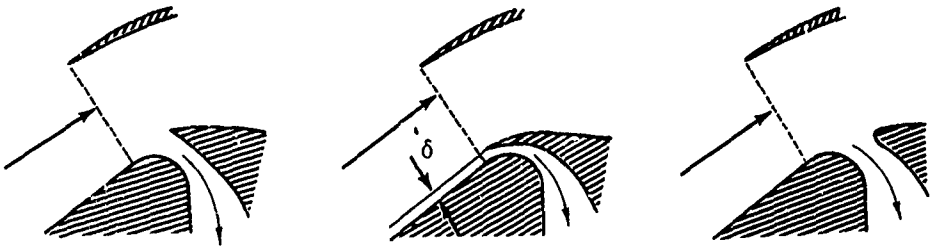

Ram Scoop 1 Ram Scoop 2 Flush Slot

The first two are ram scoops and the third is a flush slot. The middle one, with a sharp entrance tip in the flow direction, and height equal to the boundary-layer thickness, gave the most satisfactory results. Figure 3-55 shows the critical pressure recovery and the supercritical mass-flow ratio as a function of Mach number in the test range from M = 1.97 to the design Mach number of 3.0. It may be noted that the maximum recovery improvement occurred at the design Mach number using the first ram scoop, but at all test Mach numbers below this value the shock detached. The best performance through the test range was shown by the scoop with its entrance normal to the stream.

The recovery gains are reduced as the Mach number decreases. Part of the reduction in mass-flow ratio is due to the 2% by-passed flow. The effectiveness of the optimum bleed system at angles of attack up to 10 deg is shown in Fig. 3-56. The gain in pressure recovery is reduced as both the angle of attack and the free-stream Mach number increase, but even at 10 deg and M = 3.0 the bleed system still has a slight advantage over the system without bleed. The increase in cowl and flow-spillage drag with this scoop is shown in Fig. 3-57 together with the net thrust ratio $(F - D_C - D_A)/F_{ideal}$ which is based on the assumption of engine matching at the critical condition for each Mach number. At M = 3.0 the use of bleeds increases the propulsive thrust by 22%.

In diffusers with a considerable amount of compression the boundary layer reacts with the normal shock and creates an extensive shock region. Elongating the throat tends to stabilize the shock, but at the same time increases the boundary-layer thickness and often creates flow separation. In such a case the desired pressure recovery may be bought at the cost of a poor pressure distribution at the diffuser exit, as well as the penalty of additional weight due to the long throat.

One of the most successful ways of improving the throat flow is by means of what is known as a dump or sometimes as a vortex trap. In the sketch below the dump is preceded by a boundary-layer bleed gap.

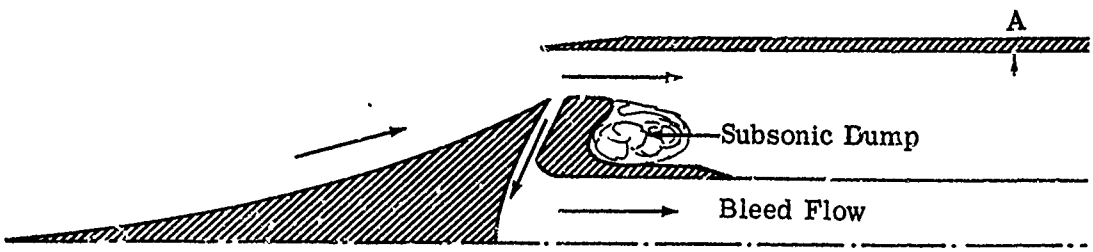

In tests of such a diffuser at M_D = 3.85 (Ref. 120) it was shown that the over-all performance was the same as for a well-designed conventional diffuser. However, the pressure recovery had achieved its peak value at a distance equal to 1.25 diameters from the cowl lip (point A on the sketch) which is about one-quarter of the length of the conventional diffuser. This saving in weight and internal drag is of considerable importance in assessing the over-all performance of the vehicle. The frictional losses of the long, conventional annulus are traded for losses in dynamic head due to the incomplete mixing at the abrupt area discontinuity. The pressure distribution at three stations along the dump diffuser is shown in Fig. 3-58 for recovery levels corresponding to supercritical, critical, and subcritical flow regimes. The flow distortion is seen to be quite small, especially in the case of the critical flow. It may also be noted from this figure that the high-energy air is at the inner wall of the annulus in supercritical flow and moves across to the outer wall during subcritical operation. The diffuser gave good recovery characteristics up to 8 deg angle of attack.

Another method of improving the conditions at the minimum annulus section is by means of a scoop or pitot device. Many modifications of such a method were incorporated by Carr and Gunther in a two-dimensional diffuser (Ref. 121) and were tested at Mach numbers of 3.5 to 5.0. The essentials of the diffuser are shown in the sketch below.

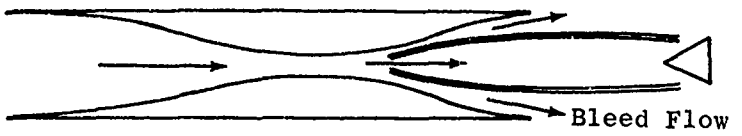

Both the contoured compression plates and the enclosing side plates were flexible and capable of being shaped by means of mechanical actuation in order to provide suitable area ratios for starting and for steady supersonic flow. The throat height was also adjustable. The supersonic compression of the diffuser proved very efficient but the normal-shock system was stable only when situated far downstream of the minimum section. Since the relatively high Mach number at that station resulted in poor normal-shock recovery, this part of the diffuser to a great extent nullified the good performance of the supersonic portion. The remedy consisted of capturing only the high-energy central core of the throat flow. By this means the subsonic pressure recovery was much improved. The penalties, however, are high. Compensation must be made for the internal drag of the scoop itself as well as its additional weight. In these particular tests up to one-third of the air mass was bled off. This presents not only the problem of reduced mass flow to the engine face but also the problem of either using the bleed or dumping it overboard. If the by-passed air is re-expanded to free-stream static pressure and ejected as a rearward jet it will, at least theoretically, provide a source of thrust to compensate for a part of the drag increase. Many design refinements have been tried with both subsonic and supersonic flow in the by-pass ducts and though considerable improvements have been made in the net thrust, the standard of achievement is still below that required. This problem is discussed further in Subsec. 6.4.3.

An axially-symmetric diffuser with much less boundary-layer suction than that described in the above paragraph has already been discussed and illustrated on page 119 and its pressure recovery shown in Fig. 3-9. The drag penalty associated with the by-pass flow was not estimated. It may be noticed that in the second sketch on page 119 that there is also a rearfacing step in the innerbody of the diffuser. This device has been found helpful in stabilizing the normal shock and also in preventing separation of the boundary layer.

In most of the preceding examples the penalties of extra weight and of additional drag have been pointed out. In the final analysis the complexity of operation and of manufacture as well as the cost would have to be considered.

3.7.3 Boundary Layer in the Subsonic Diffuser

Shoemaker and Henry (Ref. 122), in an effort to obtain high performance in a short subsonic diffuser, investigated the effectiveness of boundary-layer suction in the annulus downstream of the minimum section. The boundary

layer was removed through four, six, or eight rows of equally spaced holes on both outer and inner walls of the diffuser as shown in the sketch below.

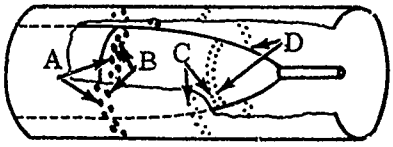

A (1/2" d.)
B. (3/8" d.)
C,D (1/4" d.)

Four-row suction employed rows A and B; six-row and eight-row suction added row C and rows C and D respectively. The equivalent conical angle of the diffuser was 10 deg. It was found that the pressure recovery was quite sensitive to the ratio of the mass flows through the inner and outer walls. Figures 3-59a and b show the improvement in pressure recovery due to removing 5% and 10% of the total mass flow. Measured pressure recoveries (from Ref. 131) of a 10 deg and a 5 deg diffuser without suction are shown for comparison. It may be seen that less than 5% suction in the short diffuser achieves a pressure recovery as good as that in a 5 deg diffuser without the penalty of added weight and skin-friction drag. This gain has to be weighed against the power required to perform the suction.

3.7.4 Fuselage Boundary Layer

So far only the diffuser of an independently operating ramjet has been considered. Sometimes a two-dimensional diffuser or a part of an axisymmetric diffuser may be located along the fuselage or under the wing of a larger craft. In this case the accumulated boundary layer of the fuselage may enter the inlet. This condition is usually alleviated by lifting the inlet partially or completely above the boundary layer.

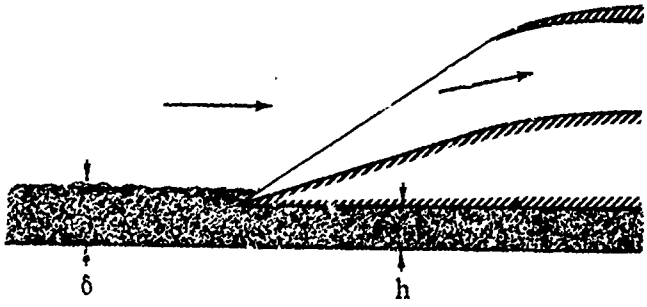

The diverted air may often be used for auxiliary systems, but in any case as much momentum as possible must be recovered and the drag taken into account in the net thrust of the system.

3.8 Diffuser Buzz

Diffuser "buzz" may be defined as unstable, subcritical operation associated with fluctuating internal pressures and a shock pattern oscillating about the diffuser entrance. In stable subcritical operation such as (a) of the next sketch, the normal shock may be situated at any point upstream of the cowl lip. Its position, and hence its motion, is intimately related to the pressure recovery. During buzz the shock pattern (and the pressure ratio) vibrates rapidly about the stable position. A typical succession of shock configurations is shown in the sketch below.

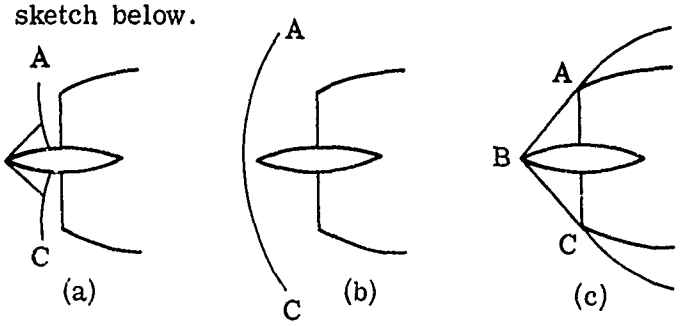

In (a) the expelled shock, AC, is moving upstream resulting in increased spillover and drag. In the limiting upstream position, (b), the shock detaches from the cone and allows a large volume of air to be expelled from the inlet. The shock reattaches and instantaneously moves to its limiting position downstream, which may or may not be within the inlet. This cycle is repeated.

The alternate swallowing and expelling of the normal shock thus creates an intermittent flow of air to the burner, resulting in inefficient combustion or, in the extreme case, in extinction of the flame. In addition to this, it creates intermittent additive drag which places further penalties on the gross thrust of the missile.

A number of theories, some based on analogies to other forms of oscillation, have been proposed in an effort to explain this phenomenon. Although no single theory so far has been able to explain all the characteristics of buzz, each one has added to the understanding of the problem. Some of the more fruitful theories, along with their application, will be discussed in the following subsection.

3.8.1 Theories of Buzz

According to Ferri's vortex-sheet theory (Ref. 119) the intersection of the conical shock with the expelled normal shock creates a vortex sheet, as shown in the sketch below (see also Subsec. 3.4.1).

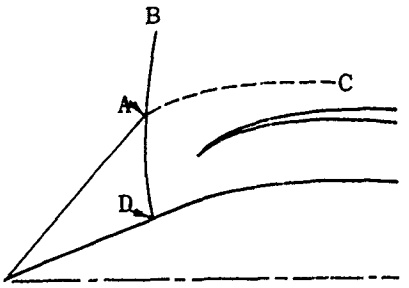

As the normal shock system (BD) moves upstream, the vortex sheet (AC) approaches the cowl lip and ultimately, under certain off-design conditions, may enter the diffuser. The entrance of the vortex sheet within the inlet triggers the oscillatory cycle. Since this vortex sheet is associated with a low-energy field, it causes boundary-layer separation which in turn chokes the diffuser. This choking expels more air, creating a stronger shock and allowing the vortex sheet to move upstream and turn toward the innerbody. This permits the boundary layer to reattach and the vortex sheet to move toward the inner cowl lip, thus re-entering the buzz cycle.

When boundary layer separation occurs on the innerbody, a lambda shaped shock wave is present as illustrated in the sketch below.

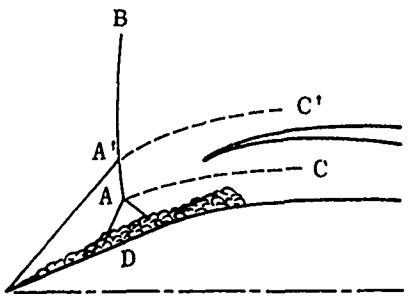

A vortex sheet arises from the lambda shock and approaches the cowl lip. This initiates the oscillatory cycle in the same manner as the vortex sheet described previously.

Ferri and Nucci (Ref. 119) tested a number of inlets at Mach numbers from 1.9 to 2.7 in order to confirm the vortex-sheet theory. It was found that the minimum entering mass flow for stable operation is essentially a function of the Mach number and of the external geometry upstream of the inlet. Figure 3-60, taken from this reference, shows the minimum stable mass flow as a function of the cowling parameter for a cone tip of 40 deg at various Mach numbers. The effect of varying the cone angle is shown in Fig. 3-61. As with the other theories that have been advanced, Ferri's vortex-sheet theory provides an adequate explanation for some cases but by no means for all. In one conical-nose inlet, the vortex sheet traveled along the entire inlet at a below-design Mach number without inciting buzz and, in the same inlet, buzz occurred at an above-design Mach number when the vortex sheet was observed to be far removed from the cowl lip.

Pearce (Ref. 123) noted that if the stagnation pressure vs mass-flow ratio curve has a positive slope of sufficient magnitude, then the system is unstable under the influence of small disturbances. However, if the slope is negative or very slightly positive, the flow will be stable in the presence of these same disturbances. Thus the diffuser characteristic curve is an indication of the stability of the system. It may be said that a positive slope is necessary for the oscillations to begin, but is not in itself sufficient to originate the instability.

According to Dailey (Ref. 124), an initial disturbance causes choking of the inlet which in turn forces the normal-shock system to move upstream

along the cone. The pressure in the combustion chamber builds up and is discharged from both ends of the engine, so that the engine resonates as would an organ pipe. The normal shock then moves toward the inlet and is swallowed to a supercritical position. Since the inlet flow rate is then greater than the exit discharge rate, the pressure in the combustion chamber again increases rapidly and the shock pattern moves upstream, re-entering the cycle.

Sterbentz and Evvard (Ref. 125) found that the frequency and wave characteristics of the oscillations occurring in a given diffuser are dependent upon the internal geometry of the ramjet. This led to the idea of comparing the buzz phenomenon to a Helmholtz resonator. During a buzz cycle the air is alternately accelerated and decelerated as the shock is swallowed and expelled. A portion of this mass flow could then act as an inertial plug resonating against the combustion chamber in a manner analogous to that of an organ pipe or a Helmholtz resonator. The frequency of pulsation is given by the expression

$$f = \frac{a_2}{2\pi}\sqrt{\frac{A_1}{\ell\, V_c}} \qquad (3\text{-}10)$$

where

ℓ = length of diffuser

V_c = volume of combustion chamber

a_2 = velocity of sound at a point downstream of the perturbations

A_1 = cross-sectional area of inlet

Experimental and calculated values of the frequency are compared in Fig. 3-62 (Ref. 125). It may be seen that the experimental values agree with the theoretical within 15%. Experimental and calculated values of the slope of the pressure-recovery curve, $d(p_{t_2}/p_{t_\infty})/d(m_2/m_\infty)$ are also given in Fig. 3-62. It may be seen that Pearce's condition of a small positive slope as a condition of instability holds for most of these data.

In spite of its success, there have been several criticisms of the resonator theory. One objection which would tend to support the vortex-sheet theory is the fact that buzz begins abruptly; in resonance it would build up slowly. However, the two theories may be compatible rather than opposing, since the entrance of the vortex sheet within the diffuser may provide the initial disturbance which is then propagated as a resonating column of air.

3.8.2 Methods of Control

The onset and character of diffuser buzz are dependent upon many factors, some of which have been theoretically analyzed or experimentally tested in order to find a means of controlling or delaying the buzz phenomenon. One method of eliminating buzz would be to prevent subcritical operation by assuring that the exit nozzle is large enough to maintain the normal-shock system

within the annular ducting of the diffuser at all missile or engine operating conditions.

According to Eq. 3-10 the frequency is inversely proportional to the square root of the resonating volume. Theoretically, at least, it would be possible to reduce the frequency to a negligible value by ensuring a large enough resonator. Computed values of the frequency for two combustion chamber volumes, one of which was more than twice the size of the other, are compared with test results at M = 2 in Fig. 3-63. As was expected, the frequency decreased when the volume was increased. However, a resonating chamber which would phase-out the oscillations would demand a volume prohibitively large for most practical applications.

More recently the problem has been substantially solved for two specific types of diffusers, although neither method offers a complete understanding of the phenomenon. One type of diffuser employed dampers in the form of can combustors. The effect of the dampers on buzz frequency and amplitude are shown in Fig. 3-64 in which it may be seen that the largest can combustor completely stabilized the system at zero angle of attack. Unfortunately the dampers also reduced the pressure recoveries by about 4%.

Since a positive slope of the diffuser characteristic curve is associated with the oscillation, anything which can prolong a negative slope will delay buzzing. Rae, in unpublished OAL tests, designed and tested a two-shock step-nose diffuser. This diffuser has a characteristic curve which "knees-over" rather than turning abruptly, as shown in Fig. 3-65 for two angles of attack at M = 2.23. It may be seen that not only was the range of stable operation increased with this type of diffuser, but the pressure recovery was also improved.

It should be noted that although diffuser buzz is definitely a detriment to efficient combustion, it is ultimately of more academic than practical interest. The undue emphasis that has been placed on it by ramjet designers stems from the fact that most diffuser performance data are derived from wind-tunnel tests where conditions are particularly favorable to unstable operation. In actual flight where the diffuser operates as an integral part of an entire engine system, buzz is less likely to occur partly because of the stabilizing effect of the combustion and partly because of the presence of such factors as the air scoops that are included for many purposes.

3.8.3 Engine-Inlet Stability

In designing a propulsion system the problem of practical importance is to ensure stable operation at all times. The application of transient flow theory is concerned more with the problem of avoiding instability than with the description of the modes of unstable operation. The techniques of mass-flow matching between the inlet and the engine to ensure efficient performance over the range of flight conditions are well understood. It is standard practice to determine the relations between inlet mass flow and efficiency for a given inlet geometry from wind-tunnel tests, since one-dimensional theory is not sufficiently well developed to permit its determination. It is possible to derive similar transient functions for the propulsion system and thus permit the application of one-dimensional theory to the complete system.

Mirels in Ref. 126 analyzes buzz by means of the acoustic analogy and comes to the same conclusion as Pearce; i.e., that decreasing the slope of the inlet characteristic curve during subcritical operation will tend to increase the range of stable operation. He also deduces a relationship between stability and the real part of the acoustic impedance of the inlet.

The conceptual approach is that of a complete propulsion system comprising an inlet and an engine separated by a mass-less, non-resisting diaphragm at the plenum chamber of the system. The acoustic impedance of the inlet as seen looking forward from this station is measured experimentally by use of a wind-tunnel model. Pressure measurements are made with a sensitive transducer, and velocity measurements are made with a hot wire anemometer. Sinusoidal excitation of the system is provided by oscillation of the sonic throttle area. In a similar manner the acoustic impedance of the engine can be measured by locating a hot wire and a pressure transducer at the corresponding station in front of the engine mounted on a bell mouth or direct connect test stand. Excitation in the latter case is more difficult because of the size of the object required and because of the necessity for generating, as nearly as possible, one-dimensional disturbances. Furthermore, in order that the impedance measured for the engine correspond to that which the engine will exhibit in flight, it is necessary that the disturbance mechanism provide adiabatic disturbances simulating stagnation pressure losses which would result from the oscillating shock system encountered in actual operation.

Once these impedances have been measured it is a simple matter to find the combination impedance for the system. The following sketch shows the components and their impedances as well as that for the system.

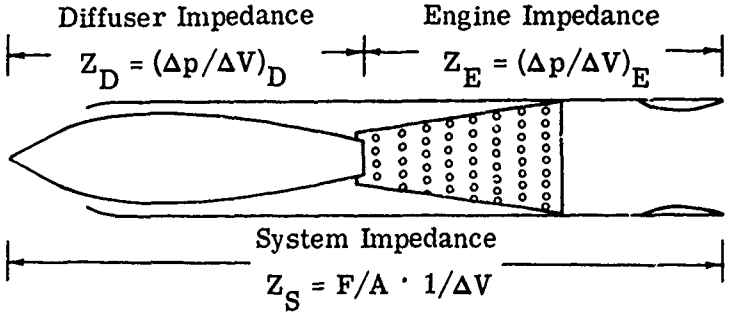

For the system

$$F = (\Delta p_E - \Delta p_D)A$$
$$= (Z_E - Z_D)\, A\Delta V \qquad (3\text{-}11)$$

i.e.,

$$\frac{F}{A\Delta V} = Z_S = Z_E - Z_D$$

The system impedance can be set equal to zero and the resulting complex roots of the system determine both the frequency and damping of the modes.

One difference between the present problem and that of the classical acoustic case is that a steady mass flow is allowed. The acoustic motion here refers to the disturbance pressures and velocities relative to the uniform flow. The diaphragm connecting the two systems in the present case is therefore a transient one which is instantaneously located at the plenum chamber interface. In spite of this difference and the fact that the impedances must be determined empirically, it is clear that the conceptual formulation of the problem is identical with that of the classical acoustic approach. These impedances therefore represent the experimental counterpart of the inlet performance with steady flow and make possible the analysis of transient effects in a propulsion system.

It is clear from the above discussion that the use of a wind-tunnel model to determine transient characteristics of a complete propulsion system is valid only when carried out in the manner described. The stability boundaries and even the transient characteristics themselves for the complete diffuser system are different from those of a geometrically similar inlet which is mounted in front of an engine.

The acoustic analysis described above may be extended to the case of a propulsion system containing a controller attached to an inlet, or to the engine controls. This simply requires the measurement of additional acoustic transfer functions relating the motion of the controller to the sensory unit which commands the control motion.

In carrying out the measurements described above or in making flight measurements of transient system characteristics, it is always important to be sure that the properties measured really correspond to the aerodynamic phenomena and are not intrinsically tied to the method of measurement. For instance, care must be taken to ensure that there are no natural modes of the recording element, the transducer, or the mounting of the transducer in the duct system which might interfere with the validity of the determination.

Table 3-1

Coefficients in the Equation of the Curved Shock of a Biconic Diffuser

θ_{S_1}	θ_{S_2}	M_∞	A	B	C	D
20	10	2.1297	0.00300	0.41889	0.014181	0.0001995
		2.4431	0.00172	0.56011	0.014385	0.0002264
		2.8387	0.00095	0.68393	0.015033	0.0002682
		3.3694	0.00052	0.80130	0.015889	0.0003286
		4.1538	0.00020	0.91795	0.016811	0.0004121
		5.5457	0.00009	1.04145	0.017531	0.0005204
20	12.5	2.1297	0.00267	0.33701	0.015552	0.0002356
		2.4431	0.00144	0.49121	0.014633	0.0002341
		2.8387	0.00076	0.61930	0.014956	0.0002819
		3.3694	0.00035	0.73369	0.015466	0.0003310
		4.1538	0.00006	0.84559	0.015859	0.0003847
20	15	2.1297	0.00302	0.24096	0.018494	0.0003274
		2.4431	0.00118	0.42031	0.015433	0.0002752
		2.8387	0.00057	0.55024	0.015208	0.0003060
		3.3694	0.00035	0.66545	0.015209	0.0003413
		4.1538	0.00014	0.77296	0.015577	0.0004131
		5.5457	0.00006	0.88047	0.015850	0.0005149
20	20	2.4431	0.00134	0.24045	0.019465	0.0004315
		2.8387	0.00048	0.40333	0.016134	0.0003658
		3.3694	0.00005	0.52581	0.014625	0.0003360
		4.1538	0.00007	0.62818	0.014956	0.0004476
		5.5457	0.00004	0.72099	0.016271	0.0006712
25	10	2.0665	-0.00025	0.13050	0.019890	0.0003524
		2.3604	0.00086	0.31332	0.016952	0.0003122
		2.7296	0.00077	0.44802	0.016448	0.0003467
		3.2188	0.00039	0.56032	0.016834	0.0004147
		3.9260	0.00012	0.66438	0.016555	0.0004260
25	15	2.3604	-0.00051	0.14089	0.021571	0.0004826
		2.7296	0.00045	0.31503	0.017628	0.0004089
		3.2188	0.00019	0.43879	0.016428	0.0004080
		3.9260	0.00012	0.54276	0.016086	0.0004468
		5.1233	0.00003	0.63992	0.015888	0.0005148
25	20	2.7296	0.00034	0.13727	0.022852	0.0006600
		3.2188	0.00012	0.30283	0.017201	0.0004587
		3.9260	0.00006	0.41575	0.015952	0.0004837
		5.1233	0.00002	0.51109	0.015225	0.0005259

Equations of the shock fronts: $x = -A + By + Cy^2 - Dy^3$ (see Subsec. 3.3.2) where the origin is at the juncture of the cone surfaces.

Table 3-2

Parameters at Point of Intersection of Curved and Conical Shocks of a Biconic Diffuser

θ_{S_1}	θ_{S_2}	M_∞	x_P	y_P	M_P	φ_P	θ_{W_1}
20	10	2.1297	11.065	18.129	1.441	19.093	36.124
		2.4431	10.775	14.883	1.640	20.852	33.045
		2.8387	833	11.919	1.871	22.491	30.435
		3.3694	8.576	9.314	2.148	24.018	28.180
		4.1538	7.146	7.035	2.500	25.433	26.199
		5.5457	5.625	5.038	2.976	26.751	24.433
20	12.5	2.1297	8.641	16.359	1.351	21.409	36.124
		2.4431	8.791	13.592	1.547	23.304	33.045
		2.8387	8.225	10.974	1.769	25.034	30.435
		3.3694	7.243	8.600	2.036	26.589	28.180
		4.1538	6.062	6.502	2.369	28.011	26.199
20	15	2.1297	6.589	14.861	1.256	23.635	36.124
		2.4431	7.138	12.517	1.449	25.726	33.045
		2.8387	6.840	10.160	1.667	27.517	30.435
		3.3694	6.121	7.999	1.923	29.122	28.180
		4.1538	5.163	6.059	2.238	30.560	26.199
		5.5457	4.068	4.331	2.652	31.863	24.433
20	20	2.4431	4.246	10.635	1.234	30.33	33.045
		2.8387	4.546	8.813	1.442	32.51	30.435
		3.3694	4.271	7.008	1.677	34.30	28.180
		4.1538	3.693	5.336	1.956	35.84	26.199
		5.5457	2.959	3.827	2.329	36.861	24.433
25	10	2.0665	4.193	12.798	1.215	23.13	41.644
		2.3604	5.181	11.175	1.402	25.14	38.495
		2.7296	5.370	9.392	1.607	26.90	35.873
		3.2188	5.097	7.669	1.842	28.49	33.651
		3.9260	4.559	6.083	2.127	29.842	31.737
25	15	2.3604	2.779	9.265	1.203	29.84	38.495
		2.7296	3.429	7.988	1.408	31.92	35.873
		3.2188	3.485	6.595	1.634	33.63	33.651
		3.9260	3.228	5.261	1.895	35.12	31.737
		5.1233	2.812	4.042	2.224	36.279	30.066
25	20	2.7296	1.781	6.797	1.187	36.456	35.873
		3.2188	2.226	5.758	1.417	38.413	33.651
		3.9260	2.224	4.639	1.666	39.971	31.737
		5.1233	1.994	3.568	1.958	41.301	30.066

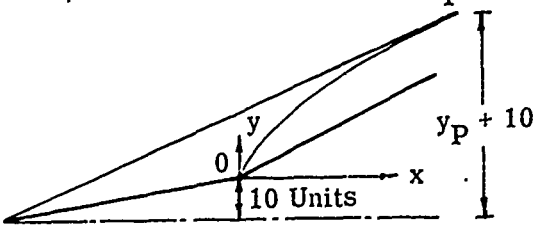

The units of x_P and y_P are determined by the required dimensions of the inlet.

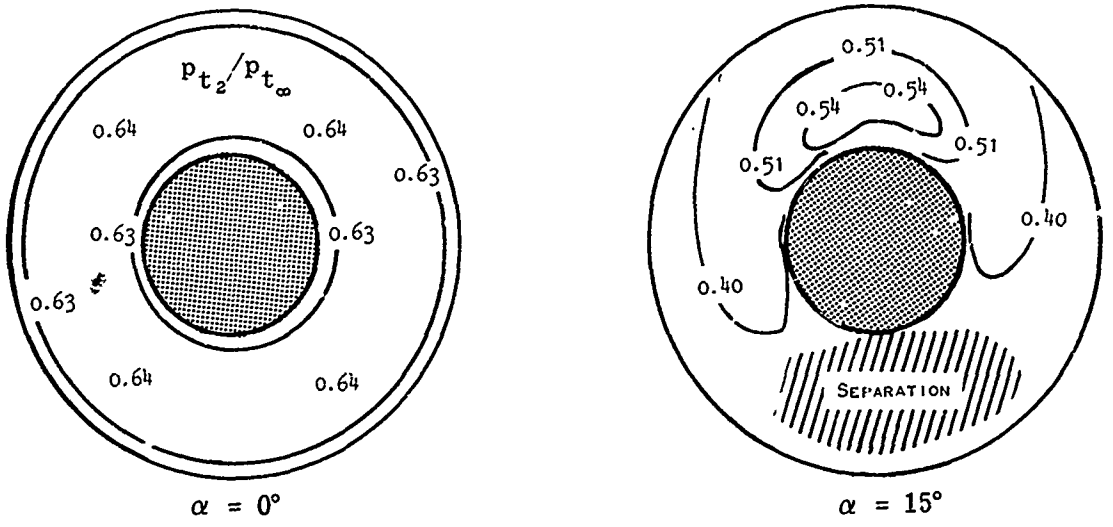

Source Ref. 103

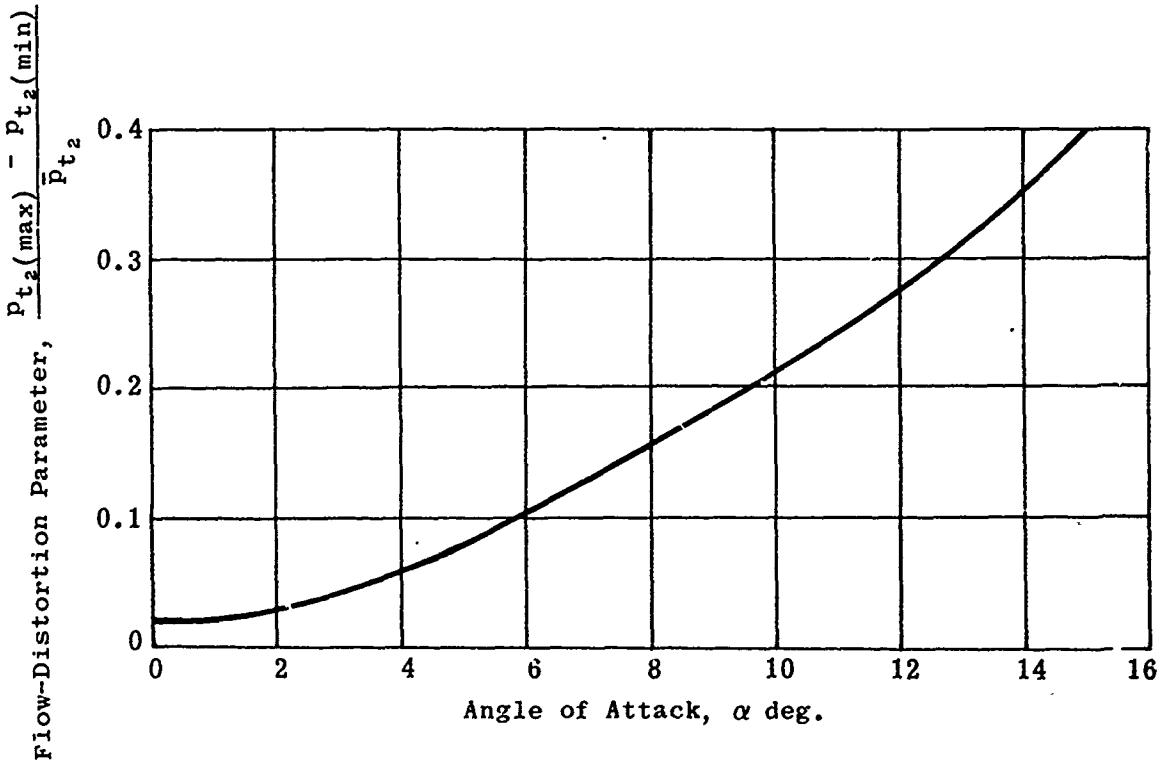

Fig. 3-1. Typical flow distortion at diffuser exit; M = 3.

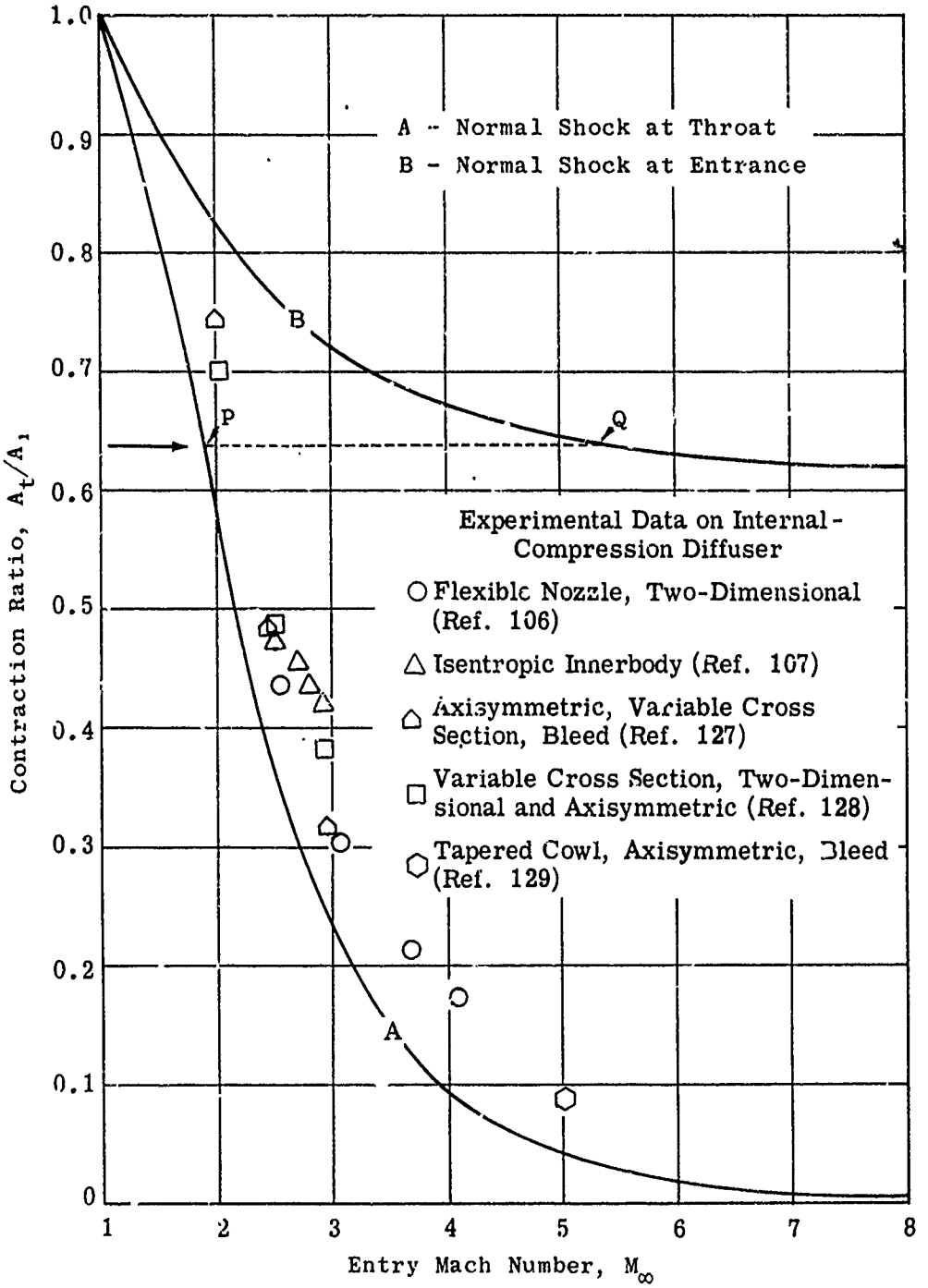

Fig. 3-2. Comparison of theoretical and experimental contraction ratio vs Mach number; M_∞ = 1 to 8; γ = 1.4.

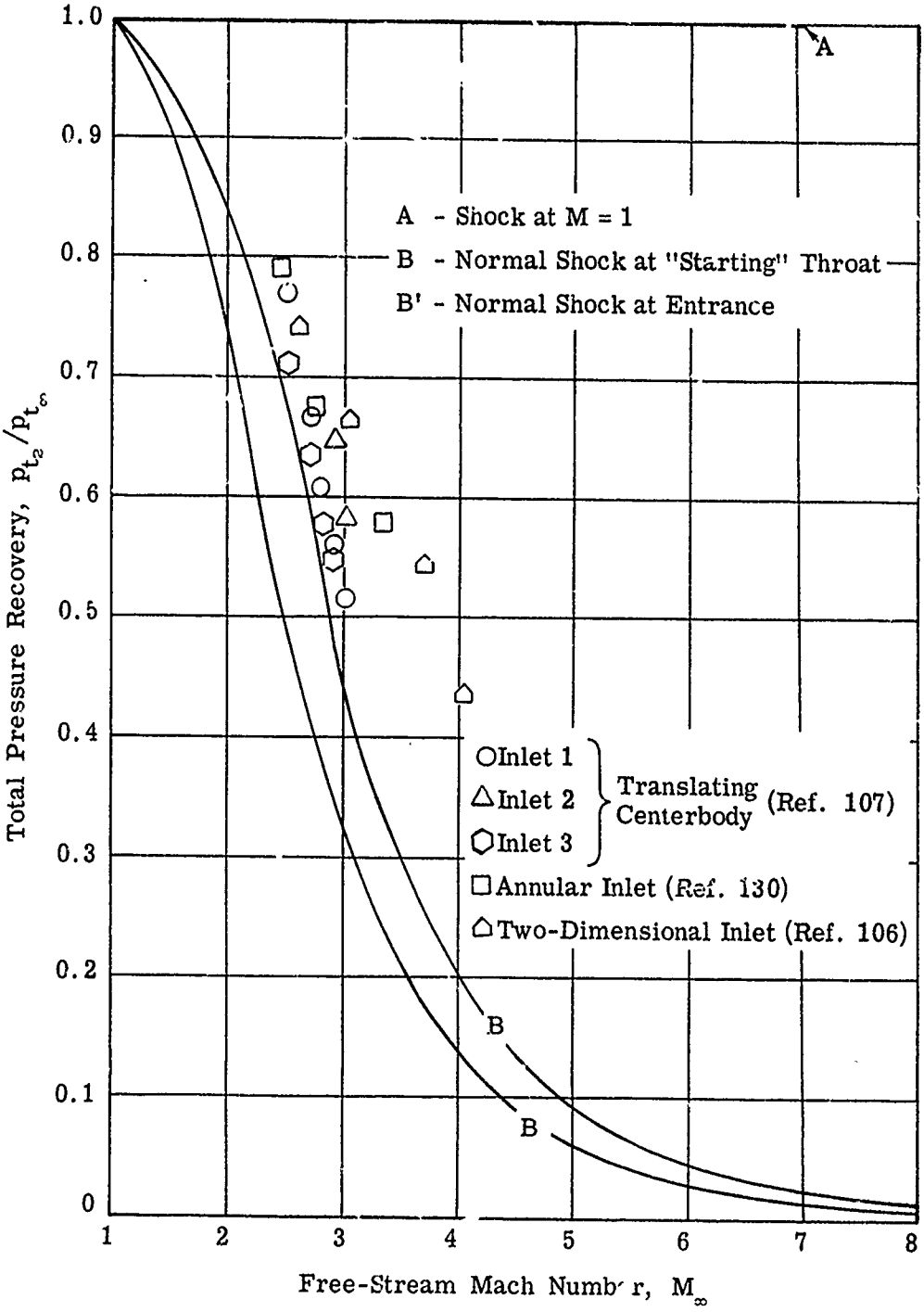

Fig. 3-3. Comparison of theoretical and experimental total pressure recovery vs Mach number; all internal compression; M_∞ = 1 to 8; γ = 1.4.

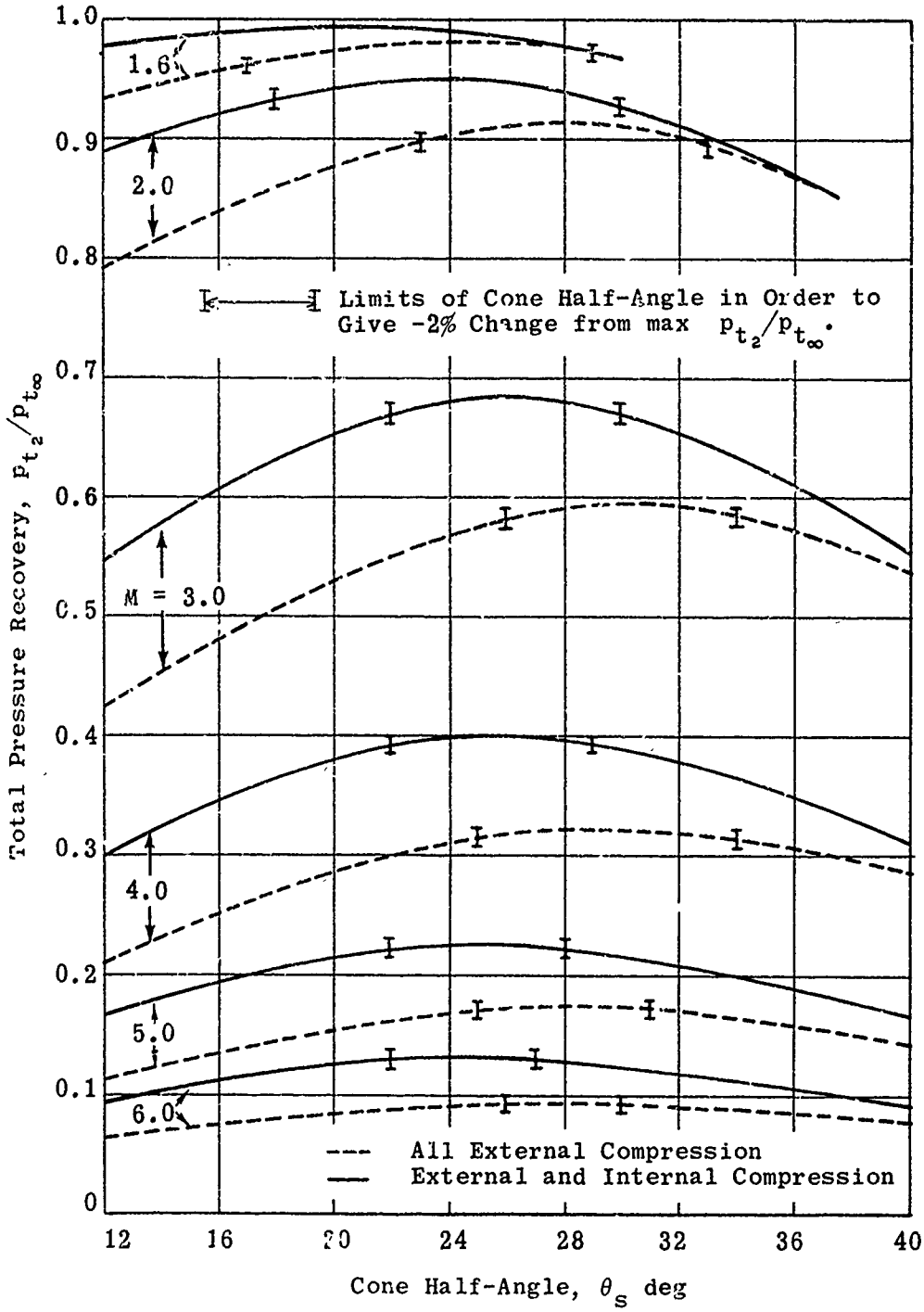

Fig. 3-4. Theoretical total pressure recovery for a single-cone diffuser vs cone half-angle; M = 1.6, 2, 3, 4, 5, and 6; γ = 1.4.

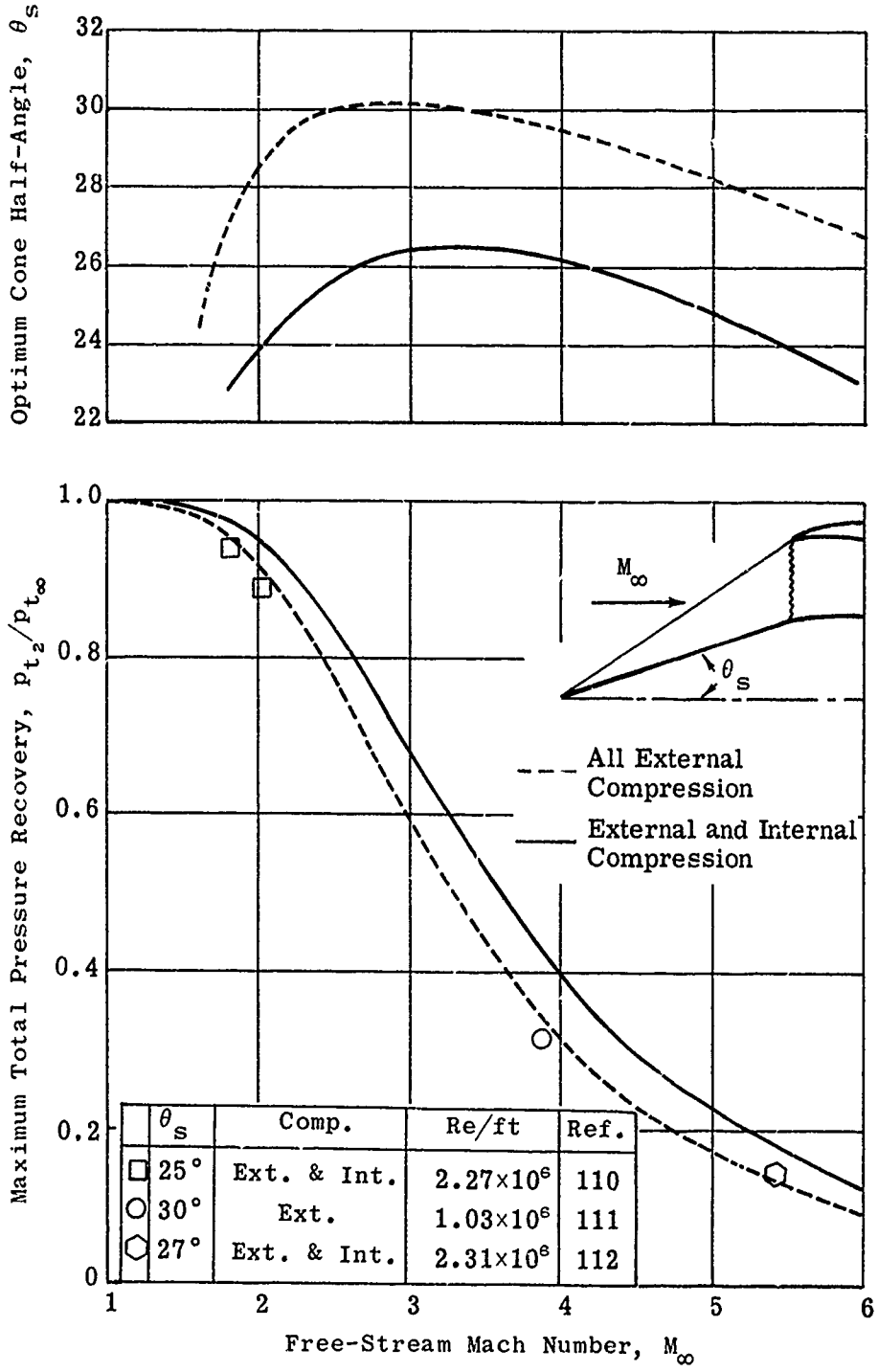

Fig. 3-5. Maximum total pressure recovery and the cone angle at which it occurs as a function of Mach number (some experimental values); M_∞ = 1 to 6; γ = 1.4.

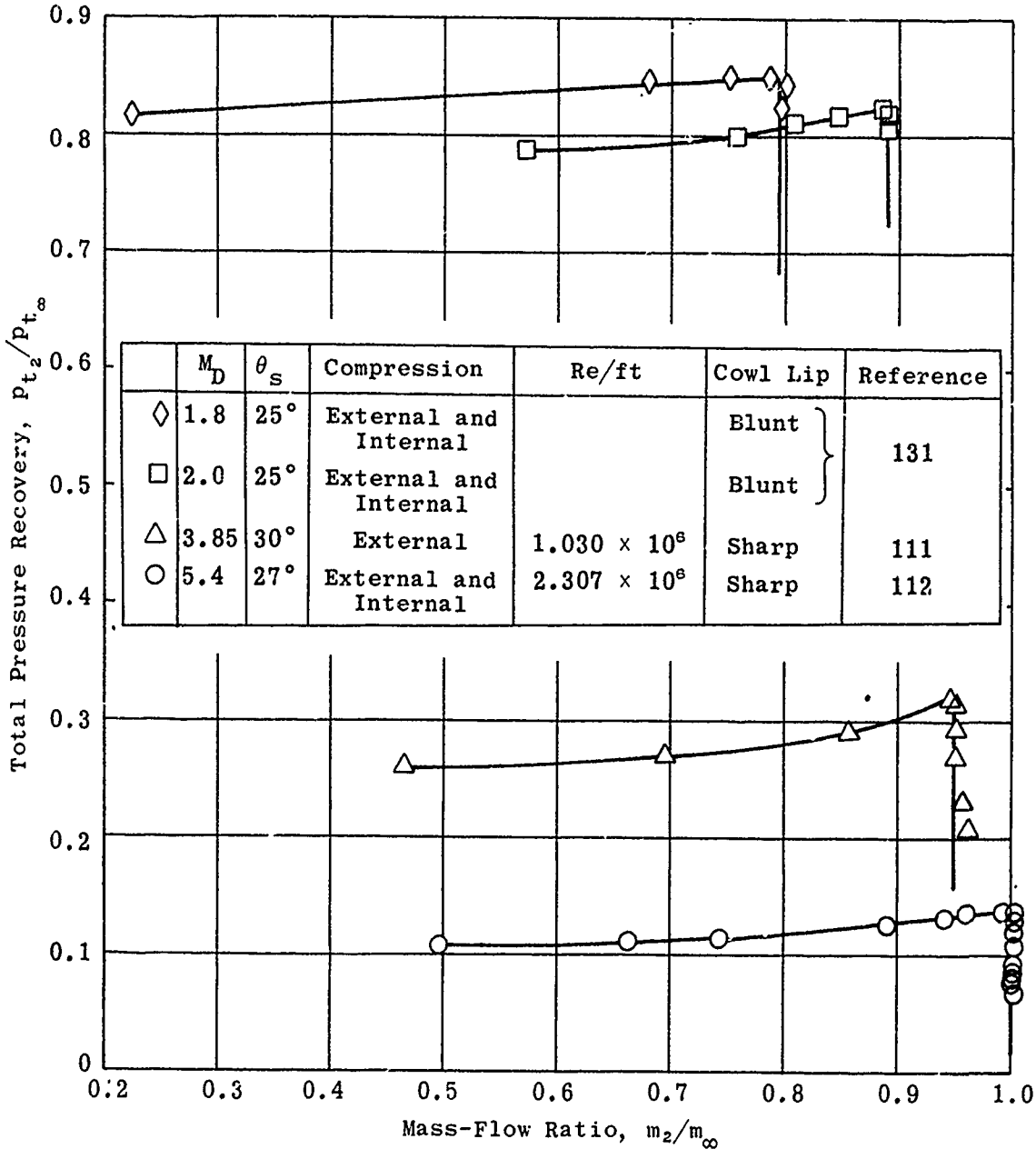

	M_D	θ_s	Compression	Re/ft	Cowl Lip	Reference
◇	1.8	25°	External and Internal		Blunt	131
□	2.0	25°	External and Internal		Blunt	
△	3.85	30°	External	1.030×10^6	Sharp	111
○	5.4	27°	External and Internal	2.307×10^6	Sharp	112

Fig. 3-6. Experimental total pressure recovery vs mass-flow ratio for single-cone inlets operating at design Mach number; M = 1.8, 2.0, 3.85, and 5.4; γ = 1.4.

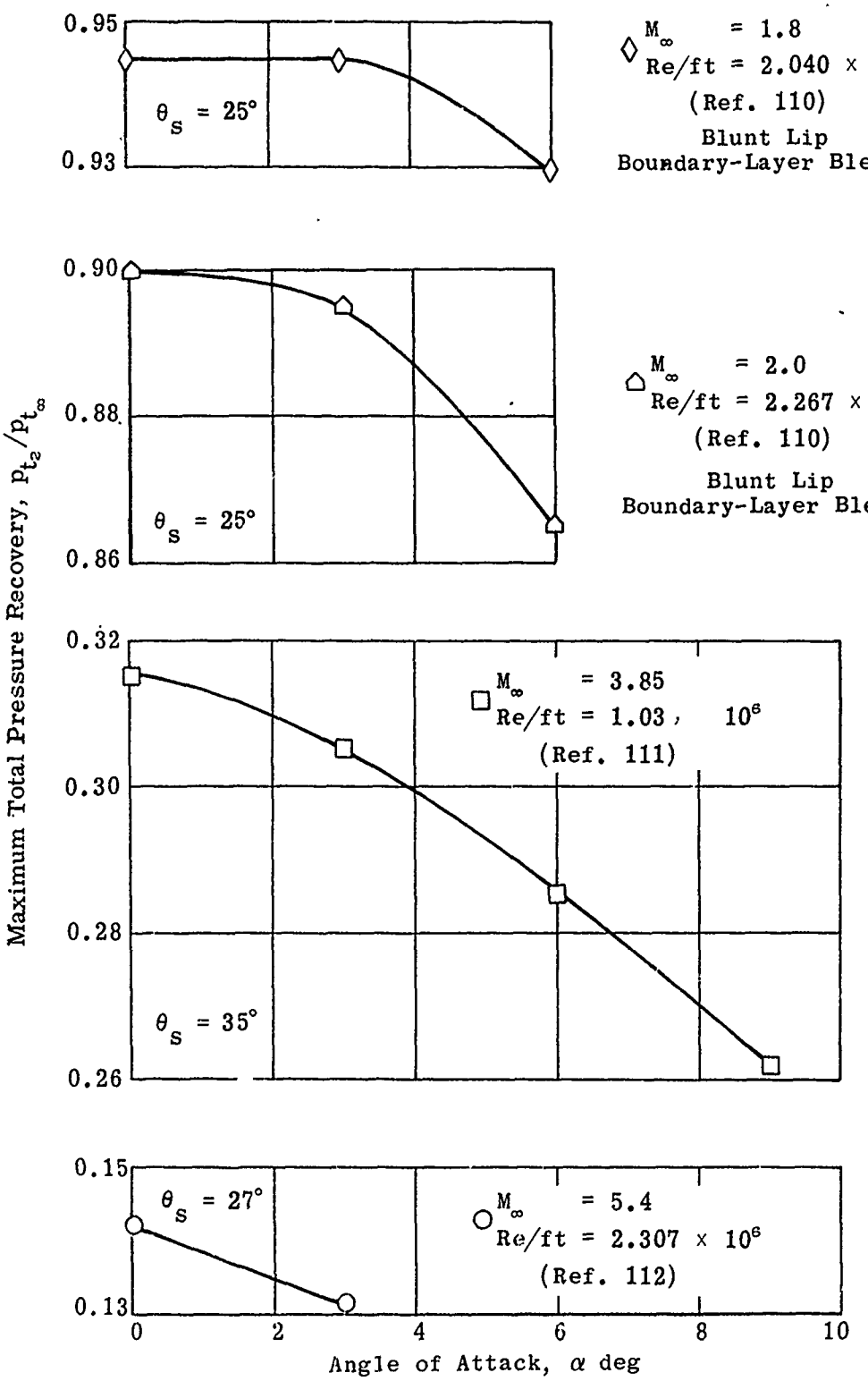

Fig. 3-7. Experimental maximum total pressure recovery vs angle of attack for single-cone inlets; M_∞ = 1.8, 2.0, 3.85, and 5.4; γ = 1.4; α = 0 to 9°.

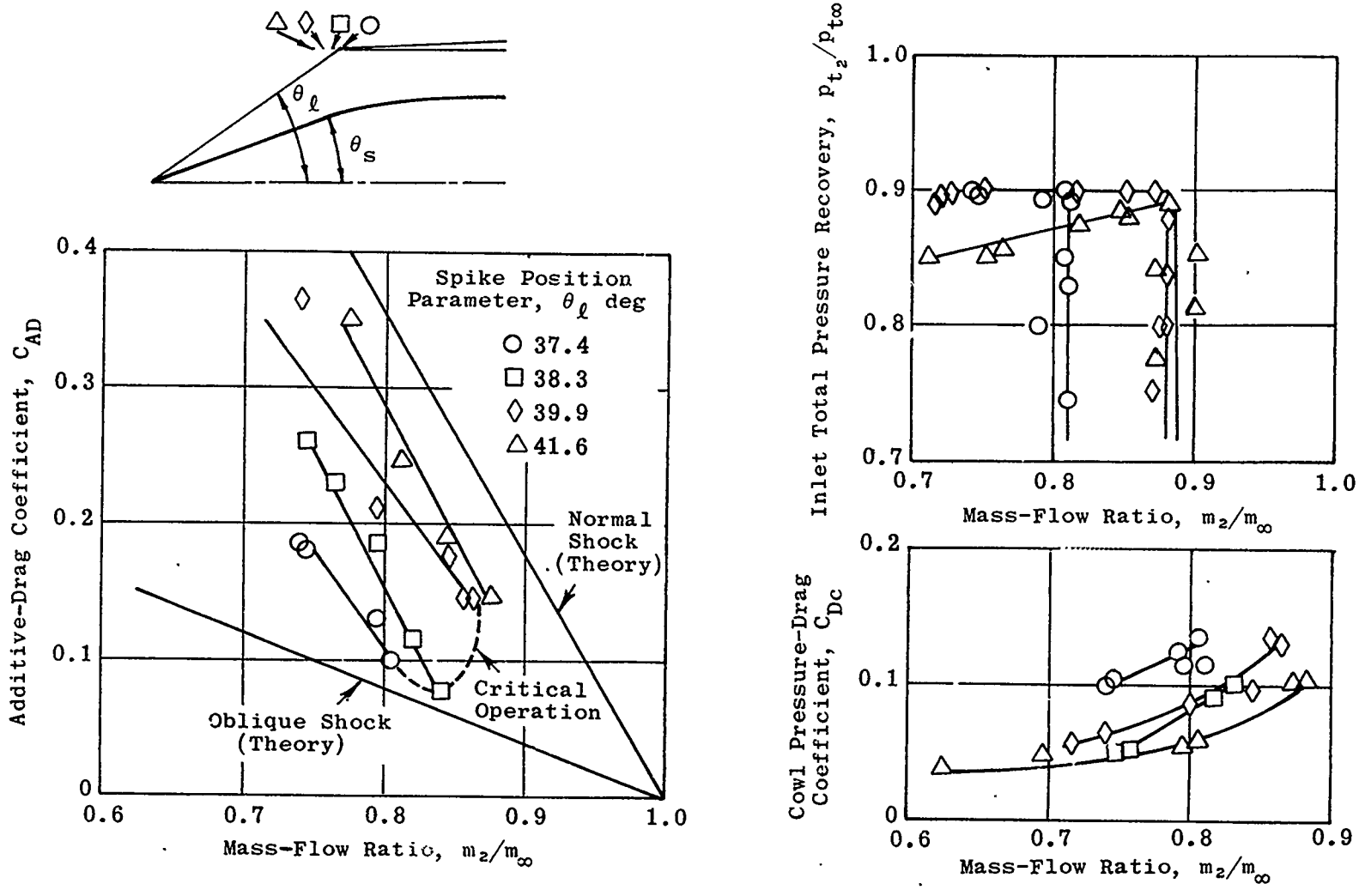

Fig. 3-8. Effect of spike translation on the additive drag, cowl-pressure drag, and total pressure recovery as a function of mass-flow ratio for single-cone inlets; $M_D = 2.0$; $\gamma = 1.4$; Re/ft = 2.267×10^6. (Source: Ref. 110)

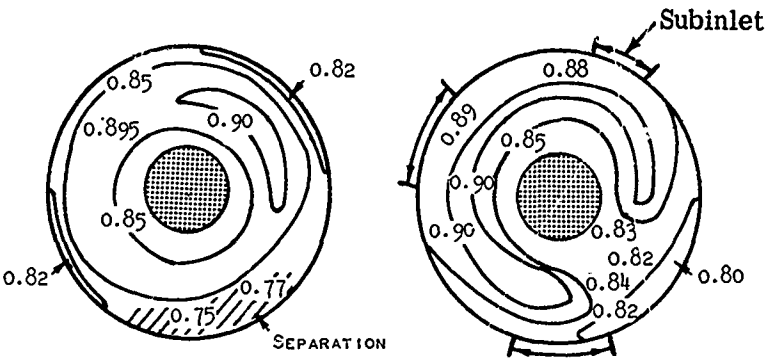

Inlets Closed
$\alpha = 6°$
$\theta_\ell = 41.6°$
Distortion = 18.2%

Inlets Open
$\alpha = 6°$
$\theta_\ell = 41.6°$
Distortion = 12%

Source: Ref. 110

Single-Cone Diffuser

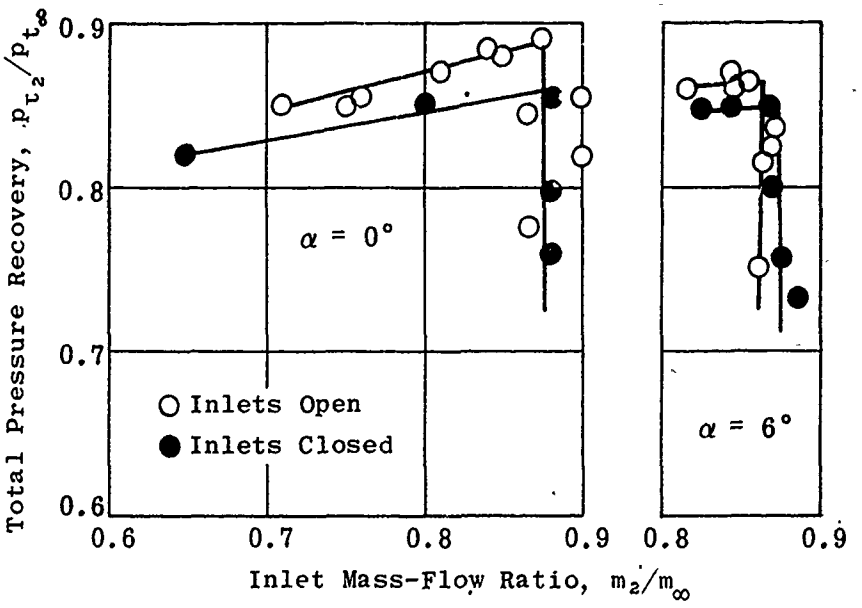

Fig. 3-9. Experimental total pressure recovery vs mass-flow ratio with and without boundary-layer bleed; $M_D = 2.0$; $\alpha = 0$ and 6°; $\gamma = 1.4$; Re/ft = 2.267×10^6.

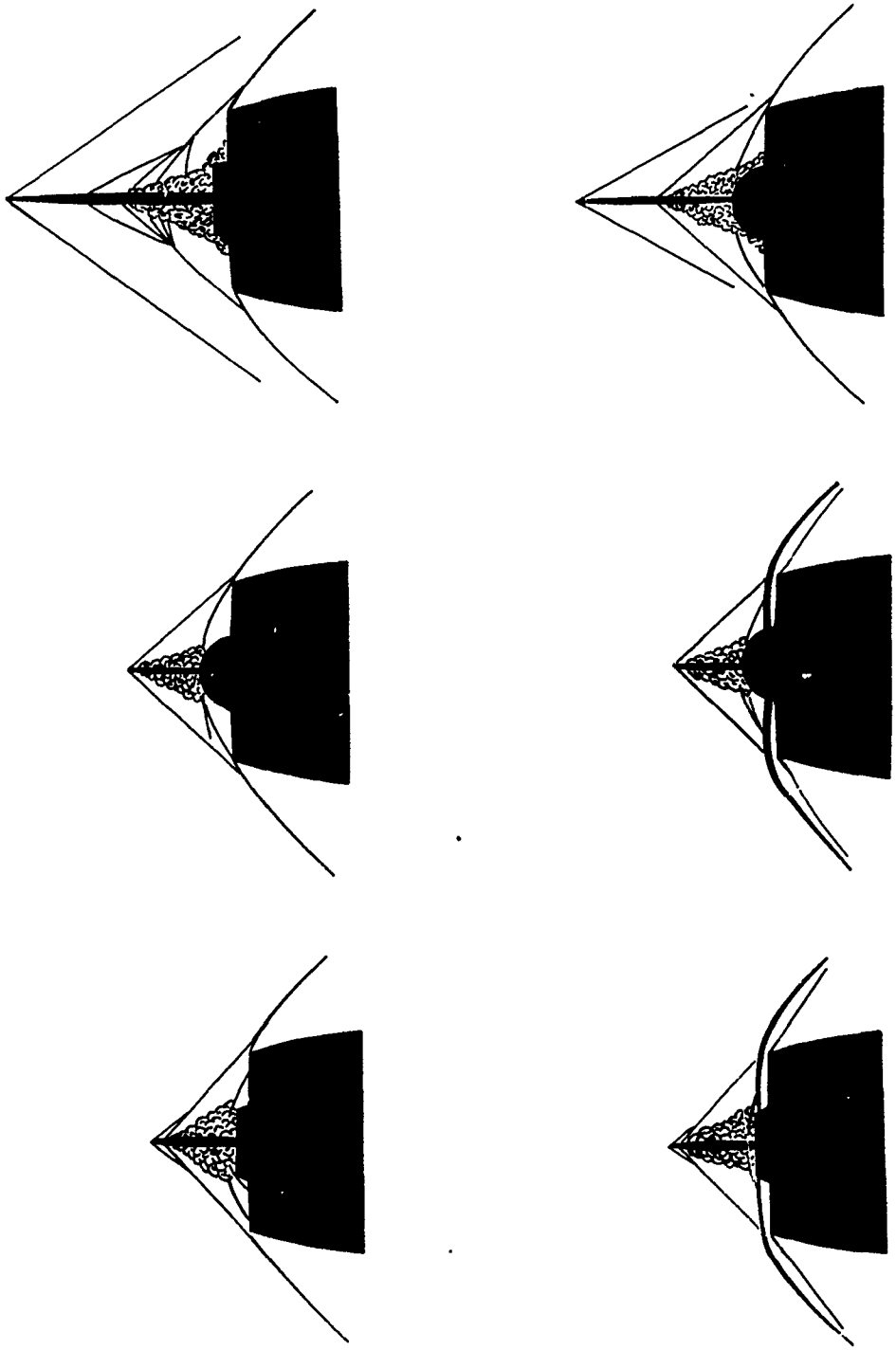

Fig. 3-10. Sketches of typical flow conditions with long and short probes on blunt-nosed diffusers; shock detached and swallowed; M = 1.8; γ = 1.4. (Source: Ref. 113)

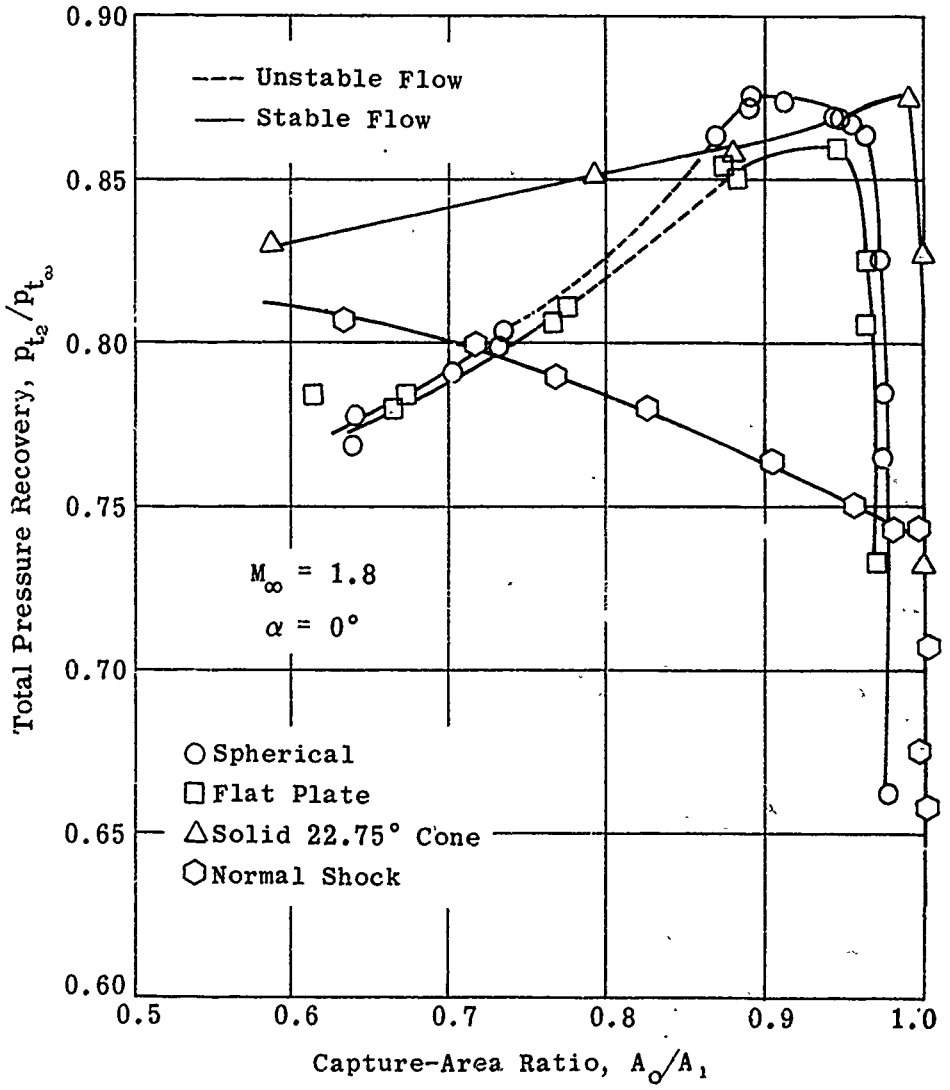

Fig. 3-11. Comparison of experimental total pressure recovery for two probe diffusers, a single-cone diffuser, and a normal-shock diffuser vs capture-area ratio; M_∞ = 1.8; α = 0°; γ = 1.4. (Source: Ref. 113)

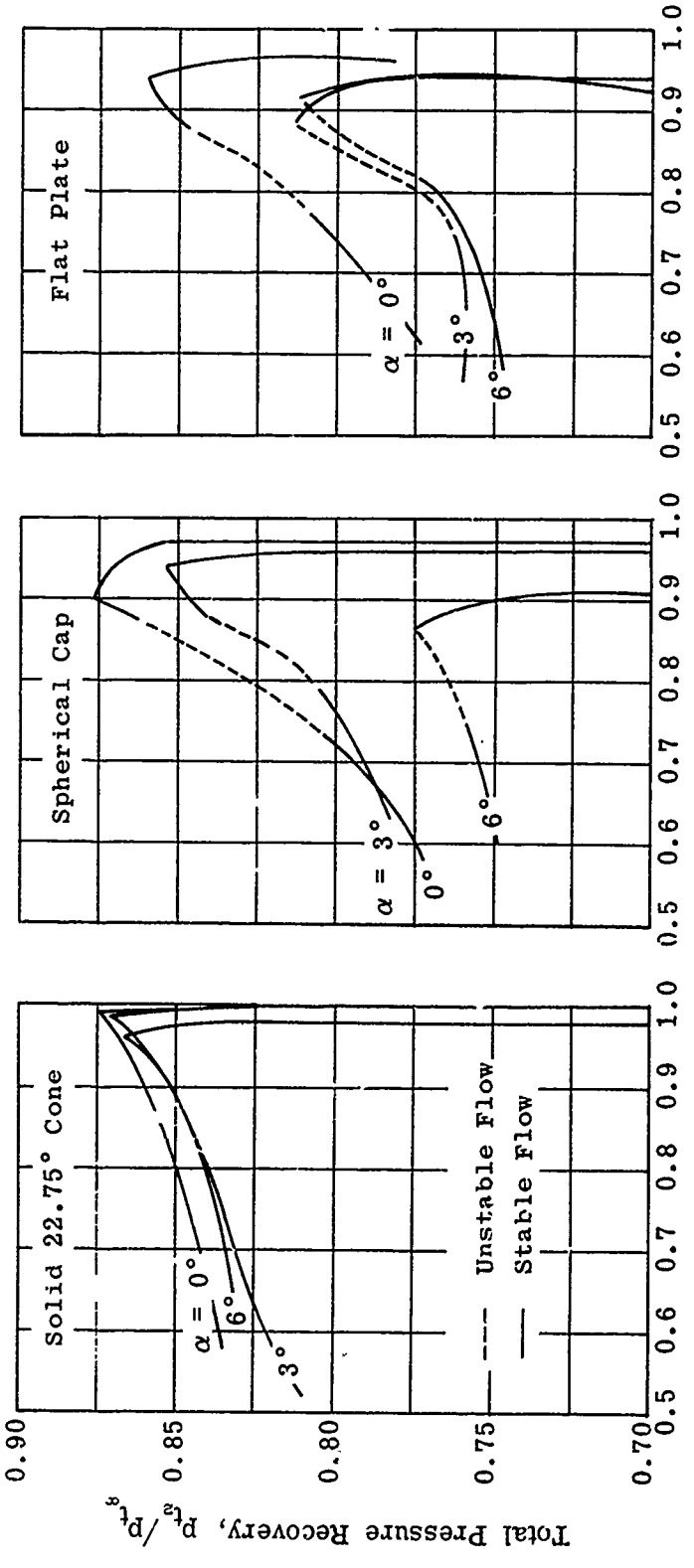

Fig. 3-12. Comparison of the measured total pressure recovery vs capture-area ratio for a single-cone inlet and two probe diffusers; α = 0, 3, and 6°; M_∞ = 1.8; γ = 1.4. (Source: Ref. 113)

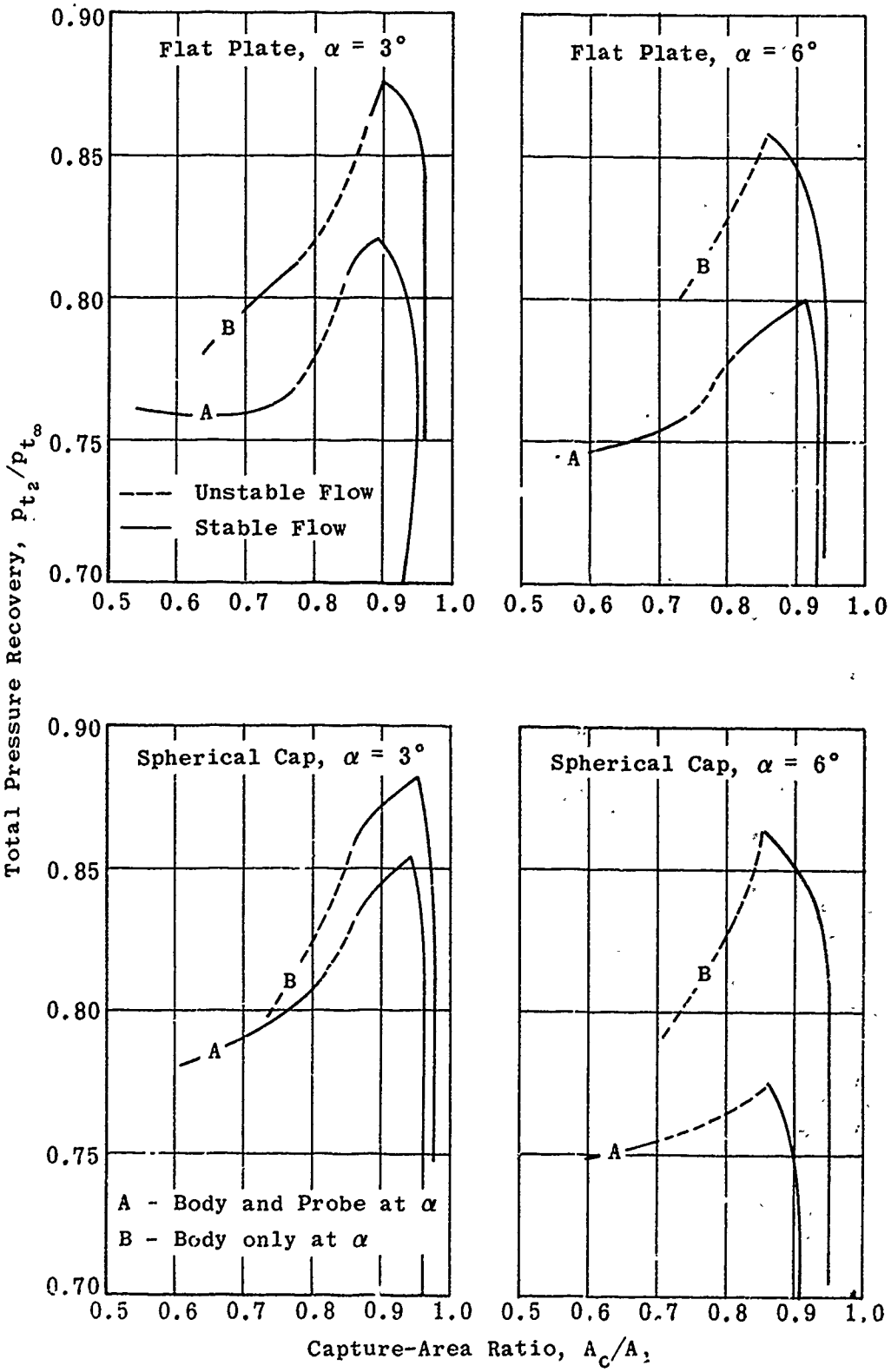

Fig. 3-13. Effect of off-axis probe alignment for two probe diffusers at angle of attack; $M_\infty = 1.8$; $\alpha = 3$ and 6°; $\gamma = 1.4$. (Source: Ref. 113)

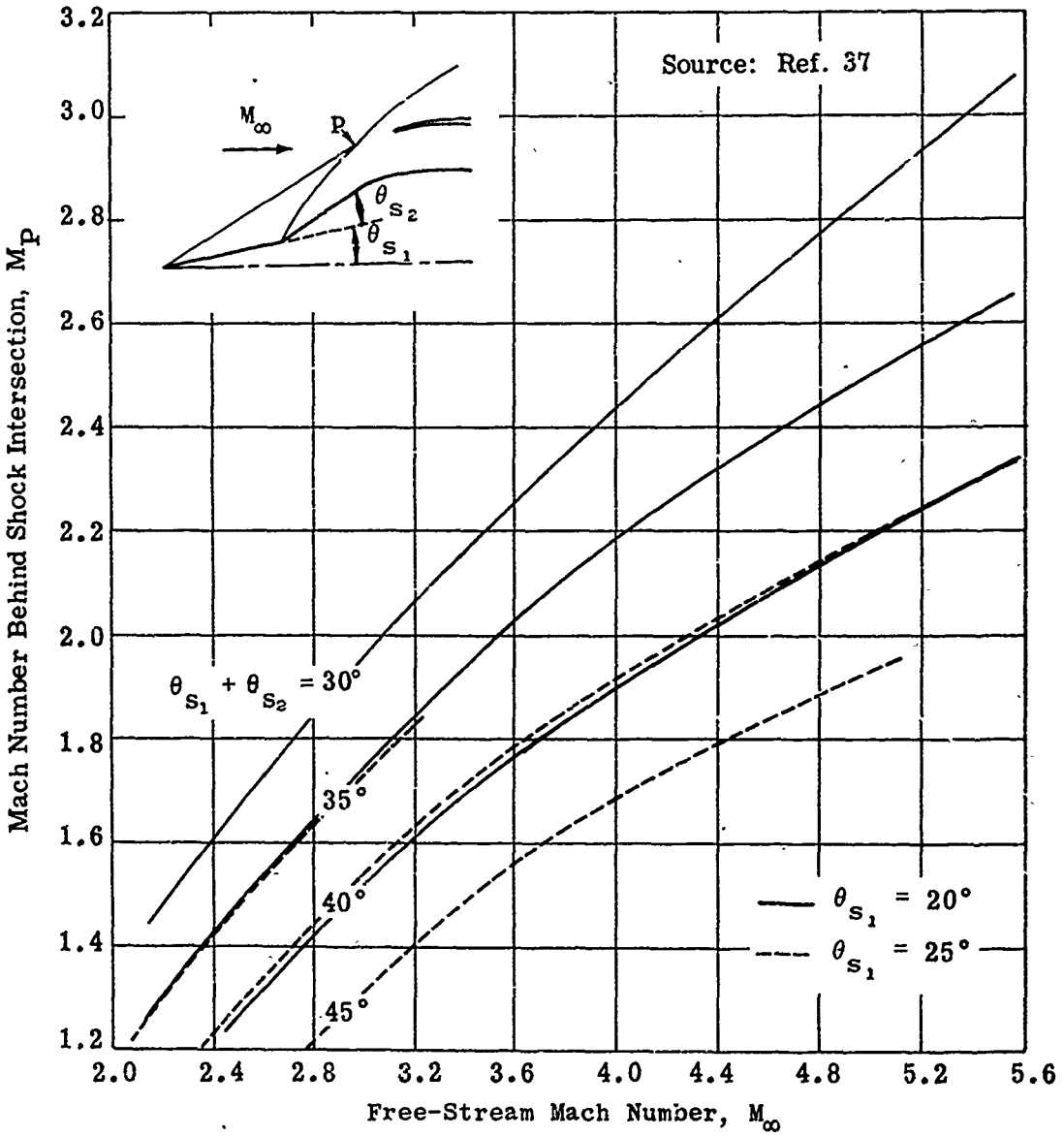

Fig. 3-14. Mach number behind point of shock intersection vs free-stream Mach number for biconic inlets; M_∞ = 2 to 5.6; θ_{S_1} = 20 and 25°; $\theta_{S_1} + \theta_{S_2}$ = 30, 35, 40, and 45°; γ = 1.4.

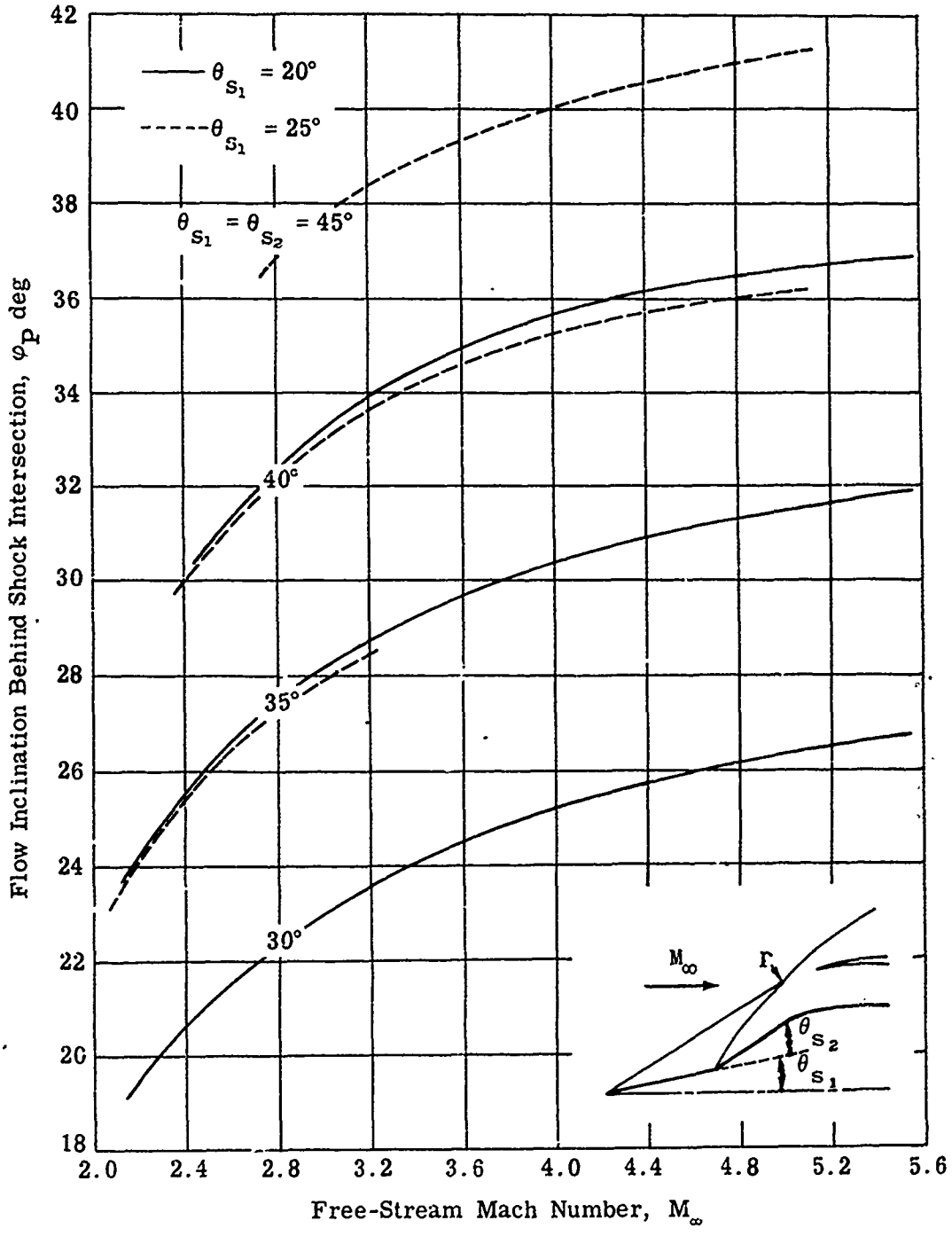

Fig. 3-15. Flow inclination behind point of shock intersection vs free-stream Mach number for biconic inlets; M_∞ = 2 to 5.6; θ_{S_1} = 20 and 25°; $\theta_{S_1} + \theta_{S_2}$ = 30, 35, 40, and 45°; γ = 1.4. (Source: Ref. 37)

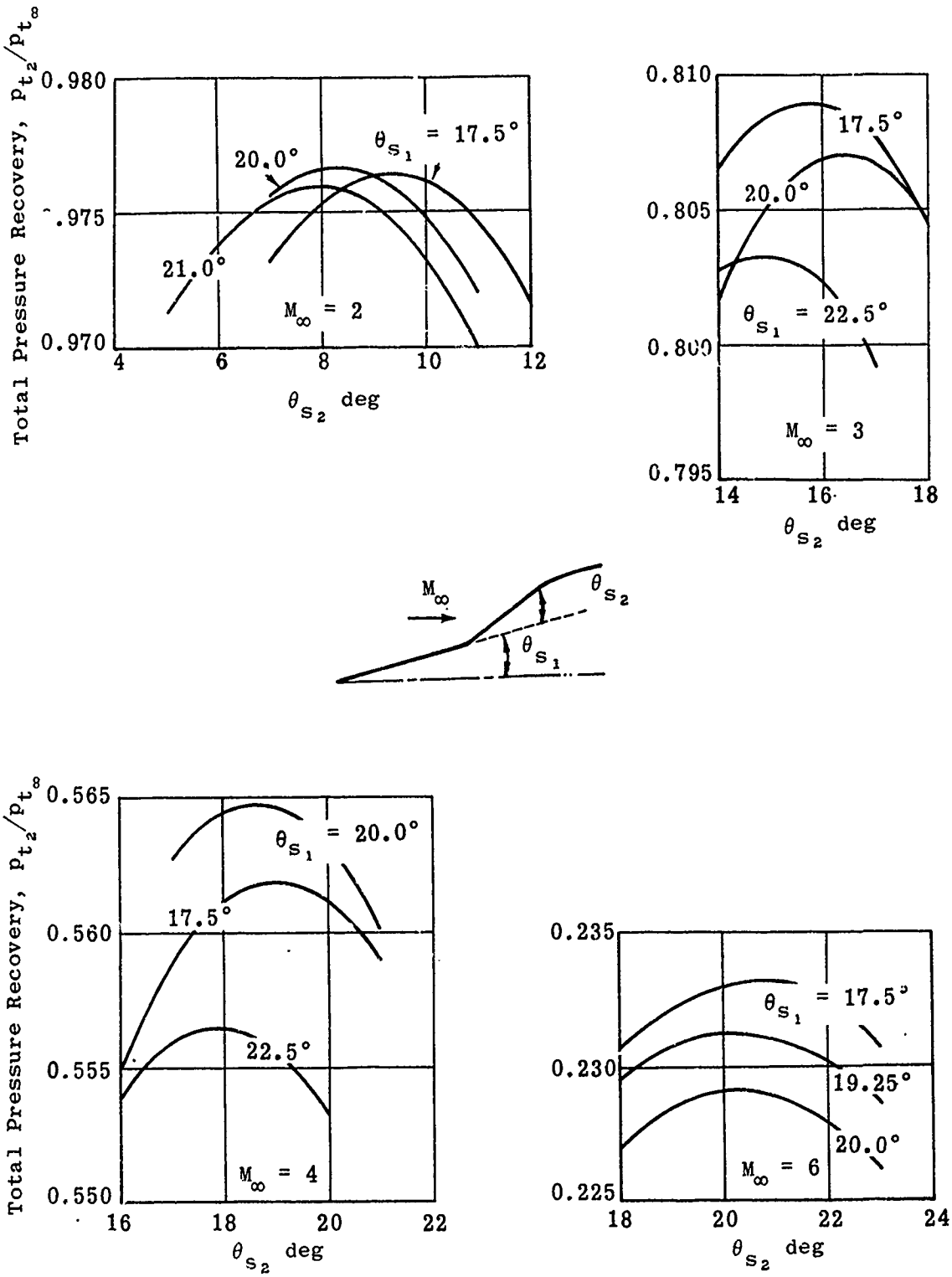

Fig. 3-16a. Calculated total pressure recoveries of biconic inlets as a function of cone angles and free-stream Mach number; external and internal compression; M_∞ = 2, 3, 4, and 6; γ = 1.4.

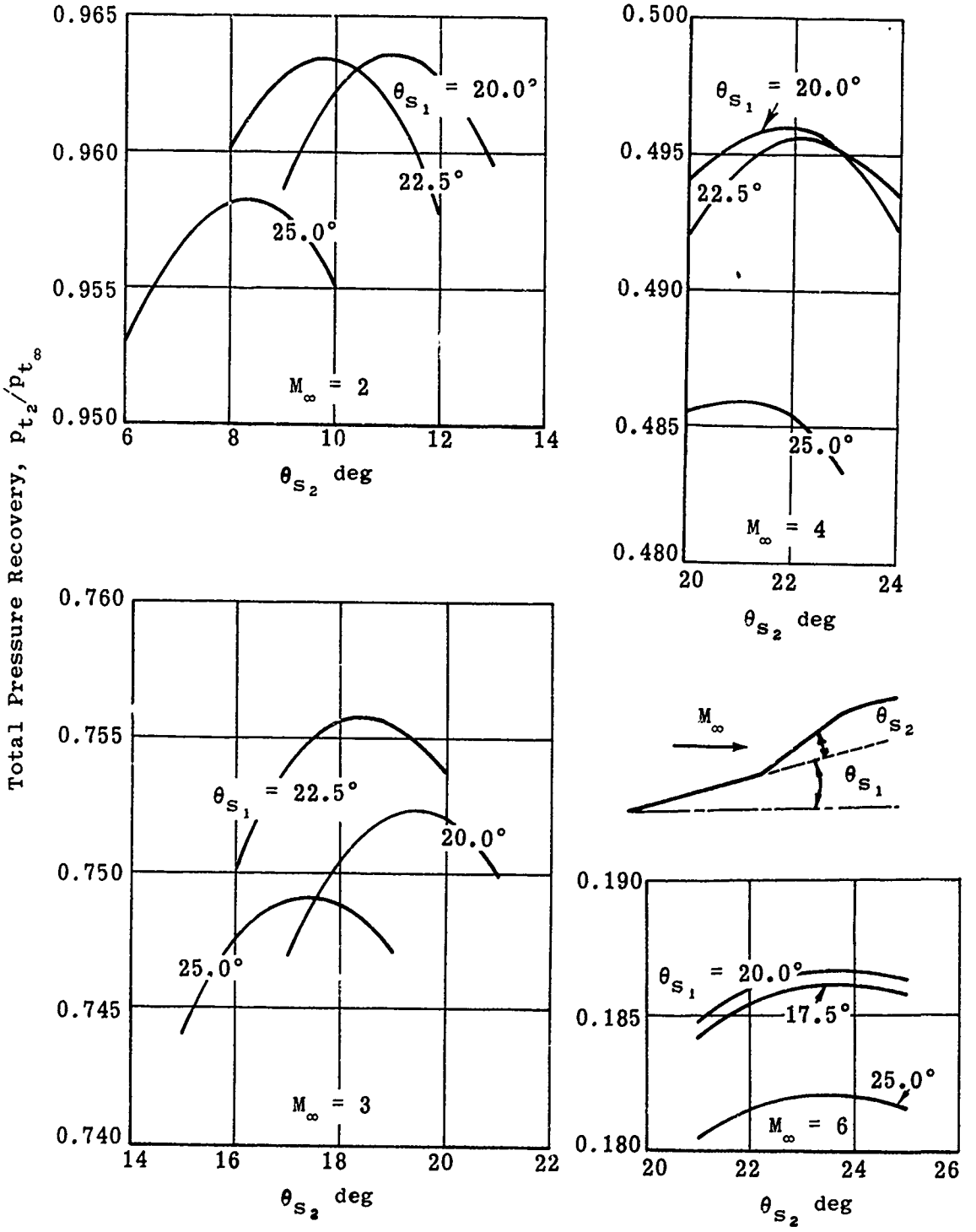

Fig. 3-16b. Calculated total pressure recoveries of biconic inlets as a function of cone angles and free-stream Mach number; all external compression; M_∞ = 2, 3, 4, and 6; γ = 1.4.

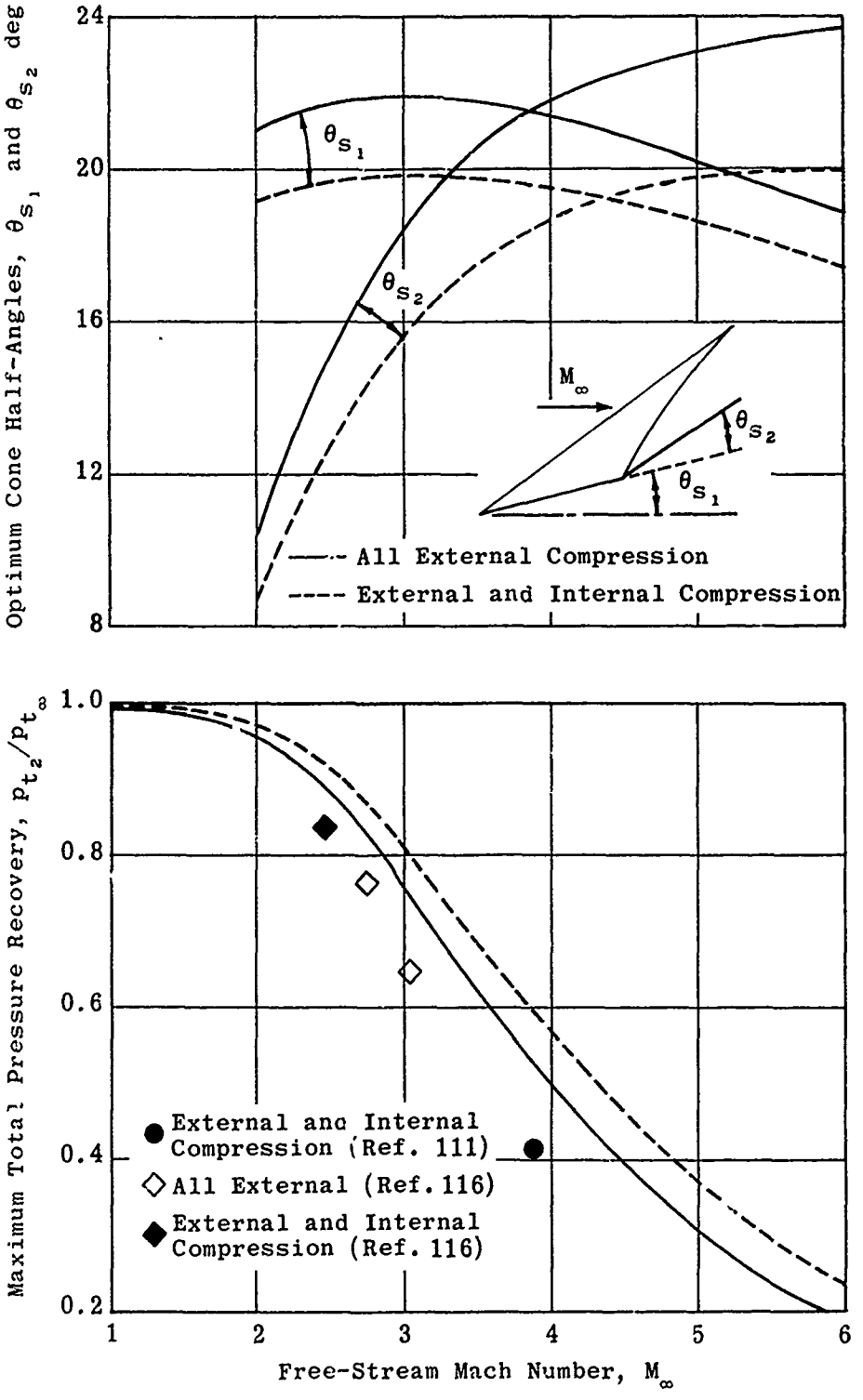

Fig. 3-17. Comparison of calculated and experimental maximum pressure recovery and associated cone half-angles for biconic inlets vs free-stream Mach number; M_∞ = 1 to 6; γ = 1.4.

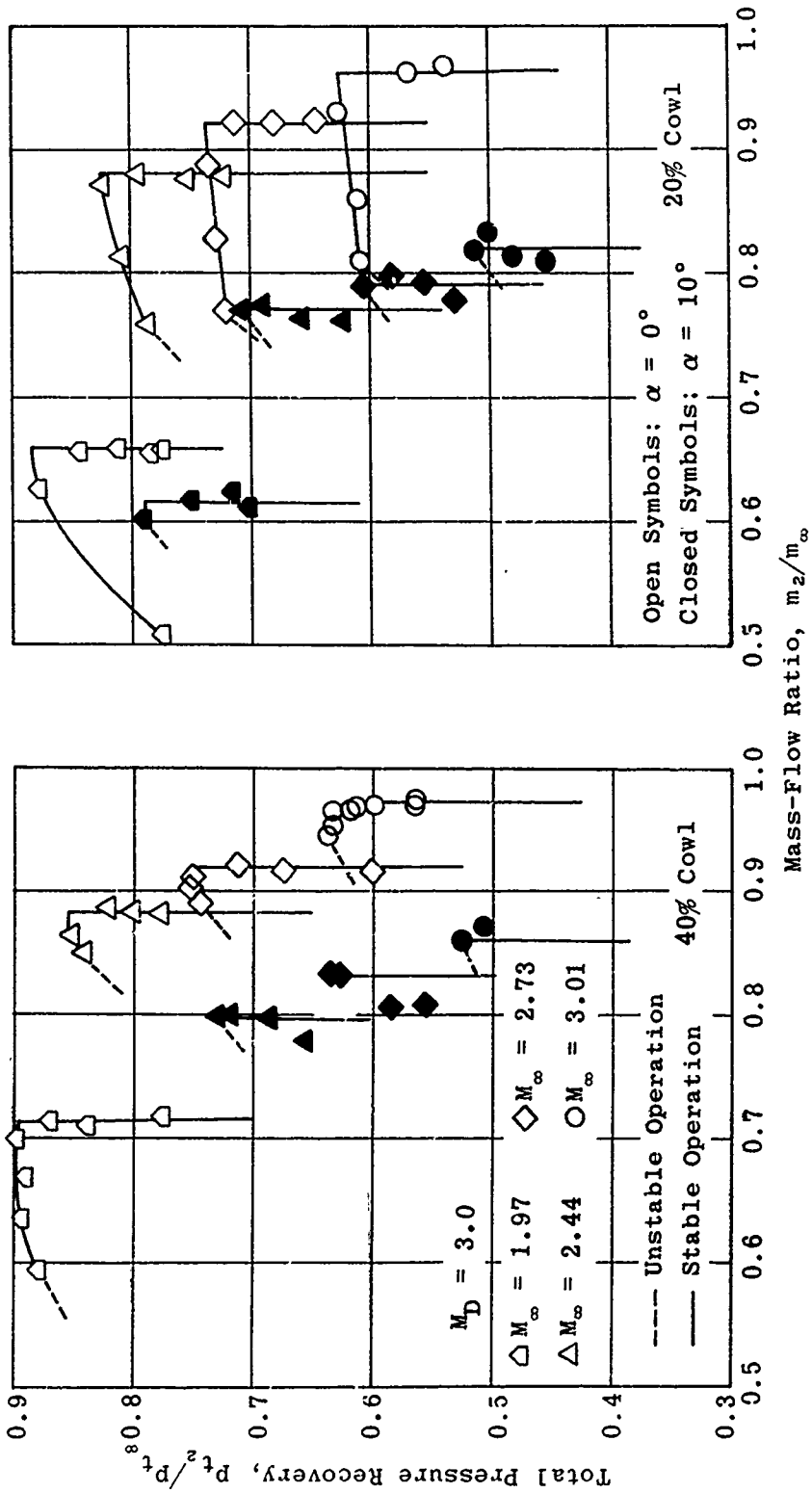

Fig. 3-18. Experimental total pressure recovery vs mass-flow ratio for high- and low-drag cowls; biconic spike, M_∞ = 1.97, 2.44, 2.73, and 3.01; α = 0 and 10°; Re/ft = 2.5 × 10^6; γ = 1.4. (Source: Ref. 103)

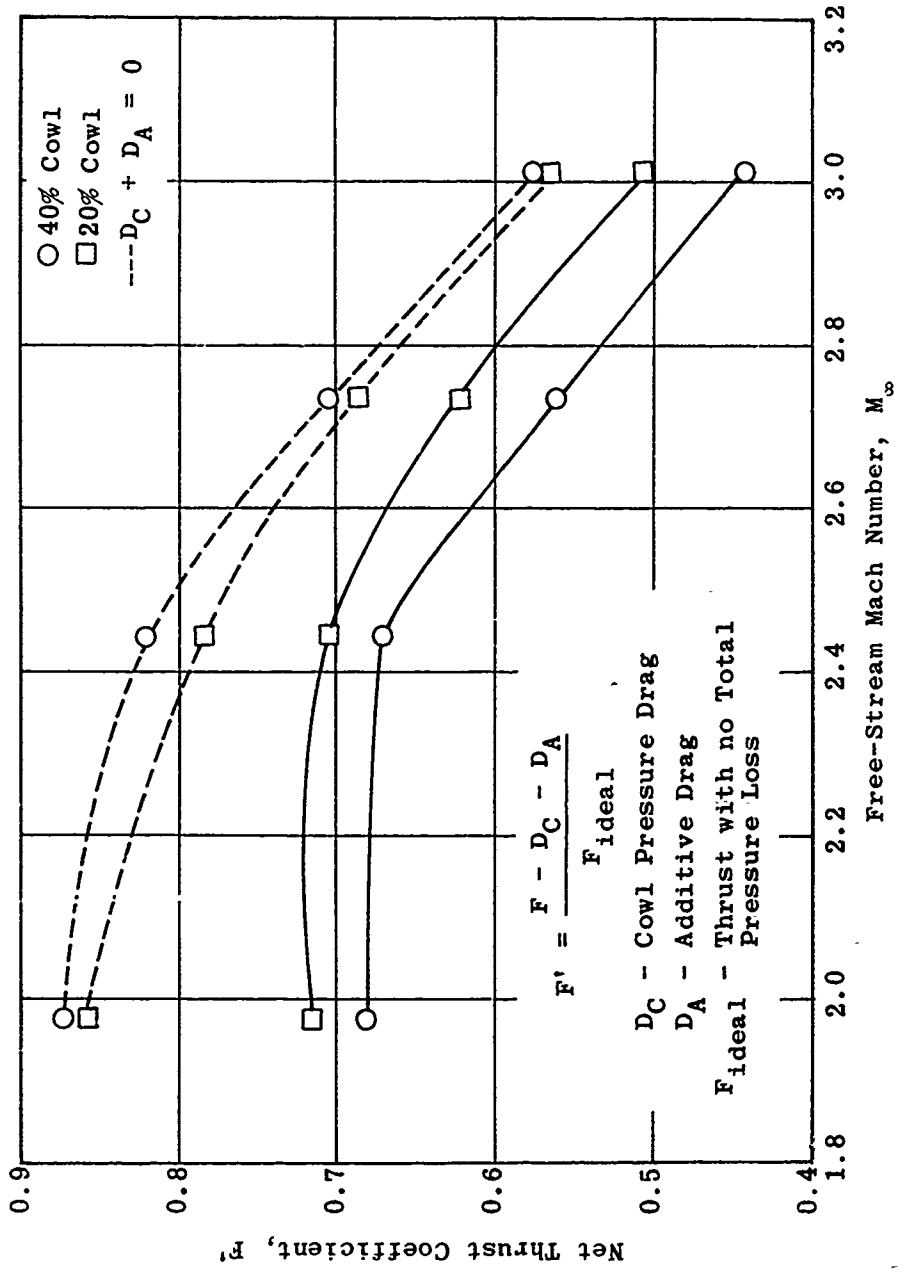

Fig. 3-19. Experimental values of thrust minus drag as a function of free-stream Mach number for high- and low-drag cowls; biconic spikes; $\gamma = 1.4$; Re/ft = 2.5×10^6. (Source: Ref. 103)

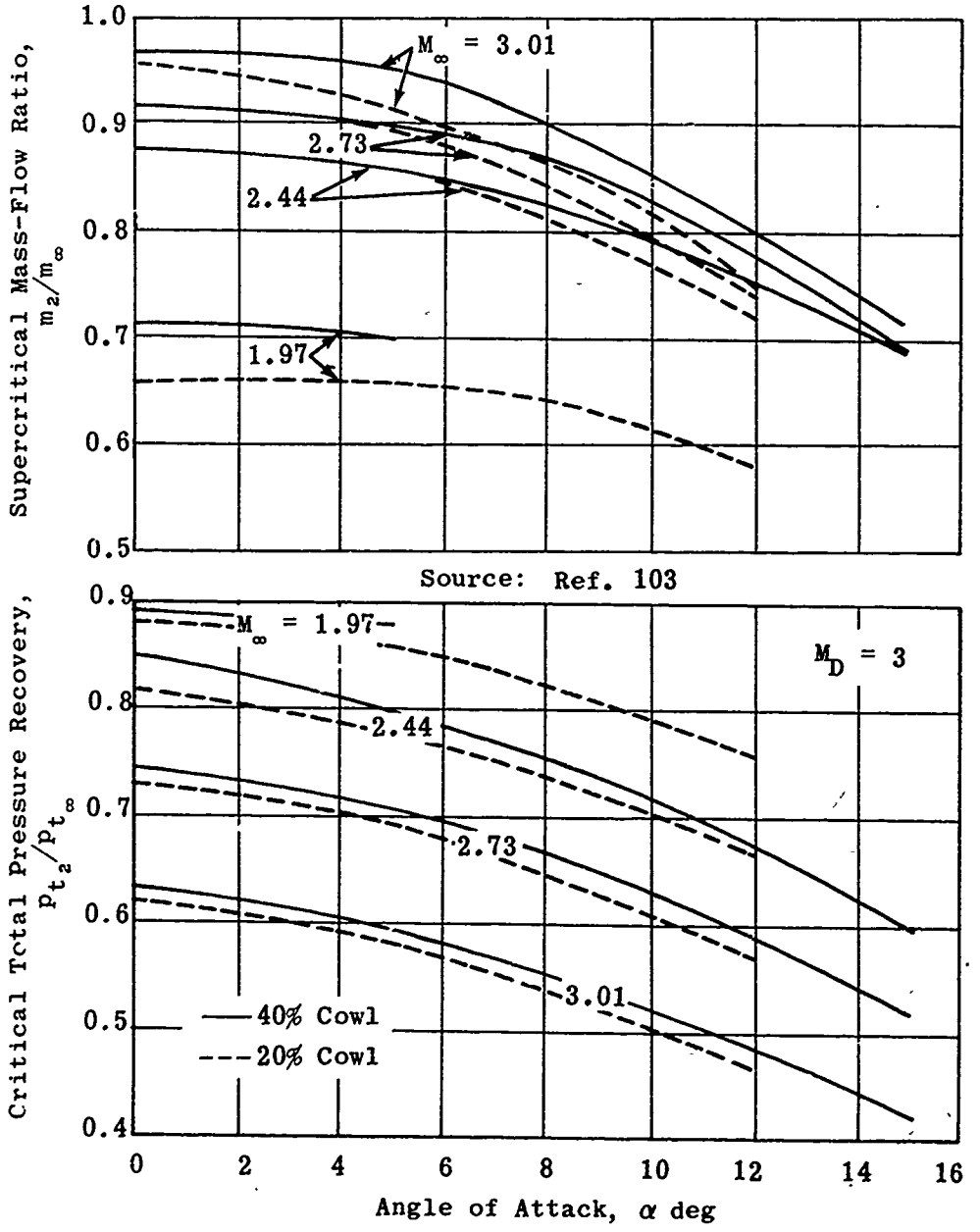

Fig. 3-20. Critical total pressure recovery and associated supercritical mass-flow ratio as a function of angle of attack for high- and low-drag cowls; biconic spikes; M_∞ = 3.01, 2.73, 2.44, and 1.97; Re/ft = 2.5 x 10^6.

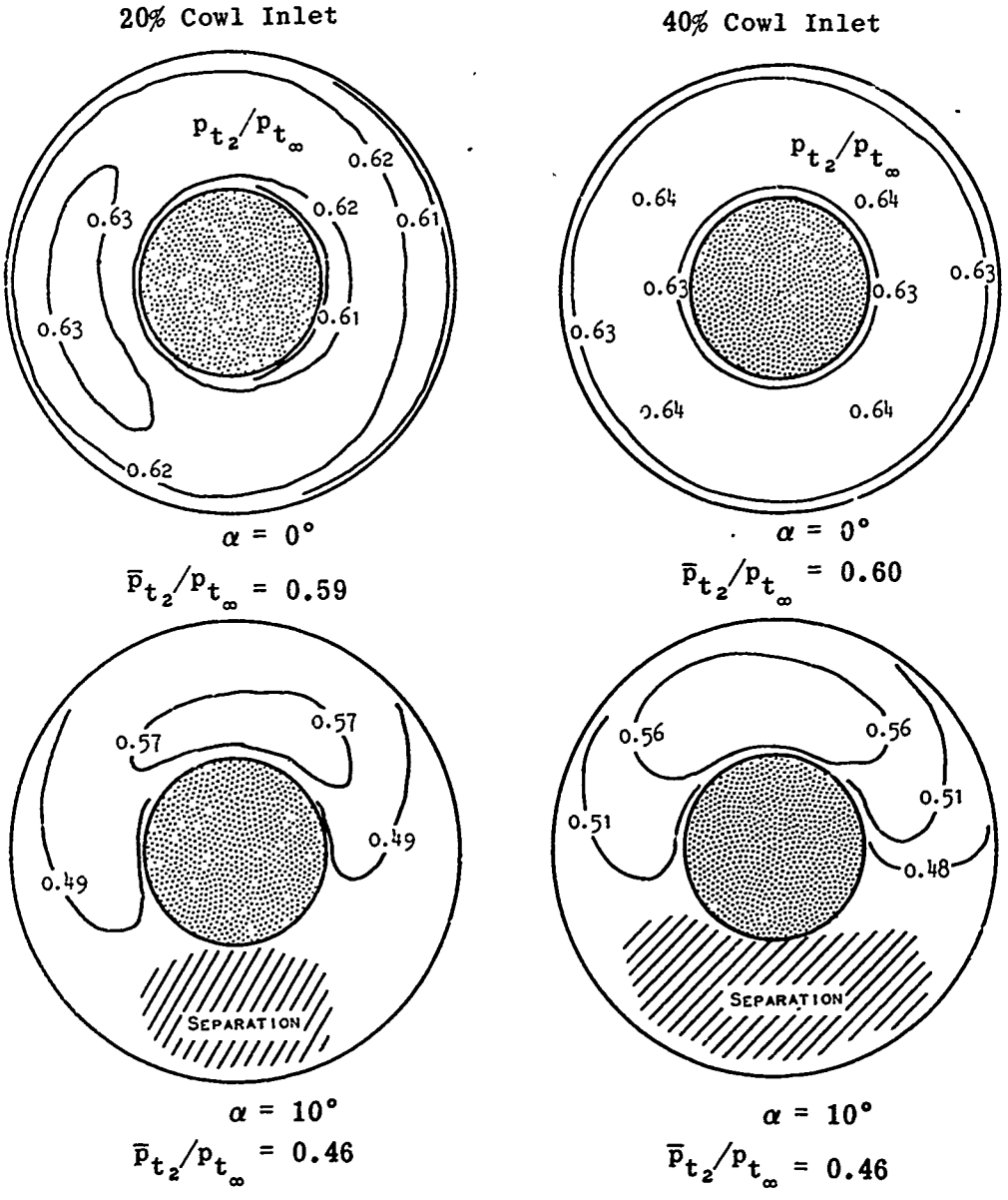

Fig. 3-21. Flow-distortion contours at the diffuser exit for two cowls at $M_\infty = 3.01$; $\alpha = 0$ and 10°; $\gamma = 1.4$; Re/ft = 2.5×10^6. (Source: Ref. 103)

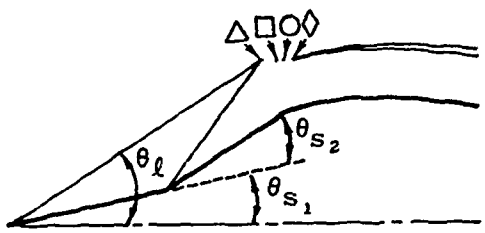

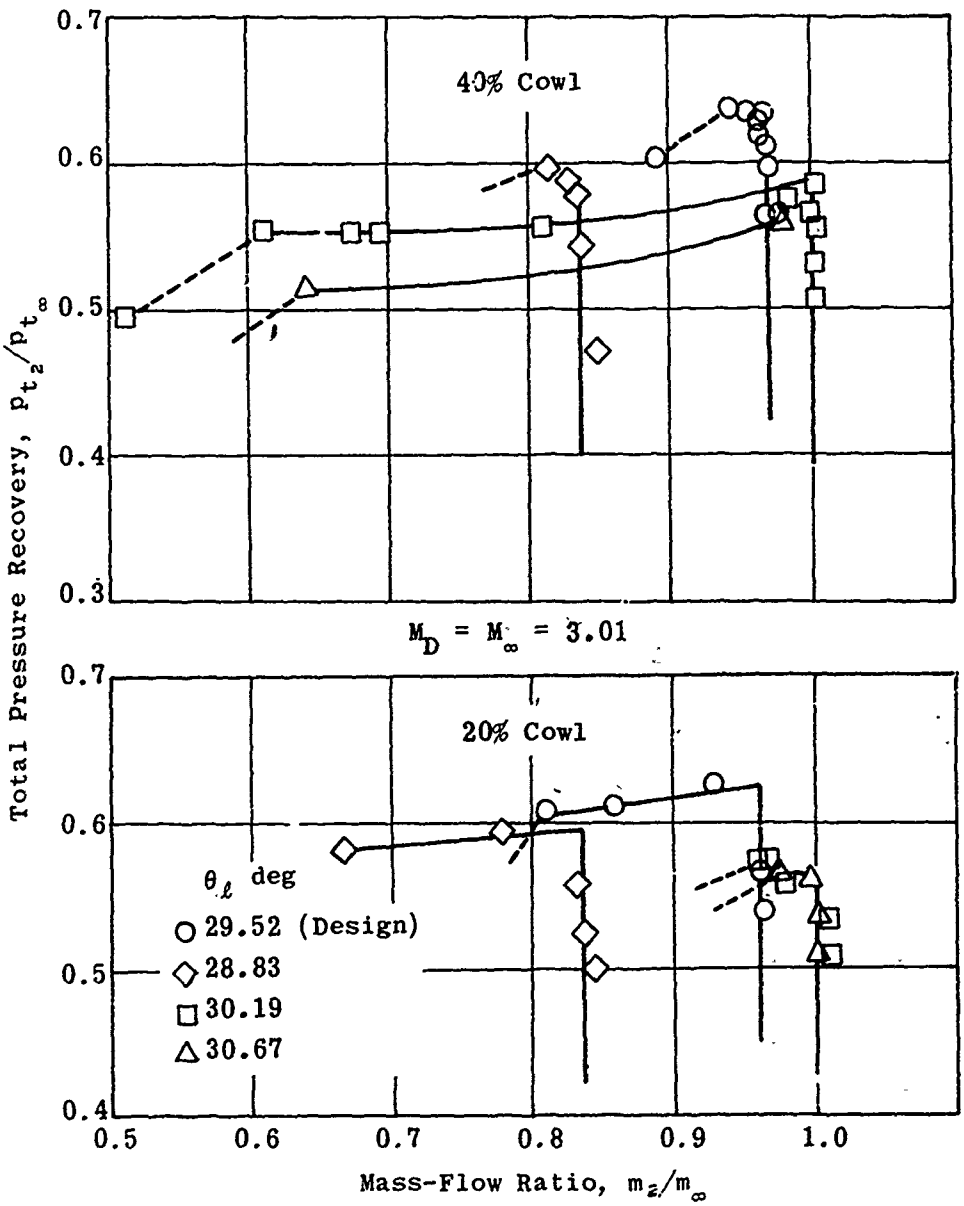

Fig. 3-22. Measured total pressure recovery vs mass-flow ratio as a function of biconic spike position; $M_D = 3.01$; $\gamma = 1.4$; $\alpha = 0°$; Re/ft = 2.5×10^6. (Source: Ref. 103)

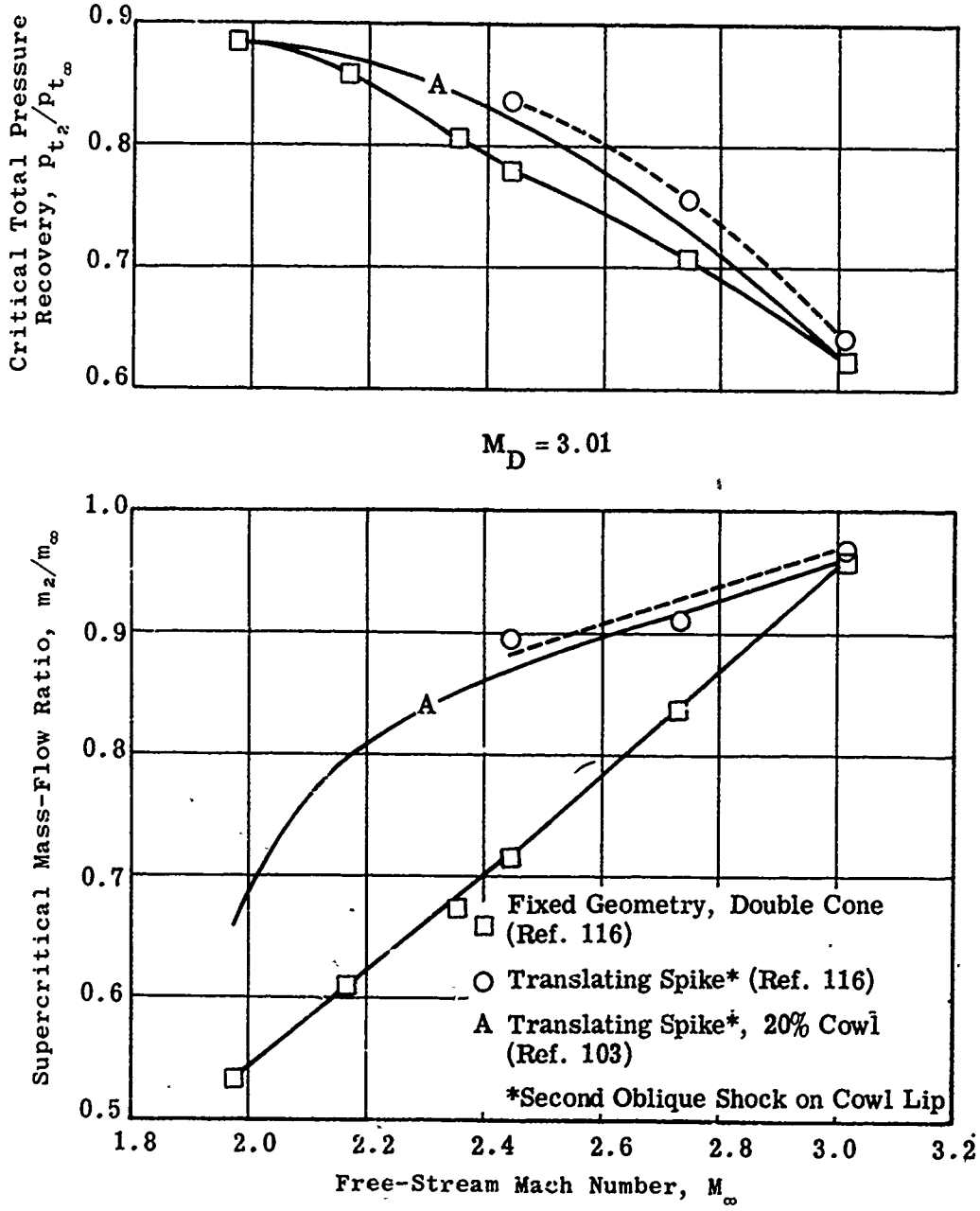

Fig. 3-23. Off-design performance of translating biconic-spike inlets as a function of free-stream Mach number; $\gamma = 1.4$; Re/ft = 2.5×10^6. (Source: Ref. 116)

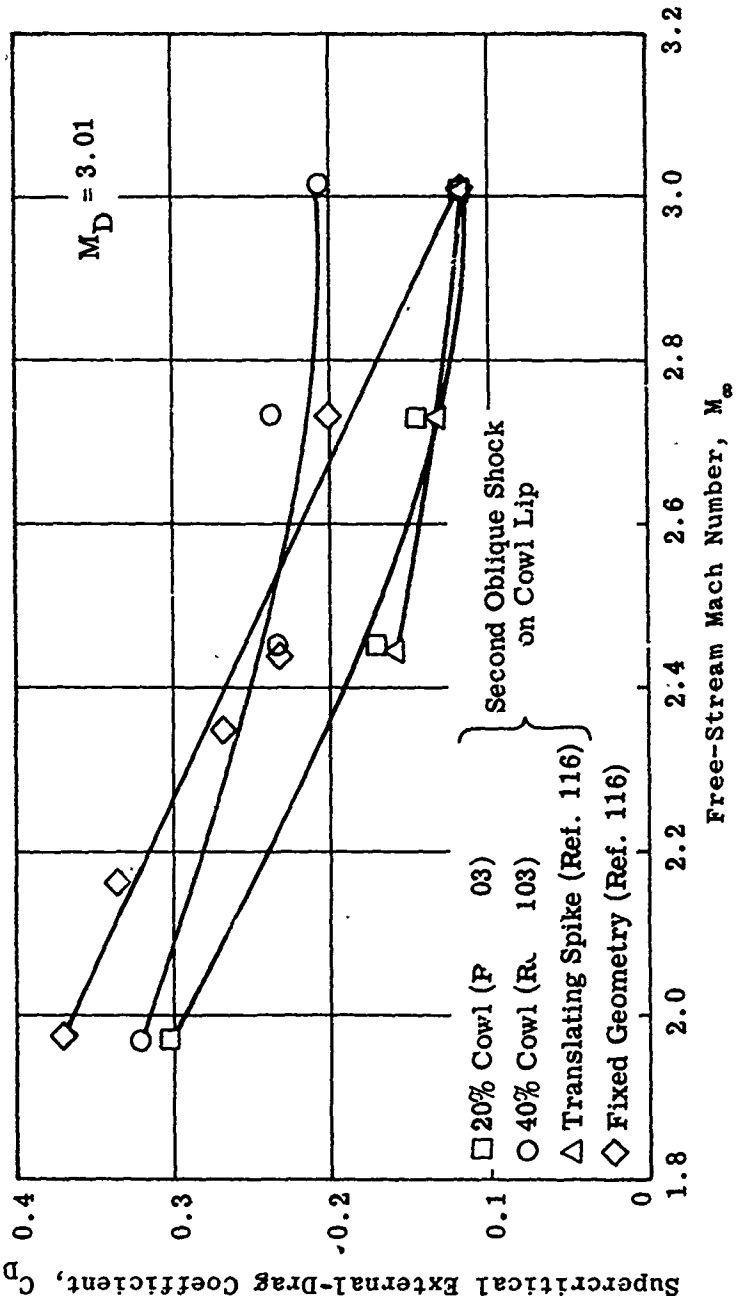

Fig. 3-24. Comparison of supercritical external-drag coefficient vs free-stream Mach number for various biconic spikes; $2 \leq M_\infty \leq 3$; Re/ft = 2.5×10^6.

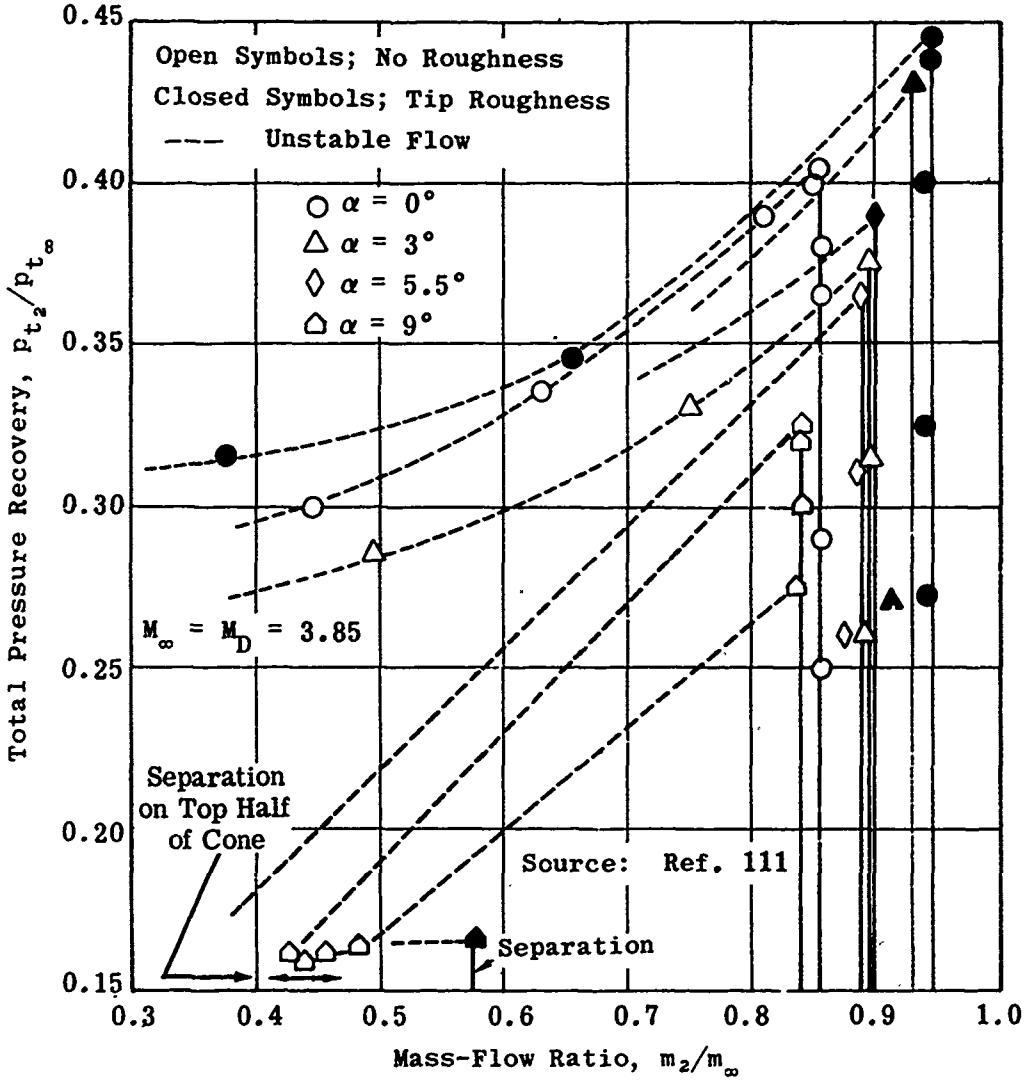

Fig. 3-25. Effect of tip roughness and angle of attack on measured total pressure recovery vs mass-flow ratio for biconic inlets; $M_\infty = 3.85$; $\alpha = 0$, 3 , 5.5 , and 9°; $\gamma = 1.4$; Re/ft = 1.0×10^6.

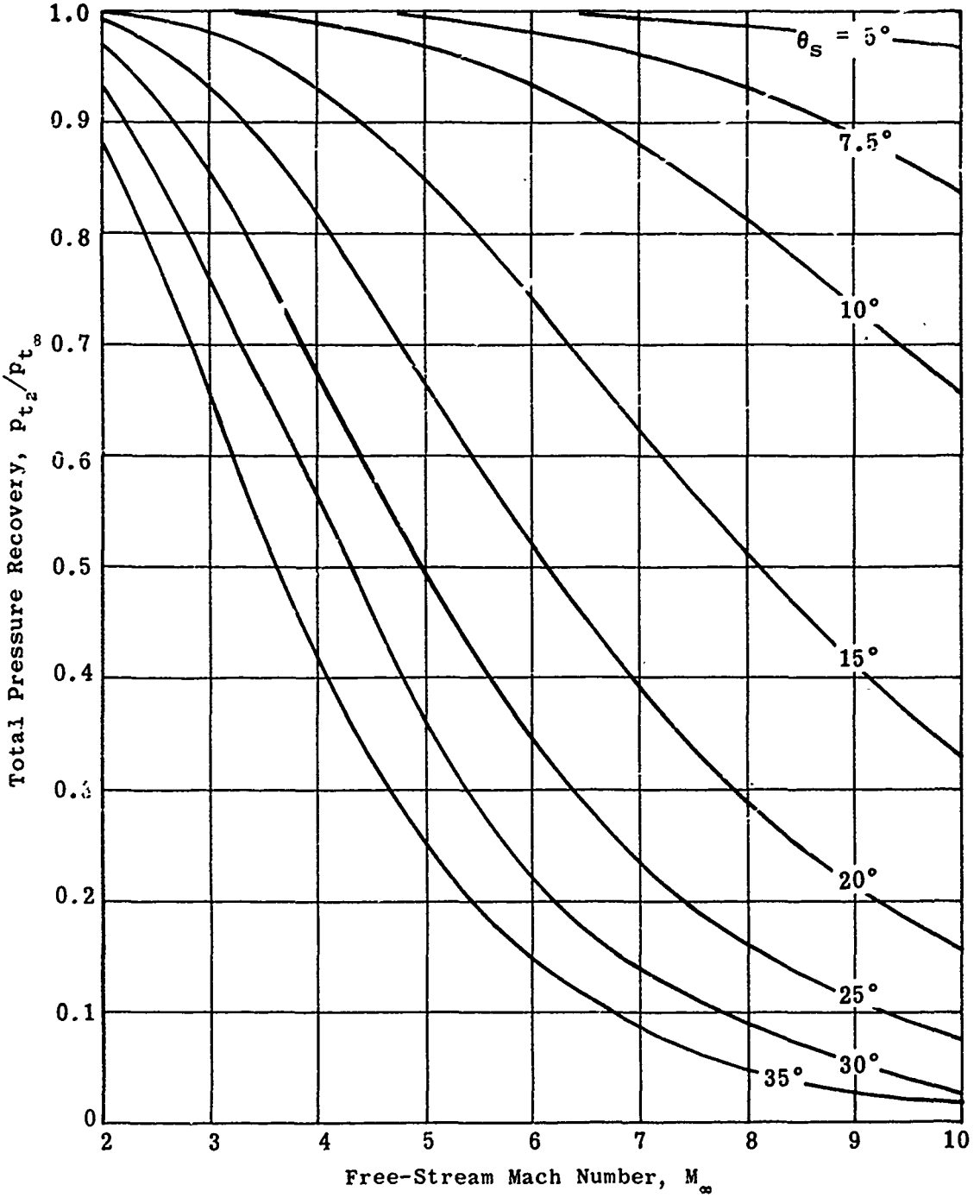

Fig. 3-26. Calculated total pressure recovery through a conical shock as a function of free-stream Mach number and cone semi-angle; $2 \leq M_\infty \leq 10$; $5° \leq \theta_s \leq 35°$; $\gamma = 1.4$.

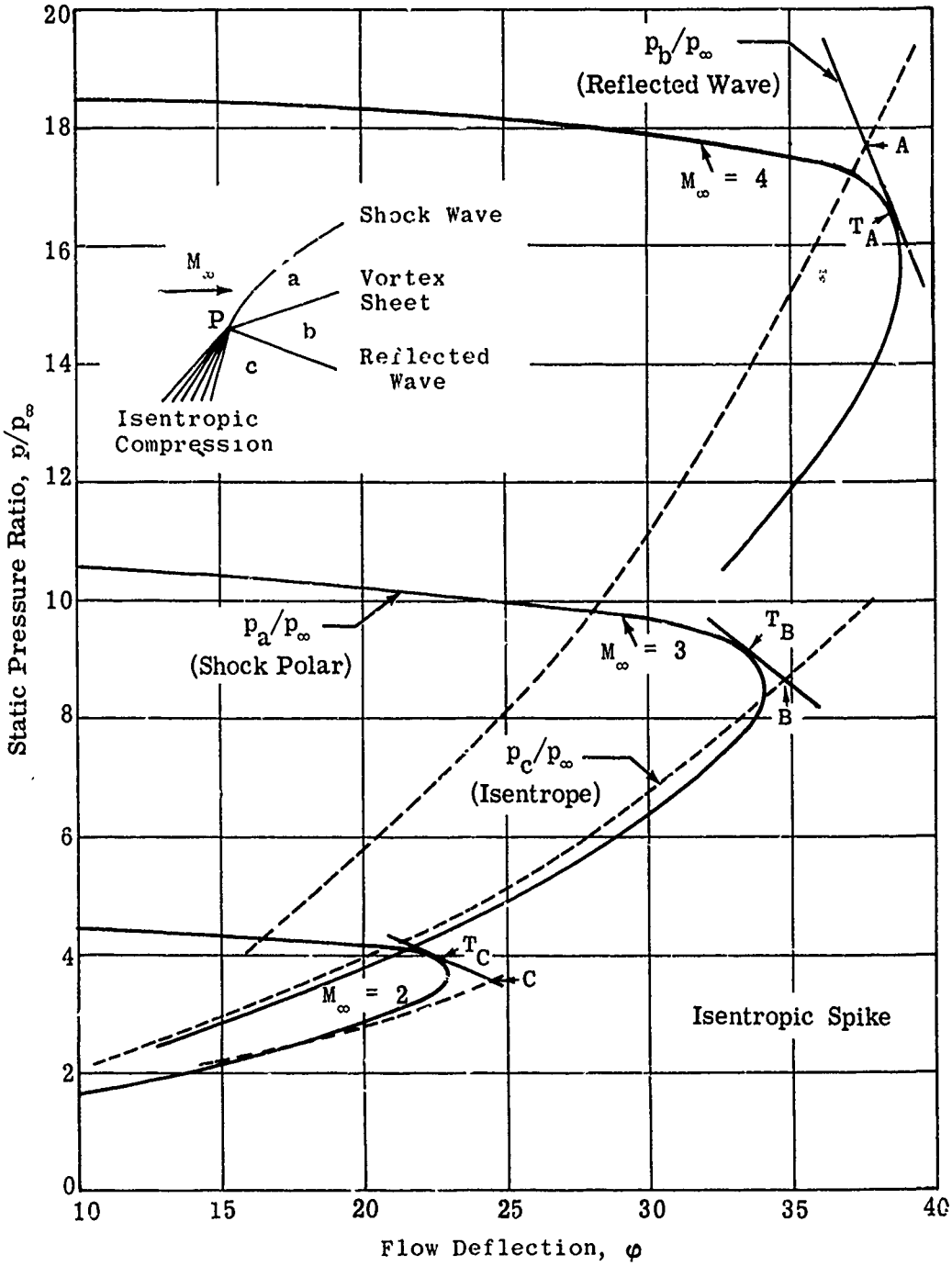

Fig. 3-27. Theoretical pressure-deflection polars; γ = 1.4; M_∞ = 2, 3, and 4.

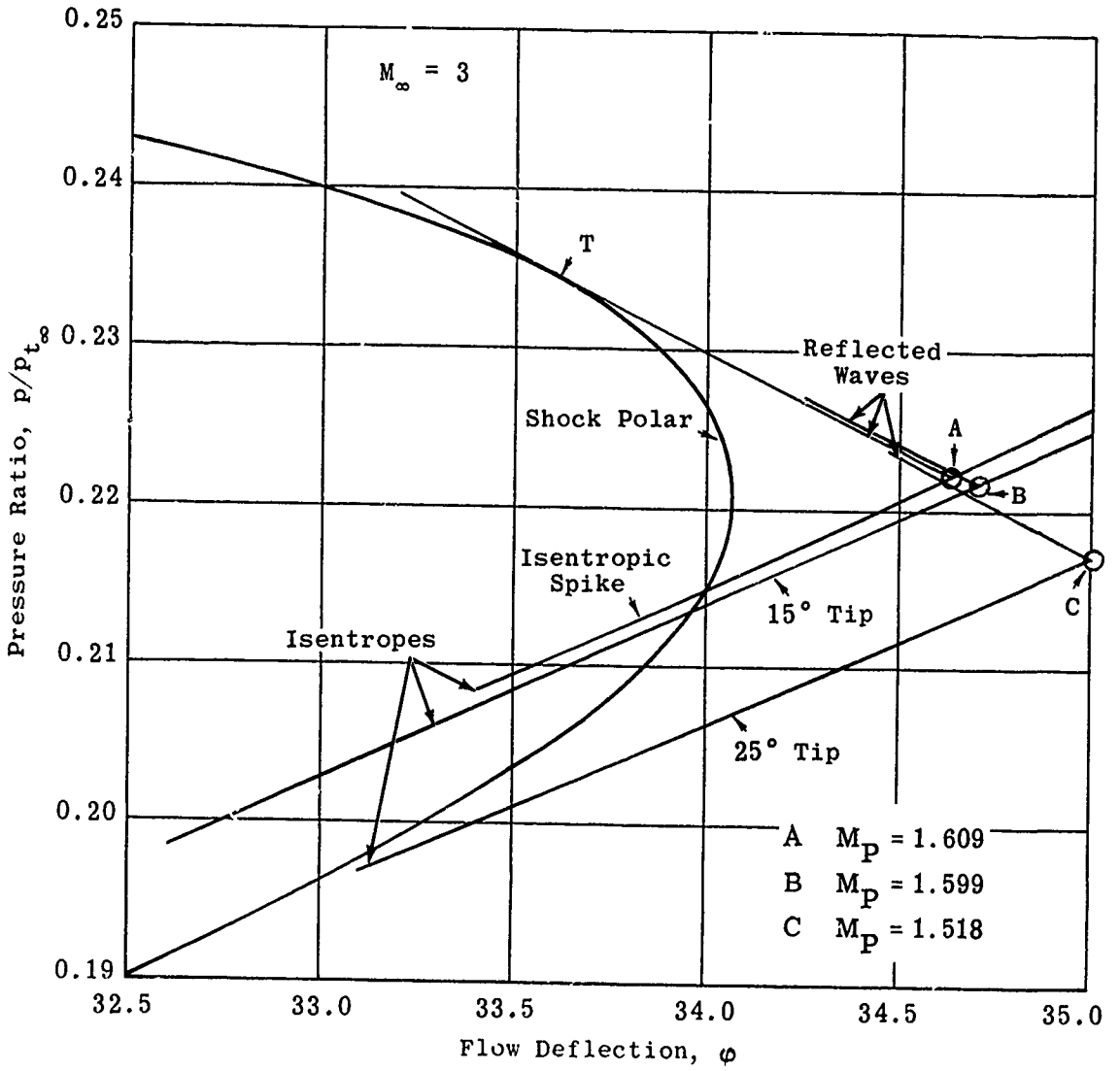

Fig. 3-28a. Critical regions of shock polars showing compressive reflection waves; $M_\infty = 3$; $\gamma = 1.4$.

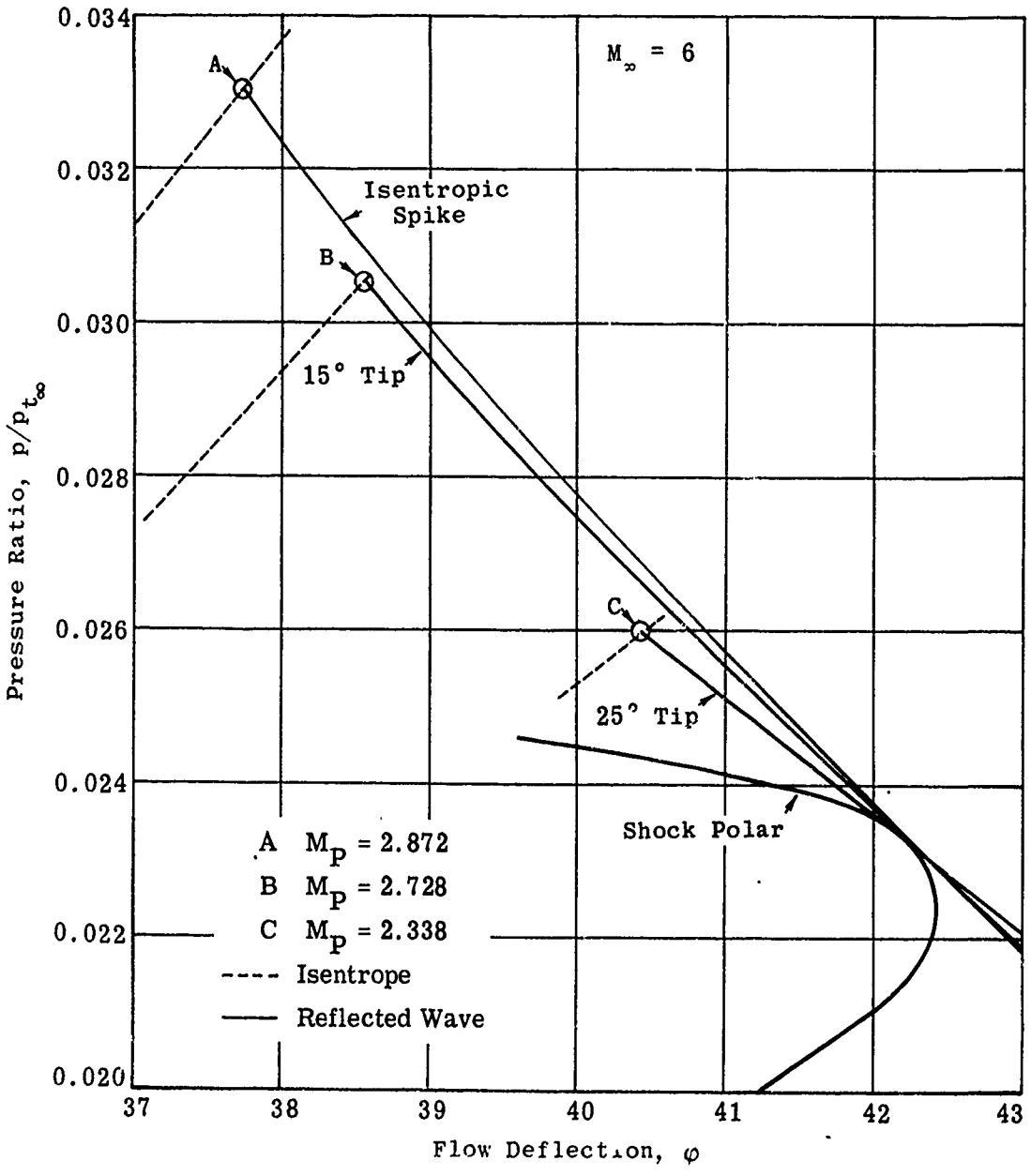

Fig. 3-28b. Critical regions of shock polars showing expansive reflection waves; $M_\infty = 6$; $\gamma = 1.4$.

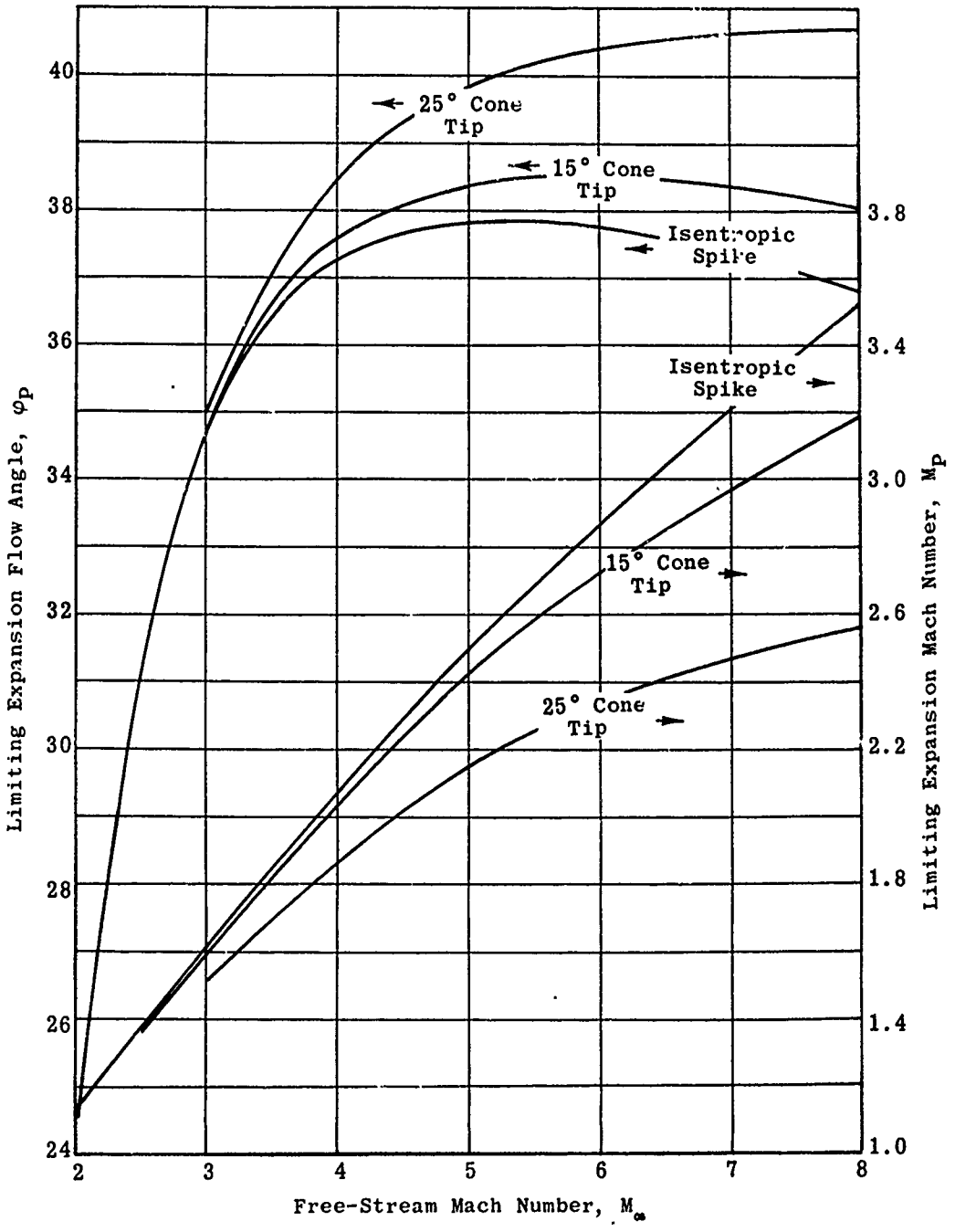

Fig. 3-29. Limits imposed on flow parameters by the vortex-sheet criterion vs free-stream Mach number; isentropic spike, 15 and 25° tip; $\gamma = 1.4$; $2 \leq M_\infty \leq 8$.

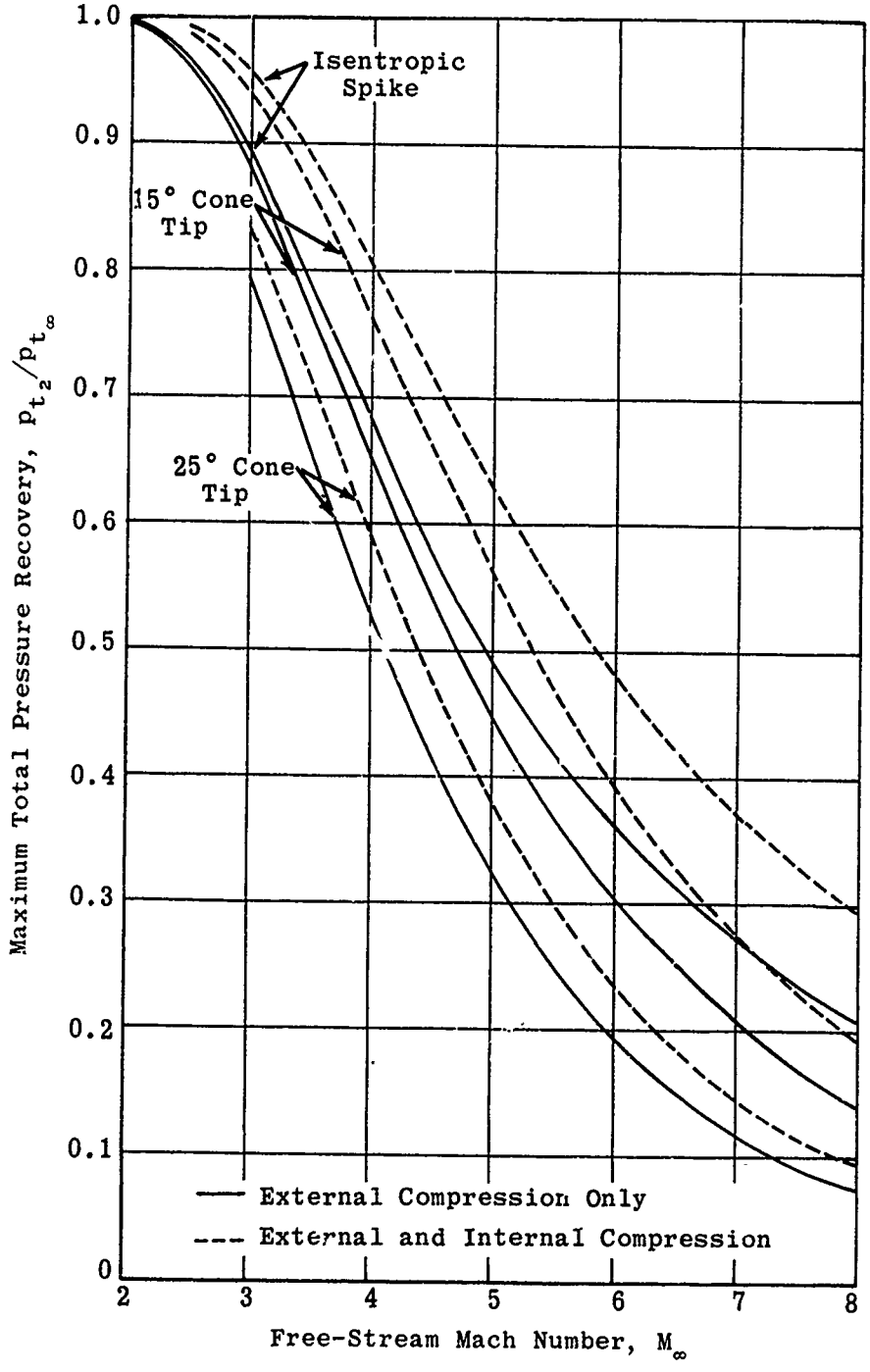

Fig. 3-30. Maximum pressure recovery allowed by vortex-sheet criterion as a function of free-stream Mach number; isentropic spike, 15 and 25° tip; $\gamma = 1.4$; $2 \leq M_\infty \leq 8$.

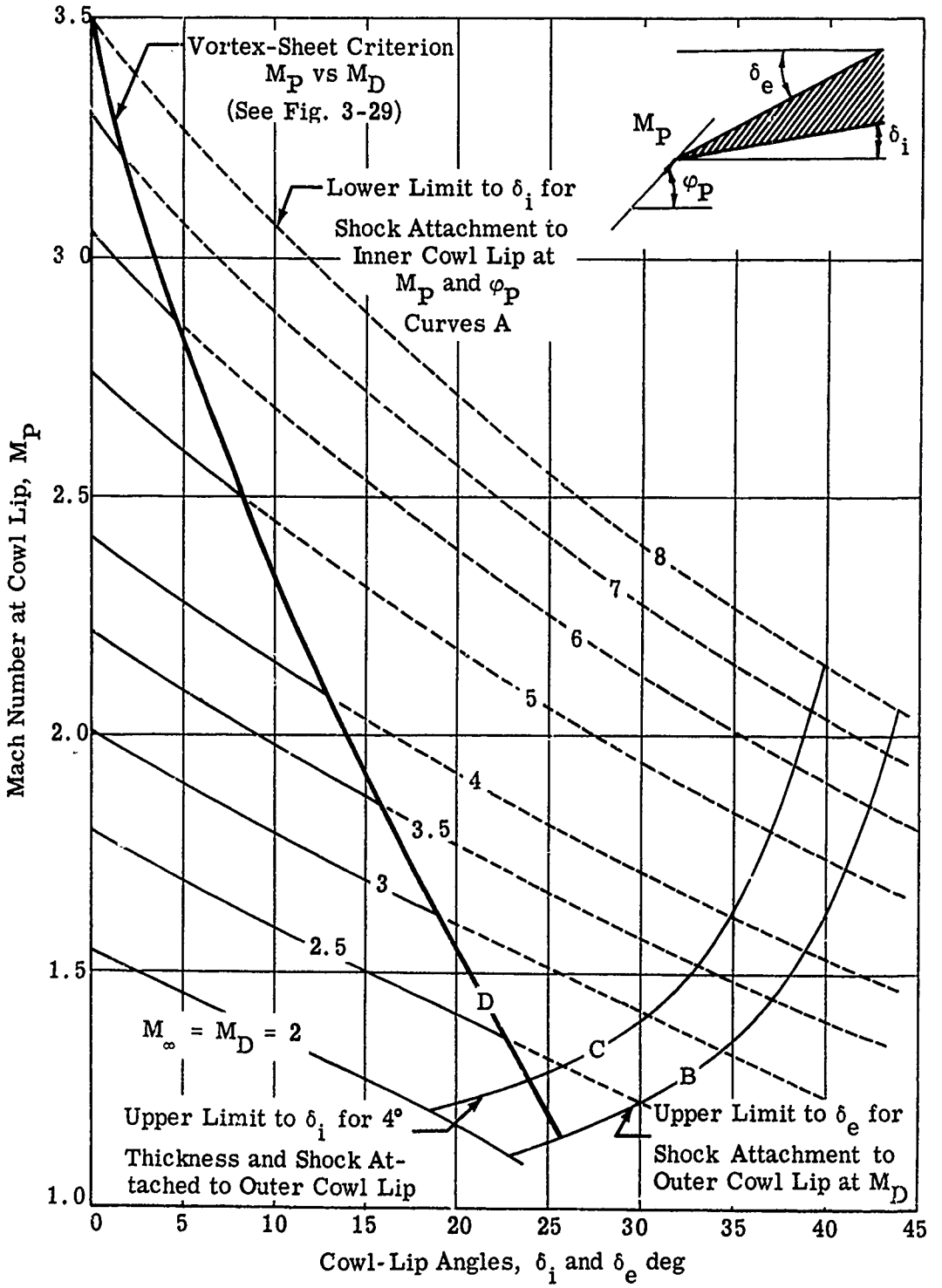

Fig. 3-31a. Critical cowl-lip angles determined by vortex-sheet criterion and shock attachment for various free-stream Mach numbers; isentropic spike; M = 2 to 8; $\gamma = 1.4$.

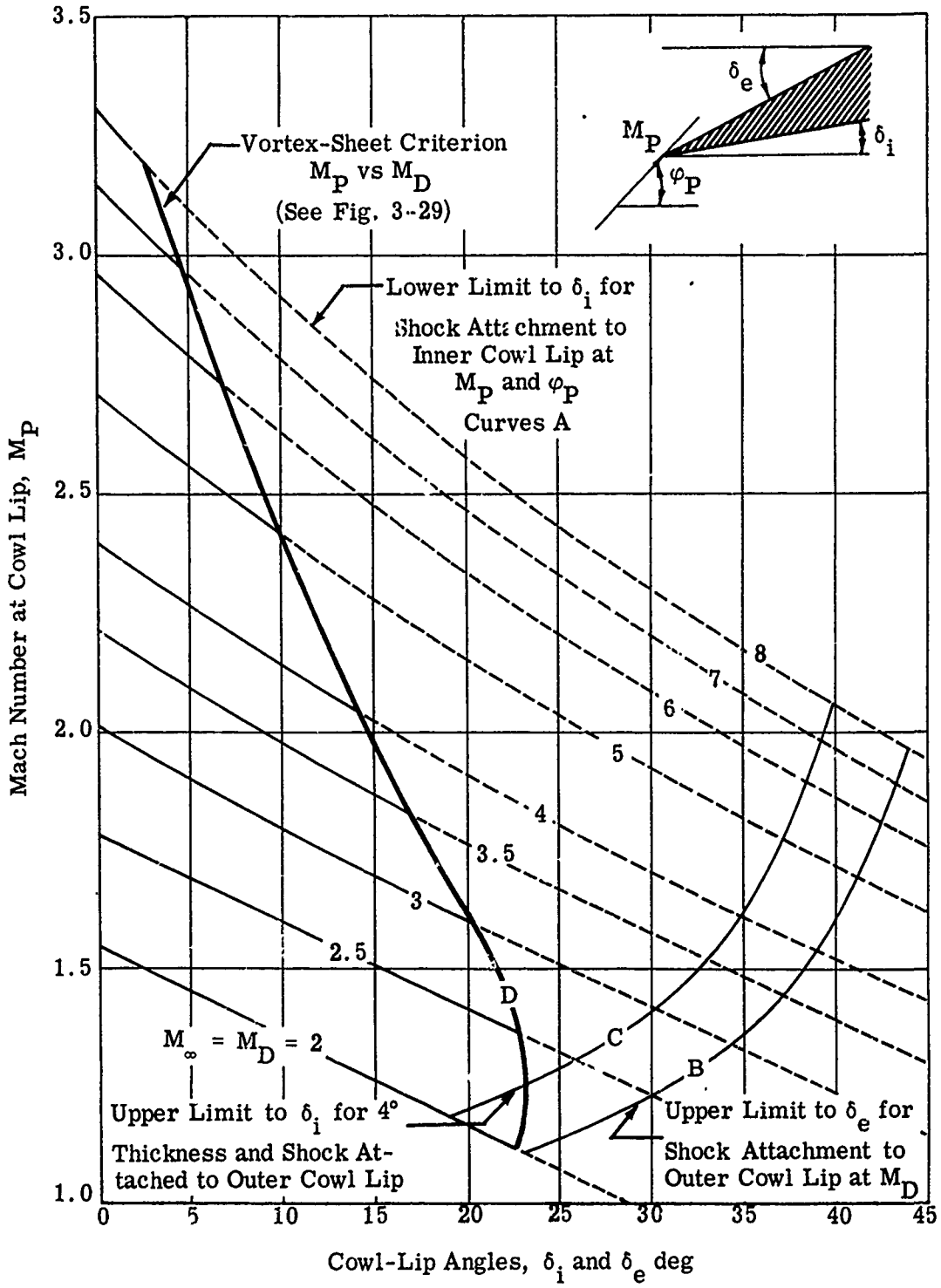

Fig. 3-31b. Critical cowl-lip angles determined by vortex-sheet criterion and shock attachment for various free-stream Mach numbers; 15° cone tip; M_∞ = 2 to 8; γ = 1.4.

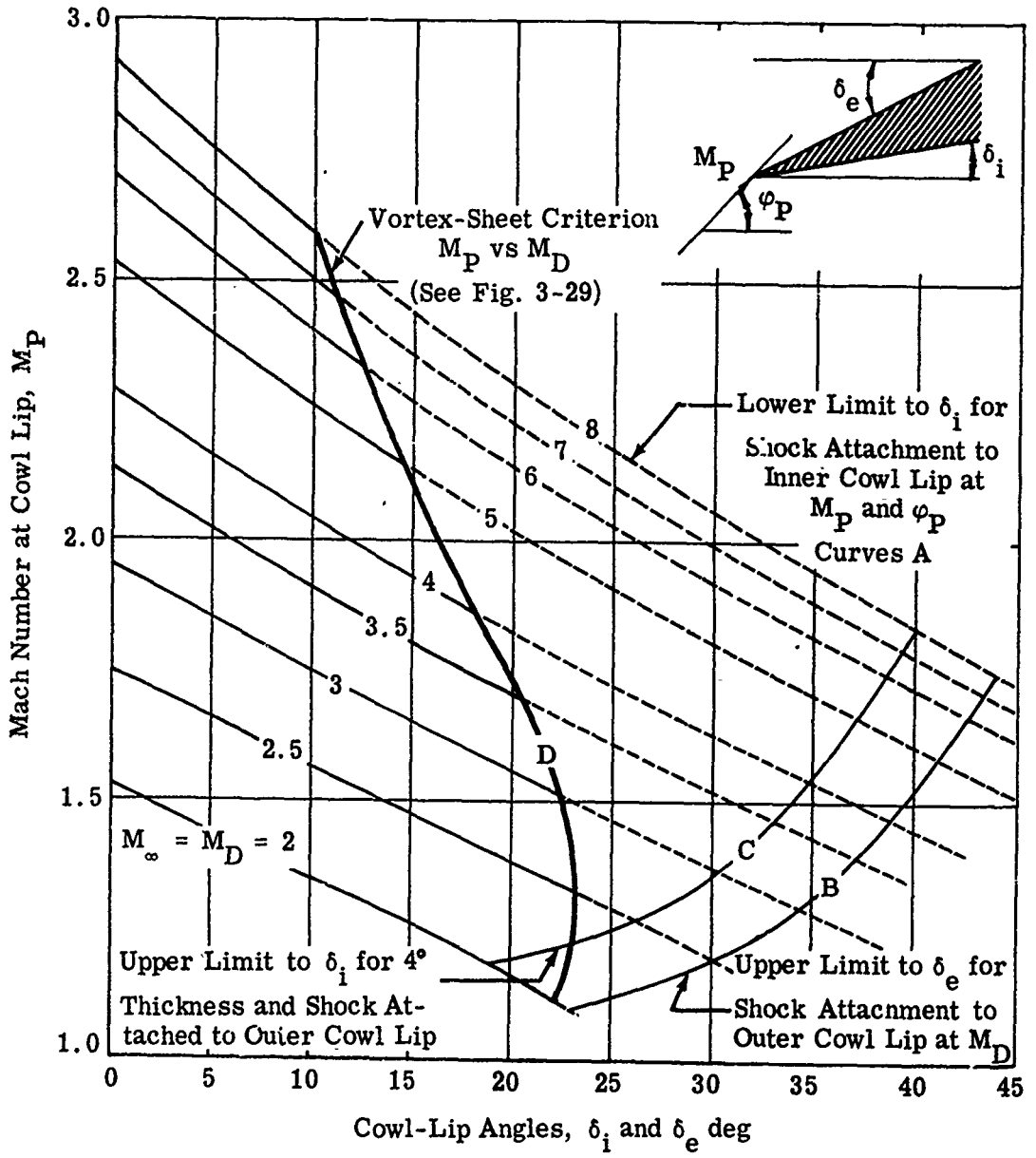

Fig. 3-31c. Critical cowl-lip angles determined by vortex-sheet criterion and shock attachment for various free-stream Mach numbers; 25° cone tip; M = 2 to 8; $\gamma = 1.4$.

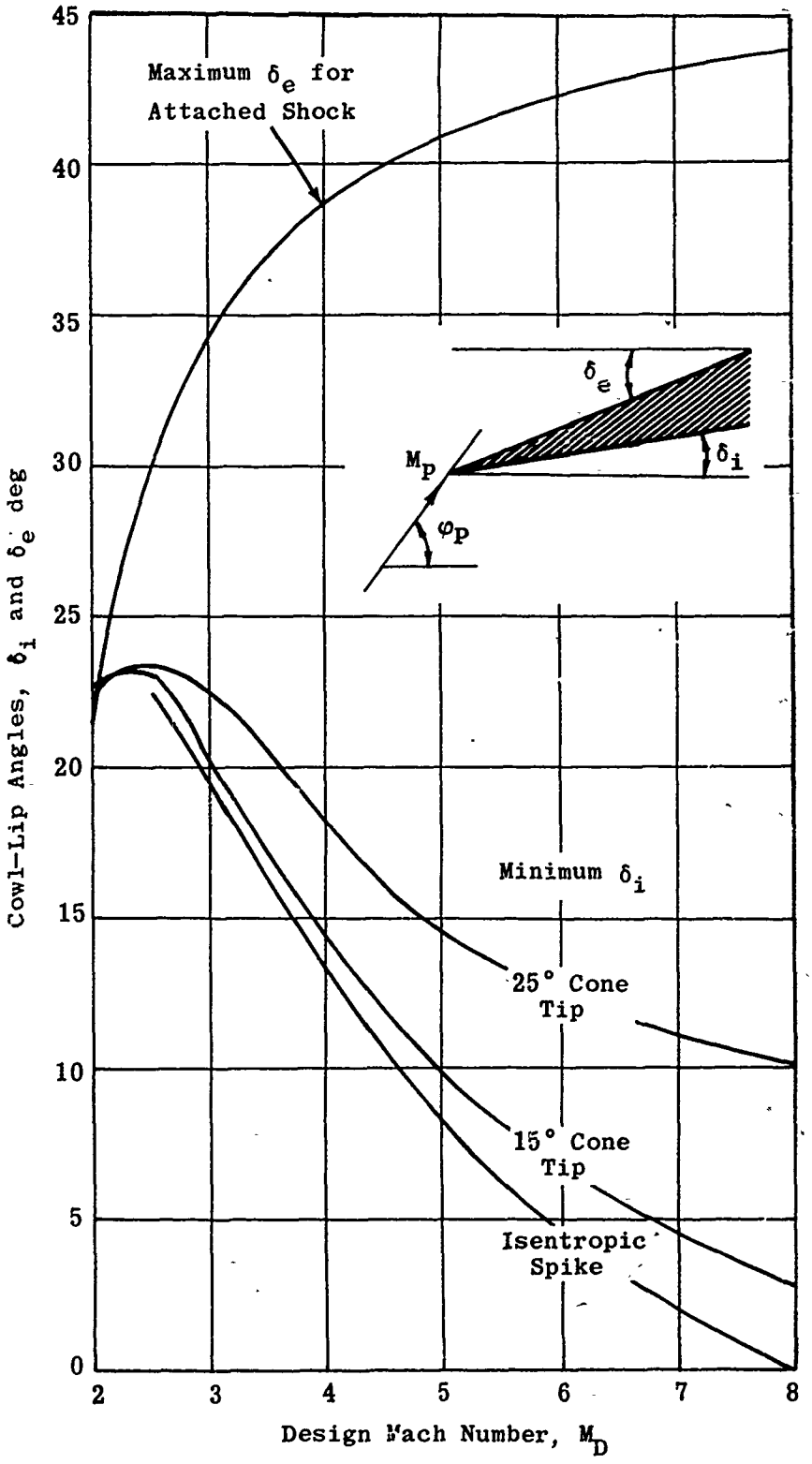

Fig. 3-32. Maximum and minimum cowl-lip angles determined by vortex-sheet and shock-attachment criteria vs design Mach number; isentropic spike, 15 and 25° tip; γ = 1.4

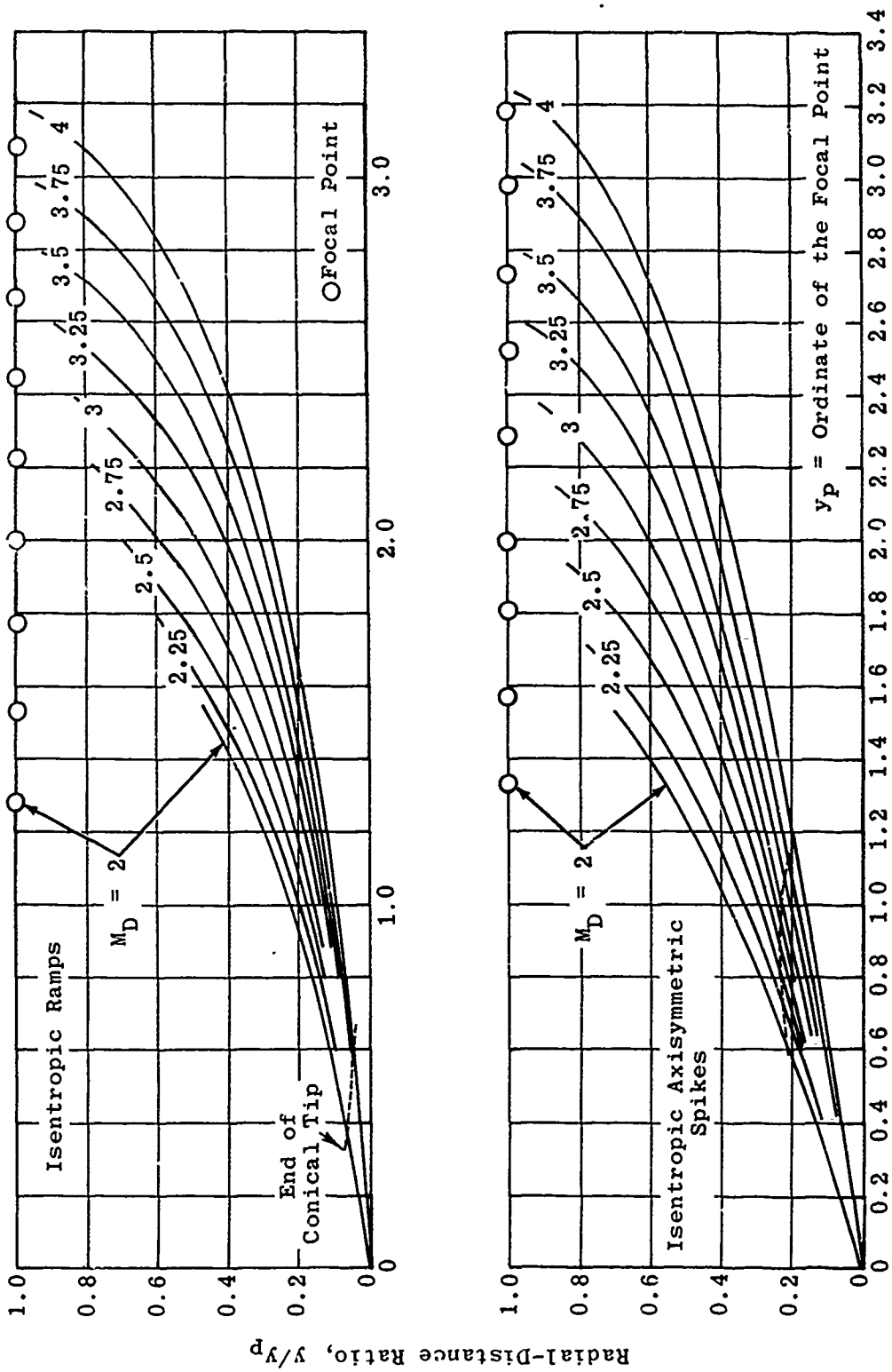

Fig. 3-33. Coordinates of isentropic spikes and ramps with 1% pressure loss due to nose shock; M_D = 2 to 4; γ = 1.4. (Source: Ref. 115)

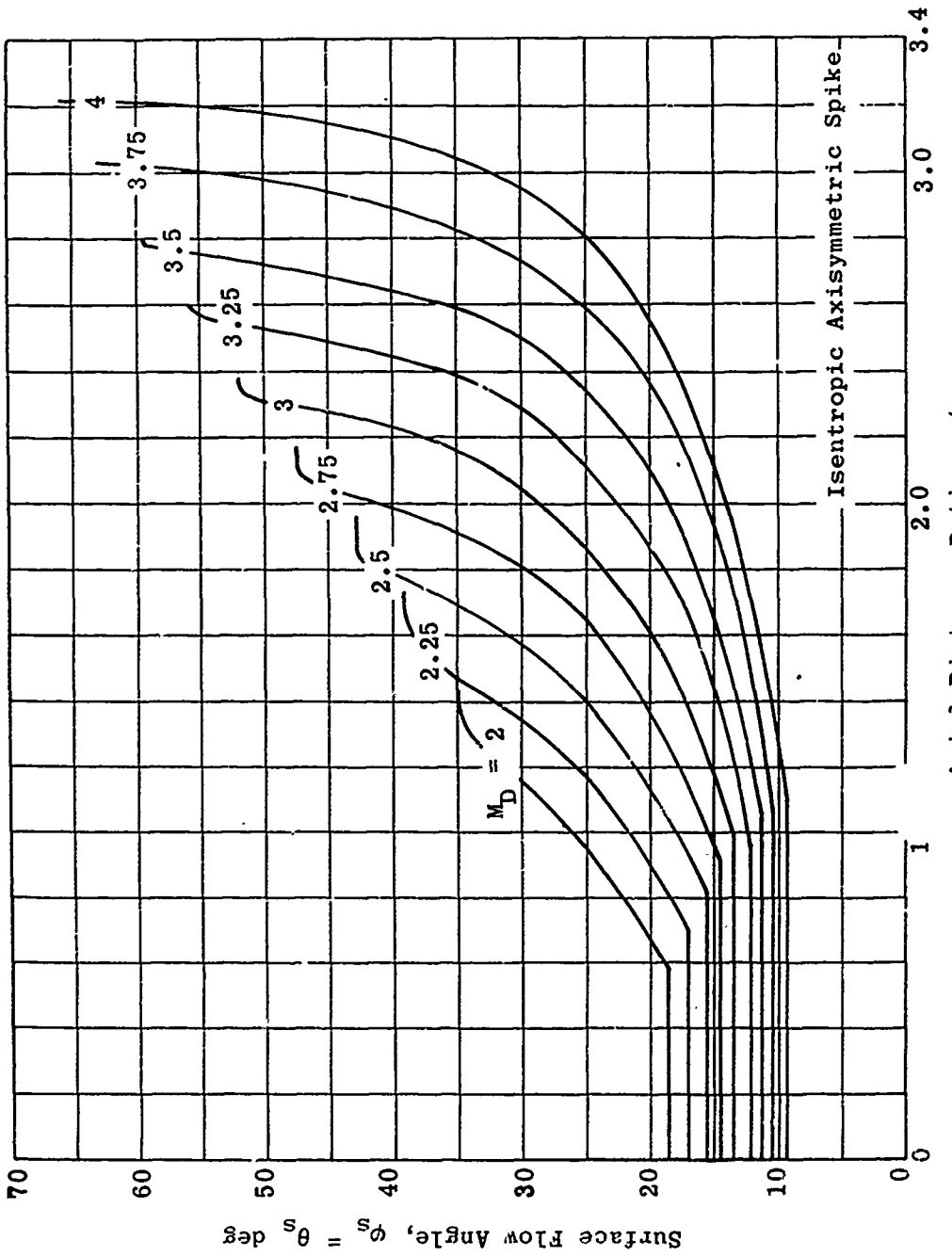

Fig. 3-34a. Surface flow angle vs axial-distance ratio; isentropic axisymmetric spike; M_D = 2 to 4; γ = 1.4. (Source: Ref. 115)

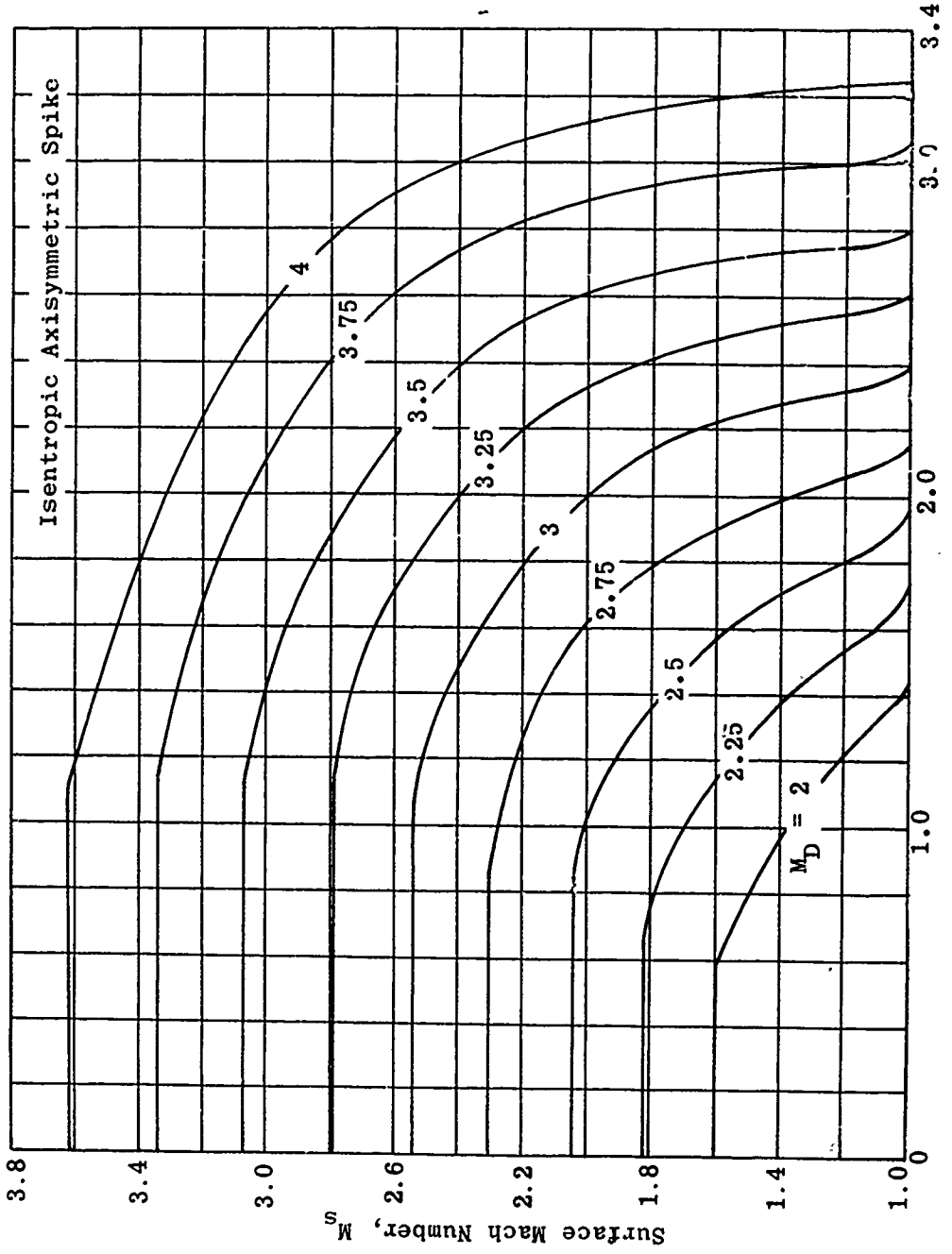

Fig. 3-34b. Surface Mach number vs axial-distance ratio; isentropic axisymmetric spike; M_D = 2 to 4; γ = 1.4. (Source: Ref. 11[illegible]

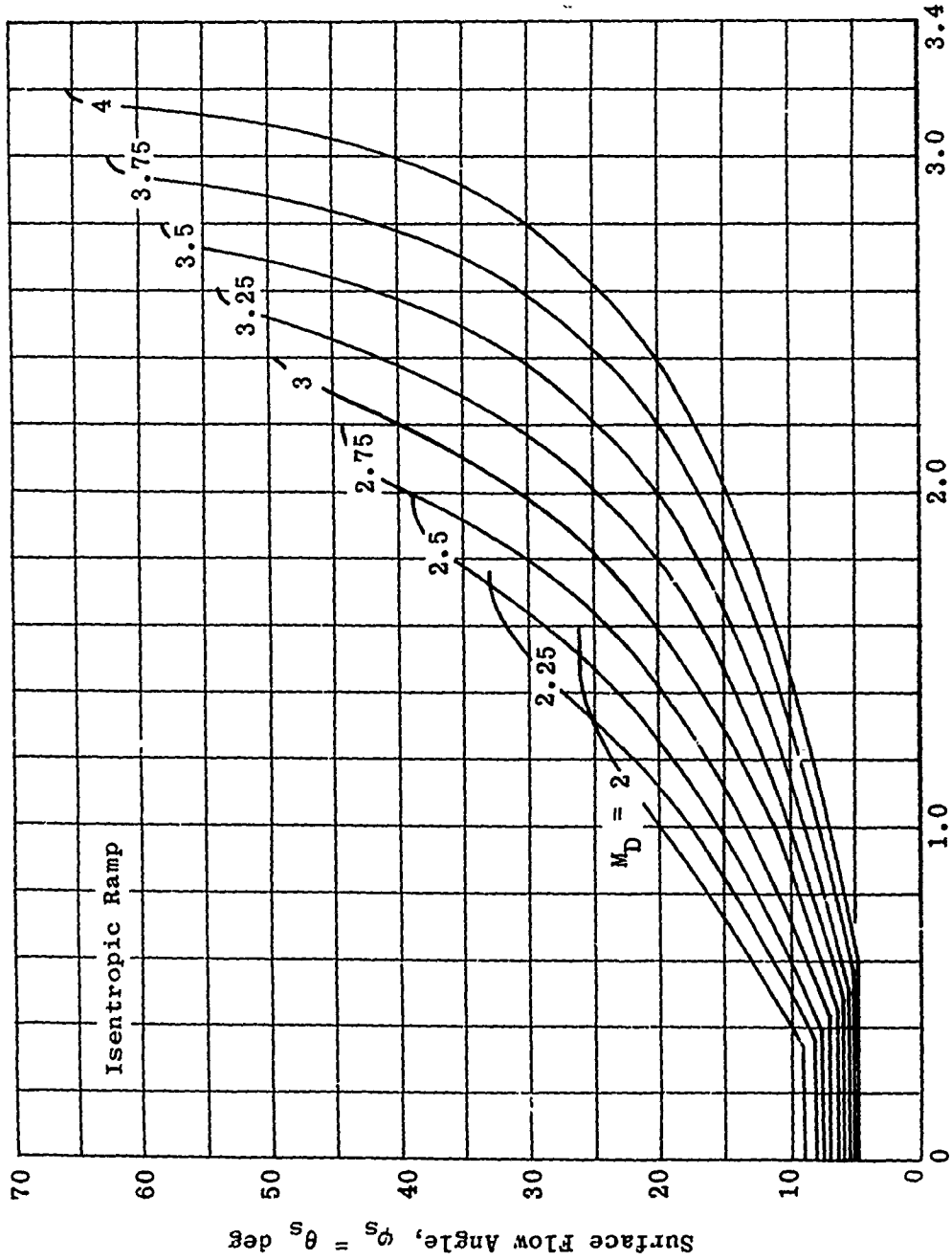

Fig. 3-35a. Surface flow angle vs axial-distance ratio; isentropic ramp; M_D = 2 to 4; γ = 1.4 (Source: Ref. 115)

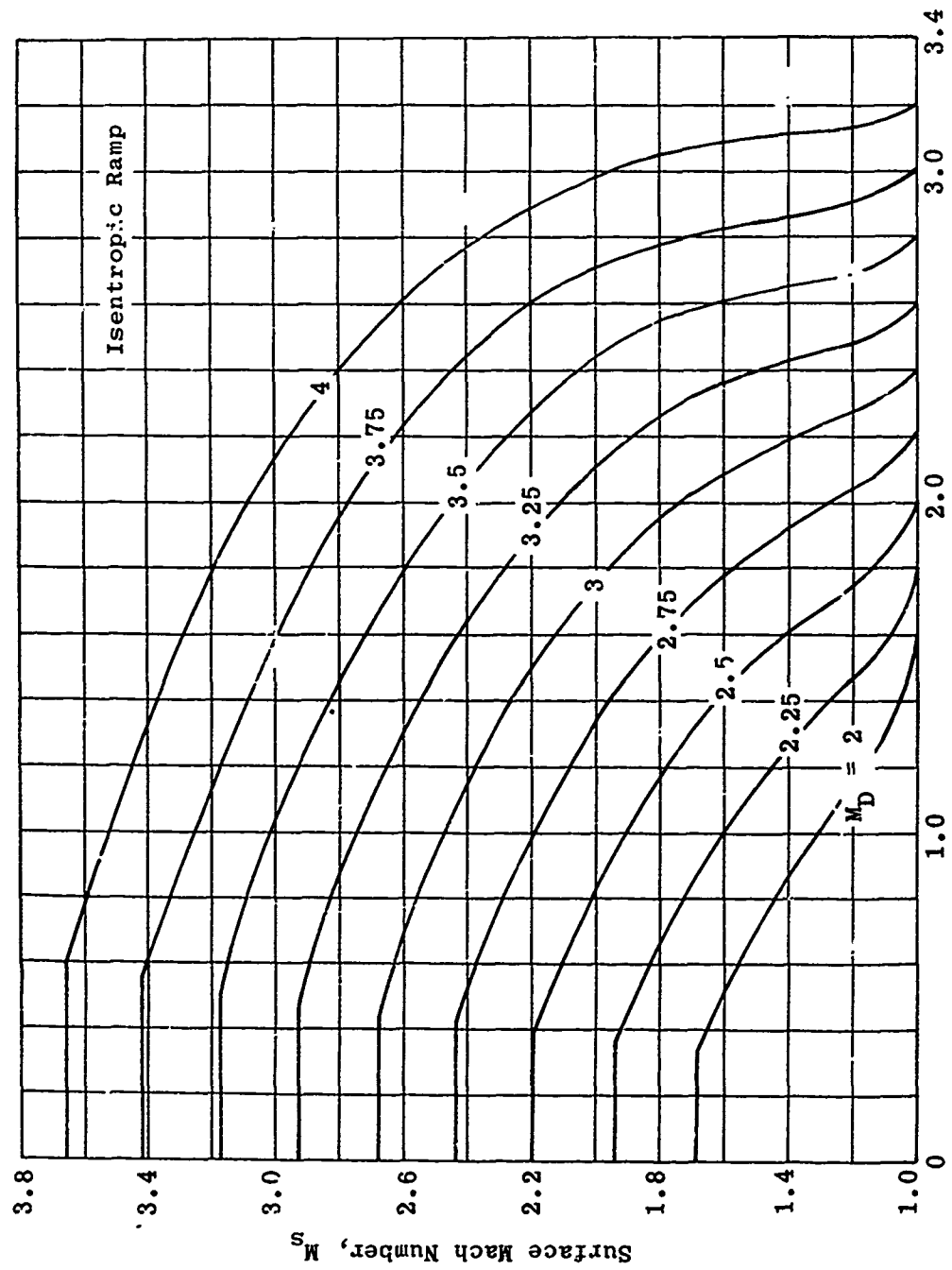

Fig. 3-35b. Surface Mach number vs axial-distance ratio; isentropic ramp; M_D = 2 to 4; γ = 1.4. (Source: Ref. 115)

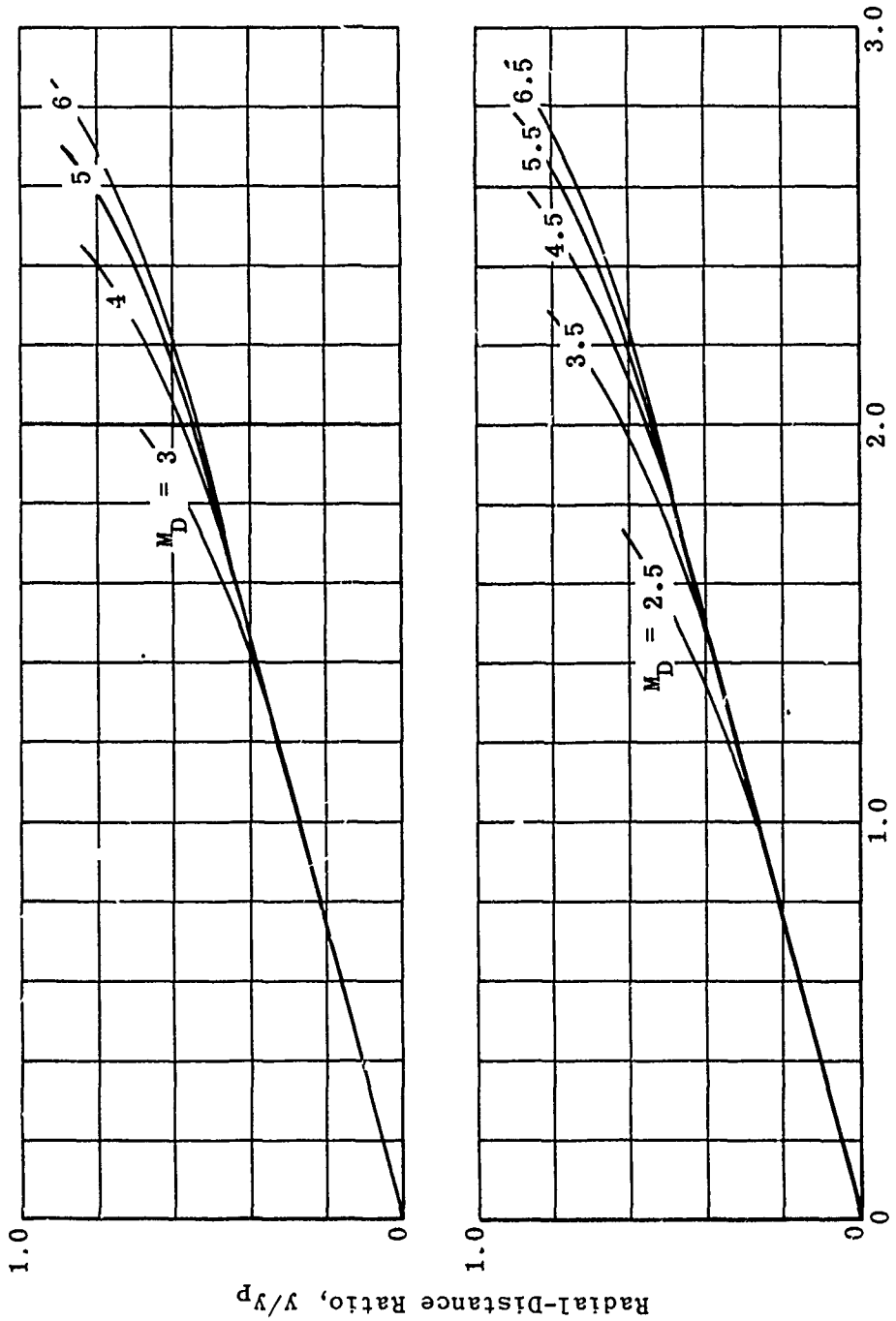

Fig. 3-36. Coordinates of 15° tip isentropic spike; M_D = 2.5 to 6.5; γ = 1.4.

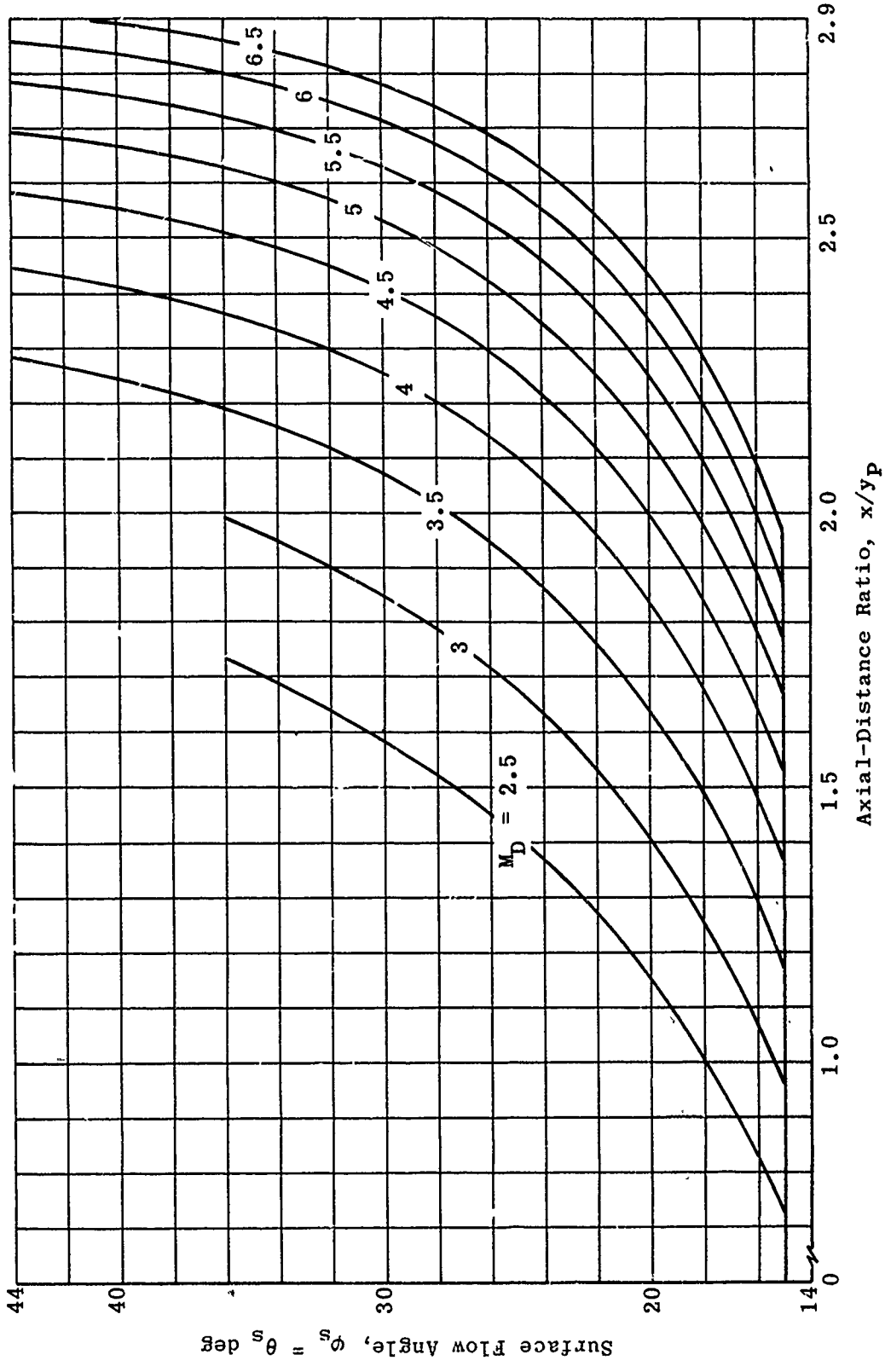

Fig. 3-37a. Surface flow angle vs axial-distance ratio; 15° tip isentropic spike; M_D = 2.5 to 6.5; γ = 1.4.

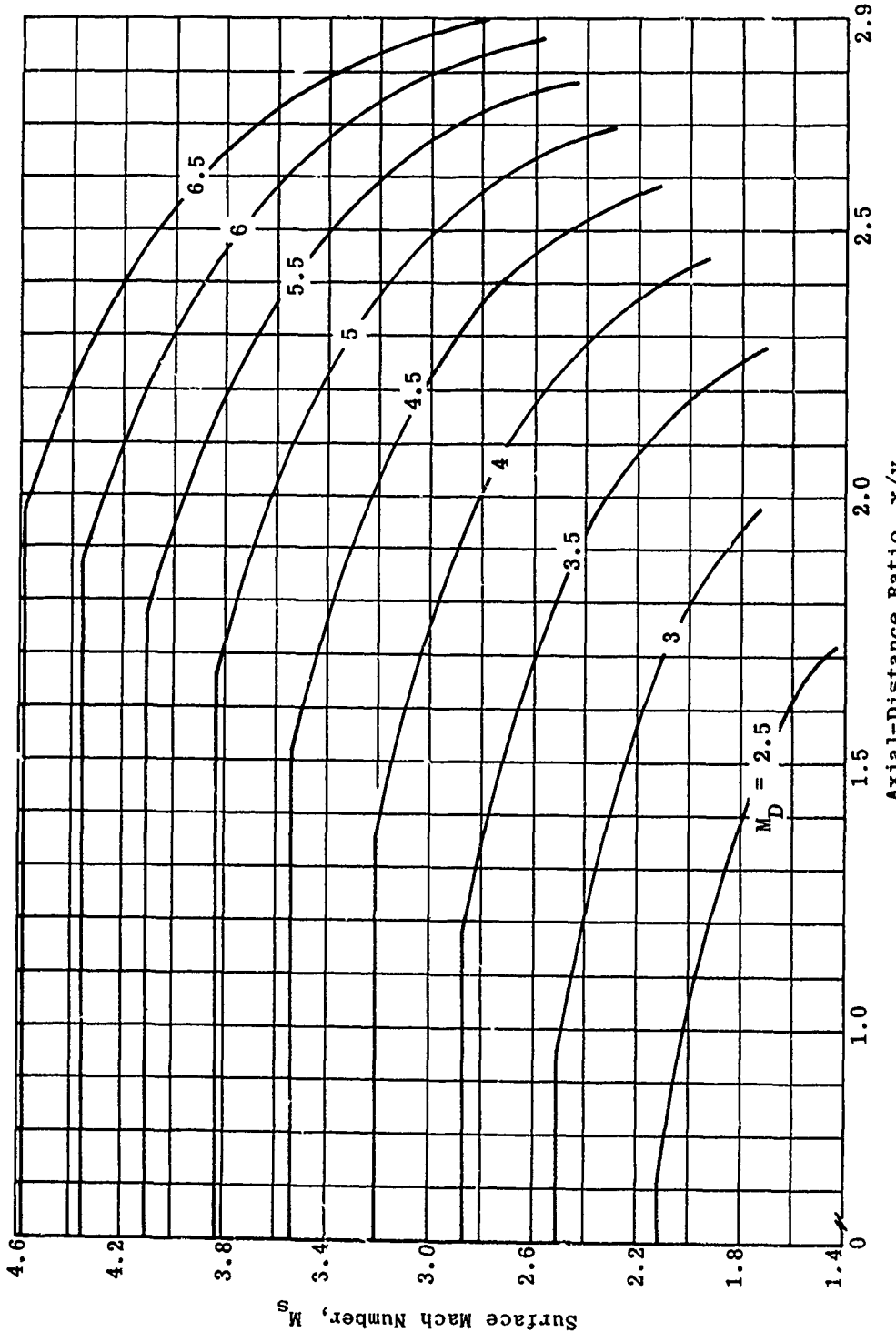

Fig. 3-37b. Surface Mach number vs axial-distance ratio; 15° tip isentropic spike; M_D = 2.5 to 6.5; γ = 1.4.

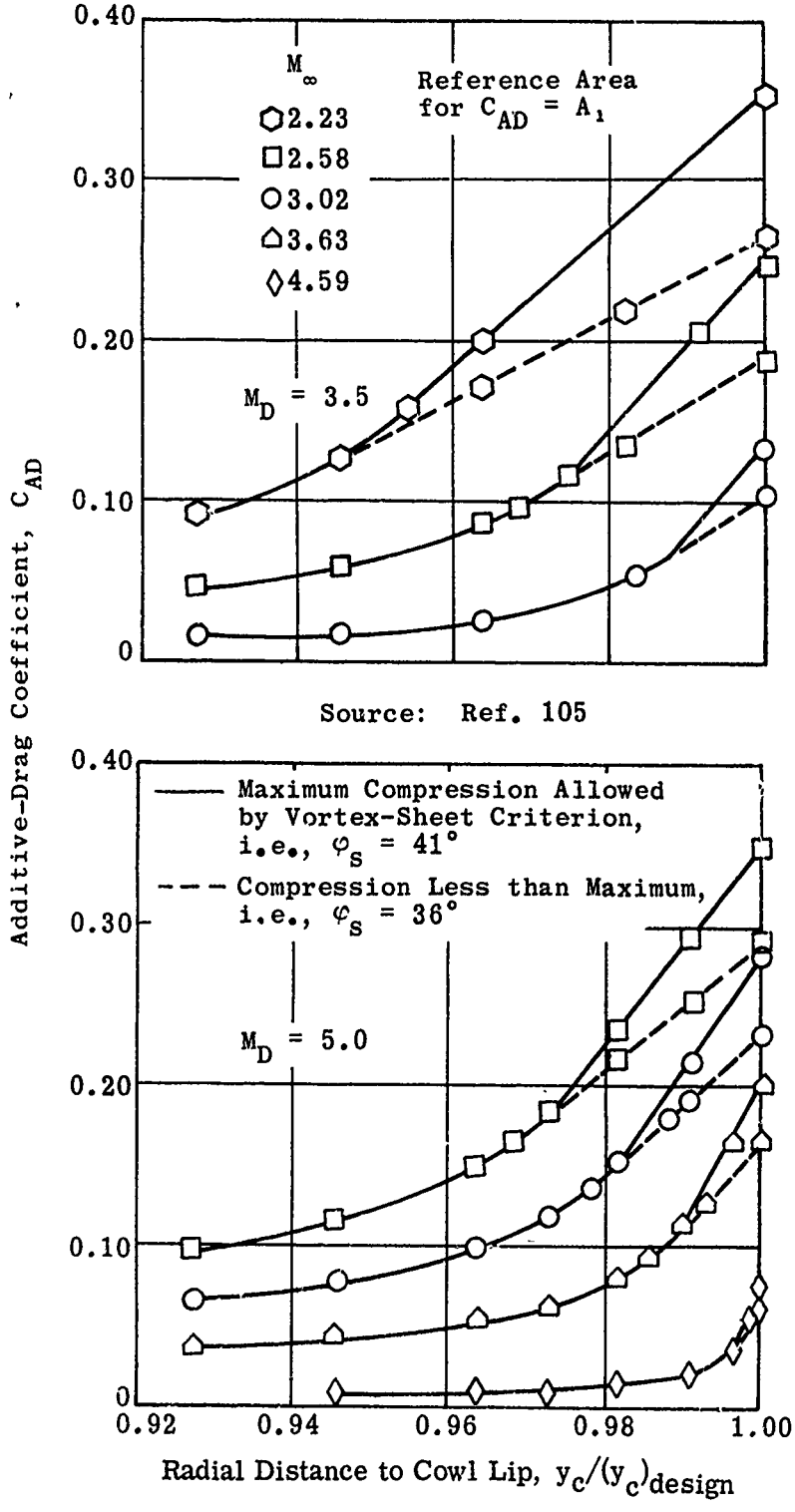

Fig. 3-38. Calculated additive-drag coefficient at off-design Mach numbers; cowl lip on design conical shock; $M_D = 3.5$ and 5.0; $2.23 \leq M_\infty \leq 4.59$; 15° tip isentropic spikes.

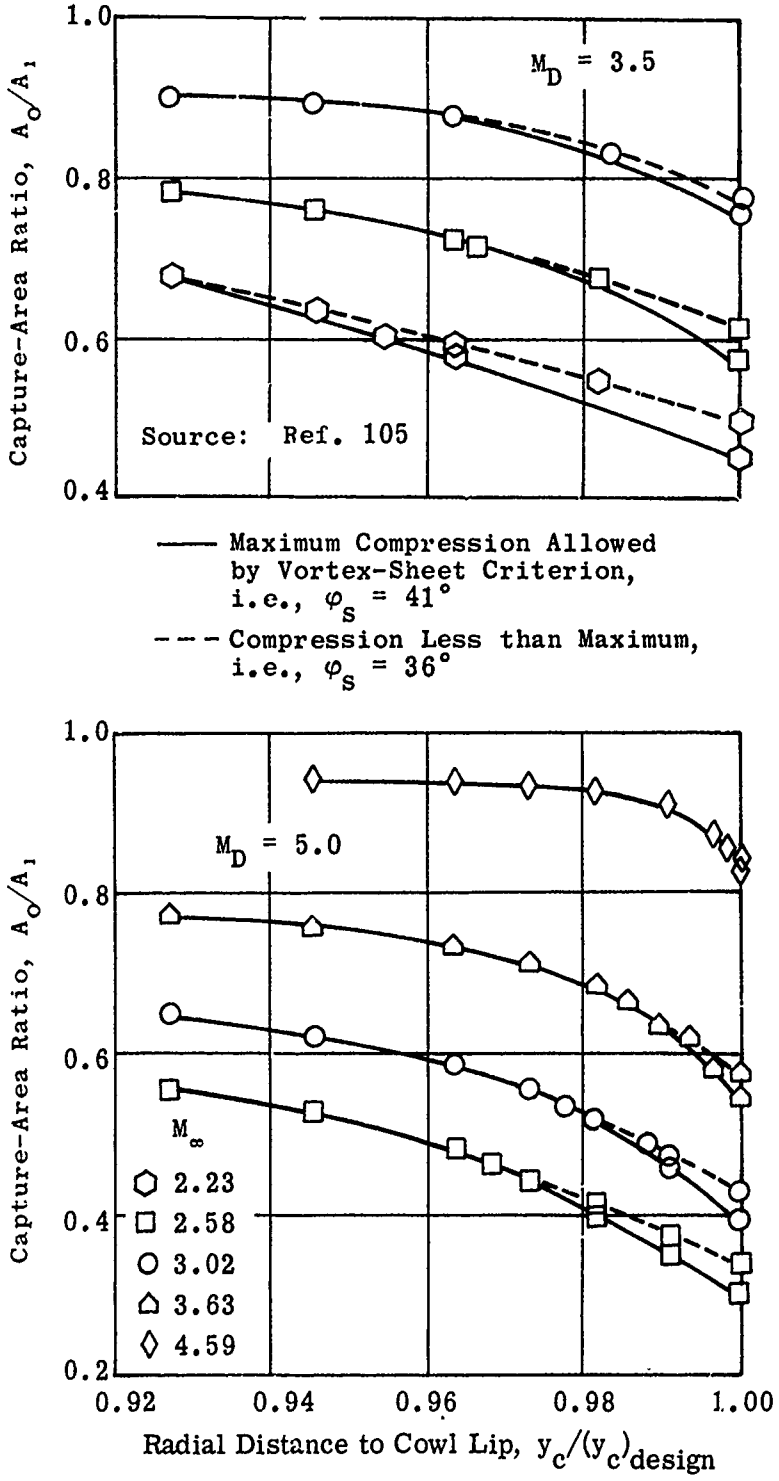

Fig. 3-39. Calculated capture-area ratio at off-design Mach numbers; cowl lip on design conical shock; 15° tip isentropic spikes; M_D = 3.5 and 5.0; 2.23 ≤ M_∞ ≤ 4.59.

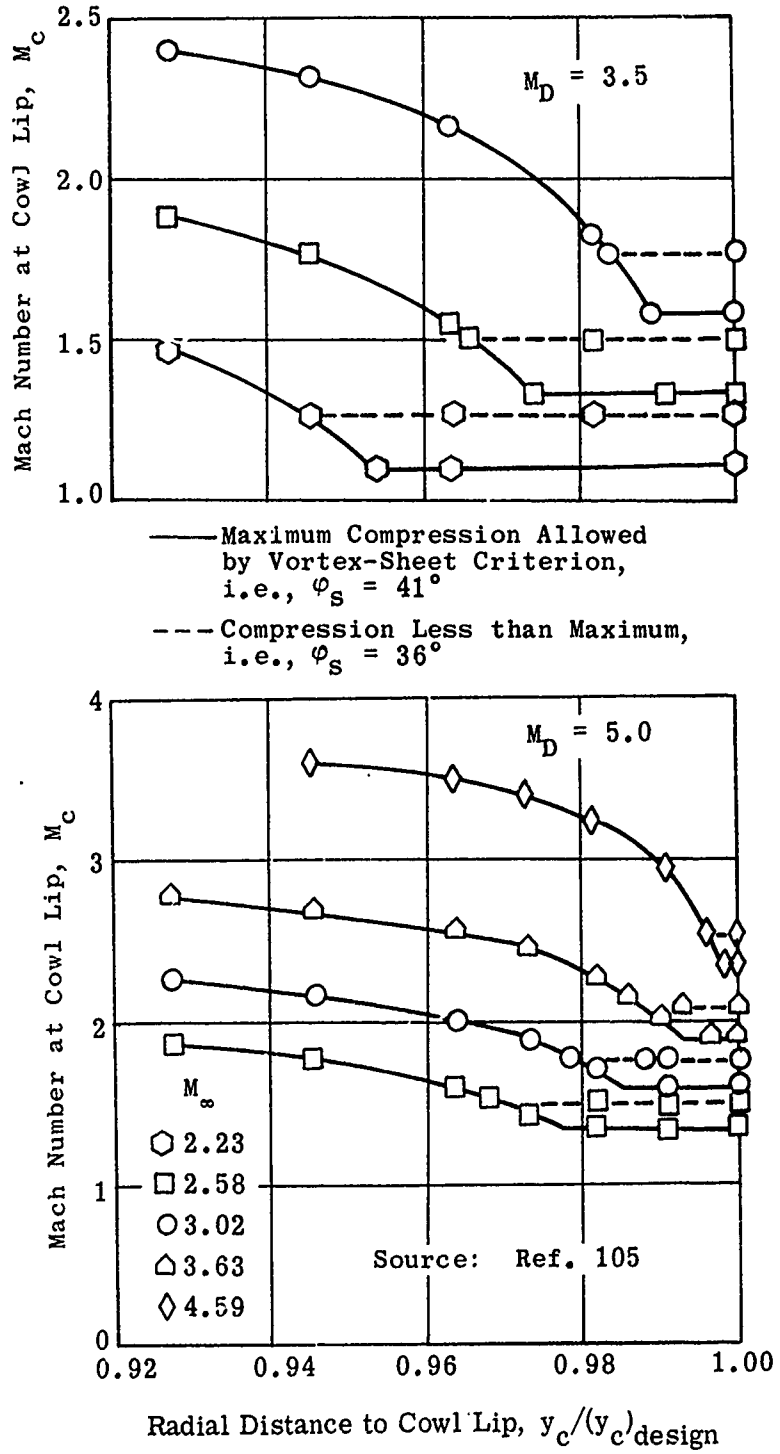

Fig. 3-40. Calculated Mach number at cowl lip at off-design Mach numbers; cowl lip on design conical shock; 15° tip isentropic spikes; M_D = 3.5 and 5.0; 2.23 ≤ M_∞ ≤ 4.59.

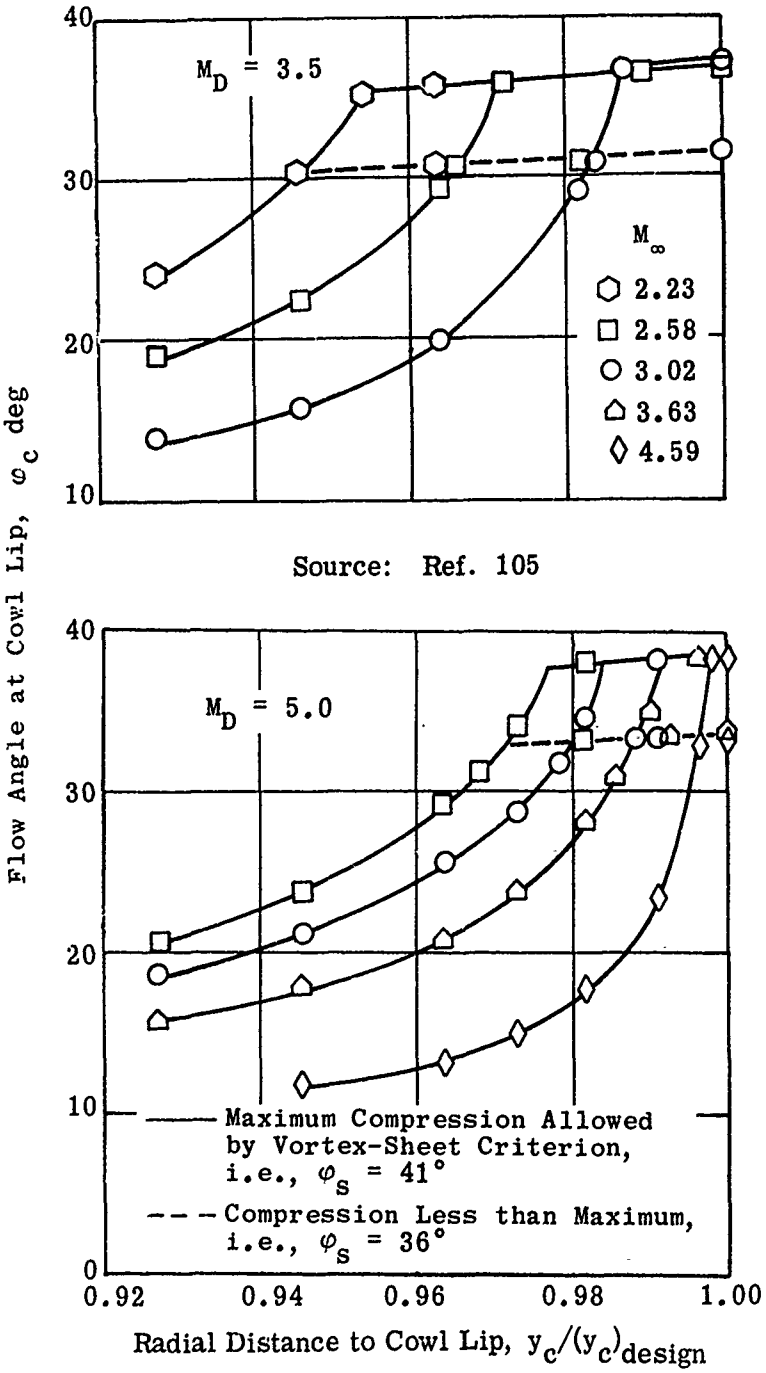

Fig. 3-41. Calculated flow angle at cowl lip at off-design Mach numbers; cowl lip on design conical shock; 15° tip isentropic spikes; M_D = 3.5 and 5.0; 2.23 ≤ M_∞ ≤ 4.59.

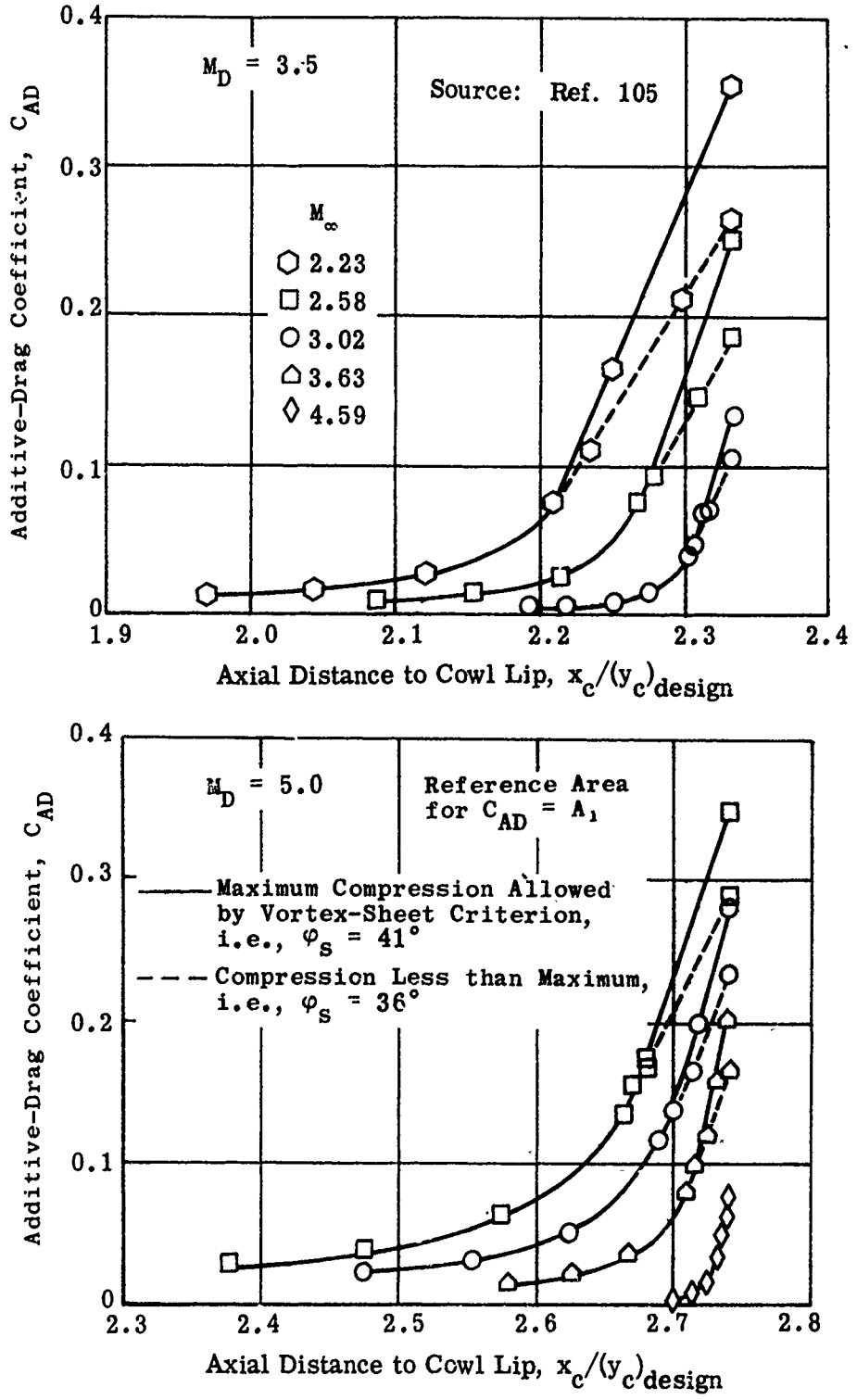

Fig. 3-42. Calculated additive-drag coefficient at off-design Mach numbers; cowl lip at constant radial distance; 15° tip isentropic spikes; M_D = 3.5 and 5.0; 2.23 ≤ M_∞ ≤ 4.59.

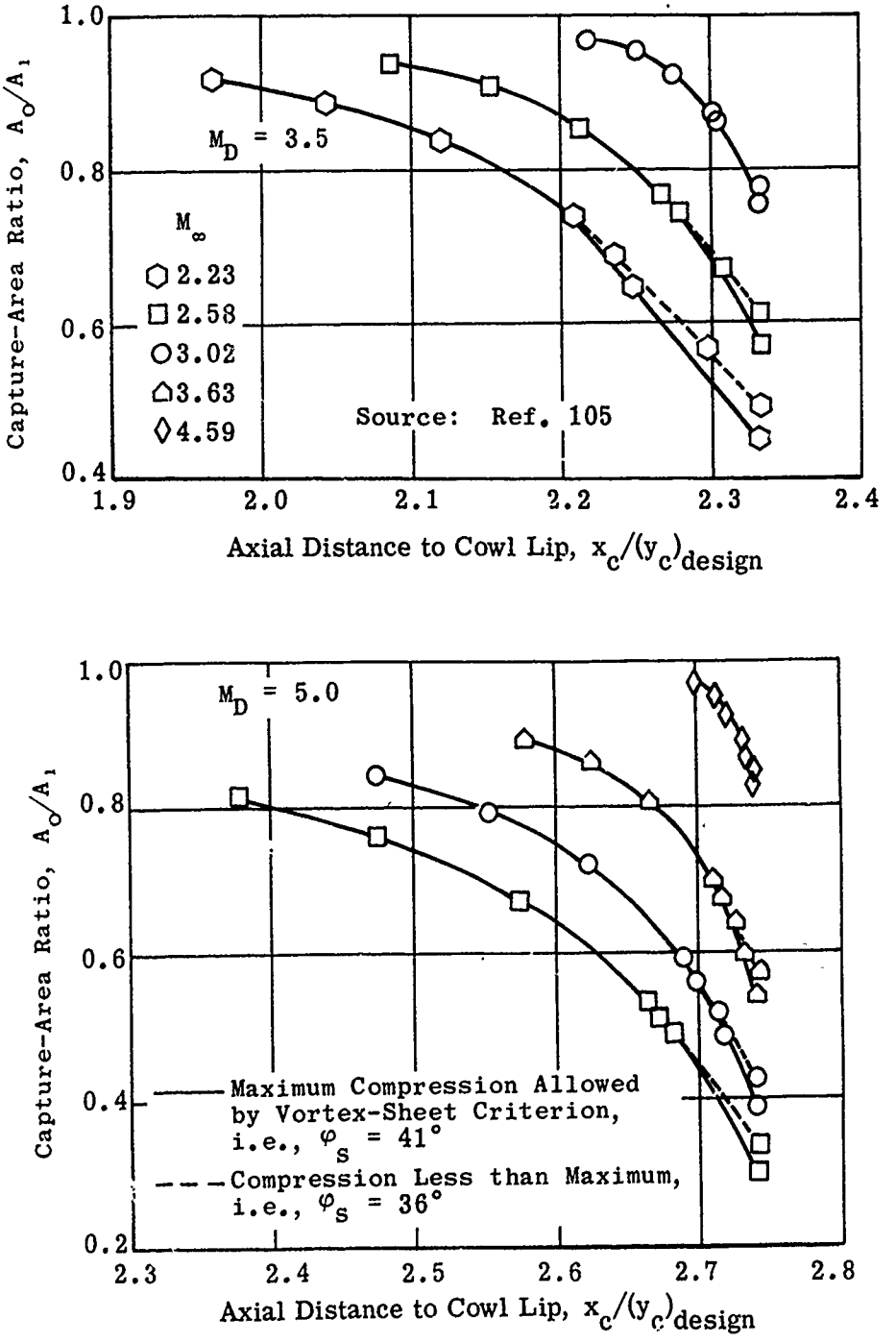

Fig. 3-43. Calculated capture-area ratio at off-design Mach numbers; cowl lip at constant radial distance; 15° tip isentropic spikes; M_D = 3.5 and 5.0; 2.23 ≤ M_∞ ≤ 4.59.

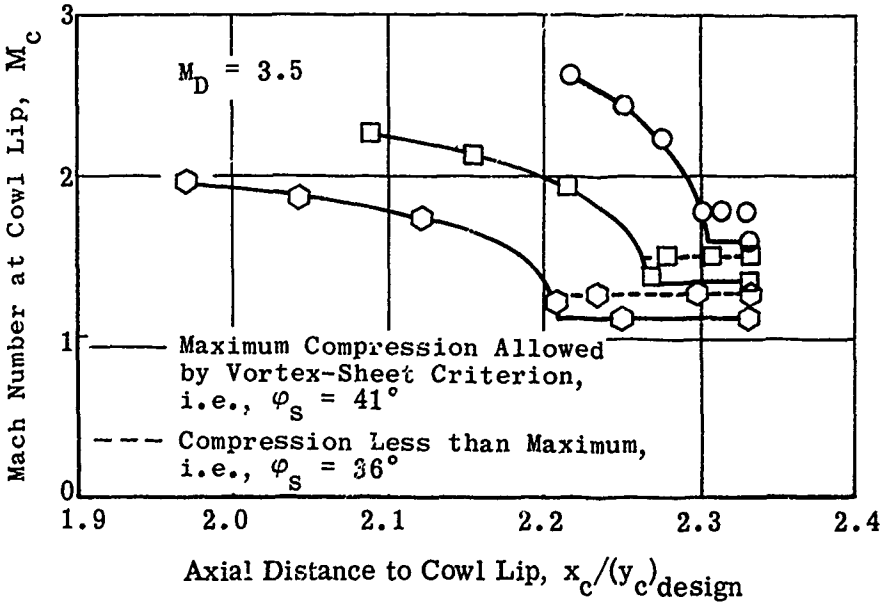

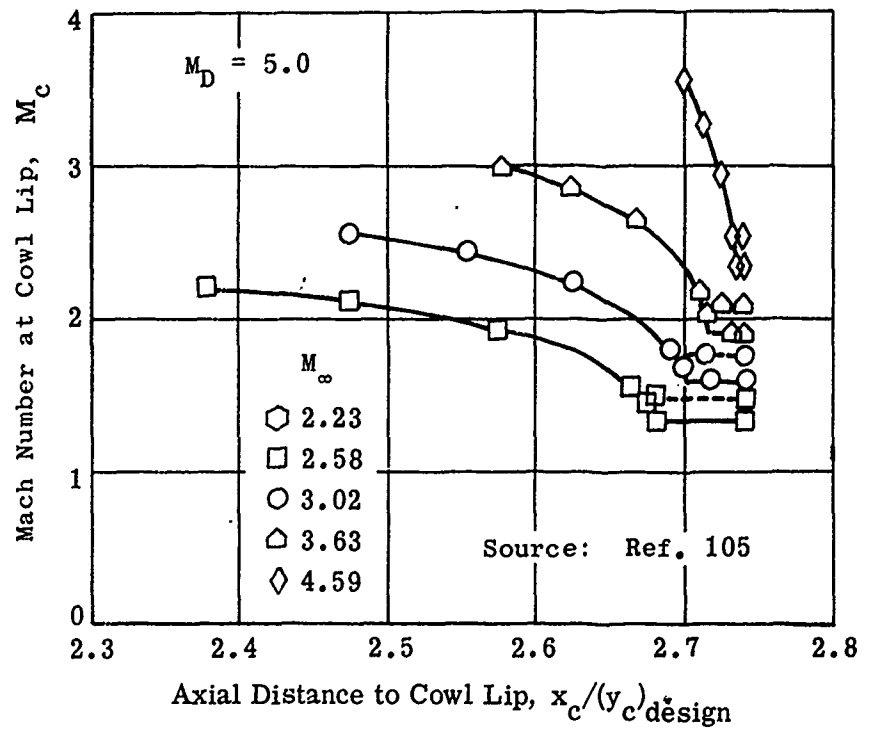

Fig. 3-44. Calculated Mach number at cowl lip at off-design Mach numbers; cowl lip at constant radial distance; 15° tip isentropic spikes; M_D = 3.5 and 5.0; $2.23 \leq M_\infty \leq 4.59$.

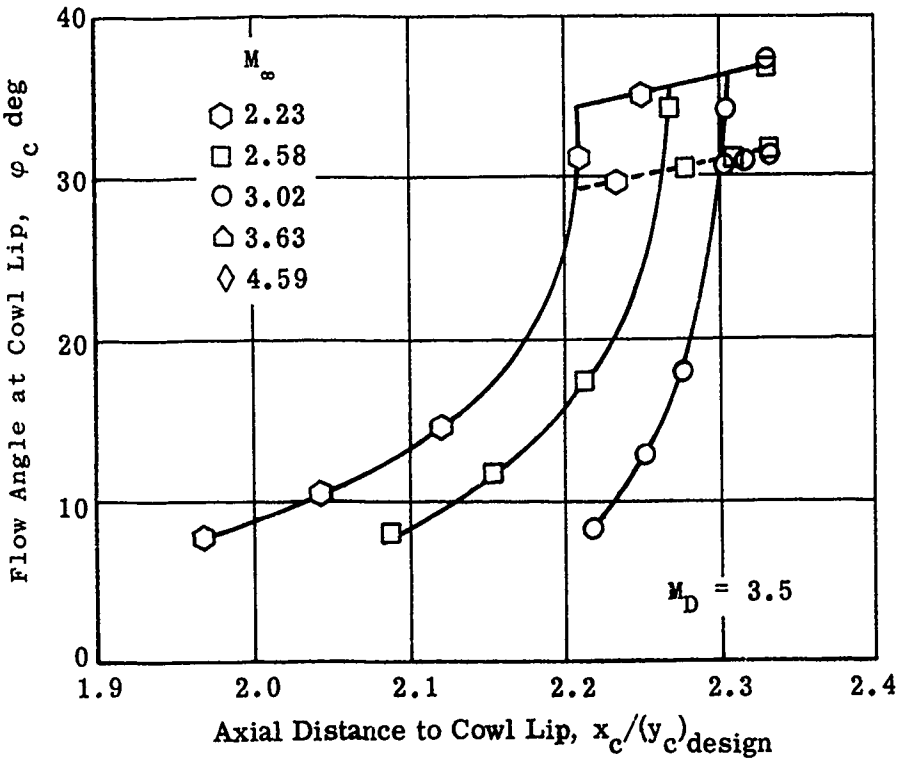

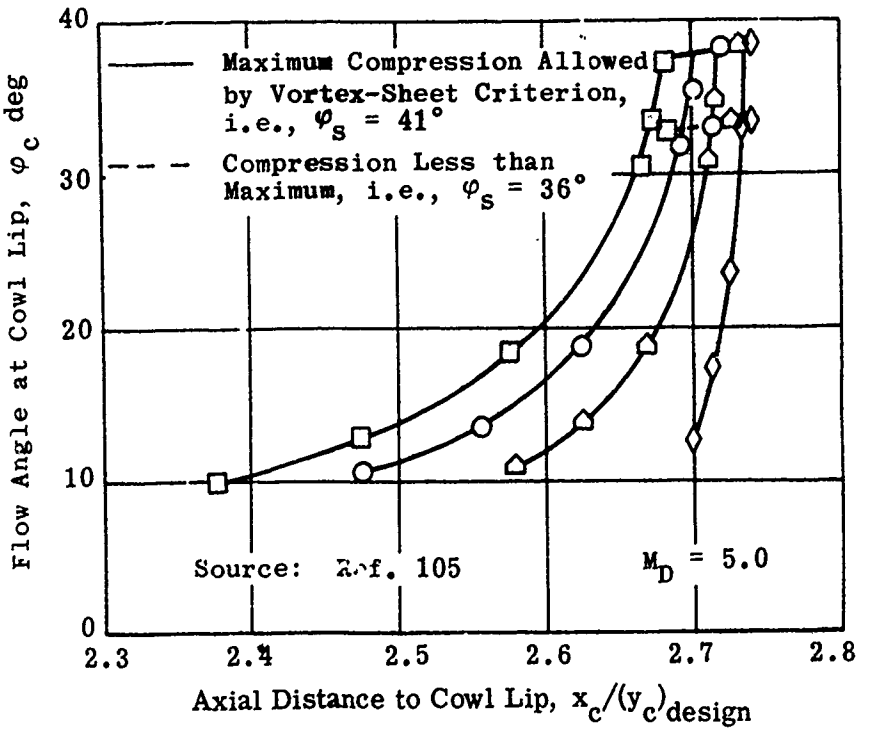

Fig. 3-45. Calculated flow angle at cowl lip at off-design Mach numbers; cowl lip at constant radial distance; 15° tip isentropic spikes; M_D = 3.5 and 5.0; 2.23 ≤ M_∞ ≤ 4.59.

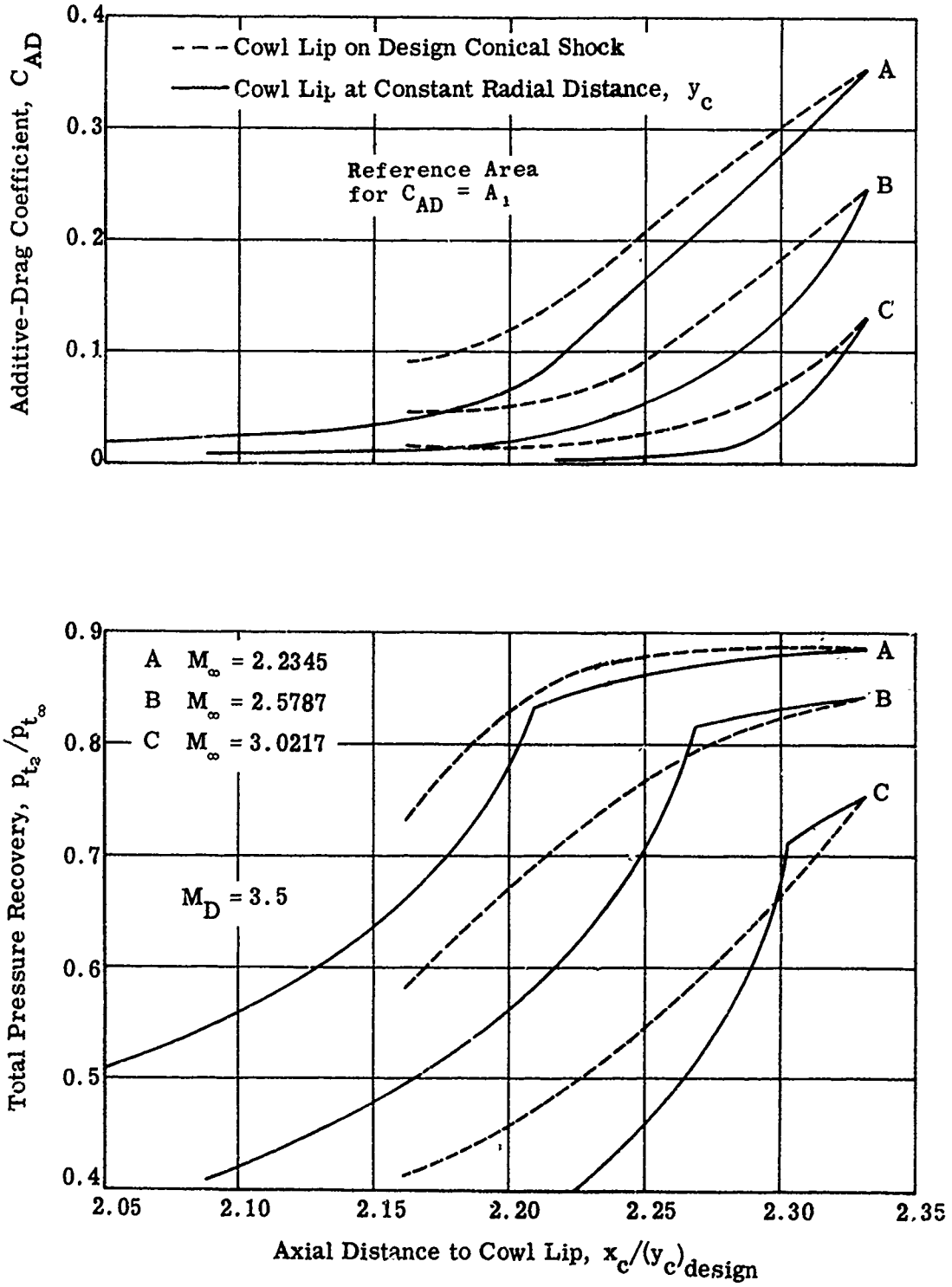

Fig. 3-46. Calculated total pressure recovery and associated additive-drag coefficient at off-design Mach numbers; $M_D = 3.5$, 15° tip isentropic spikes, $\gamma = 1.4$.

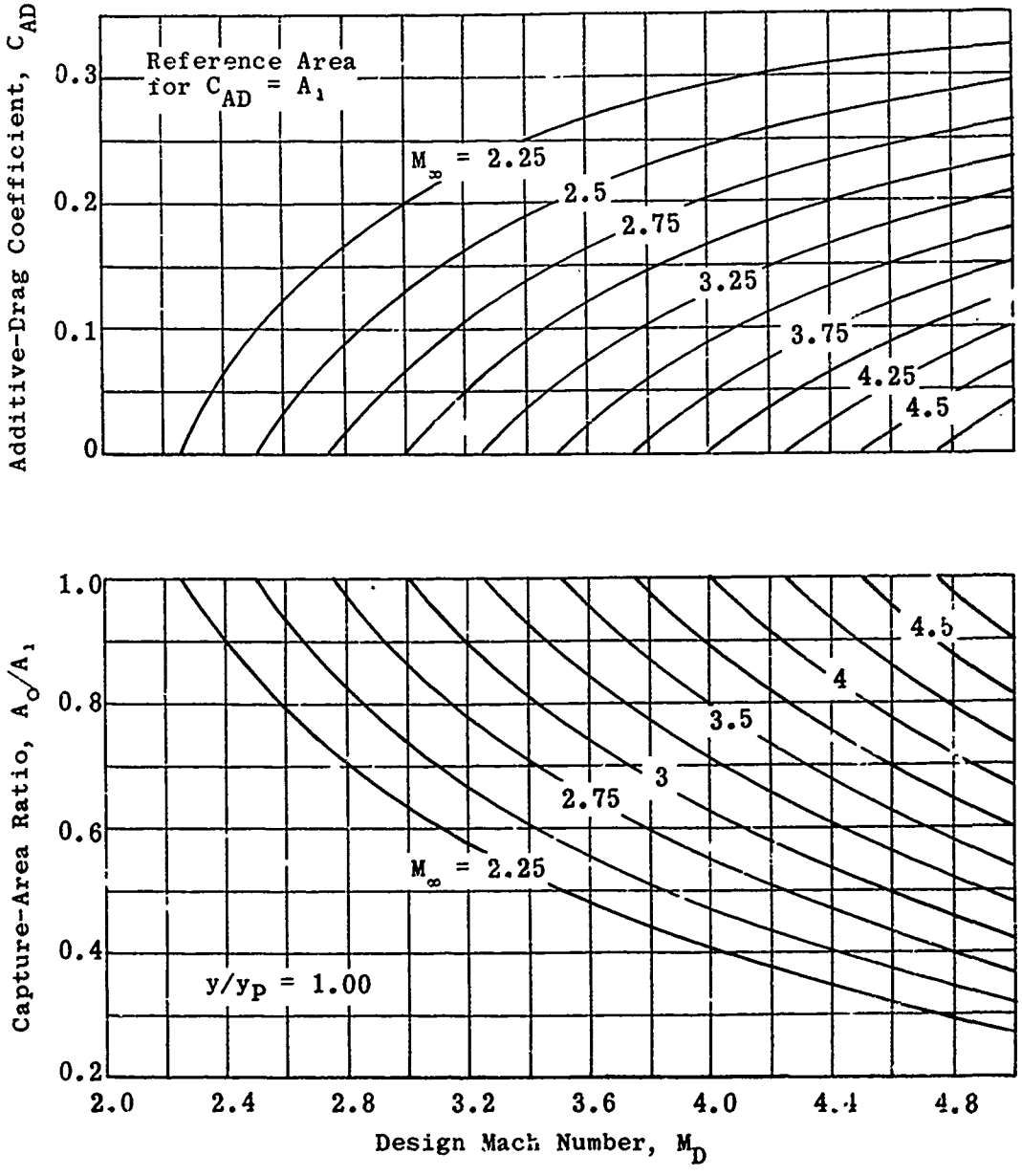

Fig. 3-47. Theoretical additive-drag coefficient and capture-area ratio for 15° tip isentropic-spike diffusers at below-design Mach numbers; cowl lip at design focal point; $2.0 \leq M_D \leq 5.0$; $2.25 \leq M_\infty \leq 4.75$.

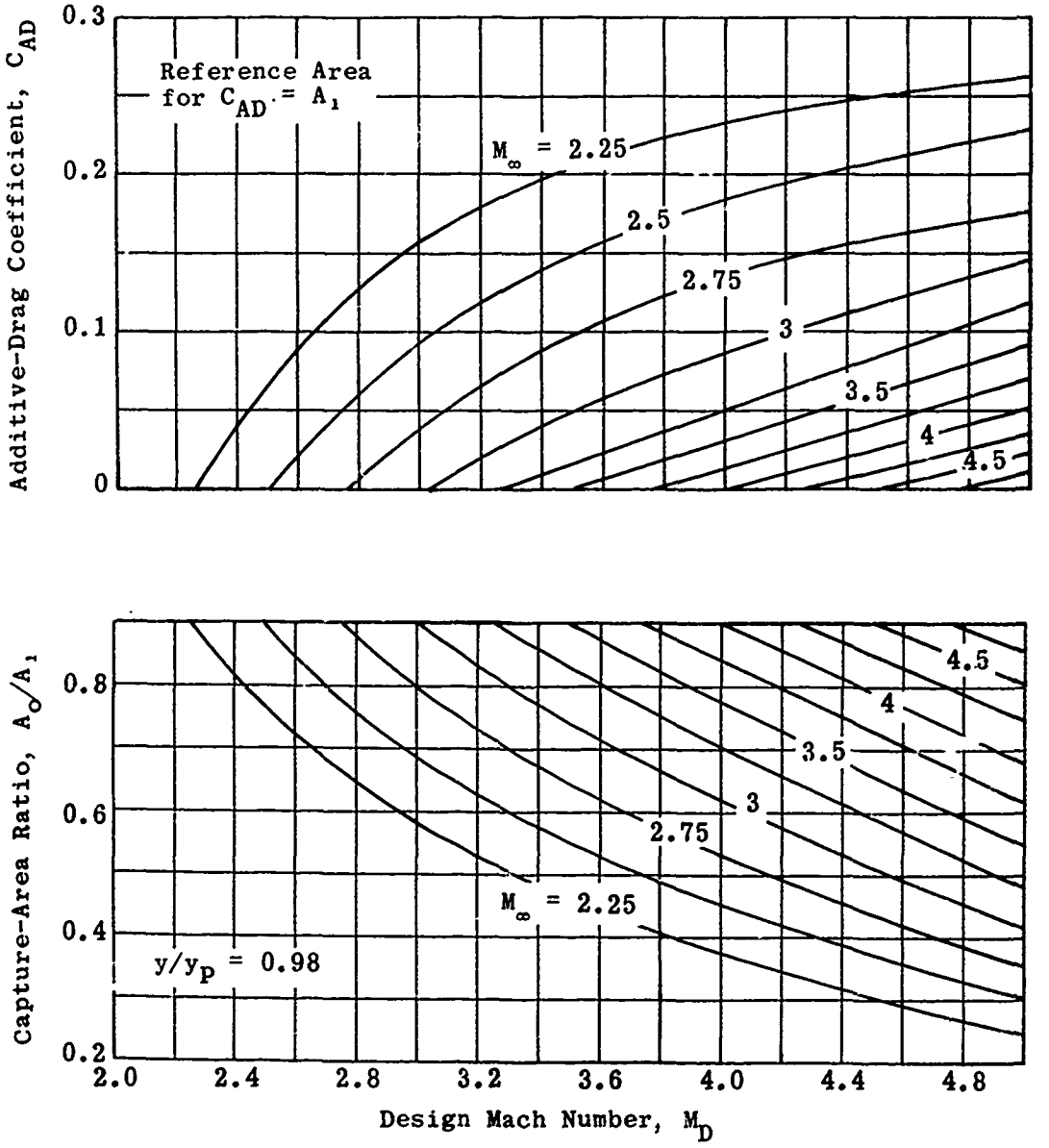

Fig. 3-48. Theoretical additive-drag coefficient and capture-area ratio for 15° tip isentropic-spike diffusers at below-design Mach numbers; cowl lip on design conical shock; $2.0 \leq M_D \leq 5.0$; $2.25 \leq M_\infty \leq 4.75$; radial-distance ratio = 0.98.

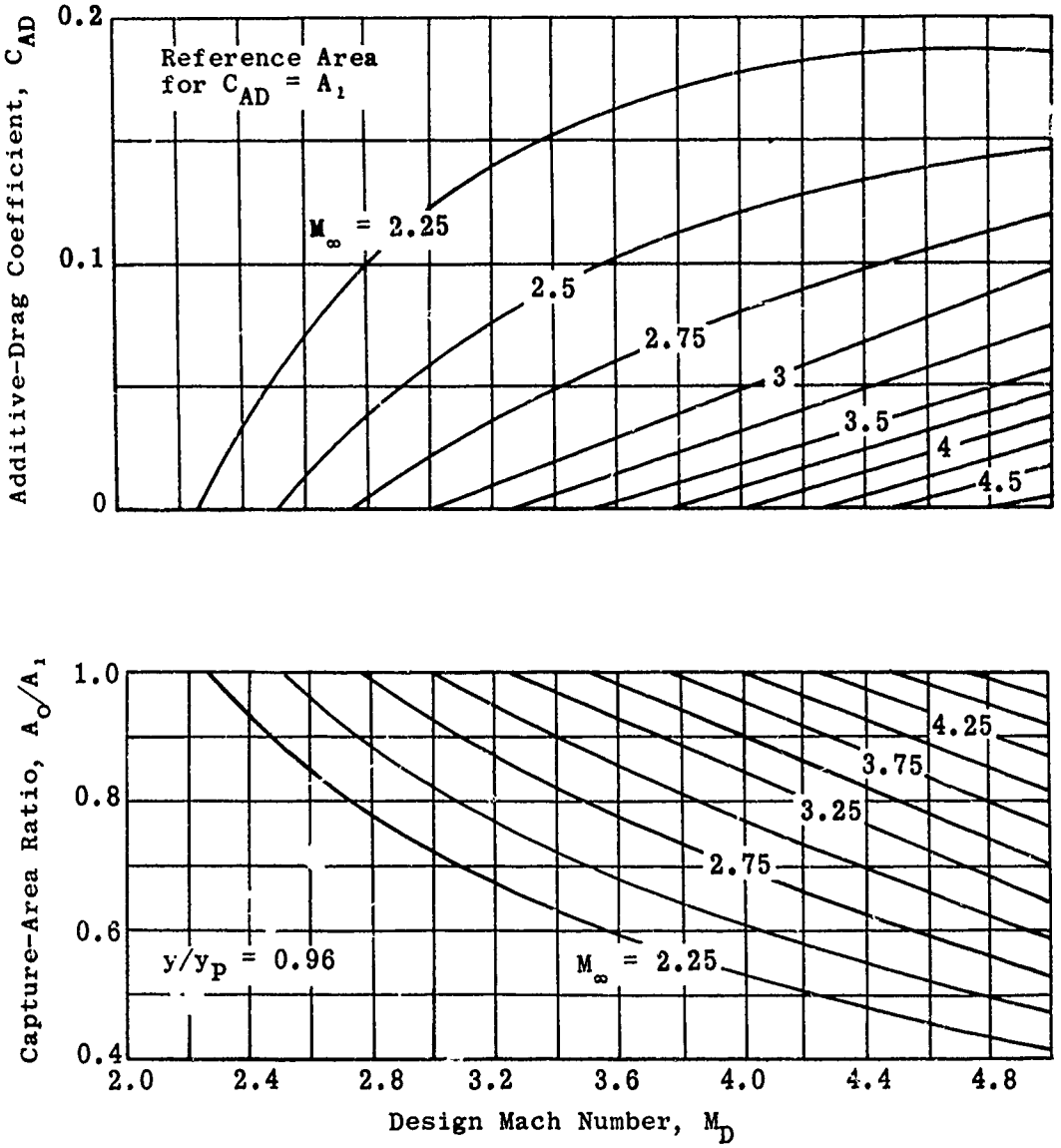

Fig. 3-49. Theoretical additive-drag coefficient and capture-area ratio for 15° tip isentropic-spike diffusers at below-design Mach numbers; cowl lip on design conical shock; $2.0 \leq M_D \leq 5.0$; $2.25 \leq M_\infty \leq 4.75$; radial-distance ratio = 0.96.

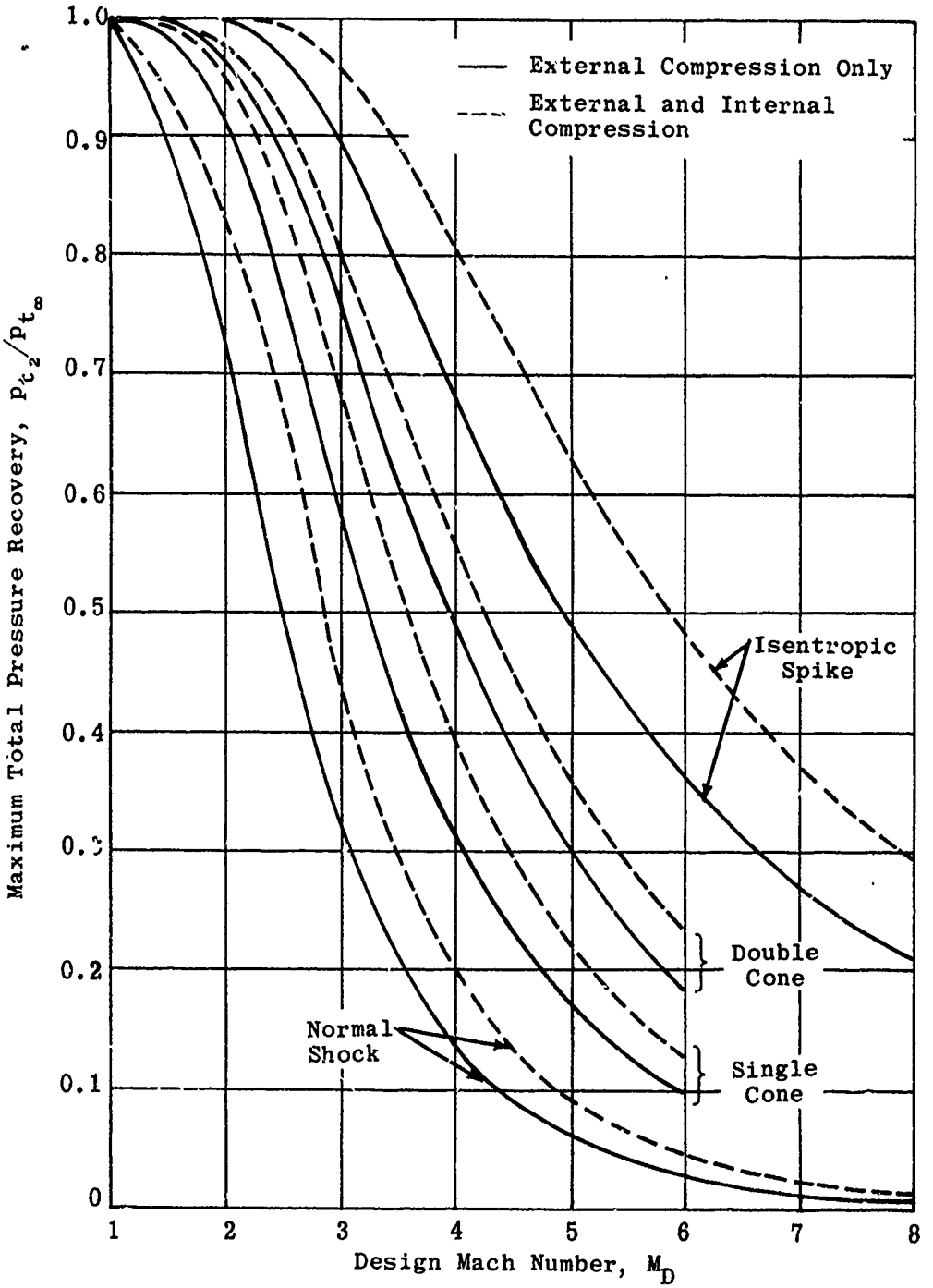

Fig. 3-50. Maximum theoretical total pressure recovery vs design Mach number for various basic diffusers; M_D = 1 to 8; γ = 1.4.

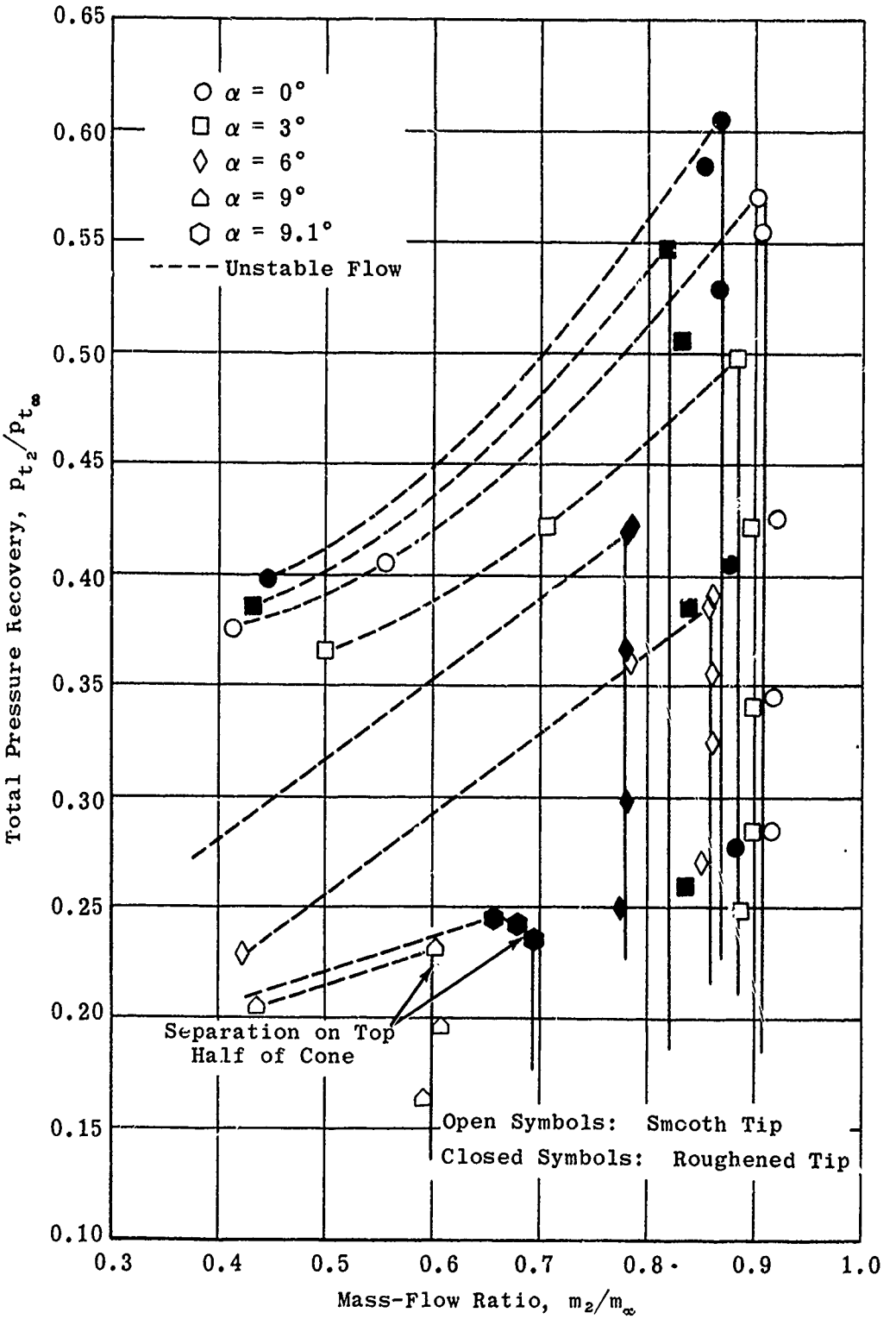

Fig. 3-51. Effect of tip roughness on total pressure recovery of an isentropic-spike inlet vs mass-flow ratio; α = 0 to 9°; M_∞ = 3.85; γ = 1.4; Re/ft = 1.0 × 10^6. (Source: Ref. 111)

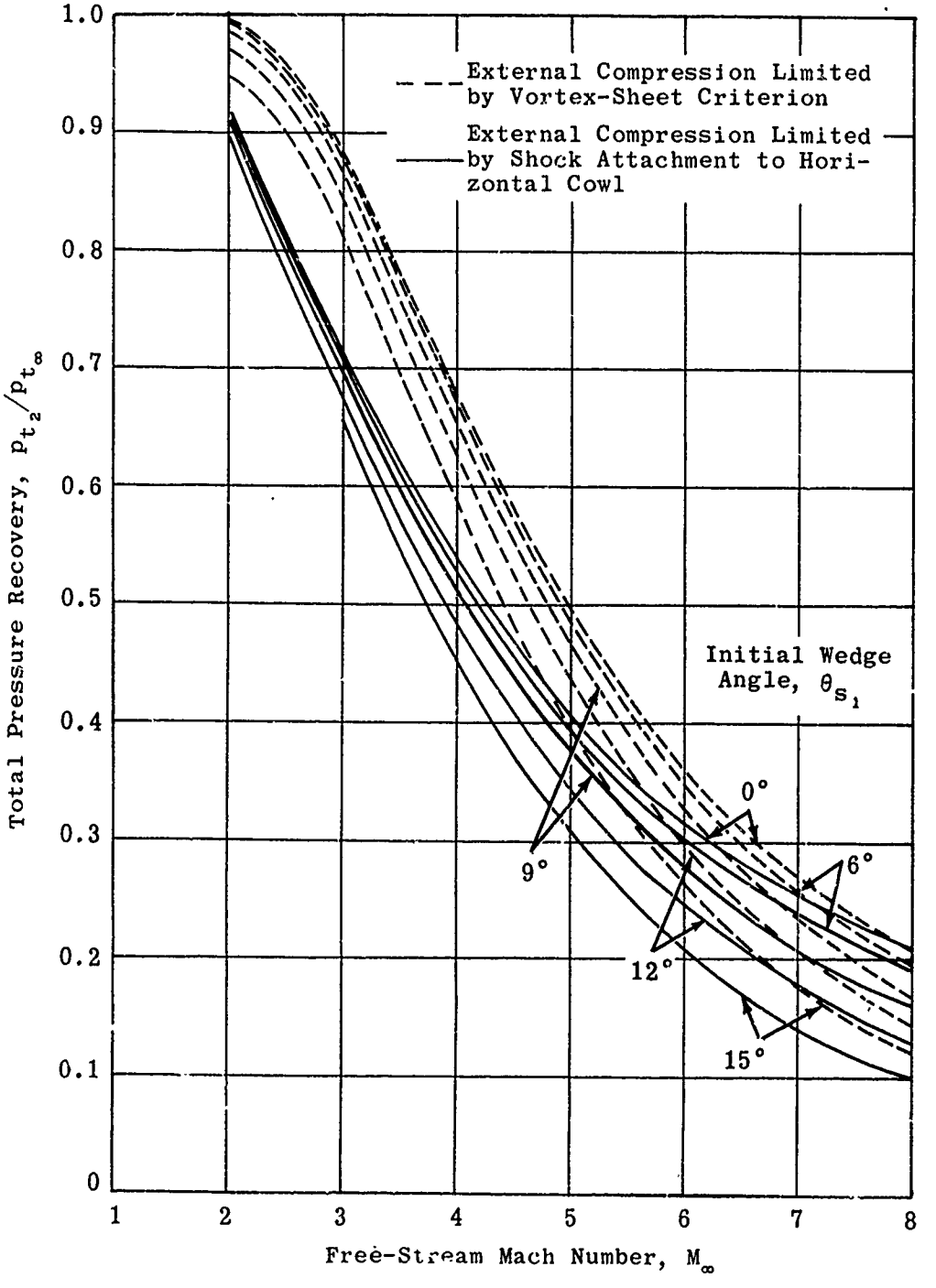

Fig. 3-52. Theoretical total pressure recovery based on limits imposed on compression by the vortex-sheet criterion and shock attachment; isentropic wedge, θ_{S_1} = 0 to 15°; shock attached to horizontal cowl; M_∞ = 2 to 8.

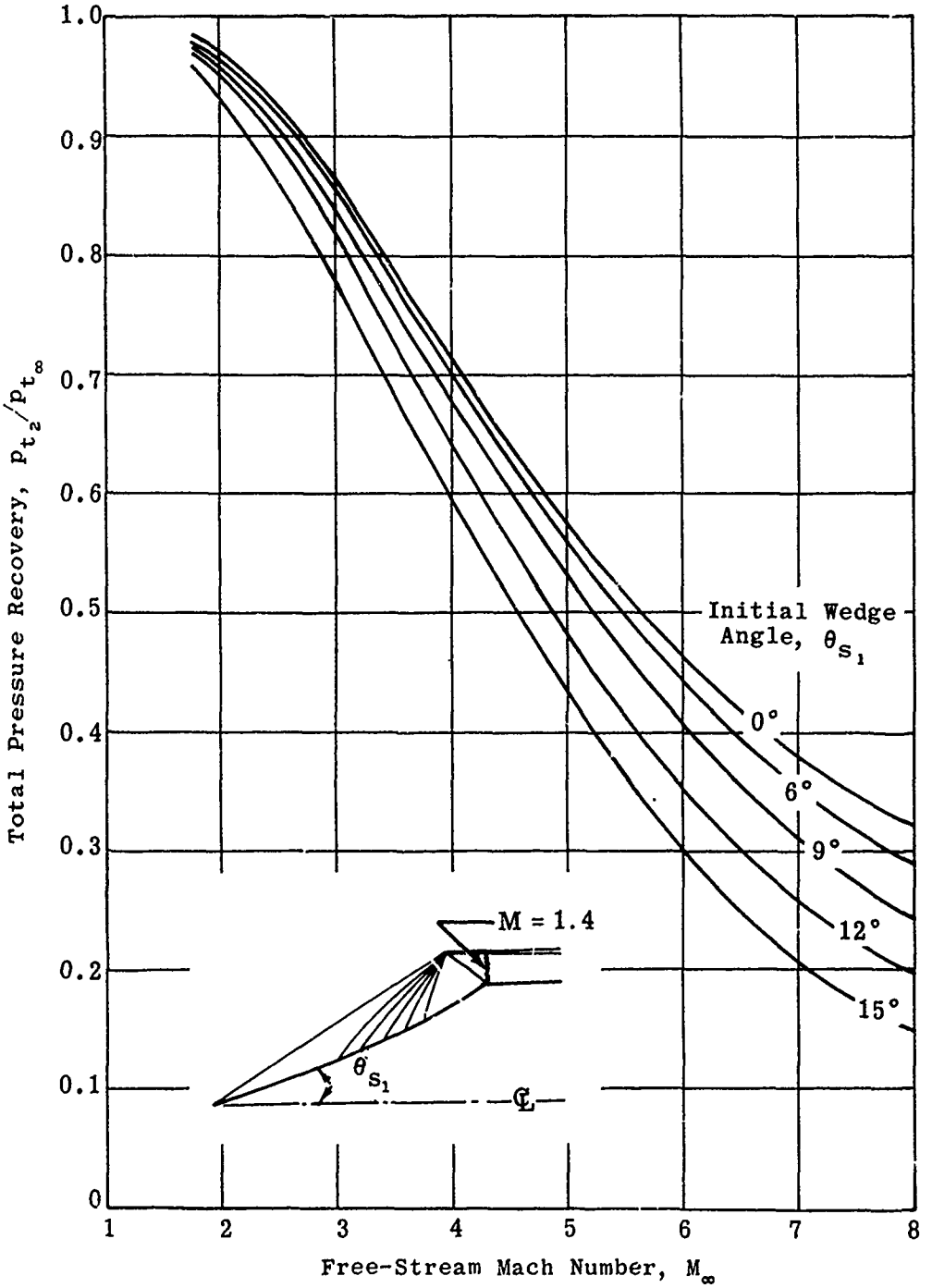

Fig. 3-53. Theoretical total pressure recovery vs free-stream Mach number for an isentropic-wedge diffuser operating at on-design Mach numbers; θ_{s_1} = 0 to 15°; horizontal cowl; M_∞ = 1 to 8.

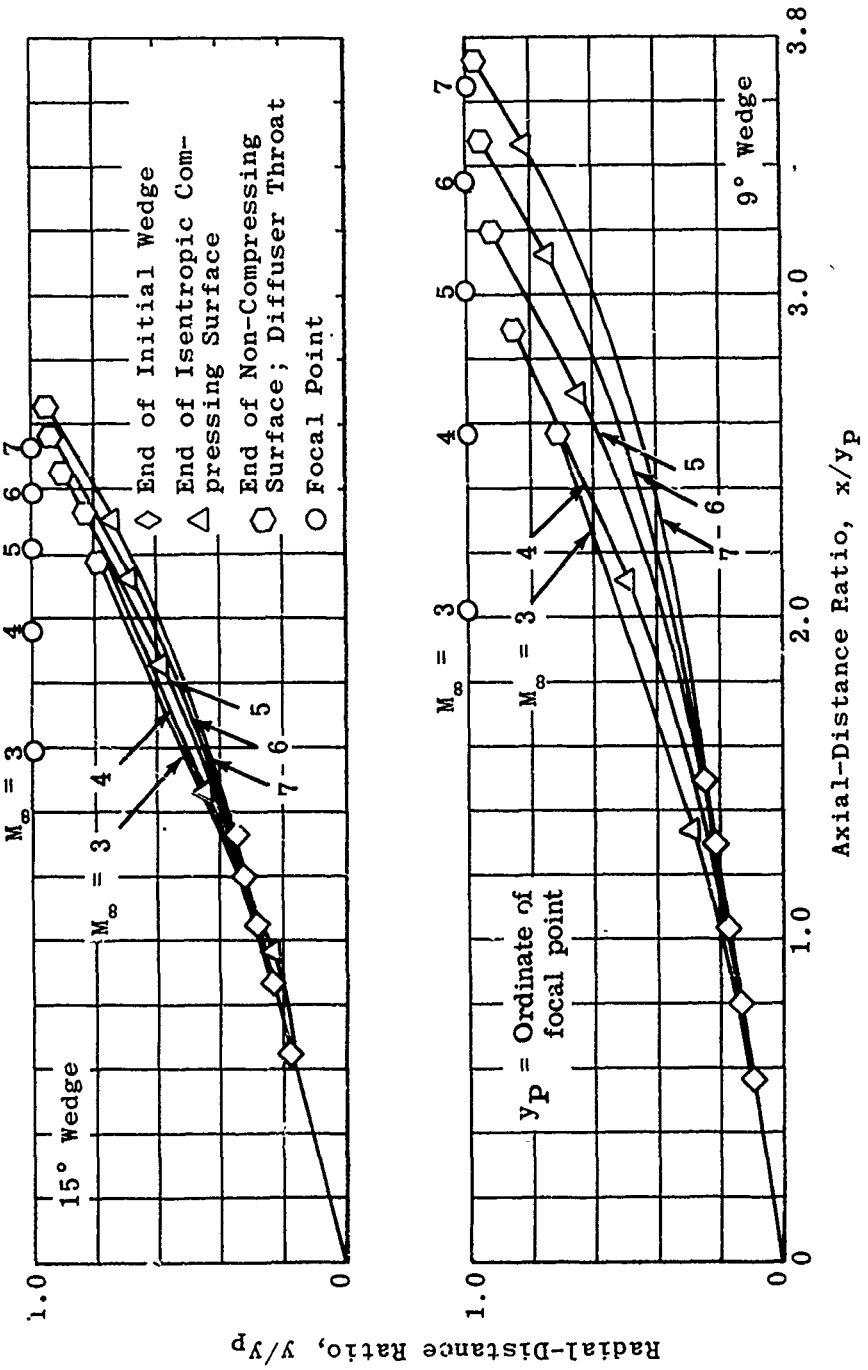

Fig. 3-54. Geometry of two isentropic wedges designed for Mach numbers from 3 to 7; $\gamma = 1.4$.

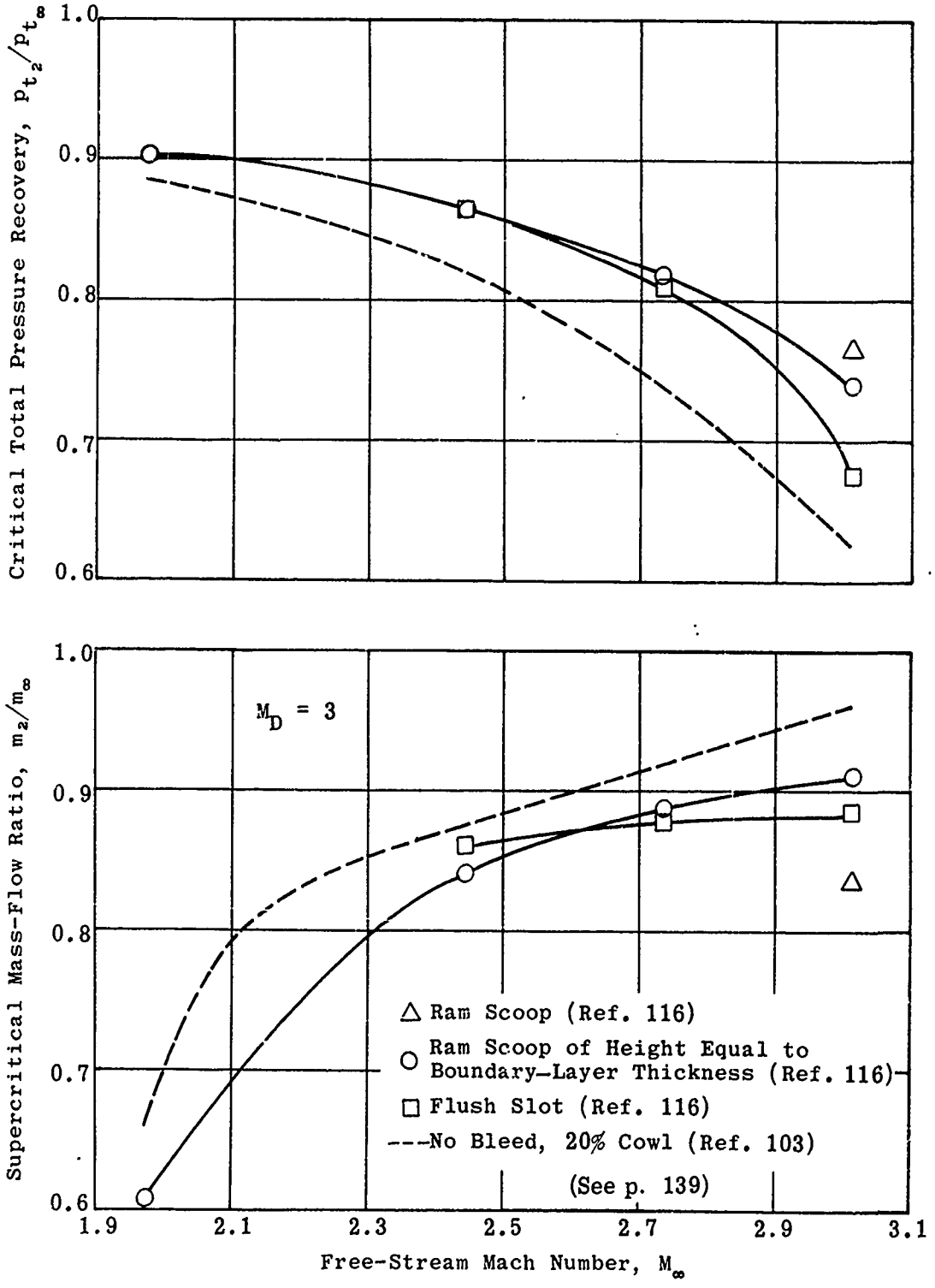

Fig. 3-55. Comparison of critical performance of double-cone diffusers utilizing various types of suction slots for boundary-layer control; $1.9 < M_\infty < 3.1$; $Re/ft = 2.5 \times 10^6$.

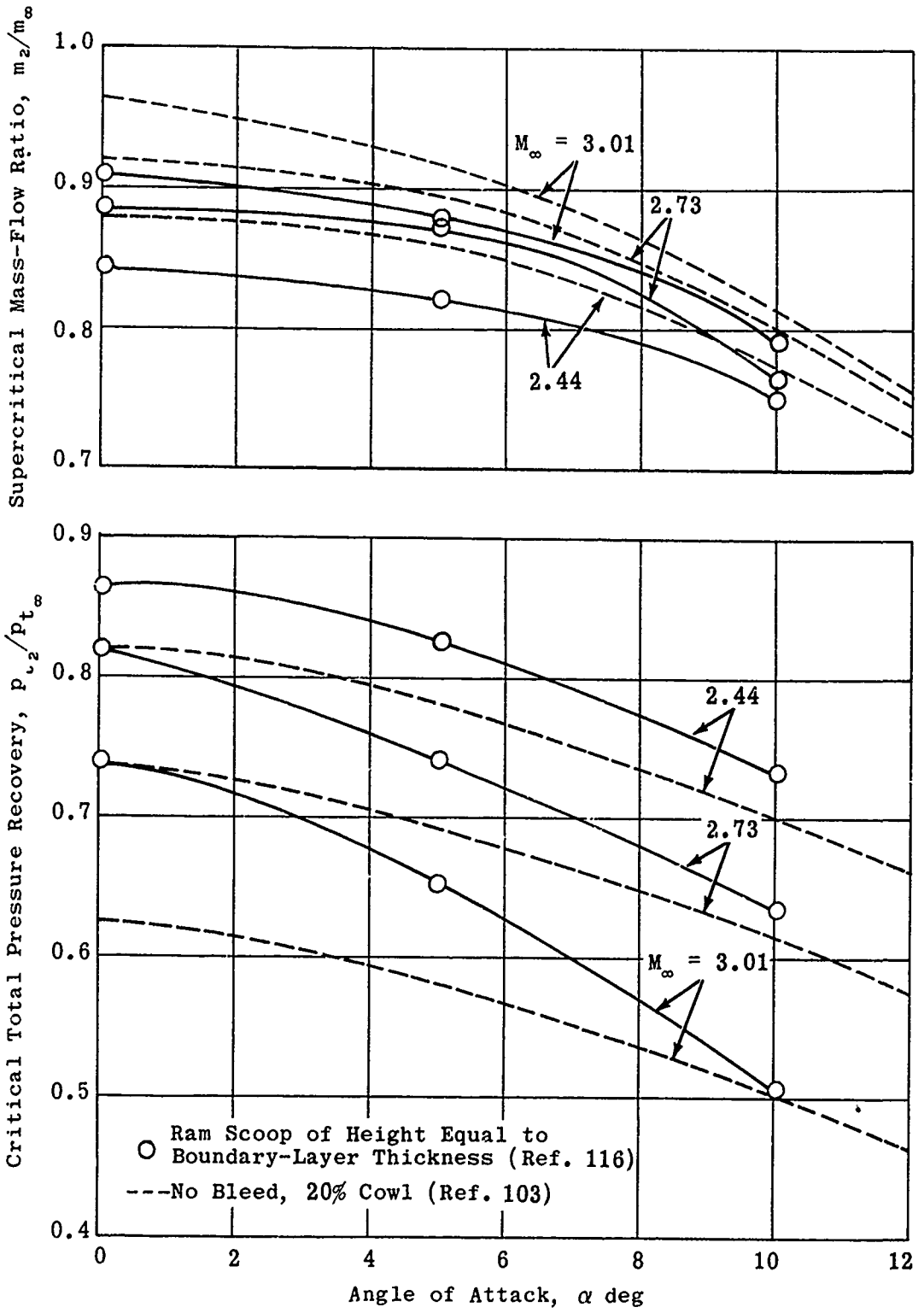

Fig. 3-56. Effect of boundary-layer bleed on critical performance of double-cone diffusers at angle of attack; α = 0 to 12°; 2.44 ≤ M_∞ ≤ 3.01; γ = 1.4; Re/ft = 2.5 × 10^6.

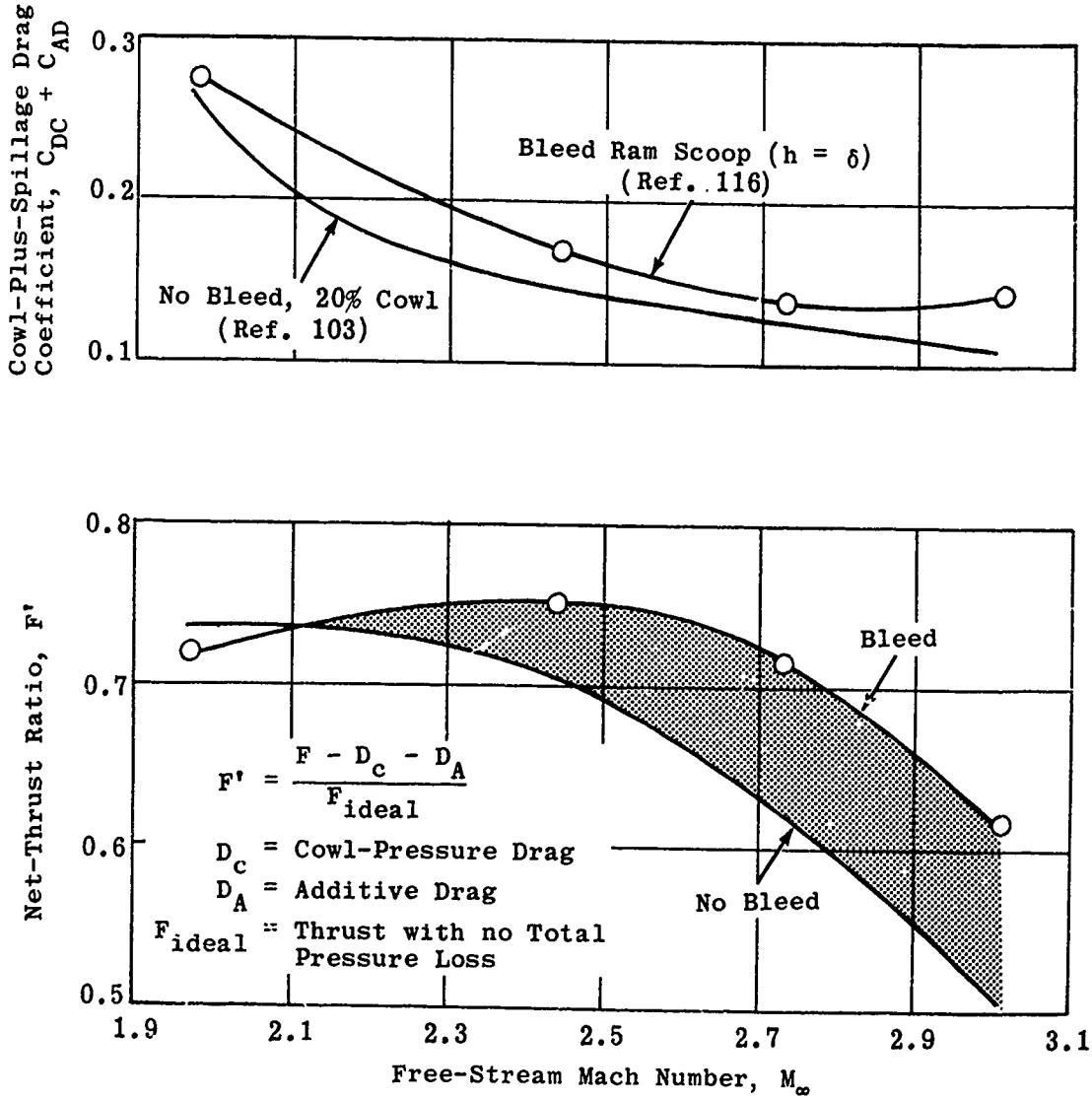

Fig. 3-57. Effect of ram scoop on net-thrust ratio and cowl-plus-spillage drag coefficient; double-cone diffuser; $1.9 < M_\infty < 3.1$; Re/ft = 2.5×10^6; $\gamma = 1.4$.

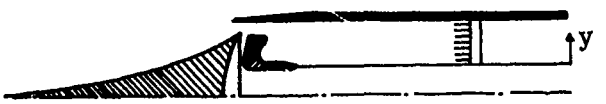

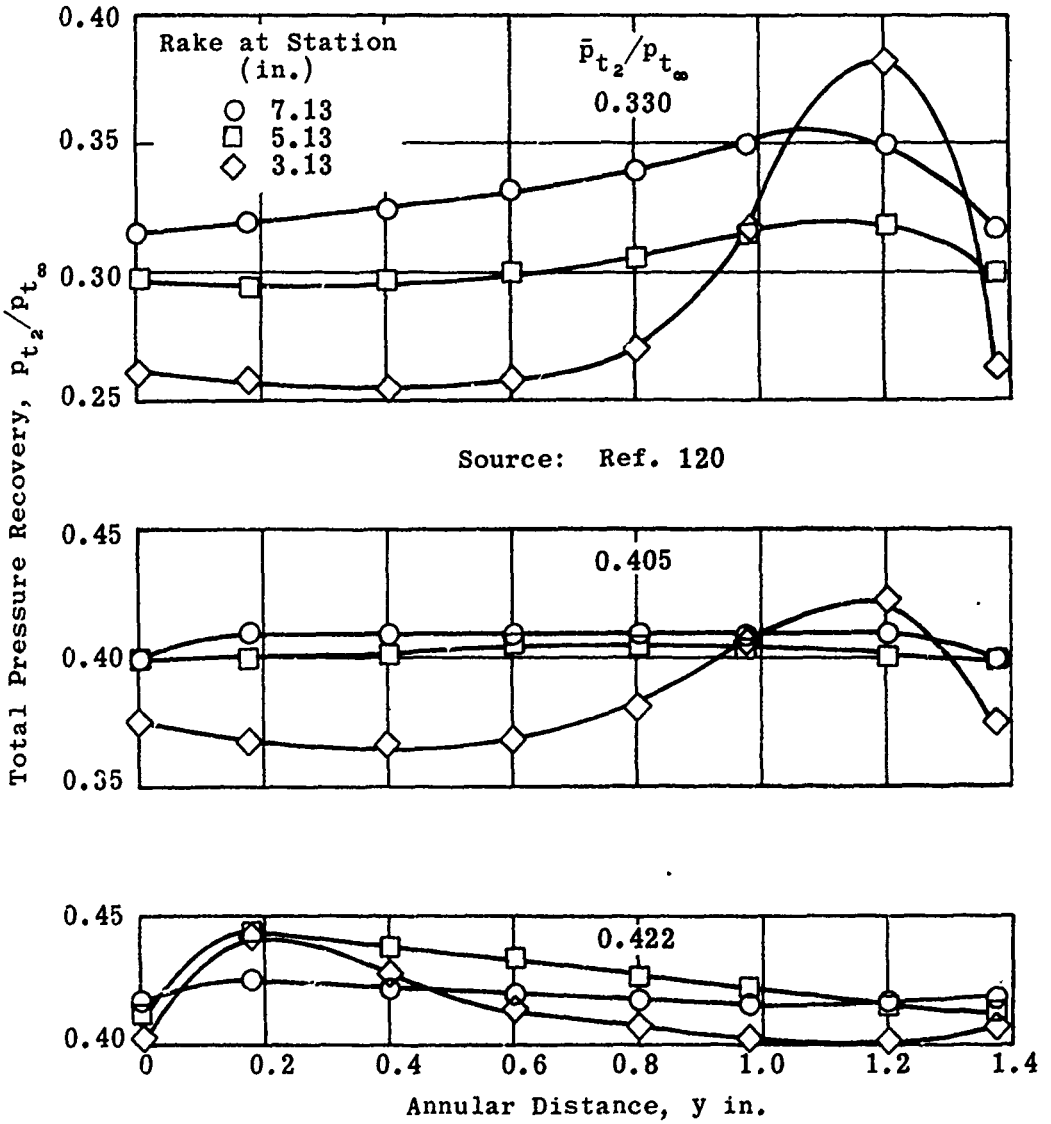

Source: Ref. 120

Fig. 3-58. Total pressure profile at various axial stations along a dump diffuser; $M_\infty = 3.85$; Re/ft = 8.6×10^4.

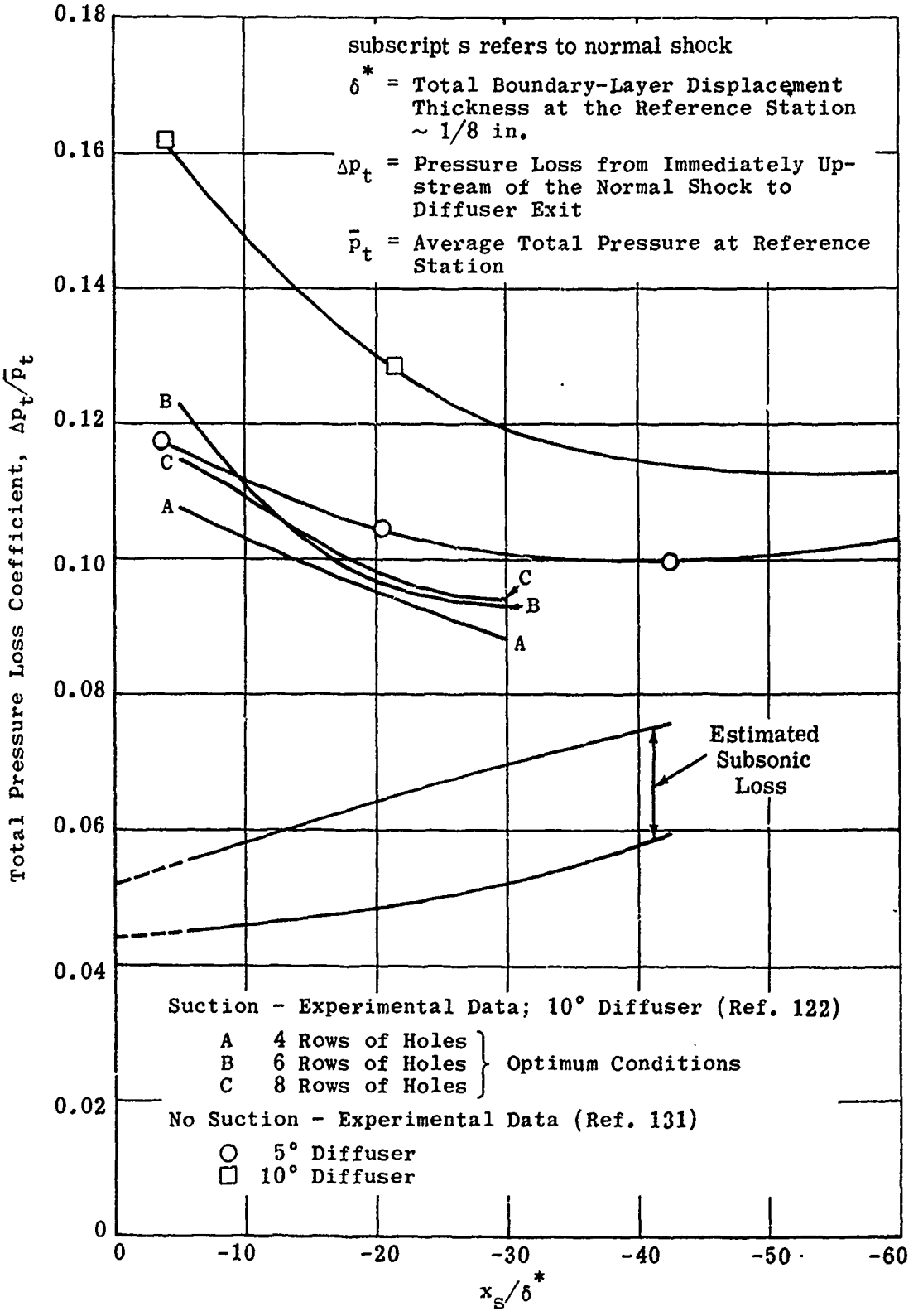

Fig. 3-59a. Effect on total pressure loss of suction in subsonic ducting; suction = 5% of total mass flow; $1.41 < M_s < 1.46$.

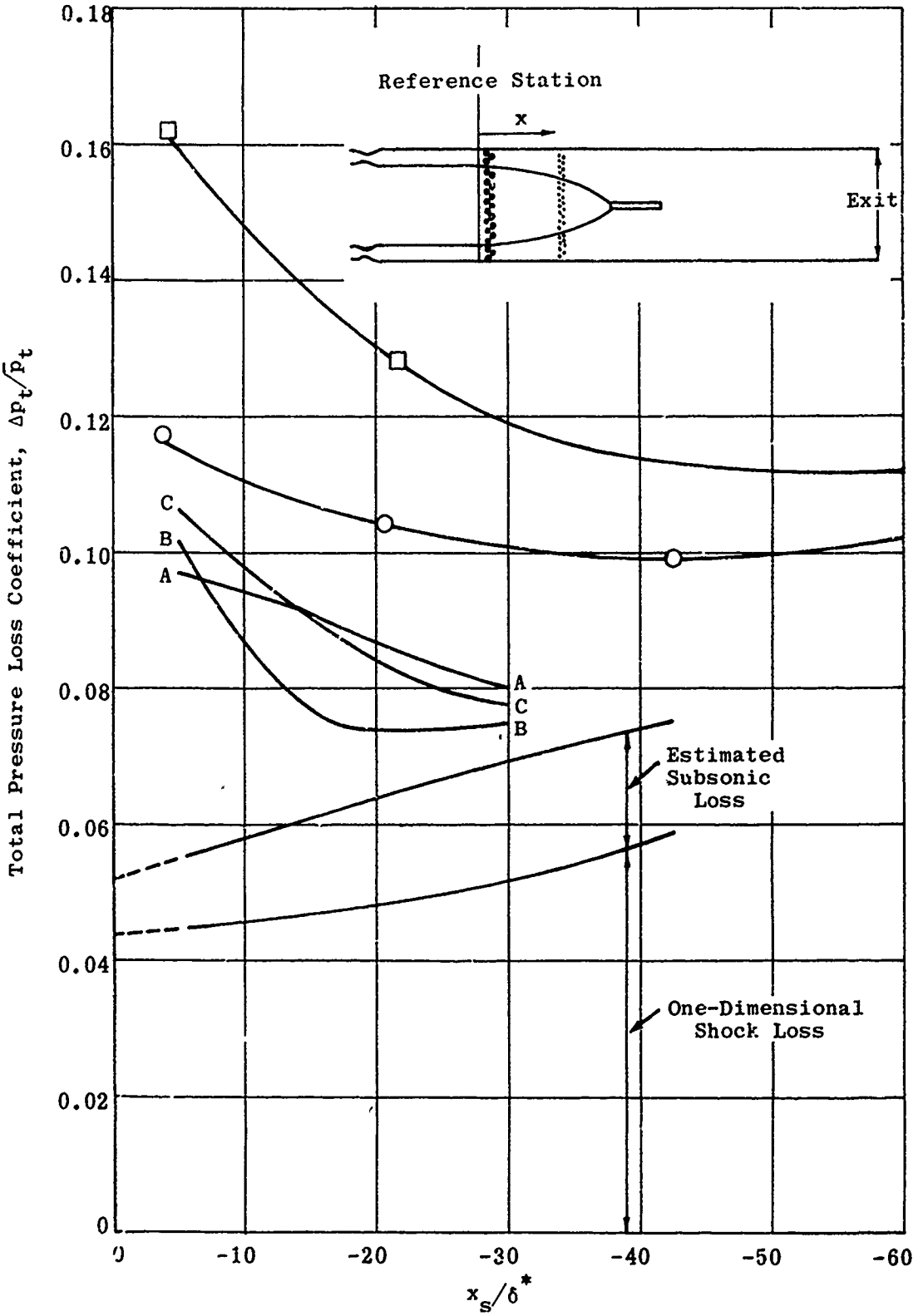

Fig. 3-59b. Effect on total pressure loss of suction in subsonic ducting; suction = 10% of total mass flow; $1.41 < M_s < 1.46$.

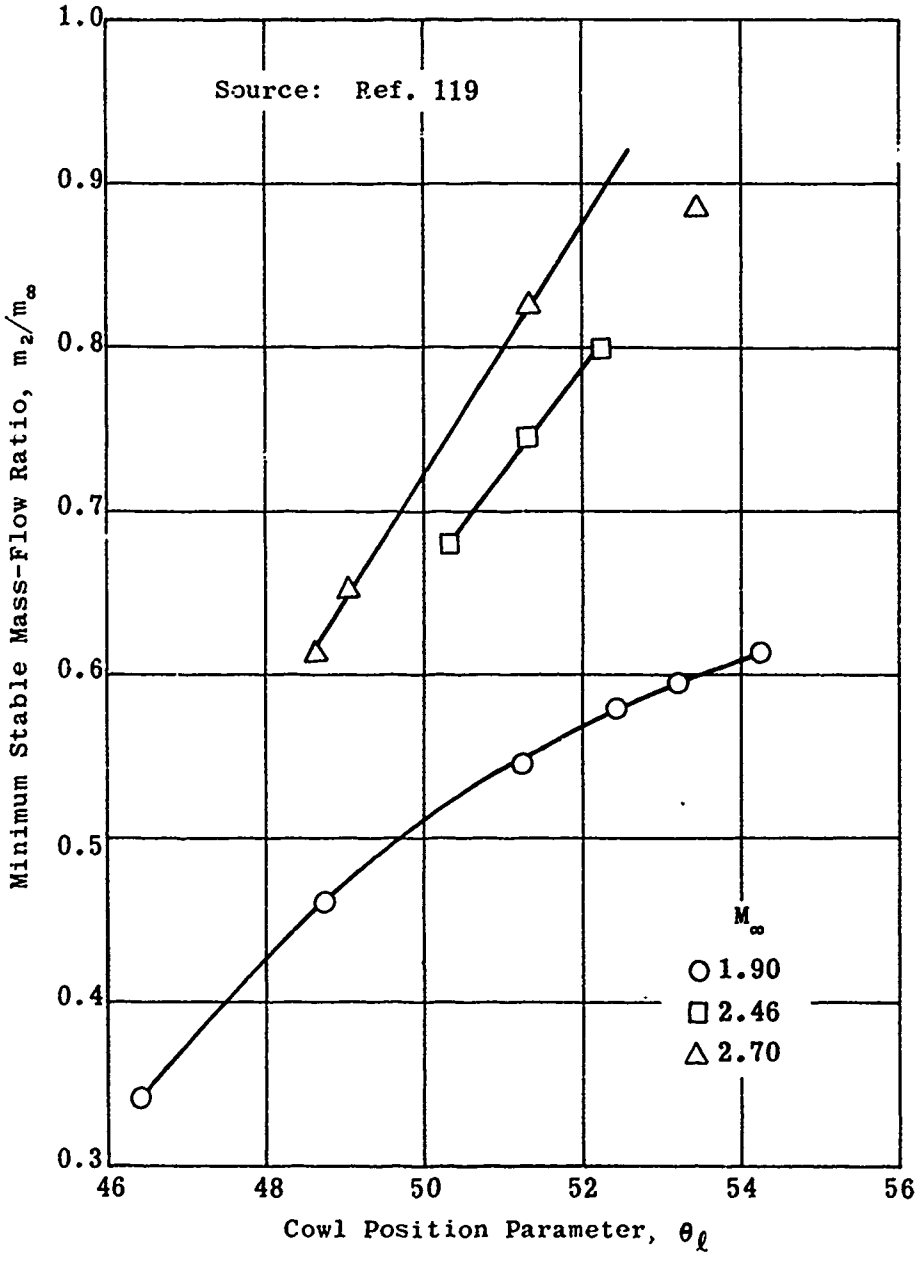

Fig. 3-60. Minimum stable mass-flow ratio vs cowling parameter; single-cone diffuser; M_∞ = 1.90, 2.46, and 2.70; θ_s = 40°; $2.3 \times 10^7 \leq$ Re/ft $\leq 2.9 \times 10^7$.

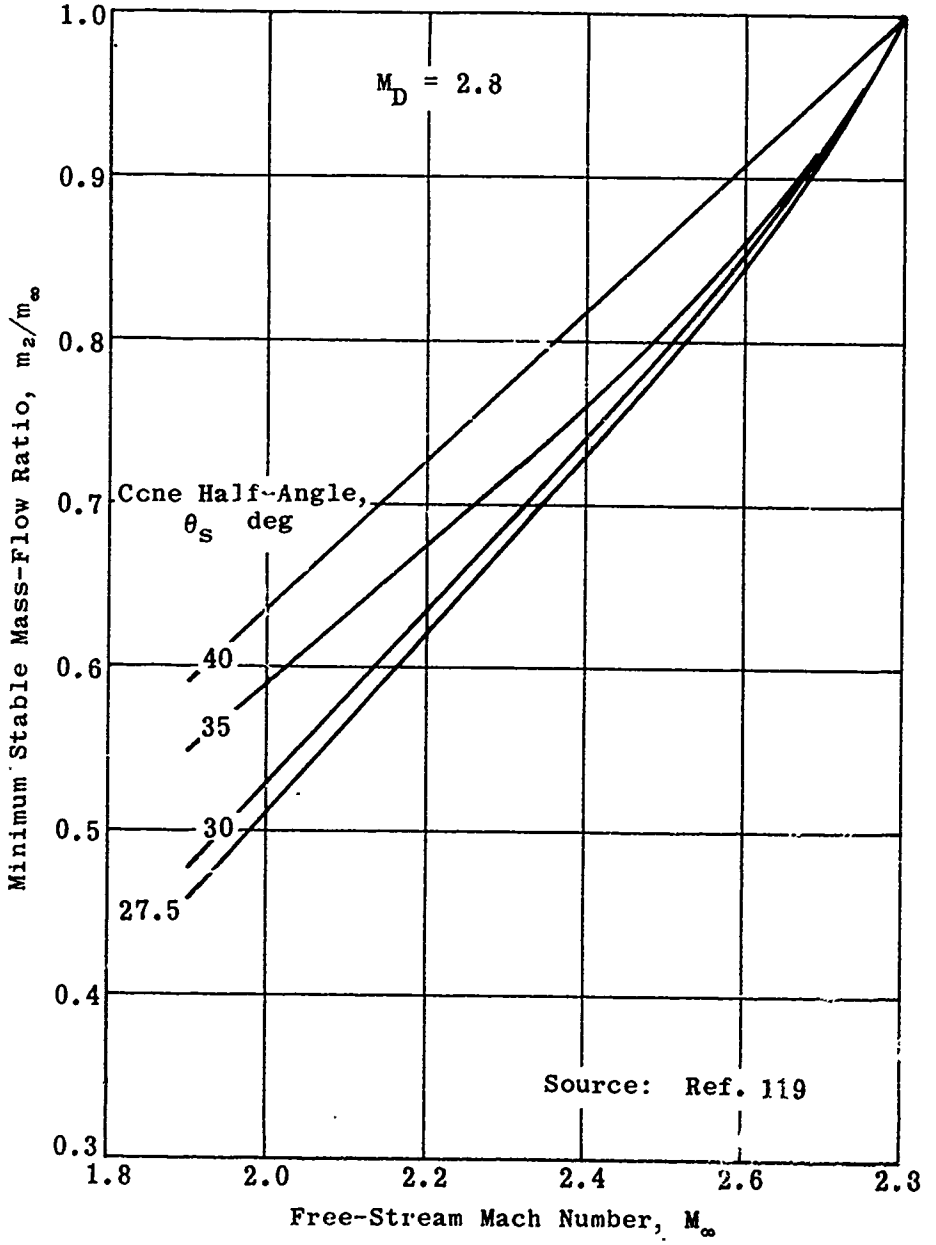

Fig. 3-61. Minimum stable mass-flow ratio vs free-stream Mach number; single-cone diffuser; θ_s = 27.5 , 30 , 35 , and 40°; $2.3 \times 10^7 \leq$ Re/ft $\leq 2.9 \times 10^7$.

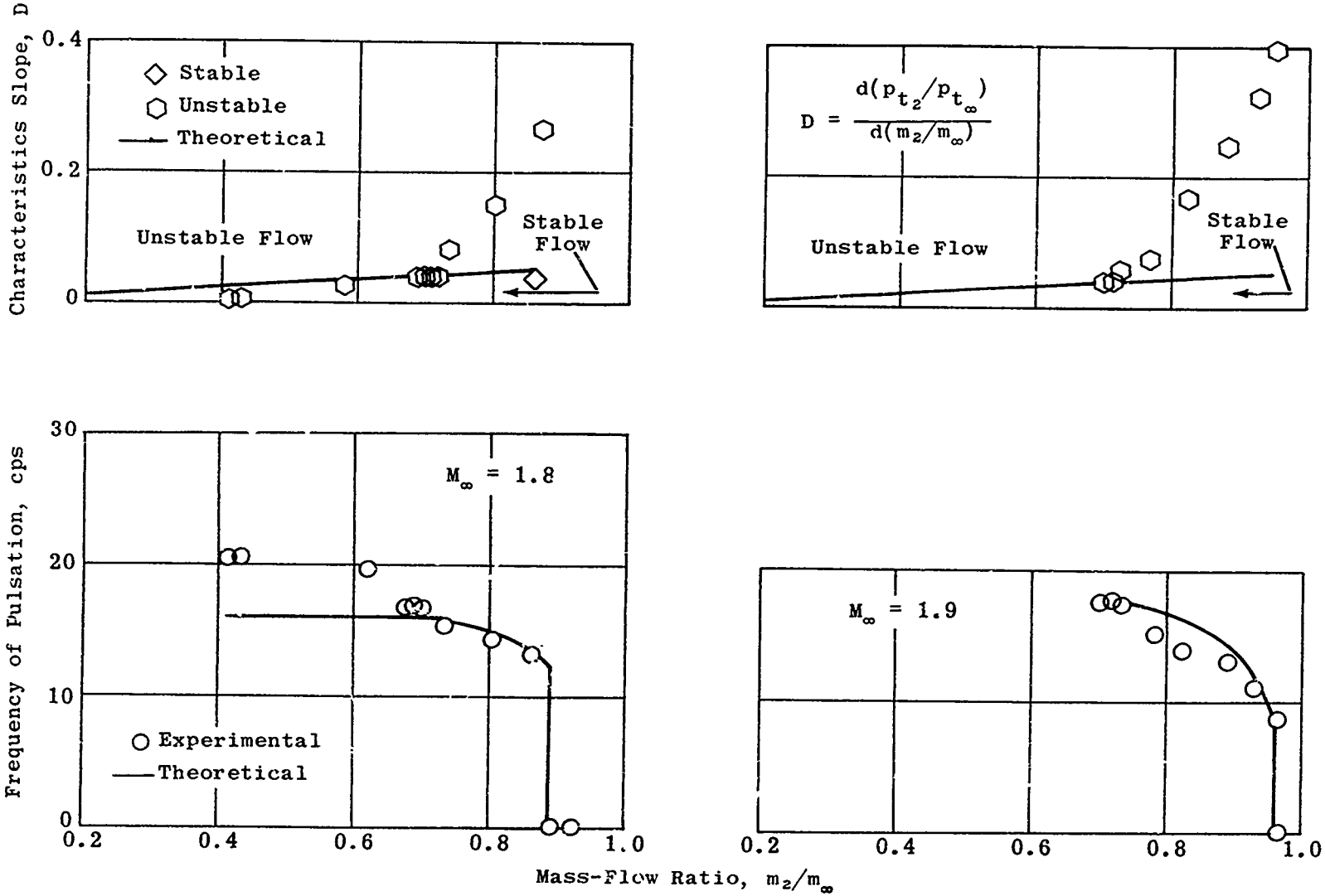

Fig. 3-62. Frequency of pulsation and slope of diffuser pressure-recovery curve vs mass-flow ratio (experimental and calculated values); single-cone diffusers; M_∞ = 1.8 and 1.9. (Source: Ref. 125)

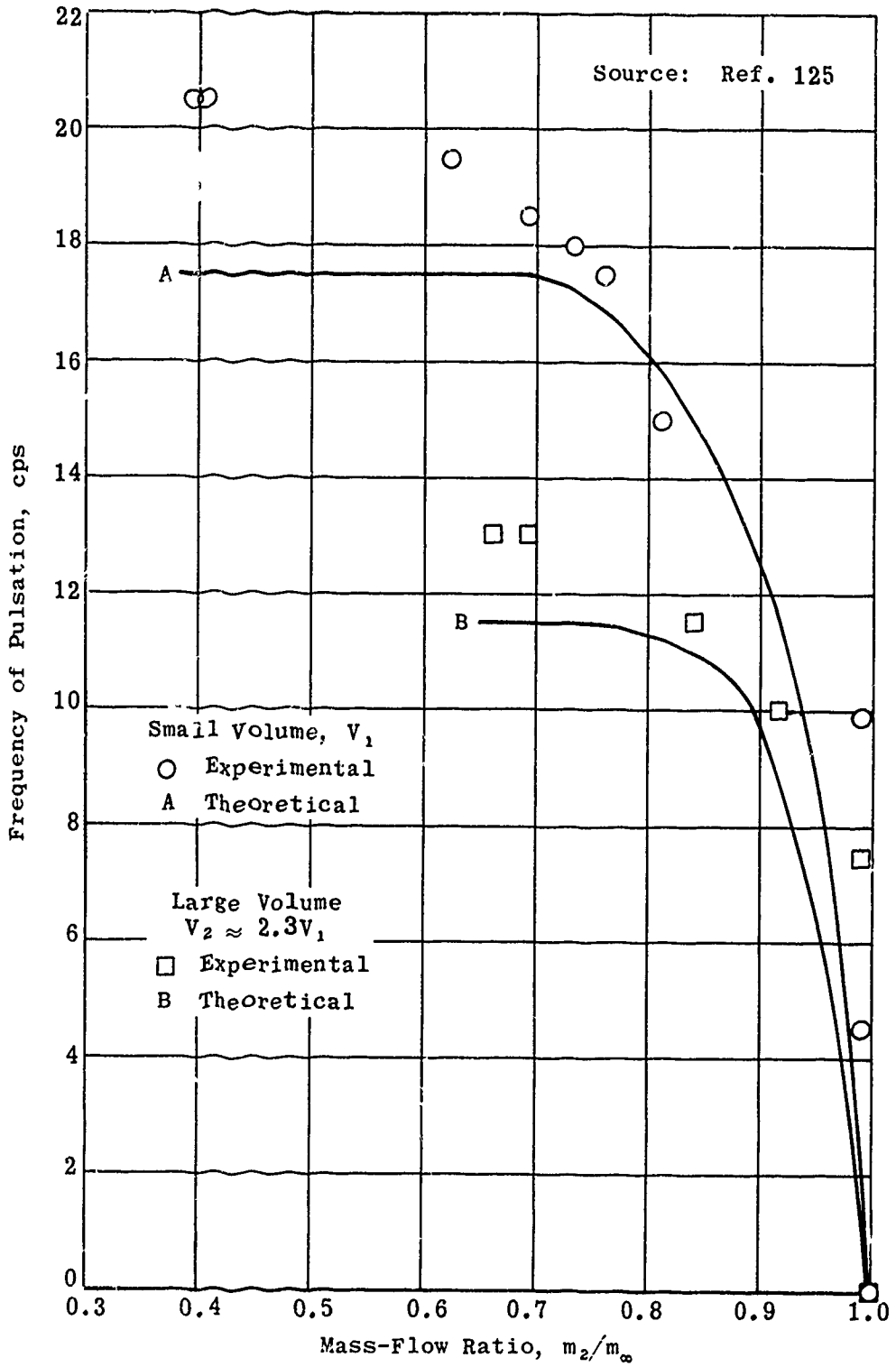

Fig. 3-63. Effect of combustion-chamber volume on frequency of pulsation in various single-cone diffusers (experimental and theoretical values); $V_2 \approx 2.3V_1$; $M_\infty = 2.0$.

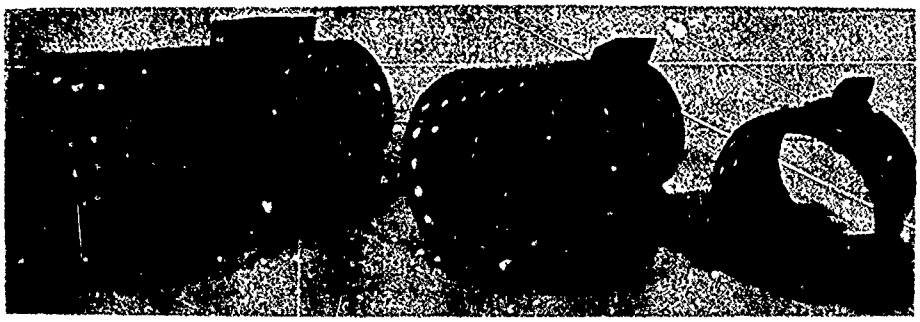

Can Combustion-Type Dampers

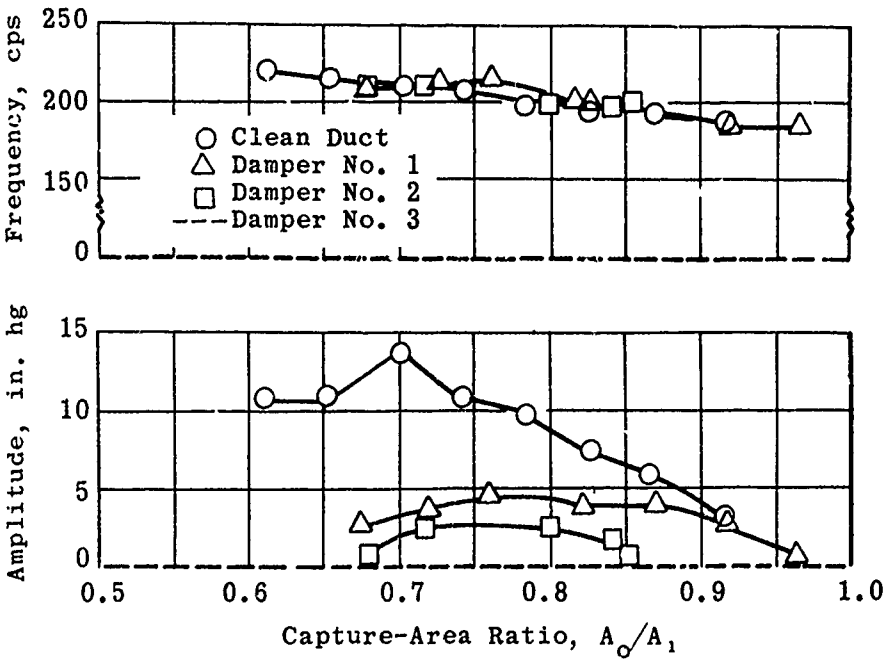

Fig. 3-64. Effect of dampers on frequency and amplitude of diffuser buzz; single-cone diffuser; $\theta_s = 22.75°$; $M_\infty = 1.73$.

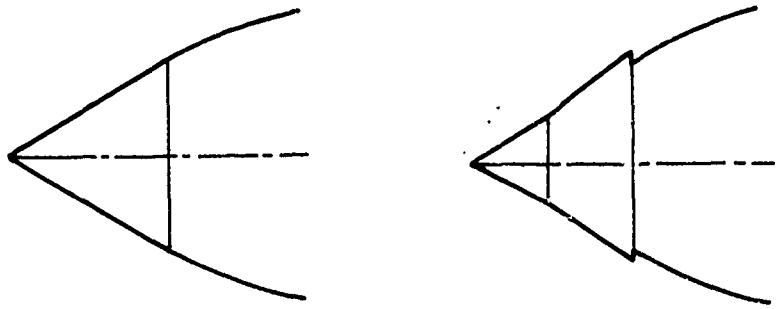

Single-Cone Diffuser

Two-Shock Step-Nose Diffuser

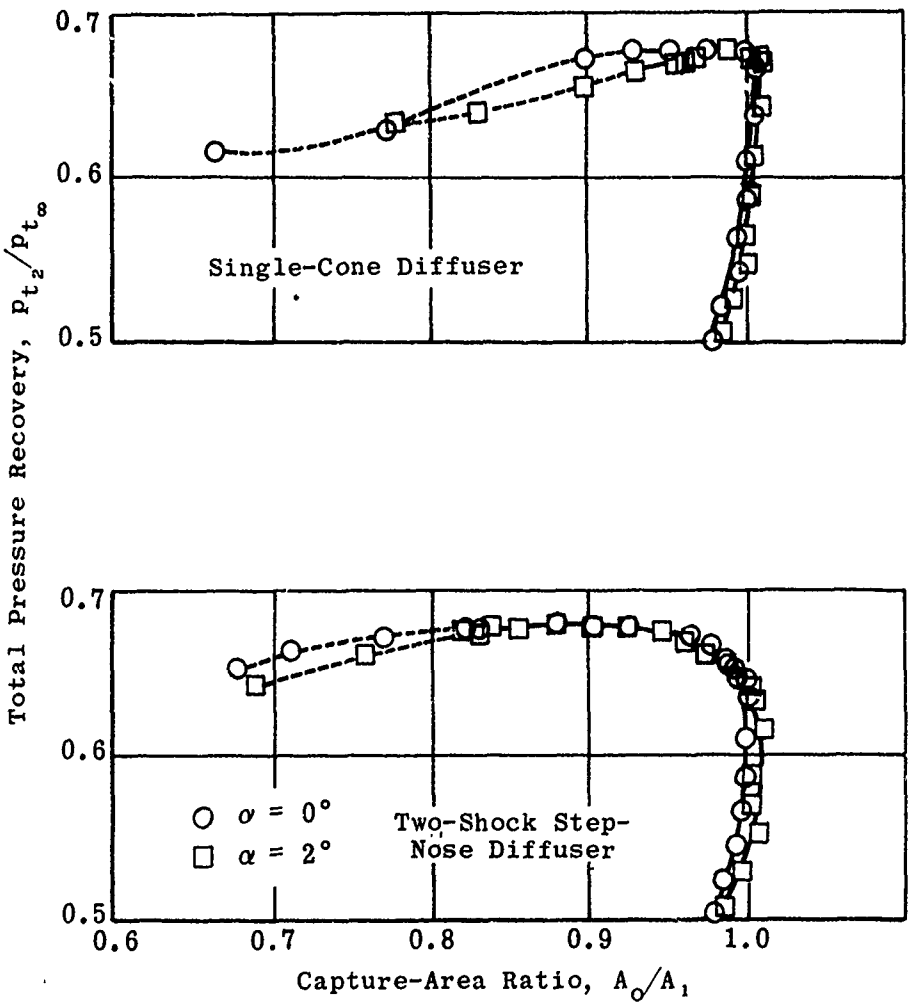

Fig. 3-65. Performance of single-cone and step-nose diffusers; $M_D = 2.23$.

Intentionally Blank

4. Wind-Tunnel Nozzles

A wind-tunnel nozzle is a simple Laval nozzle with subsonic flow on one side of a sonic throat and supersonic flow on the other. The divergent, or supersonic, section should be designed to assure a constant Mach number distribution across the exit area. It is also required that the flow at the exit be uniformly parallel to the tunnel axis. Methods of achieving such flow for a fixed Mach number will be discussed in Subsec. 4.3. The design of nozzles in which the Mach number may be varied will be treated in Subsec. 4.4.

The conventional nozzle may be said to consist of the four basic parts shown in the sketch below.

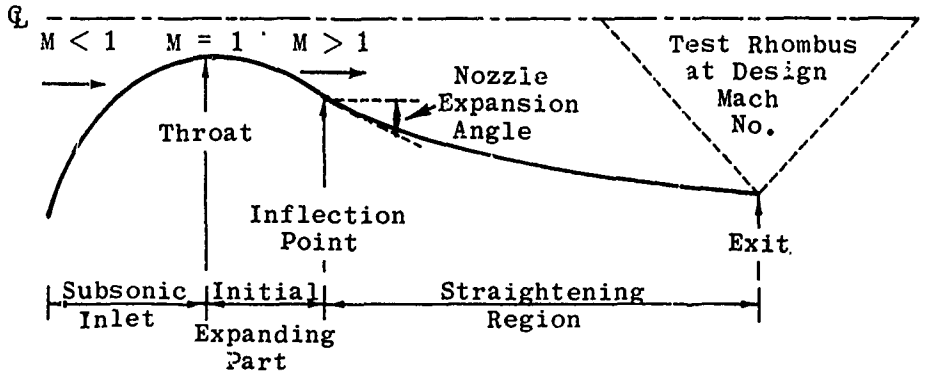

In the subsonic inlet, or effusor, the flow is accelerated from rest at the upstream end to sonic velocity at the throat. The inlet may house screens or honeycombs to reduce the turbulence level. Heating of the working fluid, where this is necessary, is often accomplished in the effusor. The inlet section of the nozzle is discussed in Subsec. 4.2.

In the sketch above, the throat is generated by a single line; however, in practice it is considered as an arbitrary region in the neighborhood of this unique cross section. The minimum area of the sonic throat is of critical importance in determining the exit Mach number of the flow. The surface contour and finish of the throat region are also important factors in the production of shock-free flow. The nozzle throat is discussed in Subsec. 4.1.

In the third region of the nozzle, the sonic flow is further accelerated as the slope of the contour increases from zero at the throat to a maximum expansion angle at the inflection point. The fourth region is one of increasing cross-sectional area but decreasing wall slope. In this region the flow is "straightened" in order that it may emerge parallel to the nozzle axis.

The nozzle contours are usually designed with the assumption that the gas flow is isentropic and non-viscous. The contour thus determined is then corrected for viscosity and heat-transfer effects. The viscous correction has been discussed in Subsec. 2.4 of this volume and additional material is given in Subsec. 4.8. Heat-transfer effects are touched upon in Subsec. 4.6 but will be treated fully in Section 14 of the Handbook.

4.1 The Nozzle Throat

It will be seen in Subsecs. 4.3 and 4.4 that most nozzle calculations, whether based on simple area relationships or on complex characteristics nets, are dependent upon the flow properties in the sonic throat and therefore this region should logically be examined first. It is usually assumed that the actual flow in the minimum-area throat is uniform over the cross section and that the velocity is equal to the local velocity of sound. Sauer in Ref. 132 and Oswatitsch in Ref. 3 (p. 478) examine the flow properties in detail for both two-dimensional and axially-symmetric nozzles and show that this assumption, while not exact, is acceptable under certain conditions to be discussed later. The basic geometry for both cases is illustrated in the sketch below.

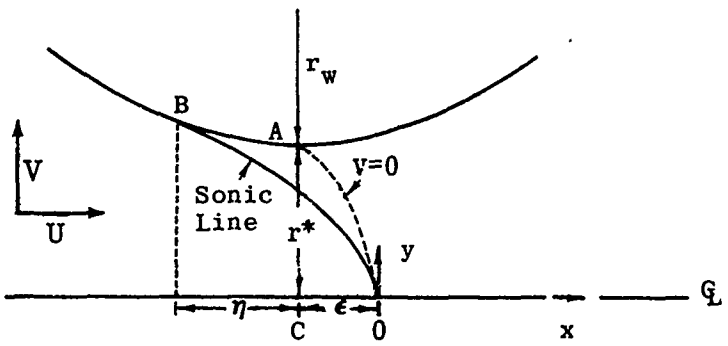

The x-axis is taken along the nozzle centerline and the origin is the point on it at which M = 1, i.e., U = a. It is further assumed that along this axis the flow may be defined by

$$\left.\begin{aligned} U_o/a^* &= 1 + \alpha x \\ \text{and} \qquad V_o/a^* &= 0 \end{aligned}\right\} \qquad (4\text{-}1)$$

where

U and V = the velocity components in the x and y directions

a = local sonic velocity

α = axial flow acceleration

superscript * = condition at nozzle throat

subscript o = condition along x-axis.

Near the throat it is further assumed that U differs from a* by only a small quantity and that V is always small.

Two-Dimensional Throat.--In this case the flow field is defined by

$$\left.\begin{aligned} U/a &= 1 + \alpha x + \frac{\gamma + 1}{2}\,\alpha^2\, y^2 + \ldots \\ \text{and} \qquad V/a &= (\gamma + 1)\,\alpha^2\, xy + \frac{(\gamma + 1)^2}{6}\,\alpha^3\, y^3 + \ldots \end{aligned}\right\} \qquad (4\text{-}2)$$

The nozzle contour is designed to conform to a streamline and hence at the vertex of the throat wall, where $y = r^*$ and $V = 0$,

$$x = -\epsilon = -\frac{(\gamma + 1)}{6}\,\alpha\, r^{*2} \,. \tag{4-3}$$

Since also at $x = -\epsilon$, $dy/dx = \tan\theta \doteq V/U = 0$, then the radius of curvature of the wall, r_w, is given by

$$r_w = \frac{\left[1 + \left(\frac{dy}{dx}\right)^2\right]^{3/2}}{\left|d^2y/dx^2\right|} = \frac{1 + \frac{(\gamma + 1)}{3}\,\alpha^2 r^{*2}}{(\gamma + 1)\,\alpha^2 r^*} \,. \tag{4-4}$$

Equation 4-4 may be rearranged so that α may be expressed in terms of r_w and r^*, giving

$$\alpha^2 = \frac{1}{(\gamma + 1)\, r^{*2}\left[r_w/r^* - 1/3\right]} \,. \tag{4-5}$$

By means of Eq. 4-5 the values of U/a, V/a, and ϵ may be expressed in terms of r_w and r^* rather than α, i.e., in terms of the known throat geometry rather than the unknown flow acceleration along the nozzle axis.

The vertex of the parabolic sonic line is on the nozzle axis a distance $|\epsilon|$ downstream of the narrowest section. The accuracy of this measurement is limited only by the basic assumptions of small velocity gradients and non-viscous isentropic flow. In order to determine the point, B, at which the sonic line intersects the contour wall, Sauer employs further simplifying assumptions. He assumes that the difference between y_B and r^* is negligible and also that $V/a = 0$ at B, i.e., $(U/a)_B = 1$ and obtains

$$x_B - x_A = \eta = -\frac{(\gamma + 1)}{3}\,\alpha\, r^{*2} = -2\epsilon \,. \tag{4-6}$$

The accuracy of this value of η will be discussed a little later.

Axially-Symmetric Throat. --In the case of axial symmetry the streamlines are defined by

$$\left.\begin{aligned} U/a &= 1 + \alpha x + \frac{\gamma + 1}{4}\,\alpha^2\, y^2 + \ldots \\ \text{and} \\ V/a &= \frac{\gamma + 1}{2}\,\alpha^2\, xy + \frac{(\gamma + 1)^2}{16}\,\alpha^3\, y^3 + \ldots \end{aligned}\right\} \tag{4-7}$$

with

$$\epsilon = -x_A = \frac{\gamma + 1}{8}\,\alpha\, r^{*2} \,, \tag{4-8}$$

$$r_w = \frac{1 + \frac{\gamma + 1}{8} \alpha^2 \, r^{*2}}{\frac{\gamma + 1}{2} \alpha^2 \, r^*} \tag{4-9}$$

and

$$\alpha^2 = \frac{8}{(\gamma + 1) \, r^{*2} \left[4 \frac{r_w}{r^*} - 1 \right]} . \tag{4-10}$$

Using the same assumptions with respect to the point B as were made in the two-dimensional case, one obtains

$$x_B - x_A = \eta = - \frac{\gamma + 1}{8} \alpha \, r^{*2} = -\epsilon . \tag{4-11}$$

Sonic lines calculated by Sauer's method for both the axially-symmetric and the two-dimensional nozzle throat are shown in Fig. 4-1 for values of r_w/r^* of 1.5, 2, 4, and 10. (Actually in the two-dimensional case the values were 1.5333, 2.333, etc., in order to simplify the calculations from Eq. 4-5.) It may be seen from Fig. 4-1 that the usual assumption of a straight sonic line is more nearly realized in the three-dimensional case than in the two-dimensional case. It also may be noted that in both cases the condition of linearity is approached as the ratio r_w/r^* increases. No solution exists for $r_w/r^* = 1.5$ in the two-dimensional case. A comparison of the Mach number distribution in a two-dimensional and in a three-dimensional nozzle is given in Fig. 4-2 for $r_w/r^* = 10$.

The effect of the additional simplifications employed to obtain the values of η computed from Eqs. 4-6 and 4-11 is shown in the following sketch, where Sauer's value of η is compared with the abscissa of the intersection of the calculated sonic line and the actual throat (calculated from Eq. 4-2 or 4-7).

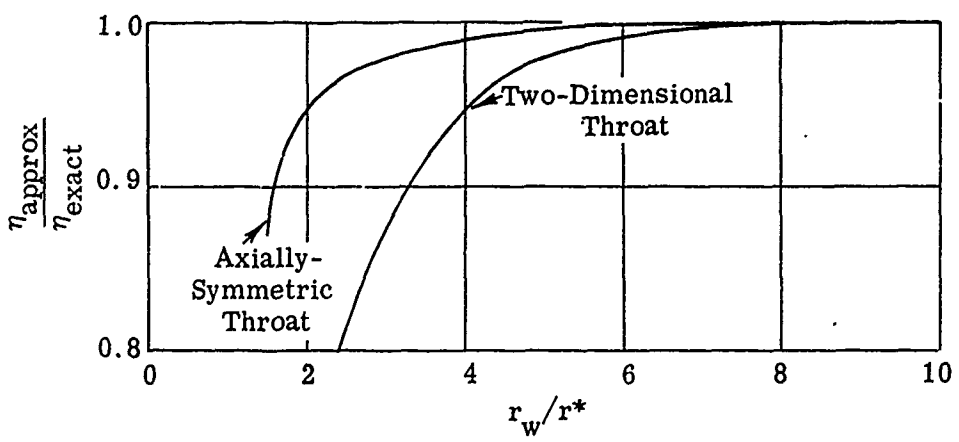

It may be seen that Sauer's approximation of $|\eta| = 2\epsilon$ (two-dimensional) or $|\eta| = \epsilon$ (three-dimensional) is very good for all but small values of r_w/r^*.

The sketch on page 226 shows the curve for which V = 0, i.e., along which the flow is axially aligned. Between the sonic line and the nozzle contour the flow is supersonic and accelerating, and hence the streamlines are diverging. One of the approximations to the actual throat conditions makes use of this fact and assumes that the flow is emanating from some point along the axis upstream of the throat (radial or source flow). The most common assumption is that the flow is sonic and parallel to the axis at the minimum cross section. This becomes more nearly true as the radius of curvature of the throat wall is increased. In the sliding nozzles of Ref. 133, to be discussed in Subsec. 4.4.3, the throat walls are made parallel and planar (i.e., with an infinite radius of curvature) in order to maintain a normal sonic line.

It is customary to make the throat wall radius of curvature from two-thirds to four times the throat height or diameter, though many values from a sharp throat (zero radius of curvature, Ref. 134) to the planar throat (infinite radius of curvature, Refs. 133 and 135) have been tested. A two-dimensional nozzle for a Mach number of 8 was designed and tested by Oliver and Nagamatsu (Ref. 136) in which the throat wall radius was 12 in. and the throat height 0.084 in. (see sketch on page 243). The large radius successfully eliminated from the throat side-walls the waves and flow separation which had been noted with more severe curvature (see Subsec. 4.5). The calculated mass flow through the throat is slightly in error when the sonic line is assumed to be rectilinear at the minimum-area cross section. The extent and nature of this error are discussed in Subsec. 6.2.4 and shown in Fig. 6-16. For values of the wall radius of curvature which are greater than 1.25 times the throat diameter (or height), the error is less than 1%.

4.2 The Subsonic Contraction

The design of the inlet contraction section in which the flow is accelerated to sonic speed is not critical. The contour shape cannot be obtained by straightforward calculation as in the case of the supersonic portion, since the differential equations are of the elliptic type rather than hyperbolic. The method of characteristics may no longer be applied. A solution to problems of elliptic or mixed elliptic-hyperbolic types has been developed by Dorodnitsyn (Ref. 137) and extended by Holt (Ref. 138). By means of integral relations, problems governed by non-linear partial differential equations may be solved with the aid of electronic computers. Holt has applied this method to the design of the transonic nozzle contour and also to an analysis of the flow field within a known contour. The method may be used for both two-dimensional and axisymmetric nozzles.

In order to check the assumption that the inlet shape is not critical, Armstrong and Smith (Ref. 139) were able to calculate three inlet profiles which would produce the same flow properties along the line M = 0.6 in the throat as those obtained from Eqs. 4-2 to 4-5. For the first contour they extended the basic supersonic equations through the transonic region. The result is curve 1 as shown in the sketch on the following page. It is not surprising that it becomes impractical for an inlet as it moves away from the throat, since the equations from which it is derived are first approximations even at the

throat itself. The second and third calculations were based on the Karman-Tsien approximation which derives a compressible flow from a corresponding incompressible one. The two solutions which were obtained are shown as curves 2 and 3 in the sketch below. It may be seen that the three profiles differ widely and yet each of them has the same slope and curvature at the point A and produces a flow of M = 0.6 along the dashed line shown in the sketch.

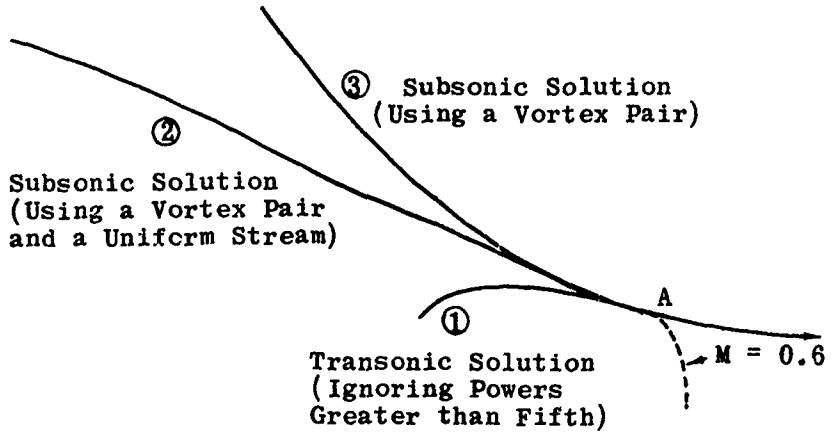

Source: Ref. 139

The authors conclude that if such widely differing profiles can produce almost identical flows near the throat, then it is safe to assume that provided the shape of the subsonic inlet is correctly chosen near the throat, the remainder of the inlet may be shaped arbitrarily without appreciably changing the transonic flow.

Oswatitsch and Rothstein (Ref. 140) also made calculations which led them to conclude that flows in the subsonic zone may exhibit marked differences in the inlet section and still produce the same flow field in the throat.

The subsonic contour is usually taken as a smooth curve such as an ellipse, a parabola, or an arc of a circle having the required radius of curvature at the minimum cross section.

4.3 Fixed Mach Number Nozzles

Fixed Mach number supersonic nozzles or effusors are designed to establish uniform parallel flow at a specific predetermined Mach number. The four main parts of such a nozzle block are shown in the first sketch of Subsec. 4. The subsonic inlet has been discussed in Subsec. 4.2 and the sonic throat in Subsec. 4.1. Nearly all methods of designing the straightening section are based on the method of characteristics, and in some cases the expansion section is included in this calculation. Since details of the basic method of characteristics are readily available in the literature, they will not be repeated here. For nozzles with two-dimensional symmetry, i.e., two plane walls and two contoured walls, Refs. 2, 6, 7, 94, 97, and 99 give all necessary details. In the case of axially-symmetric flow, the method of characteristics is given in Refs. 95, 96, and 98.

There are two general types of fixed Mach number nozzles: those that have rounded throats and those that have sharp throats (see sketch below).

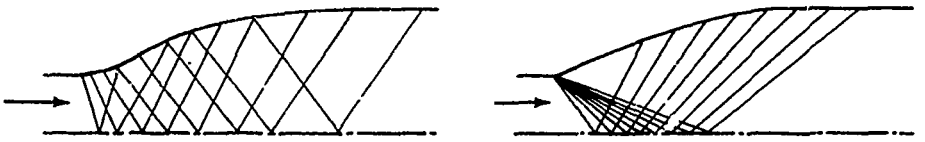

The former group may be subdivided into those whose expansion is the maximum Prandtl-Meyer angle associated with the fixed Mach number, and those whose expansion is less than the maximum. Sharp-throated nozzles usually employ maximum expansion angles and are the shortest possible contoured nozzles. The ultimate application of a supersonic nozzle is often a determining factor in the choice of its basic characteristics. Under flow conditions where the boundary layer may become a problem, a short nozzle is an advantage. When uniformity of flow in the test section is of paramount importance, the longer nozzle associated with less than maximum expansion is likely to be more satisfactory.

The methods of design differ also in their starting point. Some start the characteristics net at a sonic line considered as straight and perpendicular to the nozzle axis. Others start from a curved sonic line such as is shown in Fig. 4-1. In many others the flow up to the inflection point is considered as source flow emanating from a point on the nozzle axis. These three methods of starting the characteristics net are illustrated in the sketch below.

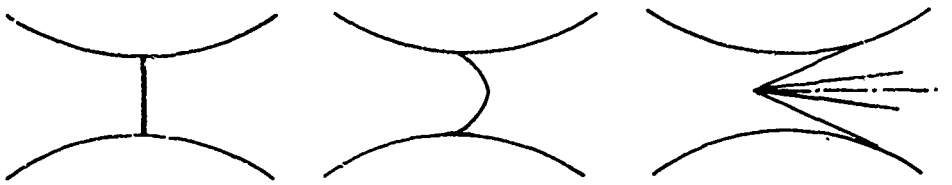

The flow field is usually fixed by the required expansion angle, i.e., it is turned until the last characteristic gives the required Mach number along the centerline. Almost the inverse process is sometimes employed, i.e., the Mach number distribution along the axis is specified and this determines the wall curvature. Such a method is outlined in Ref. 160. Most nozzles in common use are two-dimensional since they are easier to design and fabricate. Pressure fluctuations due to construction (or design) errors are distributed over the centerplane, and thus the source may often be located and the error eliminated (see Subsec. 4.7). Axially-symmetric nozzles for moderate Mach numbers are harder to design and fabricate, and have the added disadvantage that all irregularities are concentrated on the tunnel axis and are harder to trace to their source. However, axisymmetric nozzles have proven very successful for hypersonic research tunnels (see Subsec. 4.5).

732-359 O - 64 - 17

The actual design procedure may be wholly graphical, semi-graphical, or analytical. Many short cuts and helpful series of tables have been developed to assist in nozzle design. Rather than discuss them separately, the salient features of some of the best known methods that are readily available have been tabulated for easy reference. Table 4-1 analyzes design methods for two-dimensional, constant Mach number nozzles. Table 4-2 deals with two-dimensional nozzles designed for variable Mach number operation and Table 4-3 treats axially-symmetric nozzles. The type of throat, the design Mach number, and the basic design method are tabulated. A brief description of helpful tables and graphs is listed and a notation made where nozzles actually have been fabricated and tested. The listing includes as many types and different methods as possible; it is by no means either complete or comprehensive but merely a tabulation of readily available material from many sources. Further useful information may be found in Refs. 163-171.

4.3.1 Nozzles with Continuous Curvature

Many of the design methods referred to in the preceding subsection result in a discontinuity in curvature at the point of inflection. For a fixed-geometry solid-walled nozzle block, the discontinuities may not cause any serious problem as long as extremes of pressure and temperature are avoided. When the expansion angle is large the relaxation of the pressure gradient at the point of inflection may cause undue boundary-layer growth, and in critical cases flow separation may result. If pressure and temperature conditions are such that the value of γ may no longer be considered constant, the flow pattern itself may shift. The effects of such a shift are minimized where the curvature is both continuous and small.

In flexible-walled nozzles (see Subsec. 4.4.1), the presence of a discontinuity in the wall curvature may be more critical. Although the wall may be flexed accurately enough to include such discontinuities, their presence will cause unequal stresses in the plate. It is, however, more probable that the flexed wall will fair the curvature across the discontinuity and thus cause the flow pattern to differ from its theoretical design with consequent imperfections in the test-section flow. Therefore, it is desirable in this application to have a nozzle wall along which the curvature is continuous.

Evvard and Marcus (Ref. 145) have derived two auxiliary boundary conditions which will assure continuity of curvature in the design of two-dimensional symmetrical supersonic nozzles by means of the method of characteristics. The first condition is that the point of inflection must be upstream of the characteristic point. The second is that the first derivatives of the characteristics, $d\psi^+/ds$ and $d\psi^-/ds$, must be continuous functions. This implies that ψ^+ must first reach its test-section value at the characteristic point and that the axial Mach number gradient is continuous and approaches zero at the upstream vertex of the test rhombus.

The terminology and symbols are explained by the sketch on the opposite page, and the fact that the local flow angle, φ, may be expressed as

$$\varphi = \psi^+ - \psi^- .$$

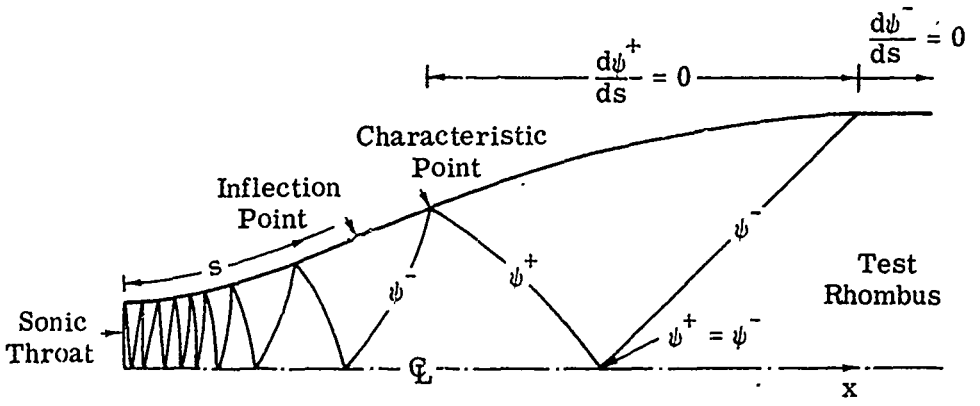

The use of this technique is exemplified in Fig. 4-3 which gives plots of ψ^+, ψ^-, and φ for a M = 4 nozzle. The flow is expanded from a sonic throat by the method of Ref. 148 until the curves of ψ^+ and ψ^- have the same slope. This gives the point of inflection. The ψ^+ is then faired from this value to the horizontal. The point at which it becomes horizontal is the characteristic point. The values of ψ^- and φ, determined from the characteristics net, will approach horizontal tangency at the test section as shown in Fig. 4-3. The value of the Mach number, both along the axis and along the nozzle contour, is also given in Fig. 4-3.

4.3.2 Multi-Nozzles

A multi-nozzle, consisting of a planar set of small nozzles mounted normal to the stream direction, is sometimes used to produce supersonic flow. A common form of multi-nozzle is a perforated plate which is from 0.25 to 1.0 in. thick. Each hole constitutes an individual nozzle which may be either two-dimensional or three-dimensional. An optimum hole shape has not been determined nor has an optimum array.

The chief advantages of the multi-nozzle are its very short length and the ease and speed with which the Mach number of a facility may be changed. However, the flow is far from uniform due to wake flows, jet impingement, and edge shocks whose origin and strength depend on the geometric relation between the outer nozzles and the duct walls. The use of multi-nozzles is restricted to tests in which the disadvantages of flow non-uniformity and large pressure losses are outweighed by the advantages of a wide range of Mach numbers at which data may be quickly and easily obtained.

Reshotko and Haefeli (Ref. 172) describe tests on four multi-nozzles: one two-dimensional nozzle designed for M = 3, and three axisymmetric nozzles with M_D = 3.0, 3.5, and 7. Three types of disturbance were observed in the flow field: oblique shock waves, strong corner shock waves, and wake flows. The oblique shock waves predominated at large exit turning angles, whereas wake losses predominated at small exit turning angles. The type of flow that

was observed is shown in the following sketch.

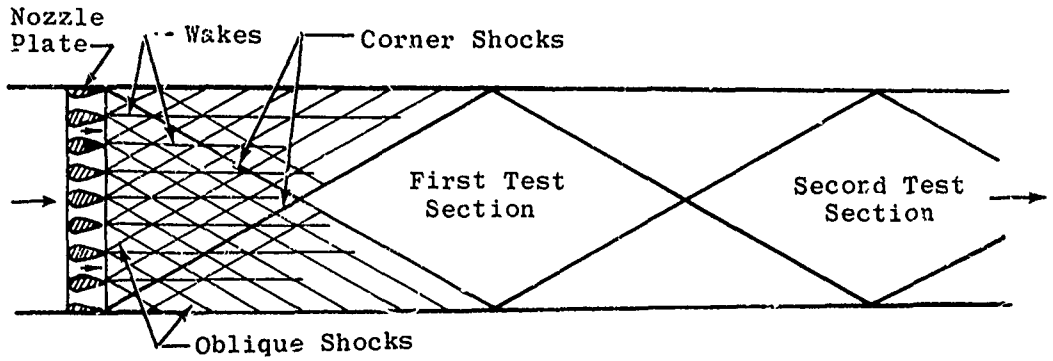

The most uniform flow was obtained in the second test section where the Mach number was about 60% of the design value with a maximum variation across the section of 4.5% of the average Mach number. The pressure recovery was as much as 60% less than that obtained with conventional nozzles. Kurzweg (Ref. 149) evaluated, by means of schlieren photography, the flow from a multi-nozzle designed for M = 2.86. Although the turbulence level was high, the over-all efficiency was equal to that of a conventional nozzle. Measurements made in two-dimensional and conical multi-nozzles (Ref. 173) showed substantial variation of the static pressure at any cross section downstream of the nozzle plate.

4.4 Variable Mach Number Nozzles

Fixed Mach number nozzle blocks for two-dimensional flow are relatively simple to design and fabricate, but as the size of the tunnel increases the weight of the blocks makes nozzle changing a difficult and time-consuming task. Furthermore, since the blocks are designed only for one specific Mach number, it is necessary to change them every time a change in Mach number is required. A series of fixed Mach number blocks usually has fairly large Mach number increments, whereas the use of a variable Mach number nozzle generally permits increments as small as may be desired. Furthermore, with the latter it is often possible to vary the Mach number continuously during a run and thus determine acceleration effects which cannot be studied in constant-velocity flow. To overcome these difficulties, many types of variable Mach number nozzles have been proposed. The salient features of several designs will be presented in this subsection together with some appraisal of their performance and advantages. Table 4-2 analyzes many references dealing with variable Mach number nozzles.

4.4.1 Flexible Nozzles

One of the simplest ways of varying the Mach number of a nozzle is by means of a pair of opposite flexible walls and a pair of stationary parallel walls. The contour of the flexible walls may be set by a system of jacks to provide flow of the desired Mach number in the test section. This system has the advantage that any Mach number within the design range may be obtained by proper positioning of the jacks, and furthermore the changes may be

made without dismantling the tunnel or disturbing the model. Since the change is relatively simple and fast, it is more economical of time and effort than changing heavy, fixed Mach number nozzle blocks. However, the setting must be extremely precise in order to provide uniform flow in the test section. To prevent excessive stresses in the plates, the total change is often made in small iterative steps. If this is accomplished manually, the operation may also be very time consuming. It is important that each setting have a high degree of repeatability, i.e., that the Mach number may be accurately predicted for each setting. Remote control mechanisms which set the profile to within ±0.001 in. are described by Leavy in Ref. 174. In a completely flexible nozzle the whole contour from inlet to test section is variable. The more commonly used semi-flexible nozzle may have either a fixed throat block or a fixed test section and usually has both. The blocks are connected by means of flexible plates. Since the thermal and elastic stresses are most severe in the throat region, many of the problems of the flexible nozzle are minimized by the use of a solid throat block. Where the throat is flexible, it is necessary to have a large radius of curvature in order to prevent overstressing. This implies a longer nozzle for the same Mach number than one with a sharper throat. Figures 4-4 and 4-5, taken from Ref. 174, show sections of a semi-flexible nozzle and jack system designed for Mach numbers from 1.6 to 3.5 in increments of ~0.2. The subsonic inlet terminates in hinged plates which are constrained by stiff springs to bear on the fixed-contour blocks forming the nozzle throat. The flexible plates are made of 1/2 in. thick steel. The jacks operate through crossheads and links at eleven points on the plate.

The sequence of jack movements is programmed on a coded, perforated tape which is fed through a standard Ferranti tape reader. Suitable decoder circuits are included so that only one station receives a signal at a time, and an interlock ensures that the tape reader cannot continue unless the preceding instruction has been carried out. By this method damage to the plates due to overstrain is avoided. The total time to change from one extreme Mach number to the other is about twenty minutes.

One of the major problems in the design of the flexible wall is the thickness of the plate. It must be thin enough to prevent overstressing when fully flexed, and it must be thick enough to prevent buckling or sagging between the jacks. Overstressing of the plates may also result from incorrect operation of the jacks. Although a thin plate is desirable for precise contours, it requires a greater number of jacks than a thicker plate and hence a more complex positioning system.

A second problem of the flexible-walled nozzle is the mechanical complexity of the jack system and its controls which must be constructed so as to have a minimum of backlash. The pressure seals between the fixed block and the movable plate also present technical difficulties. Although the total time to change from one Mach number to another is relatively short, the time rate of change of Mach number is too slow for acceleration tests. Installation costs may be so high that they outweigh the saving of time and effort in later use.

Insofar as the actual design of the nozzle contour is concerned, the discontinuity in curvature at the inflection point is much more critical for a flexible plate than for a solid nozzle block. As has been pointed out, the plate

will either smooth out the discontinuity and change the flow pattern or, if the shape is accurately maintained by a jack at the inflection point, the stresses will be severe. However, the basic characteristics method may be modified to ensure continuous curvature of the nozzle surface (see Subsec. 4.3.1). A form of modification which is particularly applicable to flexible nozzles is given by Riise in Ref. 154. The method gives control of the first and second derivatives of the wall slope both upstream and downstream of the inflection point, but does so at the expense of an increased nozzle length. Reference 154 gives tables and graphs which facilitate nozzle design and enable a final check to be made between the aerodynamic and thermoelastic properties of the designed plates. An order-of-magnitude estimate of the quality of flow to be expected may be derived in terms of the flow parameters. The procedure is intended primarily for a completely flexible nozzle, but has been modified for use in the design of nozzles which have solid throat blocks and are based on either a constant nozzle length or a constant expansion angle. Reference 154 also gives an example in which the plate contour, the spacing of the jacks, and the plate stresses are computed for a nozzle to give Mach numbers from 1.3 to 4.8.

4.4.2 Scissors-Type Nozzles

The Mach number may also be varied by the relative movement of two solid nozzle blocks. Careful design ensures flow of reasonable uniformity for a limited range of Mach numbers, but it is naturally not of as good quality as the flow in a nozzle designed for a unique Mach number. A nozzle having a 10 × 14 in. geometric test section and designed to operate at Mach numbers from 2.7 to 6.3 is described briefly by Eggers and Nothwang (Ref. 151). The tunnel is two-dimensional and the nozzle blocks are continuous, rigid, built-up steel structures which include the inlet, the effusor, and the diffuser sections. Mach number variation is effected by two jacks only: one at the sonic throat and one at the diffuser throat. The jacks at the first, or sonic, throat are connected through a chain drive to a common motor so that the symmetry of the throat is maintained at all times. The jacks at the second, or diffuser, throat are similarly connected to another common motor. A sketch of the nozzle assembly is shown below.

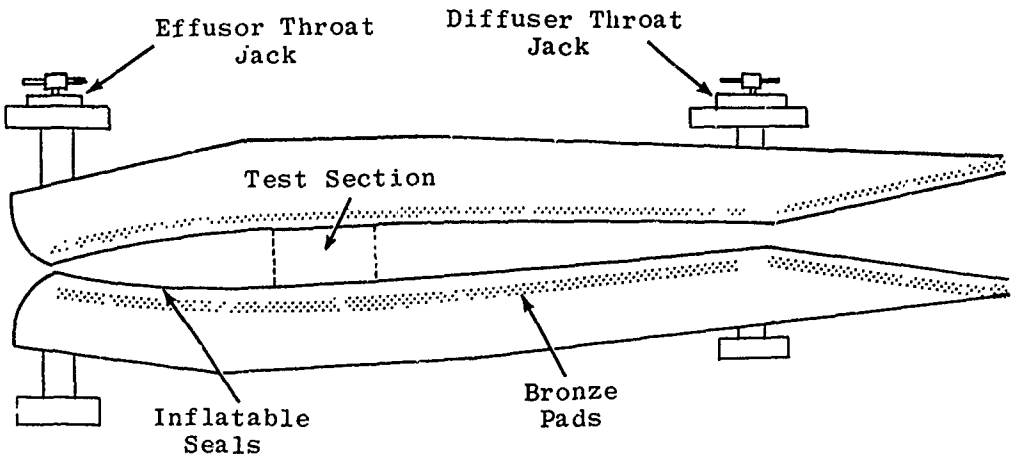

This arrangement allows efficient use of available power, since the supersonic flow may be established at the lowest supersonic Mach number and the nozzle then adjusted to give the required Mach number. At the same time the second throat may be adjusted to give the most efficient diffusion. Since Mach number adjustment is obtained by the operation of a single control, it is possible to make tests under conditions of acceleration.

Pressure surveys reported in Ref. 151 show that the flow is sufficiently uniform for general test purposes within a region about 10 inches in length and 4 × 4 inches in cross-sectional area. Thus the usable test section is about 11% of the geometric one, giving a rough estimate of the penalty incurred by using a surface not accurately designed for a specific Mach number. The Mach number variation along the tunnel centerline is within ±1% of the design value at the lowest Mach number and within ±0.5% at intermediate Mach numbers, and has a maximum variation of ±2% at the highest test-section Mach number. The variation in flow direction along the tunnel centerline is less than ±0.2 deg at all Mach numbers.

The major problem in a tunnel of this type is the seal between the movable blocks and the stationary walls. In the above case the seals were of rectangular rubber tubing inflated to 100 psig. Since neither the blocks nor the walls may be made perfectly planar, bearing pads of bronze are attached to the nozzle blocks as shown in the sketch on the previous page.

4.4.3 Asymmetric Sliding-Block Nozzles

By means of asymmetric sliding blocks it is possible to produce a variable Mach number flow of reasonably good uniformity without the use of flexible walls. Such a nozzle is shown in the sketch below.

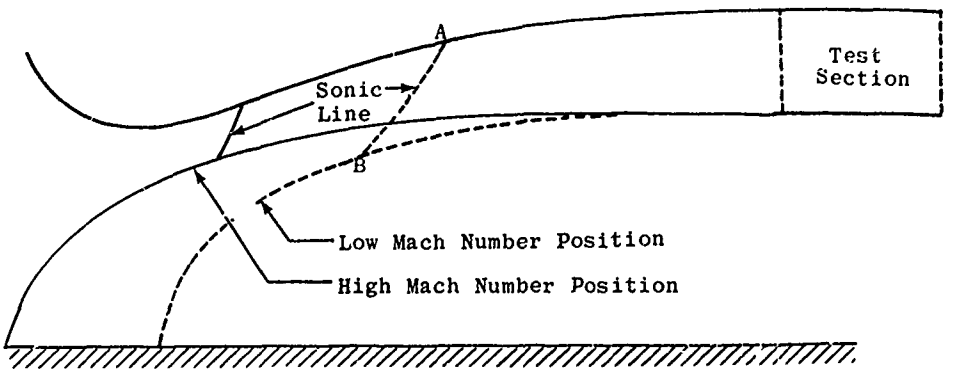

In this case the lower wall is translated parallel to the direction of the free stream in the test section. As the block slides, the throat area changes while the test-section area remains constant and hence the Mach number varies. Aerodynamically the problem reduces to contouring the walls in such a way as to produce reasonably uniform flow for all positions of the lower wall. Three methods of doing this will be discussed in this subsection.

The structural and mechanical advantages of such a nozzle are readily apparent. It avoids the possibilities of overstress and deformation which may occur with flexible nozzles. It also has the advantage that the Mach number may be varied during a run. This fact also permits a lower starting compression ratio since the tunnel can be started at the low Mach number position and the sliding block later moved to give a higher Mach number. This operation also reduces the starting shock loads on models and model supports.

The major disadvantage of such a nozzle is that it is about twice as long as a fixed nozzle of the same exit Mach number, since all expansion waves originate on one wall and all cancellation is accomplished on the other wall. This increased length, coupled with the large radius of curvature of the lower wall, causes a relatively thick boundary layer which has a tendency to separate.

Syvertson and Savin (Ref. 153) developed two methods for designing asymmetric supersonic nozzles for which the calculated exit flows are uniform over a wide range of Mach numbers. One method applies at Mach numbers less than about 3, and the other at Mach numbers greater than 3.

In the first case, the method is noniterative and comparatively simple. The first step is to construct a contour for a Mach number slightly higher than the lowest design Mach number. These calculations are based on a curved and sloping sonic line as shown in the sketch below. Starting from the sonic line AB, using the equations of Subsec. 4.1, the flow field is determined along AC, from which line a characteristics net is constructed. Constant curvature

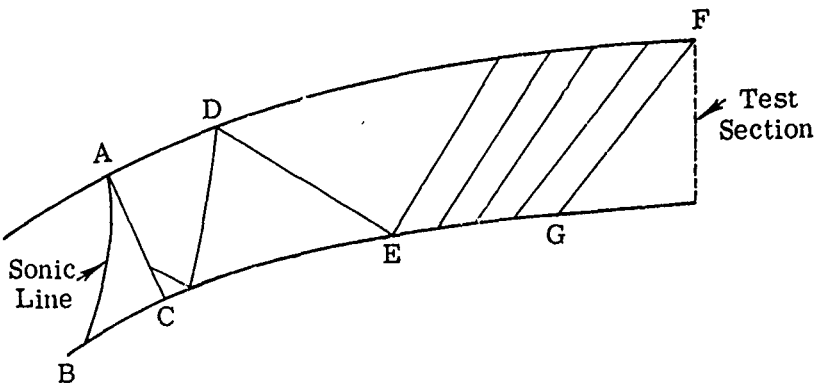

is maintained in the upper wall until Prandtl-Meyer flow is obtained at D, and in the lower wall to the point E. It is then gradually decreased to zero at G where the design Mach number is reached.

The second major step is to calculate the flow field that will exist with the contours of step 1 when the sliding block is translated to give a test section Mach number slightly less than the maximum design Mach number.

The third step is to determine contours in the region bounded by the sonic lines at the high and low Mach number positions. These contours must produce a flow field to match the high Mach number field starting from AC. In the low Mach number nozzle this region upstream of AB forms the subsonic inlet and therefore, except at the minimum section, the contour is not critical (see Subsec. 4.2).

These three steps, which are worked out in detail in Ref. 153, will produce uniform flow at the two limiting Mach numbers. It has been found by actual tests that the flow also has a high degree of uniformity at intermediate Mach numbers and at Mach numbers slightly above the high and slightly below the low design points.

Experience gained by designing and testing many nozzles by the above procedures has shown that it is desirable to have the throat move continuously upstream along both walls as the exit Mach number is increased. This condition is satisfied when the wall contours in this region have a finite radius of curvature everywhere and no inflection points. It is furthermore required that the local radius of curvature of the lower wall shall always be sufficiently less than that of the upper wall to ensure a unique throat (minimum section) for each position.

Practical difficulties limit the use of this procedure to Mach numbers below 3. An averaging procedure is given in Ref. 153 for the design of high Mach number asymmetric nozzles. The part of the contour determined by the characteristics net is computed for the highest Mach number. The lower block is then moved to give the required throat area for the lowest Mach number, and using the contour already computed, the characteristics net for the lowest Mach number is obtained. Corrections are made to the contour of the flow-straightening section in order to give uniform exit flow. This process is repeated for two intermediate Mach numbers, and finally a mean contour is selected from the four that have been constructed. Although the resulting design does not give a high degree of uniformity over the entire Mach number range, experience has shown that flow deviations of as little as a quarter of a degree may be obtained by this method.

The two methods just outlined use a curved contour at the throat and a curved sonic line. In contrast to this, Burbank and Byrne (Ref. 133) give details of a design procedure based on a throat of zero curvature and the associated straight sonic line perpendicular to the throat walls. The stationary upper block (see the sketch below) accordingly had a straight section along which the sonic line moved as the lower block was translated in the flow direction. A unique throat was thus created at each Mach number setting.

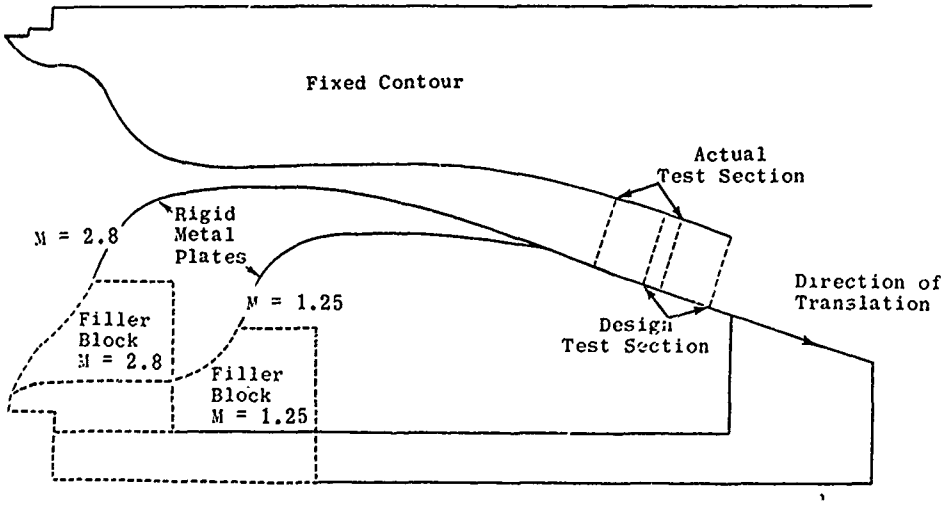

The method of characteristics was used in the design of the contours which had the following features: the first derivative of the contour was smooth and continuous; there were no inflection points and no compression waves. Reference 133 not only gives full details of the design procedure, but includes the coordinates for a pair of nozzle blocks for the design Mach number range 1.25 to 2.8. Through this Mach number range the longitudinal translation of the lower block was equal to slightly over twice the test-section height. Calibration tests gave the Mach number range as 1.27 to 2.75. At M = 2.75 the nozzle length was about five times the test-section height. In calibration tests the flow direction was shown to be accurate to ±0.10 deg and the Mach number to ±0.01.

4.4.4 The Tilting-Plate Nozzle Adapter

Fixed Mach number nozzle blocks may be adapted for variable Mach number flow by means of a tilted plate at the test-section entrance. Such an adapter is described by Drougge (Ref. 175) and is shown in the sketch below.

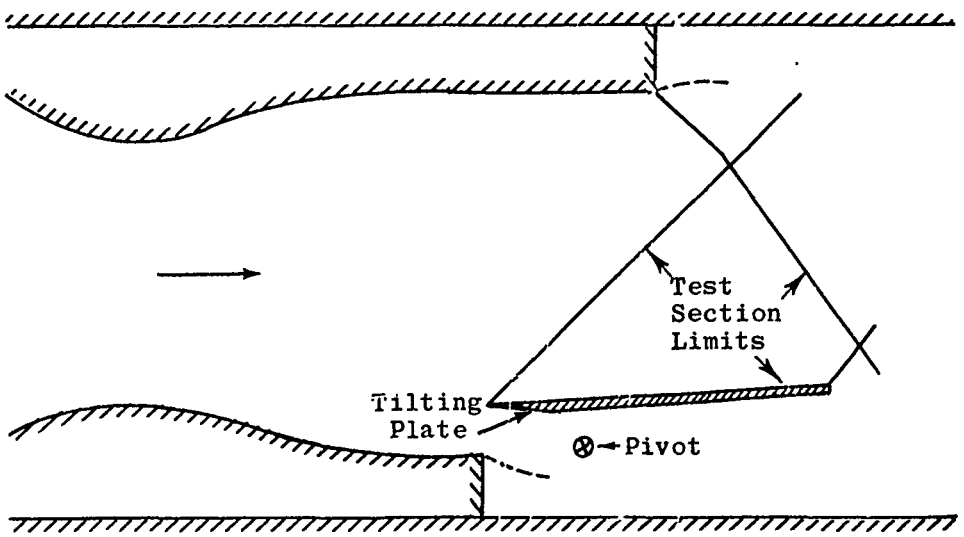

The plate has a sharp leading edge and spans the tunnel. As long as the shock is attached, the area between the shock and the plate will constitute a test region of uniform flow. The extent to which the velocity may be varied is strongly dependent upon the original Mach number. Continuous adjustment of the plate angle allows the Mach number to be varied during a run and may, under some circumstances, achieve "acceleration" conditions. To prevent choking, it is necessary to relieve the test section in the region of the plate leading edge and also where the leading edge of the shock will strike.

4.4.5 Plug-Type Nozzles

Silverstein, of the Flight Propulsion Research Laboratory of NASA, in an effort to avoid some of the disadvantages of the flexible-walled nozzle, proposed what is now known as the plug nozzle. This nozzle consists of a fixed-contour supersonic nozzle with a symmetrical body, or plug, mounted in the

throat. The plug may be either two-dimensional, or in the case of an axisymmetric tunnel, a body of revolution. Its shape may be calculated by the method of characteristics but is more often determined experimentally. A typical shape is shown in the sketch below.

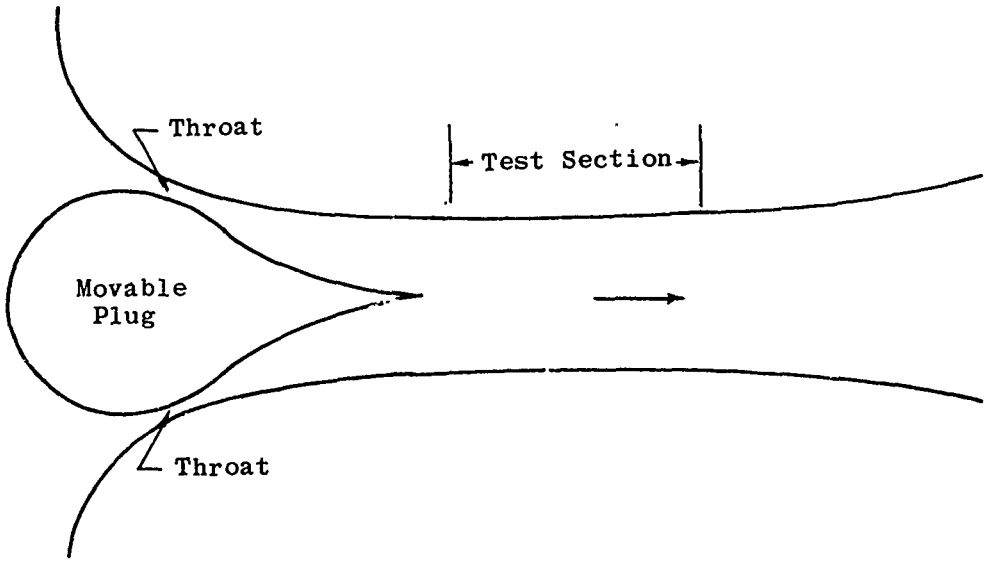

The Mach number may be varied through a considerable range by moving the plug and thus changing the effective throat area. The above sketch shows the plug in position to yield the minimum throat area, i.e., the maximum Mach number. Provided that the shape has been carefully chosen the test section may be free of adverse pressure gradients. The use of such a configuration is quite limited because of disturbances which traverse the test section. These disturbances consist mainly of a viscous wake from the plug and of shock waves emanating from its tip.

Two methods of obviating the wake have been tried. The first was to cut boundary-layer suction slots in the tail of the plug. The suction decreased but did not remove the wake. The second corrective method was to split the plug in two similar parts and apply them to the parallel walls in the throat region. Such bosses are often known as Menard inserts. In Ref. 150, Amick, Harrington, and Liepman describe tests of Menard inserts in fixed Mach number nozzles for M from 1.5 to 3.0. The inserts were designed by means of modified area-ratio considerations, since the contours are neither strictly two-dimensional nor axisymmetric, and therefore are not easily amenable to analytical treatment. Reference 150 concludes that at low Mach numbers the Menard inserts are effective, and that their shape is not critical. At a test Mach number of 1.5 the inserts increased the Mach number by 10% without appreciable loss in uniformity. At Mach numbers above 2 the design of the insert is more critical and must be achieved by trial-and-error methods. The possible increase in Mach number is less than 10%, and flow deterioration in tests at M = 2 was more pronounced than it was at M = 1.5.

4.4.6 Slotted Nozzles

Slotted nozzles are used to give rapid variation of the Mach number in the low supersonic and transonic regimes. The Mach number variation is produced by bleeding by-pass air from the stagnation chamber to a plenum chamber surrounding the test section. A tunnel using such a nozzle is described by Little and Cubbage (Ref. 176). The by-pass ducts contain quick-opening valves and flow-metering orifices. The rate of Mach number change is dependent primarily upon the rate of opening or closing the valves that control the bleed flow. For a 2% bleed flow the Mach number was reduced 5% in 1/8 sec, and with a 10% bleed the reduction was 30% in 1/4 sec. Increases in test-section Mach number accompanied a diminishing bleed flow.

The bleed air is allowed to flow in longitudinal slots in one pair of nozzle walls, the other pair of walls being solid. One design of a slotted wall is shown in the sketch below.

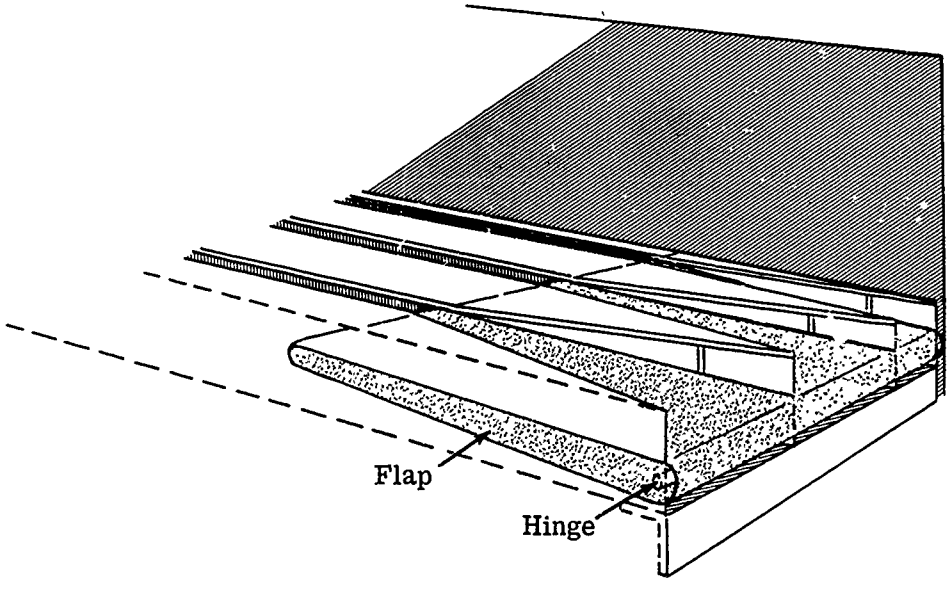

Although the geometry of the slot depends on many factors, certain basic guidelines have been set down in Ref. 176. It is suggested that the slot length should be twice the test-section height and the slot width such as to make the open area about 1/14 to 1/7 of the total area of the test-section walls. One of the most critical regions in the nozzle design is the diffuser entrance where the slot flow merges with the main flow. When the test-section length is increased at the expense of the slot flow re-entry length, the pressure losses are increased. Various forms of boattailed wall plates were tested by Little and Cubbage in terms of the efficiency of the total pressure recovery. They concluded that the total pressure losses in the re-entry region were lowest when the wall plates ended abruptly rather than when they were boattailed. Flaps (see sketch above) of various shapes were also tried. The flap is hinged at the downstream end and, when deflected, changes the channel cross-sectional area. Both the flow diffusion and the test-section Mach number distribution were found to be optimum when the flaps were deflected so that their upper surface was parallel to the tunnel centerline.

4.5 Hypersonic Nozzle Design

Although nozzles to produce hypersonic flow may be designed by most of the methods outlined in Subsecs. 4.3 and 4 4, simpler designs are very often used. Not only does the characteristics method become unduly tedious as the characteristics net is elongated, but the error in graphical methods becomes relatively greater. In addition to the difficulties of obtaining a potential-flow contour, there is also the problem of correcting the contour to account for boundary-layer thickness (see Subsecs. 2.4 and 4.8). The large temperature difference between the flow in the throat and that in a high Mach number test section not only involves real-gas effects but also gives rise to large variation in heat-transfer rates along the nozzle. For these reasons, the design of hypersonic nozzles either has been very much simplified or has included viscous corrections step by step as the contour is defined. Real-gas effects are usually concentrated in the throat region and may be taken into account by an adjusted source flow. The simple nozzles lend themselves easily to the study of flow problems such as heat transfer and real-gas effects. Where models are to be tested to obtain force or pressure data, a conventional nozzle is required to produce the uniform flow over the model. Examples of both types of nozzles will be given.

A simple two-dimensional wedge nozzle with a rounded throat is described in Ref. 152. This nozzle produces a shock-free, almost isentropic expansion having a test-section Mach number distribution comparable to that obtained by conventional nozzles at lower Mach numbers. The use of small wedge angles inhibits the separation which is often a problem in conventional nozzles requiring a high turning angle to give the necessarily large area ratio within a reasonably short nozzle length. The Mach number variation is effected by rotating the blocks about the center of the small circular-arc throat contour. Although the test-section flow is not parallel and uniform, it so closely approximates source flow that it is easily amenable to theoretical analysis. The cooling of the nozzle is discussed in Subsec. 4.6.

The design of a throat of large radius of curvature and small expansion angle is described in Ref. 136. A sketch of the throat is given below.

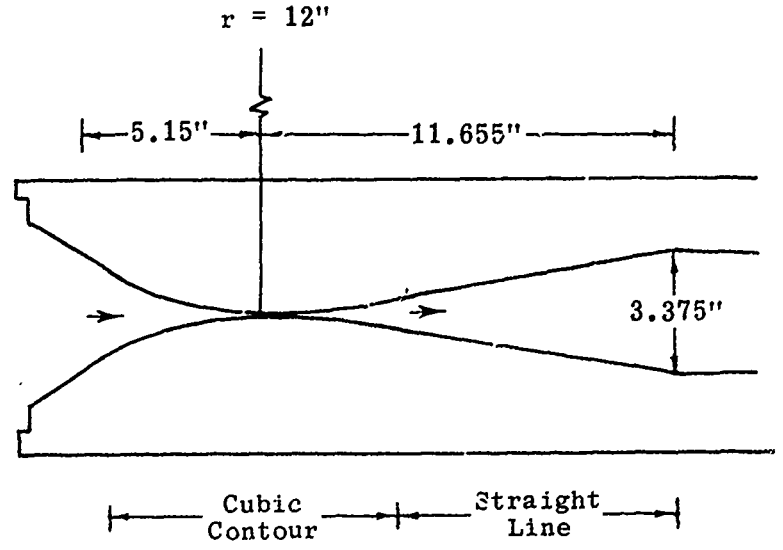

The flow along the expanding section was investigated experimentally and found to correspond very closely to radial flow and to be free of any sidewall waves emanating from the throat. The exit Mach number was about 5.5. The satisfactory throat shape having been confirmed, an exit section for the nozzle was designed by the method of characteristics to give a test-section Mach number of 8.

A small conical nozzle which proved to be a useful research tool is described by Hill, et al (Ref. 159). The test section Mach number is 10 with nitrogen as the working fluid and 16 with helium. A sketch of the nozzle assembly is given below.

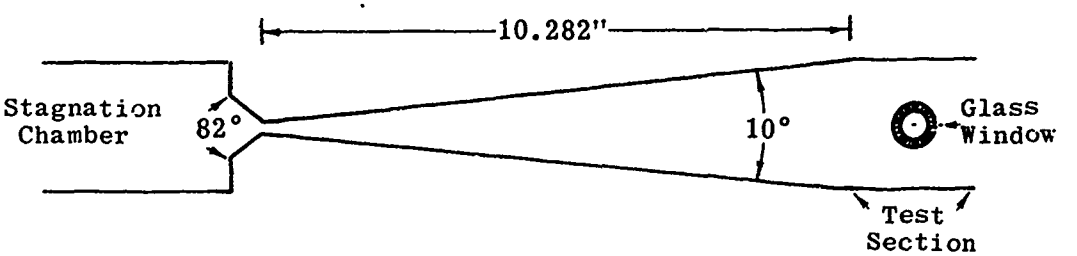

The conical nozzle has the following advantages:

1. The relatively small expansion angle provides an essentially constant Mach number at every cross section.

2. Its comparatively short length minimizes viscous and heat-transfer effects. The boundary layer grows uniformly resulting in a symmetrical flow pattern.

3. The solid block that constitutes the throat provides an excellent heat sink and minimizes geometric changes in the throat due to expansion.

4. The nozzle may use any convenient streaming gas, e.g., air, He, N, or CO_2 since the contour is not dependent on the value of γ.

5. The construction is simple, quick and inexpensive.

The nozzle has the following disadvantages:

1. The circular cross section not only restricts window size but complicates the interpretation of optical measurements.

2. If a constant-area test section is added (as in the sketch), shocks arise at the junction of cylinder and cone, thus restricting the usable test area.

Since the current trend is toward higher Mach number testing, much effort has been put into the design of hypersonic nozzles producing flow whose properties are at least as predictable as those in the supersonic regime.

Erickson and Creekmore in Ref. 185 present extensive charts of the thermodynamic properties of air and show how they may be employed to design

a hypersonic nozzle. Ideal and real-gas axisymmetric contours are calculated for a Mach number 12 nozzle operating at a stagnation pressure of 300 atm and a stagnation temperature of 2790°R. The cross section of the real-gas contour is less in the throat region than that of the ideal gas but is larger than the ideal beyond the inflection point. The maximum deviation occurs in the test section where the real-gas contour is 10% greater than the ideal contour. No correction is made to account for the boundary layer.

A method similar to that above is used by Johnson (Ref. 177) to design a nozzle for a Mach number of 17 with nitrogen as the working fluid. It is noted that in this case the radius of the axisymmetric nozzle exit must be increased by 9% to account for real-gas effects. The complete computer program (in Fortran language) is presented in this reference together with a modification by which the method may be applied to gases other than nitrogen.

The hypersonic nozzles currently in use in the NOL facility were designed by a method which incorporates three well-known procedures. The Friedrichs method is used for the throat region, a lattice-point characteristics network for the intermediate section, and the straightening region is based on simple wave theory. The contour is specified by a Mach number distribution along the nozzle centerline and by the dimensions of the nozzle exit. The method, which is suitable for fixed-block, semi-flexible, or flexible nozzles, is easily adapted for high-speed computers. This procedure is fully documented by Squires, Roberts and Fisher (Ref. 160) and was adapted to axisymmetric nozzle design by Thickstun, Schroth and Lee (Ref. 161). This latter reference gives a description of the nozzle construction as well as all the necessary equations for its design. A nozzle designed by this method produced satisfactory flow characteristics and achieved the design Mach number of 8 within 1.3%. Pressure measurements indicated that disturbances do indeed focus on the centerline as one would anticipate. The disturbances in this case were traced to their source and eliminated. Boundary-layer corrections were included in the design (see Subsecs. 2.4 and 4.8).

The above method of nozzle design has been further amended by Enkenhus and Maher (Ref. 162) to take into account the properties of high-temperature gases. The gas is assumed to expand isentropically and to remain in thermodynamic equilibrium. Turbulent boundary-layer growth and convective heat-transfer rates are found from numerical integration of the Von Karman momentum integral equation. The design method has been coded on an IBM 704 computer and has been used to investigate the performance characteristics of a family of nozzles having exit Mach numbers from 11 to 19 for supply pressures from 50 to 500 atmospheres and supply temperatures up to 7500°K.

4.6 Nozzle Cooling

The heat-transfer rate at the nozzle throat becomes extremely high in hypersonic tunnels where elevated stagnation temperatures are required either to simulate atmospheric Reynolds numbers or to obviate condensation of the working fluid. Many methods of alleviating the heating problem and the configuration changes associated with it have been suggested. The most attractive seems to be that of transpiration cooling. The porous surface through which transpiration occurs provides an effectively large wetted area for heat

transfer. Furthermore, the characteristics of the boundary layer are radically changed by the coolant, significantly reducing both the skin friction and the heat transfer.

Bernicker (Ref. 178) describes an experimental investigation in which both helium and air were injected into the boundary layer through a porous strip located in the subsonic region of a two-dimensional nozzle. Such a technique gives the maximum cooling effect in the throat where the heat-transfer rate is highest, and also inserts the porous strip where it is least likely to present any structural problem. Test results indicate an appreciable reduction in the equilibrium temperature compared with the zero-injection case. The effect of helium injection not only is substantially greater than that of air for a given coolant weight flow, but also persists for a greater distance. The cooling effect of helium even at moderate injection rates is felt downstream for a distance of about twenty times the width of the porous strip. With air at the same rate of flow, the cooling effect reaches about twelve times the strip width.

The results for two positions of the strip have been correlated in terms of a wall cooling parameter, θ, and an injection parameter, F. It is shown in Ref. 178 that for constant F,

$$\theta = \theta^* \left(\frac{x}{x_p} \right)^{K\, F^{3/4}} \tag{4-12}$$

where

$$\theta = \frac{T_w - T_t}{T_{aw} - T_t}$$

T_{aw} = adiabatic wall temperature, zero injection

x = distance along the nozzle measured from the upstream edge of the strip

x_p = width of porous strip

K = an empirical constant associated with the coolant

= 0.032 for air

= 0.110 for helium

F = injection parameter = injection ratio $\sqrt{\text{Reynolds No. of coolant}}$

$$= \frac{(\rho v)_w}{(\rho v)_\infty} \sqrt{Re_c}$$

and

$\theta^* = \theta$ at $x = x_p$, a function of F only.

The values of θ^* in terms of F, calculated from Eq. 4-12, are given in Fig. 4-6 together with some of the test data. The experimental data lie within ±15% of the calculated values.

Water cooling of a small wedge nozzle at hypersonic Mach numbers is described in Ref. 152. The water flows in transverse tubes as shown in the sketch below. The flow in each tube may be separately controlled in order to provide a means of assessing the heat-transfer characteristics along the wall. The nozzle itself is discussed in Subsec. 4.5.

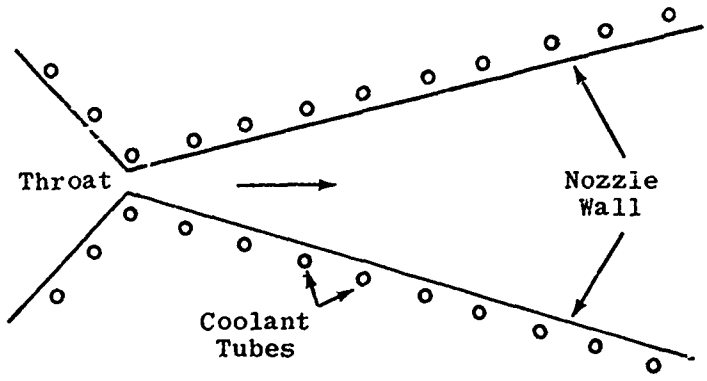

Pasqua (Ref. 179) made analytical studies of the problems associated with the expansion of plasma with extremely high temperature and pressure through the subsonic section and throat of a hypersonic wind tunnel. Graphs are given from which the heat flux to the nozzle wall may be read in terms of the stagnation pressure and temperature in the presence of either laminar or turbulent boundary layer. It is shown that a laminar boundary layer effectively insulates the wall from the hot plasma whereas the turbulent boundary layer promotes extreme rates of heat transfer. The thermal radiation is shown to be a major contributor to the heat flux in the assumed spherical plenum region and hence it is advisable to maintain the effective radius of this section as small as other considerations will allow. The analysis also shows that transpiration cooling is capable of handling all convective and radiative heat loads but may present the practical problems of coolant pumping and coolant compatibility with the plasma stream. A combination of film cooling on the inner surface and conductive cooling behind the walls could also be used satisfactorily, according to the calculations.

4.7 Nozzle Calibration

The two basic requirements for a good nozzle are that it shall have a uniform Mach number distribution over the test region and that the flow shall be both shock-free and parallel to the tunnel axis.

The Mach number is usually determined by extensive pressure surveys, static pressure measurements being taken in both horizontal and vertical planes over the test rhombus and on the contoured walls of the nozzle and test section. Pitot-static measurements are also made. The Mach number is taken from the flow tables. The Mach number, and to some extent the flow inclination, may also be checked by means of calibrated cones with pressure taps.

732-359 O - 64 - 18

The flow quality is best determined by optical methods. Weak shocks may often be traced to their sources, especially in the case of two-dimensional nozzles, and the roughness or irregularity which is the cause can then be removed. Very fine lines scribed on the contour perpendicular to the flow direction cause Mach shocks from which the flow alignment, as well as the Mach number, may be checked. The Mach number is also determined from schlieren or shadow photographs of wedges and cones with their attached bow shocks. Measurement techniques, associated equipment, and data reduction are treated fully in Section 20 of the Handbook (Ref. 13).

4.8 Boundary-Layer Correction of Nozzle Contours

The boundary-layer corrections discussed fully in Subsec. 2.4 may also be applied to contoured nozzles. In two-dimensional nozzles, corrections are applied step-by-step along the contoured walls. Plane side walls are often set at a small angle to allow for the calculated displacement thickness of the boundary layer in the test section. When optical flow-measuring techniques are employed, it is better to leave the side walls parallel. In this case either the correction for the side walls is neglected or it is combined with that for the contoured walls. The "corner-effect" in two-dimensional nozzles is customarily neglected in boundary-layer corrections; Ruptash (Ref. 180) has shown that the radius of the corner fillet is of the order of the boundary-layer thickness.

In many cases it is assumed that the boundary layer has zero thickness at the throat. Tucker (Ref. 100) uses the source of the radial flow that most closely represents the flow through the throat as the zero point of boundary-layer development.

Most boundary-layer corrections are based on δ^*, the displacement thickness (see Eqs. 2-173 and 2-174). This is considered the most suitable criterion, since it satisfies the requirement of mass-flow continuity and gives the required Mach number. A second criterion for nozzle flows, pointed out by Tucker, is that the test section should be free of expansion waves and shock waves. To satisfy this condition the contour correction logically should be based on the interaction of the Mach waves and the boundary layer. A simplified sketch of the interactions is shown below.

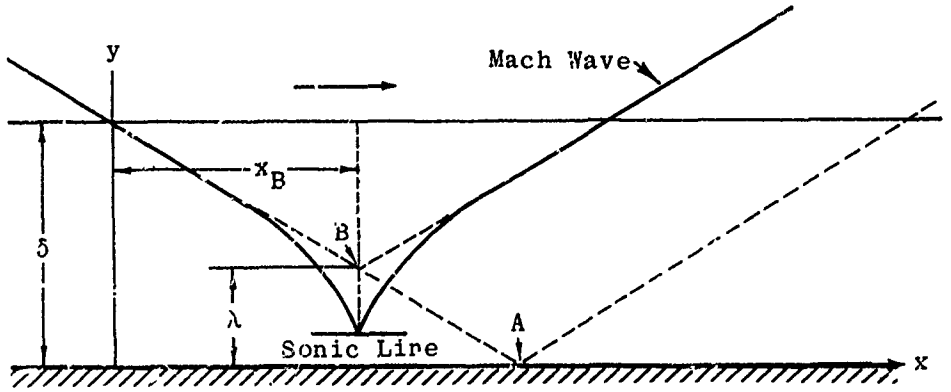

It may be seen from the sketch that λ/δ at any point is given by

$$\lambda/\delta = 1 - \frac{1 - x_B}{\delta\sqrt{M^2 - 1}} \tag{4-13}$$

When changes in the slope of the Mach lines due to penetration of the boundary layer are neglected, a reflection thickness, λ, may be defined as the displacement of the reflection point from the surface, or as the distance from the "effective" reflection point to the surface. The value of x_B is obtained by the integration of

$$\frac{d(y/\delta)}{dx} = -\frac{1}{\delta\sqrt{M^2 - 1}} \tag{4-14}$$

A comparison of λ/δ and δ^*/δ for Mach numbers from 1 to 10 and a 1/7 power velocity profile is shown in Fig. 4-7 for the case of zero heat transfer.

The values of λ near M = 1 are of doubtful accuracy since the assumption of no change in the sonic line due to shock impingement is no longer valid in this region.

Within the accuracy of the skin-friction values which enter into the computation of δ, there is reasonable correspondence between λ and δ^*, and thus both requirements of the flow are simultaneously approximated. At present there is insufficient knowledge of the behavior of the skin friction under conditions of varying pressure gradient to allow any choice to be made between λ and δ^* as a criterion for the boundary-layer correction of a contoured nozzle.

The boundary-layer thickness in a rocket nozzle is discussed in Subsec. 6.2.3. Much of the information there is also applicable to a wind-tunnel nozzle.

4.8.1 Boundary-Layer Correction in Hypersonic Nozzles

In moderate Mach number nozzles, the boundary-layer correction (see Subsec. 2.4) is usually small compared with the dimensions of the core of potential flow. Hypersonic nozzles are generally designed on a relatively small scale (due to power requirements) and since the boundary-layer thickens rapidly with increasing Mach number it may easily occupy a large part of the cross-sectional area. Elevated stagnation temperatures are usually required to prevent condensation in the test section. The large differential between the high temperature in the throat and the low one in the test section gives rise to great variation in the heat-transfer rates between the gas and the walls. It becomes evident that the viscous effects may no longer be regarded as corrections to the potential flow, but must be taken into account in the basic flow equations.

The general boundary-layer equations which include the effects of pressure gradient and heat transfer will be presented and discussed fully in

Sections 13 and 14 of the Handbook. However, it is the intent in the current section to present sufficient information to enable the reader to include boundary-layer corrections to nozzle designs.

The necessary equations for turbulent boundary-layer development in the presence of a pressure gradient but with no heat transfer (Ref. 100) have been given in Subsec. 2.4.

Persh and Lee (Refs. 182 and 183) have refined the methods of calculating turbulent boundary layer by including the variation in skin friction due to heat transfer. The effects of pressure gradient have not been included. However, it is felt that their influence on the skin friction and on the velocity profile will be relatively small. Both the two-dimensional and the axially-symmetric cases are fully worked out by Persh and Lee. Table 4-4, taken from Ref. 183, presents values of δ^*/δ and θ/δ for Mach numbers from 0 to 20, $(T_w - T_e)/T_\infty$ from -10 to +10, and n = 5, 7, 9, and 11. In the foregoing, T_w is the actual wall temperature, T_e is the equilibrium wall temperature, and n is the velocity exponent (see Eq. 2-166).

Reference 182 gives many graphs of boundary-layer thickness and nozzle temperature for Mach numbers of 5 and 8 with stagnation pressures of 10 and 100 atm, stagnation temperatures of 900 and 1500°F, coolant rates of 10, 100, and 1000 gals/min, and heat-transfer rates from 67 to 1400 BTU/sec. The method of these calculations assumes that the boundary layer is not an appreciable fraction of the nozzle diameter and hence the method should be used with caution where such a condition is violated.

Van Driest (Ref. 184) gives turbulent skin-friction and heat-transfer coefficients for a flat plate as a function of Reynolds number for M from 0 to 10 and T_w/T_∞ from 1.0 to T_t/T_∞ at each Mach number. The Prandtl number is assumed to be unity. Equations are given from which the boundary-layer thickness may be calculated.

Enkenhus and Maher (Ref. 162) have made boundary-layer calculations which include real-gas effects. The factors taken in account are:

1. The change in the thermodynamic and transport properties of air at high temperatures.

2. The diffusion of atomic species which recombine and release additional heat to the wall.

3. The effect on skin friction and heat transfer of a highly cooled wall.

Since the formulas used are of a semi-empirical nature, the results must be treated with some reservation until they have been experimentally justified. In particular, it is known that the boundary-layer thickness is very sensitive to the skin-friction law employed. IBM computer calculations have been made by this method for seven axially-symmetric nozzles for M = 11, 15, and 19 with stagnation temperatures up to 6000°K. The nozzle contours with associated

boundary-layer thicknesses are given in tables and graphs. The boundary-layer thickness near the throat was found to be almost independent of the arbitrary initial value assigned to it. A typical value of the thickness at the throat is a few thousandths of an inch, while at the exit it has increased to several inches. The boundary layer grows almost linearly with distance from the throat. Test results gave the following correlation for the displacement thickness at the nozzle exit:

$$\delta_e^* \text{ (ft)} = 1.45 \times 10^{-6} \, (T_t)^{3/4} \, (\ell)^{4/5} \, (p_t)^{-1/3} \, (M_e)^{5/2}$$

$$= 1.45 \times 10^{-6} \, \alpha$$

where ℓ is the length of the nozzle from throat to exit. The test range of α was from 2.5×10^5 to 10^6.

Intentionally Blank

Table 4-1

Design of Two-Dimensional Fixed Mach Number Supersonic Nozzles
(Analysis of References)

Source and Range	Basic Method and Assumptions	Information Included
Ref. 134 M: 1.2 to 10	Semi-graphical (kernel) Straight sonic line Sharp throat Maximum expansion angle	Calculations for M = 4 nozzle Tables of design parameters for M from 1 to 10
Ref. 139 Any M	Semi-graphical Parabolic sonic line Curved throat Maximum expansion angle	Emphasis on transonic region Theory only
Ref. 141 Any M	Analytical (Foelsch Eqs.) Curved throat Maximum expansion angle Radial flow	Calculations for M = 2, 3, 4, and 5 Graphs, formulas and tables of design parameters for M from 1 to 12
Ref. 142 Any M	Semi-graphical Straight sonic line Sharp throat Maximum expansion angle	Calculations for M = 1.503 Tables of all required functions
Ref. 143 Ref. 144 M: 1.5 to 2.5	Semi-graphical Curved sonic line Curved throat	Calculations for M = 1.5 Tables and graphs of design parameters. Method of boundary-layer correction included
Ref. 147 Any M	Analytical (exact) Curved throat Radial flow	Tables of φ functions Coordinates of duct to convert radial flow at M = 1.15 to uniform axial flow at M = 1.5
Ref. 148 Any M	Semi-graphical Straight sonic line Flat throat	Flow tables for M from 1 to 11 Calculations for M = 1.64 Coordinates for M = 1.99, 2.42, 2.82, 3.24, 3.62, and 4.04
Ref. 160 Any M	Analytical (exact) Continuous curvature M distribution along centerline	Nozzles for M = 4 and M = 5 have proven satisfactory. Nozzles up to M = 5 fabricated and tested. Adapted for machine calculation
Ref. 181 M: 1.5 to 3.5	Analytical (Friedrichs' method) Straight sonic line Curved throat	Extensive tables of design parameters. Fabrication and calibration techniques. Corrections for heat transfer and viscous effects

Table 4-1 (cont)

Source and Range	Basic Method and Assumptions	Information Included
Ref. 187 M: 1.5 to 5	Analytical Radial flow Curved sonic line	Nozzle surface expressed by two equations. Graphs of necessary parameters. Example given in Ref. 188
Ref. 189 Any M	Graphical Curved sonic line Curved throat	Example for M = 2 nozzle Details of testing and recorrection for boundary layer

Table 4-2

Design of Variable Mach Number Nozzles
(Analysis of References)

Source, Type and Range	Basic Method and Assumptions	Information Included
Ref. 133 Sliding Block M: 1.27 to 2.75	Graphical No inflection point Straight sonic line Flat throat Maximum expansion angle	Tables of design parameters Test results
Ref. 150 Menard Inserts M: 1.5 to 3.0	Semi-graphical Two-dimensional nozzle Curved throat	Low and high Mach number inserts designed and tested
Ref. 152 Wedge M: 5 to 8	Analytical Sharp throat Source flow	Water-cooled. Tested at M = 7.6 and 8.0. Boundary-layer and heat-transfer measurements
Ref. 153 Sliding Block a) M < 3 b) M > 3	Graphical Inclined, curved sonic line Curved throat Maximum expansion angle	Designed and tested for M = 1.5 and 2.6
Ref. 154 Flexible Plate Any M	Semi-graphical	Sample work sheets for M from 1.3 to 4.8. Tables and graphs of design parameters. May be used for all flexible and semi-flexible nozzles
Ref. 186 Flexible Plate M: 1.71 to 3.23	Semi-graphical Curved throat	Solid transonic blocks rotated to effect change in M. Flesible plates downstream of inflection point

Table 4-3

Design of Axisymmetric Supersonic Nozzles
(Analysis of References)

Source and Range	Basic Method and Assumptions	Information Included
Ref. 146 M: 1.6 to 4.0	Analytical Radial flow	Graphs of all required functions Basic theory
Ref. 155 M: 1.008 to 8.238	Analytical Straight sonic line Both round and sharp throats	Fundamental equations Tables of nozzle coordinates and flow parameters (interpolation possible)
Ref. 156 M = 2.7203 Ref. 157 M = 3.0413 Ref. 158 M = 3.8532	Analytical (based on method of Ref. 155) Sharp throat Maximum expansion angle	Complete set of coordinates for each nozzle. Boundary-layer growth calculated for M = 3.8532
Ref. 159 M = 10	Truncated 10° cone Curved throat Source flow	Experimental results at M = 10.05 for air and 16.2 for helium
Ref. 161 M = 8	Modification of method of Ref. 160 (see Table 4-1)	Computer programmed Nozzles fabricated, calibrated and tested Boundary-layer corrections
Ref. 162 M: 11 to 19	Analytical Curved throat Curved sonic line Maximum expanion angle	Charts and information for nozzle design. Real-gas effects and boundary-layer corrections Temperatures up to 7500°K Adapted for machine computation
Ref. 177 M = 17 (Nitrogen)	Analytical Curved throat Curved sonic line Source flow Maximum expansion angle	Sample calculations adaptable to other gases. Real-gas effects and temperatures up to 5000°R Fortran program
Ref. 190 M: 5 to 27 γ = 7/5, 6/5, and 5/3	Analytical Source flow (not fully expanded) Partial cancellation Centerline Mach number distribution	Coordinates for 52 different nozzles. Boundary-layer corrections Computer flow chart

Table 4-4

Displacement Thickness Ratio and Momentum Thickness Ratio as a Function of Mach Number and Heat Transfer for n = 5, 7, 9, and 11*

M_∞	n = 5 δ^*/δ	n = 5 θ/δ	n = 7 δ^*/δ	n = 7 θ/δ	n = 9 δ^*/δ	n = 9 θ/δ	n = 11 δ^*/δ	n = 11 θ/δ
			$\frac{T_w - T_e}{T_\infty} = -10$					
8	0.5924	0.0402	0.5304	0.0366	0.4826	0.0335	0.4441	0.0310
10	0.7099	0.0242	0.6552	0.0229	0.6110	0.0216	0.5742	0.0205
12	0.7774	0.0165	0.7304	0.0159	0.6915	0.0153	0.6581	0.0147
14	0.8215	0.0121	0.7810	0.0118	0.7468	0.0115	0.7170	0.0112
16	0.8525	0.0093	0.8173	0.0092	0.7870	0.0090	0.7604	0.0087
18	0.8753	0.0074	0.8443	0.0073	0.8174	0.0072	0.7934	0.0070
20	0.8927	0.0060	0.8651	0.0060	0.8409	0.0059	0.8191	0.0058
			$\frac{T_w - T_e}{T_\infty} = -8$					
8	0.6205	0.0358	0.5590	0.0330	0.5112	0.0306	0.4725	0.0285
10	0.7220	0.0226	0.6682	0.0215	0.6248	0.0204	0.5883	0.0194
12	0.7837	0.0158	0.7375	0.0153	0.6991	0.0146	0.6662	0.0142
14	0.8253	0.0117	0.7853	0.0115	0.7515	0.0112	0.7221	0.0109
16	0.8549	0.0091	0.8201	0.0089	0.7901	0.0088	0.7637	0.0086
18	0.8769	0.0072	0.8462	0.0072	0.8195	0.0071	0.7957	0.0069
20	0.8938	0.0059	0.8664	0.0059	0.8424	0.0058	0.8208	0.0057
			$\frac{T_w - T_e}{T_\infty} = -6$					
6	0.4827	0.0574	0.4189	0.0507	0.3720	0.0454	0.3355	0.0412
8	0.6438	0.0324	0.5833	0.0302	0.5358	0.0282	0.4971	0.0264
10	0.7328	0.0213	0.6801	0.0204	0.6373	0.0194	0.6012	0.0185
12	0.7896	0.0152	0.7442	0.0147	0.7063	0.0142	0.6738	0.0137
14	0.8288	0.0114	0.7894	0.0112	0.7560	0.0109	0.7269	0.0106
16	0.8572	0.0088	0.8227	0.0088	0.7931	0.0086	0.7669	0.0084
18	0.8784	0.0071	0.8480	0.0071	0.8215	0.0070	0.7979	0.0068
20	0.8948	0.0058	0.8677	0.0058	0.8438	0.0057	0.8223	0.0056
			$\frac{T_w - T_e}{T_\infty} = -4$					
6	0.5334	0.0484	0.4683	0.0438	0.4195	0.0398	0.3812	0.0366
8	0.6637	0.0297	0.6042	0.0278	0.5573	0.0261	0.5187	0.0246
10	0.7426	0.0201	0.6909	0.0193	0.6487	0.0185	0.6131	0.0177
12	0.7952	0.0146	0.7504	0.0142	0.7131	0.0137	0.6810	0.0133
14	0.8322	0.0111	0.7933	0.0109	0.7603	0.0106	0.7314	0.0103
16	0.8593	0.0087	0.8253	0.0086	0.7959	0.0084	0.7700	0.0082
18	0.8799	0.0070	0.8497	0.0069	0.8235	0.0068	0.8000	0.0067
20	0.8959	0.0057	0.8689	0.0057	0.8452	0.0057	0.8239	0.0056

*Two-dimensional flow; see Subsec. 4.8.1.

Table 4-4 (cont)

M_∞	n = 5 δ^*/δ	n = 5 θ/δ	n = 7 δ^*/δ	n = 7 θ/δ	n = 9 δ^*/δ	n = 9 θ/δ	n = 11 δ^*/δ	n = 11 θ/δ
			$\frac{T_w - T_e}{T_\infty} = -2$					
4	0.3916	0.0726	0.3287	0.0630	0.2846	0.0557	0.2515	0.0499
6	0.5722	0.0422	0.5072	0.0387	0.4579	0.0356	0.4187	0.0330
8	0.6809	0.0274	0.6226	0.0259	0.5763	0.0244	0.5380	0.0231
10	0.7516	0.0191	0.7009	0.0184	0.6593	0.0176	0.6241	0.0169
12	0.8003	0.0140	0.7563	0.0137	0.7195	0.0133	0.6877	0.0128
14	0.8354	0.0107	0.7970	0.0106	0.7644	0.0103	0.7358	0.0101
16	0.8614	0.0085	0.8277	0.0084	0.7987	0.0082	0.7730	0.0081
18	0.8814	0.0068	0.8515	0.0068	0.8254	0.0067	0.8021	0.0066
20	0.8969	0.0056	0.8701	0.0057	0.8466	0.0056	0.8254	0.0055
			$\frac{T_w - T_e}{T_\infty} = 0$					
0	0.1674	0.1188	0.1257	0.0970	0.1005	0.0817	0.0837	0.0704
2	0.2847	0.0927	0.2278	0.0786	0.1904	0.0680	0.1638	0.0599
4	0.4669	0.0584	0.4000	0.0523	0.3516	0.0471	0.3146	0.0429
6	0.6032	0.0375	0.5391	0.0348	0.4899	0.0323	0.4504	0.0301
8	0.6959	0.0254	0.6389	0.0242	0.5932	0.0229	0.5554	0.0217
10	0.7598	0.0182	0.7100	0.0176	0.6691	0.0169	0.6344	0.0162
12	0.8052	0.0135	0.7619	0.0132	0.7255	0.0129	0.6942	0.0124
14	0.8384	0.0104	0.8006	0.0103	0.7683	0.0101	0.7401	0.0098
16	0.8635	0.0083	0.8301	0.0082	0.8013	0.0081	0.7758	0.0079
18	0.8828	0.0067	0.8531	0.0067	0.8272	0.0066	0.8042	0.0065
20	0.8979	0.0056	0.8713	0.0056	0.8479	0.0055	0.8269	0.0054
			$\frac{T_w - T_e}{T_\infty} = 2$					
0	0.3315	0.0820	0.2682	0.0712	0.2258	0.0626	0.1953	0.0558
2	0.3967	0.0700	0.3302	0.0618	0.2839	0.0551	0.2495	0.0496
4	0.5204	0.0494	0.4528	0.0450	0.4026	0.0412	0.3638	0.0379
6	0.6289	0.0338	0.5660	0.0317	0.5172	0.0296	0.4776	0.0278
8	0.7093	0.0237	0.6534	0.0227	0.6085	0.0216	0.5711	0.0205
10	0.7674	0.0173	0.7185	0.0168	0.6782	0.0162	0.6439	0.0155
12	0.8098	0.0131	0.7671	0.0128	0.7313	0.0125	0.7003	0.0121
14	0.8414	0.0102	0.8040	0.0100	0.7721	0.0098	0.7441	0.0096
16	0.8654	0.0081	0.8324	0.0081	0.8039	0.0079	0.7786	0.0078
18	0.8841	0.0066	0.8547	0.0066	0.8291	0.0065	0.8061	0.0064
20	0.8988	0.0055	0.8725	0.0055	0.8492	0.0054	0.8283	0.0054

Table 4-4 (cont)

M_∞	n = 5 δ^*/δ	n = 5 ϑ/δ	n = 7 δ^*/δ	n = 7 ϑ/δ	n = 9 δ^*/δ	n = 9 ϑ/δ	n = 11 δ^*/δ	n = 11 ϑ/δ
				$\frac{T_w - T_e}{T_\infty} = 4$				
0	0.4249	0.0644	0.3562	0.0576	0.3079	0.0518	0.2717	0.0470
2	0.4691	0.0571	0.4000	0.0516	0.3503	0.0469	0.3125	0.0428
4	0.5613	0.0430	0.4942	0.0397	0.4438	0.0367	0.4039	0.0341
6	0.6506	0.0308	0.5890	0.0291	0.5408	0.0274	0.5014	0.0258
8	0.7213	0.0223	0.6666	0.0214	0.6224	0.0204	0.5854	0.0195
10	0.7744	0.0166	0.7264	0.0161	0.6867	0.0155	0.6528	0.0150
12	0.8141	0.0126	0.7721	0.0124	0.7367	0.0121	0.7060	0.0117
14	0.8442	0.0099	0.8073	0.0098	0.7757	0.0096	0.7480	0.0094
16	0.8673	0.0079	0.8347	0.0079	0.8064	0.0078	0.7813	0.0076
18	0.8854	0.0065	0.8563	0.0065	0.8308	0.0064	0.8081	0.0063
20	0.8998	0.0054	0.8736	0.0054	0.8505	0.0054	0.8297	0.0053
				$\frac{T_w - T_e}{T_\infty} = 6$				
0	0.4887	0.0536	0.4189	0.0489	0.3683	0.0446	0.3294	0.0410
2	0.5214	0.0486	0.4523	0.0446	0.4014	0.0410	0.3618	0.0378
4	0.5939	0.0382	0.5280	0.0357	0.4777	0.0332	0.4376	0.0310
6	0.6693	0.0284	0.6091	0.0269	0.5615	0.0255	0.5224	0.0241
8	0.7321	0.0210	0.6785	0.0203	0.6350	0.0194	0.5985	0.0185
10	0.7809	0.0159	0.7337	0.0155	0.6946	0.0149	0.6612	0.0144
12	0.8182	0.0122	0.7768	0.0120	0.7419	0.0117	0.7116	0.0114
14	0.8469	0.0097	0.8104	0.0096	0.7792	0.0094	0.7518	0.0092
16	0.8691	0.0078	0.8368	0.0078	0.8088	0.0077	0.7840	0.0075
18	0.8867	0.0064	0.8578	0.0064	0.8325	0.0063	0.8099	0.0062
20	0.9007	0.0053	0.8747	0.0053	0.8518	0.0053	0.8311	0.0052
				$\frac{T_w - T_e}{T_\infty} = 8$				
0	0.5361	0.0461	0.4669	0.0427	0.4155	0.0394	0.3754	0.0365
2	0.5617	0.0424	0.4936	0.0395	0.4424	0.0366	0.4021	0.0340
4	0.6208	0.0344	0.5565	0.0323	0.5065	0.0304	0.4663	0.0285
6	0.6856	0.0263	0.6267	0.0251	0.5799	0.0238	0.5412	0.0226
8	0.7419	0.0199	0.6873	0.0198	0.6466	0.0185	0.6105	0.0177
10	0.7869	0.0152	0.7406	0.0149	0.7021	0.0144	0.6690	0.0139
12	0.8221	0.0119	0.7813	0.0117	0.7468	0.0114	0.7168	0.0111
14	0.8494	0.0094	0.8134	0.0093	0.7825	0.0092	0.7554	0.0090
16	0.8709	0.0076	0.8389	0.0076	0.8111	0.0075	0.7865	0.0074
18	0.8879	0.0063	0.8593	0.0063	0.8342	0.0062	0.8118	0.0061
20	0.9016	0.0053	0.8758	0.0053	0.8530	0.0052	0.8324	0.0052

Table 4-4 (cont)

M_∞	n = 5 δ^*/δ	n = 5 θ/δ	n = 7 δ^*/δ	n = 7 θ/δ	n = 9 δ^*/δ	n = 9 θ/δ	n = 11 δ^*/δ	n = 11 θ/δ
			$\frac{T_w - T_e}{T_\infty} = 10$					
0	0.5732	0.0406	0.5053	0.0380	0.4539	0.0353	0.4133	0.0330
2	0.5940	0.0378	0.5273	0.0355	0.4764	0.0332	0.4358	0.0310
4	0.6435	0.0313	0.5805	0.0297	0.5313	0.0280	0.4914	0.0264
6	0.7000	0.0245	0.6424	0.0235	0.5964	0.0224	0.5582	0.0214
8	0.7509	0.0189	0.6994	0.0183	0.6573	0.0176	0.6217	0.0169
10	0.7926	0.0146	0.7470	0.0143	0.7091	0.0139	0.6765	0.0134
12	0.8257	0.0115	0.7855	0.0114	0.7515	0.0111	0.7218	0.0108
14	0.8519	0.0092	0.8163	0.0091	0.7857	0.0090	0.7588	0.0088
16	0.8726	0.0075	0.8409	0.0075	0.8134	0.0074	0.7890	0.0072
18	0.8892	0.0062	0.8607	0.0062	0.8359	0.0061	0.8136	0.0060
20	0.9025	0.0052	0.8768	0.0052	0.8542	0.0052	0.8337	0.0051

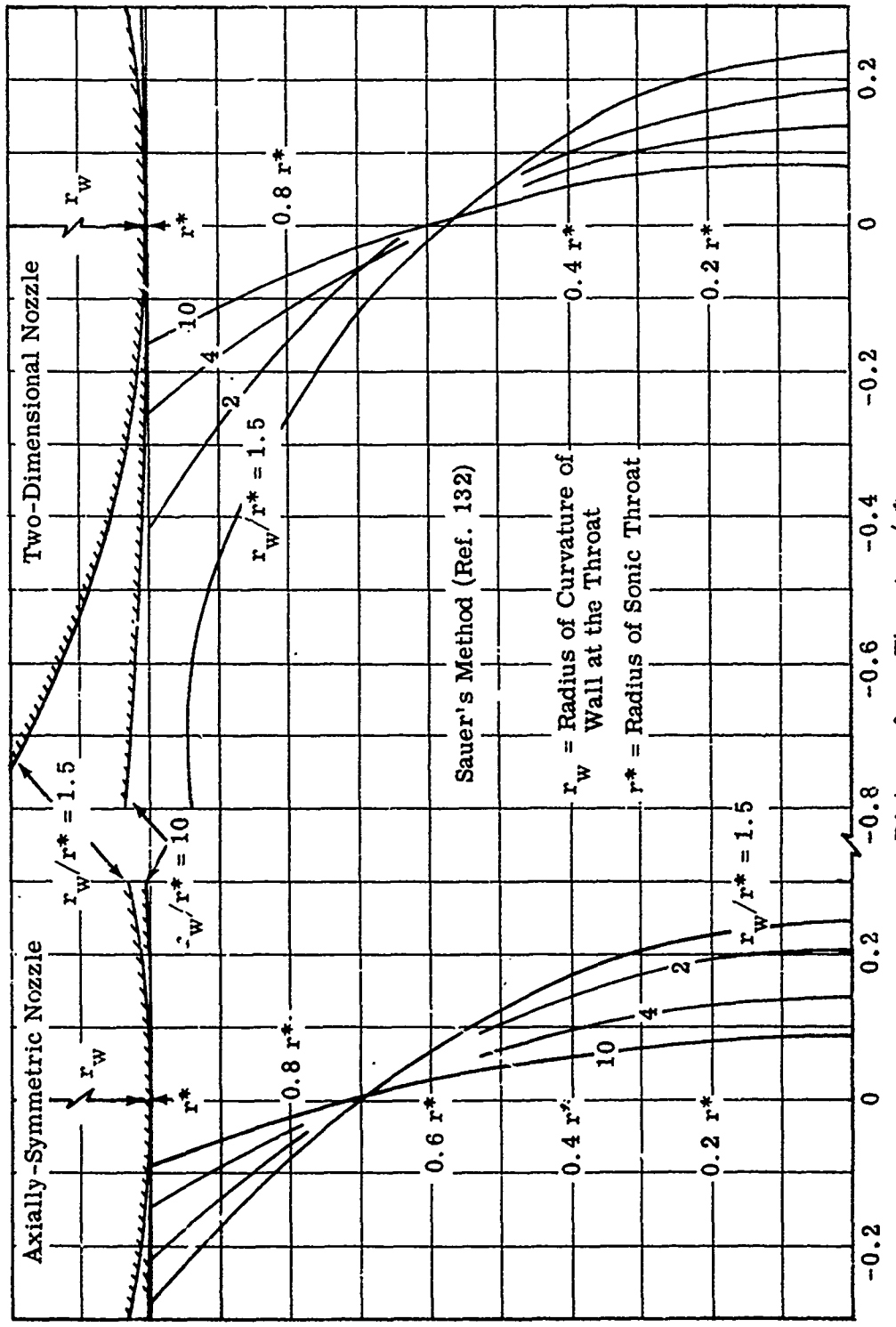

Fig. 4-1. Position of the sonic line for various values of r_w/r^*; axially-symmetric and two-dimensional nozzles; $\gamma = 1.4$.

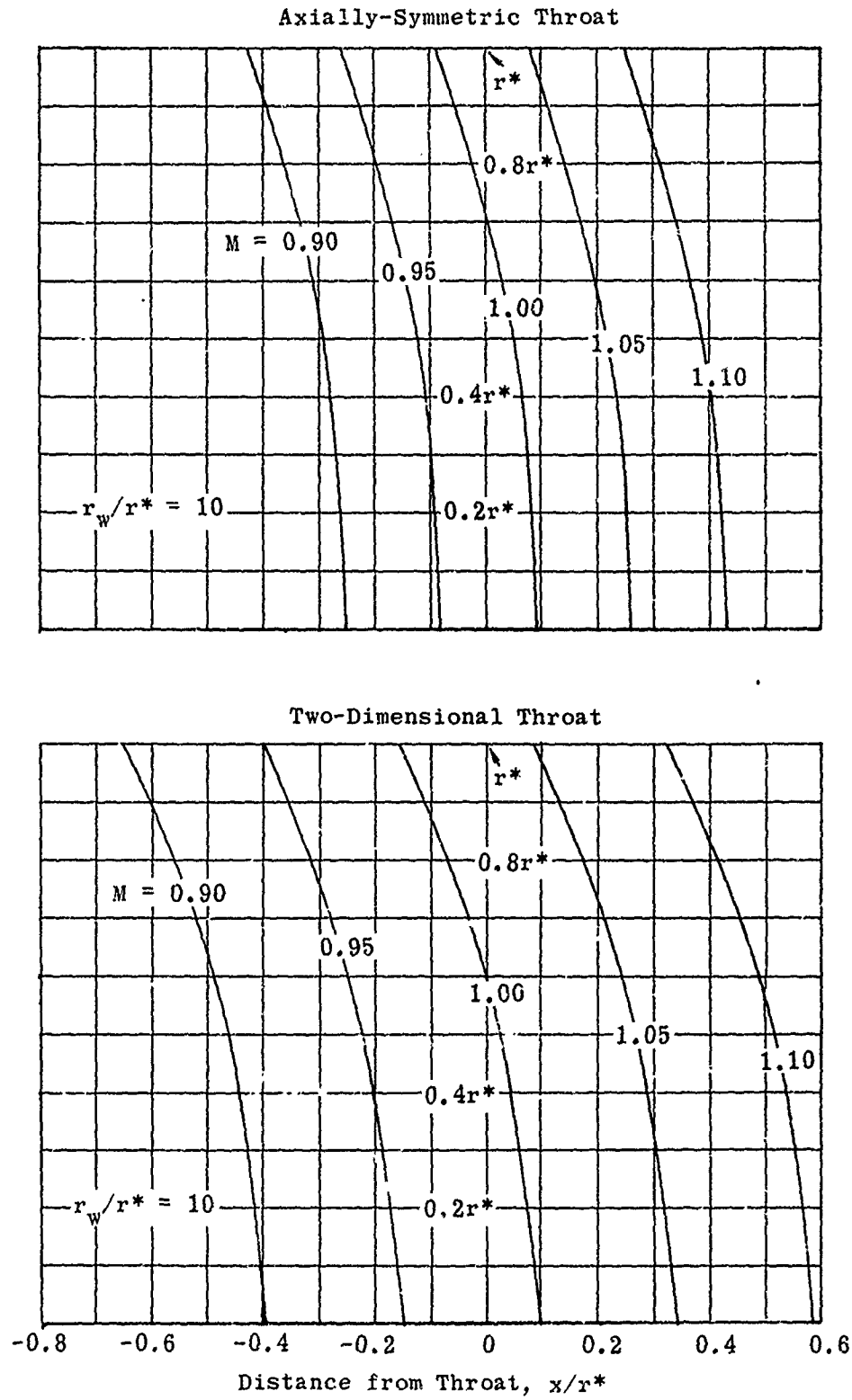

Fig. 4-2. Mach number distribution in a sonic throat of axially-symmetric and two-dimensional nozzles; $r_w/r^* = 10$; $\gamma = 1.4$.

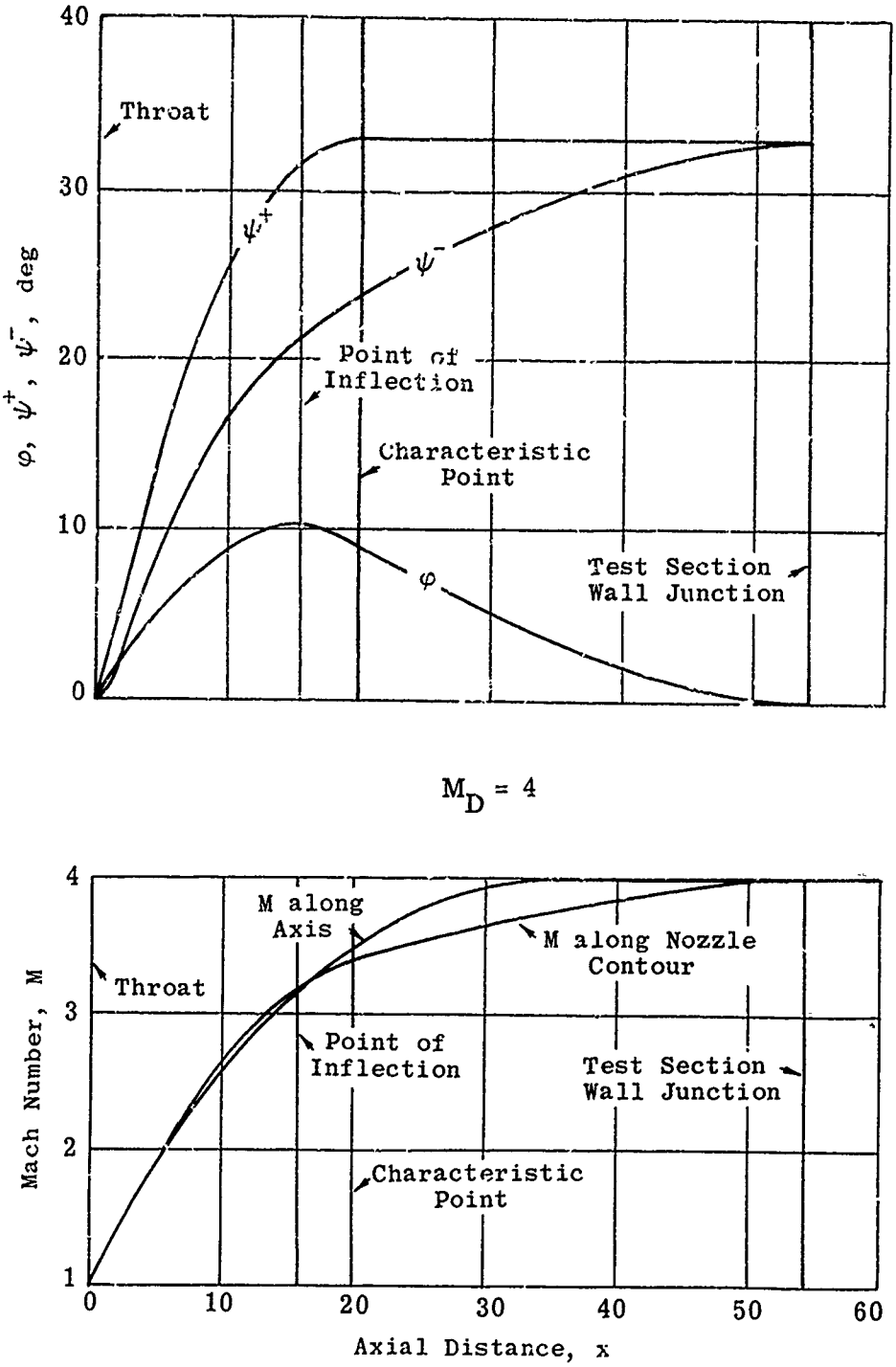

Fig. 4-3. Values of ψ^+, ψ^-, φ, and M as a function of distance from throat (see Subsec. 4.3.1). (Source: Ref. 145)

732-359 O - 64 - 19

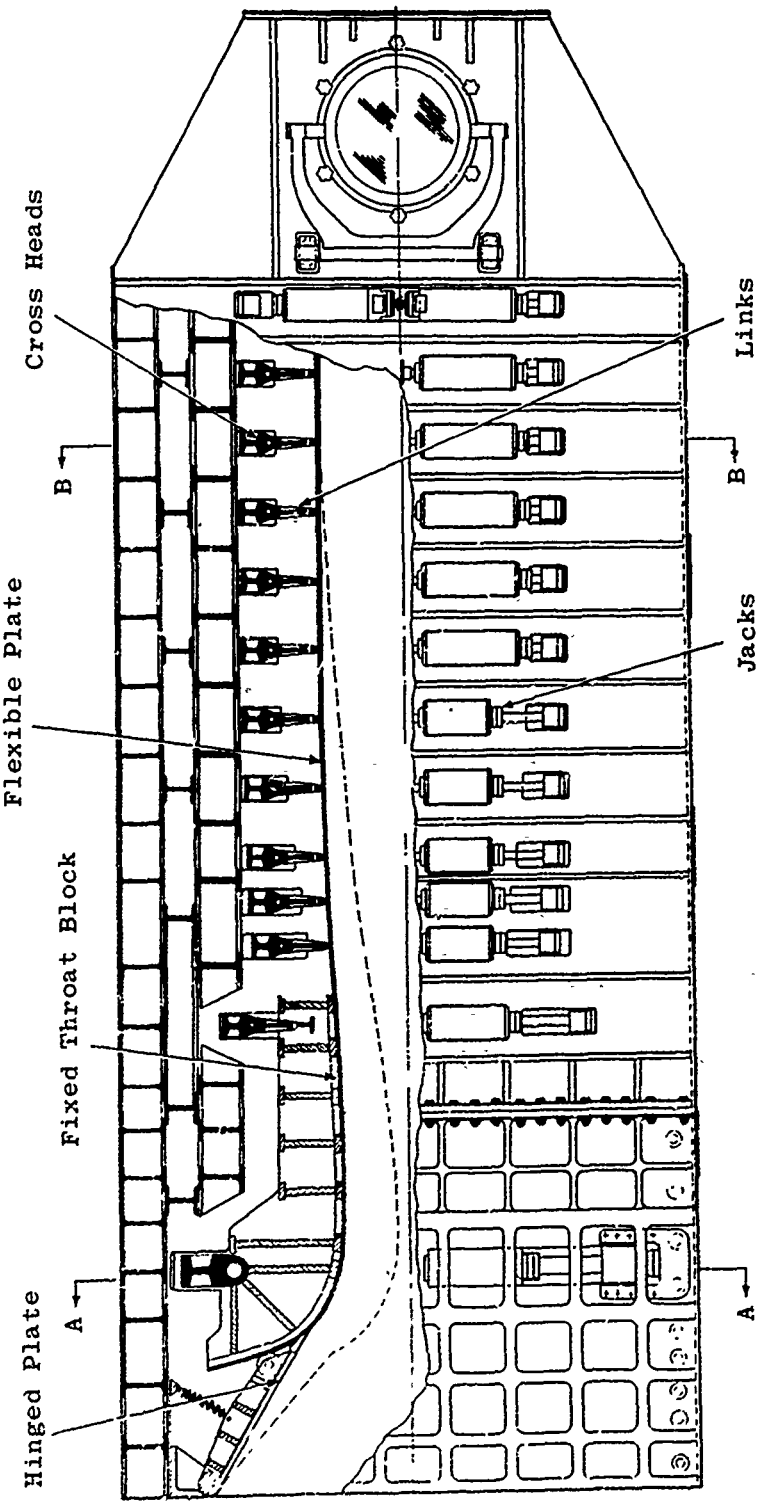

Fig. 4-4. Proposed flexible nozzle and working section for Mach number range of 1.6 to 3.5. (Source: Ref. 174)

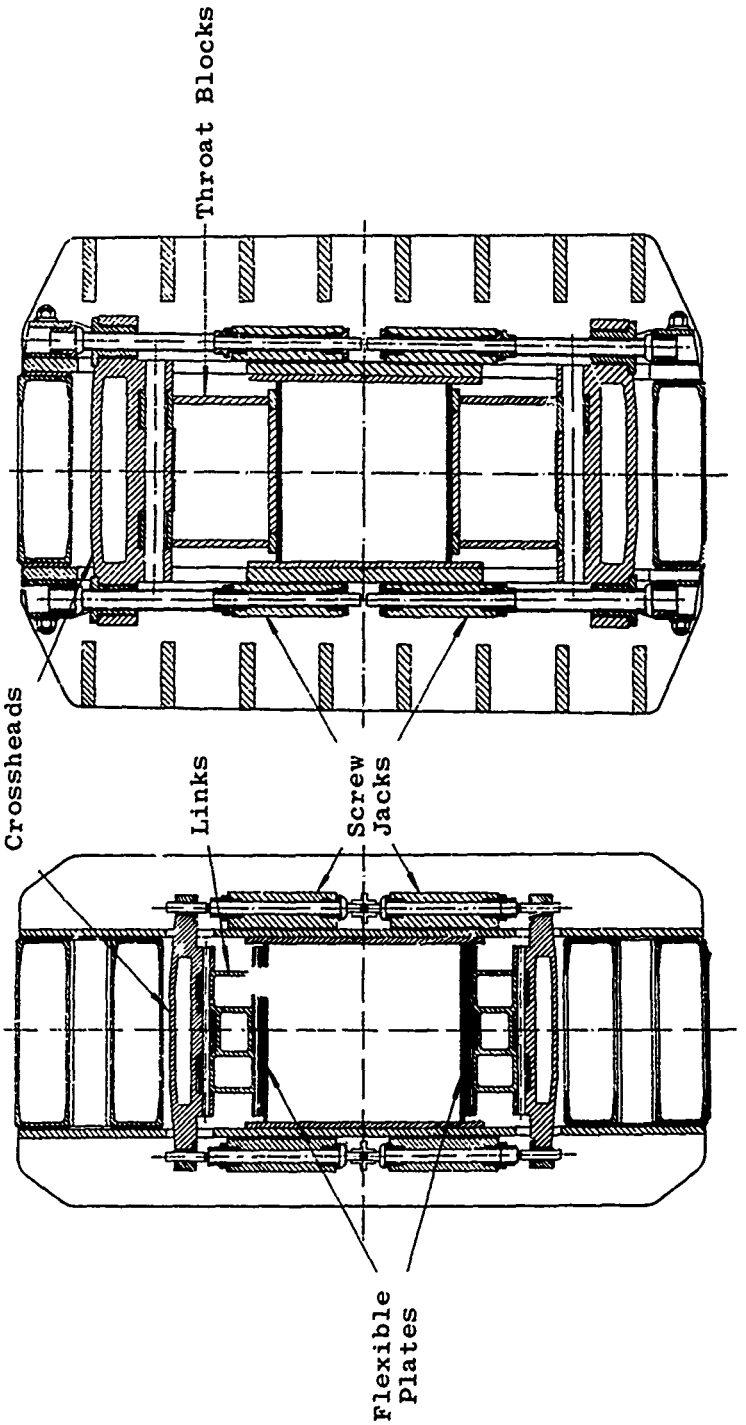

Fig. 4-5. Cross sections of a proposed nozzle section for Mach number range of 1.6 to 3.5. (Source: Ref. 174)

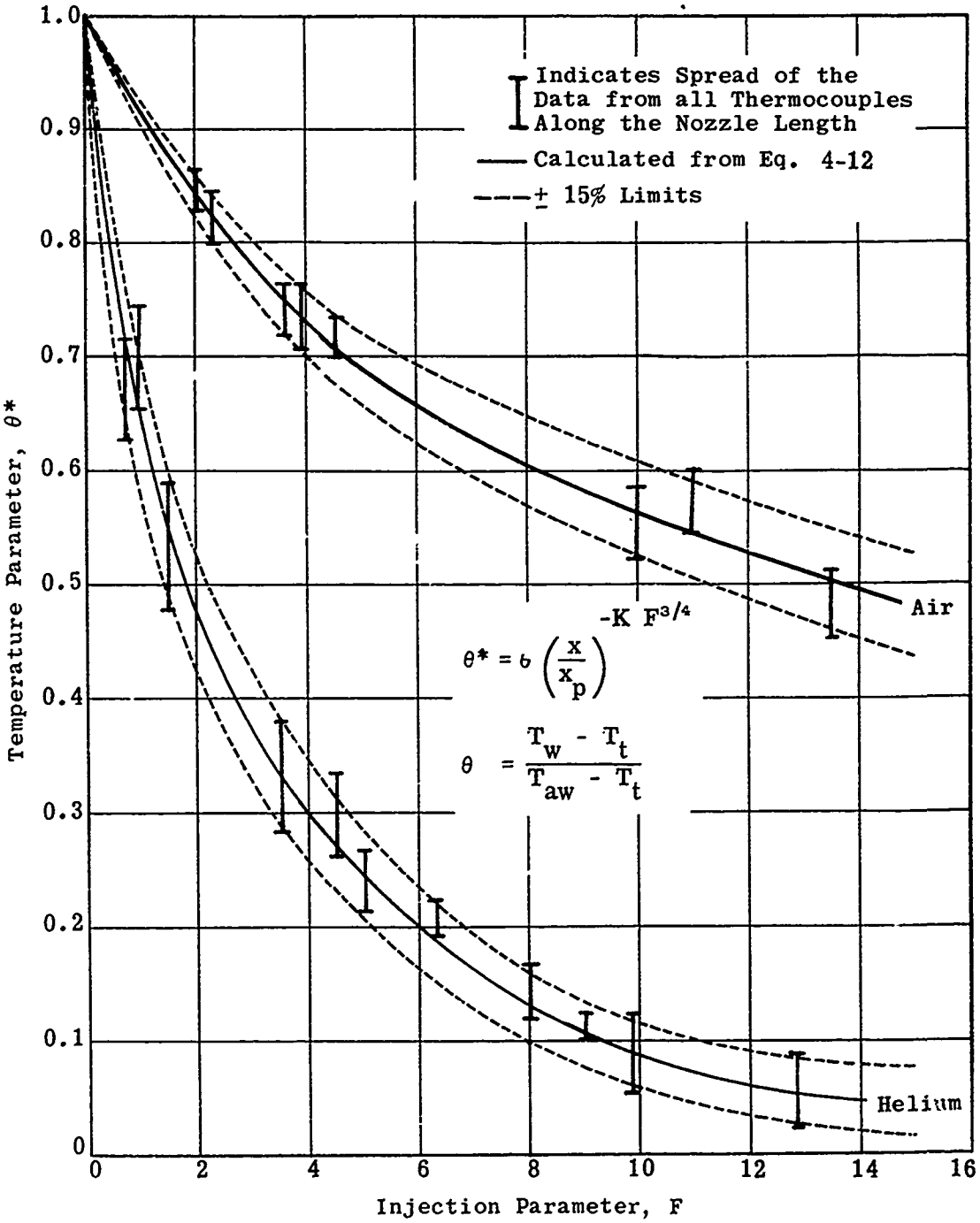

Fig. 4-6. Variation of normalized recovery temperature with injection parameter for a water-cooled hypersonic nozzle; air and helium. (Source: Ref. 178)

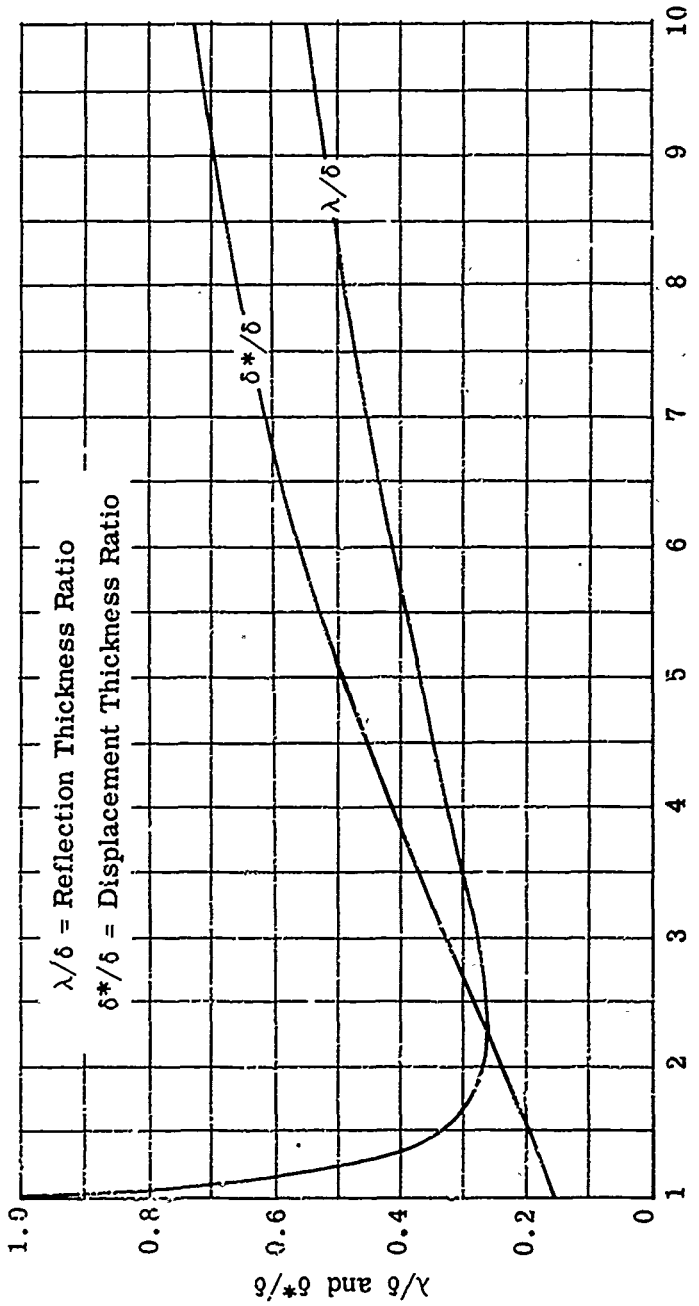

Fig. 4-7. Comparison of reflection and displacement thickness ratios vs M for a velocity-profile parameter of 7; $\gamma = 1.4$. (Source: Ref. 100)

Intentionally Blank

5. Supersonic Wind-Tunnel Diffusers

The function of the wind-tunnel diffuser is comparable to that of the ramjet diffuser (Subsec. 3), i.e., to reconvert the kinetic energy of the working fluid into pressure energy as efficiently as possible. The most important difference between the two diffusers is that in the wind tunnel all the diffusion must take place within the confines of the duct, whereas the ramjet diffuser may spill air at the cowl lip under off-design flow conditions. Secondly, the entering stream of the ramjet diffuser is usually uniform and hence is amenable to analytical treatment, whereas the entering stream of a wind-tunnel diffuser is often highly turbulent, as it is largely the wake flow from the test-section model and support system. A third difference is that the boundary layer originates at the lip of the ramjet diffuser, while at the entrance to the wind-tunnel diffuser there is already a well-developed boundary layer. It will be shown that the performance of all forms of diffusers is dominated by the behavior of the boundary layer. Theoretically, in the absence of boundary layer, it would be possible to diffuse the airstream isentropically, without total pressure loss, by means of a second sonic throat and a suitably shaped duct. In nonisentropic flow the simplest diffusion would be achieved by a single normal shock. Both the isentropic compression and the normal-shock method are complicated in practice by the presence of the boundary layer. Diffuser designs and research problems are concerned chiefly with ways of combining area variation and shock systems in the most efficient manner for a particular set of flow characteristics.

Complete diffusion includes both supersonic and subsonic diffusions. The former is usually considered the reduction of supersonic velocity to sonic or near sonic velocity, either by means of a series of shocks or a second duct contraction. Subsonic diffusion converts the remaining kinetic energy to a level negligible in comparison with that of the test-section flow. Although subsonic diffusion is physically the last stage of diffusion, the subsonic diffuser will be discussed first (Subsec. 5.2), since it is a factor common to all the methods of supersonic diffusion which will be outlined in Subsecs. 5.3 to 5.6.

5.1 Definitions of Diffuser Efficiency

Before discussing the various forms of diffusers it is necessary to have some standard by which their performance may be assessed and compared. There are two definitions of diffuser efficiency in common use and both of them assume that the diffusion process continues until the residual kinetic energy of the flow is a negligible fraction of its value at the diffuser entrance.

The polytropic efficiency, η_D, is defined as the ratio of the actual increase in pressure energy to the actual decrease in kinetic energy. This ratio may be expressed in the following forms.

For incompressible flow,

$$\eta_D = \frac{p_2 - p_1}{\frac{1}{2}\rho V_1^2 - \frac{1}{2}\rho V_2^2} \tag{5-1}$$

For compressible fluids, η_D cannot be stated explicitly but may be found (Ref. 12) from

$$\frac{p_2}{p_1} = \left(1 + \frac{\gamma - 1}{2} M_1^2\right)^{\eta_D\left(\frac{\gamma}{\gamma-1}\right)} \tag{5-2}$$

or

$$\frac{p_2}{p_1} = \left(\frac{p_{t_1}}{p_1}\right)^{\eta_D} \tag{5-3}$$

or since $p_2 \approx p_{t_2}$

$$\frac{p_{t_2}}{p_{t_1}} = \left(\frac{p_1}{p_{t_1}}\right)^{1-\eta_D} \tag{5-4}$$

Subscripts $_1$ and $_2$ refer to the diffuser entrance (usually the test section) and its exit, at which station the gas is assumed to be at rest.

The isentropic efficiency, η_σ, is the ratio of the kinetic energy which could be transformed isentropically to give the observed exit pressure to the kinetic energy which is actually transformed. It is expressed (Ref. 12) as

$$\eta_\sigma = \frac{2}{\gamma - 1} \frac{1}{M_1^2} \left[\left(\frac{p_2}{p_1}\right)^{\frac{\gamma-1}{\gamma}} - 1\right] \tag{5-5}$$

From Eqs. 5-2 and 5-5 the relationship between η_D and η_σ may be derived as

$$\left(1 + \frac{\gamma - 1}{2} M_1^2\right)^{\eta_D} = 1 + \frac{\gamma - 1}{2} M_1^2 \eta_\sigma \tag{5-6}$$

This relationship for air ($\gamma = 1.4$) is shown graphically in Fig. 5-1 from which it may be seen that for incompressible flow, $\eta_D = \eta_\sigma$.

5.2 Subsonic Diffusers

Subsonic diffusion is achieved primarily by expanding the cross section of the duct. The adverse pressure gradient thus introduced causes rapid boundary-layer thickening with consequent flow separation and velocity reversal in the boundary layer. For this reason subsonic diffusion is never completely efficient. Lukasiewicz (Ref. 191) has collected experimental data on subsonic diffusion which indicate that for $0.4 < M < 0.9$ the total pressure recovery is virtually constant and lies between 0.88 and 0.89. These results are for the case of an empty test section (no model) and thus represent an upper limit (see Subsec. 5.9). At very low speeds the pressure recovery approaches 1.0.

It has been shown experimentally that the diffuser losses are minimized by restricting the divergence angle to about 7 degrees. On the other hand, when the length becomes excessive, the losses due to skin friction may outweigh the improvement due to reducing the gradient. The design is thus always a compromise.

Several devices have been suggested whereby flow separation may be prevented or delayed. Suction may be applied at the region where the boundary layer becomes critical or a jet of compressed air may be injected to re-energize the flow adjacent to the wall. Successful applications of the injection and suction principles will be described in Subsec. 5.6. It has also been suggested that a series of director vanes inserted in the diffuser would accelerate the flow along the walls. However, the drag of such plates in a high-velocity duct would place excessive penalties on the power system.

5.3 Diffusers Without Contraction

The simplest type of supersonic diffusion is by means of a normal shock at the end of the working section. In this case, if the subsequent complete subsonic diffusion could be achieved without further losses, then the final static pressure, p_2, would be equal to the stagnation pressure behind the normal shock at M, and Eq. 5-5 could be written as

$$\eta_\sigma = \frac{2}{\gamma - 1} \frac{1}{M^2} \left[\frac{\gamma + 1}{2} M^2 \left(\frac{\gamma + 1}{2\gamma M^2 - (\gamma - 1)} \right)^{1/\gamma} - 1 \right] \qquad (5\text{-}7)$$

The value of η_σ from Eq. 5-7 for values of M from 1 to 10 in air is shown as curve A in Fig. 5-2, where it is compared with experimental data from several sources (solid symbols).

In practice, the actual efficiency is lower than this partly because the theory does not take into account any viscous losses, but chiefly because the normal shock occurs as a shock system strongly affected by the state of the boundary layer rather than as a single shock.

The following sketch shows possible types of shock compression taking place in the entrance to the subsonic diffuser.

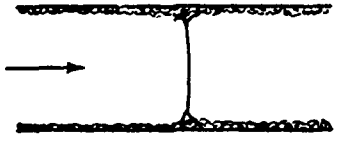

Shock System for Thin Boundary-Layer

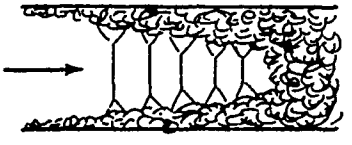

Shock System for Thick Boundary-Layer

The efficiency may be improved by the insertion of an elongated constant-area duct between the test section and the subsonic diffuser. This length allows the flow to reattach itself to the wall. Since the angle of the shock wave is dependent on the Mach number of the flow, and the slope of the reflected wave is dependent on the boundary-layer thickness as well as the characteristics of the incident wave, the optimum length of such a shock duct is a strong function of the Mach number and to a lesser degree of the Reynolds number (see Subsec. 4.8).

Figure 5-3, derived from data in Ref. 192, shows the improvement in efficiency for a Mach number two diffuser without contraction as the constant-area duct is increased in length. Although the data do not show a definite optimum length, it may be noted that the curve is flattening at $\ell/h \sim 4$ (ℓ is the length of the constant-area duct and h is its height). In this example the constant-area duct is followed by a diffuser with an average divergence of ~5.5 deg. Collected data from Ref. 193 have been replotted in Fig. 5-4. The shock length, ℓ_s/h, has been plotted against 1/M rather than M in order to show the almost linear relationship between 1/M and ℓ_s/h. The duct height in these data is sometimes less than that of the test section. The Mach number is the average in the duct rather than in the test section.

Although a dissipative system such as the one described above is inefficient, it has the advantage of being stable for a wide range of inlet flow conditions, and has the added merit of simple construction and maintenance. It is generally considered adequate for supersonic Mach numbers less than about two. The effect of suction along the walls of a constant-area shock duct is discussed in Subsec. 5.6.2.

5.4 Diffusers With Contraction

In the absence of heat-transfer and viscous effects, it would be theoretically possible to achieve shock-free supersonic diffusion by introducing a second convergent-divergent channel with a throat equal in area to the first sonic throat. However, the change in entropy due to the boundary layer makes this impossible, and in practice a normal shock occurs either in the working section or beyond the second throat. Oswatitsch (Ref. 3, p. 55) has shown that the shock is unstable when it occurs between the two throats and that it will always move either upstream or downstream, thus causing either the breakdown of supersonic flow or its stabilization at the required Mach number. Hence in order to start the tunnel, the second throat must be large enough to "swallow" a normal shock at the design Mach number. Once the shock has passed the second throat establishing the required flow regime, a reduction of the diffuser throat area improves the total pressure recovery. The choice between the simplicity of a fixed throat and the added efficiency of an adjustable one depends on many factors, among which are the design Mach number, the available power and the required run time. Diffusers with fixed-area throats will be discussed in Subsec. 5.4.1. Diffusers using different techniques for varying the contraction ratio will be discussed in Subsec. 5.4.2.

5.4.1 Fixed-Area Second Throat

In order to establish stable supersonic flow, the normal-shock system associated with the test-section Mach number must be compatible with the second throat. Hence, for each Mach number, the diffuser throat has a minimum area below which the flow will choke. This starting area, A_2, may be derived by equating the mass flow at the two throats, i.e.,

$$\rho_1^* A_1^* a_1^* = \rho_2^* A_2^* a_2^* \tag{5-8}$$

where the starting nomenclature is shown by the following sketch.

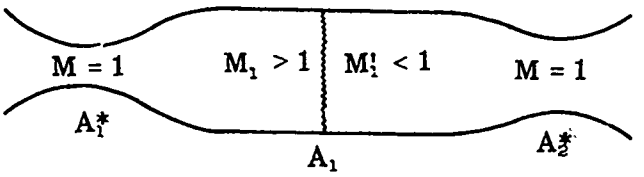

Since the total temperature, T_t, and the critical velocity of sound, a*, are constant across the shock, then

$$\frac{\rho_1^*}{\rho_2^*} = \frac{p_1^*}{p_2^*} = \frac{p_{t_1}}{p_{t_2}} \tag{5-9}$$

Equations 5-8 and 5-9 combine to give

$$\frac{A_2^*}{A_1^*} = \frac{p_{t_1}}{p_{t_2}} \tag{5-10}$$

i.e., the limiting ratio of the throat areas is equal to the stagnation pressure ratio across a normal shock at the test-section Mach number, M_1. The ratio of the diffuser throat to the test-section area is given by

$$\frac{A_2^*}{A_1} = \frac{A_2^*}{A_1^*} \cdot \frac{A_1^*}{A_1} = \frac{p_{t_1}}{p_{t_2}} \left(\frac{A_1^*}{A_1}\right)_{M_1} \tag{5-11}$$

or in terms of M_1, by

$$\frac{A_2^*}{A_1} = \left(\frac{\gamma - 1}{\gamma + 1}\right)^{\frac{\gamma+1}{2(\gamma-1)}} \left(\frac{2\gamma}{\gamma - 1} - \frac{1}{M_1^2}\right)^{\frac{1}{\gamma-1}} \left(1 + \frac{2}{(\gamma - 1)\, M_1^2}\right)^{1/2} \tag{5-12}$$

Equation 5-12 is shown as curve A in Fig. 5-5 for Mach numbers from 1 to 8 and is compared with experimental data from several sources (open symbols).

It is surprising to find that nearly all the measured values of the minimum starting throat are less than the theory would predict. One would expect that the viscous effects would create larger losses and demand an increased second throat. The anomaly may be explained by the fact that the starting shock occurs and passes through the throat before the design Mach number has been reached. The pressure losses (see Eq. 5-11) are not as great and at the same time the areas remain constant since they are the geometric ones rather than those associated with the Mach number of the shock.

It has already been stated that the flow is stable only when the normal shock is slightly downstream of the second throat. As the normal shock moves upstream towards the throat, the efficiency improves, reaching a maximum when the shock is at the narrowest section. This latter location is the only one readily amenable to simple calculation. The running conditions with the minimum starting throat are shown in the sketch below.

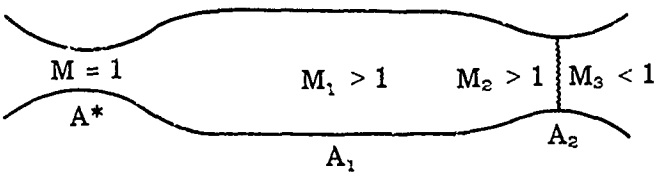

It must be remembered that A_2 is no longer a sonic throat and that once the flow is established M_2 is supersonic. The diffuser efficiency, η_σ, is a function of M only but cannot be stated explicitly; however, it may be computed in the following manner:

1. $M_1 \longrightarrow A_2/A^*$, from normal-shock tables (Eq. 2-24) and Eq. 5-10.
2. $A_2/A^* \longrightarrow M_2$, from isentropic-flow tables or Eq. 2-4.
3. $M_2 \longrightarrow p_3/p_{t_2}$, from Eqs. 2-2, 2-22, and 2-24.
4. Since $p_{t_2} = p_{t_1}$, then $p_3/p_{t_2} = p_3/p_{t_1}$.
5. $M_1 \longrightarrow p_1/p_{t_1}$, from isentropic-flow tables or Eq. 2-2.
6. $p_3/p_1 \longrightarrow \eta_\sigma$, from Eq. 5-5.

The isentropic efficiency so calculated is shown as curve B in Fig. 5-2; experimentally determined efficiencies for diffusers with second throats of minimum starting area are presented in the same figure for comparison (half-shaded symbols). The discrepancies between these values are accountable to viscous effects and additional shock losses. The shock actually occurs downstream of the throat and hence at a higher Mach number giving the slightly greater shock losses.

The shape of the supersonic portion of the diffuser, i.e., the contraction to the second throat, is of critical importance. The deceleration of the air is not usually an isentropic process but is accomplished by a series of oblique shocks reflecting from the diffuser walls. The turning angle of the waves is equal to the diffuser wall angle, and hence a more abrupt contraction implies stronger shock waves and a greater pressure loss. Furthermore, since

there is an adverse pressure gradient there is always the possibility that the boundary-layer will separate at the points of shock-wave reflection. It is generally accepted that the turning angle should be limited to a few degrees and that the diffuser length should be from 5 to 10 times the height (or diameter) of the test section. The three typical two-dimensional supersonic diffusers shown in Fig. 5-6 utilize constant-area second throats. They have been tested and proved satisfactory for Mach numbers from 4 to 10. A hypersonic diffuser designed for use in a helium tunnel will be described in Subsec. 5.10.

5.4.2 Variable-Area Second Throat

Once the normal shock has passed through the second throat and supersonic flow has been established in the test section, the area of the second throat may be reduced. Theoretically the most efficient running condition would be with the normal shock exactly at M = 1 in the second throat, in which case the two sonic throats would be equal in area and A_2/A_1 (curve B of Fig. 5-5) would be given by Eq. 2-4. Viscous effects preclude such ideal diffusion.

The diffuser throat area is usually changed by means of hydraulic jacks working against either continuous flexible plates or rigid hinged plates. In general, the first method is preferred since it provides a long, smooth throat transition of large radius of curvature. The second method gives a sharper, short throat which, under critical conditions, may cause flow separation. A third method of changing the diffuser throat area is by means of a centerbody moved into the throat after supersonic flow is established. This body creates its own shock pattern, the effect of which is discussed in the next subsection. As the throat is contracted the efficiency rises to an optimum value and then drops until, at the critical area ratio, the flow is choked. This is shown clearly in Fig. 5-7 where the experimentally determined polytropic efficiency of diffusers at M = 2.83, 6.86, 10 and 20 is given in terms of the contraction ratio. The data at M = 20 is for a helium tunnel and hence quantitatively not comparable with the other two curves. Actually, the quantitative aspect of all the curves is less significant than the trends typified by them, since the efficiency is dependent upon the boundary layer, i.e., the Reynolds number, as well as the diffuser design and flow Mach number. The optimum contraction ratio has also been shown to be a function of the supersonic contraction angle and of the length of the contraction section. The contraction angle should be of the order of 5 to 10 deg for $M < 4$, but may be increased to 15 or 20 deg at very high Mach numbers, i.e., $7 < M < 10$. The contraction length is usually about 5 to 10 times the test-section diameter (or height). Figure 5-5 shows the calculated minimum starting contraction ratio as a function of the test-section Mach number and compares it with experimentally determined minimum starting and running as well as optimum running contraction ratios. It may be seen that as the Mach number is increased, the optimum contraction is much less than that required for establishing the flow. At low Mach numbers little is to be gained by varying the contraction ratio. Experimentally derived efficiencies for several diffusers with the optimum throats discussed above and shown in Fig. 5-5 are given in Fig. 5-2 (open symbols). It may be seen that the isentropic efficiency associated with a variable throat is much higher than that for the same diffusers operating with no second throat (solid symbols) or with the minimum starting throat (half-shaded symbols).

The power requirements and the available running time are dependent on the variable-throat area. These relationships will be discussed in Subsecs. 5.7 and 5.8.

5.5 Oblique-Shock Diffusers

The principle of the Oswatitsch ramjet diffuser (see Subsec. 3.3) may also be applied to a supersonic wind-tunnel diffuser. The design is based upon the improved efficiency of diffusion through a series of oblique shocks as compared with that of a single normal shock. An innerbody is usually placed on the centerline of the tunnel (a cone or isentropic spike for an axially-symmetric tunnel; a simple wedge or double wedge for a two-dimensional tunnel). The shock system is of the type shown in the sketch below.

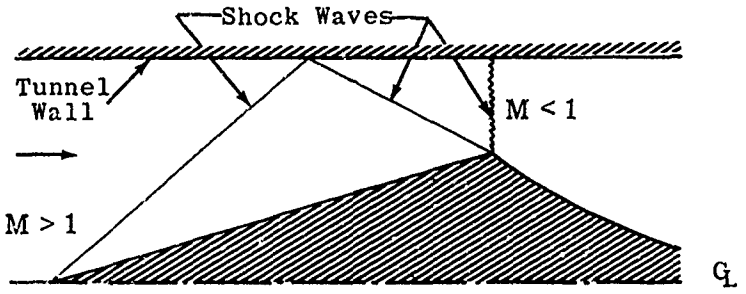

The most efficient oblique-shock diffusers are those designed to give near-sonic velocity just downstream of the last shock. The theoretical isentropic efficiency, η_σ, of such diffusers is compared with the simple normal-shock diffuser in Fig. 5-8. It may be seen that if a sufficient number of shocks are produced, the efficiency may approach a very high value. A diffuser of several shocks must be carefully designed for a specific Mach number and hence will operate only within a narrow range of off-design conditions. Beyond this range it will either choke the tunnel or operate at a much lower efficiency. A simple bridge or strut across the tunnel gives moderate efficiencies through a wide range of Mach numbers.

Little (Ref. 207) describes tests made with a variable-throat diffuser both with and without a wedge at the diffuser entrance. The polytropic efficiency, η_D, for both cases is shown in Fig. 5-9 as a function of the throat to test-section area ratio, A_2/A_1. It may be seen that the presence of the wedge made very little difference to the minimum compression ratio at which the tunnel would run; 0.665 with and 0.715 without the wedge. However, it greatly affected the starting ratio; 0.76 with and 1.146 without the wedge. For optimum conditions with the wedge, the throat area was about 0.875 of the test-section area and gave $\eta_D = 0.364$, whereas without the wedge, the optimum throat was approximately equal to the entrance area and η_D was 0.353.

The technique of using an innerbody is often incorporated into other forms of diffusers. The diffuser for a wind tunnel designed to operate at Mach number 3.5 is described by Leavy in Ref. 174. The incidence gear on which models are mounted acts as a partial diffuser. During starting and stopping

at high stagnation pressures it is below the tunnel floor. When the tunnel is running it is raised to the centerline of the diffuser section and, together with a jack-operated hinged wall, provides the optimum area of the second throat. The layout of the diffuser and details of the incidence gear are illustrated in Figs. 5-10 and 5-11.

5.6 Diffusers With Air Injection or Suction

A thick boundary layer not only gives rise to high viscous losses but under many circumstances it may separate from the diffuser walls and thus create even greater losses. Separation losses may be reduced either by injecting high-energy air into the boundary layer or by removing some of the boundary layer by suction.

Suction has also been employed in diffusers to remove the contaminating exhaust gases consequent upon ramjet and turbojet tests in a wind tunnel. The effect of such a scavenging action on the diffuser operation is discussed in Subsec. 5.6.3.

5.6.1 Air Injection

An ingenious piece of research has been done by Hasel and Sinclair (Ref. 198) to determine the effectiveness of supersonic injection at the diffuser throat. Part of the diffuser is shown in the sketch below.

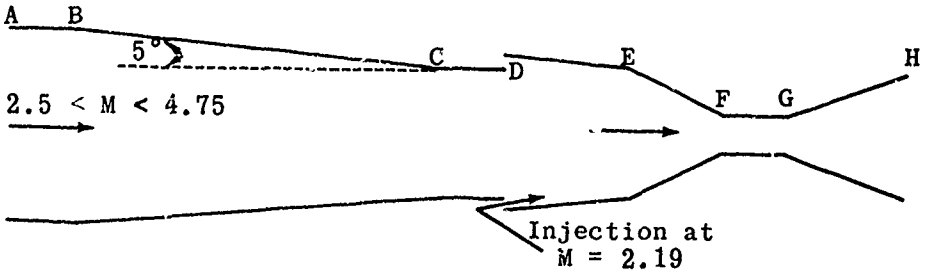

The Mach number in the test section, AB, may vary from 2.5 to 4.75. The supersonic diffuser, BC, of 5 deg inclination is long in order to minimize shock and boundary-layer interaction effects. It is followed by a short parallel shock duct, CD. The air which is injected at D is the excess mass flow from a constant-volume compressor and is capable of achieving high mass-flow ratios (injector to main stream), i.e., from 1 at M = 3 to 4.8 at M = 4.75. The by-pass air is fed through a sonic throat in the injector section from which it emerges at M = 2.19 and mixes with the stream in section DE before passing through a second supersonic diffuser, EF, a shock duct, FG, and a subsonic diffuser, GH.

The supersonic injected air improves the diffuser efficiency in the following ways:

1. It raises the total head slightly. The by-pass is short and hence the stagnation pressure of the injected air is higher than that of the main stream, which has already suffered viscous and oblique-shock losses.

2. The injection re-energizes the boundary layer and reduces further shock-interaction losses.

3. Except when the free-stream Mach number is low, the static pressure of the injectant is higher than that of the free stream and thus exerts a decelerating effect.

At a stagnation pressure of 120 psia, the experimental data (given in Fig. 5-12) in the range of $2.5 \leq M \leq 4.75$ show that the isentropic efficiency of the diffuser without air injection varies from 0.84 to 0.54. With air injection it is virtually constant at 0.89 for all Mach numbers, pointing up the increased advantage of this technique for high Mach numbers.

The effect of injection on the power requirements is discussed in Subsec. 5.7, and the effect of a model in the test section in Subsec. 5.9.

5.6.2 Air Suction

An experimental study of the effect of distributed boundary-layer suction on the efficiency of a diffuser without contraction has been made by Cohen and Valerino and is reported in Ref. 192. The test-section Mach number of the 3.84 × 10 in. tunnel was 2.0. Suction was applied to the two porous sidewalls of the constant-area section whose length was 46 inches. Following this constant-area section was a subsonic diffuser with the horizontal walls diverging at 5 deg and the vertical ones at 6 degrees. A schematic diagram of the tunnel is given below.

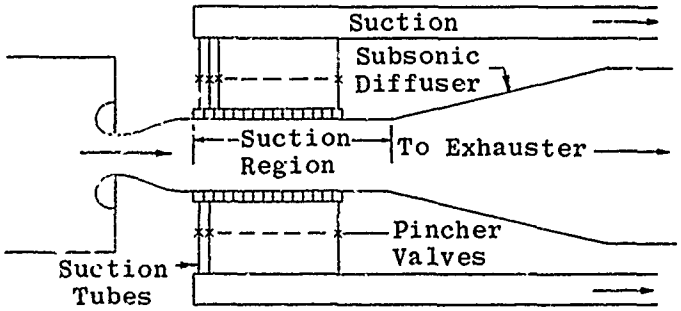

The weight ratio of the bleed air to the main-stream air varied from 0 to 8%. The length of the shock system in the parallel duct was varied by adjusting the tunnel outlet valve connected to a bank of reciprocating exhausters which also furnished the suction for the boundary layer. As the bleed ratio was increased the efficiency of the diffuser improved, reached a maximum, and then decreased. The optimum bleed ratio was dependent on the shock length and varied from 1.5% at $\ell_s/h = 2$ to 4.5% at $\ell_s/h = 4.5$. Schlieren photographs of the flow indicated that with no suction the shock system was highly unstable, oscillating in the streamwise direction by as much as 10 inches. Boundary-layer separation was noted and a gradual static pressure rise measured. When suction was applied, the amplitude of the instability was reduced to about one-fifth of its previous value, and the shock system appeared to be reattached to the tunnel walls while the measured pressure and Mach number approached

those predicted by theoretical one-dimensional normal-shock values. The efficiency improvement due to the suction varied from 4 to 6%, and is shown in Fig. 5-13 as a function of the length of the shock system in the constant-area duct. The maximum efficiency (taken from Fig. 5-13), with and without suction, is shown in Fig. 5-12.

5.6.3 Scavenger Scoop

It is often necessary in ramjet and turbojet engine tests to use a scavenger duct in the diffuser section to collect the contaminating exhaust gases. Hastings and Roberts (Ref. 193) developed a method of calculating the performance of such a diffuser and showed that their analytical results agreed well with experimental data at several Mach numbers. The following sketch shows the general configuration which they tested.

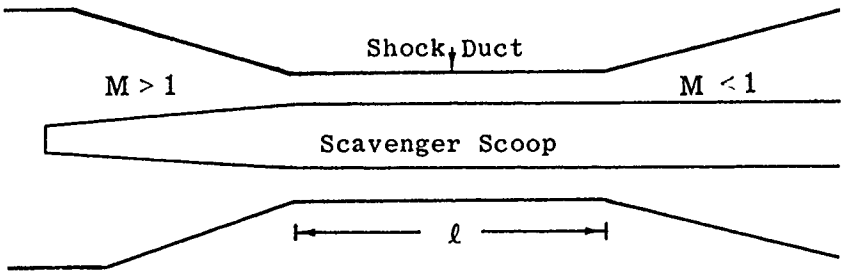

Tests of the diffuser without the scoop showed that the most critical feature of the diffuser is the relative length of the shock duct, ℓ/h. The optimum length will be that of the actual shock system associated with any set of flow characteristics (see Subsec. 5.3). A compilation of measured values of the shock length, ℓ_s/h, as a function of the average Mach number in the duct has already been given in Fig. 5-4. It was found that in the presence of the scoop the length of the shock duct is still of critical importance; the performance of the diffuser as a whole was relatively insensitive to the length of the supersonic contraction. It was impossible either to establish or to maintain supersonic flow in the tunnel unless the scoop suction was sufficient to swallow the shock. Once the shock was swallowed the addition of the scoop did not materially affect the performance of the diffuser provided the cross section of the scoop was constant throughout the length of the shock duct, i.e., as long as the effective duct area did not vary along its length. The starting and running power requirements of the diffuser with two scoop configurations are given in Subsec. 5.7, and the effect of a model in the test section is discussed in Subsec. 5.9.

5.7 Power Requirement and Diffuser Efficiency

In order to start a wind tunnel it is theoretically necessary to have a pressure ratio between the stagnation chamber and the diffuser exit (p_{t_o}/p_{t_e}) sufficient to maintain a normal shock in the test section. In practice a slightly lower pressure ratio suffices since the shock actually occurs before the Mach

number has reached its maximum value (see page 274). This starting ratio (taken from normal-shock tables with $\gamma = 1.4$) is shown as curve A in Fig. 5-14 together with experimental data from several sources (open symbols).

Once supersonic flow is established and the shock system stabilized beyond the second throat (Subsec. 5.4), the flow may be maintained with a lower compression ratio than is required for starting. The more efficient the diffuser the less the actual power consumption. In blowdown or intermittent tunnels the power saving is most significantly reflected in longer running time (Subsec. 5.8). For a normal shock assumed to occur at a second throat with the minimum area ratio for starting, the pressure ratio is given by curve B of Fig. 5-14. This corresponds to a constant-geometry diffuser under its most efficient conditions. Data points for diffusers operating with the minimum starting throats (closed symbols) and optimum positions of variable throats (flagged symbols) have been added to Fig. 5-14 for comparison with the theoretical curves.

When diffuser efficiency is improved by suction the power requirements for the suction must be weighed against the power saving due to the reduced compression ratio in order to assess the economy of the system as a whole. In the tests of Ref. 192, the optimum bleed-weight ratio (see Subsec. 5.6.2) produced a net saving of 6 to 8% of the total power required. It was determined that although the suction was applied in the test section, the greatest power reduction (50%) occurred in that which was required for the subsonic diffusion. This suggests that the improvement is effected by a change in the nature of the flow entering the subsonic diffuser.

For the scoops of Ref. 193 (see Subsec. 5.6.3), the compression ratio for starting and running the tunnel is given in Fig. 5-15, together with the basic configuration of the two scoops that were tested. In the presence of the scoops the contraction ratio is corrected to represent the actual cross-sectional area of the free-stream flow in the test section and the shock duct. With Scoop II, which is designed to maintain a long constant annular shock duct, the starting compression ratio is about 6% greater than that for the empty diffuser; with Scoop I, which reduced the constant-area section by half its length, the compression ratio was increased by a further 3%. During operation the difference between the two scoops increased to about 8%. The effect of two different models in the test section will be discussed in Subsec. 5.9.

The excess pressure ratio made available by varying the second throat after tunnel stabilization has occasionally been utilized to allow an increase in the test-section Mach number. The Mach number increase has been achieved by the insertion of a small pin along the centerline of an axisymmetrical nozzle throat which effectively reduces the throat area.

5.8 Run Time and Diffuser Efficiency

Since a compression ratio high enough to start the tunnel must always be available, the power economy of highly efficient diffusers is not always of paramount importance. However, the length of time that an intermittent or blowdown tunnel can operate is nearly always of prime consideration. The run time is strongly affected by the diffuser efficiency. To show this, consider a tunnel running at constant stagnation pressure, p_t, with test-section

Mach number, M, emptying into a vacuum tank of volume V_2 which is originally at zero pressure.

The mass in the tank at any time, τ, is given by the mass flow through the test section, i.e.,

$$(V_2\rho_2)_\tau = \rho VA\tau$$

which, from Eqs. 2-2 and 2-3, gives

$$(V_2\rho_2)_\tau = AM(\gamma p_t \rho_t)^{1/2}\ \tau \left(1 + \frac{\gamma - 1}{2} M^2\right)^{-\frac{(\gamma+1)}{2(\gamma-1)}} \tag{5-13}$$

According to Eq. 5-4, the relation between the critical pressure in the tank at time τ and the diffuser efficiency is

$$\frac{(p_2)_\tau}{p_t} = \left(\frac{p}{p_t}\right)^{1-\eta_D}$$

where

p = the test-section static pressure.

Equation 5-13 thus becomes

$$\tau = \left(\frac{p}{p_t}\right)^{1-\eta_D} \frac{V_2}{AMRT_2} \left(\frac{p_t}{\gamma\rho_t}\right)^{1/2} \left(1 + \frac{\gamma - 1}{2} M^2\right)^{\frac{\gamma+1}{2(\gamma-1)}} \tag{5-14}$$

For constant values of the stagnation conditions and for constant geometry this reduces to

$$\tau \propto \left(\frac{p}{p_t}\right)^{1-\eta_D} \cdot \frac{1}{T_2} \tag{5-15}$$

or by assuming $T_2 \propto (p_2)^{\frac{\gamma-1}{\gamma}}$ and using Eq. 5-4 once more

$$\tau \propto \left(\frac{p}{p_t}\right)^{\frac{1-\eta_D}{\gamma}} \tag{5-16}$$

From this

$$(d\tau/\tau)/(d\eta_D/\eta_D) = \frac{\eta_D}{\gamma} \log_e (p_t/p) \tag{5-17}$$

Values derived from Eq. 5-17 are shown as a function of η_D and M in Fig. 5-16, from which it may be noted that the percentage increase of the run time may be many times that of the diffuser efficiency. In order to get a rough estimate of the increased run time that might be expected at any Mach number a curve of η_D vs M has been added to Fig. 5-16. The theoretical η_D is that obtained with a normal shock in the minimum starting throat. From Ref. 195, pressure ratios required to maintain various run times of 10, 40 and 90 sec for a tunnel at M = 6.86 have been used to compute values of $d\tau/\tau$ and $d\eta_D/\eta_D$. The three points representing $d\tau$ of 30, 50 and 80 sec are shown in Fig. 5-16 where they are in good agreement with the theoretical curves.

When the stagnation pressure is also a function of time, as it often is in blowdown tunnels, the run time is even more strongly dependent on the diffuser efficiency. Reference 209 compares a varying-area second throat diffuser with one having a constant-geometry. The efficiencies (η_D) were 0.623 and 0.415 for a test-section Mach number of 4.2 while the run times were 17 and 9 seconds. The value of $(d\tau/\tau)/(d\eta_D/\eta_D)$ is 1.77 which is higher than the associated value from Fig. 5-16. This is to be expected since stagnation pressure decreases with time.

It was estimated that the variation of the flexible throat (for the tunnel shown in Figs. 5-10 and 5-11) and the oblique shocks from the centerbody would so improve the diffuser efficiency that at M = 3.5 the run time would be increased from 10 to 40 seconds.

5.9 Effect of a Model on Diffuser Efficiency

It is generally assumed that when there is a model in the test section the diffuser efficiency is reduced. Comparison is made in Fig. 5-17 between data in which "model" and "no model" tests were made with all other conditions remaining constant. The data from all tests but one indicate that the presence of a model reduces the diffuser efficiency.

In tests with air injection in the diffuser (Ref. 198) the isentropic efficiency remained virtually constant for Mach numbers from 2.9 to 4.75. With no model in the test section, the value of η_σ was 0.82, but when a typical research model was present η_σ dropped to 0.78. With neither a model nor air injection, the efficiency varied as shown in Fig. 5-17. When the typical research model was reintroduced, the efficiency dropped 5 to 10%. This reduced efficiency is due principally to the fact that choking occurs with a larger diffuser throat than it does with an empty test section.

In suction tests at M = 2 (Ref. 192), where the efficiency is dependent on the length of the shock system, the average value of η_σ for the empty diffuser is also higher than when a model is present. However, the spread of the data with the model is less than the spread with no model. When the tunnel is empty the shock system oscillates back and forth in the diffuser and creates undesirable disturbances. When a model is present the bow shock, or

its reflection from the tunnel walls, stabilizes the shock system (see Subsec. 5.5). Static pressures measured along the diffuser of a Mach 4.2 tunnel (Ref. 209) at different times during a run showed wide fluctuations when no model was used, but were much steadier as a function of time when a cone was located in the test section.

The total shock loss may also be reduced by the oblique shocks from the model. This is especially true of sharp-nosed models such as cones and wedges in high Mach number flow. Little (Ref. 207) reports higher efficiencies at Mach 10 with a wedge model present in the test section than with an empty tunnel (see Fig. 5-9).

Ducted bodies and cone-cylinders were tested in combination with the scavenging-scoop diffusers described in Subsec. 5.6.3. A comparison of the starting and running pressure ratios is given in Fig. 5-18 from which it may be noted that while a cone-cylinder model requires a somewhat larger second throat than either the ducted body or the empty test section, it nevertheless permits a reduced compression ratio both for running and for starting.

5.10 Hypersonic Diffusers

The problems of hypersonic diffusion are basically the same as those encountered in the supersonic regime; the effects, however, are usually more pronounced. The strong shock waves, for instance, and thicker boundary layers normally occurring in hypersonic tunnels may cause more extensive regions of separated flow than in the supersonic case, resulting in reduced diffuser efficiency. There are also new problems inherent in hypersonic diffusion. For the most part they are associated with the use of high-enthalpy flows producing real-gas effects too significant to be neglected with impunity.

The few systematic investigations of hypersonic diffusers that have been made up to the present are reported in Refs. 194, 195, 206 and 207. In all of these save one (Ref. 206), the Mach number is less than 10 and stagnation conditions are such that real-gas effects are negligible. The data therefore have been summarized in the previous subsections, where it is shown that the efficiency decreases rapidly with increasing Mach number. It has also been shown that the efficiency may be improved by means of a shock duct, i.e., a constant-area throat section. However, in high-enthalpy tunnels, the structural and cooling problems introduced by the high heat-transfer rates in the shock duct may more than offset the gain in efficiency. The heat-transfer phase of the problem will be treated in Section 14 of the Handbook.

Johnson and Witcofski (Ref. 206) investigated the effectiveness of variable geometry supersonic diffusers designed for a 3-in. helium tunnel operating at a Mach number of 20. The length of the converging section of the diffuser was varied from 8.8 to 20.5 inches. The lowest value of the compression ratio required to maintain supersonic flow was obtained with the shortest convergent section. The contraction angle varied from 0 to 4.7 deg, the latter angle being that associated with the shortest length. The diffuser efficiency, η_D, varied from 0.476 to 0.483.

The effectiveness of the shock-duct diffuser at the higher Mach numbers has been shown by Makofski and Rea (Ref. 210) from data obtained during

the development of a helium hypersonic wind tunnel. The nozzle, referred to on page 244, produces a test-section Mach number which varies from 16.4 17.8 with constant supply pressures from 400 to 1000 psia. The test diffus. was constructed in three major parts in order to facilitate geometric changes. The two entrance sections (see sketch below) had angles of 2.5 and 4 degrees. The exit section had a 10 deg divergence. Straight sections of 2.5, 5, 10 and 15 in. allowed the shock duct length to be varied from 0 to 32.5 inches. The internal diameter of the shock duct was changed by boring out the initial channel in successive increments.

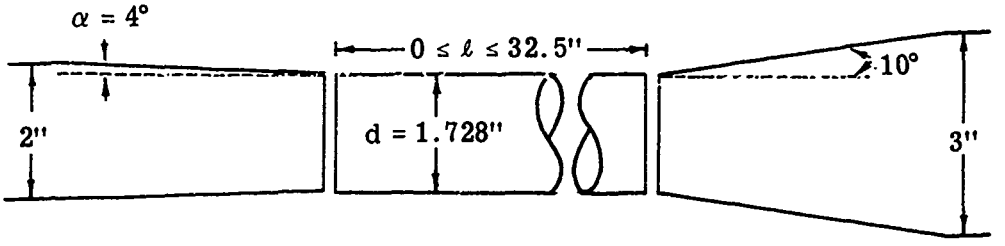

Although there is a wide scatter in the data, the compression ratio follows a general trend when it is plotted as a function of the length to diameter ratio of the constant-area section. Figure 5-19a and b gives typical plots for α = 2.5 and 4 deg and stagnation pressures from 400 to 1000 psia. From these and additional data (Ref. 210) it may be concluded that the optimum value of ℓ/d lies between 9 and 16. Within the limited cases there is no apparent dependence of the optimum ℓ/d on either stagnation pressure or convergence angle.

The minimum operating compression ratio is plotted against α and p_{t_o} in Fig. 5-19c from whence it may be seen that the best value for α is in the neighborhood of 2.5 degrees. From the chart that accompanies Fig. 5-19c it may be seen that the minimum compression ratio is a strong se function of the Reynolds number. This is of course to be expected si. he character of the shock formation in the constant-area duct is primarily determined by the type and thickness of the boundary layer.

Since the diffuser throat area was enlarged in discrete increments, it can hardly be considered a variable throat; however, the pressure recovery was the highest at the minimum throat which allowed starting, i.e., a contraction ratio of 0.712.

Earlier studies were made of the effect of a movable hemispherical-nosed innerbody in the diffuser. After the tunnel was started the innerbody was moved slowly up the divergent section of a short-duct diffuser (ℓ/d = 1.25). The highest pressure recovery was noted when the nose reached the exit of the constant-area shock duct. In this case the diffuser efficiency, η_D, was 0.41 compared with 0.37 for an empty diffuser. Other nose-shapes were tested but none gave as high an efficiency as the hemispherical cap.

When the above short diffuser was used the tunnel pressure ratio was found to be quite sensitive to the configuration and location of typical test models, whereas with a longer diffuser (ℓ/d = 5.93) this sensitivity was very much reduced. The effect is apparently due to the stabilizing influence of the additional reflections occurring in the shock duct.

In general, it appears that the shock-duct diffuser can significantly increase the pressure recovery, but that structural and cooling requirements may severely limit its effectiveness. Unfortunately, the lack of experimental data prevents any estimate of optimum configurations for a given Mach number and set of stagnation conditions.

Intentionally Blank

p. 286

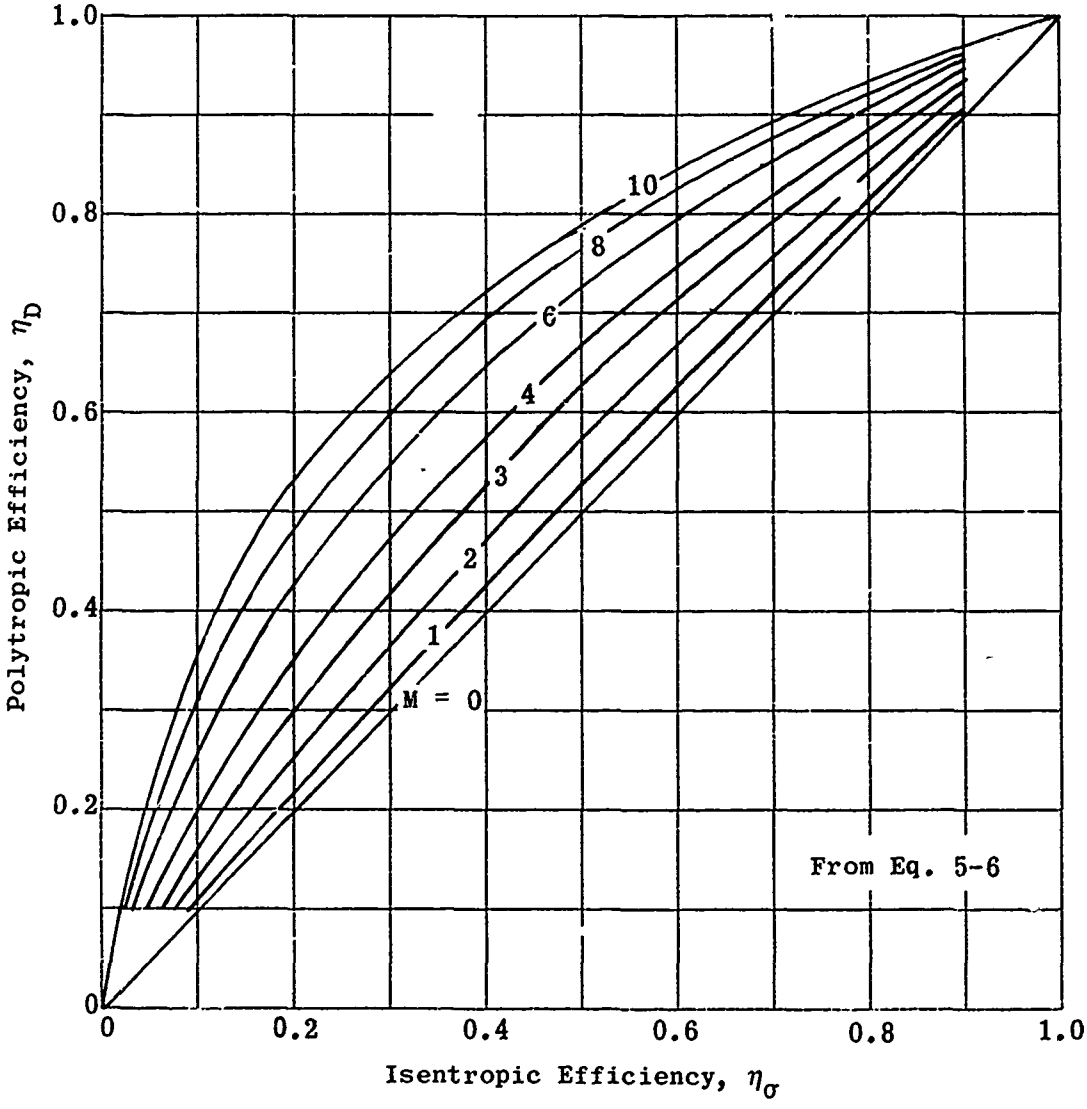

Fig. 5-1. Comparison of calculated isentropic efficiency (η_σ) with calculated polytropic efficiency (η_D) for supersonic diffusers; M = 0 to 10; γ = 1.40.

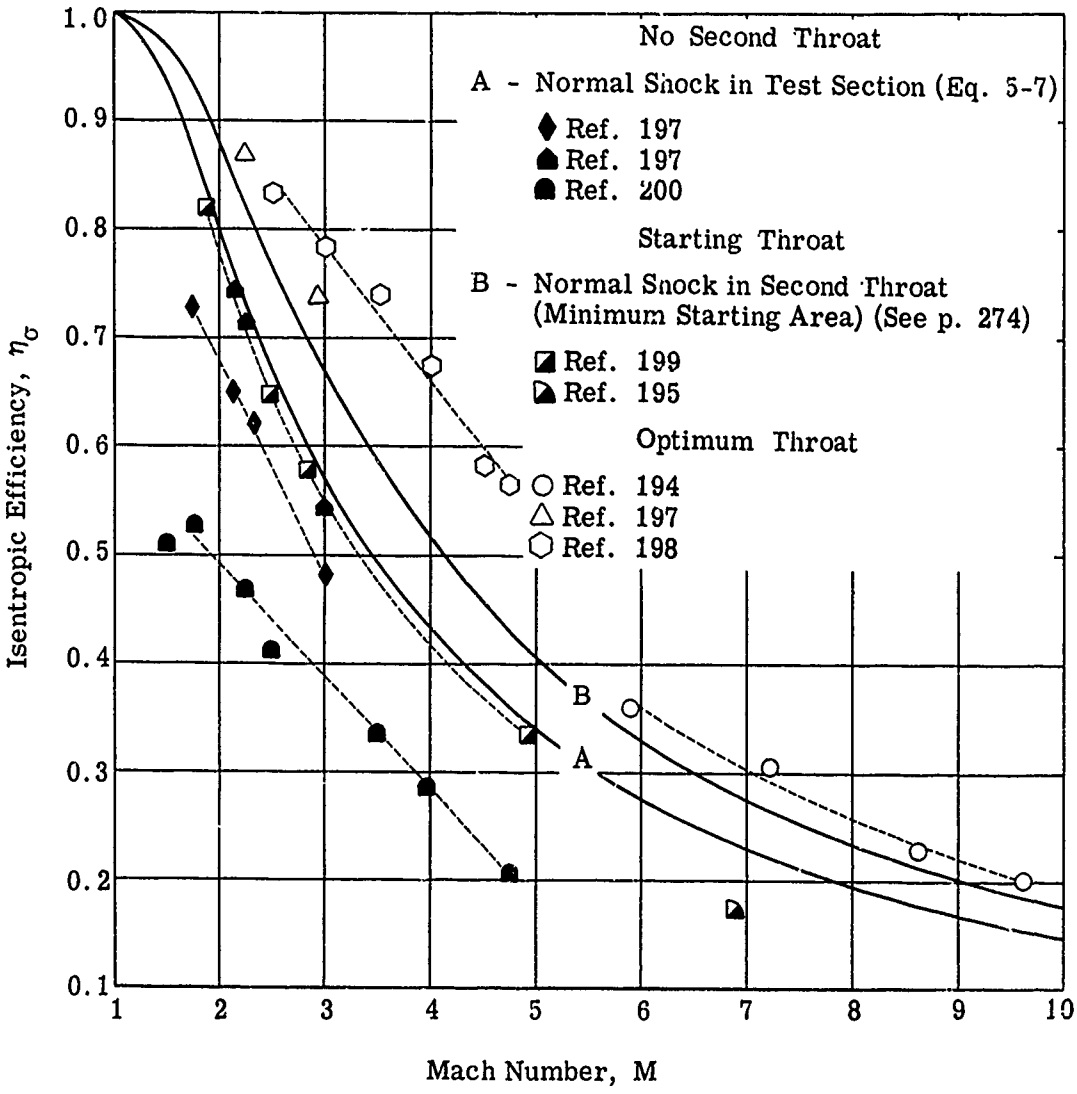

Fig. 5-2. Calculated and experimental isentropic efficiency of supersonic diffusers with full subsonic recovery as a function of Mach number; $\gamma = 1.4$; M = 1 to 10.

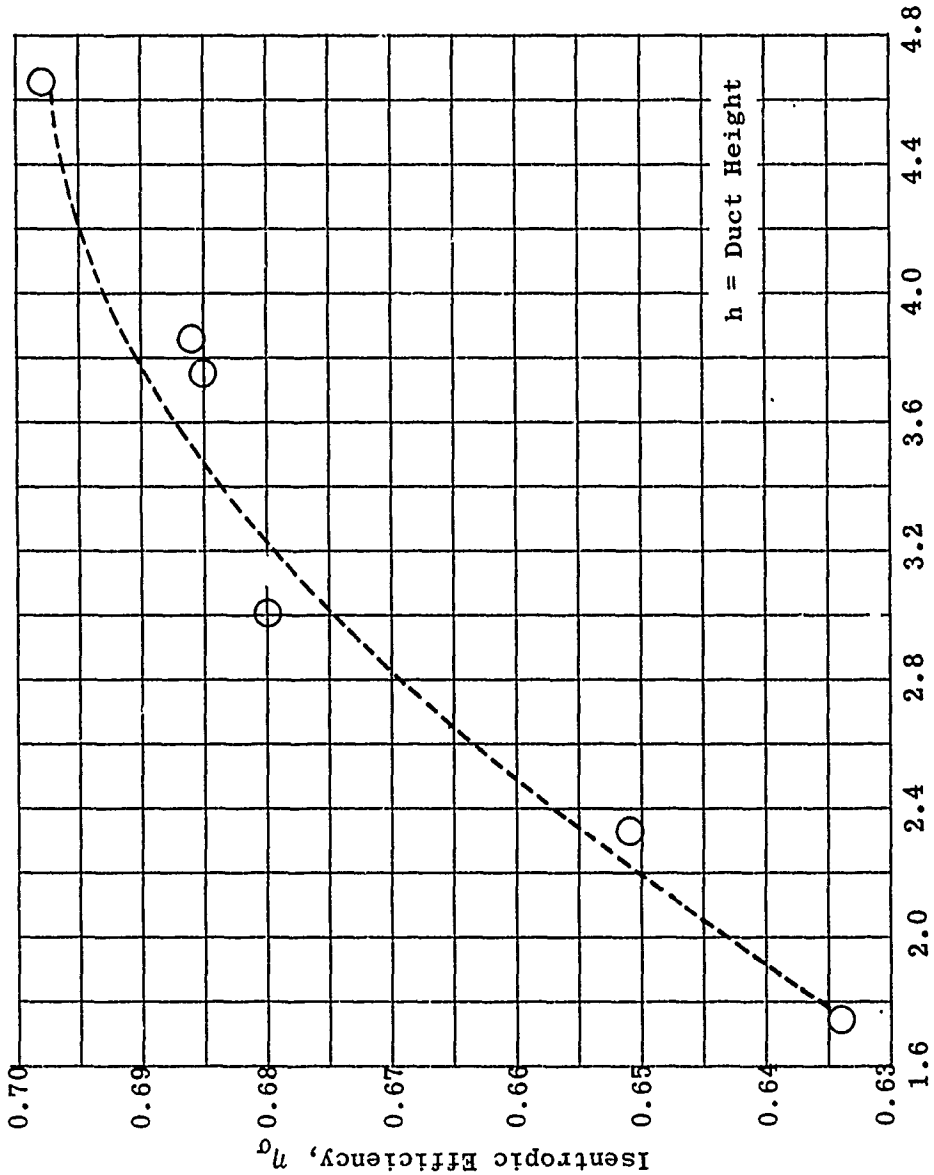

Fig. 5-3. Effect of length of constant-area duct on diffuser efficiency; M = 2. (Source: Ref. 192)

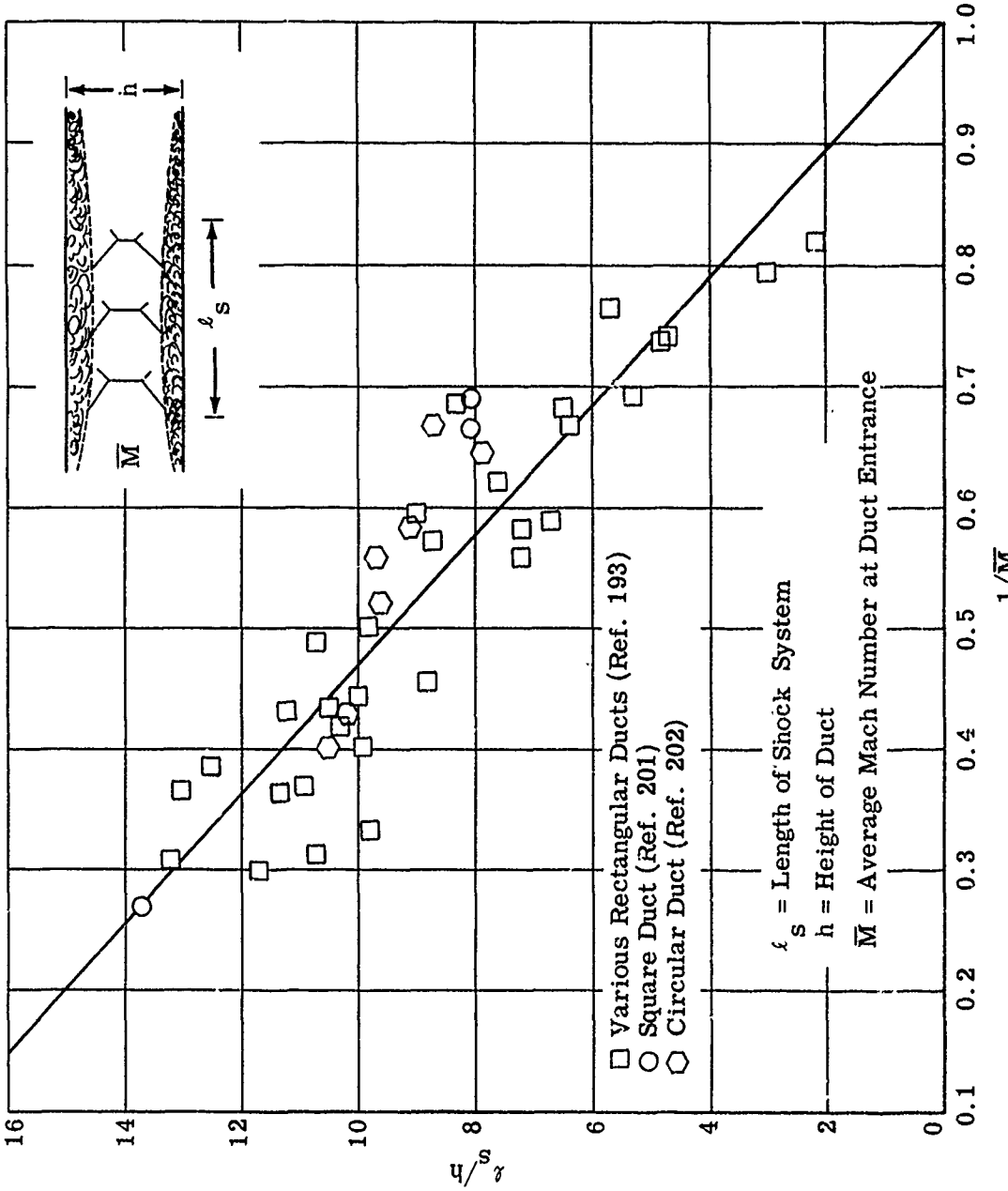

Fig. 5-4. Shock length as a function of Mach number in a constant-area duct. (Source: Ref. 193)

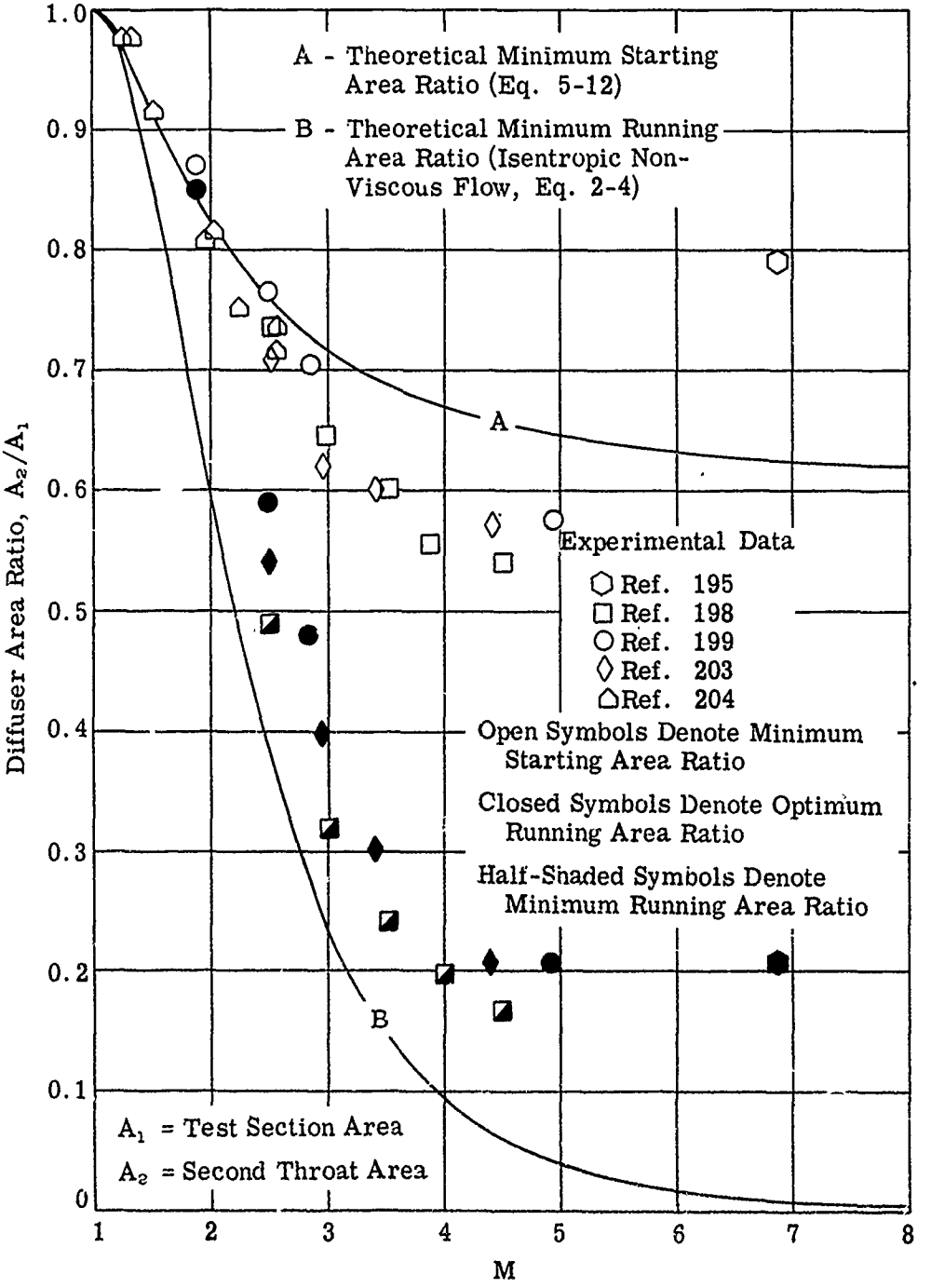

Fig. 5-5. Calculated and experimental contraction ratio of supersonic diffusers as a function of Mach number; $\gamma = 1.4$; M = 1 to 8.

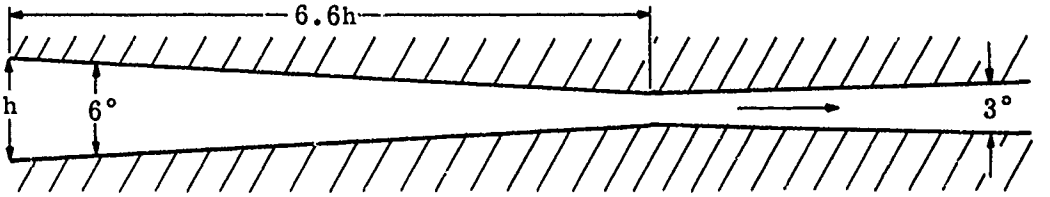

Side View of a Two-Dimensional Hypersonic Diffuser; $6 < M < 10$. (Source: Ref. 194)

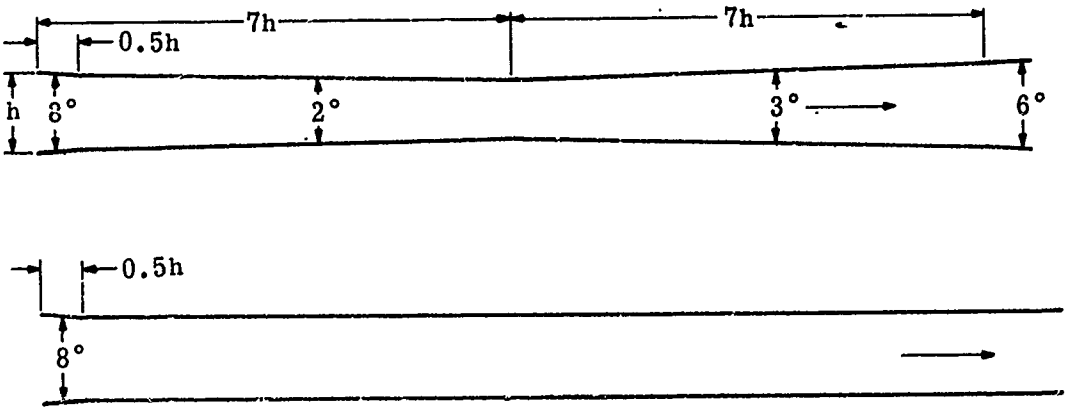

Side View and Plan View of a Quasi-Two-Dimensional Diffuser for a Mach 4 Nozzle. (Source: USCEC)

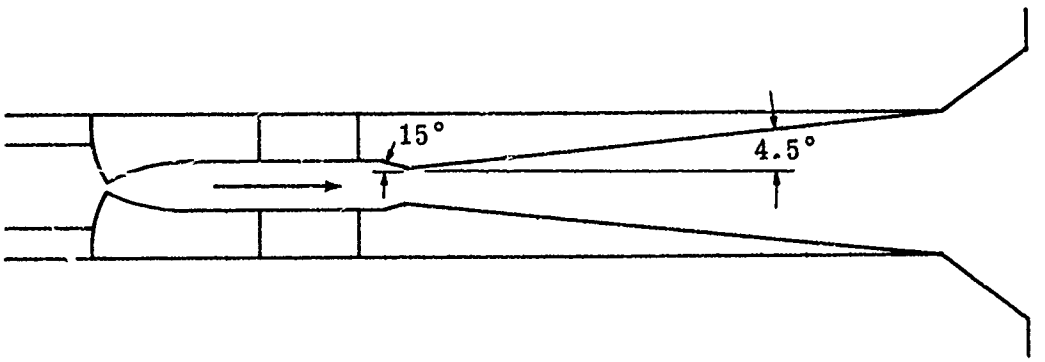

Side View of a Quasi-Two-Dimensional Diffuser for a Mach 4.4 Nozzle. (Source: Ref. 209)

Fig. 5-6. Sketches of two-dimensional diffusers for high supersonic Mach number nozzles.

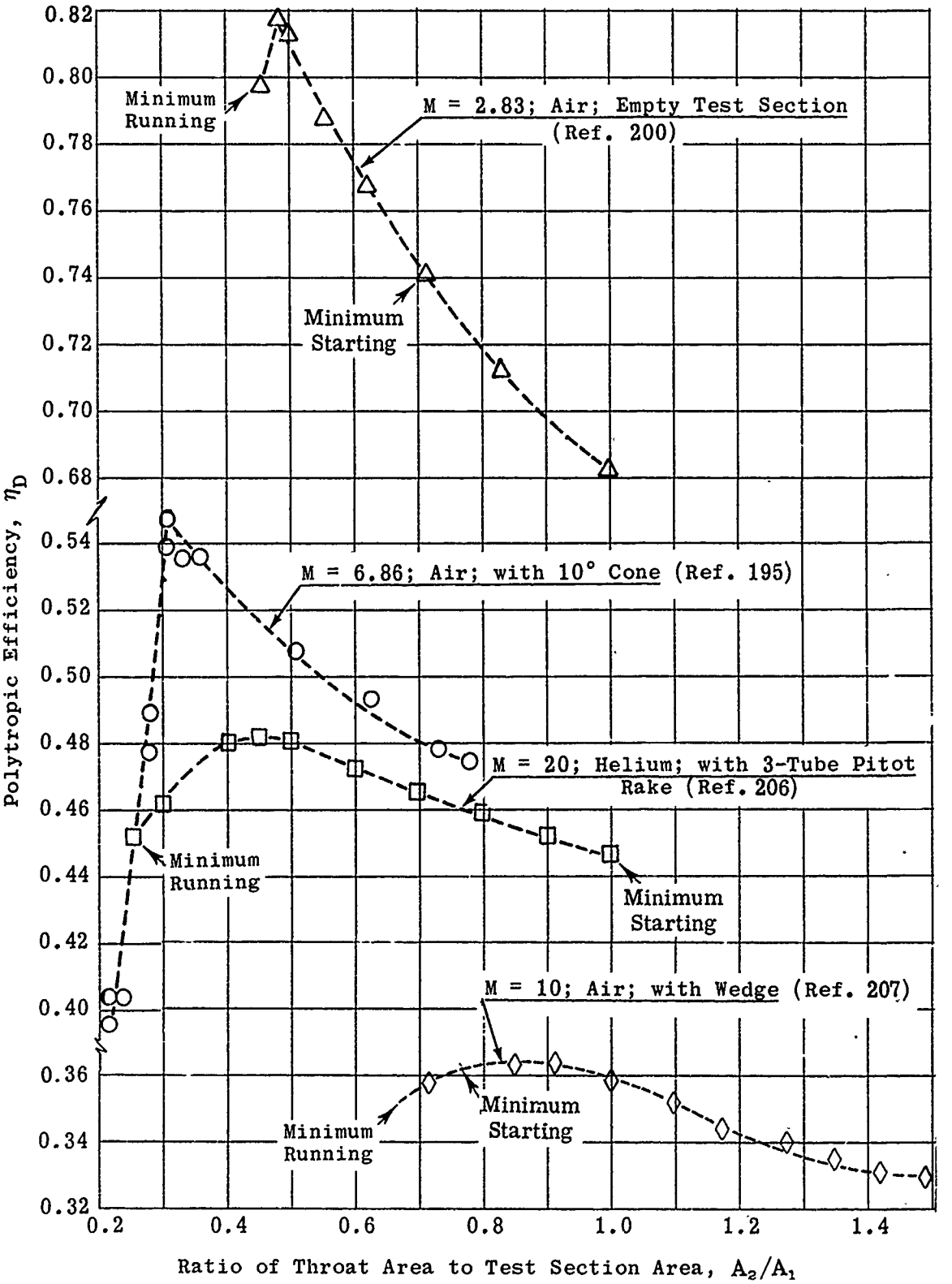

Fig. 5-7. Experimentally determined polytropic efficiency as a function of area ratio for various Mach numbers.

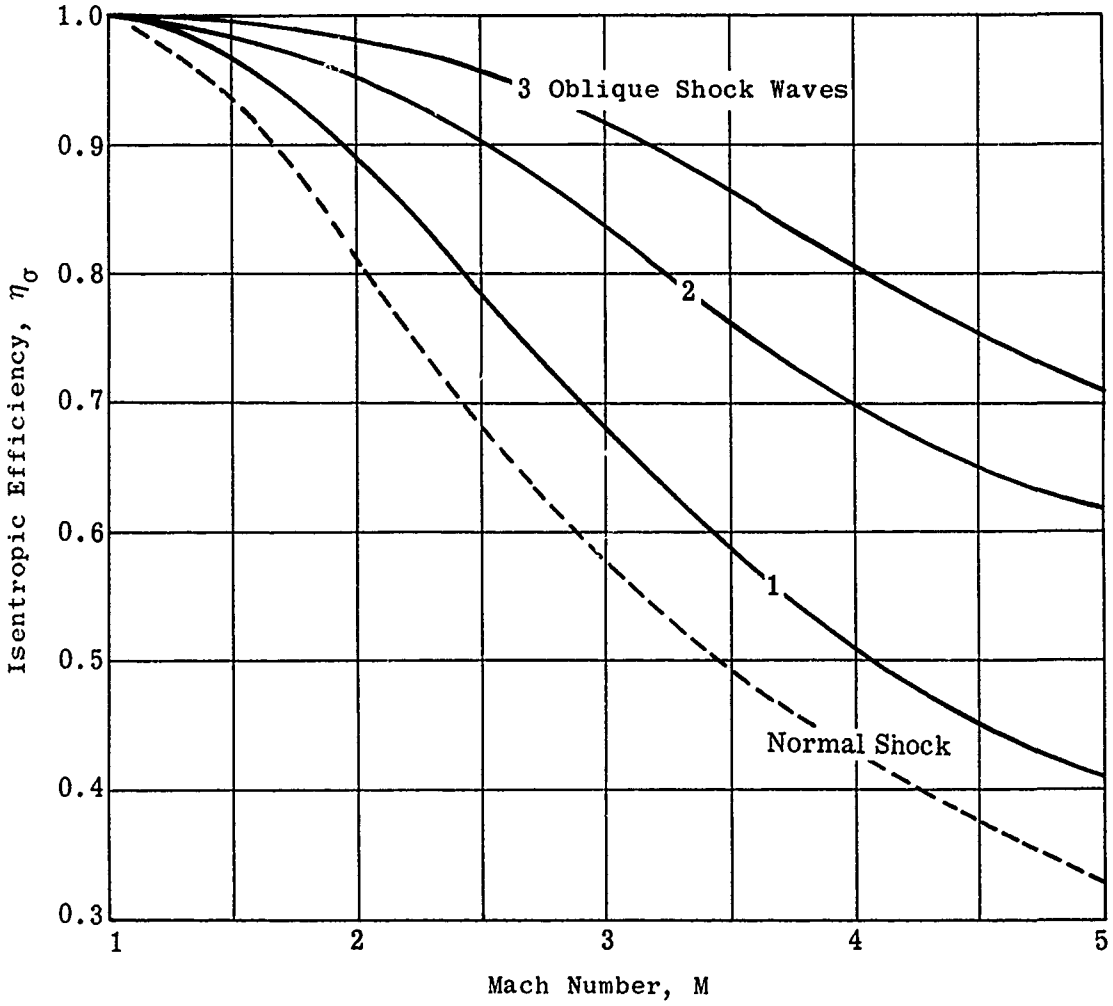

Fig. 5-8. Theoretical isentropic efficiency of normal-shock and oblique-snock diffusers with sonic velocity behind the last shock wave and full subsonic recovery. (Source: Ref. 12)

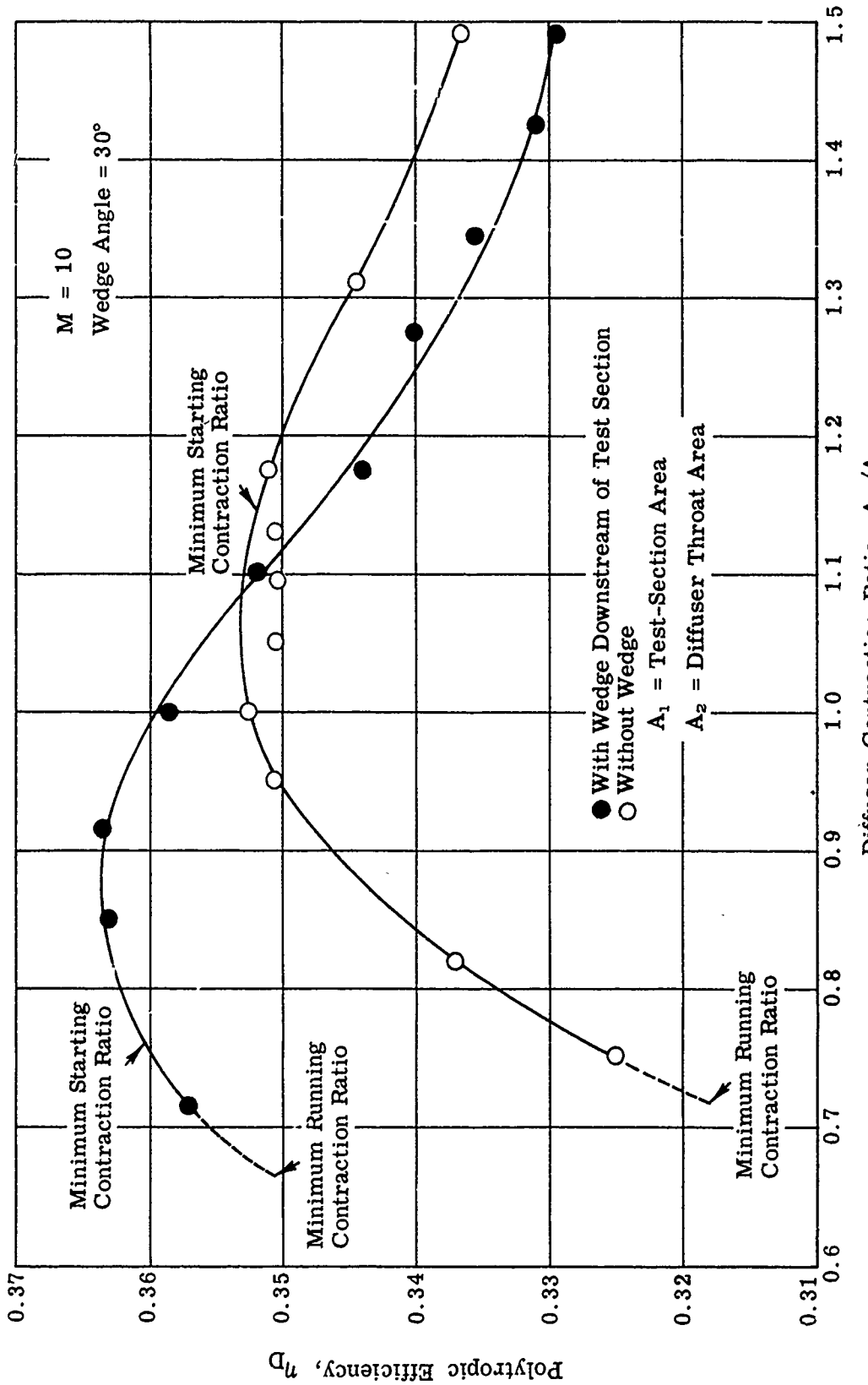

Fig. 5-9. Experimentally determined effect of an oblique shock on the polytropic efficiency of a variable-geometry diffuser. (Source: Ref. 207)

731-359 O - 64 - 21

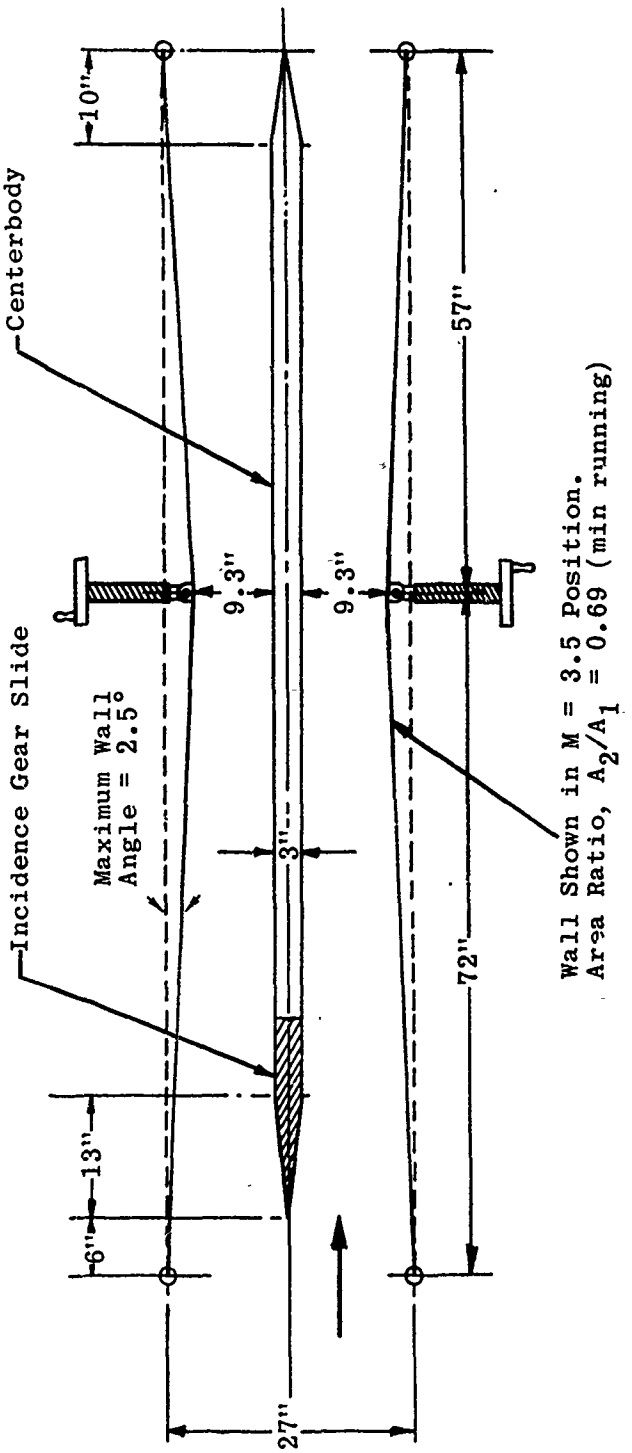

Fig. 5-10. Layout of supersonic diffuser. (Source: Ref. 174)

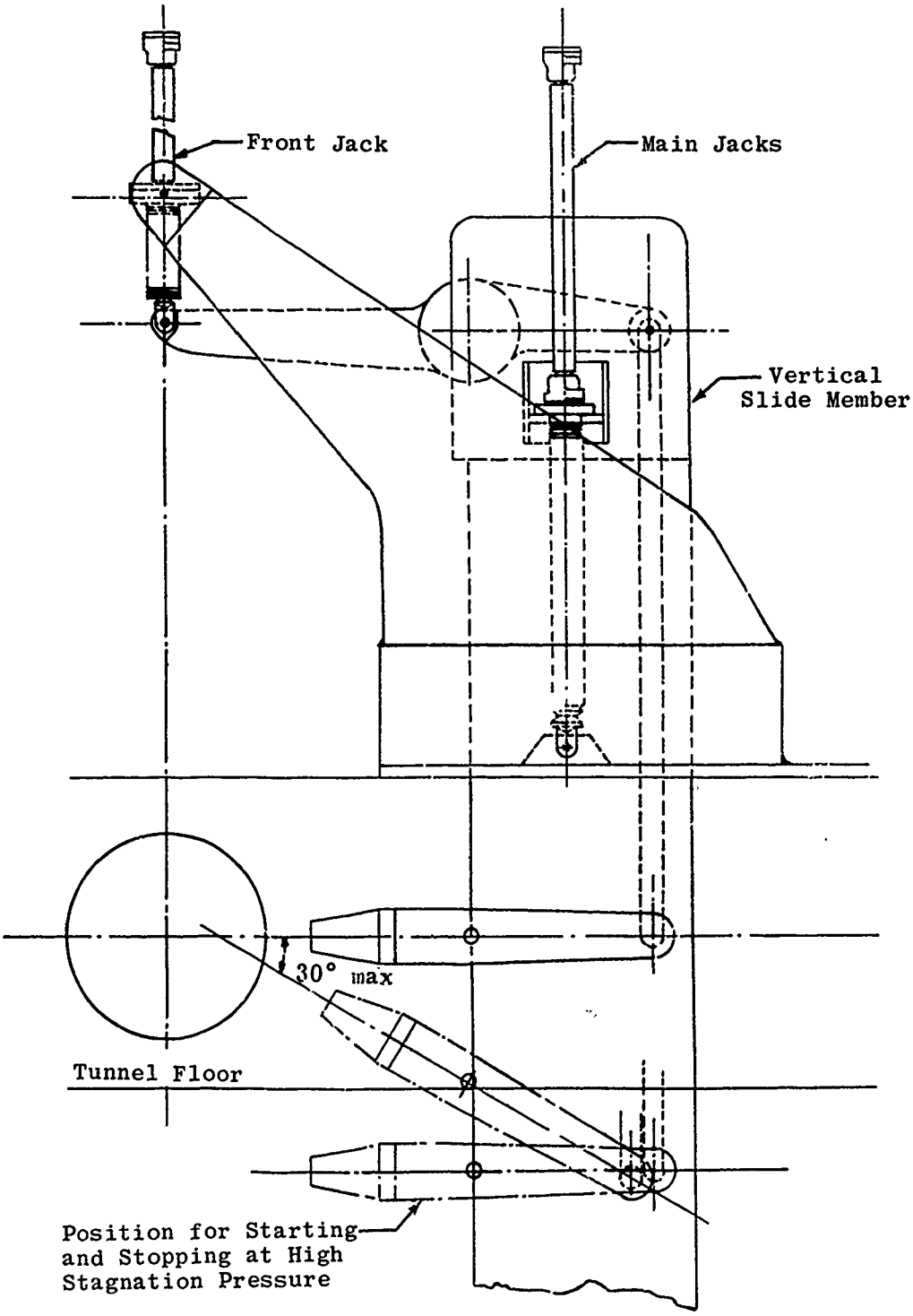

Fig. 5-11. Supersonic tunnel incidence gear. (Source: Ref. 174)

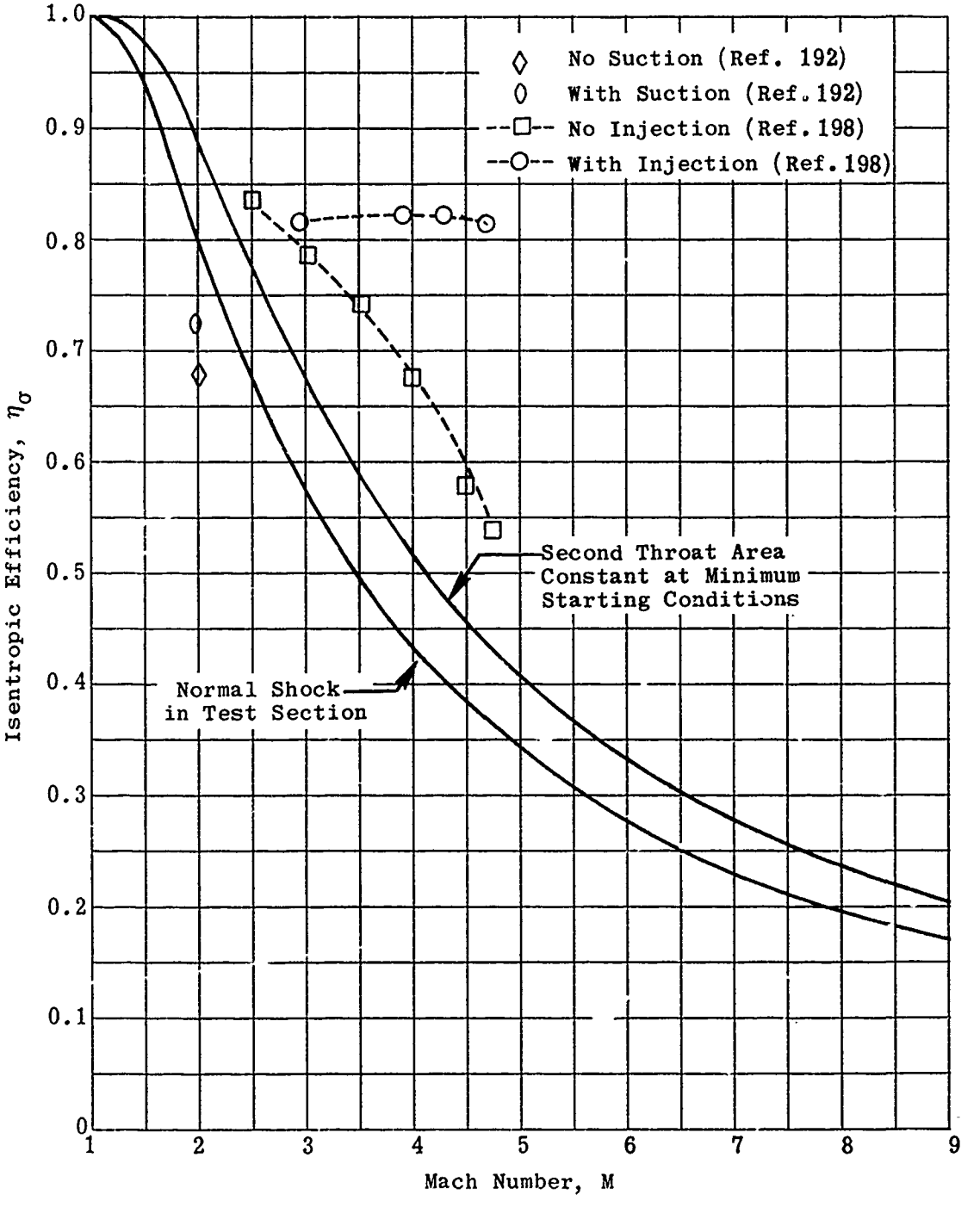

Fig. 5-12. Effect of injection and suction on isentropic diffuser efficiency.

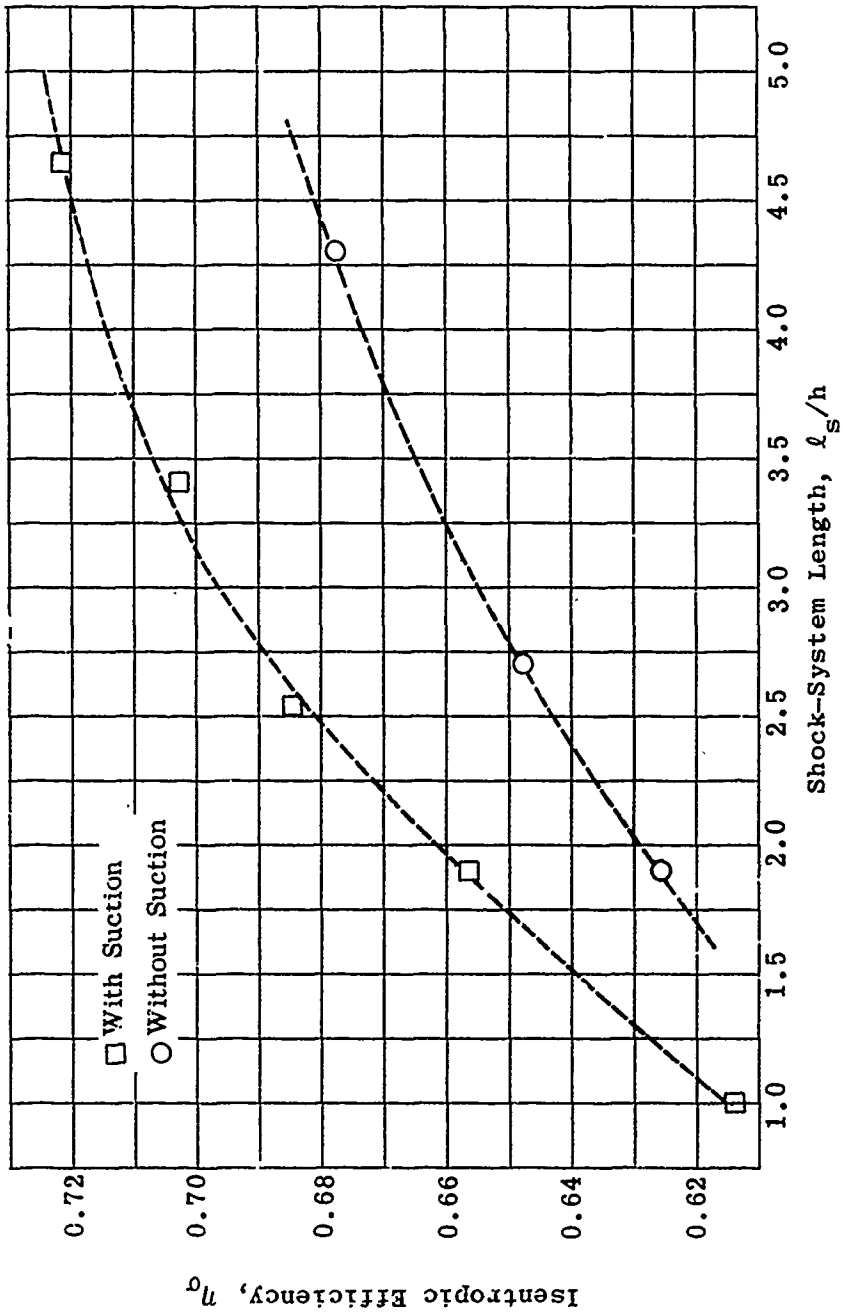

Fig. 5-13. Experimentally determined effect of suction on isentropic diffuser efficiency as a function of shock-system length; M = 2. (Source: Ref. 192)

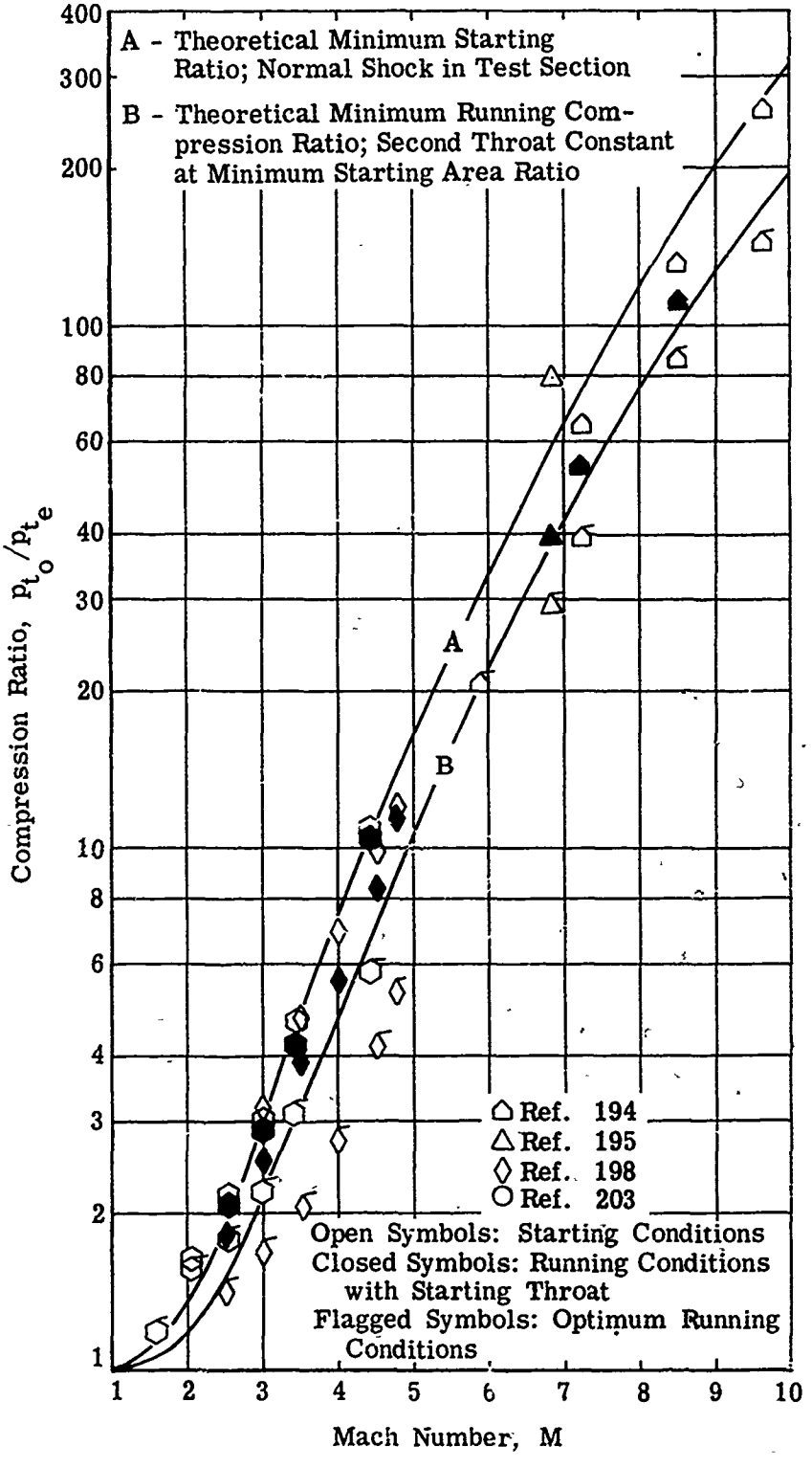

Fig. 5-14. Comparison of theoretical and experimental compression ratios as a function of Mach number.

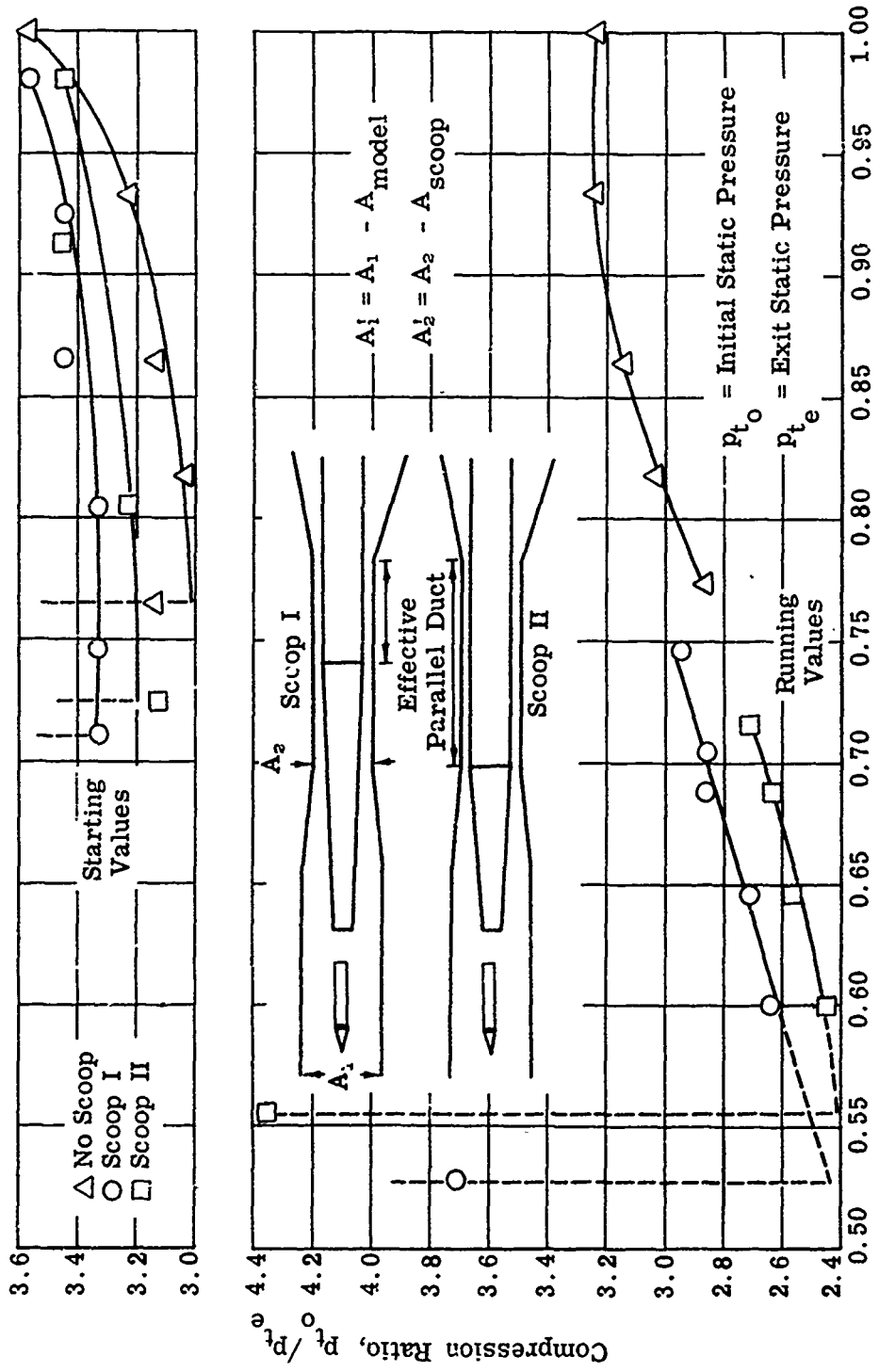

Fig. 5-15. Starting and running compression ratios as a function of contraction ratio for scoop diffusers; M = 2.86. (Source; Ref. 193)

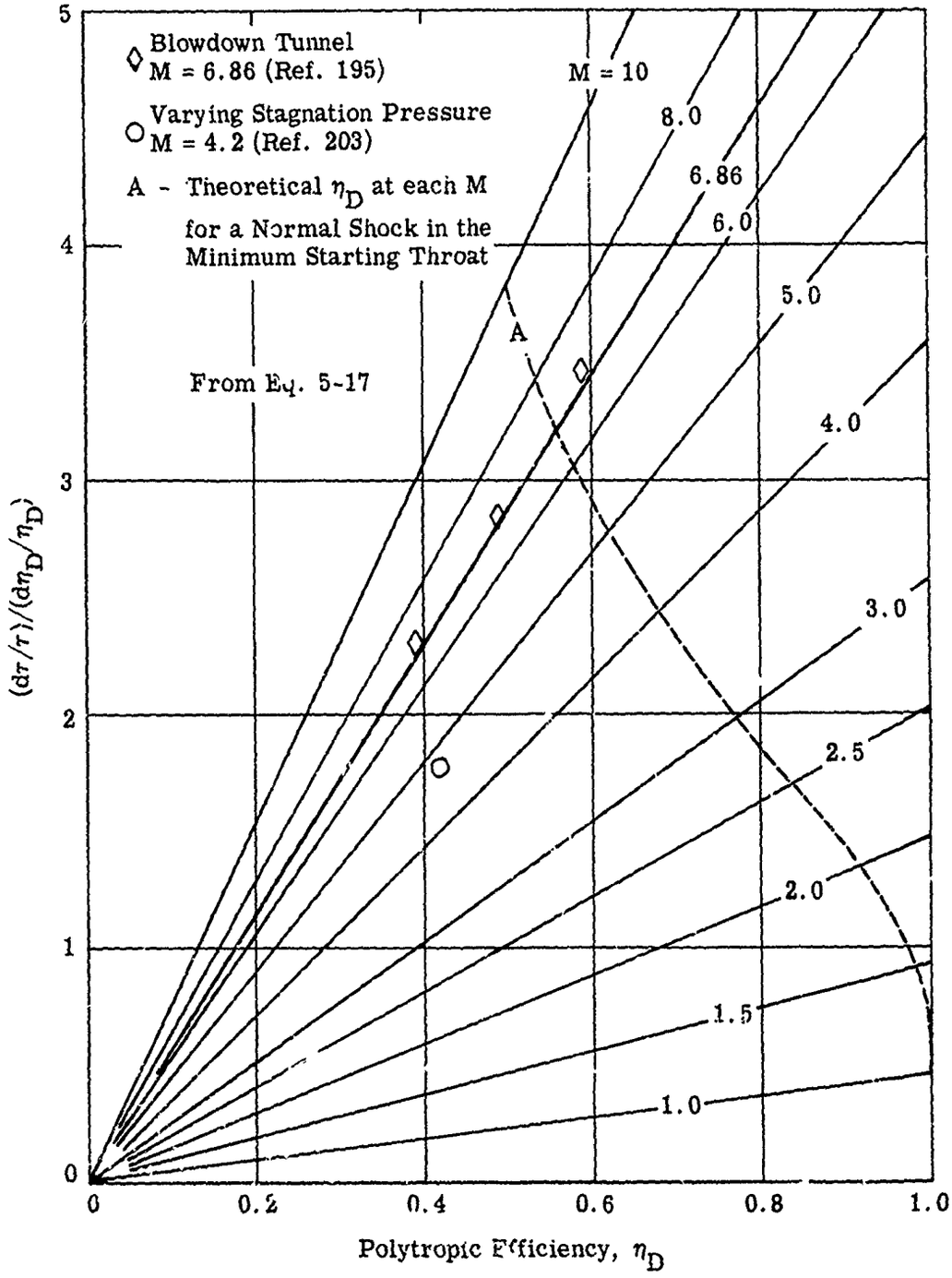

Fig. 5-16. Theoretical and experimental values of run time as a function of diffuser efficiency; M = 1 to 10; $\gamma = 1.4$. (See Sub Sec. 5.8)

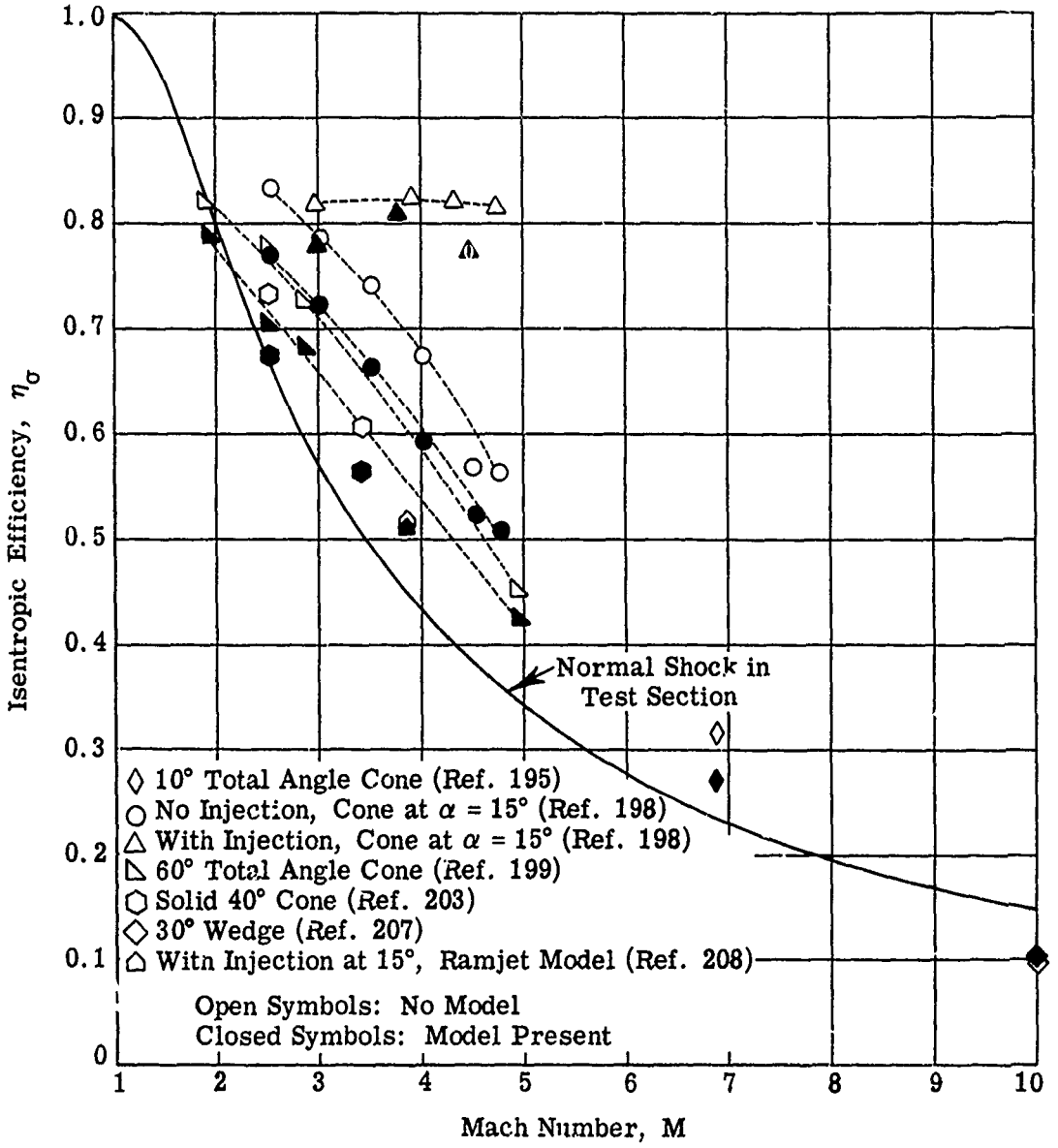

Fig. 5-17. Effect of a model on the isentropic efficiency of variable geometry diffusers; optimum running conditions.

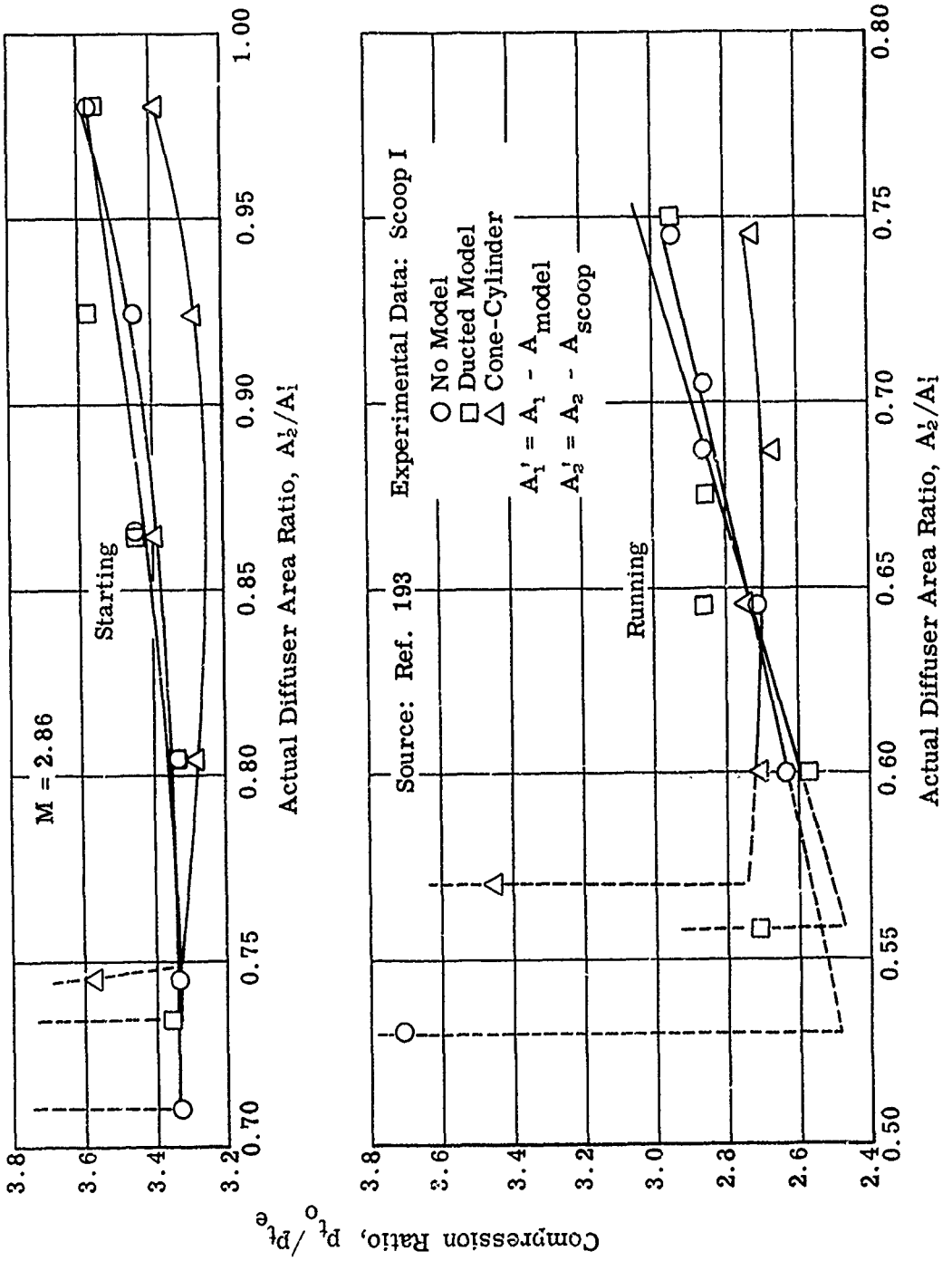

Fig. 5-18. Effect of models on starting and running compression ratio for scoop diffusers.

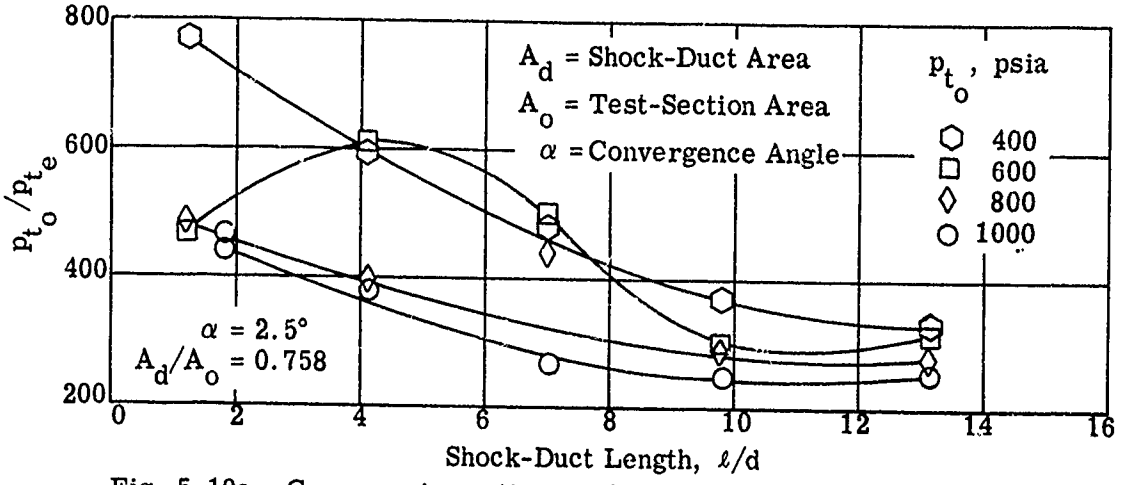

Fig. 5-19a. Compression ratio as a function of shock-duct length; α = 2.5°.

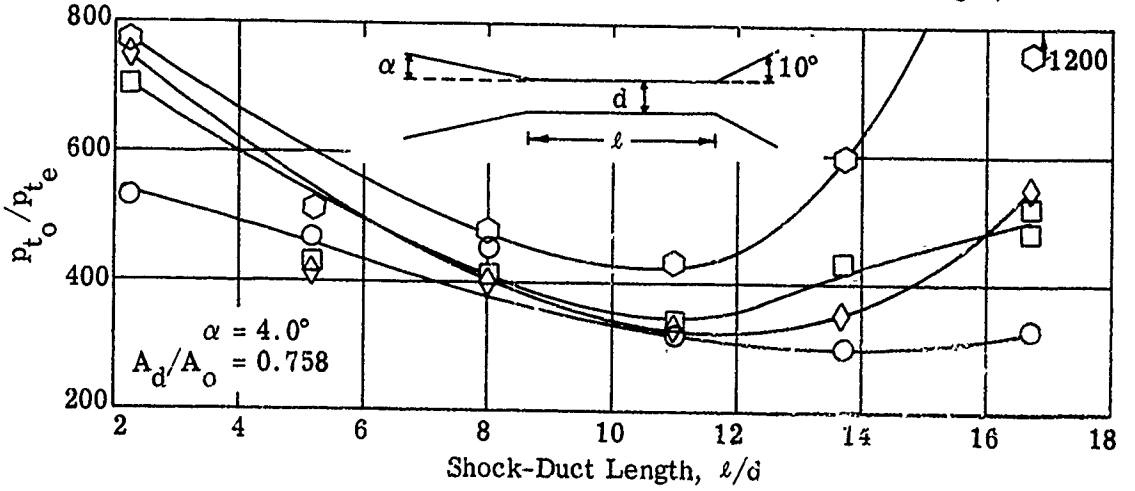

Fig. 5-19b. Compression ratio as a function of shock-duct length; α = 4°.

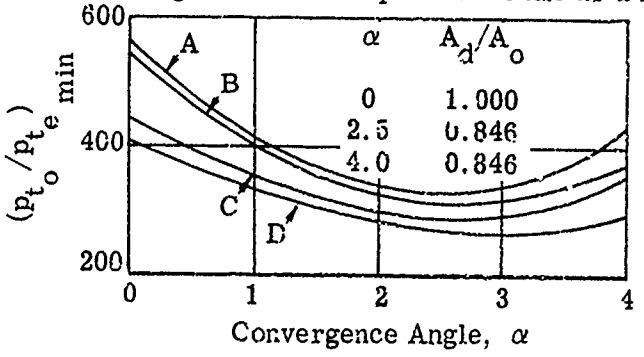

	p_{t_c}	M	Re/in. × 10^{-6}
A	400	16.4	2.09
B	600	17.0	2.92
C	800	17.4	3.82
D	1000	17.8	4.89

Fig. 5-19c. Minimum operating compression ratio as a function of convergence angle. (Source: Ref. 210)

Intentionally Blank

p. 306

6. Propulsion Nozzles

It has been seen in Subsec. 3 that efficient diffusion is an important factor in the operation of ramjet engines. It is necessary that the air reach the combustor at a low Mach number and with high total pressure and a uniform distribution.

To assure efficient performance in a propulsion nozzle it is necessary to consider not only the essential flow relations for ideal and real gases, but also the geometry which affects this flow. This subsection presents the basic flow equations and defines their relationship to the physical factors governing nozzle design. Included in this discussion are the elements of design for conical, contoured, and plug nozzles; the interaction effects of clusters of simple nozzles; real-gas effects; and the effect of chemical recombination of the combustion products. Thrust vector control is discussed briefly.

6.1 Rocket Performance Relations for Ideal Nozzle Flows

Many parameters enter into the combustion and flow relationships of rocket nozzles, and the basic equations may be expressed in many ways. For the one-dimensional flow of an ideal gas, some of the most frequently used equations are given below.

Gross thrust, F_G (see Eq. 2-45), is defined by

$$F_G = \rho_e A_e V_e^2 + (p_e - p_\infty) A_e \tag{6-1}$$

i.e.,

$$F_G = m V_e + (p_e - p_\infty) A_e \tag{6-2}$$

where m = mass flow = ρVA and subscript e denotes conditions at the exit.

Exit velocity, V_e, may be expressed as

$$V_e = M_e \sqrt{\gamma R T_e} \tag{6-3}$$

By using Eqs. 2-1 and 2-2 and assuming zero velocity in the combustion chamber (subscript c)

$$V_e^2 = \frac{2\gamma R T_c}{\gamma - 1} \left[1 - \left(\frac{p_e}{p_c} \right)^{\frac{\gamma-1}{\gamma}} \right] \tag{6-4}$$

For expansion into a vacuum, i.e., for $p_e = 0$, this equation becomes

$$V_{e_{max}}^2 = \frac{2\gamma R T_c}{\gamma - 1} \tag{6-5}$$

Mass flow, m, may be expressed as

$$m = \rho^* V^* A^* = \sqrt{\frac{\gamma}{RT^*}} \cdot p^* A^*$$

$$= \sqrt{\frac{\gamma}{R}} \left(\frac{2}{\gamma + 1}\right)^{\frac{\gamma+1}{2(\gamma-1)}} \cdot \left(\frac{p_c}{\sqrt{T_c}}\right) \cdot A^* \qquad (6\text{-}6)$$

where the superscript * denotes conditions in a sonic throat.

In rocket literature, the characteristic velocity, C*, is often used to evaluate the performance of a rocket chamber. It is defined as

$$C^* = \frac{p_c A^*}{m}$$

and therefore, from Eq. 6-6 it follows that

$$C^* = \sqrt{\frac{R}{\gamma}} \left(\frac{\gamma + 1}{2}\right)^{\frac{\gamma+1}{2(\gamma-1)}} \sqrt{T_c} \qquad (6\text{-}7)$$

Since the characteristic velocity depends on the temperature reached in the combustion chamber, it may be used as a measure of combustion efficiency; however, its validity for this purpose is questionable whenever non-isentropic nozzle expansion processes occur.

Thrust coefficient, C_F (see Eq. 2-51), is defined by

$$C_F = \frac{\text{thrust}}{p_c A^*}$$

and thus, from Eq. 6-2,

$$C_F = \frac{m V_e}{p_c A^*} + \frac{A_e}{A^*}\left(\frac{p_e}{p_c} - \frac{p_\infty}{p_c}\right) \qquad (6\text{-}8)$$

i.e.,

$$C_F = \frac{p_e \gamma M_e^2 A_e}{p_c A^*} + \frac{A_e}{A^*}\left(\frac{p_e}{p_c} - \frac{p_\infty}{p_c}\right) \qquad (6\text{-}9)$$

The ideal thrust coefficient, $C_{F_{ideal}}$, is defined as the thrust produced when the exit pressure, p_e, is equal to the ambient pressure, p_∞, and hence from Eq. 6-9

$$C_{F_{ideal}} = \frac{p_e \gamma M_e^2 A_e}{p_c A^*} \qquad (6\text{-}10)$$

Using Eqs. 2-2 and 2-4, Eq. 6-10 may be written as

$$C_{F_{ideal}} = \gamma \sqrt{\frac{2}{\gamma - 1}} \left(\frac{2}{\gamma + 1}\right)^{\frac{\gamma+1}{2(\gamma-1)}} \left[1 - \left(\frac{p_e}{p_c}\right)^{\frac{\gamma-1}{\gamma}}\right]^{1/2} \qquad (6\text{-}11)$$

Since p_e/p_c is directly related to the expansion ratio, $C_{F_{ideal}}$ may be calculated as a function of A_e/A^* and γ using isentropic flow tables (see Appendix A). The results of such calculations are shown for $\gamma = 1.1$, 1.2, 1.3, and 1.4 on Fig. 6-1 from which it may be clearly seen that the thrust has reached about 90% of its maximum value at $A_e/A^* \approx 10$ and that considerably larger exit areas produce only slightly greater thrust.

For a fixed geometry and hence a given value of p_e/p_c, the maximum thrust is obtained when the nozzle discharges into a vacuum, i.e., when $p_\infty = 0$. The vacuum thrust coefficient, $C_{F_{vac}}$, derived from Eq. 6-9 is

$$C_{F_{vac}} = \frac{p_e}{p_c} \frac{A_e}{A^*} (1 + \gamma M_e^2) \qquad (6\text{-}12)$$

The values of $C_{F_{vac}}$ and $C_{F_{ideal}}$ are given in the tables of Ref. 38 for a large number of useful values of γ and expansion ratios from 1 to 1000. They are also shown in Fig. 6-1 for $\gamma = 1.1$, 1.2, 1.3, and 1.4, and A_e/A^* from 1 to 36.

The maximum thrust is obtained when A_e is infinite, in which case, $p_e = 0$. From Eq. 6-11 it may be seen that when $p_e = 0$

$$\left(C_{F_{ideal}}\right)_{max} = \gamma \sqrt{\frac{2}{\gamma - 1}} \left(\frac{2}{\gamma + 1}\right)^{\frac{\gamma+1}{2(\gamma-1)}} \qquad (6\text{-}13)$$

It may be shown that $C_{F_{vac}}$ also has a maximum and that

$$\left(C_{F_{vac}}\right)_{max} = \left(C_{F_{ideal}}\right)_{max}.$$

This limiting value is plotted as a function of γ in Fig. 6-2. Although $p_e = 0$ seems unrealistic, it is nevertheless a convenient and useful parameter for nondimensionalizing thrust coefficients for purposes of comparison. At very high altitudes the pressure actually does approach zero.

When $p_e = p_\infty$, the specific impulse, I (see Eq. 2-47), becomes I_{ideal}, which may be expressed as

$$I_{ideal} = \frac{m V_e}{W} = \frac{V_e}{g} \tag{6-14}$$

and when $p_\infty = 0$, I becomes I_{max}, which may be expressed as

$$I_{max} = \frac{1}{g}\sqrt{\frac{2\gamma}{\gamma - 1} RT_c} \tag{6-15}$$

For any particular combination of fuel and oxidizer, theoretically attainable values of T_c may be computed if the heat release due to the reaction is known. When such values of T_c are inserted in Eqs. 6-7 and 6-15, C* and I_{max} may be computed.

It should be remembered that all equations in this subsection are valid only for ideal gases under equilibrium conditions. In actual rocket chambers the combustion is often incomplete, with dissociation and recombination taking place in the exhaust gases (see Subsec. 6.3). Although γ is far from constant along the nozzle, a value between 1.23 and 1.25 is usually taken for rocket exhaust gases. The exhaust gases of air-breathing engines may be represented by $\gamma = 1.27$. Tables of pressure, temperature, density, and other functions of Mach number for values of γ from 1.0 to 1.67 are found in many references (see Appendix A).

6.2 Nozzle Efficiency

The deviation of actual or measured parameters in a nozzle from those calculated by the methods of Subsec. 6.1 for ideal-gas flow in a one-dimensional nozzle may be termed coefficients of efficiency. As such they may be considered as corrections to the basic physical assumptions either of the nature of the gas itself or the properties of its streamlines. They will treat actual rather than ideal flow properties and will include viscous effects, the completeness of the combustion process, and the nature of the exhaust gases.

6.2.1 Over-All Efficiency

The over-all efficiency of a nozzle is based upon the thrust it can produce and is usually defined as η or η_n where

$$\eta = \frac{\text{actual thrust}}{\text{ideal thrust}} \tag{6-16}$$

The ideal thrust is derived from the best possible thermochemical estimate for the fuel-oxidizer combination and nozzle area ratio employed in a given experiment. It is based on the assumption of the one-dimensional flow of an ideal gas.

In adiabatic flow the energy equation may be written as

$$h + \frac{1}{2} V^2 = \text{constant} \tag{6-17}$$

where h is the enthalpy. If the gas is in equilibrium at stations 1 and 2, then

$$h_1 + \frac{1}{2} V_1^2 = h_2 + \frac{1}{2} V_2^2 \tag{6-18}$$

even if non-equilibrium conditions exist between the two stations. Thus, regardless of friction, velocity profile, or other effects, the ratio of integrated kinetic energy over the exit area to the difference between ideal combustion-chamber enthalpy and the enthalpy integrated over the exit area must be unity for adiabatic flow.

A measure of how closely an actual flow approaches this condition of an adiabatic expansion of a perfect gas is given by the kinetic energy efficiency, η_{KE}, which is defined as

$$\eta_{KE} = \frac{\overline{V}_e^2}{2\Delta h} \tag{6-19}$$

where

$\overline{V}_e$ = average value of the exit velocity (see Subsec. 2.1.8)

Δh = theoretical enthalpy change from combustion chamber to exit station for an ideal gas based on nozzle area ratio and the fuel and oxidizer used.

This definition of efficiency is based on momentum and is thus a more valid measure of the thrust loss due to heat transfer, viscous stresses, and other irreversible effects than η defined by Eq. 6-16. Snyder (Ref. 219) investigated the actual flow in the nozzle throat and derived an expression relating the throat Mach number to η_{KE} and γ (see Subsec. 6.2.4).

The efficiency of a nozzle may be affected by the non-uniform distribution of both the magnitude and direction of the velocity across the exit. Some of these non-uniformities may be due to irregularities in construction or poor design of the nozzle walls as well as to viscous effects. A velocity coefficient, η_V (sometimes called C_{V_e}), may be defined as

$$\eta_V = \frac{V_{e\ \text{effective}}}{V_{e\ \text{theoretical}}} \tag{6-20}$$

The effective velocity thus defined could properly replace $V_{e\ \text{theoretical}}$ in the one-dimensional equations.

The discharge correction factor, η_d (sometimes called C_d), is the ratio of the actual flow rate in a real nozzle to the ideal critical flow at the

throat of the nozzle, i.e.,

$$\eta_d = \frac{m_{actual}}{m^*_{ideal}} \tag{6-21}$$

The ideal mass-flow rate is based on one-dimensional, isentropic flow assuming stagnation conditions in the combustion chamber.

For a liquid-fueled rocket, the actual mass-flow rate is known from the pump characteristics, and for a solid-fueled rocket it is found from a simultaneous solution of Eq. 6-6 and the equation defining the burning rate in terms of pressure and temperature. In computing the ideal mass flow from Eq. 6-6 the pressure is usually measured but the chamber temperature has to be calculated on the assumption of a complete reaction of oxidizer and fuel. Poor mixing and consequent incomplete combustion, as well as heat loss to the walls, make the actual temperature somewhat lower than that which is calculated. However, this is offset by the fact that mixing and combustion continue down the nozzle and are also accompanied by some recombination (see Subsec. 6.3). The discharge coefficient in an actual rocket nozzle has been found to vary from 0.98 to 1.15. Sutton in Ref. 211 gives the following reasons for the fact that η_d is usually greater than one:

1. The molecular weight of the gases increases slightly when flowing through a nozzle, thereby changing the density.

2. The heat transferred to the walls lowers the gas temperature and raises the density.

3. The density of the exhaust gases is further increased by incomplete combustion.

4. The change in γ down the nozzle is such as to increase η_d.

The discharge coefficient may also be expressed in terms of the characteristic velocity (see Eq. 6-7), i.e.,

$$\eta_d = \frac{C^*_{theoretical}}{C^*_{actual}} \tag{6-22}$$

The shape of the combustion chamber and the design of the fuel injector have a great influence on the combustion efficiency and hence on the discharge coefficient. One useful parameter in chamber design is the characteristic length, ℓ^*, defined by

$$\ell^* = \frac{\text{combustion chamber volume up to throat section}}{\text{cross-sectional area of throat}} \tag{6-23}$$

Increasing ℓ^* enhances the degree of completeness of combustion and hence gives values of C* closer to the theoretical.

In summary, for a nozzle operating with $p_e = p_\infty$, since the thrust is given directly by the momentum of the exhaust gases, the over-all nozzle

efficiency may be expressed by

$$\eta_n = \eta = \eta_{KE}^{1/2} \cdot \eta_V \cdot \eta_d \tag{6-24}$$

6.2.2 Divergence Factor

Exhaust nozzles designed to give parallel, uniform exit flow (see Subsec. 6.4.2) usually are excessively long and heavy. In many cases simple conical shapes have been found satisfactory. The potential flow in such a nozzle may be closely represented by source flow as shown below.

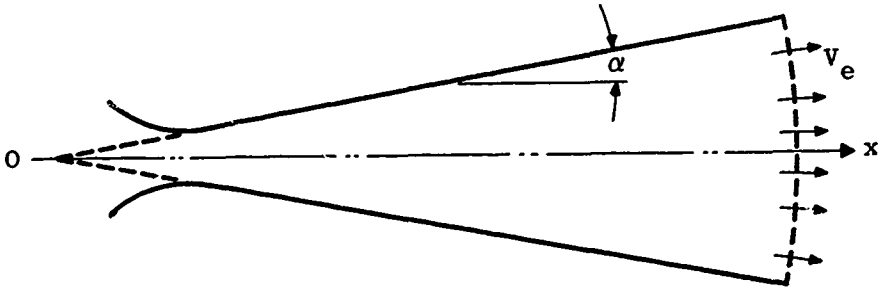

Across the spherical surface, the exit velocity is constant and normal to the surface. Since thrust is based on the axial component of momentum acting against the exit area normal to the axis, the thrust of a conical nozzle will be less than that of a contoured nozzle. Simple geometric considerations give the ratio of the momentum flux in the conical nozzle to that in the contoured nozzle as

$$\lambda = \frac{1 + \cos \alpha}{2} \tag{6-25}$$

where

λ = divergence factor

α = divergence angle of the nozzle.

Thus, for a conical nozzle, the thrust coefficient (Eq. 6-9) becomes

$$C_{F_{conical}} = \lambda \cdot \frac{p_e}{p_c} \frac{A_e}{A^*} \gamma M_e^2 + \frac{A_e}{A^*} \left(\frac{p_e}{p_c} - \frac{p_\infty}{p_c} \right) \tag{6-26}$$

Thrust measurements on conical nozzles (Foster and Cowles, Ref. 212) gave the values of λ shown in Fig. 6-3, indicating that Eq. 6-25 is valid for α of practical interest, i.e., up to about 30 degrees. In one test with increased curvature of the throat wall, the resulting shorter nozzle delayed the separation of the experimental and theoretical curves.

Figure 6-4 shows the calculated values of the comparative performance of conical nozzles ($p_\infty = 0$) in terms of the nozzle geometry. It is usually

desirable to minimize both the weight and the heat transfer of a practical rocket nozzle. Because both of these factors are closely related to the wetted area of the nozzle, the minimization of this area is of prime interest. At each value of constant thrust in Fig. 6-4 the nozzle surface area was calculated as a function of α and the minimum value determined. A line connecting the minimum area for each vacuum thrust is shown. From this line one may obtain the optimum nozzle angle for minimum weight and heat transfer as a function of the nozzle length.

6.2.3 Viscous Effects

In hypersonic tunnel nozzles and in rocket nozzles the Reynolds number is usually high enough to assure turbulent flow along most of the nozzle. Since in a rocket nozzle the origin of the flow is turbulent, the boundary layer along the nozzle is more likely to be entirely turbulent. The flow is usually shock-free within the nozzle itself, i.e., the loss in thrust is due principally to viscous and heat-transfer effects, which are inseparable. Until recently no exact solution of the boundary-layer equations had been obtained for turbulent flow in the presence of high heat-transfer rates and large negative pressure gradients. In the absence of such a solution, several semi-empirical techniques were developed by which viscous effects may be included in nozzle computations. These simplified methods will be presented before the exact solution is discussed since they will always be useful not only to those who wish to make quick estimates of performance but also to those who do not have ready access to a computation center.

Durham in Ref. 213 derives many nozzle flow relationships in terms of an average friction parameter, B, defined by

$$B = \frac{\gamma C_f}{\tan \alpha} \tag{6-27}$$

where

C_f = average value of the skin-friction coefficient

α = divergence angle.

C_f and γ will vary down the nozzle; for non-conical nozzles α will also vary. Durham uses parameters which are averaged with respect to the nozzle length in order to compute B. The required exit area, A'_e, may be calculated for a fixed exit Mach number and a given friction parameter from

$$\frac{A'_e}{A^*} = \frac{1}{M}\left(\frac{1 + \frac{\gamma - 1}{2} M^2}{\frac{\gamma + 1}{2}}\right)^{\frac{\gamma+1}{2(\gamma-1+2B)}}\left(\frac{1 - B}{1 - BM^2}\right)^{\frac{1-B}{\gamma-1+2B}} \tag{6-28}$$

The corresponding loss in stagnation pressure due to viscosity may be calculated by using

$$\frac{p'_{t_e}}{p^*_t} = \left(\frac{1 + \frac{\gamma - 1}{2} M^2}{\frac{\gamma + 1}{2}}\right)^{\frac{B(\gamma+1)}{(\gamma-1)(\gamma-1+2B)}} \left(\frac{1 - BM^2}{1 - B}\right)^{\frac{1-B}{\gamma-1+2B}} \qquad (6\text{-}29)$$

where

p'_{t_e} = effective stagnation pressure at the exit

p^*_t = stagnation pressure at the throat

$\approx p_c$ in most cases.

Figures 6-5 to 6-10 show curves of A'_e/A_e (obtained by combining Eqs. 2-4 and 6-28) and p'_{t_e}/p^*_t for $\gamma = 1.2$, 1.3, and 1.4; B = 0 to 0.06 and M = 1 to 5.

The following table indicates a practical range of values of the parameter B. The skin-friction coefficients used in computing B are those for a flat plate with zero heat transfer; γ is 1.4.

	Laminar Flow			Turbulent Flow					
	$Re = 10^5$			$Re = 10^6$			$Re = 10^8$		
M / α	2	5	10	2	5	10	2	5	10
10	0.0325	0.0286	0.0246	0.0294	0.0210	0.0159	0.0131	0.0075	0.0048
15	0.0214	0.0188	0.0162	0.0193	0.0138	0.0105	0.0086	0.0050	0.0031
30	0.0099	0.0087	0.0075	0.0090	0.0064	0.0049	0.0040	0.0023	0.0015

The effects of heat transfer and pressure gradient on skin friction are not yet fully explained. If estimates of the local wall temperature and the local Reynolds number can be made, the flat-plate skin-friction coefficient may be obtained from the nomograph in Fig. 6-11 (taken from Ref. 214), which gives both the local and mean values of the skin-friction and heat-transfer coefficients in terms of wall temperature ratio, Mach number, and Reynolds number.

A purely empirical approach to the viscous problem is suggested by Rowe in Ref. 15. The measured static pressure at the nozzle exit is compared with the theoretical value and a value of the polytropic exponent, γ, calculated to fit the expansion process. The thrust of the nozzle is then computed by means of one-dimensional theory using the effective value of γ.

Although the foregoing methods give adequate estimates of thrust loss in conical nozzles, they cannot be applied to contoured nozzles or to highly nonuniform flow. For many parameters, the concept of an average value has questionable physical meaning. As in the case of wind-tunnel nozzles, the assumption may be made that viscous forces are confined to the regions adjacent to the walls. Beyond these regions the flow may then be considered frictionless.

Using δ^* and θ as defined in Eqs. 2-167 and 2-168, the momentum of the exit flow may be written as

$$m\overline{V}_e \left[1 - \frac{2\delta^*}{r_e(\overline{M}_e^2 - 1)} - \frac{2\theta}{r_e} \right] \tag{6-30}$$

where

$\overline{V}_e$ = average exit velocity (see Subsec. 2.1.8)

r_e = radius of exit section

$\overline{M}_e$ = average exit Mach number.

The expression in brackets may also be used as a velocity efficiency factor in obtaining the effective exit velocity of the exhaust gases. Values of δ^*/δ and θ/δ may be found from Table 2-1 (no heat transfer) and Table 4-4 (with heat transfer; T_w/T_e known). The value of δ may be obtained from Eq. 2-176. Both the tables and Eq. 2-176 are based on $\gamma = 1.4$ and flat-plate values of the skin-friction coefficient.

The work done by Bartz on the viscous effects in rocket nozzles is perhaps the most precise and generally applicable. He has derived a method by which one may compute the boundary-layer growth in the presence of both heat transfer and pressure gradients.

His first solution (Ref. 216) was a hand-computed approximation, limited to simple convergent-divergent conical nozzles. The distribution of the velocity boundary-layer thickness was derived from the integral momentum equation. When these results were substituted in the integral energy equation the distribution of the ratio of the temperature boundary-layer thickness to the velocity boundary-layer thickness was obtained. Assuming an analogy between heat transfer and momentum transfer allowed the heat-transfer coefficient to be expressed as an explicit function of the boundary-layer thickness. In spite of many simplifications, the method was still cumbersome; however, the results for any specific nozzle could be extended to apply to all geometrically similar nozzles and some geometrically dissimilar nozzles.

Experience gained from these hand computations led Bartz to derive an empirical expression for the heat-transfer coefficient, h, in conical nozzles (Ref. 217). The expression for h at any cross section, A, is

$$h = \left(\frac{A^*}{A}\right)^{0.9} \cdot \sigma \left[\frac{0.026}{d^{*0.2}} \left(\frac{\mu^{0.2} c_p}{Pr^{0.6}} \right)_t \left(\frac{p_c g}{C^*} \right)^{0.8} \left(\frac{d^*}{r_w} \right)^{0.1} \right] \tag{6-31}$$

$$\sigma = \left(\frac{\rho_\infty + \rho_w}{2\rho_w} \right)^{0.8} \left(\frac{T + T_w}{2T_t} \right)^{\omega/5}$$

where

d^* = throat diameter

C^* = characteristic velocity (see Eq. 6-7)

and

subscript w denotes wall conditions.

By means of Eq. 6-31 reasonably accurate estimates of heat transfer may be made very rapidly.

More recently, employing machine computation (Ref. 218), Bartz has found a simultaneous, iterative solution of the momentum and energy equations. Although the basic procedure is similar to that of the approximate solution, the exact solution no longer requires many of the original compromises. The calculations are no longer restricted to conical nozzles but may be applied to any axisymmetric configuration. The boundary-layer thicknesses obtained may be used to correct both performance calculations and nozzle shape. Although many changes and refinements were made in the light of later information, the quantitative results of the new approach are still based on several factors which can be defined with only limited accuracy. The skin-friction and heat-transfer coefficients at each step are still those that would be found on a flat plate at the same stream and wall conditions.

Figures 6-12 to 6-15 give the calculated velocity, momentum, and displacement boundary-layer thickness distributions, as well as the heat-transfer coefficient for a specific nozzle (shown on Fig. 6-15) with three different sets of initial conditions. Although experimental confirmation is extremely limited, there are several qualitative results applicable to rocket nozzles operating under typical conditions. They are:

1. The velocity boundary layer has a minimum thickness slightly upstream of the nozzle throat.

2. This minimum thickness is fairly insensitive to the boundary-layer characteristics at the nozzle entrance; hence the usual assumption of zero boundary layer at the throat is not greatly in error.

3. The growth of the velocity boundary layer is almost linear in the supersonic part of the nozzle.

4. The maximum heat transfer occurs very close to the throat.

Altman and Carter in Ref. 16 derived an approximate temperature-pressure relationship for flow with heat transfer through rocket nozzles. The quantity of heat, Q, transferred from the gas between stations 1 and 2 during an expansive process is given by

$$Q = h_1 - h_2 + \frac{1}{2} m(V_1^2 - V_2^2) \qquad (6\text{-}32)$$

where h is the enthalpy. Provided that $Q \ll c_p T_c$ the approximate pressure-temperature relation in the nozzle is given by

$$T/T_c = (p/p_c)^{\frac{\gamma-1}{\gamma}} \left[1 - \frac{\gamma+1}{2} \cdot \frac{Q}{c_p T_c}\right] \qquad (6\text{-}33)$$

Values of h for many gases may be obtained from Ref. 41. Altman and Carter compare the exhaust velocity in a nozzle which is water-cooled with the velocity in a regeneratively cooled one.

For adiabatic expansion without heat transfer

$$\frac{1}{2} m V_e^2 = c_p T_c \left(1 - \frac{T_e}{T_c}\right) = n_i c_p T_c \tag{6-34}$$

where

$$n_i = 1 - \frac{T_e}{T_c} = 1 - (p_e/p_c)^{\frac{\gamma-1}{\gamma}}$$

For the water-cooled case, where V_e is now V_w,

$$\frac{1}{2} m V_w^2 = n_i c_p T_c \left[1 + \frac{\gamma + 1}{2} \frac{Q}{c_p T_c} \frac{(1 - n_i)}{n_i}\right] - Q \tag{6-35}$$

If the transferred heat, Q, is fed back into the combustion zone at T_c and p_c the exit velocity, V_r, is given by

$$\frac{1}{2} m V_r^2 = n_i c_p T_c \left(1 + \frac{Q}{c_p T_c}\right) \left[1 + \frac{\gamma + 1}{2} \frac{Q}{c_p T_c} \frac{(1 - n_i)}{n_i}\right] - Q \tag{6-36}$$

Heat-transfer and viscous effects will be discussed more fully in Sections 13 and 14 of the Handbook.

6.2.4 Nozzle Throat Correction

The flow characteristics in a sonic throat have been discussed in Subsec. 4.1. It was shown that the sonic line is parabolic rather than linear, and that its position relative to the minimum cross section is dependent upon the geometric parameters of the throat. Figure 4-1 shows the position of the sonic line for various values of wall-to-throat radius of curvature in both two- and three-dimensional throats. Figure 4-2 gives the Mach number distribution for a given geometry and a gas whose ratio of specific heats is 1.4. Equations are given which permit calculations for other values of γ. It is evident that mass-flow calculations, based on the usual assumption of uniform axial flow at M = 1 across the minimum section, will be somewhat in error. The ratio of the actual mass flow to that calculated by simple one-dimensional theory may be used as a throat efficiency factor, η^*.

In order to obtain a closed solution for the integral,

$$\eta^* = \frac{1}{\pi (r^*)^2} \int_{y=0}^{y=r^*} \frac{\rho U}{\rho^* U^*} \cdot 2\pi y \, dy \tag{6-37}$$

it is necessary to make some approximation. The most direct is to assume V = 0 and x = constant, i.e., integrate across the minimum cross section shown as AC in the following sketch.

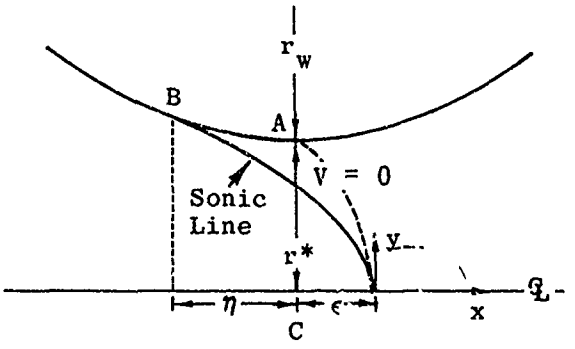

The value of M is obtained from Eq. 4-7 and the values included in the integration lie between M_A and M_C. In this case the values of M will be somewhat lower than the real ones since values of V have been neglected. V/a^* is zero at A and C, but has a minimum value of -0.07 between A and C. The integral reduces to

$$\eta^* = \frac{1}{\gamma-3}\left(\frac{\gamma+1}{2}\right)^{\frac{\gamma+1}{2(\gamma-1)}}\left(4\frac{r_w}{r^*}-1\right)\left\{\left[1+\frac{\gamma-1}{2}\left(\frac{4\frac{r_w}{r^*}}{4\frac{r_w}{r^*}-1}\right)^2\right]^{\frac{\gamma-3}{2(\gamma-1)}}\right. \tag{6-38}$$

$$\left. -\left[1+\left(\frac{\gamma-1}{2}\right)\left(\frac{4\frac{r_w}{r^*}-2}{4\frac{r_w}{r^*}-1}\right)^2\right]^{\frac{\gamma-3}{2(\gamma-1)}}\right\}$$

where r_w represents the wall radius of curvature at the throat.

A second method is to integrate over the surface of V = 0 (see sketch) which is given by

$$x = -\frac{(\gamma+1)}{8}\alpha y^3$$

where α is defined by

$$U_o/a^* = 1 + \alpha x \quad \text{(Eq. 4-1)}$$

Since the flow is always aligned with the axis, the projected area of this curve over which the flow must be integrated is equal to the area of the geometric throat, but since the curve is to the right of the throat the Mach

numbers are somewhat in excess of the true values. The value of η^* in this case is

$$\eta^* = \frac{2}{(\gamma - 3)} \left(\frac{\gamma + 1}{2}\right)^{\frac{\gamma+1}{2(\gamma-1)}} \left(4 \frac{r_w}{r^*} - 1\right) \left\{ \left[1 + \left(\frac{\gamma - 1}{2}\right) \left(\frac{4 \frac{r_w}{r^*}}{4 \frac{r_w}{r^*} - 1} \right)^2 \right]^{\frac{\gamma-3}{2(\gamma-1)}} - \left(\frac{\gamma + 1}{2}\right)^{\frac{\gamma-3}{2(\gamma-1)}} \right\} \tag{6-39}$$

A third method, given by Oswatitsch (Ref. 3, p. 478), simplifies the calculations by use of the following transonic approximation:

$$\frac{\rho q}{\rho^* a^*} = 1 - \frac{\gamma + 1}{2} (M - 1)^2 + \ldots \tag{6-40}$$

where

$$q^2 = U^2 + V^2$$

The result is

$$\eta^* = 1 - \frac{\gamma + 1}{96} \left(\frac{r^*}{r_w}\right)^2 \tag{6-41}$$

The evaluation of η^* as a function of r^*/r_w for all three methods is given in Fig. 6-16. For values of r^*/r_w less than 0.6 the correction is less than 1% of the total mass flow and the difference between the three methods is negligible. Beyond this value there is a rapid increase in the error and a wider divergence in the three calculated values. The advantages of a large radius of curvature for the nozzle wall are apparent. A value of $r^*/r_w = 2/3$ is customarily used.

The correction factor, η^*, normally is included in the discharge coefficient of a rocket nozzle. It may be thought of as a wall shape effect or an area ratio, i.e.,

$$\eta^* \sim \frac{A^*_{\text{effective}}}{A^*_{\text{actual}}} \tag{6-42}$$

In non-isentropic flow, the velocity in the physical throat is subsonic, i.e., the actual sonic throat occurs slightly downstream of the theoretical throat. According to Snyder (Ref. 219), this discrepancy is due to boundary-layer effects which are not taken into account by isentropic design methods. He has derived a throat correction factor relating the Mach number in the physical throat and the kinetic energy efficiency. By assuming that the mass velocity, ρV, is a maximum at the throat, he obtained the following

expression for the throat Mach number in terms of γ and η_{KE}.

$$M_t^2 = \frac{\frac{4}{\gamma - 1}}{\left\{\left[\frac{1}{\eta_{KE}}\left(\frac{3\gamma-1}{\gamma-1}\right) - 3\right]^2 + 8\left(\frac{1}{\eta_{KE}} - 1\right)\right\}^{1/2} + \left\{\frac{1}{\eta_{KE}}\left(\frac{3\gamma-1}{\gamma-1}\right) - 3\right\}} \quad (6\text{-}43)$$

where M_t is the Mach number in the physical throat. The values of M_t calculated from Eq. 6-43 are presented in Fig. 6-17 as a function of η_{KE} for $\gamma = 1.20$, 1.23, 1.40, and 1.67. It may be seen from this figure that the flow in the physical throat is always subsonic since the kinetic energy efficiency is always less than one. Setting $\gamma = 1$ in Eq. 6-43 yields

$$M_t = \sqrt{\eta_{KE}} \quad (6\text{-}44)$$

These values of M_t are represented in Fig. 6-17 by a dashed line which is seen to be an upper limit, i.e., since γ is always greater than one, M_t will always be less than $\sqrt{\eta_{KE}}$. If the real nozzle with boundary-layer growth is replaced by an equivalent nozzle with isentropic flow, the actual sonic throat will be downstream of the physical throat and have a reduction in area determined by M_t and A_t.

6.2.5 Flow Separation in Over-Expanded Nozzles

An exhaust nozzle is said to be operating at an over-expanded condition when the nozzle exit pressure is less than the ambient pressure. If the ratio p_e/p_∞ drops below a critical value, the exhaust gases will separate from the nozzle walls and increase the stream pressure by means of a shock system until the over-expanded condition is corrected. The pressure on the walls is usually much lower than ambient before the separation occurs.

The following sketch illustrates an over-expanded, separated flow and shows the character of the wall pressure distribution.

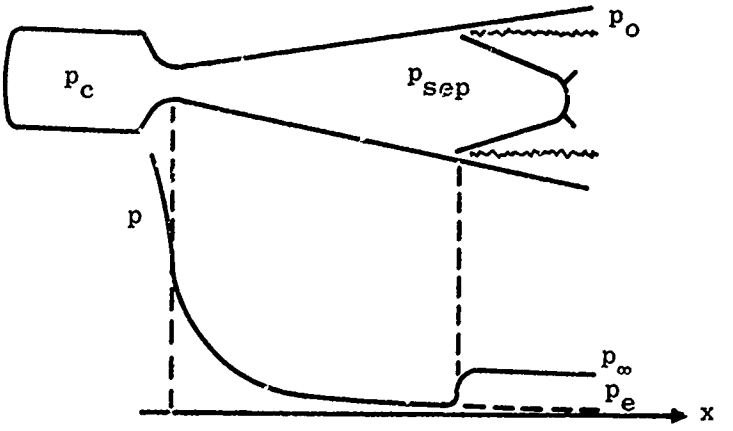

The wall pressure is predicted by the isentropic nozzle flow relations until at the point of flow detachment, the pressure rapidly jumps to the ambient value. In two-dimensional nozzles, an asymmetric shock pattern may occur, causing the flow to attach itself to one wall or the other. In some instances the flow shifts alternately from wall to wall, causing unsteady operation. Experience indicates that the flow separation in axisymmetrical nozzles is always symmetrical and stable; however, during starting and stopping operations in wind-tunnel tests, when the pressure ratio is low, an asymmetric shock pattern has sometimes been observed. The stream pressure on the jet boundary downstream of the oblique-shock system is essentially that of the ambient air and the separated flow may be regarded as a free jet.

Many measurements of the wall pressure have been made in nozzles of varying length and divergence as well as for several different gases, hot and cold, operating under a wide range of compression ratios.

Campbell and Farley (Ref. 220) tested nozzles with α = 15, 25, and 29 deg, each with area ratios of 10, 25, and 40 both with unheated and heated air (1200°F). Within the accuracy of the measurements there was no significant difference in the relationship between the separation pressure ratio due either to geometric factors or to gas heating. In consequence the nine geometric variations are shown in Fig. 6-18 by only two symbols, one for hot flow and one for cold flow.

Bloomer, Antl, and Renas (Ref. 221) tested a family of conical nozzles mounted on a water-cooled JP-4-gaseous-oxygen thrust chamber. The divergence angle varied from 15 to 30 deg and the area ratio from 8 to 75. The experimental separation pressure ratios obtained during this study are also shown on Fig. 6-18. The agreement with those of the preceding reference is good. Also included on this figure are collected data from Refs. 222, 223, and 224.

The theoretical aspect of the problems associated with flow separation has received a good deal of attention, primarily in two-dimensional flow. Reference 225 presents a comprehensive review of the literature on high-speed flow separation and gives an extensive bibliography. However, this detailed study deals principally with the underlying theory of boundary-layer separation rather than its application to exit nozzle flow, and hence will be discussed in Section 13 of the Handbook. In this subsection we shall confine ourselves to the methods or devices by which one may predict the onset of separation in conical nozzle flow and the pressure ratios involved.

The first method is due to Mager and is outlined in Refs. 226, 227, and 228. For the two-dimensional case the ratio of the ambient pressure, p_∞, to the separation pressure, p_s, may be calculated by means of

$$\frac{p_\infty}{p_s} = \left[1 + \frac{\gamma M_s^2 (1 - K)}{2 + (\gamma - 1) M_s^2}\right] \left[1 + \frac{0.328 \gamma K M_s^2 \theta_s}{1 + \frac{\gamma - 1}{2} K M_s^2}\right] \qquad (6\text{-}45)$$

where

K = an empirically determined constant
= 0.55
M_s = Mach number at which separation occurs
θ_s = angle between nozzle wall and separated flow.

The value of M_s may be determined in terms of p_s and the total pressure in the combustion chamber, p_c, from Eq. 2-2. As a first approximation

$$\theta_s = \frac{\sqrt{M_s^2 - 1}}{\gamma M_s^2} \left[(p_\infty/p_s) - 1\right] \tag{6-46}$$

Substitution of θ_s in Eq. 6-45 gives a first approximation to p_s/p_∞ from which the exact value of θ_s may be obtained, i.e.,

$$\tan^2 \theta_s = \left[\frac{(p_\infty/p_s) - 1}{\gamma M_s^2 - (p_\infty/p_s) + 1}\right]^2 \cdot \frac{2\gamma M_s^2 - (\gamma-1) - (\gamma+1)(p_\infty/p_s)}{(\gamma + 1)(p_\infty/p_s) + (\gamma - 1)} \tag{6-47}$$

Several iterations may be required before a solution is reached.

The above two-dimensional calculations have been applied to conical flow by assuming:

1. That the pressure p_2 in the separated region is the same as that for the two-dimensional case, i.e., that

$$p_2/p_s = 1 + \frac{\gamma M_s^2 (1 - K)}{2 + (\gamma - 1) M_s^2} \tag{6-48}$$

2. That p_2 may be represented by the pressure along the surface of a cone whose semi-angle is θ_s in flow at M_s as shown below.

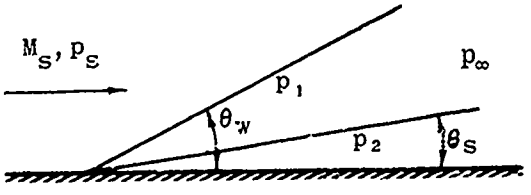

Having obtained p_2/p_s from Eq. 6-48, the values of θ_s and the pressure p_1 immediately behind the shock wave may be found from cone tables, such as Refs. 23 and 35-37 (see Appendix A). Mager assumes a parabolic pressure variation in the region behind the shock and obtains an average value,

$$p_\infty = p_2 - \tfrac{1}{3}(p_2 - p_1) \tag{6-49}$$

Graphs of p_∞/p_s, p_2/p_s, θ_w, and θ_s for Mach numbers from 1.5 to 4.0 are presented in Ref. 228 from which the values for $\gamma = 1.2$ and 1.4 are reproduced in Fig. 6-19. Curve A for which $\gamma = 1.4$ and curve B for which $\gamma = 1.2$ give the dependence of p_s/p_c on p_∞/p_c using the Mager method and are shown in Fig. 6-18. The agreement between these calculations and the measured data is very good. The difference, due to γ, between curves A and B is very slight except at high compression ratios. This has been substantiated by tests; different gases, even at different temperatures, do not reflect any change in the pressure ratio.

A second method of predicting the pressure at the onset of separation is that of assuming a constant ratio between the Mach numbers across the oblique shock. Simply by assuming that $M_2^2 = 0.58\ M_s^2$, the pressure relationship, p_s/p_c vs p_∞/p_c was calculated for $\gamma = 1.4$, shown by curve C, and for $\gamma = 1.2$, shown by curve D, on Fig. 6-18. These curves lie very close to those of Mager, especially for $\gamma = 1.2$. A closer fit for the $\gamma = 1.4$ case could easily be obtained by a very small change in the ratio of the shock Mach numbers. These curves also indicate how slight is the effect of changing γ except at high compression ratios. The location of the onset of separation may easily be calculated from the ratio p_s/p_c and isentropic flow tables. Since the flow behaves as a free jet once it has separated from the walls, the geometry of the nozzle has little or no effect upon it. Tests with nozzle lengths up to three times the distance from the throat to the initial separation point showed no effect of length on the separation pressure ratios.

For some time it was generally accepted that p_s/p_∞ had a constant value; Summerfield, Foster, and Swan gave the value as 0.4, whereas Rao suggested about 0.3. The slope of the theoretical curves A, B, C, and D of Fig. 6-18 rapidly approach a constant value as the nozzle pressure ratio, p_c/p_∞, increases; however, both theory and data show a sharp increase in the separation pressure as the compression ratio is reduced below about 30. This is shown in Fig. 6-20 which contains the same data as Fig. 6-18 in a slightly different form. Since for rockets $p_c/p_\infty \geq 30$ is common, then the use of $p_s/p_\infty \sim 0.3$ is reasonable. However, for ramjets p_c/p_∞ is usually less than 30 and hence p_s/p_∞ should be greater than 0.3.

When the separation pressure is known, the thrust performance of a nozzle operating at an over-expanded condition may be determined. As long as the nozzle flows full, i.e., does not separate, the thrust may be obtained from Eq. 6-23 using the value of p_e/p_c corresponding to A_e/A^*. For separated flow this equation may be expressed as

$$C_F = \left(\frac{1 + \cos\alpha}{2}\right)\gamma\sqrt{\frac{2}{\gamma - 1}}\left(\frac{2}{\gamma + 1}\right)^{\frac{\gamma+1}{2(\gamma-1)}}\left[1 - \left(\frac{p_s}{p_c}\right)^{\frac{\gamma-1}{\gamma}}\right]^{1/2} + \left[\left(\frac{p_s}{p_c} - \frac{p_\infty}{p_c}\right)\frac{A_s}{A^*}\right] \qquad (6\text{-}50)$$

where

p_s = separation pressure

A_s = area of cross section at which separation occurs.

Figure 6-21 shows the performance of 15 deg nozzles whose expansion ratios are 6 and 25 for $\gamma = 1.20$ and 1.26 for a wide range of compression ratios. The nozzle thrust at each pressure ratio is normalized by comparing it with the thrust of a 15 deg nozzle whose area ratio is corrected to give ambient exit pressure. The thrust under conditions of separation is independent of the actual expansion ratio since the thrust is calculated over the separation area. This assumes, of course, that the separated flow is parallel to the axis, which in turn assumes that the pressure behind the shock system is equal to the ambient pressure. In actual nozzles the pressure in the separated region is often slightly lower than ambient, due to the eddy flow between the separated stream and the nozzle wall.

6.3 Problems in Expansion Processes

Gas imperfections at high temperatures have been discussed briefly in Subsec. 2.1.7 and the effects of heat addition in Subsecs. 2.1.3 to 2.1.5. In these discussions it has been assumed that the chemical composition of the gas remains constant. In Subsec. 2.1.3, the aerodynamic effect of non-gaseous products in a chemically stable ideal exhaust gas has been treated. In the present subsection, two problems are discussed which deal with non-ideal exhaust gases in which the ratio of specific heats varies due to the dissociation and recombination of the exhaust products and also to the presence of micron-sized oxides dispersed in the exhaust gases.

6.3.1 Effect of Recombination in Exhaust Gases

In the analysis of nozzle flow discussed in the preceding subsections it has been assumed that the specific heats of the exhaust gases are constant, i.e., that the gases are ideal. The flow variables depended only on the area variation of the nozzle according to the usual isentropic relationships. The expansion process was assumed to take place without any changes in chemical composition, i.e., "frozen" flow.

However, the elevated temperatures in the combustion chambers of rockets and some high speed air-breathing engines cause appreciable dissociation of the combustion products into atoms and free radicals. For example, the products of hydrocarbon-oxygen combustion contain species such as atomic hydrogen and oxygen, hydroxyl radicals, as well as carbon monoxide, all in a state of chemical equilibrium with the major products, water and carbon dioxide. The energy required for these dissociation processes is obtained at the expense of the temperature of the gases themselves. As the gases flow through the nozzle, both the static temperature and pressure decrease. The decrease in temperature induces recombination of the atoms and radicals into stable molecules; at the same time the decrease in pressure favors further dissociation. Since the temperature decrease is by far the predominant influence, the net result is that some recombination occurs, returning some of the dissociation

energy to the gas stream. In this way a higher performance may be achieved than for completely frozen flow. The best performance one can expect is from a gas whose composition maintains a state of local chemical equilibrium associated with the temperature and pressure at each station in the nozzle. Such a shifting equilibrium flow thus represents an upper limit while frozen flow represents a lower limit to the performance. Since by definition an equilibrium flow is everywhere in chemical equilibrium it is also isentropic flow and all the variables, like those of frozen flow (including composition), depend only upon the area variation.

The nozzle flow history may be determined for either the equilibrium or frozen limits. In computing the pressure, temperature, and gas velocity at any cross section of the nozzle, the energy released by changes in the chemical composition of the exhaust gases must be accounted for in addition to the area variation. The theoretical performance of JP-4 fuel and liquid oxygen as a rocket propellant has been calculated by Huff, Fortini, and Gordon (Refs. 229 and 230) for both frozen and equilibrium compositions. The data presented in both tabular and graphical form in these two references permit interpolation of complete performance data for equivalence ratios of 1.0 to 2.0, chamber pressures of 150 to 1200 psia, and pressure ratios up to 1500.

To demonstrate the magnitude of the difference between the two flows, the specific impulse has been computed for one typical case in which the chamber pressure is 600 psia and the oxidizer-to-fuel weight ratio is 2.431. The exit Mach number and the specific impulse are shown in Fig. 6-22 as a function of A_e/A^* and apply to a rocket nozzle operating at the ideal expansion ratio, i.e., $p_e = p_\infty$. It will be noted that the increase in specific impulse between the two limits varies from about 2.5% at an area ratio of 4 to about 7% at an area ratio of 36. This is typical for rocket propellants. It is shown in Refs. 229 and 230 that the specific impulse difference is slightly dependent on the oxidizer-to-fuel ratio and strongly dependent on the pressure ratio, p_c/p_∞. High chamber pressure tends to suppress dissociation and therefore minimize the difference between frozen and equilibrium flow.

All actual flows, of course, lie between the two limiting cases. The changes in chemical composition which occur as a real gas flows through a nozzle are determined by the rate at which the various chemical reactions take place. There is a coupling between these chemical kinetic rates and the overall flow, since the chemical rates are dependent on both temperature and pressure. The flow is then non-isentropic and is no longer determined by the area variation alone, but depends on the time (or distance) required to reach a given area ratio. The gas flow variables thus depend on the configuration of the nozzle as well as the expansion ratio even in the one-dimensional approximation.

Chemically reacting flows are usually very complex. However, in a relatively simple case, striking experimental evidence for the effect of finite reaction rates was provided by the work of Wegener (Ref. 231). By passing gas mixtures of nitrogen dioxide and nitrogen tetroxide of differing concentrations through a small supersonic tunnel (M = 1.8), he was able to produce flows which would remain in chemical equilibrium or depart from it, depending on

the reactant concentration in the nozzle supply. The equation for the reaction is

$$2NO_2 \underset{\leftarrow k_d}{\overset{\rightarrow k_r}{\rightleftharpoons}} N_2O_4 \qquad (6\text{-}51)$$

where k_d and k_r were the rate constants for dissociation and recombination, respectively. As the gas flowed down the nozzle, the NO_2 concentration dropped as it recombined to N_2O_4. The measurements indicated that the mixture tended to follow the local equilibrium condition for a time and then, at a rather ill-defined point, tended to "freeze" in composition after which no appreciable changes occurred. The existence of such a freezing point had been predicted theoretically by Bray (Ref. 232) as a necessary consequence of the rapid drop in reaction rates which accompanies the drop in temperature and pressure in the nozzle. Bray's theory will in some cases allow the point of freezing, which is typical of all reacting exhaust gases, to be roughly estimated. Thus it is possible to construct a fairly good approximation to a non-equilibrium flow (if it is not too complex) by performing an equilibrium flow calculation up to the freezing point and considering the gas to be frozen thereafter.

Most exhaust gases contain many species which enter into many different elementary reactions. The theoretical calculation of the nozzle flow parameters in such complex cases is prohibitively difficult without the aid of modern high-speed computers. In recent years, however, such computers have been used to good advantage in making fairly realistic analyses of actual exhaust flows for cases where reliable kinetic data were available. Eschenroeder, Boyer, and Hall (Ref. 233) have calculated the non-equilibrium nozzle flow of air considered to contain the species O_2, N_2, O, N, and NO undergoing essentially five different reversible reactions. Westenberg and Favin (Ref. 234) have made similar calculations for hydrogen-air combustion products containing H_2, O_2, H_2O, H, O, and OH undergoing eight reversible reactions. Figure 6-23 taken from Ref. 234 shows the static temperature profiles computed for a 25 deg total angle nozzle (divergent section only). The vital role of the pressure in determining both the spread between frozen and equilibrium limits and the degree to which equilibrium can be maintained in actual flow is clearly indicated.

It should be noted that loss of dissociation energy by failure to maintain equilibrium flow in the nozzle may be much more serious in an air-breathing ramjet engine than in a rocket. In a typical rocket, where the unburned propellant is essentially at room temperature and then burns to some high flame temperature, the energy of dissociation is a small fraction of the total chemical energy released, and hence the difference between frozen and equilibrium specific impulse is usually a few per cent at most. In a high Mach number ramjet, however, the incoming air is diffused to a high static temperature before the fuel is injected. Very little temperature rise is associated with the combustion process, but a large part of the energy goes into dissociation. The pressure is a strong factor in the recovery of this energy, which may be of critical importance to the nozzle performance.

6.3.1.1 Temperature Measurements

The temperature of the expanded gas at the nozzle exit is particularly sensitive to the chemical changes that have taken place in the nozzle.

Simmons (Ref. 235) measured the temperature at both the nozzle inlet and exit in rockets using liquid oxygen and RP-1 fuel in a wide range of mixing ratios. He also measured the characteristic exhaust velocity and used the data to estimate the exit temperature. His equations are

$$\left(T_e\right)_{est} = \left(\frac{T_e}{T_c}\right)_{isen} \left(T_c\right)_{eff} + \left(\frac{c_{pc}}{c_{pe}}\right) \left[\left(T_c\right)_{theo} - \left(T_c\right)_{eff}\right] \qquad (6\text{-}52)$$

and

$$\left(T_c\right)_{eff} = \left(T_c\right)_{theo} \left[\frac{C^*_{meas}}{C^*_{theo}}\right]^2 \qquad (6\text{-}53)$$

where

C^* = characteristic velocity (see note after Eq. 6-7)

T = temperature

c_p = specific heat at constant pressure

and subscripts

c = chamber

e = nozzle exit

eff = effective

est = estimated

isen = isentropic

meas = measured

theo = theoretical flow, either equilibrium or frozen.

Figure 6-24 (taken from Ref. 235) presents a comparison of the estimated and measured exit temperatures as well as the calculated values for frozen and equilibrium flow. These data, compiled for one fuel at a fixed chamber pressure of 600 psia and a conical nozzle having an 8 to 1 area ratio, indicate a temperature nearer to the frozen case than to the equilibrium one. However, the data are too limited to allow generalization.

6.3.1.2 Acoustic Velocity in Real Gases

Application of the characteristics method to the flow of exhaust gases in chemical equilibrium becomes possible when one defines the local speed of sound as

$$a = \sqrt{\left(\frac{\partial p}{\partial \rho}\right)_s} \qquad (6\text{-}54)$$

Pressure is a function of density, temperature, and equilibrium chemical composition. The differentiation is carried out by holding entropy alone

constant. When dealing with ideal gases the foregoing relation may be shown to reduce to the more familiar

$$a = \sqrt{\gamma RT} \tag{6-55}$$

The use of acoustic velocity in the application of the method of characteristics is discussed by Rao in Ref. 236. The two differential equations in the method of characteristics depend basically upon the relationship between the gas velocity and the acoustic velocity during the isentropic expansion of the exhaust gases.

In the case of ideal gases the relationship is prescribed by the value of γ. In the case of exhaust gases it is obtained by knowing the changes in chemical composition and enthalpy, consistent with constant entropy. The interdependence of gas velocity and acoustic velocity can be readily expressed in terms of Mach number and M*, where M* is the ideal gas velocity divided by the gas velocity at M = 1. The expansion process of the exhaust gases in a nozzle may then be expressed in terms of M*. Typical examples of the relationship between M and M* are shown in Fig. 6-25. In this figure curve A gives M* vs M in an isentropic expansion of the combustion products of the propellant mixture discussed in Subsec. 6.3.1, and curve B is based on the isentropic expansion of the combustion products of the stoichiometric mixture of hydrocarbon fuel and air starting from a combustion chamber at a pressure of 15 atm and a temperature of 5000°R. The thermodynamic data for this example are taken from Ref. 39, which gives the properties for various mixture ratios and pressures. Hence both curves A and B are computed for expansion processes with equilibrium composition. For the sake of comparison, the figure also shows the dependence of M* on M in flows which have values of γ of 1.23 and 1.4. It is possible to approximate a condition of shifting equilibrium by a constant value of γ in the analysis of such supersonic flow by the method of characteristics. However, this value of γ will not be the polytropic exponent of the expansion process and should not be used in estimating the thrust performance of the exhaust nozzle. The thrust of the exhaust nozzle must be calculated as a function of the mass flow, exit velocity, and exit plane pressure associated with equilibrium composition of the exhaust gases.

6.3.2 Gas-Particle Nozzle Flows

Current solid propellant technology has introduced another complex fluid dynamic problem: gas-particle nozzle flow. High performance propellants use metallic fuels which disperse in condensed micron-sized oxides in the exhaust gases. Many analytical studies and fundamental experiments have stemmed from tests that showed that these particles cause the propellants to perform below thermochemical predictions. An excellent comprehensive survey of such studies has been prepared by Hoglund in Ref. 237 which covers 72 papers on the subject.

Gas-particle flow analyses are necessarily restricted by many assumptions. For example, Kliegel (Ref. 238) assumes:

1. No mass or energy losses from the system;
2. No mass exchange between phases;

3. Negligible particle volume;
4. Negligible thermal (Brownian) motion;
5. Non-interacting particles;
6. Inviscid gas except for particle-gas interaction;
7. Constant composition perfect gas;
8. Particle size distribution equivalent to uniform spherical particle;
9. Only convective energy exchange between particles and gas;
10. Uniform particle temperature;
11. Constant heat capacities.

Although these assumptions are generally accepted, they vary somewhat from one investigator to another. The equations of mass, energy, and momentum conservation, an equation of state, together with particle-gas energy and momentum exchange equations may in general be solved simultaneously only by machine computation. The numerical problems are limited in accuracy by the lack of knowledge of the appropriate drag and heat-transfer coefficients as well as that of particle size distribution.

In the limiting case of no particle lag (very small particles), the flow can be treated as isentropic with an effective adiabatic index,

$$\bar{\gamma} = \gamma \left[\frac{1 + (W_p/W_g)(c_{pp}/c_{pg})}{1 + \gamma\,(W_p/W_g)(c_{pp}/c_{pg})} \right] \qquad (6\text{-}56)$$

where

W_p/W_g = particle/gas weight ratio

c_{pp}/c_{pg} = particle/gas specific heat ratio (per unit mass)

γ = adiabatic index for the gas.

For a large fraction of particles, $W_p/W_g \to \infty$ and hence $\bar{\gamma} \to 1$.

Non-equilibrium particulate nozzle flows behave effectively like chemical non-equilibrium nozzle flows, i.e., a "frozen" and an "equilibrium" sound speed can be defined.

The equations lead to the formulation of a scaling parameter: particulate nozzle flows are similar in geometrically similar nozzles only if the ratios of nozzle throat size to the square of the particle size, r_t/r_p^2, are the same. Since propellant combustion gives particle sizes independent of nozzle or engine dimension, similarity through scaling is impossible.

Of primary interest is the effect of particle lag on rocket performance. Particle size for aluminized propellants usually averages between 1 and 5 microns. The sketch on the opposite page shows that the losses incurred in the region of high acceleration near the throat are not fully recovered,

although the particle velocity approaches the gas velocity in the expansion region. It is apparent that the throat region is of foremost importance in establishing the characteristics of particle nozzle flow. A gradual throat contour is most desirable for reducing lags.

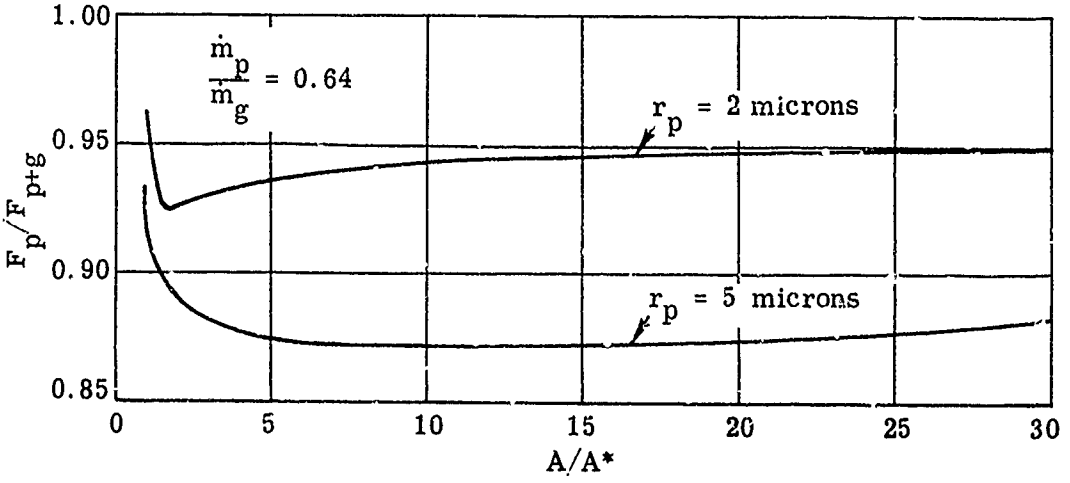

In general, theory and experiment are in reasonable agreement. Kliegel also finds that (for cases of engineering interest) appreciable particle solidification seldom occurs in the nozzle, and hence the heat of fusion of the particles is not available for useful work.

Both Bailey (Ref. 239) and Kliegel (Ref. 238) have concluded that the nozzle acts as a particle size separator. The larger particles concentrate near the nozzle axis. The very small particles follow the streamlines of the gas while the medium sized particles, due to their high inertia, follow conical streamlines. The impingement of particles on the nozzle wall, with consequent erosion and heat-transfer effects, is more severe in contoured, or skewed, nozzles than in conical ones.

Although it is possible to predict with good accuracy the effect of gas-particle mixtures on the parameters of nozzle flow there are still many problems that remain unsolved.

6.4 Design of Propulsion Nozzles

Since the shape of a nozzle largely determines its efficiency (Subsec. 6.2), the basic design problem is that of obtaining maximum thrust with minimum nozzle weight and heat transfer. Although it is designed for a specific Mach number and pressure ratio, the nozzle should be able to operate over a wide range of off-design altitudes and Mach numbers and should not involve difficult or costly fabrication problems. The many shapes that have been used or considered may be classified as simple cones, contoured nozzles, plug nozzles, and skewed nozzles. Preliminary performance calculations for a ramjet in terms of its mission and tactical requirements usually define the maximum dimensions of the exit nozzle, its expansion ratio and allowable weight.

6.4.1 Conical Nozzles

The simplest way of obtaining the required expansion ratio for the exhaust flow is by means of a cone frustum faired into a rounded throat section. Although many nozzles use an expansion angle of about 15 deg, experience has shown (see Fig. 6-3) that the expansion angle may be as great as 40 deg without incurring flow separation. The conical nozzle may thus be reasonably short, quickly designed, and easily produced. However, as indicated in Subsec. 6.2.2 and Fig. 6-3, the loss in thrust due to non-parallel flow is proportional to $(1 - \cos \alpha)/2$, which amounts to a loss of 12% in thrust when α is 40 degrees. In many practical cases the advantage of short length is more than offset by the thrust loss.

For conical nozzles of equal surface area (i.e., assumed to be of equal weight) the variation of the net thrust coefficient, $C_F - C_D$, with divergence angle is shown in Fig. 6-26. The drag is assumed to be due solely to friction on the inside surface of the nozzle. An average value of the skin friction along the nozzle was rather roughly estimated from zero heat-transfer conditions, and therefore the results should be interpreted qualitatively rather than quantitatively. The various curves of constant surface area, A_s/A^* become steeper as the surface area increases, showing that the divergence angle has become more critical for obtaining maximum thrust. The nozzle length and the exit Mach number are indicated on the curves of Fig. 6-26. A value of $\gamma = 1.26$ was used. If the nozzle exit diameter exceeds the maximum diameter of the vehicle containing it, then the additional external pressure drag as well as the drag due to the skin friction on both internal and external nozzle walls must be charged against the thrust.

6.4.2 Contoured Nozzles

A nozzle accurately designed to give parallel flow at the exit is theoretically more efficient than a conical nozzle of the same expansion ratio operating at the same exit Mach number. The design of a contoured nozzle embodies an expansion section in which the flow deviates from the axial direction, as well as a straightening section in which the flow is redirected along the axis.

In order to provide shock-free flow axially aligned at the exit, the nozzle contour should be accurately designed by means of the method of characteristics. Details of this method for axially-symmetric flow are given in Refs. 95, 96, and 98. For two-dimensional nozzles, see Refs. 2, 6, 7, 94, 97, and 99. Many of the methods used for wind-tunnel nozzles (Subsec. 4) may also be used for propulsion nozzles. Tables 4-1, 4-2, and 4-3 analyze the nozzle design features of many references.

After a contour has been designed for isentropic flow, it should then be corrected to account for the presence of the boundary layer (see Subsecs. 2.4 and 4.8). Since this correction is based on the expected Reynolds number of the flow, the optimum design of the nozzle is limited not only to one Mach number but also to a definite altitude range. However, its off-design performance may still be superior to that of a less carefully designed nozzle. Since a characteristics nozzle is about twice as long as a conical nozzle with the

same exit Mach number, the additional weight and skin friction associated with the former make it impractical as a missile exhaust nozzle. Much effort has been devoted to finding relatively rapid and simple methods of design which will produce parallel flow and have either a minimum length or a minimum surface area.

Rao in Ref. 236 has applied the calculus of variations to derive a method for designing a nozzle of given length which will produce the maximum thrust. Part of the design is still dependent upon the construction of a characteristics net and requires the use of high-speed computing machines. Compared to a conical nozzle of the same length and area ratio the improvement in thrust of such a short-length nozzle is quite small, but as the length and Mach number increase the thrust improves significantly. The calculated values of the parameters of two nozzles for $\gamma = 1.23$ (from Ref. 236) are shown below.

Nozzle	ℓ/r^*	A_e/A^*	M_e	$\frac{C_{F\ \text{contour}}}{C_{F\ \text{conical}}}$
A	8.19	19.36	3.50	1.023
B	2.94	4.973	2.60	1.005

In Ref. 240 Rao gives an approximate method for determining the contour of the optimum-thrust nozzle by purely geometric means. The nomenclature is shown in the following sketch.

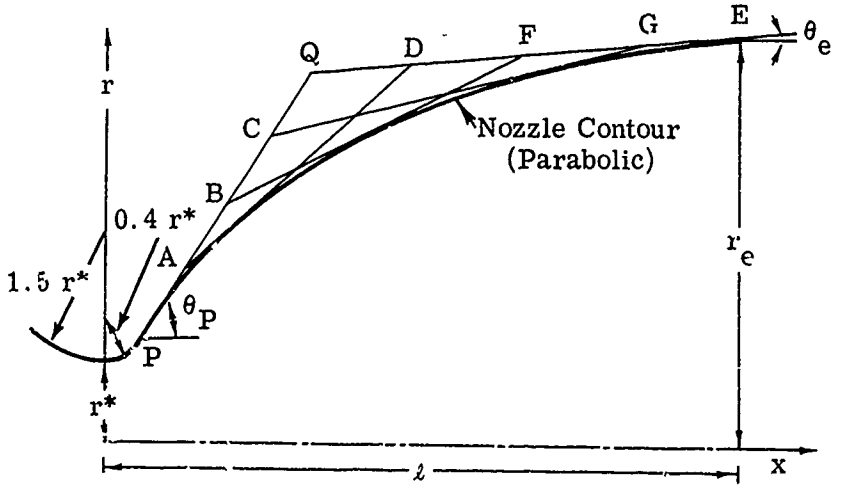

The steps of the method are as follows:

1. From the given values of r^*, r_e, and ℓ, determine θ_P and θ_e from Figs. 6-27 and 6-28.
2. Construct circular arc throat terminating at P, so that the slope at P = θ_P.
3. Construct EQ with slope θ_e and construct PQ tangent to the throat arc.
4. Divide PQ and EQ into an equal number of equal parts as shown in the sketch (as many as the accuracy requires).

5. Join AD, BF, CG, etc., giving the envelope of the required contour.

This method is accurate to within a few per cent of the exact method. It may be seen from Fig. 6-28 that for reasonably short lengths and moderate Mach numbers the maximum inclination of the exit flow is only a few degrees. The calculations of Figs. 6-27 and 6-28 are based on a value of 1.23 for γ, however, changing the value of γ does not appear to affect the nozzle contour appreciably when the length and area ratio are prescribed.

The surface area of the nozzle is more closely related to both nozzle weight and heat transfer than is the nozzle length. Consequently Knuth (Ref. 241) has considered the thrust in terms of the surface area and shown that the maximum thrust per unit of surface is obtained when

$$\tan \theta = \frac{(p_w - p_\infty)}{p_w} \cdot \frac{(M_w^2 - 1)^{1/2}}{\gamma M_w^2} \tag{6-57}$$

where

θ = wall slope

p_∞ = ambient pressure

and subscript w denotes condition at the wall. In the subsequent calculations, Knuth assumed that the gas properties were constant over each cross section.

If the maximum possible turning is allowed downstream of the throat the values of θ and M at the last tangent point P (see previous sketch) will be given by the Prandtl-Meyer equation

$$\theta_P = \left(\frac{\gamma + 1}{\gamma - 1}\right)^{1/2} \tan^{-1}\left[\left(\frac{\gamma - 1}{\gamma + 1}\right)(M_P^2 - 1)\right]^{1/2} - \tan^{-1}(M_P^2 - 1)^{1/2} \tag{6-58}$$

θ_P and M_P are found from the solution of Eqs. 6-57 and 6-58. An arbitrary set of values of M from M_P to M_e (the design exit Mach number) are chosen and from isentropic channel flow equations the corresponding values of the pressure, p, and the radius, r, of each cross section are computed.

The slope at each value of M is found from Eq. 6-57 and the distance, Δx, from one section to the next is found from

$$\Delta x = \Delta r \cot \bar{\theta} \tag{6-59}$$

where

$\bar{\theta}$ = average value of θ in this interval.

When constant flow properties are assumed at each cross section and when $p_\infty = 0$, the solution is easily obtained. Good agreement was found between a

nozzle contour computed by this method for $\gamma = 1.4$ and one calculated by the exact method of Guderley and Hantsch (Ref. 242).

One of the disadvantages of the contoured nozzle is that thrust loss is experienced when the nozzle is operating at pressure ratios and gas compositions other than those for which it was designed. Even at the design Mach number the exhaust gases may be over-expanded at altitudes lower than the altitude for which it was designed; similarly at higher altitudes the exhaust jet will be under-expanded. Over-expanded flow is discussed in Subsec. 6.2.5.

6.4.3 Skewed Nozzles

Skewed nozzles may be used for the removal of bleed flows or for achieving directional control of a missile by providing a lift component at the expense of the thrust coefficient. The former use is discussed in this subsection and the latter in Subsec. 6.5.1. The need for removing boundary-layer flow in the diffuser of a ramjet has been discussed in Subsec. 3.7. In many vehicles additional air is often scooped from the main flow to provide power for turbines. It may also be captured and re-expanded in order to be used as a coolant. After its function is performed this relatively low-velocity air should be discharged in the most efficient manner. Since the frictional losses will increase rapidly with ducting length, it is usual to exhaust laterally at some convenient station along the missile. If the by-passed flow is expanded by means of a sonic throat, a large fraction of its original momentum will be recovered as thrust.

A study by Cnossen (Ref. 243) was particularly directed towards the design of nozzles suitable for the exhaust components of boundary layer and by-pass systems associated with high-performance supersonic inlets. Three basic types of flush oblique nozzles were designed and tested. The first nozzle was fully contoured to give uniform flow at a Mach number of 2 at the exit, as shown in the sketch below.

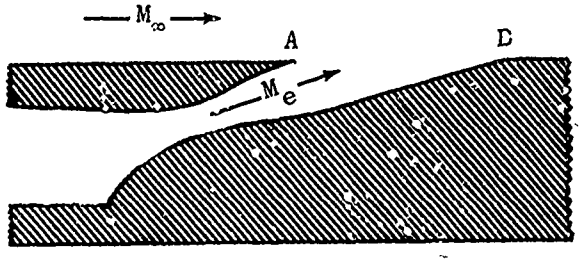

A - Full Nozzle - Both Walls Contoured

The second design was a half nozzle, i.e., one wall fully contoured and the other plane, the plane wall being the centerline of a fully contoured nozzle as

shown below. Half nozzles giving exit flow of M = 1, 2, and 3 were tested.

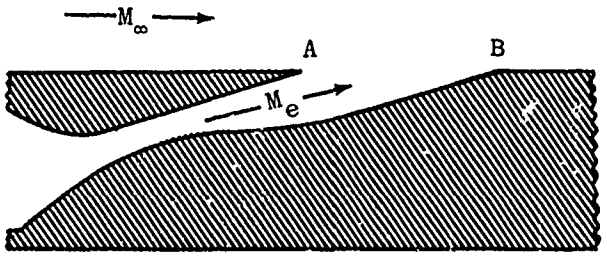

B - Half Nozzle - Lower Wall Contoured

The third type of oblique nozzle was asymmetric with straight walls as shown in the sketch below.

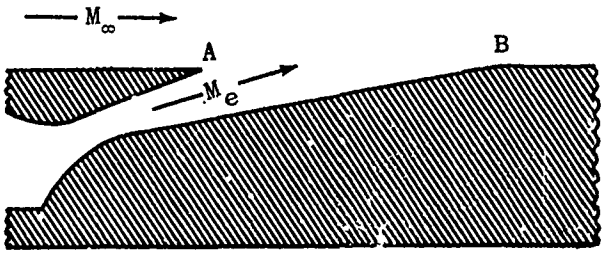

C - Asymmetric Nozzle - Both Walls Straight

The average inclination of each nozzle was 15 degrees. Since all nozzles were two-dimensional they lent themselves fairly readily to theoretical analysis for discharge into an external flow and into still air. The analyses were carried out by means of characteristics and shock-wave theories for four basic flow conditions, i.e., with the exit flow distribution: 1) less than the design value; 2) equal to the design value; 3) greater than the design value and less than the critical pressure ratio; and 4) equal to the critical pressure ratio. The design pressure ratio is such as to make the exit jet static pressure equal to the ambient pressure. During operation at a pressure ratio higher than design, an expansion fan arises from point A and is reflected from the opposite wall of the nozzle as shown in the sketch below.

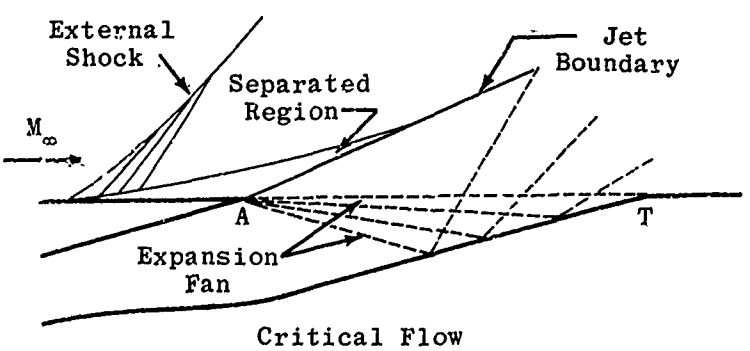

Critical Flow

When the last ray of the fan just reaches the point T, the pressure ratio is said to be critical. The stream thrust* reaches a maximum at the critical pressure ratio and remains constant at this maximum for any further increase in the pressure ratio. Calculated values of exit flow conditions and boundary-layer characteristics for the case of no external flow are compared with measured values in Ref. 243. Performance characteristics, i.e., the velocity coefficient and the stream thrust coefficient of the jet discharging into external flow at M = 0, 1.69, 2.94, and 3.87 were calculated. Comparison with experimental data shows that the calculations give reasonably accurate predictions of the nozzle performance, the differences being largely attributable to uncertainties in the skin-friction and heat-transfer characteristics of the nozzle walls.

Figure 6-29 shows the stream-thrust coefficient as a function of overall nozzle pressure ratio for the three oblique nozzles shown in the sketches. The exit Mach number of each nozzle was about 2. Tests were made with the external flow at M = 0, 1.69, 2.94, and 3.87. It is shown that within the experimental accuracy the thrust coefficient as predicted remained constant at pressure ratios greater than critical. From Fig. 6-29 it may be seen that the differences between the three nozzle shapes have very little effect on the thrust coefficient especially when the pressure ratio lies between the design and the critical values. The straight-walled nozzle appears to have the best performance of the three, but the difference is not sufficient to be really significant. The Mach number of the external flow affects, of course, the critical pressure ratio but has no effect on the maximum thrust coefficient.

Figure 6-30 compares the thrust coefficients of three half-contoured nozzles designed to give exit flow of M = 1, 2, and 3. With no external flow and with external flow at M = 1.69, increasing the velocity of the exit flow increases the thrust coefficient. With the external flow at the higher Mach numbers the data are inconclusive. The use of the skewed nozzle to obtain lift will be discussed in Subsec. 6.5.1.

6.4.4 Clustered Nozzles

Multinozzle exhausts are often incorporated in the design of modern vehicles for two general purposes: to permit the use of more than one rocket and to minimize the vehicle's exterior length and weight. With such an arrangement, moreover, pairs of nozzles may be deflected (see Subsec. 6.5) to provide directional control.

In multinozzle arrangements, the interaction of individual exhaust jets with each other and with the external flow creates complex flow patterns, which frequently include recirculation of the exhaust gases to the base region. The hot exhaust gases may have serious effects on the pressure distribution and the heat transfer at the missile base.

Goethert in Ref. 244 has made both theoretical and experimental analyses of flow and heat-transfer characteristics in the presence of four issuing jets at the base of a rocket-powered missile. These analyses show that the flow pattern is strongly dependent on the ratio of the base pressure to the ambient pressure, i.e., it is critically a function of the flight altitude.

*Stream thrust = $pA(1 + \gamma M^2)$.

At low altitudes cooling atmospheric air is sucked into the base as shown in the sketch below.

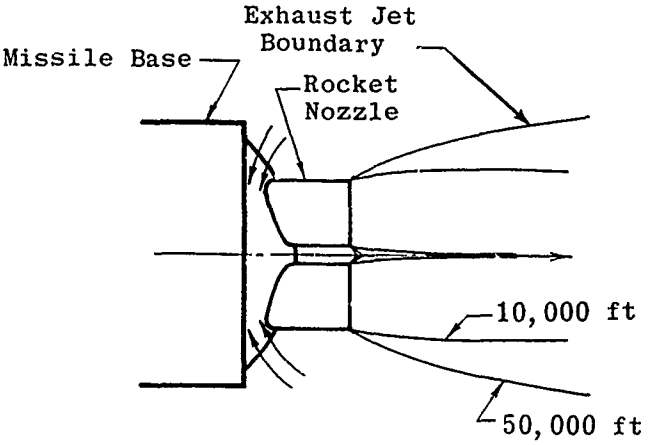

At high altitudes interference between the exhausts from the four nozzles forces the hot gases to flow back towards the base as shown in the next sketch.

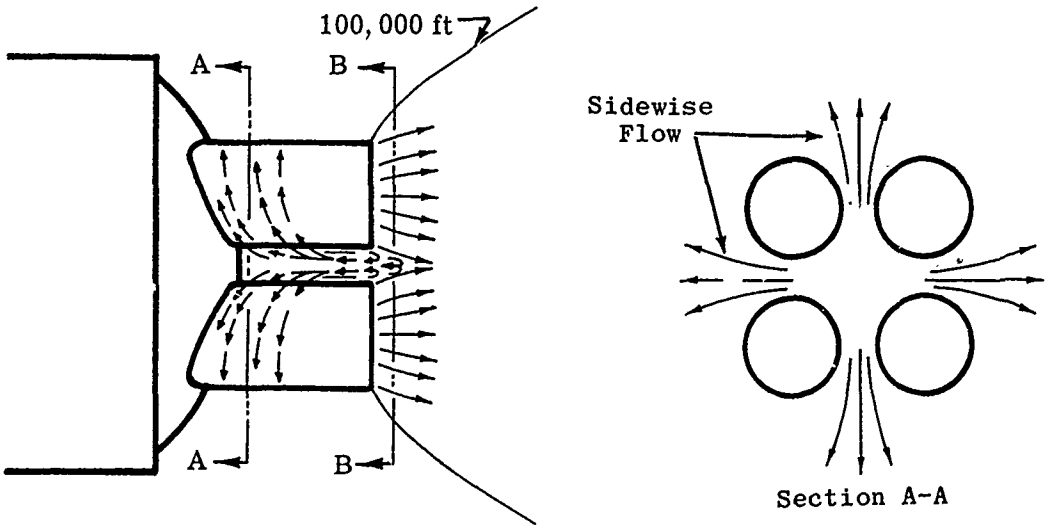

At still higher altitudes, choking conditions are reached and the base pressure remains constant. The critical altitude is determined by the nature of the exhaust gases, i.e., the value of γ, as well as by the geometry and relative position of the nozzles. The altitude bands within which the flow regimes exist are shown in Figs. 6-31 to 6-34 (taken from Ref. 244) in terms of the design geometry and a wide range of chamber pressures for exhaust gases with $\gamma = 1.2$. In spite of the fact that part of the exhaust flow is turned towards the base, the thrust under these conditions is slightly increased because of the increased base pressure. The base thrust increment (in a vacuum) is shown in Fig. 6-35 as a function of nozzle area ratio and the spacing of the four rockets. In Fig. 6-36 the base thrust increment is shown as a function of the base vent area and the exit angle. The small thrust increment can be increased appreciably by the addition of a suitable shroud. Figure 6-37 shows the thrust increment, due to the shroud, as a function of the area ratio and the spacing of

a four-nozzle cluster. The improvement due to the square shroud is estimated to run from about 2 to 10%.

6.4.5 Plug Nozzles

Another method of producing axially aligned flow is by means of a plug nozzle. The following sketch shows typical plug configurations.

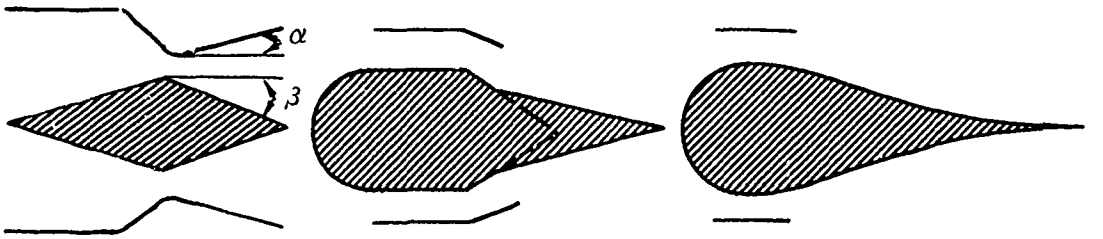

a - Complete Internal Expansion

b - Some Internal Expansion

c - Complete External Expansion

It may be seen that the expansion may be completely or partially internal or completely external.

Where the plug is used to create completely internal expansion, the performance is similar to that of the conventional convergent-divergent nozzle. In this configuration the nozzle length is decreased by use of the plug, without increasing the flow inclination; however, because of the extra wetted area the skin friction is increased.

For complete internal expansion by means of a conical plug and conical nozzle section, the flow may be assumed to be emanating from a source situated at the hypothetical intersection of the plug and nozzle surfaces. The exit momentum of such a flow may be evaluated by integrating across the exit plane. The flow divergence loss may be approximated by

$$\lambda_{plug} = \frac{1}{2} \frac{(\sin \alpha + \sin \beta)^2}{(\alpha + \beta) \sin \beta + \cos \beta - \cos \alpha} \qquad (6\text{-}60)$$

where

α = inclination of nozzle wall to axial direction

β = inclination of plug wall to axial direction.

When the outer wall is parallel to the nozzle axis this reduces to

$$\lambda_{plug} = \frac{1}{2} \frac{\sin^2 \beta}{\beta \sin \beta + \cos \beta - 1} \qquad (6\text{-}61)$$

It may be seen from these equations that conical plugs of large vertex angles may be used without undue loss from flow divergence.

Where all or most of the expansion is external, the ambient air behaves as the outer wall and thus gives this type of nozzle the advantage of an automatic adjustment of the exhaust expansion to ambient pressure and prevents

loss due to over or under expansion. In addition, the weight and volume of the engine required to produce comparable thrust may be much less for a plug nozzle than for a conventional nozzle. Cooling problems may also be simplified since the plug radiates to the ambient air. Plug nozzles of types a and b (see previous sketch) also have the advantage that the throat area may easily be varied to compensate for large changes in engine operating conditions.

At pressure ratios greater than the design value the performance of the plug nozzle is comparable with that of the conventional nozzle. However, below the design pressure ratio the thrust coefficient of the plug nozzle is less sensitive to a decreasing pressure ratio than is that of the convergent-divergent nozzle. This effect is shown in Fig. 6-38.

The upstream shape of the plug is not critical. The discussion in Subsec. 4.2 relative to the subsonic section of a wind tunnel may also be applied to the subsonic section of the plug. The shape may be varied over a wide range of design without adversely affecting the performance of the nozzle. The use of short lengths is generally an advantage.

The downstream portion of the plug is usually an isentropic spike, i.e., contoured by the method of characteristics in the same manner as an isentropic duct to give uniform axial flow with no over-expansion at the tip.

An isentropic plug, like an isentropic spike (Subsec. 3.4), is too long for practical purposes and is usually shortened by replacing the tip with a tangent cone. The effect of this conical tip on the total length is shown in Fig. 6-39 while the effect on the resultant thrust may be seen in Fig. 6-40 (from Ref. 245). In this particular example the length may be reduced to 60% of the isentropic value with virtually no loss in thrust, but beyond that limit the thrust drops very rapidly. There is no reason why the isentropic tip may not simply be lopped off since the viscous wake will create a flow field similar to that of a conical tip.

When a conical plug is used in place of an isentropic one, the optimum cone angle is dependent upon the design pressure ratio. Tests described in Ref. 246 indicate that for a design pressure ratio of 8 the total cone angle giving the highest thrust is 60 deg; for a ratio of 20 the optimum cone angle is between 60 and 80 degrees. In both cases the peak thrust coefficient of a contoured plug is about 1% greater than that obtained with the optimum conical plug with the same surface area.

Greer, in Ref. 247, gives a rapid method for designing a short plug nozzle of the external expansion type giving axially aligned exit flow. The nozzle geometry is completely defined by the two parameters, ℓ and φ, as shown below.

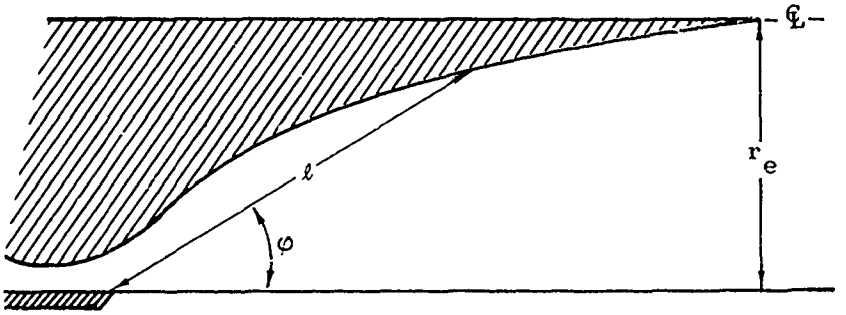

The equations necessary for this method of designing an axisymmetric nozzle with an expansion ratio of A_e/A^* are

$$\frac{\ell}{r_e} = \frac{1 - \sqrt{1 - \xi \sin(\psi + \omega)}}{\cos(\mu - \psi - \omega)} \tag{6-62}$$

and

$$\varphi = 90 - \mu - (\psi + \omega) \tag{6-63}$$

where

$\xi = A/A_e = A/A^* \cdot A^*/A_e$

$\mu = \sin^{-1} 1/M$

ω = Prandtl-Meyer expansion angle

$\psi = 90 - \omega_e$.

The value of ξ may be obtained from M, M_e, and isentropic flow tables; ω may be obtained from flow tables or from Eq. 6-58. Figure 6-41 gives the generalized nozzle contours computed by this method for $\gamma = 1.17$ and expansion ratios from 5 to 25.

The shape of the cowl lip and its position with respect to the plug surface may have a large effect on the base drag of a missile as well as on the exit nozzle performance. It is important for the throat or narrowest section to be at the cowl lip in order that all expansion waves emanate from the cowl lip to avoid performance losses. The lip and plug inclinations are such as to align the flow with the axis by the time it reaches the plug tip. As indicated in the sketch below, the location of the throat, A, for a conical plug, should be on the conical surface rather than on the curved turning surface.

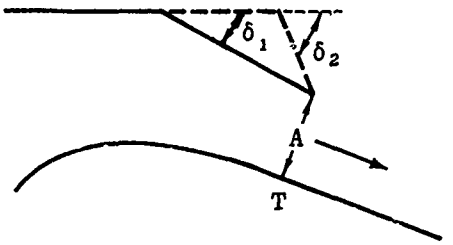

A = Constant Throat Area

Krull, et al (Ref. 246), tested both conical and contoured plugs at pressure ratios from 1.5 to 32. The theoretical lip angle, δ, required for a 60 deg conical plug nozzle was 25 deg at a pressure ratio of 7; however, the thrust coefficient remained unchanged when the lip angle was varied from 15 to 90 deg and the pressure ratio from 1.5 to 32 while the throat area remained unchanged. On the other hand when the lip angle of a contoured plug nozzle was decreased from 30 to 15 deg the thrust coefficient dropped about 1% at all but the very lowest pressure ratios where the thrust loss was even greater.

The effect of variation in throat area was also studied by Krull. The area was varied by two methods. The first employed an iris type cowl, i.e., a variation of δ as shown below.

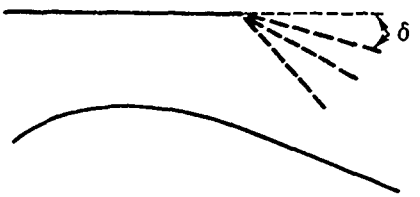

The second method employed an axial translation of either the cowl or the plug as shown below.

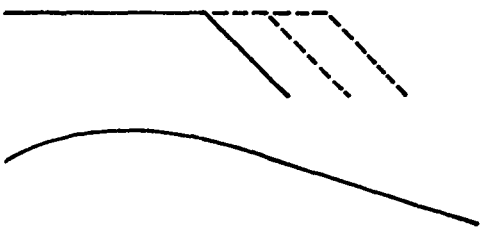

Within the range of test parameters it was found that there is virtually no decrease in thrust coefficient as the throat area is increased by changing the cowl lip angle, but translation of the cowl decreased the thrust by as much as 5%.

The feasibility of a two-dimensional plug nozzle developed by Dugger and Kiersey for flight speeds at a Mach number of 7 has been extensively surveyed by Pietrangeli and fully documented in Ref. 118. The engine, which is placed under the surface of a wing, is shown in the following sketch.

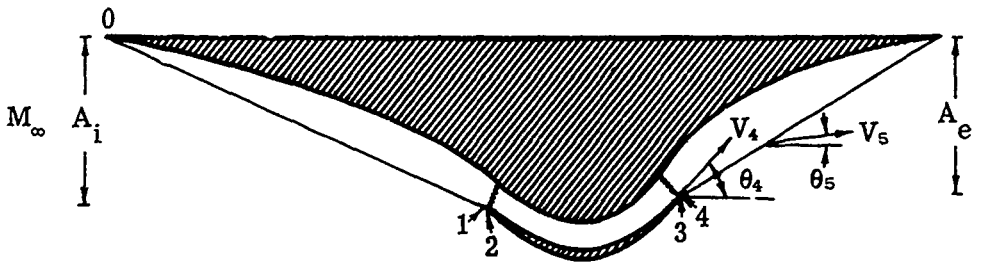

Supersonic diffusion takes place in section 0-1, subsonic diffusion in 2-3, fuel addition and combustion occur in 3-4. There is a sonic throat at station 4. Figures 6-42 and 6-43 give the thrust and lift coefficients and the specific impulse in terms of A_e/A_i. These figures also show the effects of the over-all pressure ratio and the initial turning angle of the plug, θ_4. Since these calculations are based on estimates of diffuser pressure recovery and fuel equivalence ratio, the quantitative aspects of the results are of less significance than the qualitative relationships between the parameters. Comparing C_F, C_N, and I for various fixed values of A_e/A_i shows clearly the close dependence of design parameters and desired performance. The importance of an efficient exit

nozzle is shown clearly in Fig. 6-44 which compares the specific impulse obtainable with nozzles of 100% and 97% efficiency and $A_e/A_i = 1$.

Similar extensive calculations at a Mach number of 5 have been backed up by some experimental data. Unfortunately, the results are still classified (Ref. 248) The two-dimensional ramp nozzle and the "half" axisymmetric plug nozzle also give a lift component. This aspect will be discussed in the next subsection.

6.5 Thrust Vector Control

Successful use of methods for diverting rocket exhausts has demonstrated that thrust vectoring can effectively stabilize, control, and maneuver a rocket-propelled guided missile. Where the mechanism has minimum volume and weight it may effect considerable gain in the missile performance. Jet control offers the possibility of eliminating drag-producing fins, or at least of reducing their size. Most large U.S. rockets now employ some form of jet control.

The many methods of control that have been suggested may be divided into three large groups: those that are based on movement of the nozzle itself, those that depend on vanes or paddles inserted in the flow at the nozzle exit, and those which divert the flow internally by means of oblique-shock patterns.

Most of the design and experimental work on thrust vector control has been connected with specific missiles, and the design details and test results are therefore classified. References 249 to 261, although by no means comprehensive, give generalized unclassified information on many aspects of the subject. Moak (Ref. 262) gives a brief analysis of schemes suitable for the thrust vector control of solid-propellant rockets. The following subsections outline the most common types of jet flow control.

6.5.1 Movable Nozzles

The three best known types of movable nozzles are the single-hinged, gimbaled, and rotating nozzles. The single-axis nozzle employs hinge pins and an O-ring seal, making the total weight only slightly greater than that of a similar fixed nozzle. Since the movement is confined to one plane a cluster of four such nozzles is required for pitch, yaw, and roll control. The performance is efficient and the reliability is high.

The multiaxis hinged nozzle is gimbaled at two pivot points and the gimbal ring is in turn attached to the motorcase at points 90 deg from the first pivot points. The entire nozzle is usually turned about a point in or near the nozzle throat, creating difficulties in sealing and lubrication because of the high temperatures encountered in this region.

It has been shown that a full swiveled nozzle is aerodynamically the most efficient method of diverting the exit flow. The ratio of side force to axial force is higher in terms of the percentage thrust loss than for other devices, and furthermore the swiveled nozzle has the advantage of producing no

additional drag in the jet. For a specified degree of vector control the swiveled nozzle has to be deflected through half the angle required by the single-axis hinged nozzle. Pitch and yaw control can be obtained by the use of a single gimbaled nozzle but where roll control is desired at least two nozzles must be used. Although the power requirements are high and the servo-mechanism massive, this design has been tested and used satisfactorily for both liquid- and solid-propellant rocket motors.

The rotating nozzle produces a flow deflection with an aerodynamic efficiency only slightly less than that of a swiveled nozzle. The rotation is effected about a line inclined to the nozzle axis. Since in this type of deflection an extraneous side force is produced, rotating nozzles are best used in pairs so that these extraneous forces will cancel each other. At least two nozzles are required for pitch, yaw and roll control. The large bearings and heavy bearing support structures are its major disadvantages.

Clustered nozzles (see Subsec. 6.4.4) are capable of providing attitude control about three axes if four nozzles are rotated. The weight of the control mechanism is not as critical as that of a simple nozzle, but the space requirements could be difficult to achieve. Operating more than one nozzle control may involve time lags in switching from one nozzle to another. Nozzles with flexible skirts have also been tested.

Calculations were made by Dugger and Monchick (Ref. 263) to determine whether vectoring the exhaust flow of an external-expansion ramjet would increase the value of the product $I \cdot L/D$ and hence the range of a missile. Their brief study was concerned with the configuration shown in the sketch below.

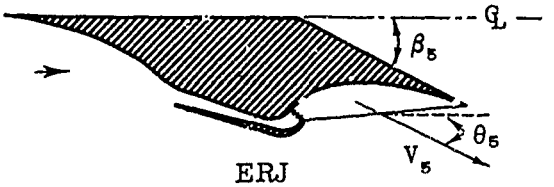

ERJ

They found that the loss in specific impulse was always equal to or greater than the gain in over-all lift-drag ratio for the expansion ratio which provides the highest value of $I \cdot L/D$. They also compared the gross thrust versus lift force due to internal flow for the conventional ramjet (see sketch below) with that of the external-expansion ramjet (above) when both have vectored nozzles.

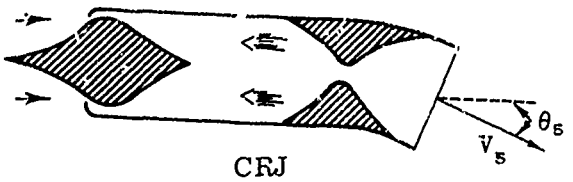

CRJ

A typical resultant curve with the ERJ having slightly more thrust than the CRJ is shown in the sketch on the opposite page. When the lift force is "gauge-corrected" for the component of lift across the exit area due to the ambient air, the curves are almost identical. These calculations are based on kerosene-fueled Mach number 5 flights at an altitude of 100,000 ft and should not

be generalized. In any case, they are chiefly of academic interest as the overall lift of the vehicle would have to include such items as the cowl lift and the effect of boattailing the nozzle; in addition, both thrust and lift would be greatly affected by the way the engine pod was integrated with the airframe. Thrust vectoring in plug nozzles may also be achieved by the relative motion, either rotational or translational, of the plug and the cowl.

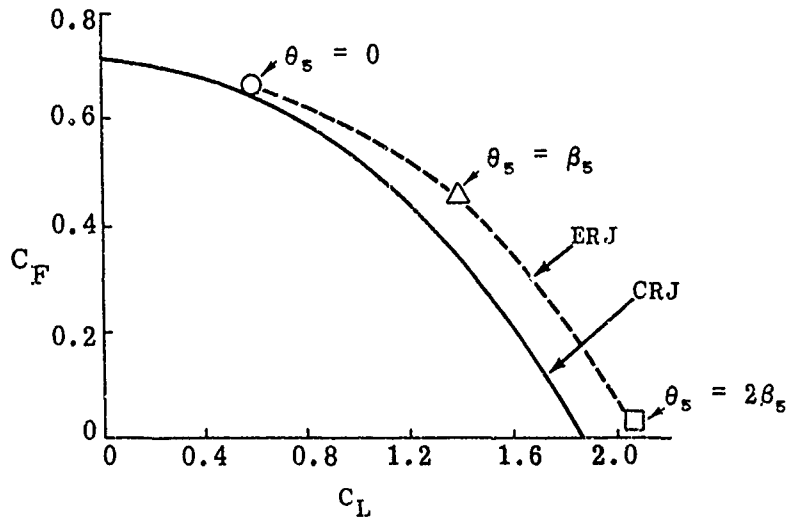

Although swiveled and rotated nozzles are usually motor-operated, they may be motivated by a secondary injection through an orifice in the wall of the exit cone. The injected fluid interacts with the main gas flow to produce a side force which tends to turn or push the nozzle towards the injected fluid. Secondary injection to provide thrust vectoring in stationary nozzles is discussed in Subsec. 6.5.3.

6.5.2 Deflecting Surfaces

A second method of producing thrust control is by means of surfaces inserted in the flow. Such insertions are critically subject to erosion, ablation, and melting due to the high temperature of the exhaust gases. They may also be adversely affected by propellant particles. Aerodynamically they produce drag which decreases the net thrust of the nozzle.

Some of the simplest aerodynamic surfaces are jet vanes which are usually inserted at the exit cross section of the nozzle. The servo power requirements are reasonable and the aerodynamic forces are large. Jet vanes may be used with either solid or liquid propellants. The thrust loss at maximum deflection is of the order of 10%. Jet vanes are simple to install and require only a moderate amount of mechanical linkage. They have been incorporated successfully into several missile designs.

Jet paddles hinged externally at the nozzle exit have been laboratory tested. The excessive weight of the necessary actuating linkage, high hinge moments, and poor frequency response make this type of control unsatisfactory. It has been suggested that a small button might be inserted in the nozzle throat

to control the flow deflection. The system requires very little operating power; however, erosion and high temperature would produce serious effects.

A jetavator is a right circular ring around the nozzle exit. In the neutral position the hinge line is normal to the nozzle centerline. It has a low hinge moment, requires a relatively small control system, and contributes little additional drag for small jetavator angles. It has been used successfully with both solid and liquid propellants.

6.5.3 Shock-Induced Deflections

A liquid or a gas injected through an orifice in the wall of the exit section of a nozzle may be used to generate a side force. The injectant causes the boundary layer to separate, which in turn creates an oblique shock as shown in the following sketch.

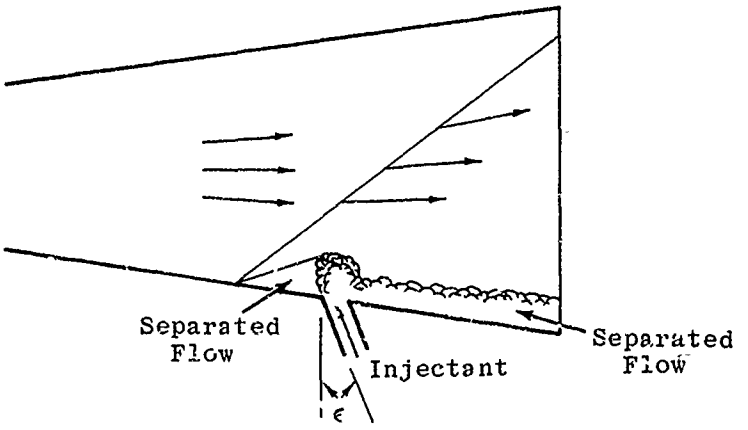

The side force has two main sources. The first is due to the change in magnitude and direction of the stream velocity as it passes through the oblique shock. The second component is due to the momentum of the injected gas. Mager, et al (Ref. 228), have evaluated analytically the ultimate potential and relative effectiveness of thrust vectoring by both gaseous and liquid injection.

For a secondary gas stream injected into a supersonic primary flow in a conical nozzle, Mager arrives at the following expression for the magnitude of the side force, F_σ, perpendicular to the nozzle axis:

$$F_\sigma = \left[\left(\frac{p_\infty}{p_s} - 1\right)(\Omega \tan \theta_w - 1)\, h^2\, \Omega + \left(\frac{p_2}{p_s} - 1\right)\left(h^2\, \Omega - \frac{A_i}{2}\right)\right] p_s \cos \alpha + p_s\, A_i \cos \epsilon \left(\frac{p_1}{p_s} - 1\right) + \dot{m}_i\, V_i \tag{6-64}$$

where

$$\Omega = \cot \theta_s + \tan (\alpha + \epsilon) \tag{6-65}$$

and

$$h = \left(\frac{2A_s}{\pi}\right)^{1/2} \left\{ \frac{2\gamma_i^2 M_i^2 \left(1 + \frac{\gamma_i - 1}{2} M_i^2\right)}{\left(\frac{A_s}{A_i}\right)^2 \left(\frac{p_s}{p_i}\right)^2 \left(\frac{p_i + 2p_2}{3p_s} - 1\right) \left[(\gamma_i + 1) + (\gamma_i - 1)\left(\frac{p_i + 2p_2}{3p_s}\right)\right]} \right\}^{1/4} \quad (6\text{-}66)$$

with

$\dot{m}$ = mass flow rate

ϵ = angle between injectant stream and a plane normal to the axis

subscript i denotes injectant properties

and all other parameters as defined in Subsec. 6.2.5. Because it is assumed that the shock caused by the injection has the same properties as that caused by separation of a turbulent boundary layer (see Subsec. 6.2.5 and in particular the sketch on page 323), the values of p_2/p_s, p_∞/p_s, θ_w and θ_s as a function of M_s are those given in Fig. 6-19 for $\gamma = 1.2$ and 1.4. Side forces computed by means of Eqs. 6-64 to 6-66 compare favorably with measured data reported in Ref. 249. However, it should be noted that the latter are obtained for the most part from the subsonic injection of cold gas, the exception being two tests with hot gas and sonic injection.

It may be noted from Eqs. 6-64 to 6-66 that the side forces are dependent upon many variables. Because the interrelationships are complex, care should be taken in making generalizations where the data are derived from a limited range of parameters. An excellent example of such nearsightedness could be pointed up by using two of the many sets of calculations of Ref. 228. By holding all quantities constant except the Mach number of the primary flow, the specific impulse of the injected fluid decreases with increasing M, leading one to assume that an injection port near the throat is desirable. If the optimum value of M_i (i.e., for $p_i = p_2$) is used rather than a constant value, then the specific impulse increases with increasing M, leading to the usual generalization that the injection should take place at as high a Mach number as possible.

Some conclusions concerning the basic parameters have been derived from various tests. The range of pressure and mass-flow ratios of the injectant and main streams were widely varied. However, only a few tests were made with supersonic injection and there are very few experimental data on the effect of the angle ϵ. The conclusions should be assessed in the light of the test conditions (see Refs. 250, 251, 252, and 264). The location of the injection port should be as far downstream as possible so that the shock will occur at a high Mach number. However, since the pressure is integrated over the shock surface, the most efficient position of the shock is that at which it reaches the opposite side of the nozzle wall at the exit. Although the dependence of the side force on the port position is usually agreed upon, there are extensive data in Ref. 250 which show no change in side force with port location with mass-flow ratios from 0 to 0.10 and sonic injectant flow.

Systematic tests reported by Walker, Stone and Shandor (Ref. 264) with normal injection at a single station in a conical nozzle showed that the

performance at a constant pressure ratio improves with increasing hole size. Both subsonic and sonic injection velocities are included in these tests. There is also an indication in Refs. 250 and 252 that for subsonic injection velocities a reduction in hole size gives a higher side force. The latter reference also gives a few test results on the use of multiple injection ports and variations of port shape

It is generally agreed that the side force ratio increases almost linearly with the mass-flow ratio, m_i/m_m, where the subscripts i and m represent the injectant and main streams. Most experimental results also show that the side force ratio increases linearly with the total pressure ratio, p_{t_i}/p_{t_m}. Reference 264 shows that the performance increases with pressure ratio until sonic speed is reached, after which the performance declines. These test data are shown in Fig. 6-45.

Both the theory of Ref. 228 and experimental data (Ref. 250) indicate that the side force increases with the injectant Mach number until an optimum M_i is reached when the static pressure of the jet is equal to the separation pressure of the nozzle. The above theory also shows that the specific impulse of the injected gas increases rapidly with increase in the injection angle, ϵ. Since most experimental data have been taken with the injection either normal to the wall ($\epsilon = -\alpha$) or to the nozzle axis ($\epsilon = 0$), it would seem that measured forces could be much improved with suitable change in the direction of the injection.

It has been shown that the side force increases slightly as γ changes from 1.4 to 1.2 but is increased by as much as 50% as the molecular weight of the injected gas is decreased by a factor of two. Tests with gases having molecular weights from 44 (CO_2) to 2(H_2) are reported in Ref. 264 where it is shown that the effective specific impulse is almost inversely proportional to the square of the molecular weight. This trend may be seen in Fig. 6-45. A more accurate correlation is provided by the same authors in Ref. 265. Using linearized supersonic flow theory an equation has been derived to give the effect on the specific impulse of γ, c_p, molecular weight, temperature and Mach number in both injectant and main flows. The equation is as follows:

$$\frac{I}{I^*} = \left[\frac{T_t}{T_{t_i}} \cdot \frac{W_i}{W} \cdot \frac{\gamma_i}{1+\gamma_i} \cdot \frac{1}{2\left(1+\frac{\gamma-1}{2}M^2\right)}\right]^{1/2} \left[\left(1+\frac{\gamma-1}{2}M^2\right)\left(1+\frac{c_{p_i}}{c_p}\cdot\frac{T_{t_i}}{T_t}\cdot\frac{W}{W_i}\right)+\frac{W}{W_i}\left(1-\frac{c_{p_i}}{c_p}\right)\right] \tag{6-67}$$

where I* is the specific impulse of an injectant for sonic flow into a vacuum, W is the molecular weight, and free-stream conditions are written without subscripts. Many tests were made with two nozzles; the first giving M = 1.86 for hot gases and M = 1.86 for cold gases, and the other one giving M = 2.90

for hot gases. The following sketch shows the basic parameters, the ranges of which are given in the table below.

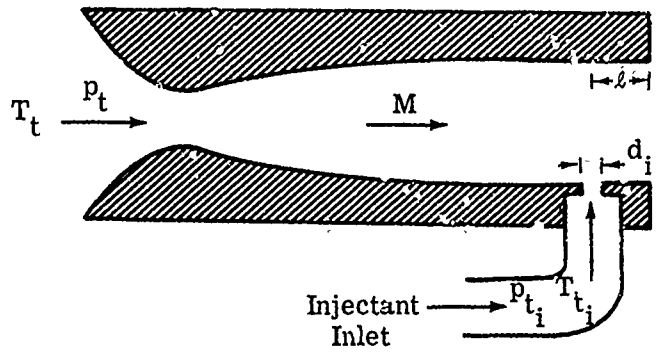

Variable	Range
p_t	50 - 200 psia
p_{t_i}	80 - 900 psia
ℓ	0.25 - 1.00 in.
d_i	0.0625 - 0.180 in.
Injectant Gas	CO_2, N_2, Ar, He + Ar, He, H_2
Propellant Gas	H_2O_2, air
T_t	530 - 1850°R
T_{t_i}	530 - 2150°R
Ambient Pressure	one atmosphere or less

Values of I/I* derived from the test results were normalized by dividing by the value of I/I* obtained from Eq. 6-67. They are plotted as a function of the weight-flow ratio, $\dot{w}_i/\dot{w}$, in Fig. 6-46. Equation 6-67 is independent of this ratio and, in fact, is based on the assumption of a "trace" flow of injectant. It may be seen from Fig. 6-46 that in the region of strict applicability of the theory, i.e., where $\frac{1}{2}(\dot{w}_i/\dot{w})(\dot{w}/\dot{w}_i)^*$ is very small, the measured effective specific impulse is slightly above the theoretical, and that it declines as the weight-flow ratio increases. This latter phenomenon may be partially accountable to induced shock wave reflections and incomplete expansion of the mixed gases.

The above theoretical approach is not restricted to the case of gas injection but has been successfully applied to liquids and gases, both active

and inert (Ref. 266). It thus appears that the linear theory is a useful tool by means of which the potential of injectant-propellant combinations may be relatively evaluated.

In spite of some uncertainty in the quantitative effect of the parameters involved in shock-induced flow deflection, there is no doubt that it is a highly advantageous method of producing thrust vector control. The only moving part is the control valve for the injectant flow. This valve may be situated in a cool environment and retain its reliability and high rate of response through changing flight conditions. The added mass flow of the injected stream more than compensates for the thrust reduction due to the shock pattern caused by the injection. There is every hope that three-dimensional control may be achieved in a single nozzle by means of secondary injection of liquids.

The shock pattern may also be induced by means of small blunt shapes introduced into the nozzle wall. The tabs are easily controlled and produce little drag, but are subject to severe erosion and high temperature effects. Jet tabs have also been suggested a a means for actuating a rotating nozzle.

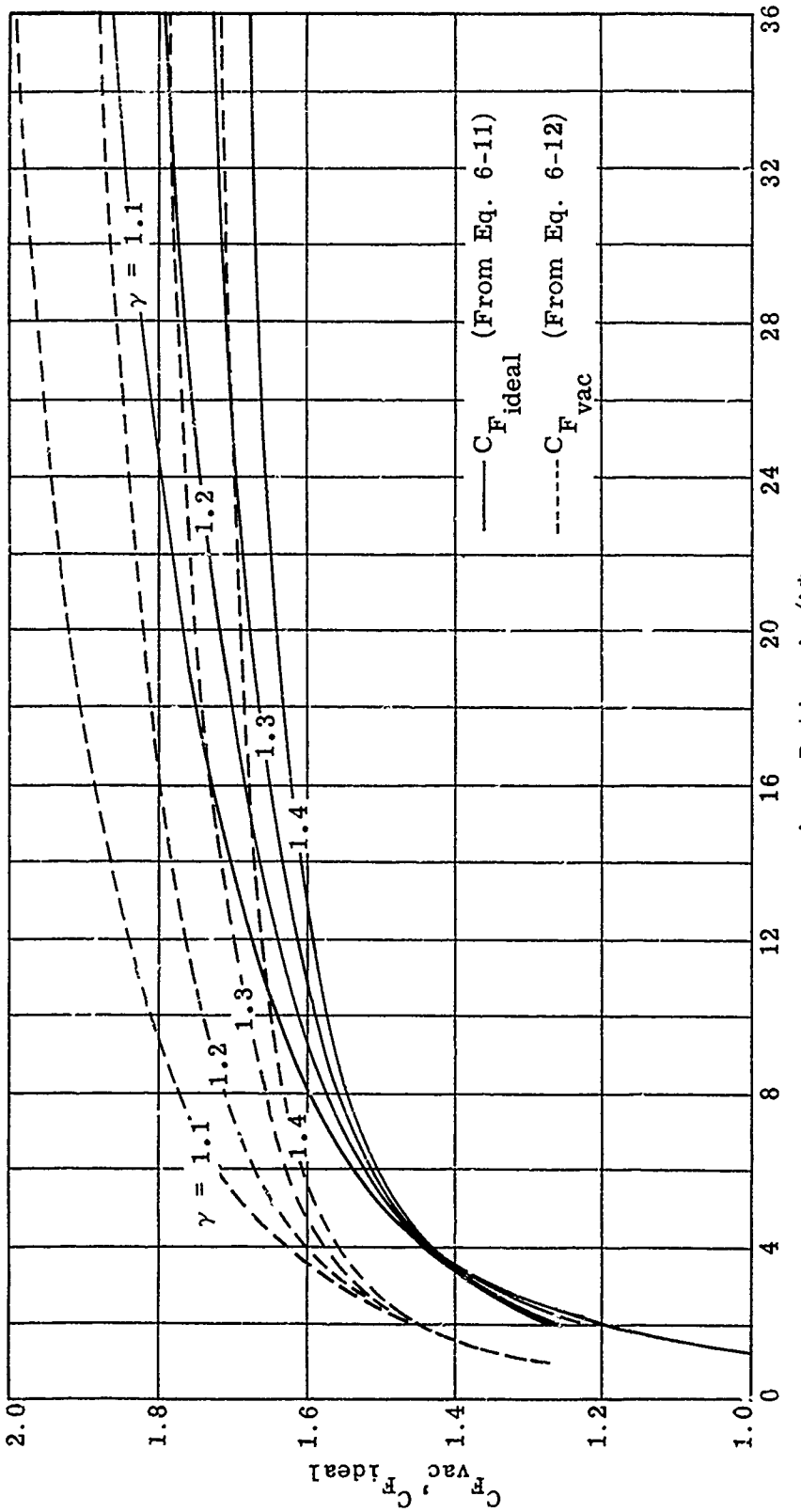

Fig. 6-1. Calculated ideal and vacuum thrust coefficients as a function of exit area ratio; γ = 1.1, 1.2, 1.3, and 1.4.

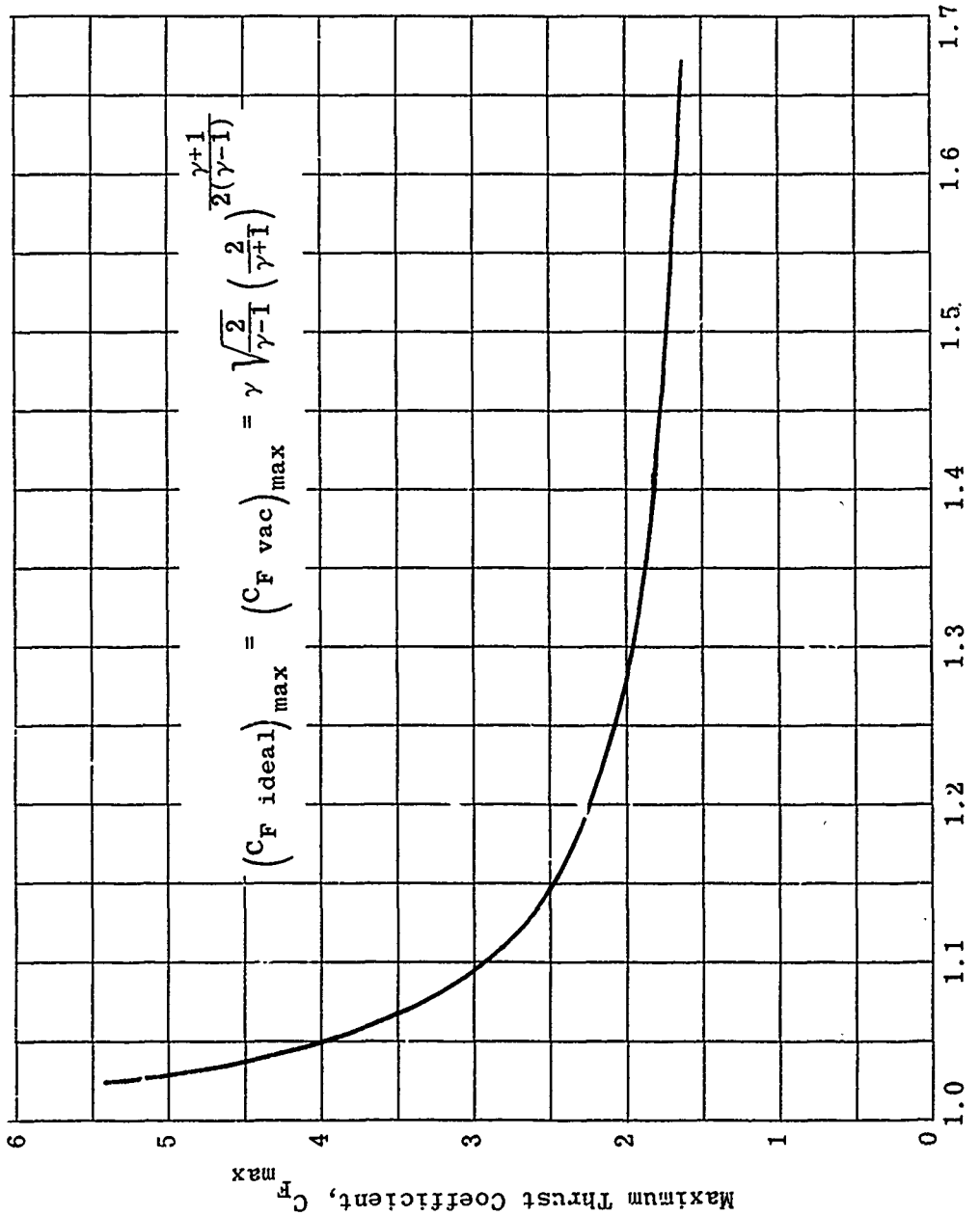

Fig. 6-2. Calculated maximum thrust coefficient as a function of γ.

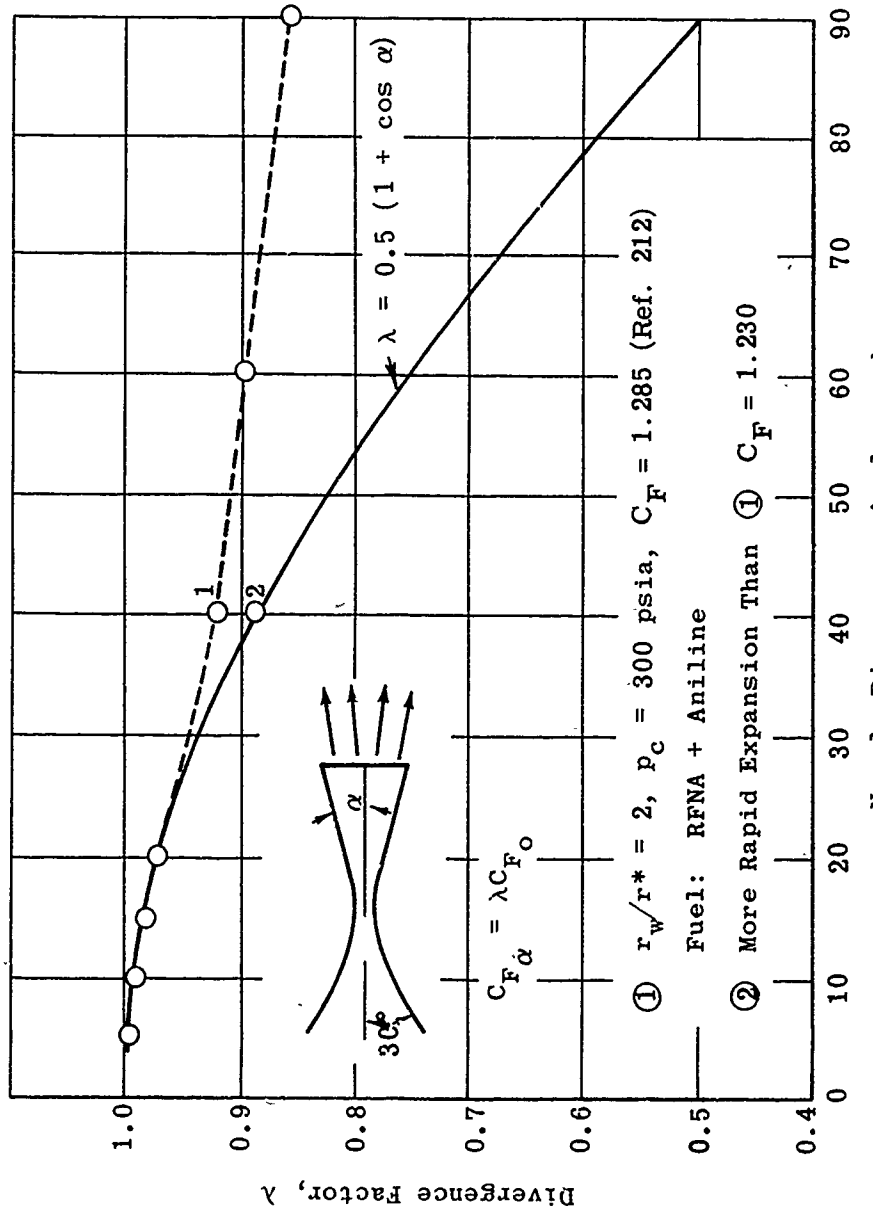

Fig. 6-3. Comparison of calculated and experimentally determined divergence factor in conical nozzles.

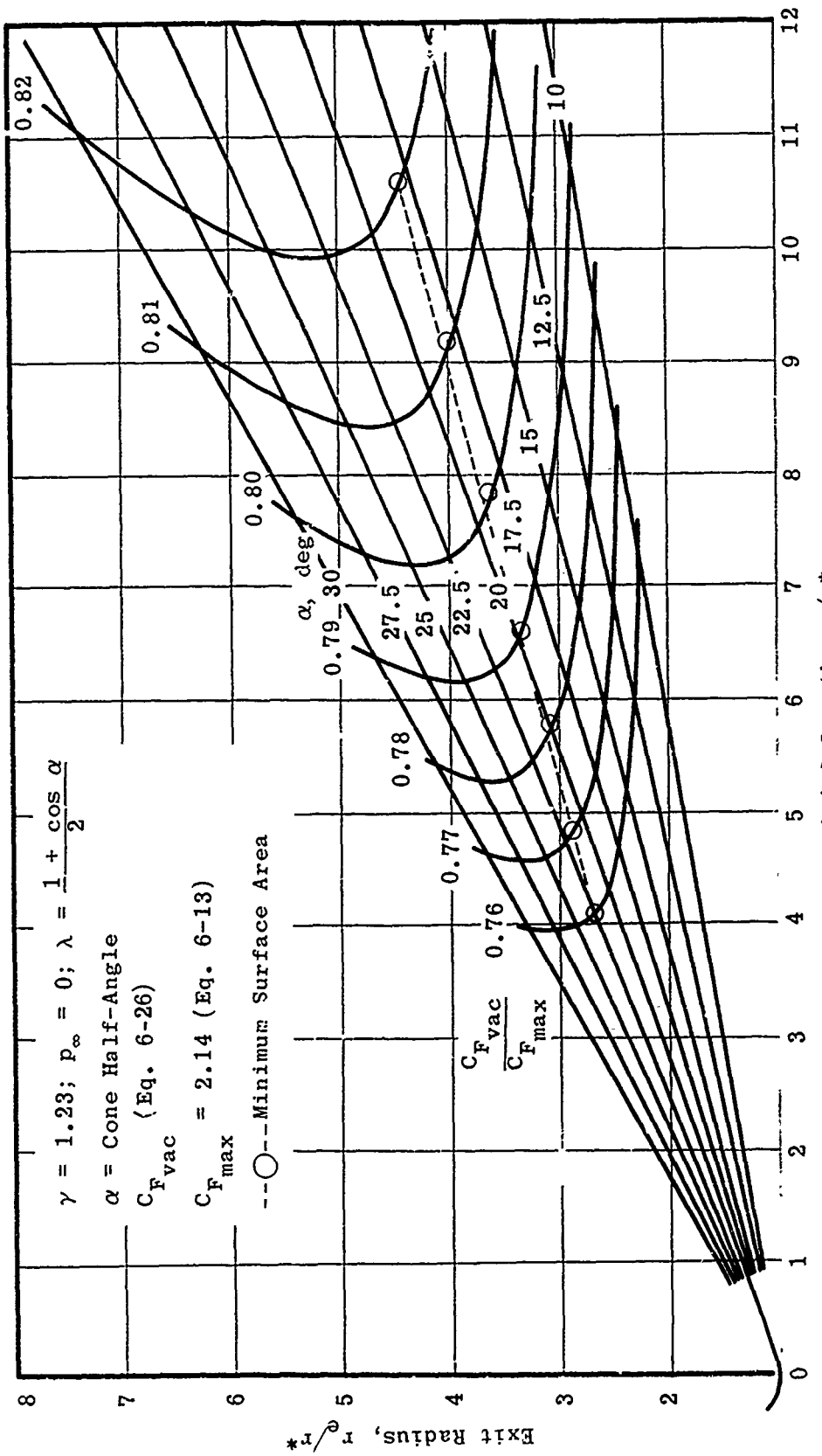

Fig. 6-4. Calculated performance of conical nozzles as a function of nozzle geometry; $\gamma = 1.23$

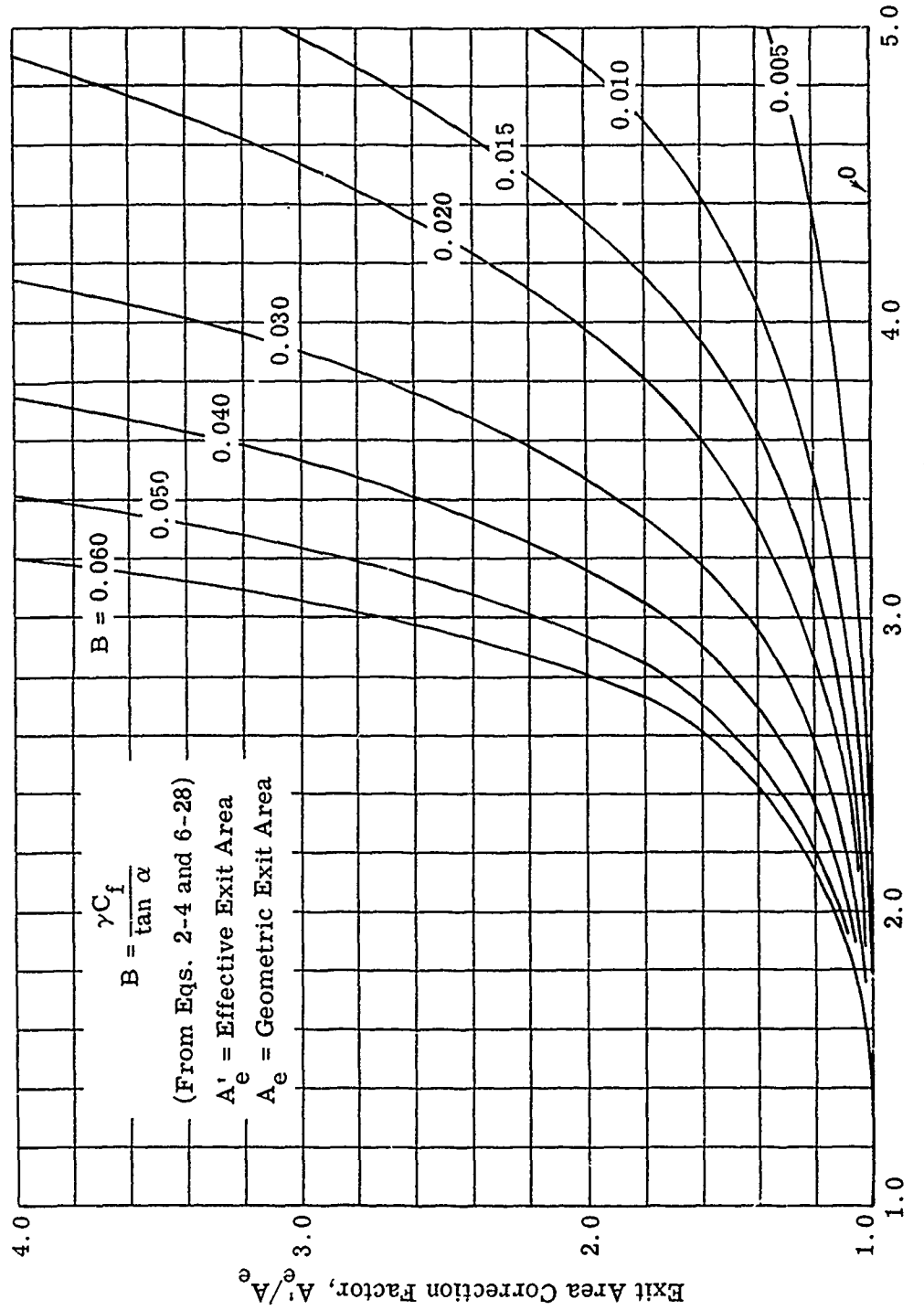

Fig. 6-5. Calculated exit area correction factor as a function of exit Mach number; $\gamma = 1.2$.

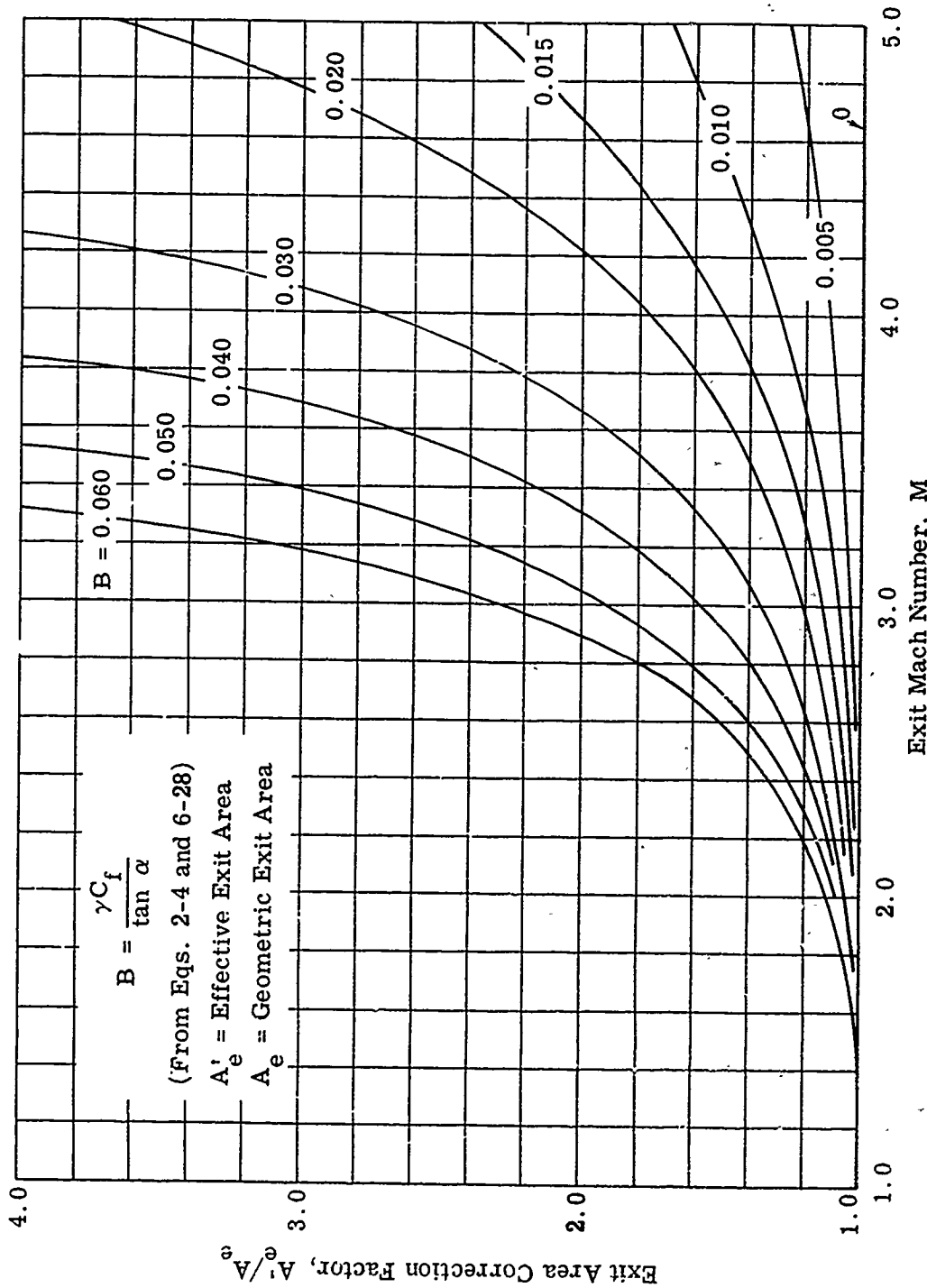

Fig. 6-6. Calculated exit area correction factor as a function of exit Mach number; $\gamma = 1.3$.

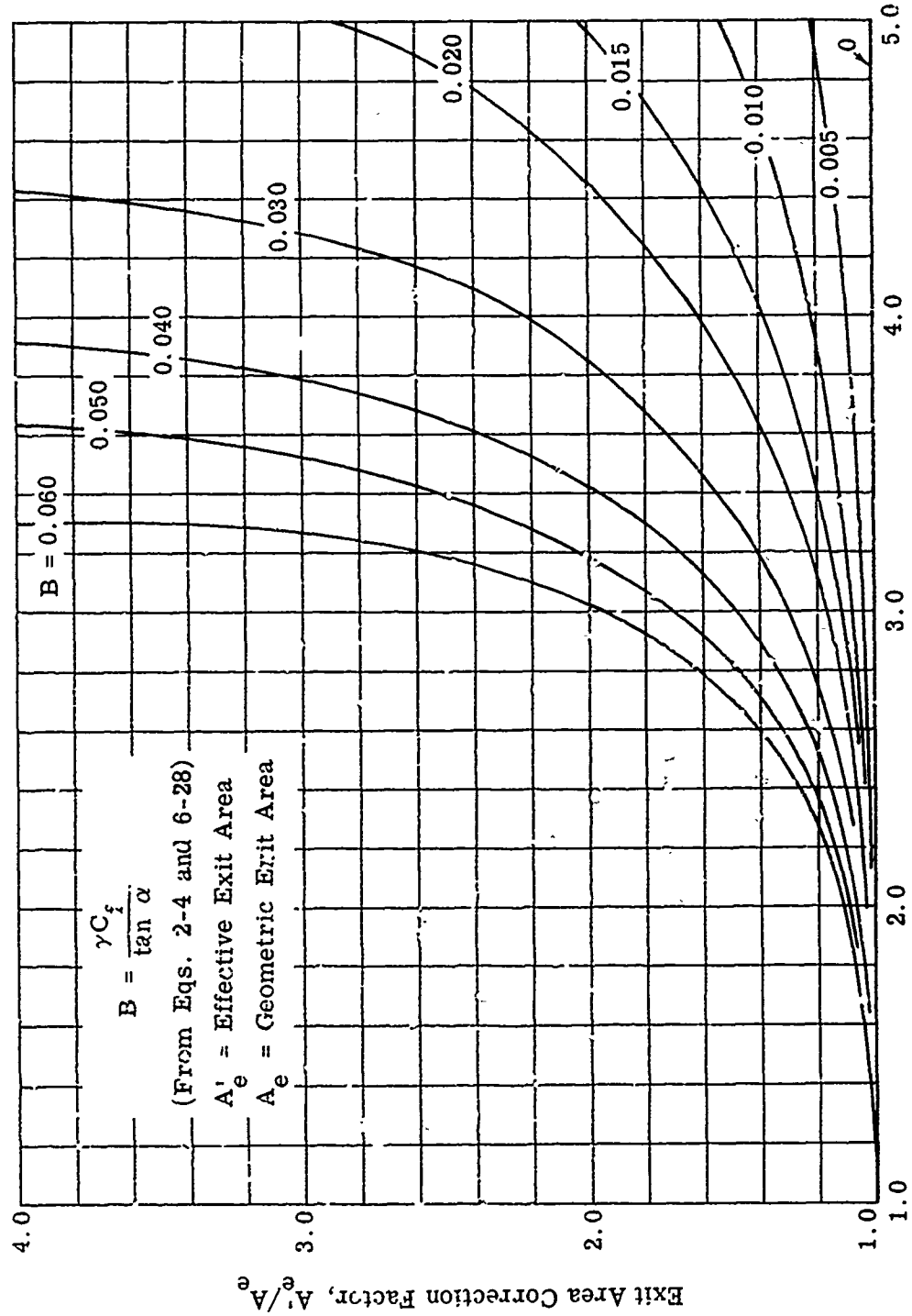

Fig. 6-7. Calculated exit area correction factor as a function of exit Mach number; $\gamma = 1.4$.

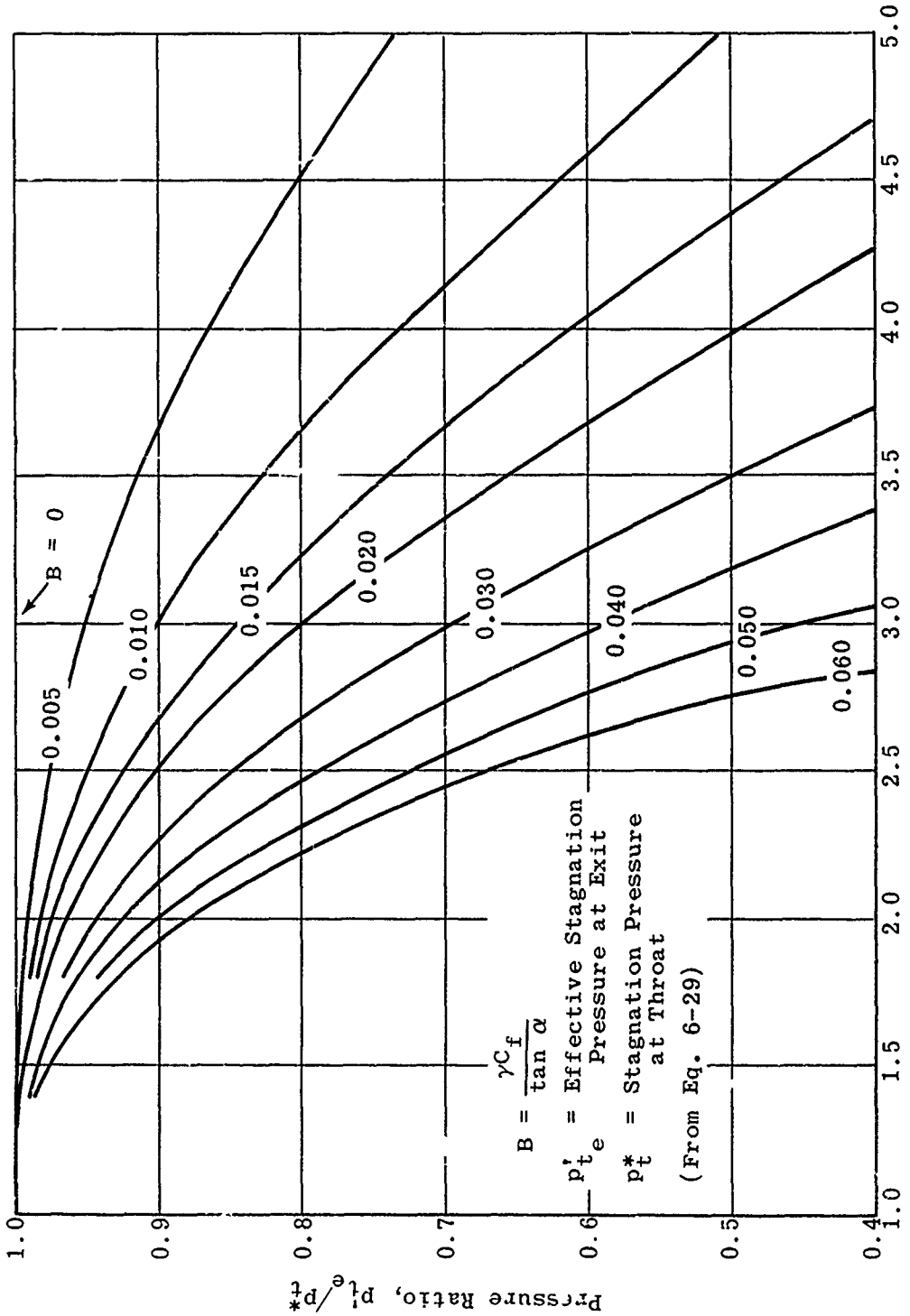

Fig. 6-8. Calculated stagnation pressure loss due to friction as a function of exit Mach number; $\gamma = 1.2$.

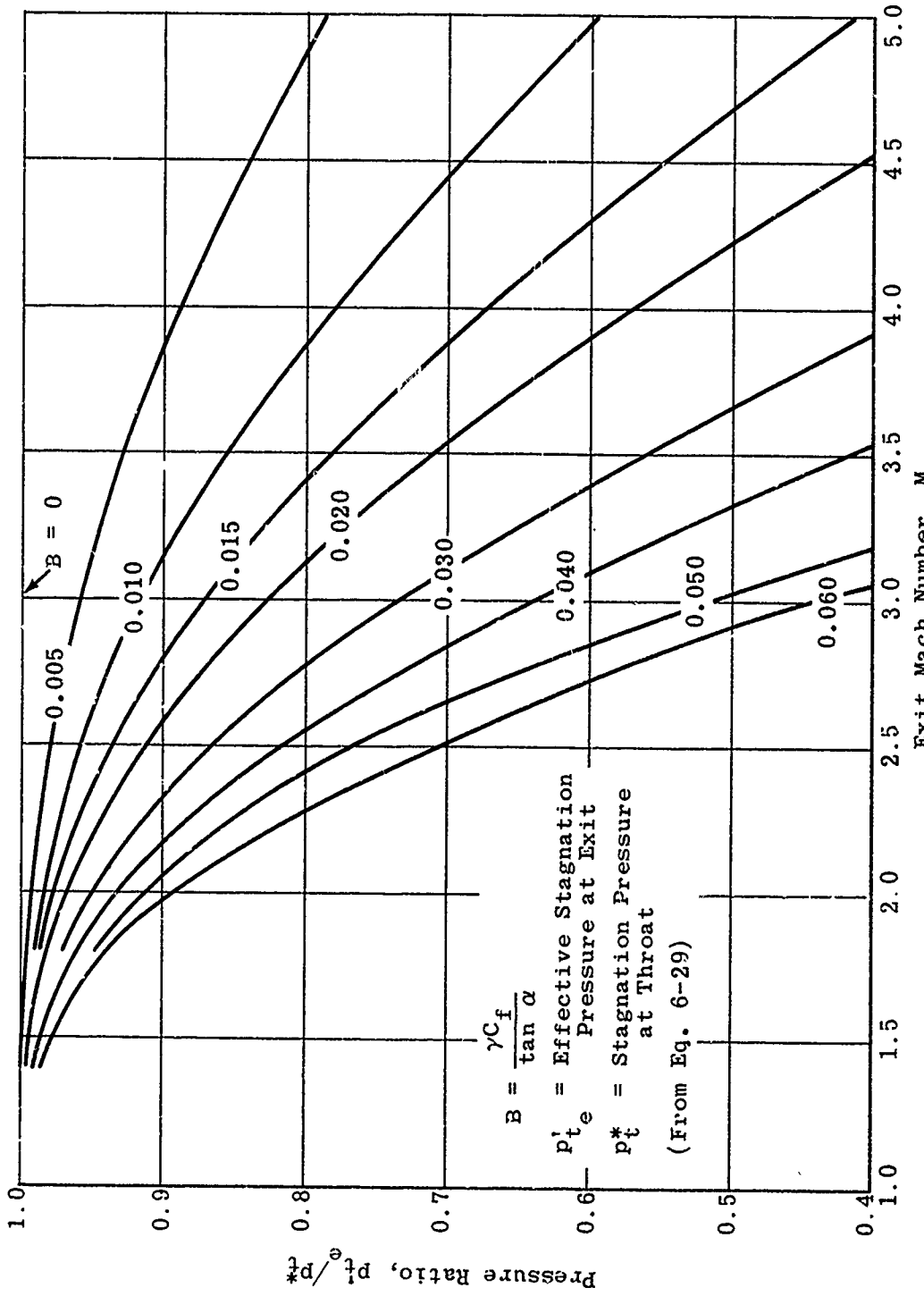

Fig. 6-9. Calculated stagnation pressure loss due to friction as a function of exit Mach number; $\gamma = 1.3$.

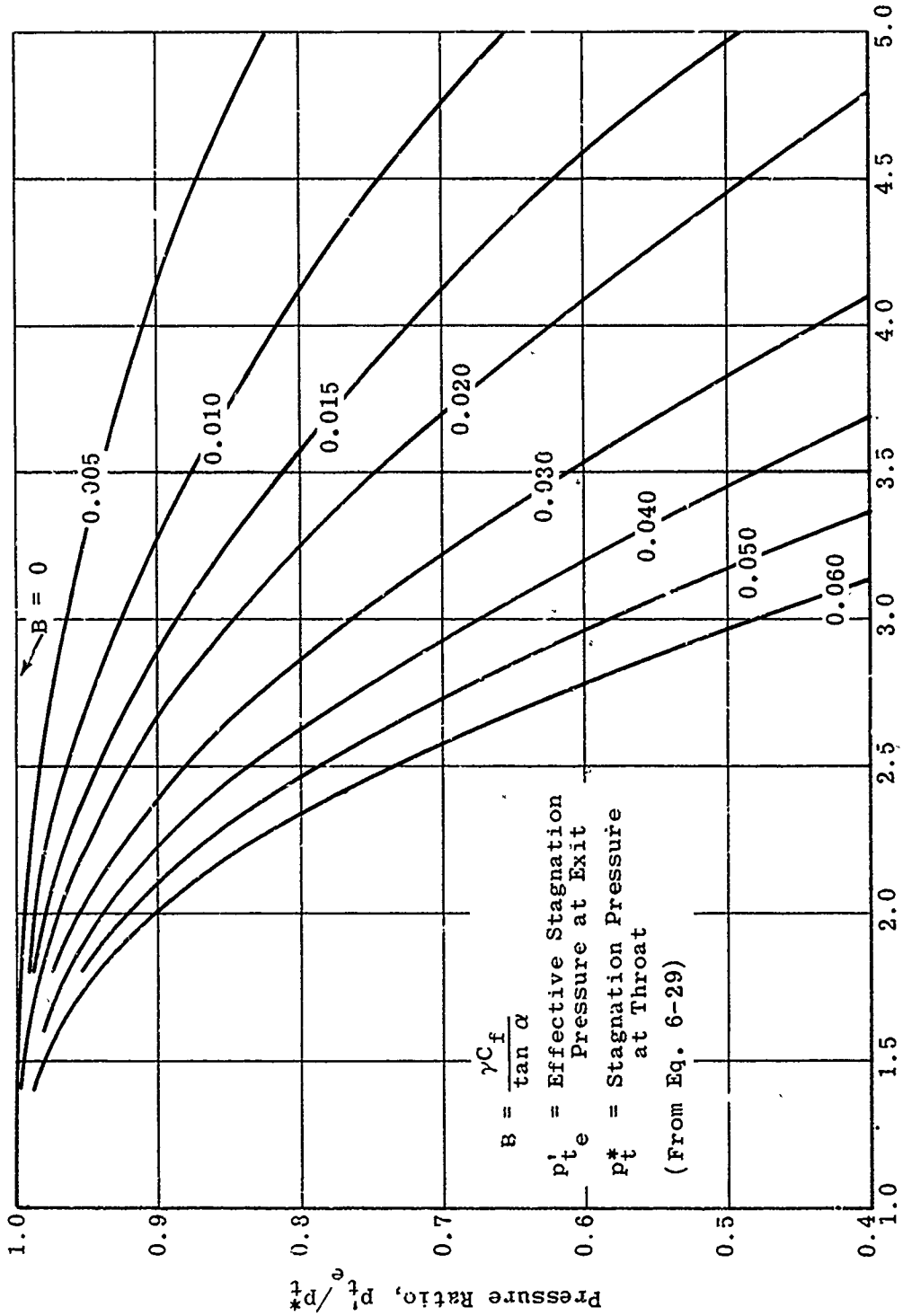

Fig. 6-10. Calculated stagnation pressure loss due to friction as a function of exit Mach number; $\gamma = 1.4$.

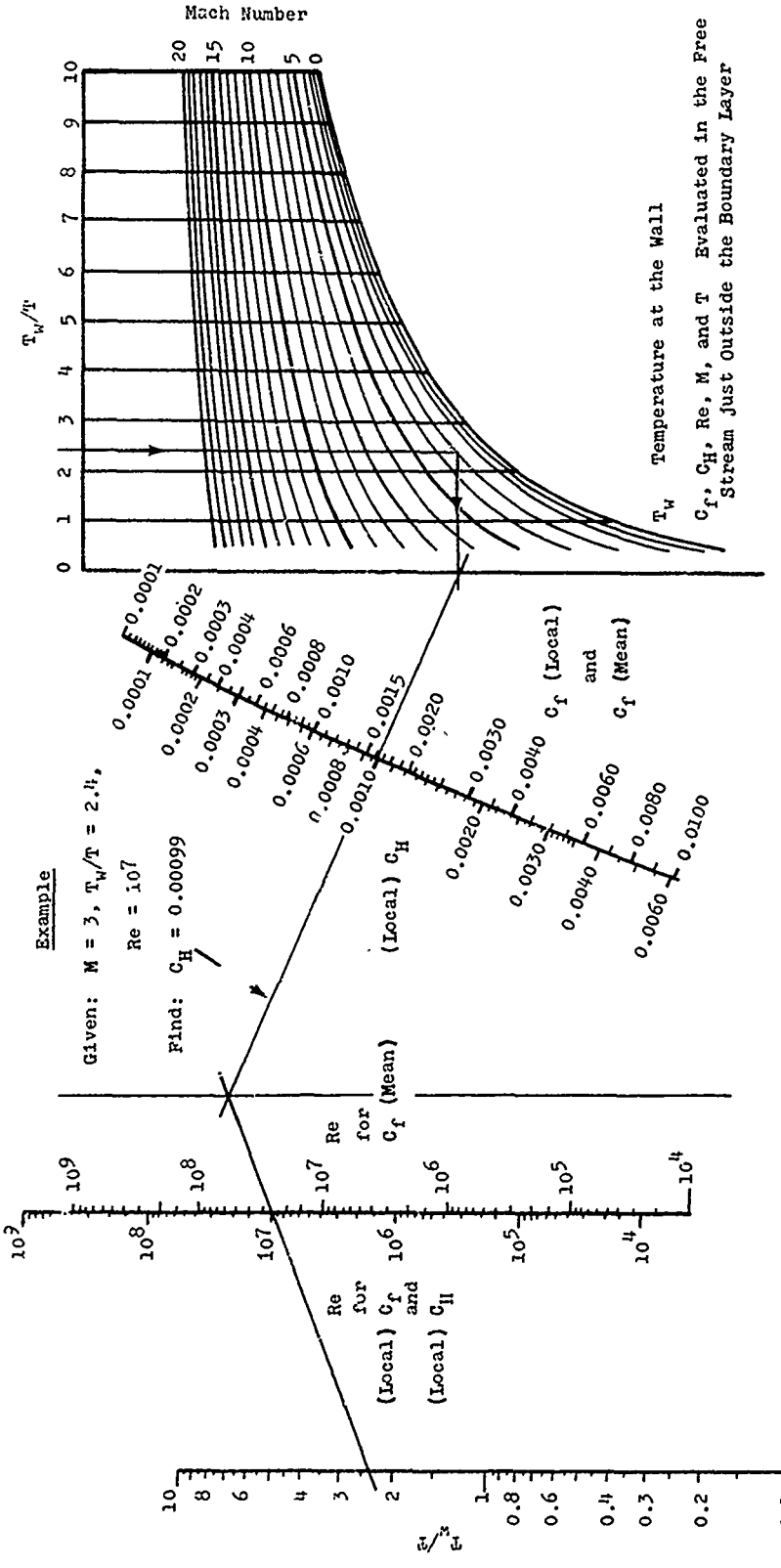

Fig. 6-11. Nomograph for coefficients of friction and heat transfer of a turbulent boundary layer on a flat plate for air. (Source: Ref. 214)

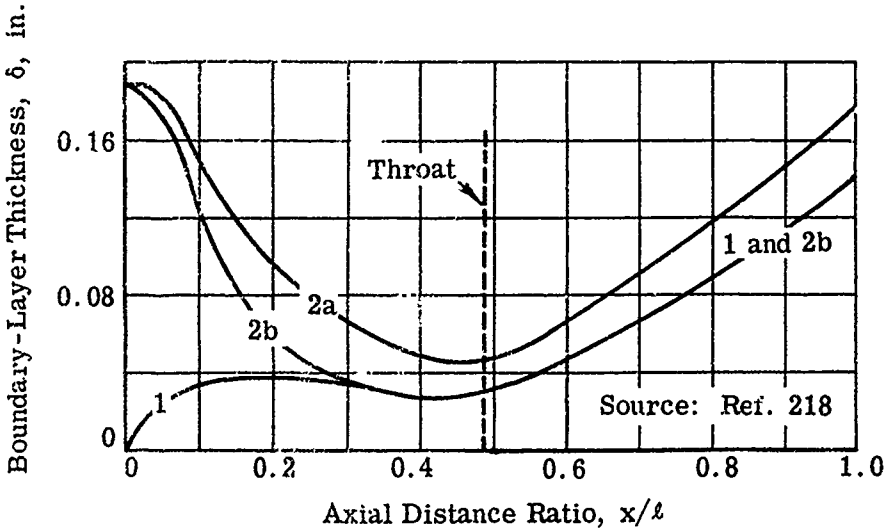

Fig. 6-12. Velocity boundary-layer thickness for nozzle shown on Fig. 6-15.

Nominal Entrance Conditions

Case	δ_o	θ_o
1	0	0
2a	0.188	0.022
2b	0.188	0.018

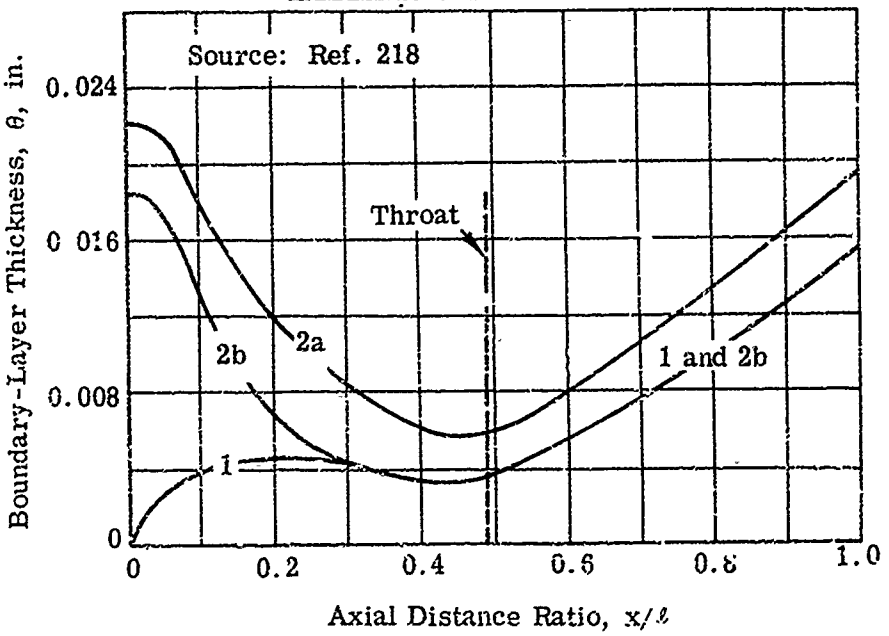

Fig. 6-13. Momentum boundary-layer thickness for nozzle shown on Fig. 6-15.

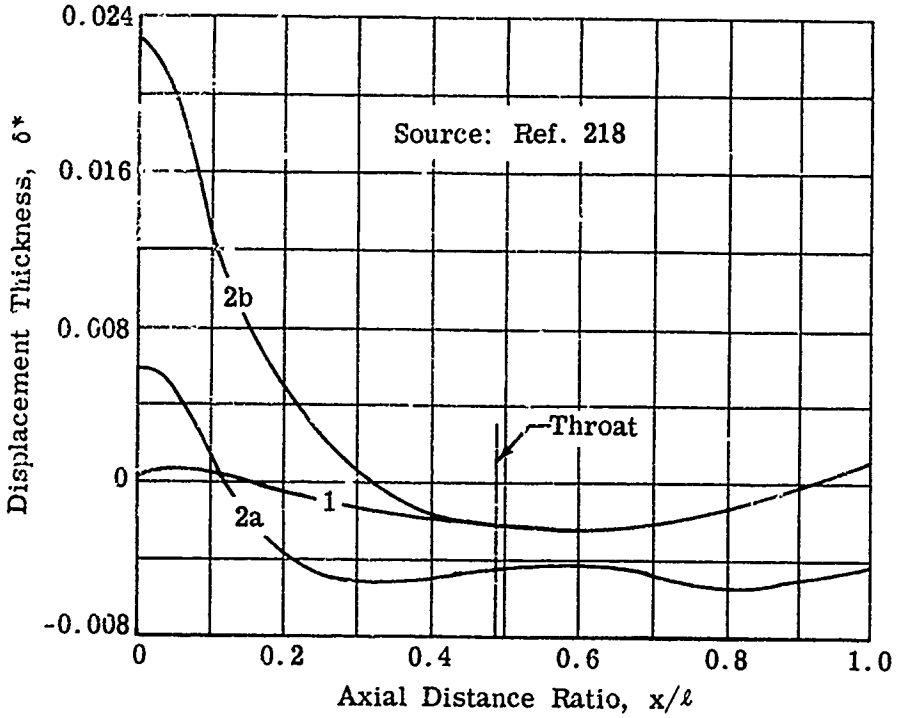

Fig. 6-14. Displacement thickness for given nozzle.

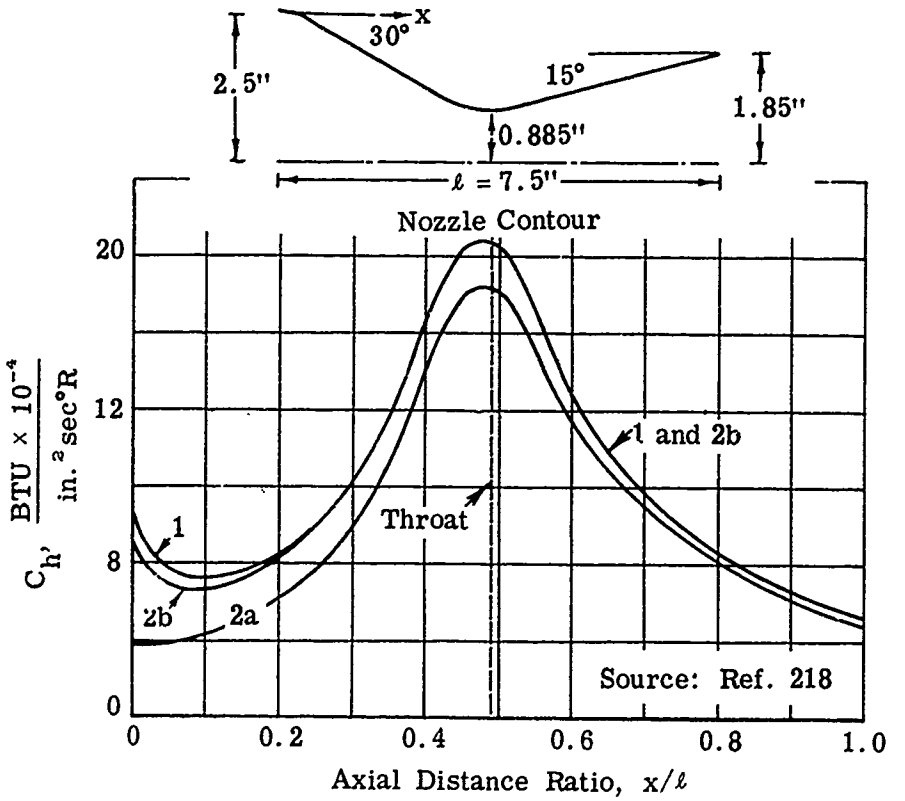

Fig. 6-15. Heat-transfer coefficient for given nozzle.

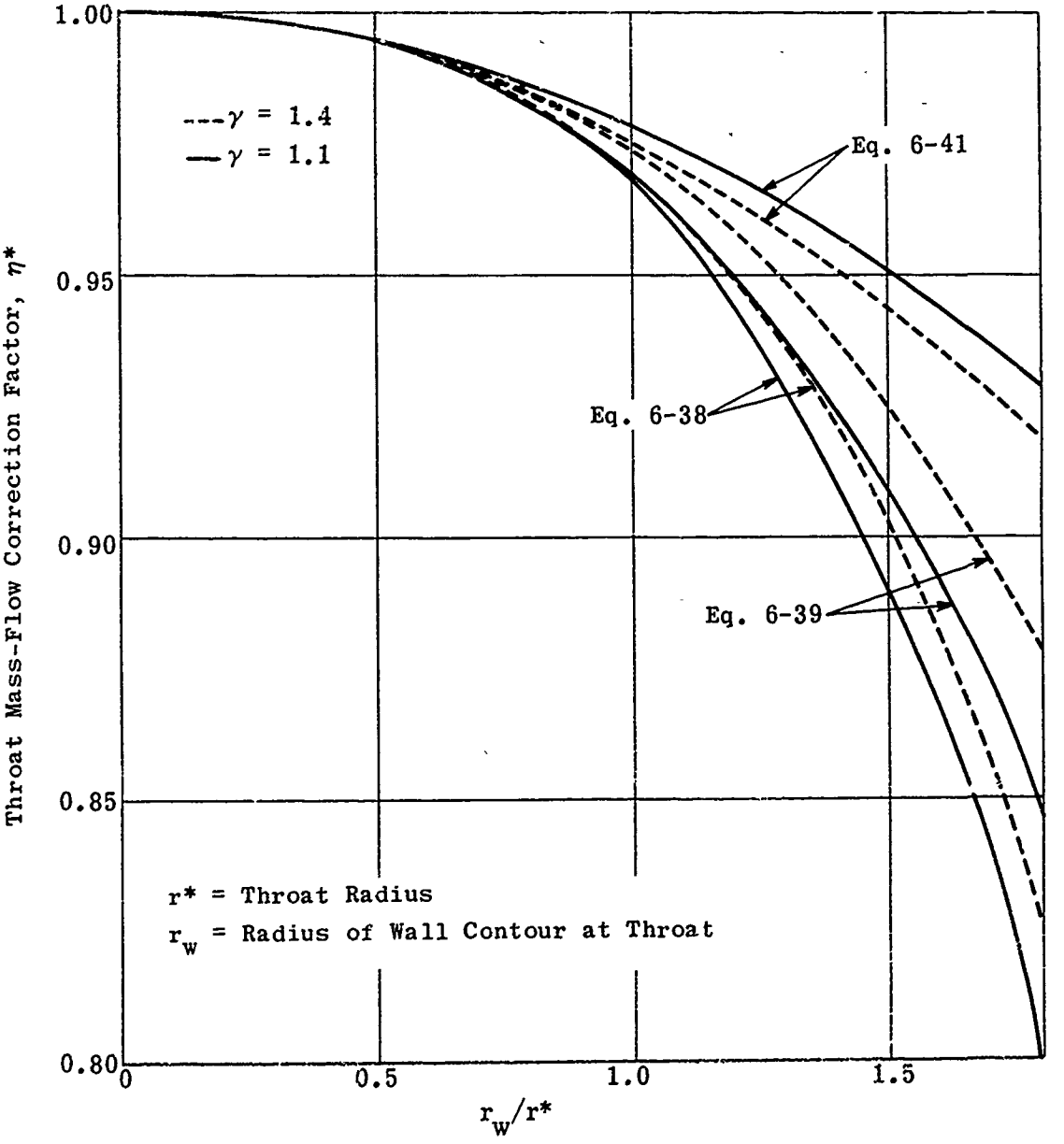

Fig. 6-16. Calculated throat mass-flow correction factor as a function of throat radius and wall radius of curvature.

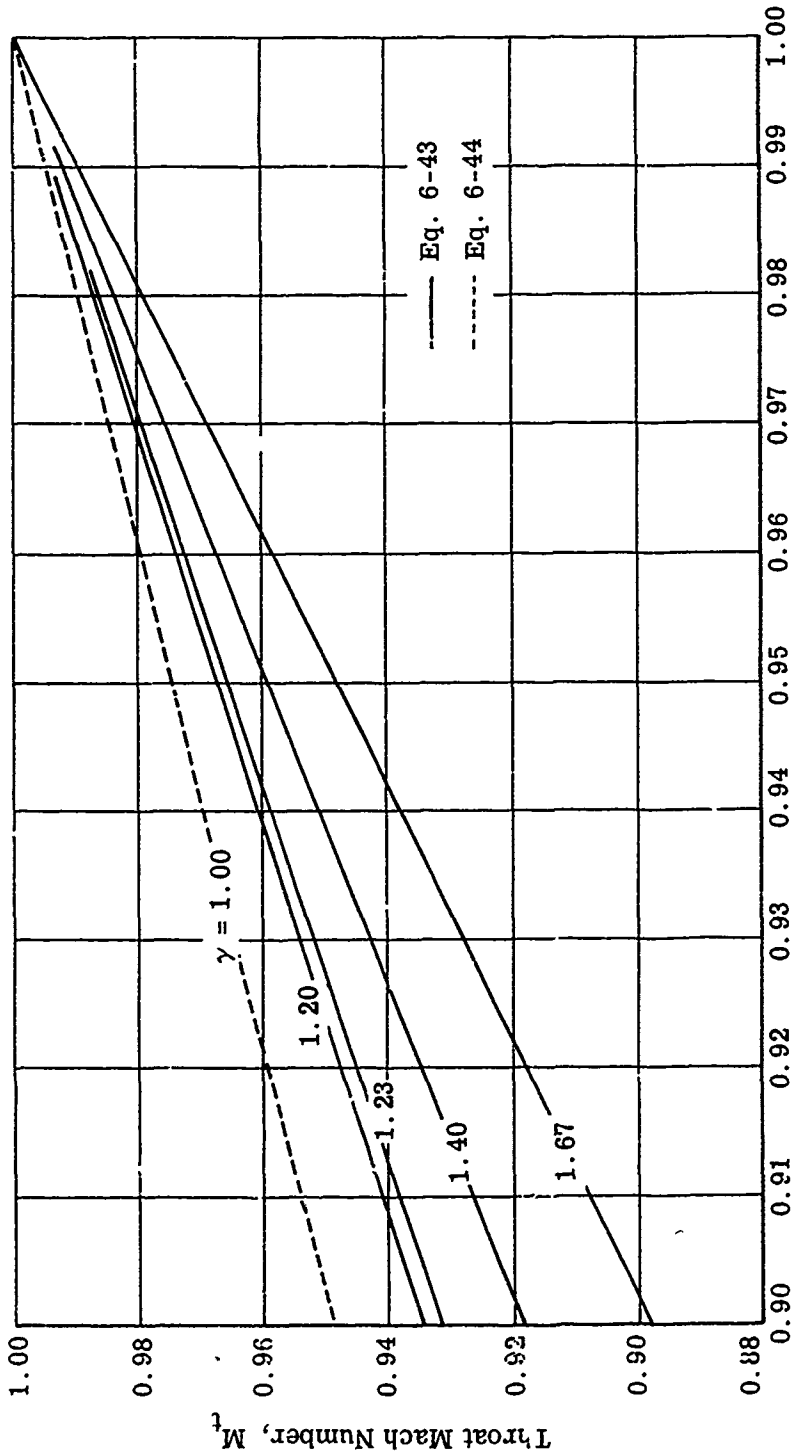

Fig. 6-17. Calculated non-isentropic throat Mach number as a function of nozzle efficiency; γ = 1.00, 1.20, 1.23, 1.40, and 1.67. (Source: Ref. 219)

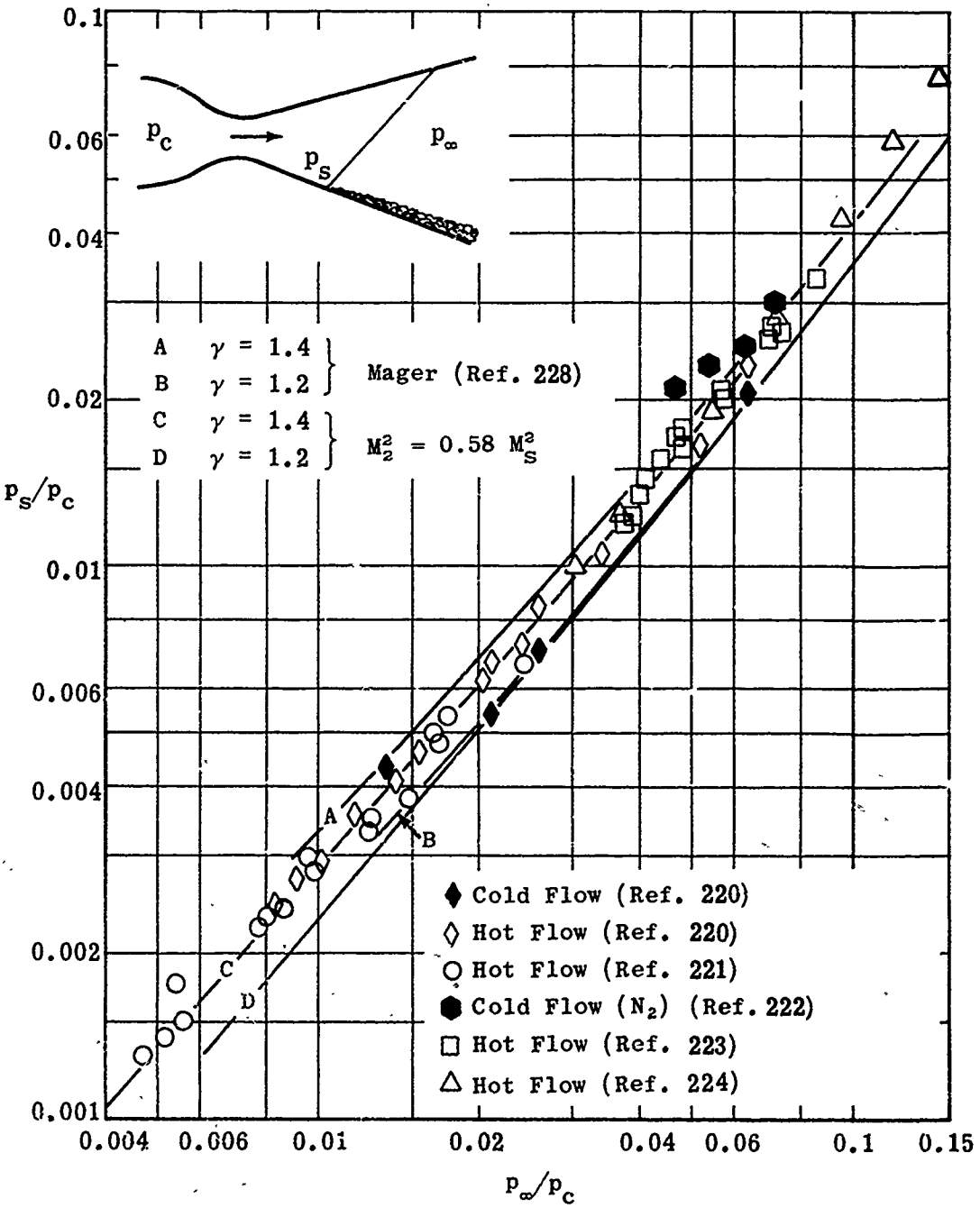

Fig. 6-18. Comparison of theoretical and experimental values of separation pressure ratio (p_s/p_c) vs nozzle pressure ratio (p_∞/p_c) for conical nozzles.

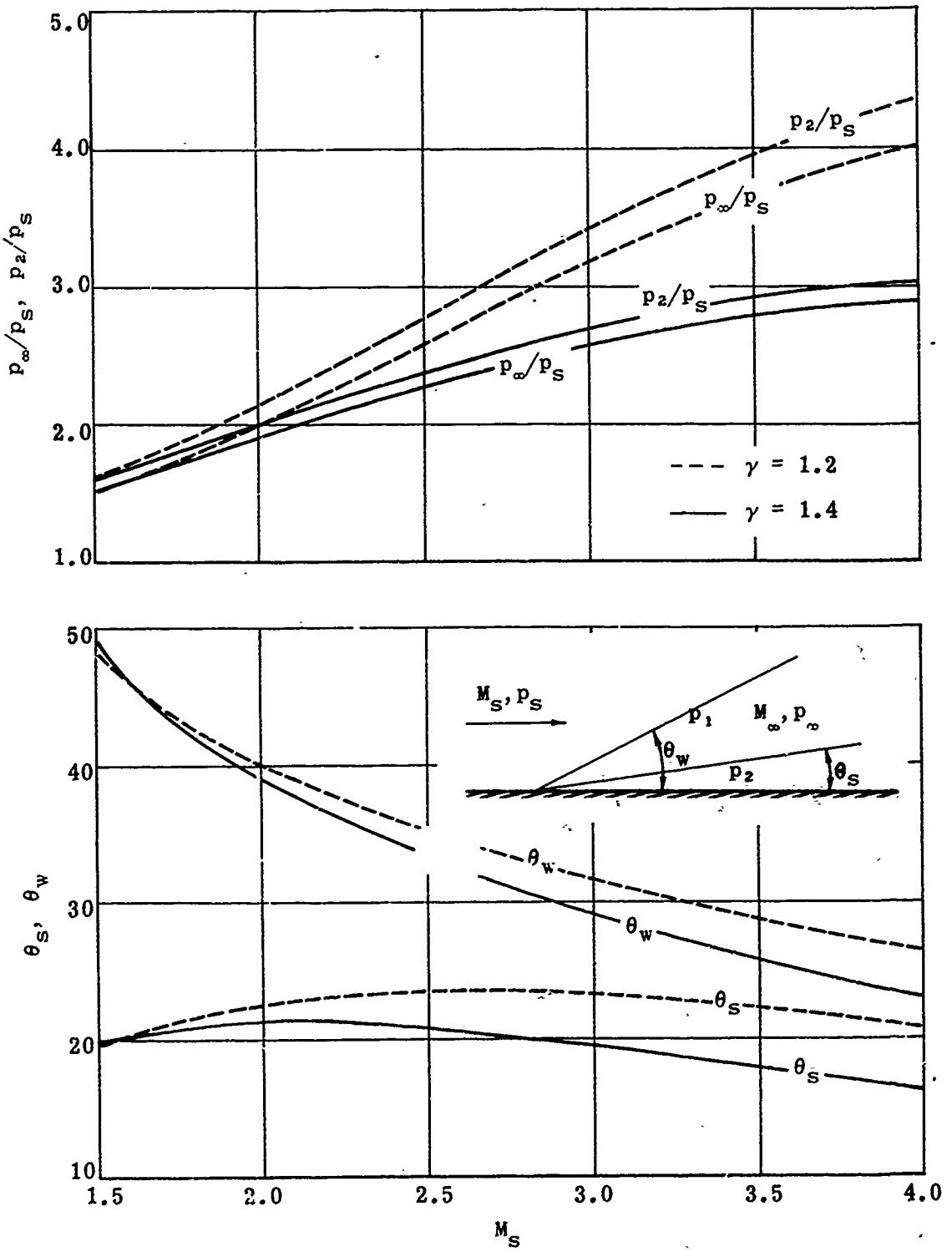

Fig. 6-19. Pressure ratios and related cone angles as a function of separation Mach number; separated turbulent boundary layer in conical nozzles; γ = 1.2 and 1.4. (Source: Ref. 228)

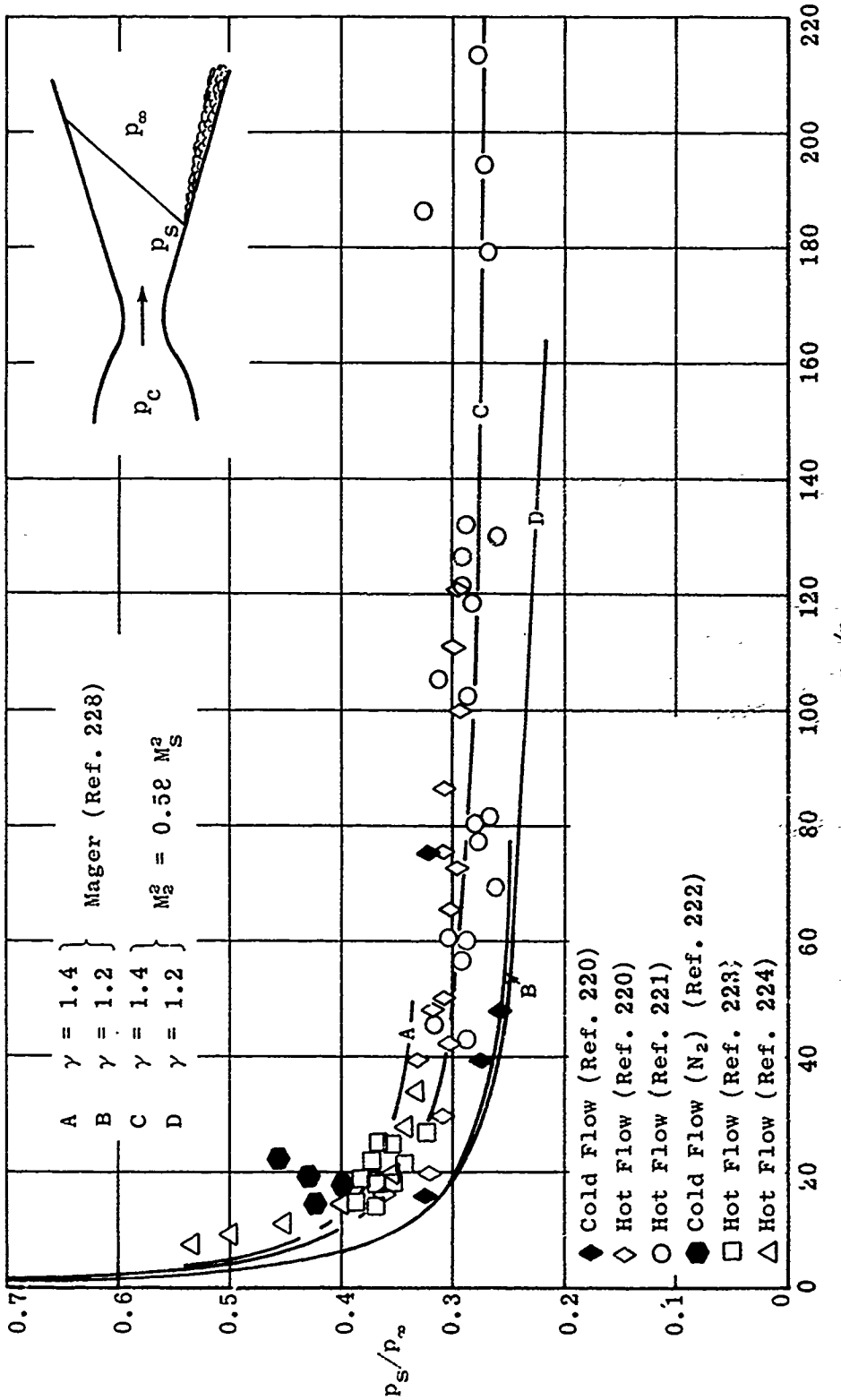

Fig. 6-20. Comparison of theoretical and experimental values of separation pressure ratio (p_s/p_∞) vs nozzle pressure ratio (p_c/p_∞) for conical nozzles.

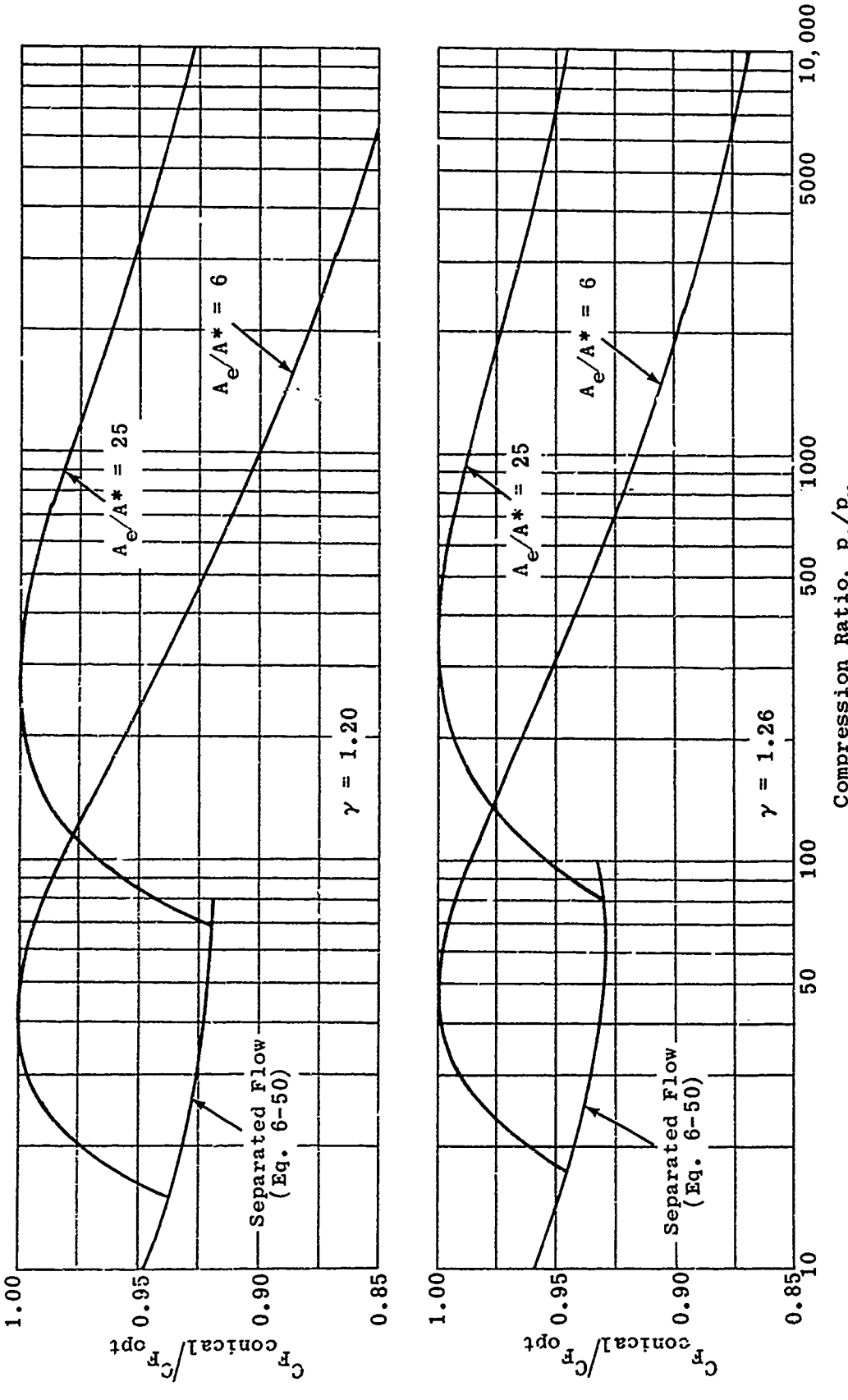

Fig. 6-21. Calculated thrust of 15° nozzle vs compression ratio; $A_e/A^* = 6$ and 25; $\gamma = 1.20$ and 1.26.

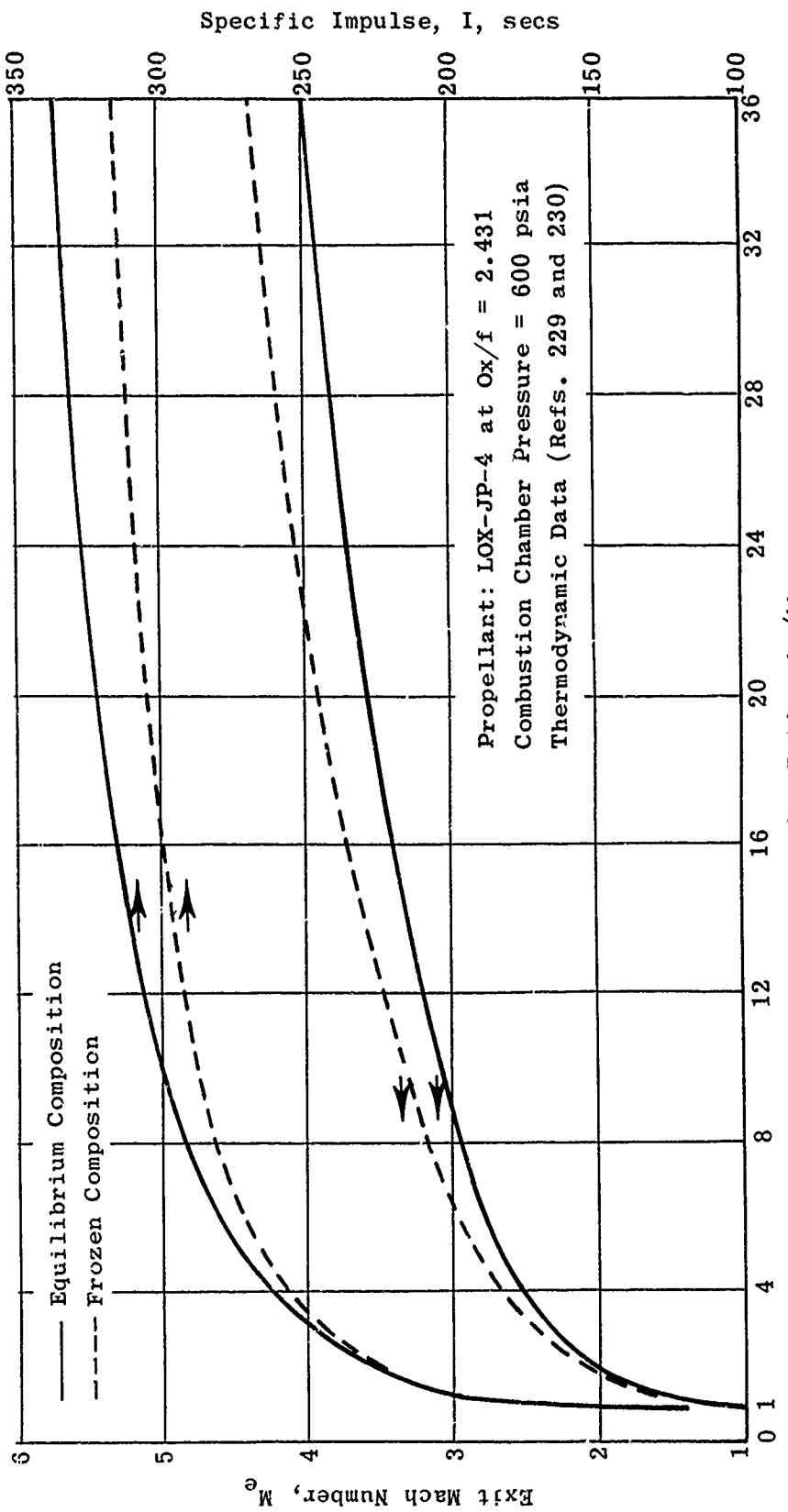

Fig. 6-22. Calculated exit Mach number and specific impulse as a function of expansion ratio for frozen and equilibrium composition.

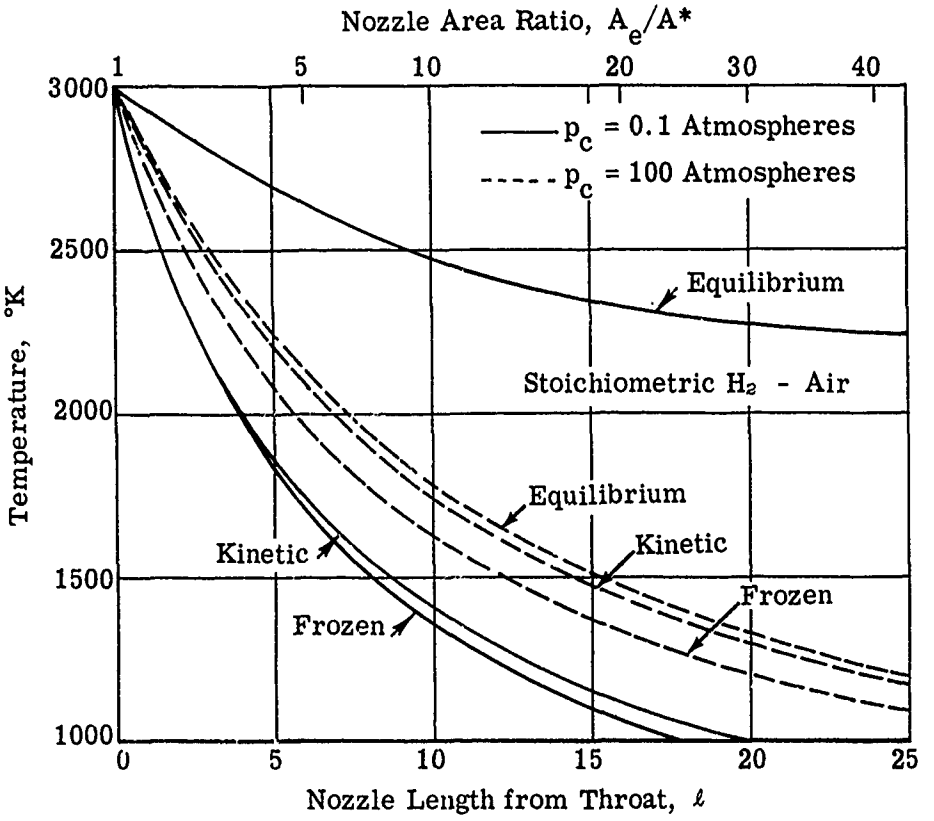

Fig. 6-23. Static temperature as a function of nozzle length; frozen and equilibrium flow; p_c = 0.1 and 100 atmospheres. (Source: Ref. 234)

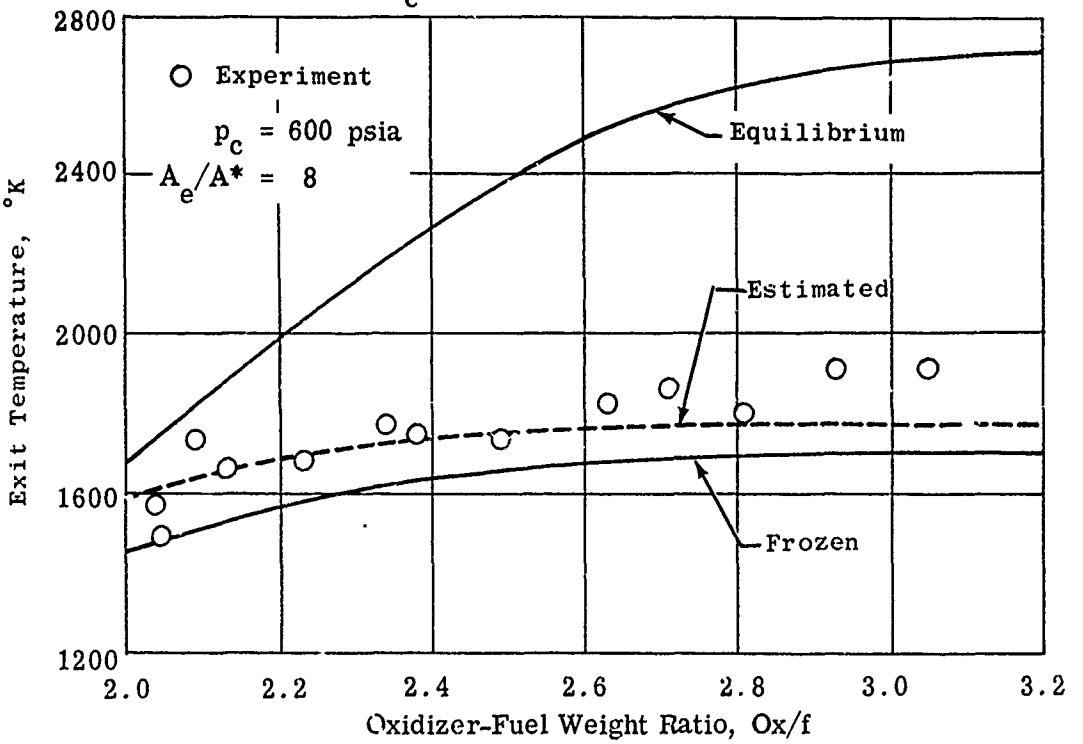

Fig. 6-24. Comparison of theoretical and experimental gas temperatures at nozzle exit. (Source: Ref. 235)

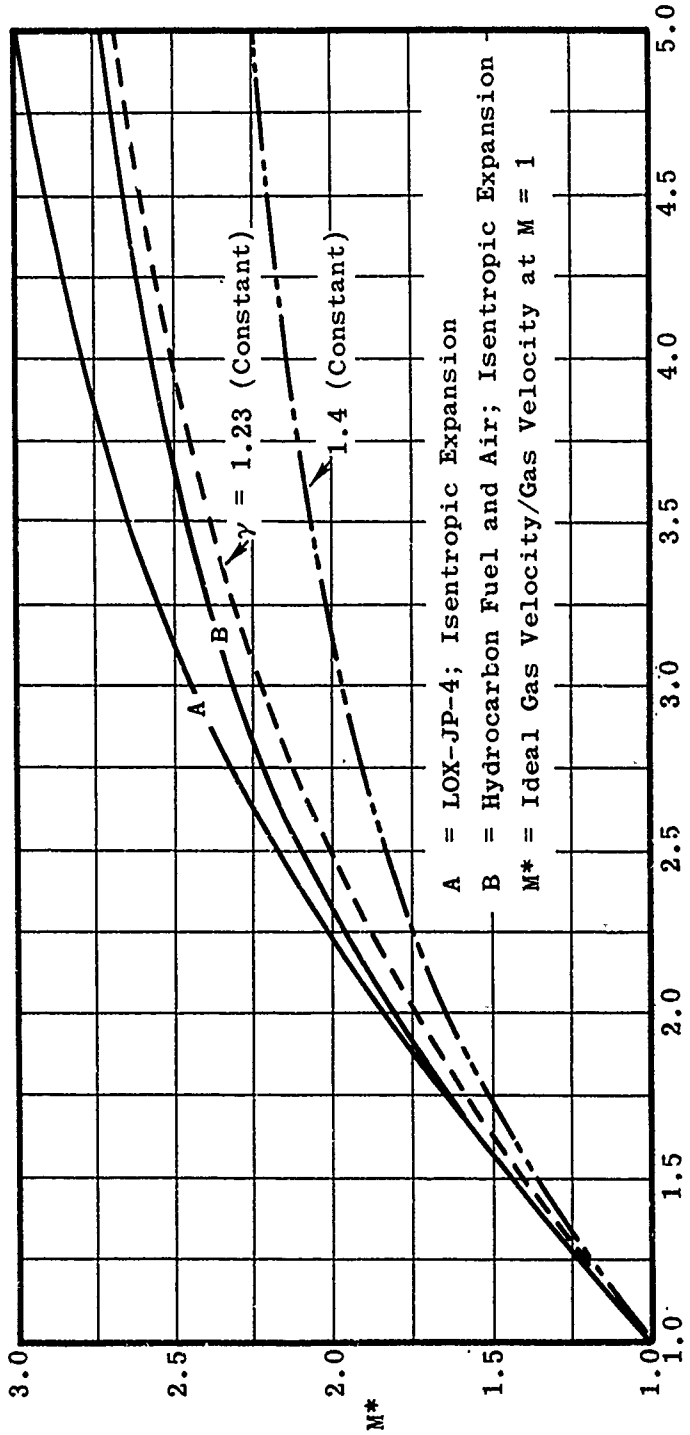

Fig. 6-25. Calculated relation between gas velocity and acoustic velocity for combustion products.

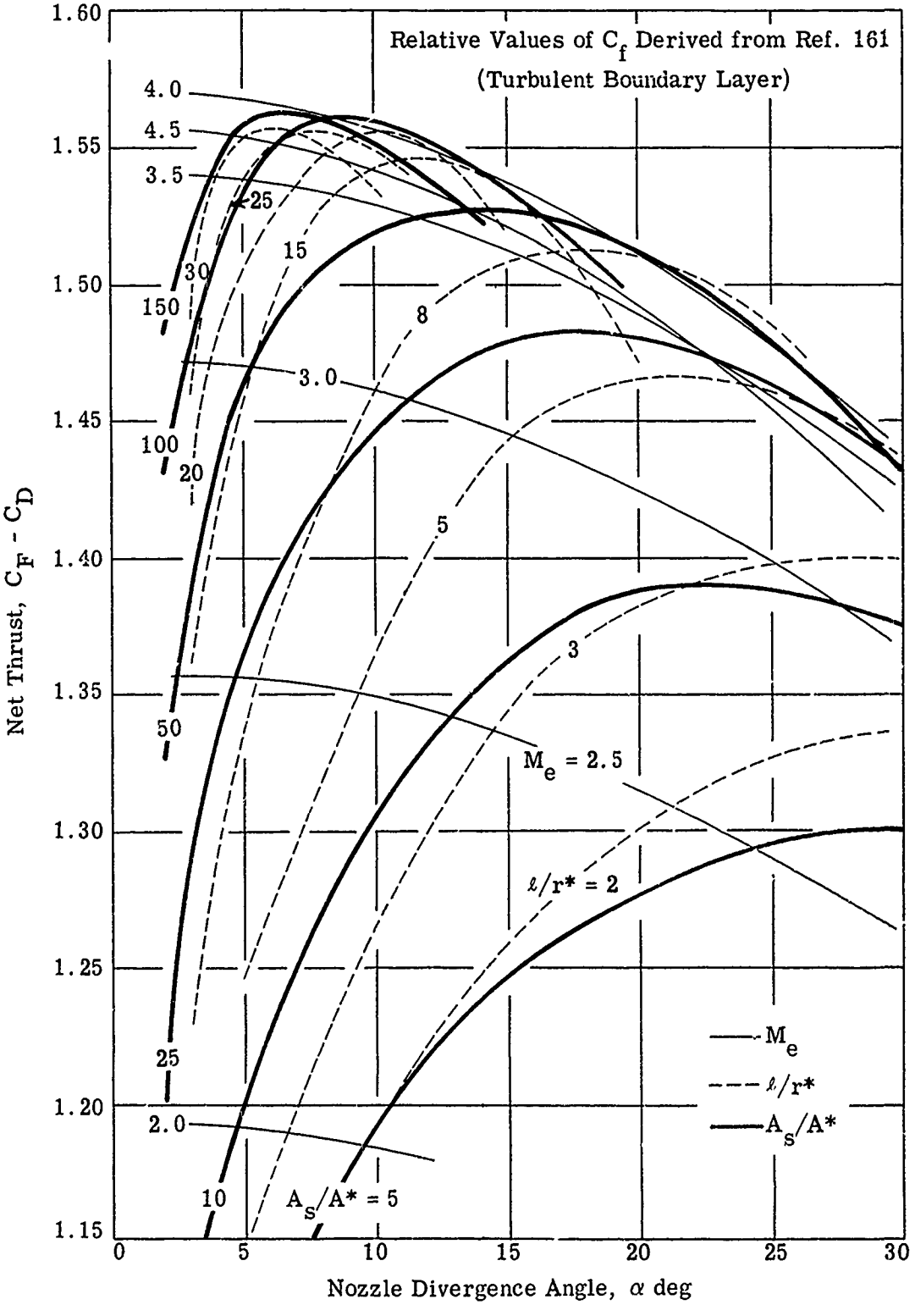

Fig. 6-26. Calculated net thrust coefficient of conical nozzles in terms of divergence angle, α, and expansion ratio; $\gamma = 1.26$.

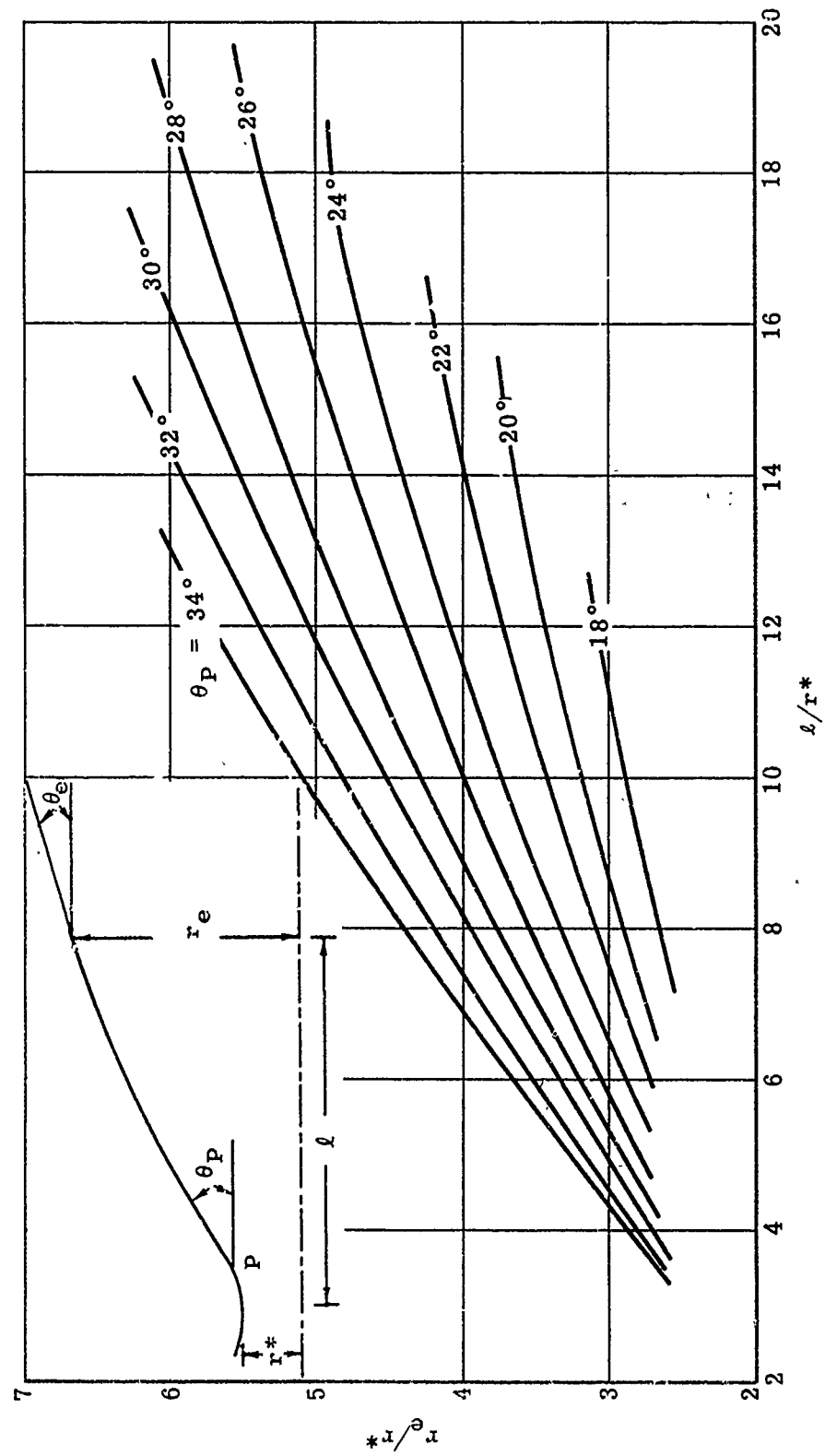

Fig. 6-27. Chart for finding the angle at point of inflection of the contour in terms of exit radius and nozzle length; $\gamma = 1.23$. (Source: Ref. 240)

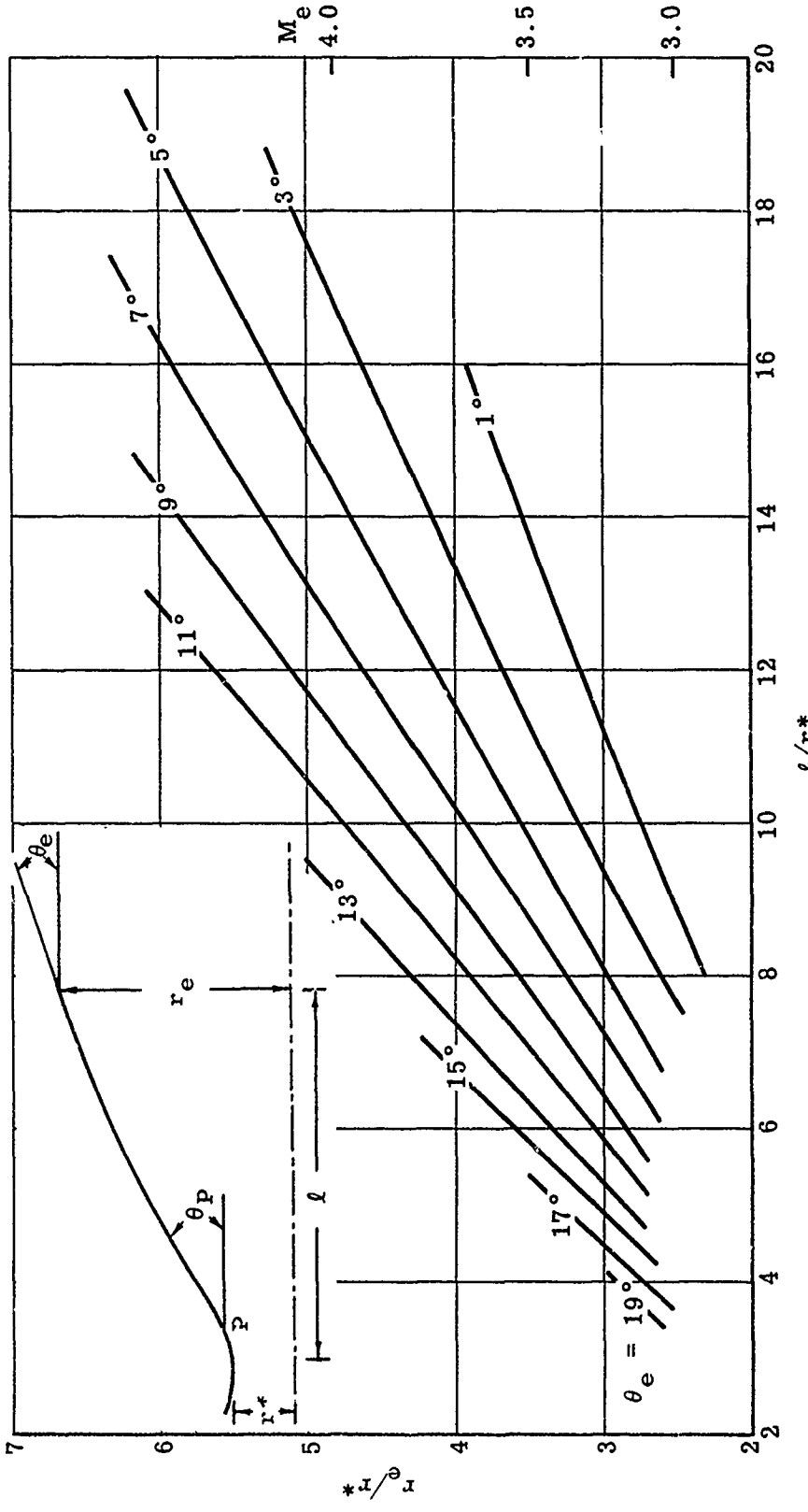

Fig. 6-28. Chart for finding contour exit angle in terms of exit radius and nozzle length; $\gamma = 1.23$. (Source: Ref. 240)

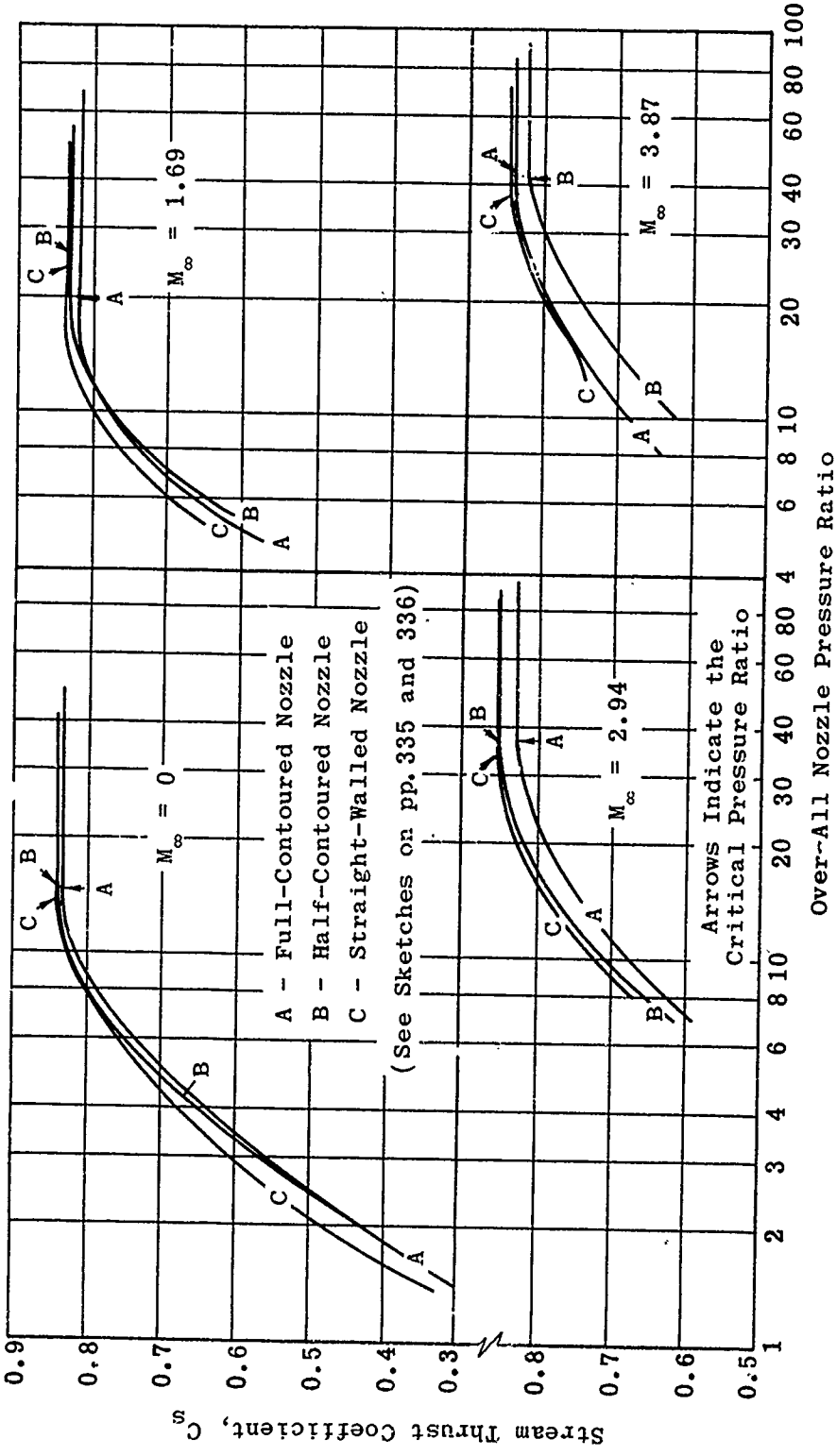

Fig. 6-29. Stream thrust coefficient vs nozzle pressure ratio for three oblique nozzles with nozzle flow at $M_e = 2$; $M_\infty = 0$, 1.69, 2.94, and 3.87; $\gamma = 1.4$. (Source: Ref. 243)

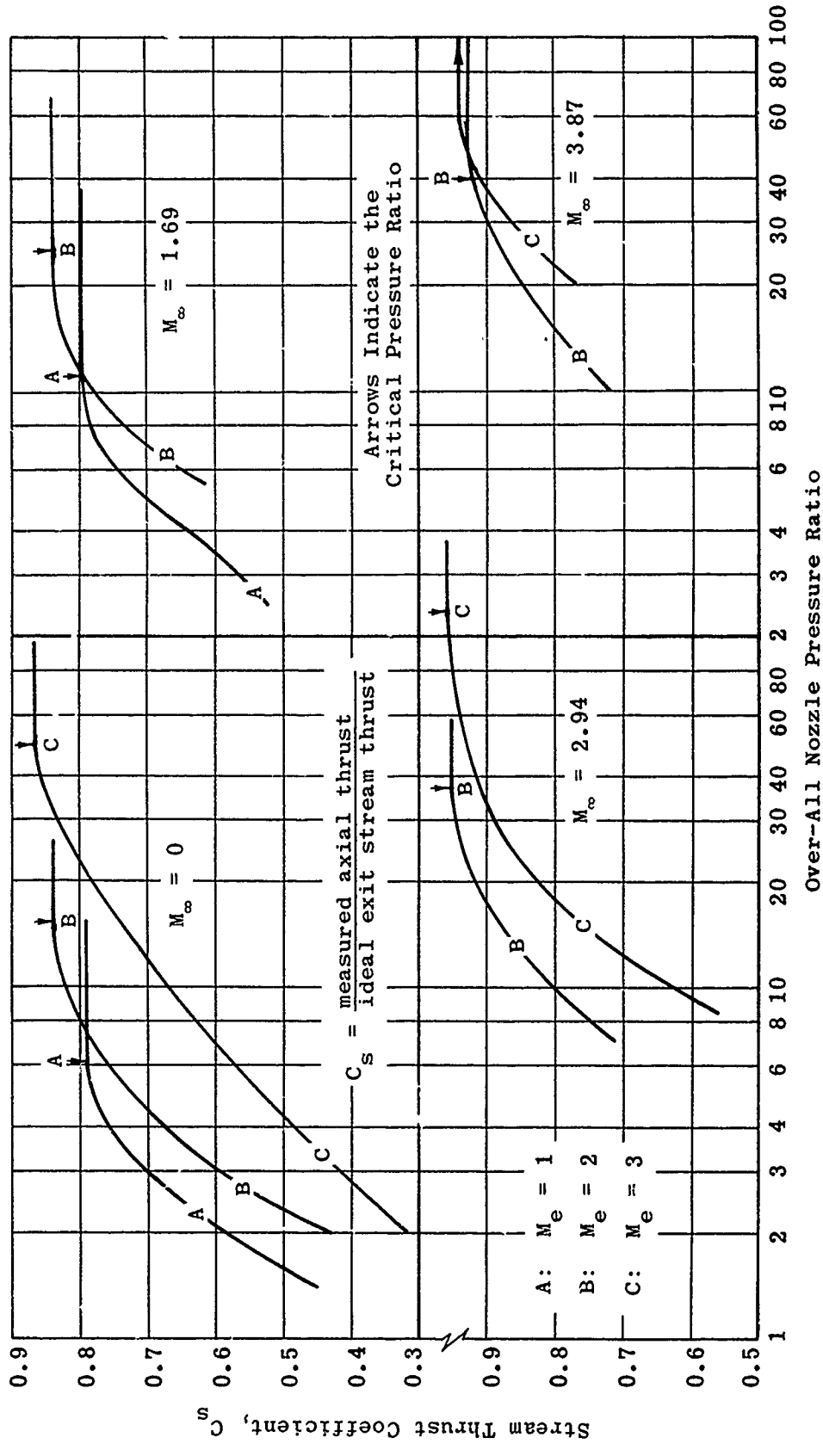

Fig. 6-30. Stream thrust coefficient vs nozzle pressure ratio for a half-contoured nozzle with nozzle flow at M_e = 1, 2, and 3; M_∞ = 0, 1.69, 2.94, and 3.87; γ = 1.4. (Source: Ref. 243)

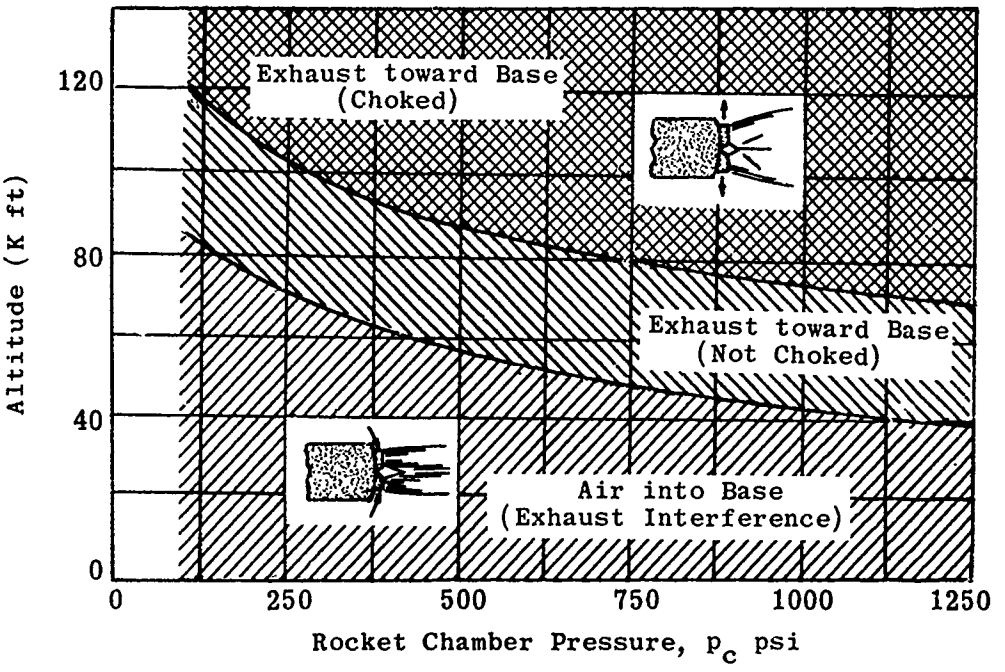

Fig. 6-31. Regions of exhaust patterns for four-nozzle cluster as a function of rocket chamber pressure; $\gamma = 1.20$, $\alpha = 15°$, $d_c/d_e = 2.4$, $A_e/A^* = 10$, $A_V/A_R = 0.50$. (Source: Ref. 244)

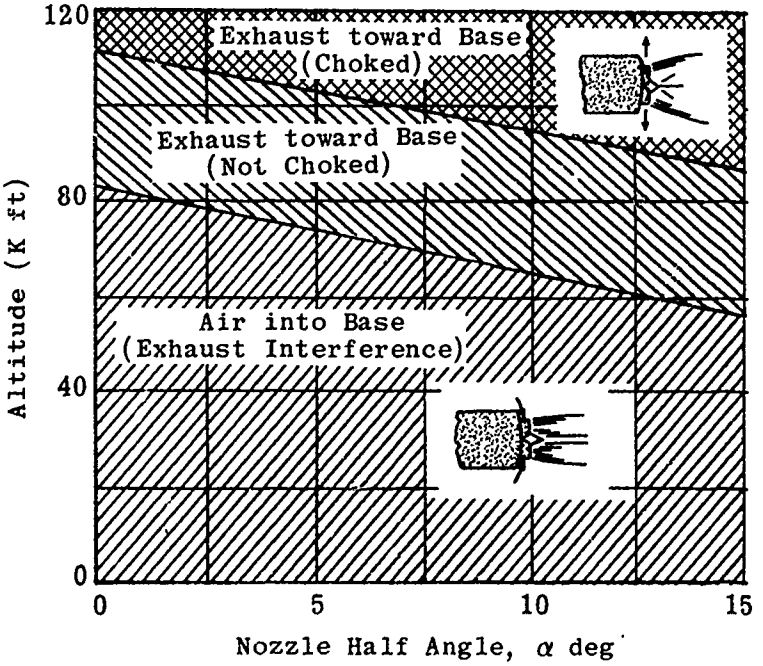

Fig. 6-32. Regions of exhaust patterns for four-nozzle cluster as a function of nozzle exit angle; $p_c = 500$ psi, $\gamma = 1.20$, $d_c/d_e = 2.4$, $A_e/A^* = 10$, $A_V/A_R = 0.50$. (Source: Ref. 244)

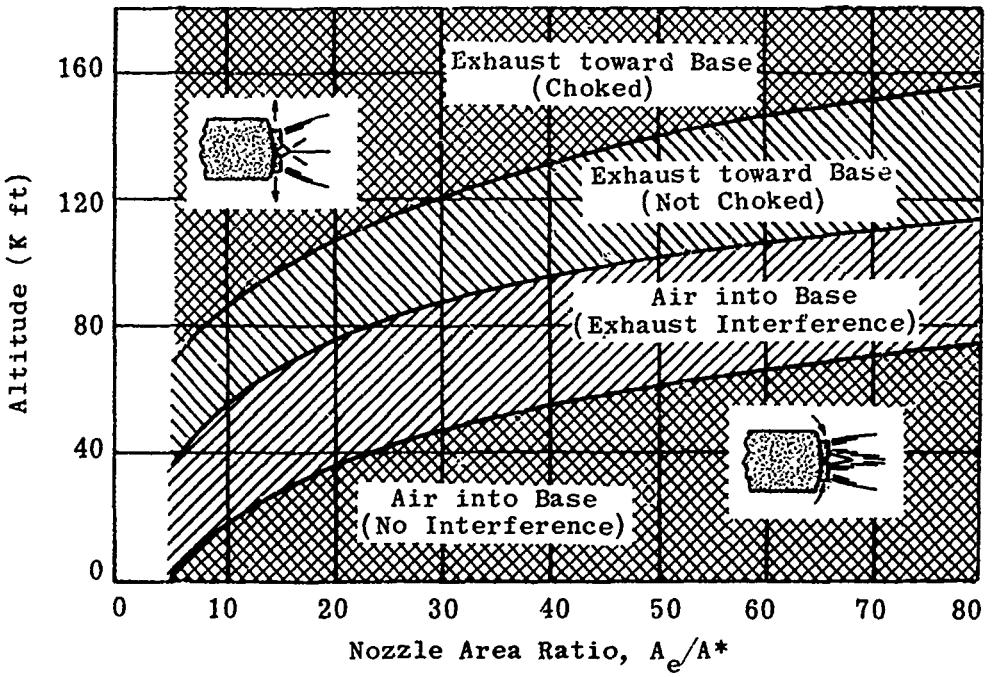

Fig. 6-33. Regions of exhaust patterns for four-nozzle cluster as a function of nozzle area ratio; p_c = 500 psi, γ = 1.20, α = 15°, d_c/d_e = 2.4, A_V/A_R = 0.50. (Source: Ref. 244)

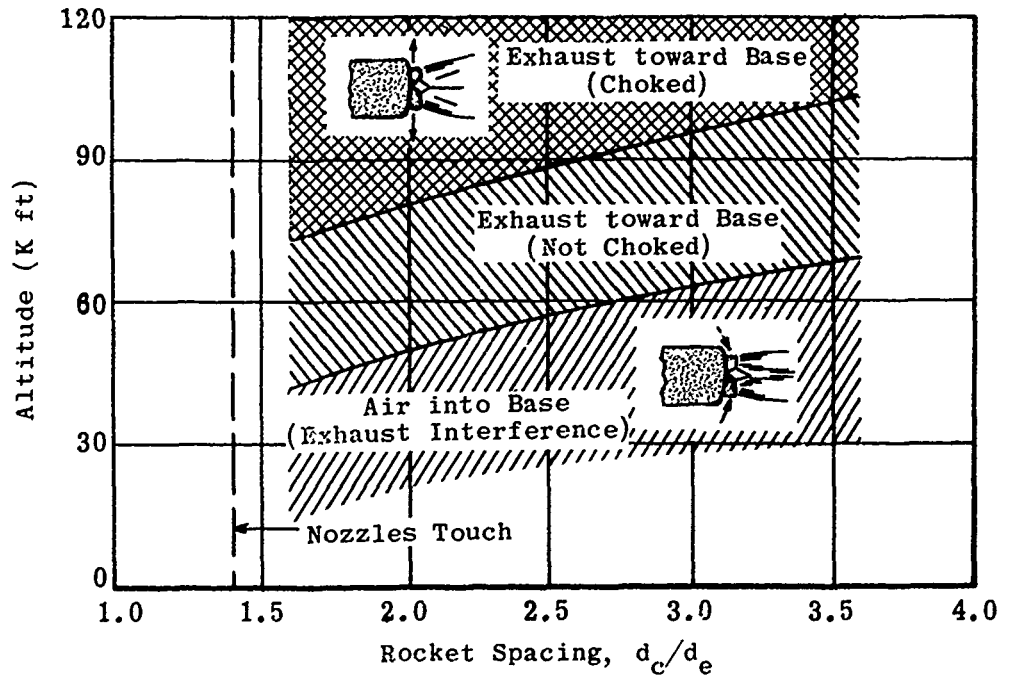

Fig. 6-34. Regions of exhaust patterns for four-nozzle cluster as a function of rocket spacing; A_e/A^* = 10, α = 15°, γ = 1.20, p_c = 500 psi, A_V/A_R = 0.50. (Source: Ref. 244)

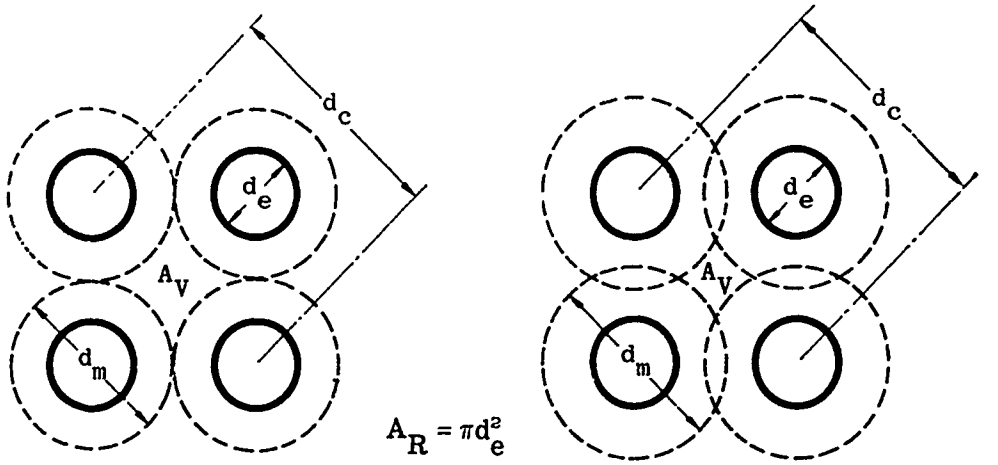

Closest Interference Mean Interference

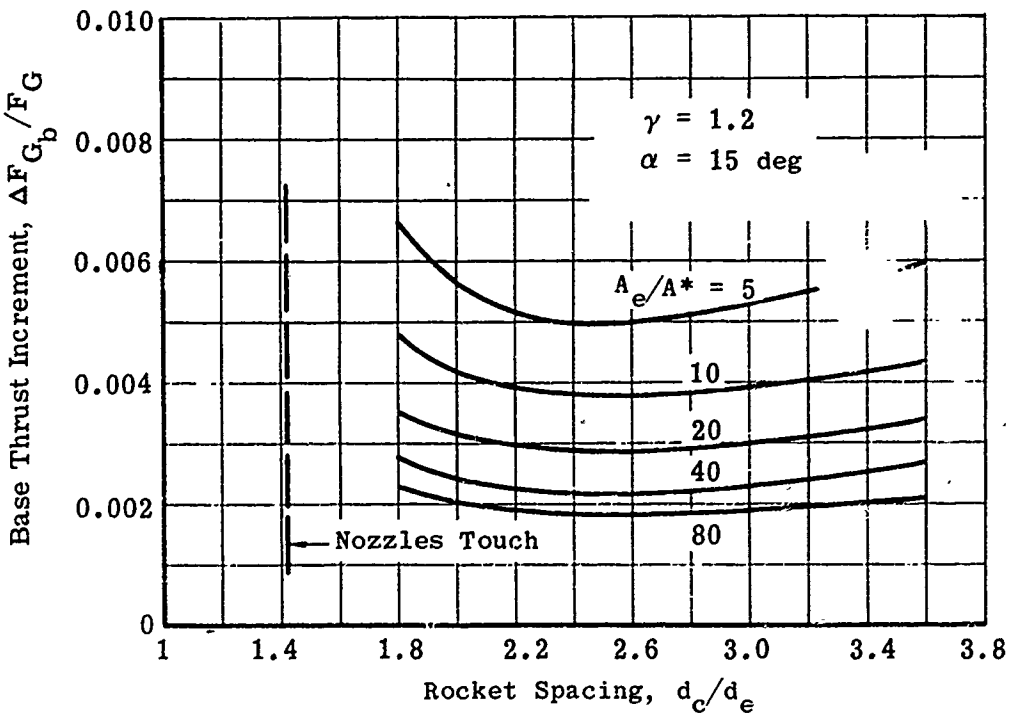

Fig. 6-35. Base thrust increment for four-nozzle cluster in vacuum as a function of nozzle area ratio and rocket spacing. (Source: Ref. 244)

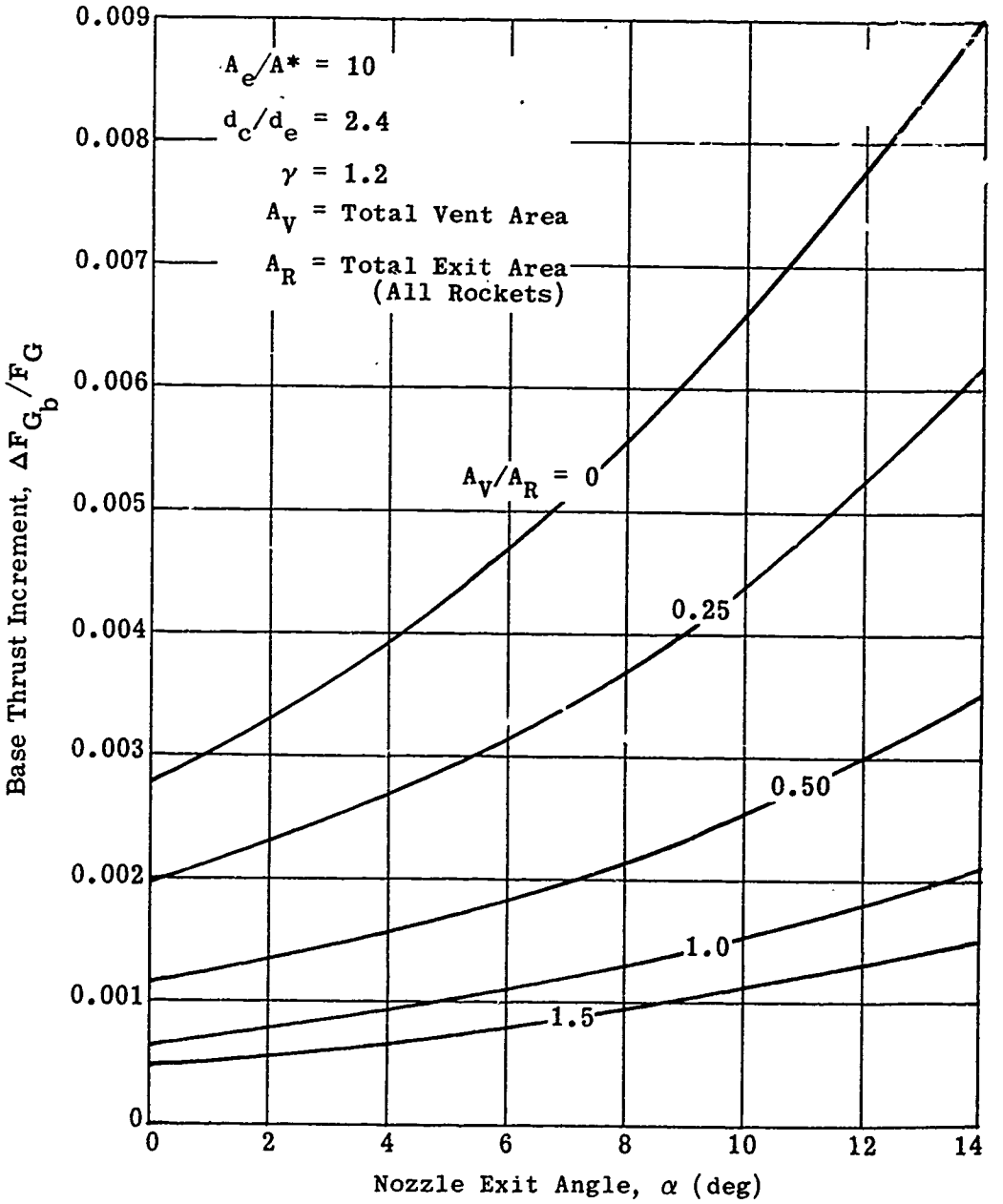

Fig. 6-36. Base thrust increment for four-nozzle cluster in vacuum as a function of base vent area and nozzle exit angle. (Source: Ref. 244)

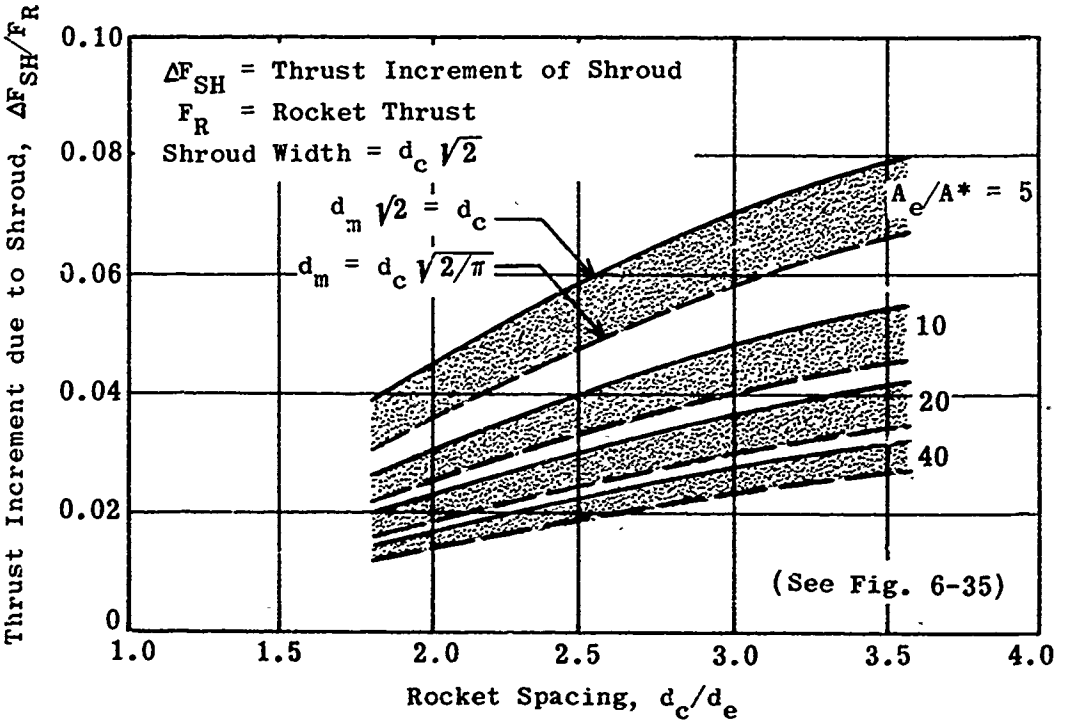

Fig. 6-37. Shroud thrust increment for four-nozzle cluster as a function of nozzle area ratio and rocket spacing (in vacuum); $\gamma = 1.20$, $\alpha = 15°$. (Source: Ref. 244)

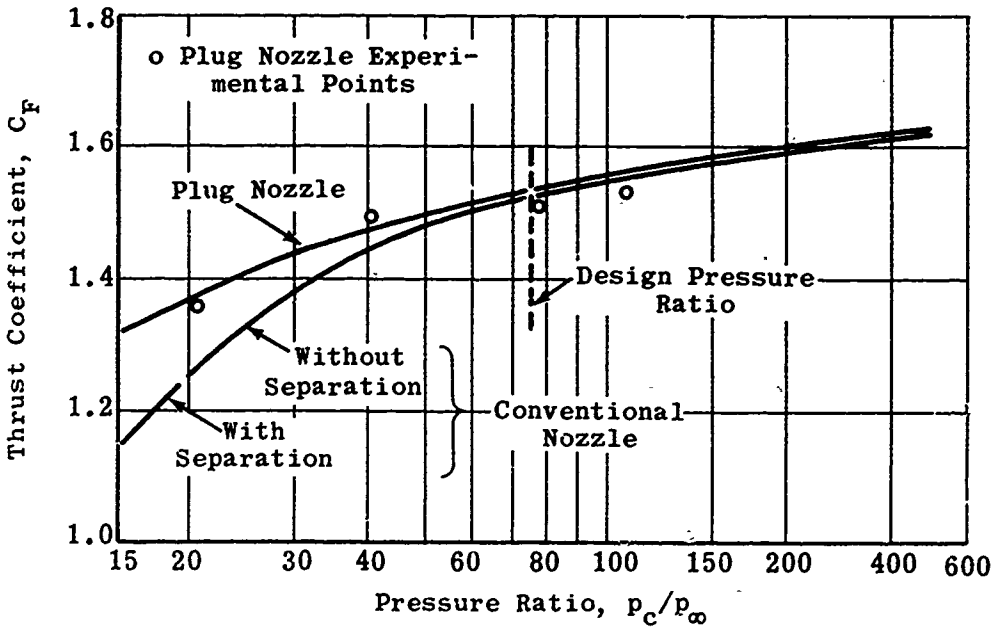

Fig. 6-38. Comparison of theoretical and experimental performances of plug and conventional nozzles; $\gamma = 1.4$. (Source: Ref. 245)

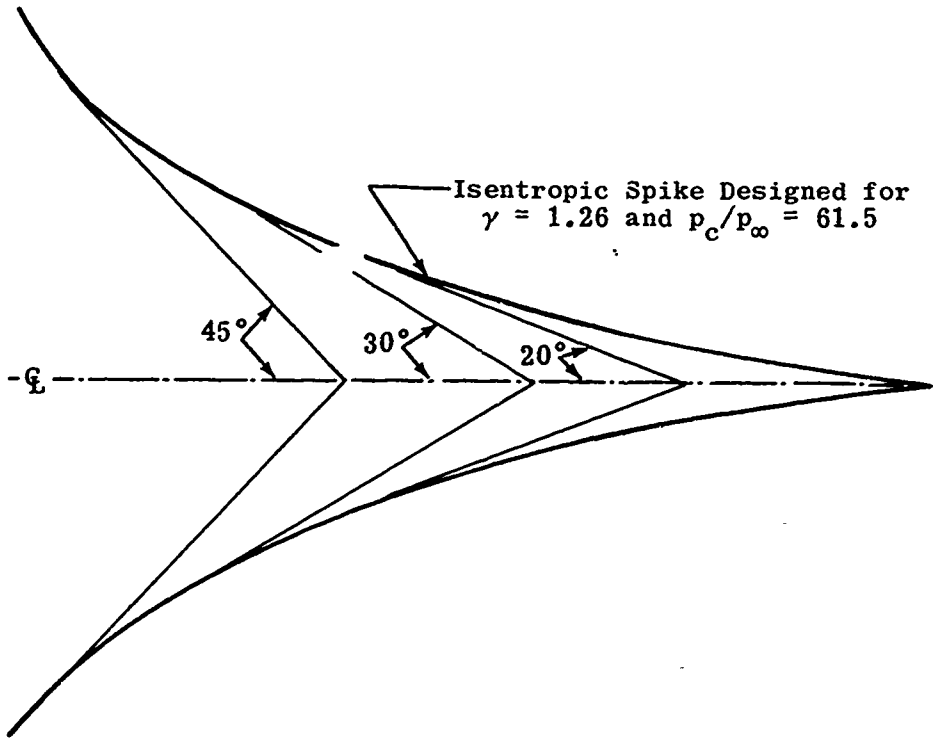

Fig. 6-39. Profiles obtained by shortening an isentropic plug using tangent cones. (Source: Ref. 245)

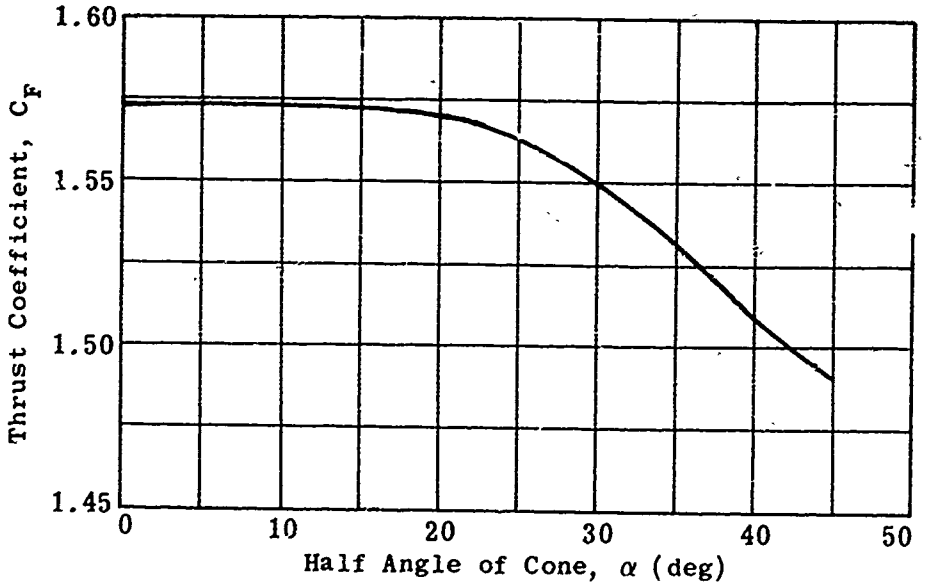

Fig. 6-40. Theoretical loss in performance caused by shortening an isentropic plug; γ = 1.26, p_c/p_∞ = 61.5. (Source: Ref. 245)

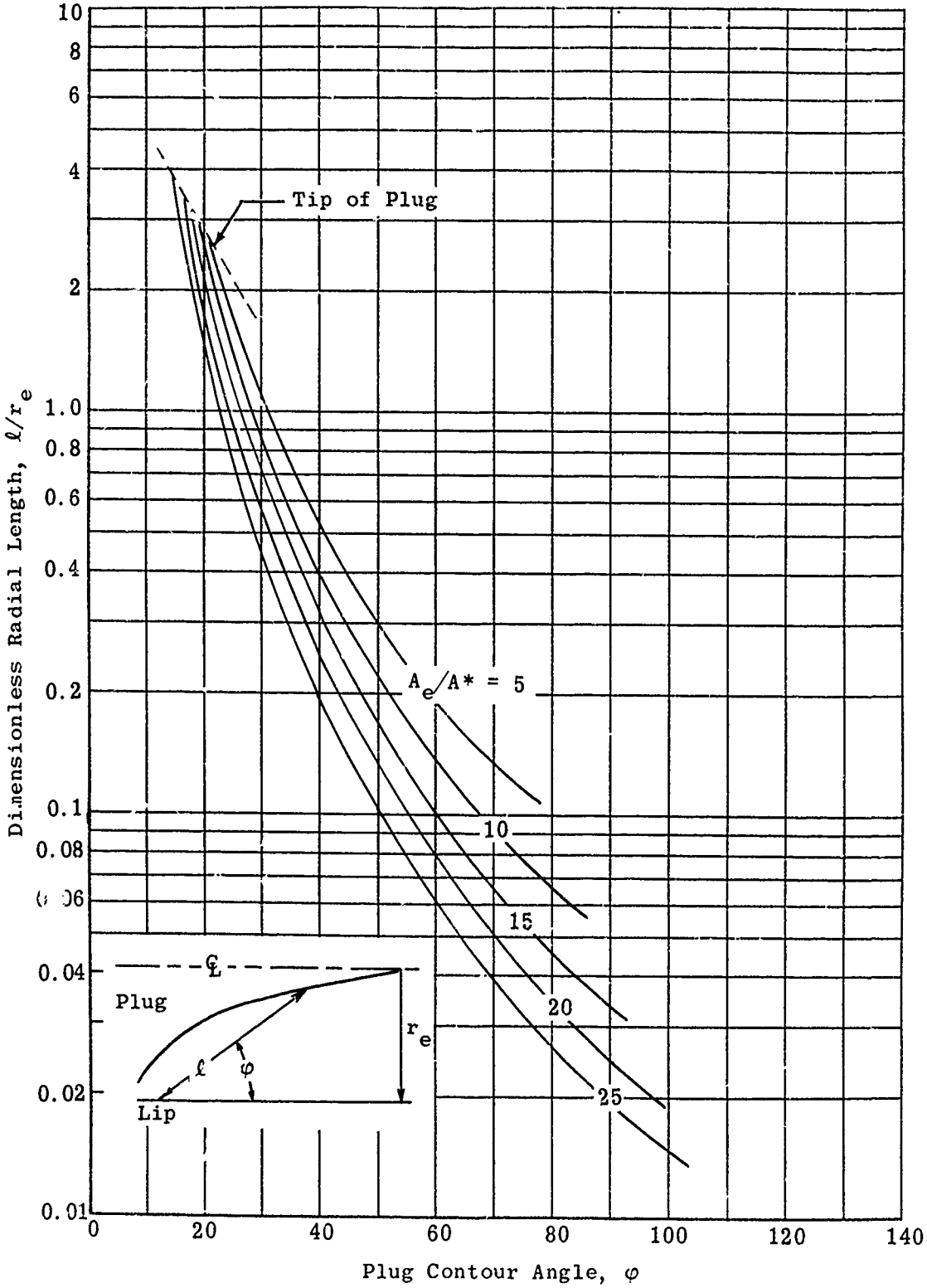

Fig. 6-41. Radial length vs contour angle for a plug nozzle; $\gamma = 1.17$, $A_e/A^* = 5$, 10, 15, 20, and 25. (Source: Ref. 247)

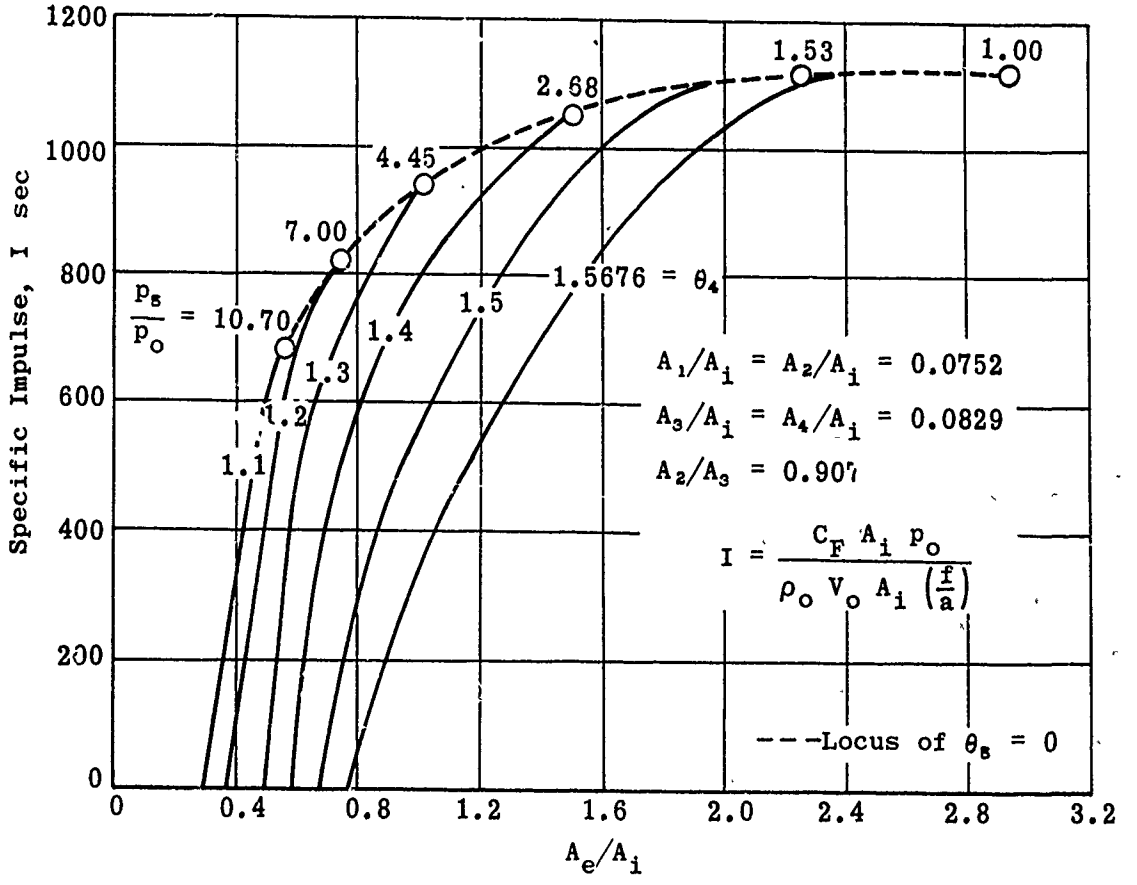

Fig. 6-42. Specific impulse vs area ratio for a two-dimensional plug nozzle; $M_\infty = 7$, $\eta_D = 0.1$, ER = 0.5. (Source: Ref. 118)

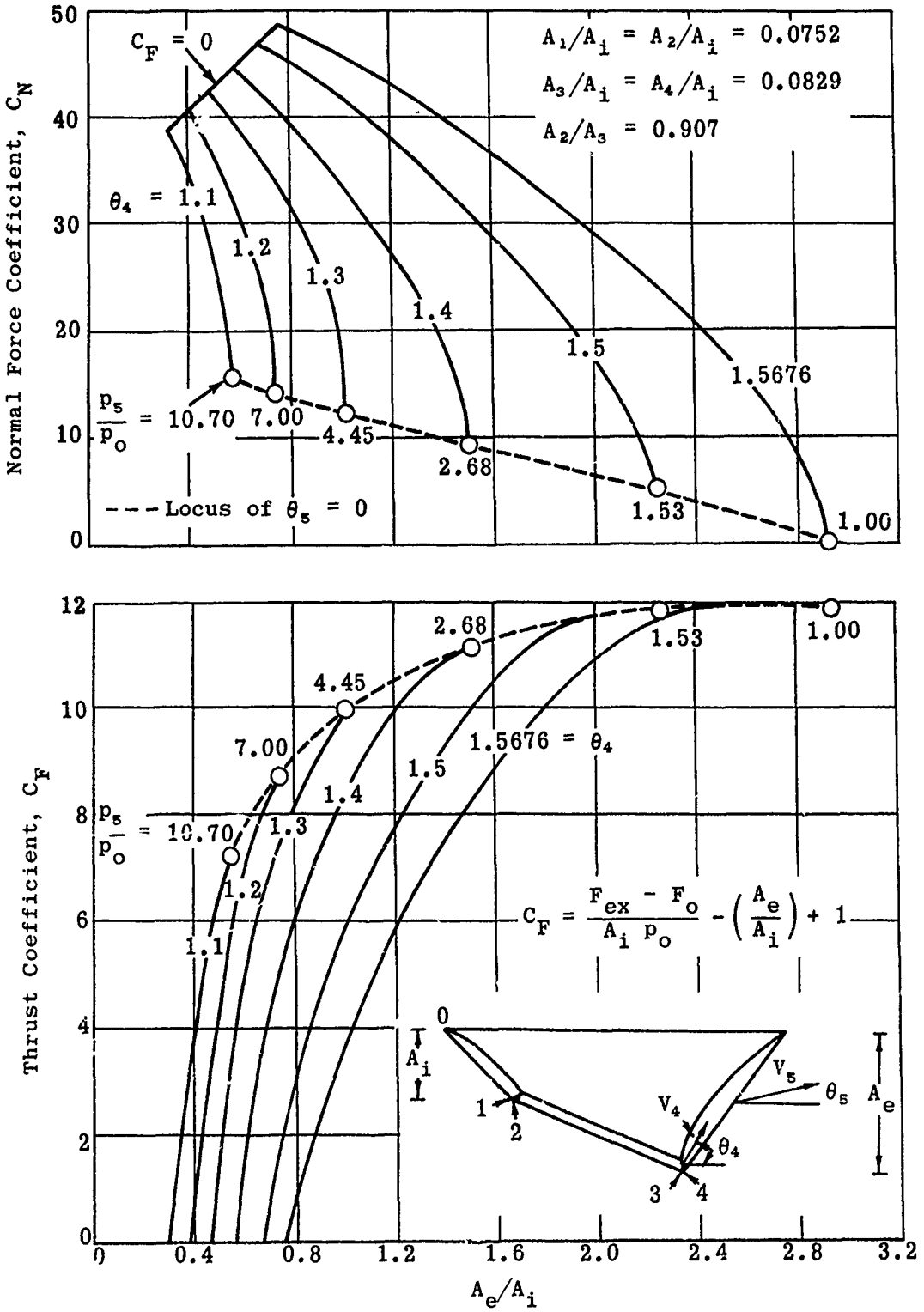

Fig. 6-43. Thrust and lift coefficients as a function of area ratio for a two-dimensional plug nozzle; $M_\infty = 7$, $\eta_D = 0.1$, ER = 0.5. (Source: Ref. 118)

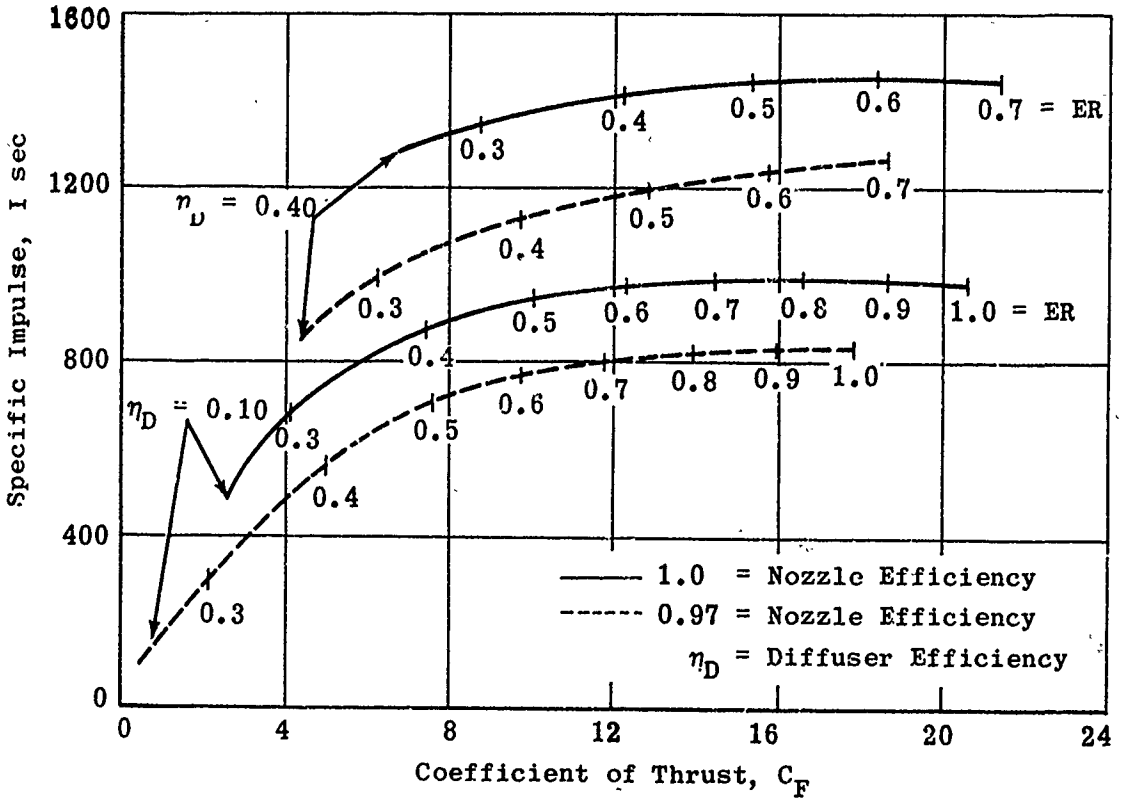

Fig. 6-44. Variation in I with C_F and nozzle efficiency for a two-dimensional plug nozzle; $M_\infty = 7$, $A_e/A_i = 1.0$. (Source: Ref. 118)

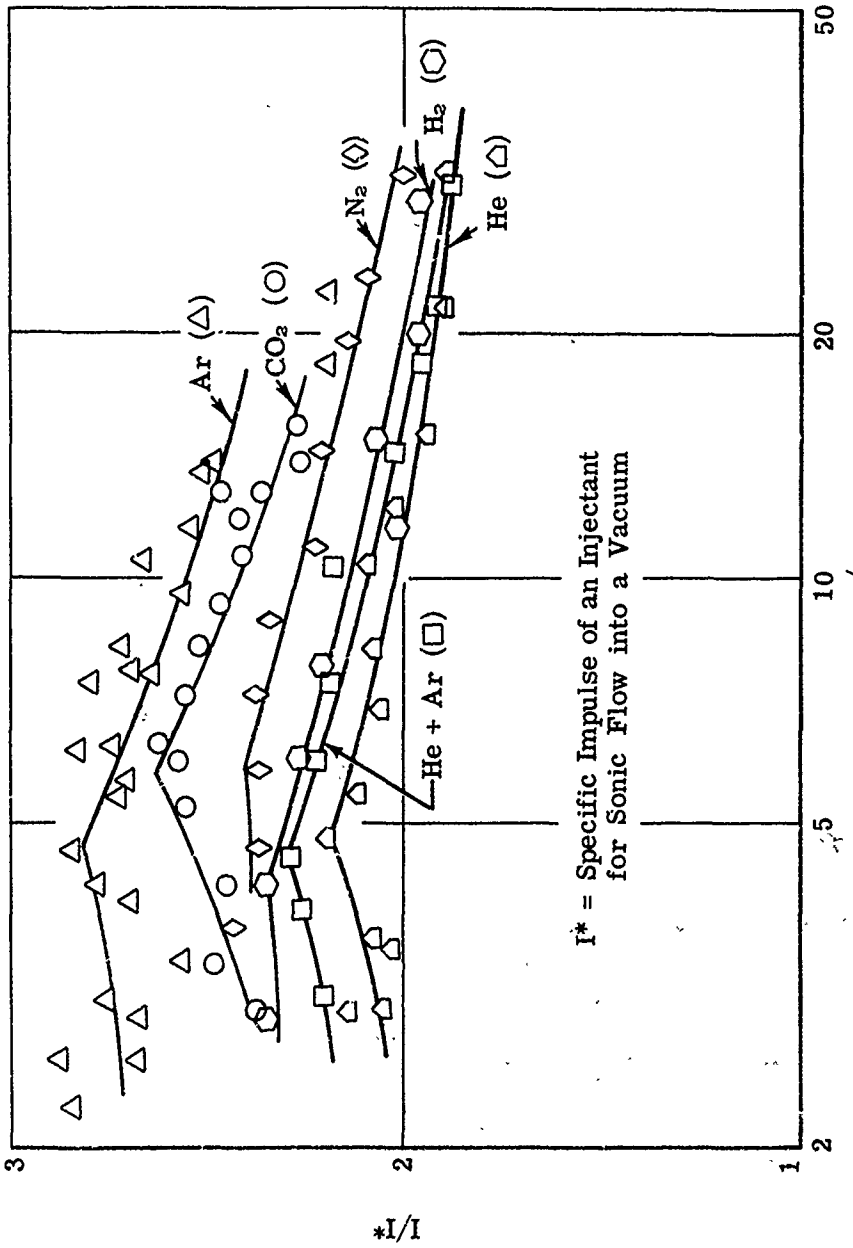

Fig. 6-45. Specific impulse ratio as a function of jet stagnation pressure ratio for various injectants. (Source: Ref. 264)

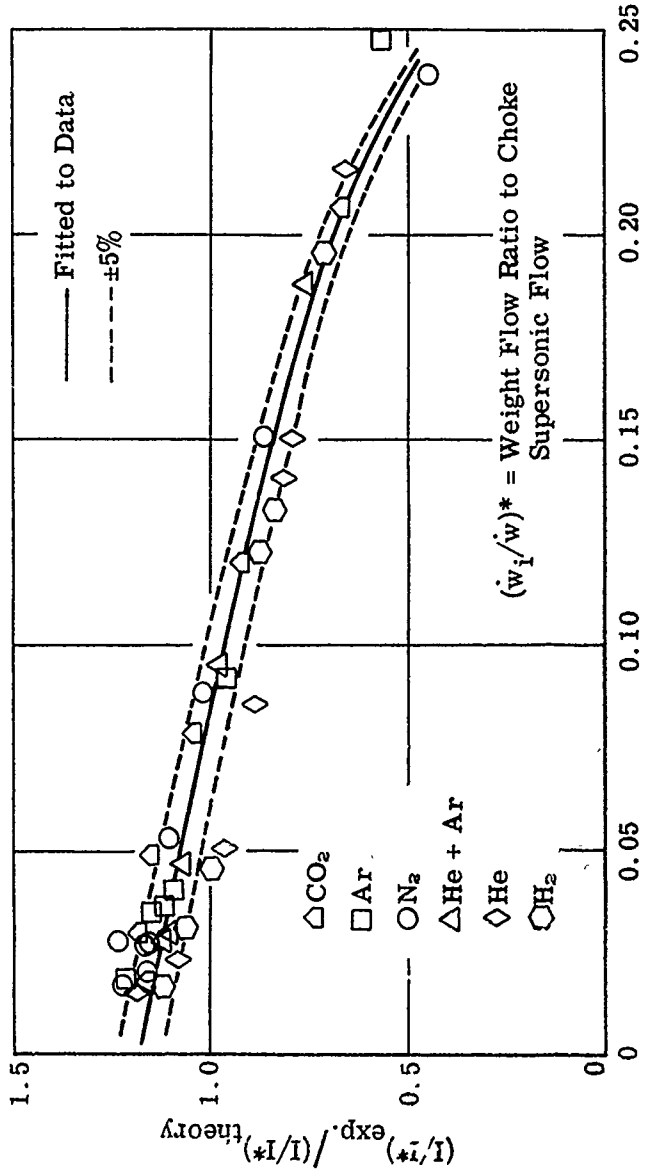

Fig. 6-46. Specific impulse ratio as a function of injectant weight-flow ratio; M = 1.86, H_2O_2 propellant, ℓ = 0.50in., d_i = 0.0625 in. (Source: Ref. 265)

Intentionally Blank

p. 390

REFERENCES

A. General

1. Applied Physics Laboratory, The Johns Hopkins University. Handbook of Supersonic Aerodynamics, NAVORD Report 1488, Vol. 1, Secs. 1 to 4, 1950.

2. Ferri, A. Elements of Aerodynamics of Supersonic Flows. New York: The MacMillan Co., 1949.

3. Oswatitsch, K. Gas Dynamics. New York: Academic Press Inc., 1956.

4. Kuethe, A. M. and Schetzer, J. D. Foundations of Aerodynamics. New York: John Wiley and Sons, Inc., 1950.

5. Bonney, E. A. Engineering Supersonic Aerodynamics. New York: McGraw-Hill Book Co., Inc., 1950.

6. Liepmann, H. W. and Puckett, A. E. Introduction to Aerodynamics of a Compressible Flow. New York: John Wiley and Sons, Inc., 1947.

7. Liepmann, H. W. and Roshko, A. Elements of Gas Dynamics. New York: John Wiley and Sons, Inc., 1957.

8. McAdams, W. H. Heat Transmission, Chap. V., Fluid Flow. New York: McGraw-Hill Book Co., Inc., 1942.

9. Applied Physics Laboratory, The Johns Hopkins University. Handbook of Supersonic Aerodynamics. NAVORD Report 1488, Vol. 3, Sec. 7, "Three-Dimensional Airfoils," August 1957.

10. Applied Physics Laboratory, The Johns Hopkins University. Handbook of Supersonic Aerodynamics. NAVWEPS Report 1488, Vol. 3, Sec. 8, "Bodies of Revolution," October 1961.

11. Schlichting, H. Boundary Layer Theory. New York: McGraw-Hill Book Co., Inc., 1955.

12. Pankhurst, R. C. and Holder, D. W. Wind Tunnel Techniques. London: Sir Isaac Pitman and Sons Ltd., 1952.

13. Applied Physics Laboratory, The Johns Hopkins University. Handbook of Supersonic Aerodynamics, NAVORD Report 1488, Vol. 6, Sec. 20, "Wind Tunnel Instrumentation and Operation," January 1961.

14. Bonney, E. A., Zucrow, M. J., and Besserer, C. W. Aerodynamics, Propulsion and Structures. Princeton, N. J.: D. Van Nostrand Co., 1956.

732-359 O - 64 - 27

15. Shapiro, A. H. The Dynamics and Thermodynamics of Compressible Fluid Flow, Vols. 1 and 2. New York: The Ronald Press Co., 1953.

16. High Speed Aerodynamics and Jet Propulsion, Vol. II. Combustion Processes. Princeton, N. J.: Princeton University Press, 1956.

17. High Speed Aerodynamics and Jet Propulsion, Vol. III. Fundamentals of Gas Dynamics. Princeton, N. J.: Princeton University Press, 1958.

18. High Speed Aerodynamics and Jet Propulsion, Vol. VI. General Theory of High Speed Aerodynamics. Princeton, N. J.: Princeton University Press, 1954.

B. Tables and Graphs

Reference 1 in the General References is largely comprised of tables (see Appendix A). Isentropic flow tables are also to be found in many of the aerodynamic texts, e.g., Refs. 2, 3, 4, 5, 6, 7, and 15.

21. Applied Physics Laboratory, The Johns Hopkins University. Handbook of Supersonic Aerodynamics, NAVORD Report 1488, Vol. 2, Sec. 5, "Compressible Flow Tables and Graphs," 1953.

22. Ames Research Staff. Equations, Tables, and Charts for Compressible Flow. NACA Report 1135, 1953.

23. Dailey, C. L. and Wood, F. C. Computation Curves for Compressible Fluid Problems. New York: John Wiley and Sons, Inc., 1949.

24. Lewis Laboratory Computing Staff. Tables of Various Mach Number Functions for Specific-Heat Ratios from 1.28 to 1.38. NACA TN 3981, 1957.

25. Tempelmeyer, K. E. and Sheraden, G. H. Compressible Flow Tables for Gases with Specific Heat Ratios from 1.10 to 1.28. Arnold Engineering Development Center, TN 58-9, Air Research and Development Command, U.S. Air Force, Washington, D.C., March 1958.

26. Hypersonic Wind Tunnel Staff. Charts and Tables for Analysis of Hypersonic Flow. GALCIT Hypersonic Wind Tunnel Memo. 4. Guggenheim Aeronautical Laboratory, California Institute of Technology, May 1951.

27. Kennedy, E. C. New Mach Number Tables for Ram-Jet Flow Analysis. $\gamma = 7/5$ and $\gamma = 9/7$. OAL Memo. 50-1 (CF-1798-A), August 1955.

28. Hoebick, C. Compressible Flow Tables, k = ____. Isentropic Process One-Dimensional Compressible Flow Tables for a Perfect Gas in Mach Number Increments of 0.001 (k = ____). Isentropic Process. Department of the Army, Army Rocket and Guided Missile Agency, Redstone Arsenal, Alabama. Series of reports with the foregoing title for specific heat ratios, k, as follows:

    k = 1.20, ARGMA TN 1H1N-6, December 1959
    k = 1.22, ARGMA TN 1H1N-7, December 1959
    k = 1.24, ARGMA TN 1H1N-9, March 1960
    k = 1.26, ARGMA TN 1H1N-1, January 1959
    k = 1.28, ARGMA TN 1H1N-8, February 1960
    k = 1.30, ARGMA TN 1H1N-10, September 1960

B. Tables and Graphs (cont)

29. Hoebick, C. Compressible Flow Tables, k = ____. Stagnation Temperature Change Without Friction. One-Dimensional Compressible Flow Tables for a Perfect Gas in Mach Number Increments of 0.001 (k = ____). Stagnation Temperature Change Without Friction. Department of the Army, Army Rocket and Guided Missile Agency, Redstone Arsenal, Alabama. Series of reports with the foregoing title for specific heat ratios, k, as follows:

k = 1.20, ARGMA TN 1H1N-11, July 1960
k = 1.22, ARGMA TN 1H1N-12, November 1960
k = 1.24, ARGMA TN 1H1N-13, August 1960
k = 1.28, ARGMA TN 1H1N-14, August 1960
k = 1.30, ARGMA TN 1H1N-15, August 1960
k = 1.40, ARGMA TN 1H1N-5, June 1959

30. Special Projects Branch, Analysis and Advanced Design Laboratory: Compressible Flow Tables, k = ____. Adiabatic Flow with Friction. Department of the Army, Army Ballistic Missile Agency, Redstone Arsenal, Alabama. Series of reports with the foregoing title for specific heat ratios, k, as follows:

k = 1.20, Report No. RA-TR-2-60, November 1960
k = 1.22, Report No. RA-TR-3-60, December 1960
k = 1.24, Report No. RA-TR-4-61, January 1961
k = 1.26, Report No. RA-TR-5-61, January 1961
k = 1.28, Report No. RA-TR-6-61, February 1961
k = 1.30, Report No. RA-TR-7-61, March 1961

31. Special Projects Branch, Analysis and Advanced Design Laboratory: Compressible Flow Tables, k = _____. Simple Gas Injection Without Forward Velocity, y = 0. Department of the Army, Army Ballistic Missile Agency, Redstone Arsenal, Alabama. Series of reports with the foregoing title for specific heat ratios, k, as follows:

k = 1.20, Report No. RA-TR-8-61, April 1961
k = 1.22, Report No. RA-TR-9-61, May 1961
k = 1.24, Report No. RA-TR-61-10, June 1961
k = 1.26, Report No. RA-TR-61-11, July 1961
k = 1.28, Report No. RA-TR-61-12, August 1961
k = 1.30, Report No. RA-TR-61-13, September 1961
k = 1.40, Report No. RA-TR-61-14, October 1961

32. Design Synthesis Branch, Analysis and Advanced Design Laboratory: Compressible Flow Tables, k = ____. Simple Gas Injection with Forward Velocity Equal to Freestream Velocity, y = 1. Department of the Army, Army Ballistic Missile Agency, Redstone Arsenal, Alabama. Series of reports with the foregoing title for specific heat ratios, k, as follows:

k = 1.20, Report No. RA-TR-61-16, October 1961
k = 1.22, Report No. RA-TR-61-17, October 1961
k = 1.24, Report No. RA-TR-61-18, November 1961
k = 1.26, Report No. RA-TR-61-19, November 1961
k = 1.28, Report No. RA-TR-61-20, December 1961
k = 1.30, Report No. RA-TR-62-21, January 1962

B. Tables and Graphs (cont)

33. Bassett, R. W. and Chappell, M. S. Compressible Gas Flow Tables for Specific Heat Ratio (γ) = 4/3 (Mach Number 0.000 to 2.000). Aeronautical Report LR-324 (N.R.C. No. 6769), National Research Council of Canada, Ottawa, January 1962.

34. Wang, C. J., Peterson, J. B., and Anderson, R. Gas Flow Tables. Guided Missile Research Division, The Ramo-Wooldridge Corp., March 1957.

35. Kopal, Z., et al. Tables of Supersonic Flow Around Cones. TR 1, Massachusetts Institute of Technology, 1947.

36. Kennedy, E. C. Tables of Supersonic Conical Flow. OAL Memo. 143 (CM-973), May 1960.

37. Kennedy, E. C. Calculation of the Flow Fields Around a Series of Bi-Conic Bodies of Revolution Using the Method of Characteristics as Applied to Supersonic Rotational Flow. OAL/CM 873, June 1956.

38. Seifert, H. S. and Crum, J. Thrust Coefficient and Expansion Ratio Tables. Guided Missile Research Division, The Ramo-Wooldridge Corp., February 1956.

39. Aircraft Gas Turbine Development Department, General Electric Company. Properties of Combustion Gases, Vol. 1: "Thermodynamic Properties." New York: McGraw-Hill Book Co., Inc., 1955.

40. Keenan, J. H. and Kaye, J. Gas Tables. New York: John Wiley and Sons, Inc., 1948.

41. Rossini, F. D., et al. Selected Values of Chemical Thermodynamic Properties. Circular 500, National Bureau of Standards. Washington, D.C.: U.S. Government Printing Office, February 1952.

42. JANAF Interim Thermochemical Tables (Vols. I and II). The Dow Chemical Co., Midland, Michigan, December 1960.

Intentionally Blank

p. 396

References for Subsec. 2

45. Chapman, D. L. "On the Rate of Explosion in Gases," Phil. Mag., Vol. 47 (1899), p. 90.

46. Jouguet, E. Mecanique des Explosifs. Paris: Doin et fils, 1917.

47. Morrison, R. B. A Shock Tube Investigation of Detonative Combustion. UMM-97, University of Michigan, 1952.

48. Eisen, C. L., Gross, R. A., and Rivlin, T. J. "Theoretical Calculations in Gaseous Detonation," Combustion and Flame, Vol. 4 (June 1960), pp. 137-147.

49. Gross, R. A. and Oppenheim, A. K. "Recent Advances in Gaseous Detonation," ARS Journal, Vol. 29 (March 1959), pp. 173-179.

50. Zeleznik, F. J. and Gordon, S. "Calculation of Detonation Properties and Effect of Independent Parameters on Gaseous Detonations," ARS Journal, Vol. 32 (April 1962), pp. 606-615.

51. Breitweiser, R., Gordon, S., and Gammon, B. Summary Report on Analytical Evaluation of Air and Fuel Specific-Impulse Characteristics of Several Nonhydrocarbon Jet-Engine Fuels. NACA RM E52L08, February 1953.

52. Tower, L. K. and Gammon, B. E. Analytical Evaluation of Effect of Equivalence Ratio, Inlet-Air Temperature, and Combustion Pressure on Performance of Several Possible Ram-Jet Fuels. NACA RM E53G14, September 1953.

53. Renich, W. T. Theoretical Combustion Performance of Ramjet Fuels: Propane. CF 2609, Applied Physics Laboratory, The Johns Hopkins University, December 1956.

54. Waiter, S. A. Heat Addition to a One-Dimensional Supersonic Flow Including Real Gas Effects. AEDC TN-60-180, USCEC-R-73-201, September 1960.

55. Bleviss, Z. O. and Inger, G. R. The Normal Shock Wave at Hypersonic Speeds. Report SM-22624, Douglas Aircraft Corporation, Santa Monica, Calif., November 1956.

56. Moeckel, W. E. Oblique-Shock Relations at Hypersonic Speeds for Air in Chemical Equilibrium. NACA TN 3895, January 1957.

57. Tyler, R. D. One-Dimensional Treatment of Non-Uniform Flow. ARC TR (R and M 2991). Ministry of Supply, Aeronautical Research Council. London: Her Majesty's Stationery Office, 1957.

58. McLafferty, G. A Generalized Approach to the Definition of Average Flow Quantities in Non-Uniform Streams. Report SR-13534-9, UAC., East-Hartford, Conn., December 1955.

References for Subsec. 2 (cont)

59. Rudinger, G. Wave Diagrams for Nonsteady Flow in Ducts. New York: D. Van Nostrand Co., Inc., 1955.

60. Courant, R. and Friedrichs, K. O. Supersonic Flow and Shock Waves. New York: Interscience Publishers, Inc., 1948.

61. Kestin, J. and Glass, J. S. "Application of the Method of Characteristics to the Transient Flow of Gases," Proc. Inst. Mech. Eng., Vol. 161, (1949), pp. 250-257.

62. Kantrowitz, A. "One-Dimensional Treatment of Nonsteady Gas Dynamics." High-Speed Aerodynamics and Jet Propulsion, Vol. III (edited by H. W. Emmons). Princeton: Princeton University Press, 1958, pp. 350-415.

63. Applied Physics Laboratory, The Johns Hopkins University. Handbook of Supersonic Aerodynamics, NAVORD Report 1488, Vol. 6, Sec. 18, "Shock Tubes," December 1959.

64. Foa, J. V. Elements of Flight Propulsion. New York: John Wiley and Sons, Inc., 1960.

65. Fox, L. Numerical Solution of Ordinary and Partial Differential Equations. London: Pergamon Press Ltd., 1962.

66. Chester, W. "The Quasi-Cylindrical Shock Tube," Phil. Mag., Vol. 45 (December 1954), pp. 1293-1301.

67. Chisnell, R. F. "The Motion of a Shock Wave in a Channel with Applications to Cylindrical and Spherical Shock Waves," J. Fluid Mech., Vol. 2 (1957), pp. 286-298.

68. Gundersen, R. "A Note on Shock Flow in a Channel," J. Fluid Mech., Vol. 4 (1958), pp. 501-504.

69. Whitham, G. B. "On the Propagation of Shock Waves Through Regions of Non-Uniform Area or Flow," J. Fluid Mech., Vol, 4, Pt. 4 (August 1958), pp. 337-360.

70. Chester, W. "The Propagation of Shock Waves Along Ducts of Varying Cross Section." Advances in Applied Mechanics, Vol. 6 (edited by H. L. Dryden and Th. von Karman). New York: Academic Press, 1960, pp. 119-152.

71. Friedman, M. P. "An Improved Perturbation Theory for Shock Waves Propagating Through Nonuniform Regions," J. Fluid Mech., Vol. 8 (1960), pp. 193-209.

72. Rosciszewski, J. "Calculation of the Motion of Non-uniform Shock Waves," J. Fluid Mech., Vol. 8 (1960), pp. 337-367.

References for Subsec. 2 (cont)

73. Jones, C. W. "On Gas Flow in One Dimension Following a Normal Shock of Variable Strength," Proc. Roy. Soc. London, Series A, Vol. 221 (1954), pp. 257-267.

74. Mirels, H. Attenuation in a Shock Tube Due to Unsteady-Boundary-Layer Action. NACA TR 1333, 1957.

75. Gundersen, J. "The Flow of a Compressible Fluid with Weak Entropy Changes," J. Fluid Mech., Vol. 3 (1958), pp. 553-581.

76. Mirels, H. Source Distribution Method for Unsteady One-Dimensional Flows with Small Mass, Momentum, and Heat Addition and Small Area Variation. NASA Memo. 5-4-59E, June 1959.

77. Benson, R. S. "Unsteady Isentropic Flow with Variable Specific Heats," J. Roy. Aeronaut. Soc., Vol. 60 (1956), pp. 347-348.

78. Riemann, B. "Uber die Fortpflanzung ebener Luftwellen von endlicher Schwingungsweite." Gesammelte Mathematische Werke, 2nd Ed., Tuebner, Leipzig (1892), pp. 156-175.

79. Rudinger, G. "On the Reflection of Shock Waves from an Open End of a Duct," J. Appl. Phys., Vol. 26 (1955), pp. 981-993.

80. Rudinger, G. "The Reflection of Pressure Waves of Finite Amplitude from an Open End of a Duct," J. Fluid Mech., Vol. 3 (1957), pp. 48-66.

81. Rudinger, G. "The Reflection of Shock Waves from an Orifice at the End of a Duct," ZAMP, Vol. 9b (1958), pp. 570-585 (J. Ackeret Anniversary Volume.)

82. Rudinger, G. "Nonsteady Discharge of Subcritical Flow," Trans. ASME, J. Basic Eng., Vol. 83(D) (1961), pp. 341-348.

83. Rudinger, G. "Nonsteady Supercritical Discharge through an Orifice," Trans. ASME. J. Basic Eng., Vol. 83(D) (1961), pp. 663-670.

84. Hall, J. G. "Transition Through a Contact Region," J. Appl. Phys., Vol. 26 (1955), pp. 698-700.

85. Taylor, G. I. "The Instability of Liquid Surfaces When Accelerated in a Direction Perpendicular to Their Planes. Part I.," Proc. Roy. Soc. London, Series A, Vol. 201 (1950), pp. 192-196.

86. Markstein, G. H. "Flow Disturbances Induced Near a Slightly Wavy Contact Surface, or Flame Front, Traversed by a Shock Wave," J. Aeronaut. Sci., Vol. 24 (1957), p. 238.

87. Foa, J. V. and Rudinger, G. "On the Addition of Heat to a Gas Flowing in a Pipe at Subsonic Speed," J. Aeronaut Sci., Vol. 16 (1949), pp. 84-95.

References for Subsec. 2 (cont)

88. Rudinger, G. "Shock Wave and Flame Interactions," Combustion and Propulsion, Third AGARD Colloquium (edited by M. W. Thring, O. Lutz, J. Fabri, and A. H. Lefebvre). London: Pergamon Press, 1958, pp. 153-182.

89. Oppenheim, A. K., Urtiew, P. A. and Stern, R. A. "Peculiarity of Shock Impingement on Area Convergence," Phys. Fluids, Vol. 2 (1959), pp. 427-431.

90. Rudinger, G. "Passage of Shock Waves Through Ducts of Variable Cross Section," Phys. Fluids, Vol. 3 (1960), pp. 449-455.

91. Chu, B. T. "On the Generation of Pressure Waves at a Plane Flame Front," Fourth Symposium (International) on Combustion. Baltimore: Williams and Wilkins Co., 1953, pp. 603-612.

92. Chu, B. T. Mechanism of Generation of Pressure Waves at Flame Fronts. NACA TN 3683, 1956.

93. Morse, P. M. Vibration and Sound. New York: McGraw-Hill Book Company, Inc., 1948.

94. Ferri, A. Application of the Method of Characteristics to Supersonic Rotational Flow. NACA Report 841, September 1946.

95. Warren, I. L., Abbadessa, R. B., and Pietrangeli, G. J. Application of the Method of Characteristics to the Supersonic Rotational Flow Through a Circular Conical Inlet. CM-668, Applied Physics Laboratory, The Johns Hopkins University, September 1951.

96. Sauer, R. Method of Characteristics for Three-Dimensional Axially Symmetric Supersonic Flows. NACA TM 1133, January 1947.

97. Cronvich, L. L. "Numerical-Graphical Methods of Characteristics for Plane Potential Shock-Free Flow Problems," J. Aeronaut. Sci., Vol. 14, No. 4 (April 1947), pp. 237-242.

98. Cronvich, L. L. "A Numerical-Graphical Method of Characteristics for Axially Symmetric Isentropic Flow," J. Aeronaut. Sci., Vol. 15, No. 3 (March 1948), pp. 155-162.

99. Shapiro, A. H. and Edelman, G. M. "Method of Characteristics for Two-Dimensional Supersonic Flow - Graphical and Numerical Procedures," J. Appl. Mech., Vol. 14, No. 2 (June 1947), pp. A-154-163.

100. Tucker, M. Approximate Turbulent Boundary-Layer Development in Plane Compressible Flow Along Thermally Insulated Surfaces with Application to Supersonic-Tunnel Contour Correction. NACA TN 2045, March 1950.

References for Subsec. 2 (cont)

101. Kuethe, A. M. and Epstein, H. T. Viscosity Effects in Transonic and Supersonic Flow. Bumblebee Report 48, University of Michigan, December 1946 (issued by APL/JHU).

102. Maxwell, H. and Jacocks, J. L. Nondimensional Calculation of Turbulent Boundary-Layer Development in Two-Dimensional Nozzles of Supersonic Wind Tunnels. AEDC-TN-61-153, January 1962.

Also cited in this Subsection: Refs. 1-3, 7-11, 15, 17, 18, 21-34 and 39

References for Subsec. 3

103. Connors, J. F., Wise, G. A., and Lovell, J. C. Investigation of Translating-Double-Cone Axisymmetric Inlets with Cowl Projected Areas 40 and 20 Percent of Maximum at Mach Numbers from 3.0 to 2.0. NACA RM E57C06, May 1957.

104. Moeckel, W. E. Approximate Method for Predicting Form and Location of Detached Shock Waves Ahead of Plane or Axially Symmetric Bodies. NACA TN 1921, July 1949.

105. Kennedy, E. C. Axisymmetric Isentropic Spike Surface of a Ramjet Diffuser Operating at Below-Design Mach Numbers. OAL/CM 957, August 1959.

106. Gunther, F. Development of a Two-Dimensional Adjustable Supersonic Inlet. JPL/CIT Progress Report 20-247, November 1954.

107. Mossman, E. A. and Pfyl, F. A. An Experimental Investigation at Mach Numbers from 2.1 to 3.0 of Circular-Internal-Contraction Inlets with Translating Centerbodies. NACA RM A56G06, October 1956.

108. Evvard, J. C. and Blakey, J. W. The Use of Perforated Inlets for Efficient Supersonic Diffusion. NACA TN 3767, September 1956.

109. Hunczak, H. R. and Kremzier, E. J. Characteristics of Perforated Diffusers at Free-Stream Mach Number 1.90. NACA RM E50B02, May 1950.

110. Hearth, D. P., Anderson, B. H., and Dryer, M. Performance Comparison at Mach Numbers 1.8 and 2.0 of Full-Scale and Quarter-Scale Translating-Spike Inlets. NACA RM E57D16, October 1957. (Confidential)

111. Connors, J. F. and Woollett, R. R. Performance Characteristics of Several Types of Axially Symmetric Nose Inlets at Mach Number 3.85. NACA RM E52I15, November 1952.

112. Bernstein, H. and Haefeli, R. C. Investigation of Pressure Recovery of a Single-Conical-Shock Nose Inlet at Mach Number 5.4. NACA RM E53A12, April 1953.

References for Subsec. 3 (cont)

113. Dean, F. A. Study of a Probe Diffuser. CM-723, Applied Physics Laboratory, The Johns Hopkins University, April 1952.

114. Moeckel, W. E. and Evans, P. J., Jr. Preliminary Investigation of Use of Conical Flow Separation for Efficient Supersonic Diffusion. NACA RM E51J08, December 1951.

115. Connors, J. F. and Meyer, R. C. Design Criteria for Axisymmetric and Two-Dimensional Supersonic Inlets and Exits. NACA TN 3589, January 1956.

116. Connors, J. F., Lovell, J. C., and Wise, G. A. Effects of Internal-Area Distribution, Spike Translation, and Throat Boundary-Layer Control on Performance of a Double-Cone Axisymmetric Inlet at Mach Numbers from 3.0 to 2.0. NACA RM E57F03, August 1957.

117. Kennedy, E. C. "Calculation of Axisymmetric Isentropic Spike Surfaces," J. Aeronaut. Sci., Vol. 25, No. 7 (July 1958), p. 463.

118. Pietrangeli, G. J. and Nice, E. V. The Feasibility of a Mach 7 Transport Employing Airbreathing Propulsion Systems. CF-2900, Applied Physics Laboratory, The Johns Hopkins University, November 1960.

119. Ferri, A. and Nucci, L. M. The Origin of Aerodynamic Instability of Supersonic Inlets at Subcritical Conditions. NACA RM L50K30, January 1951.

120. Connors, J. F. and Flaherty, R. J. High Mach Number, Low-Cowl-Drag, External-Compression Inlet with Subsonic Dump Diffuser. NACA RM E58A09, May 1958. (Confidential)

121. Carr, J. H. and Gunther, F. C. Further Development of Adjustable Supersonic Internal-Compression Air Inlets. JPL/CIT Report No. 20-121, June 1958.

122. Shoemaker, C. J. and Henry, J. R. Effects of Suction Boundary-Layer Control on the Performance of a Short Annular Diffuser with an Upstream Terminal Normal Shock. NASA TN D-1241, April 1962.

123. Pearce, R. B. "Causes and Control of Powerplant Surge," Aviation Week, Vol. 52, No. 3 (January 1950), pp. 21-25.

124. Dailey, C. L. "Supersonic Diffuser Instability," J. Aeronaut. Sci., Vol. 22, No. 11 (November 1955), pp. 733-749.

125. Sterbentz, W. H. and Evvard, J. C. Criterions for Prediction and Control of Ram-Jet Flow Pulsations. NACA TN 3506, August 1955.

126. Mirels, H. Acoustic Analysis of Ram-Jet Buzz. NACA TN 3574, November 1955.

References for Subsec. 3 (cont)

127. Luidens, R. W. and Flaherty, R. J. Use of Shock-Trap Bleed to Improve Pressure Recovery of Fixed- and Variable-Capture-Area Internal-Contraction Inlets, Mach Number 2.0 to 3.0. NACA RM E58D24, August 1958.

128. Scherrer, R. and Anderson, W. E. Investigation of the Performance and Internal Flow of a Variable-Area, Variable-Internal-Contraction Inlet at Mach Numbers of 2.00, 2.50 and 2.92. NACA RM A58C24, July 1958.

129. Stitt, L. E. and Obery, L. J. Performance of an All-Internal Conical Compression Inlet with Annular Throat Bleed at Mach Number 5.0. NACA RM E58E14, August 1958.

130. Ferri, A. and Nucci, L. M. Theoretical and Experimental Analysis of Low Drag Supersonic Inlets Having a Circular Cross Section and a Central Body at Mach Number 3.30, 2.75, and 2.45. NACA RM L8H13, November 1948.

131. Gorton, G. C. and Dryer, M. Comparison at Supersonic Speeds of Translating Spike Inlets Having Blunt- and Sharp-Lip Cowls. NACA RM E54J07, January 1955.

Also cited in this Subsection: Refs. 2, 3, 10, 14, 21-23, 26, 35, 36, 95, 97, and 98.

References for Subsec. 4

132. Sauer, R. General Characteristics of the Flow through Nozzles at Near Critical Speeds. NACA TM 1147, 1947.

133. Burbank, P. B. and Byrne, R. W. The Aerodynamic Design and Calibration of an Asymmetric Variable Mach Number Nozzle with a Sliding Block for the Mach Number Range 1.27 to 2.75. NACA TN 2921, April 1953.

134. Shames, H. and Seashore, F. L. Design Data for Graphical Construction of Two-Dimensional Sharp-Edge-Throat Supersonic Nozzles. NACA RM E8J12, 1948.

135. Allen, H. J. The Asymmetric Adjustable Nozzle for Wind-Tunnel Application. NACA TN 2919, March 1953.

136. Oliver, R. E. and Nagamatsu, H. T. Investigation of Flow in the Throat Region for a Hypersonic Nozzle. GALCIT Memo No. 24, January 1955.

137. Dorodnitsyn, A. A. Trans. Third All Union Math Congress, 1956.

138. Holt, M. The Design of Plane and Axisymmetric Nozzles by the Method of Integral Relations. AFOSR3140, University of California, September 1962.

References for Subsec. 4 (cont)

139. Armstrong, A. H. and Smith, M. G. Two-Dimensional Supersonic Nozzle Design. Part I: Theory. ARE Report No. 5/51, London, October 1951.

140. Oswatitsch, K and Rothstein, W. Flow Pattern in a Converging-Diverging Nozzle. NACA TM 1215, March 1949.

141. Beckwith, I. E. and Moore, J. A. An Accurate and Rapid Method for the Design of Supersonic Nozzles. NACA TN 3322, February 1955.

142. Shapiro, A. H. and Edelman, G. M. "Method of Characteristics for Two-Dimensional Supersonic Flow - Graphical and Numerical Procedures," J. Appl. Mech., Vol. 14, No. 2 (June 1947).

143. Nilson, E. Design of an Inlet for a Two-Dimensional Supersonic Nozzle. Meteor Report UAC-13, December 1947.

144. Nilson, E. Analytical Correction of a Two-Dimensional Nozzle for Uniform Exhaust Flow. Meteor Report UAC-15, 1948.

145. Evvard, J. C. and Marcus, L. R. Achievement of Continuous Wall Curvature in Design of Two-Dimensional Symmetrical Supersonic Nozzles. NACA TN 2616, 1952.

146. Foelsch, K. "The Analytical Design of an Axially-Symmetric Laval Nozzle for a Parallel and Uniform Jet," J. Aeronaut. Sci., Vol. 16, No. 3 (March 1949).

147. Atkin, A. O. L. Two-dimensional Supersonic Channel Design: Part I. ARC R and M 2174. London: Her Majesty's Stationery Office, 1945.

148. Puckett, A. E. "Supersonic Nozzle Design," J. Appl. Mech., Vol. 13, No. 4 (December 1946), pp. A265-270.

149. Kurzweg, H. H. The Use of Grating Nozzles and Diffusers. NOL Memo 9848, July 1948.

150. Amick, J. L., Harrington, S. A., and Liepman, H. P. On Menard Inserts in Supersonic Nozzles. CF-2656, Engineering Research Institute, University of Michigan, May 1957.

151. Eggers, A. J., Jr., and Nothwang, G. J. The Ames 10 by 14-Inch Supersonic Wind Tunnel. NACA TN 3095, January 1954.

152. Wegener, P., et al. Experimental and Theoretical Investigation of a Cooled Hypersonic Wedge Nozzle. NAVORD Report 2701, April 1953.

153. Syvertson, C. A. and Savin, R. C. The Design of Variable Mach Number Asymmetric Supersonic Nozzles by Two Procedures Employing Inclined and Curved Sonic Lines. NACA TN 2922, March 1953.

References for Subsec. 4 (cont)

154. Riise, H. N. Flexible-Plate Nozzle Design for Two-Dimensional Supersonic Wind Tunnels. JPL/CIT Report No. 20-74, June 1954.

155. Clippinger, R. F. Supersonic Axially Symmetric Nozzles. BRL Report 794, December 1951.

156. Kennedy, E. C. Design of an Axially Symmetric Contraction-Expansion Nozzle for Exit Mach Number 2.7203. OAL Memo 89, July 1956.

157. Kennedy, E. C. Design of an Axially Symmetric Contraction-Expansion Nozzle for Exit Mach Number 3.0413. OAL Memo 91, November 1956.

158. Kennedy, E. C. Design of a Supersonic Axiallv Symmetric Contraction-Expansion Nozzle Exit Mach No. 3.8532, Exit Radius 12.4200. OAL Memo 138, February 1958.

159. Faro, I. D. V Small, T. R., and Hill, F. K. "Hypersonic Flow at a Mach Number of 10," J. Appl. Phys., Vol. 22, No. 2 (February 1951), pp. 220-222.

160. Squires, R. K., Roberts, R. C., and Fisher, E. R. A Method for Designing Supersonic Nozzles Using the Centerline Mach Number Distribution. NAVORD Report 3995, U.S. Naval Ordnance Laboratory, October 1956.

161. Thickstun, W. R., Schroth, R., and Lee, R. The Development of an Axisymmetric Nozzle for Mach 8. NAVORD Report 5904, U.S. Naval Ordnance Laboratory, May 1958.

162. Enkenhus, K. R. and Maher, E. F. The Aerodynamic Design of Axisymmetric Nozzles for High-Temperature Air. NAVWEPS Report 7395, U.S. Naval Ordnance Laboratory, February 1962.

163. Ruptash, J. Supersonic Wind Tunnels - Theory, Design and Performance. UTIA Review No. 5, Institute of Aerophysics, University of Toronto, June 1952.

164. Crown, J. C. Supersonic Nozzle Design. NACA TN 1651, 1948.

165. Frost, R. C. Nozzle Design Considerations. WTM-188, University of Michigan, 1950.

166. Heybey, W. H. Nozzle Design and Correction for Two-Dimensional Supersonic Flow. NOLM 9132, 1947.

167. Peterson, J. W. Nozzle Design for the Supersonic Wind Tunnel. EMP-7, University of Michigan, 1948.

168. Pinkel, I. I. Equations for the Design of Two-Dimensional Supersonic Nozzles. NACA Report 907, 1948.

References for Subsec. 4 (cont)

169. Shapiro, A. H. "Nozzles for Supersonic Flow without Shock Fronts," J. Appl. Mech., Vol. 11 (June 1944), pp. A-96-100.

170. Sauer, R. Method of Characteristics for Three-Dimensional Axially Symmetric Supersonic Flows. NACA TM 1133, January 1947.

171. Kenney, J. T. and Webb, L. M. A Summary of the Techniques of Variable Mach Number Supersonic Wind Tunnel Nozzle Design. AGARDograph 3, October 1954.

172. Reshotko, E. and Haefeli, R. C. Investigation of Axially Symmetric and Two-Dimensional Multinozzles for Producing Supersonic Streams. NACA RM E52H28, October 1952.

173. Royle, J. K., Bowling, A. G., and Lukasiewicz, J. Calibration of Two Dimensional and Conical Supersonic Multi-nozzles. Aero 2221 S.D. 23. Farnborough, England: Royal Aircraft Establishment, September 1947.

174. Leavy, L. E. A Supersonic Wind Tunnel for Mach Numbers up to 3.5. AGARD Report No. 70, August 1956.

175. Drougge, G. A Method for Continuous Variation of the Mach Number in a Supersonic Wind Tunnel and Some Experimental Results Obtained at Low Supersonic Speeds. Report No. 29, Technical Research Institute of Sweden, 1949.

176. Little, B. H., Jr. and Cubbage, J. M., Jr. The Development of an 8-inch by 8-inch Slotted Tunnel for Mach Numbers up to 1.28. NASA TN D-908, August 1961.

177. Johnson, C. B., et al. Real-Gas Effects on Hypersonic Nozzle Contours with a Method of Calculation. NASA TN D-1622, April 1963.

178. Bernicker, R. P. An Experiment with a Transpiration-Cooled Nozzle. M.I.T. TR 447 (AFOSR TN 60-1484), July 1960.

179. Pasqua, P. F., et al. Analytical Studies on Nozzle Throat Cooling. AEDC-TDR-63-58, April 1963.

180. Ruptash, J. Boundary Layer Measurements in the UTIA 5- x 7-Inch Supersonic Wind Tunnel. UTIA Report 16, May 1952.

181. Baron, J. R., et al. Analytic Design of a Family of Supersonic Nozzles by the Friedrichs Method, Including Computation Tables and a Summary of Calibration Data. WADC TR 54-279, June 1954.

182. Persh, J. and Lee, R. A Method for Calculating Turbulent Boundary Layer Development in Supersonic and Hypersonic Nozzles Including the Effects of Heat Transfer. NAVORD Report 4200, U.S. Naval Ordnance Laboratory, June 1956.

References for Subsec. 4 (cont)

183. Persh, J. A Theoretical Investigation of Turbulent Boundary Layer Flow with Heat Transfer at Supersonic and Hypersonic Speeds. NAVORD Report 3354, U.S. Naval Ordnance Laboratory, May 1955.

184. Van Driest, E. R. "Turbulent Boundary Layer in Compressible Fluids," J. Aeronaut. Sci., Vol. 18, No. 3 (March 1951), pp. 145-160.

185. Erickson, W. D. and Creekmore, H. S. A Study of Equilibrium Real-Gas Effects in Hypersonic Air Nozzles, Including Charts of Thermodynamic Properties for Equilibrium Air. NASA TN D-231, April 1960.

186. Orlin, J., Heins, A., and Douglas, B. A New Type Symmetrical Two-Dimensional Variable Mach Number Nozzle. Nozzle Project Report 2, ARO, Inc., RJA Branch, January 1953.

187. Foelsch, K. A New Method of Designing Two-Dimensional Laval Nozzles for a Parallel and Uniform Jet. Report No. NA-46-235-2, North American Aviation, Inc., May 1946.

188. Wes.kaemper, J. C. The Design of a Mach Number 2.75 Nozzle and Variable Throat Diffuser for the OAL Supersonic Wind Tunnel. OAL Memo 80, September 1954.

189. Harrop, R. and Bright, P. I. Design and Testing of Supersonic Nozzles. Part I. Method of Design and Experimental Improvement of Mach Number Distribution. AERO 2293. Farnborough, England: Royal Aircraft Establishment, October 1948.

190. Ying-Nien Yu. A Summary of Design Techniques for Axisymmetric Hypersonic Wind Tunnels. AGARDograph 35, November 1958.

Also cited in this Subsection: Refs. 2, 3, 6, 7, 13, 94-100

References for Subsec. 5

191. Lukasiewicz, J. "Diffusers for Supersonic Wind Tunnels," J. Aeronaut. Sci., Vol. 20, No. 9 (September 1953), pp. 617-626.

192. Cohen, C. B. and Valerino, A. S. Investigation of Operating Pressure Ratio of a Supersonic Wind Tunnel Utilizing Distributed Boundary-Layer Suction in Test Section. NACA RM E50H04, 1950.

193. Hastings, S. M. and Roberts, R. C. Analysis of the Performance of a Two-Dimensional, Variable-Area Supersonic Wind Tunnel Diffuser With and Without Scavenging Scoop and Model. NAVORD Report 4384, U.S. Naval Ordnance Laboratory May 1957.

194. Wegener, P. P. and Lobb, R. K. NOL Hypersonic Tunnel No. 4 Results II: Diffuser Investigation. NAVORD Report 2376, U.S. Naval Ordnance Laboratory, 1952. Also "An Experimental Study of a Hypersonic Wind Tunnel Diffuser," J. Aeronaut. Sci., Vol. 20. No. 2 (February 1953), pp. 105-110.

References for Subsec. 5 (cont)

195. Bertram, M. H. Investigation of the Pressure-Ratio Requirements of the Langley 11-Inch Hypersonic Tunnel With a Variable-Geometry Diffuser. NACA RM L50I13, 1950.

196. Neumann, E. P. and Lustwerk, F. High-Efficiency Supersonic Diffusers. Meteor Report No. 56, Massachusetts Institute of Technology, June 1950.

197. Neumann, E. P. and Lustwerk, F. "Supersonic Diffusers for Wind Tunnels," J. Appl. Mech., Vol. 16, No. 2 (June 1949), pp. 195-202.

198. Hasel, L. E. and Sinclair, A. R. A Preliminary Investigation of Methods for Improving the Pressure-Recovery Characteristics of Variable-Geometry Supersonic-Subsonic Diffuser Systems. NACA RM L57H02, October 1957.

199. Diggins, J. L. and Lange, A. H. A Systematic Study of a Variable Area Diffuser for Supersonic Wind Tunnels. NAVORD Report 2421, U.S. Naval Ordnance Laboratory, December 1952.

200. Castagna, A. "Experimental Research on the Transformation of Energy of a Gas Flowing in a Pipe," Atti della Reale Academia delle Scienze di Torino, Vol. 70 (1935), pp. 284-317.

201. Wilson, R. E. Aerodynamic Characteristics of Nozzles and Diffusers for Supersonic Wind Tunnels. DRL Report 281, Defense Research Laboratory, April 1951.

202. Neumann, E. P. and Lustwerk, F. "High-Efficiency Supersonic Diffusers," J. Aeronaut. Sci., Vol. 18, No. 6 (June 1951), pp. 369-374.

203. DeLeo, R. V. and Huerta, J. Experimental Evaluation of Supersonic Wind Tunnel Performance With Solid Wall Test Section -- Supersonic Diffuser -- Scavenging Scoop Combinations. AEDC-TR-56-6 (ASTIA No. AD-88602), May 1956.

204. Eggink, H. The Pressure Regain in Supersonic Wind Tunnels. ARC 11270 - FM 11276(British R and T 948), September 1947.

205. Fallis, W. B., et al. Design and Calibration of the Institute of Aerophysics 16 in. × 16 in. Supersonic Wind Tunnel. UTIA Report No. 15. Institute of Aerophysics, University of Toronto, March 1953.

206. Johnston, P. J. and Witcofski, R. D. Effect of a Variable-Geometry Diffuser on the Operating Characteristics of a Helium Tunnel Designed for a Mach Number in Excess of 20. NASA TN D-237, February 1960.

207. Little, T. J. Hypersonic Wind Tunnel Diffuser Investigation. CF 2625, Applied Physics Laboratory, The Johns Hopkins University, March 1957.

References for Subsec. 5 (cont)

208. Hunczak, H. R. and Rousso, M. D. Starting and Operating Limits of Two Supersonic Wind Tunnels Utilizing Auxiliary Air Injection Downstream of the Test Section. NACA TN 3262, September 1954.

209. Faro, I. D. V. Preliminary Study of a Diffuser for Use with the 4.38 M Nozzle in the 1" F.G.S. Tunnel. CF-878, Applied Physics Laboratory, The Johns Hopkins University, January 1948.

210. Makofski, R. A. and Rea, S. N. A Preliminary Study of Shock-Duct Diffusers in a Hypersonic Helium Tunnel. TG 461, Applied Physics Laboratory, The Johns Hopkins University, January 1963.

Also cited in this Subsection: Refs. 3, 12 and 174.

References for Subsec. 6

211. Sutton, G. P. Rocket Propulsion Elements. New York: John Wiley and Sons, Inc., 1956.

212. Foster, C. R. and Cowles, F. B. Experimental Study of the Divergence-Angle Effect in Rocket-Motor Exhaust Nozzles. JPL/CIT Progress Report No. 20-134, January 1952.

213. Durham, F. P. Approximate Analysis of Rocket Nozzle Scale and Dynamic Effects. Report 5, Engineering Experiment Station, University of Colorado, May 1955.

214. van Driest, E. R. "The Problem of Aerodynamic Heating," Aero. Eng. Rev., Vol. 15, No. 10 (October 1956), pp. 26-41.

215. Rowe, P. N. "The Thrust of a Supersonic Conical Nozzle with Non-Isentropic Flow," Institution of Mechanical Engineers, Vol. 172 (1958).

216. Bartz, D. R. "An Approximate Solution of Compressible Turbulent Boundary-Layer Development and Convective Heat Transfer in Convergent-Divergent Nozzles," Trans. ASME, Vol. 77 (November 1955), pp. 1235-1245.

217. Bartz, D. R. "A Simple Equation for Rapid Estimation of Rocket Nozzle Convective Heat Transfer Coefficients," Jet Propulsion, January 1957.

218. Elliott, D. G., Bartz, D. R., and Silver, S. Calculation of Turbulent Boundary-Layer Growth and Heat Transfer in Axi-Symmetric Nozzles. JPL/CIT Technical Report No. 32-387, February 1963.

219. Snyder, W. T. "Nonisentropic Nozzle Flow," ARS Journal (March 1960), p. 270.

220. Campbell, C. E. and Farley, J. M. Performance of Several Conical Convergent-Divergent Rocket-Type Exhaust Nozzles. NASA TN D-467, September 1960.

221. Bloomer, H. E., Antl, R. J., and Renas, P. E. Experimental Study of Effects of Geometric Variables on Performance of Conical Rocket-Engine Exhaust Nozzles. NASA TN D-846, June 1961.

222. McKenney, J. D. An Investigation of Flow Separation in a Two-Dimensional Transparent Nozzle. JPL/CIT Progress Report No. 20-129, April 1951.

223. Foster, C. R. and Cowles, F. B. Experimental Study of Gas-Flow Separation in Overexpanded Exhaust Nozzles for Rocket Motors. JPL/CIT Progress Report No. 4-103, May 1949.

224. Scheller, K. and Bierlein, J. A. "Some Experiments on Flow Separation in Rocket Nozzles," ARS Journal, Vol. 23 (1953), pp. 28-32.

225. Kaufman, L. G., II, et al. A Review of Hypersonic Flow Separation and Control Characteristics. ASD TDR 62-168, Grumman Aircraft Engineering Corp., March 1962.

226. Mager, A. "Prediction of Shock-Induced Turbulent Boundary-Layer Separation," J. Aeronaut. Sci., Vol. 22, No. 3 (March 1955), p. 201.

227. Mager, A. "On the Model of the Free, Shock-Separated, Turbulent Boundary Layer," J. Aeronaut. Sci., Vol. 26 (February 1956), pp. 181-184.

228. Wu, J. M., Chapkis, R. L., and Mager, A. "An Approximate Analysis of Thrust Vector Control by Fluid Injection." Paper presented at the ARS Solid Propellant Rocket Conference in Utah, February 1961.

229. Huff, V. N. and Fortini, A. Theoretical Performance of JP-4 Fuel and Liquid Oxygen as a Rocket Propellant. I - Frozen Composition. NACA RM E56A27, April 1956.

230. Huff, V. N., Fortini, A., and Gordon, S. Theoretical Performance of JP-4 Fuel and Liquid Oxygen as a Rocket Propellant. II - Equilibrium Composition. NACA RM E56D23, September 1956.

231. Wegener, P. P. "Experiments on the Departure from Chemical Equilibrium in a Supersonic Flow," ARS Journal, Vol. 30 (April 1960), pp. 322-329.

232. Bray, K. N. C. "Atomic Recombination in a Hypersonic Wind-Tunnel Nozzle," J. Fluid Mech., Vol. 6 (July 1959), pp. 1-32.

233. Eschenroeder, A. Q., Boyer, D. W., and Hall, J. G. "Nonequilibrium Expansions of Air with Coupled Chemical Reactions," Phys. Fluids, Vol. 5, No. 5 (May 1962), p. 615.

234. Westenberg, A. A. and Favin, S. "Complex Chemical Kinetics in Supersonic Nozzle Flow," Ninth Symposium on Combustion. New York: Academic Press, Inc., 1962.

235. Simmons, F. S. "Expansion of Liquid-Oxygen RP-1 Combustion Products in a Rocket Nozzle," ARS Journal, Vol. 30 (February 1960), pp. 193-194.

236. Rao, G. V. R. "Exhaust Nozzle Contour for Optimum Thrust," Jet Propulsion, Vol. 28, No. 6 (June 1958), pp. 377-382.

237. Hoglund, R. F. "Recent Advances in Gas-Particle Nozzle Flows," ARS Journal, Vol. 32, No. 5 (May 1962), pp. 662-671.

238. Kliegel, J. R. "Gas Particle Nozzle Flows." Paper presented at the Ninth International Combustion Symposium, Cornell University, Ithaca, New York, August 1962.

239. Bailey, W. S., et al. "Gas Particle Flow in an Axisymmetric Nozzle," ARS Journal, Vol. 31, No. 6 (June 1961), pp. 793-798.

240. Rao, G. V. R. "Approximation of Optimum Thrust Nozzle Contour," ARS Journal, Vol. 30 (June 1960), p. 561.

241. Knuth, E. L. "Optimum Contours for Propulsion Nozzles," ARS Journal, Vol. 30 (October 1960), p. 983.

242. Guderley, G. and Hantsch, E. Beste Formen fur Achsensymmetrische Uberschallschubdusen," Zeitschrift fur Flugwissenschaften, Vol. 3 (September 1955), pp. 305-313.

243. Cnossen, J. W. Efficiency of Flush Oblique Nozzles Exhausting into Supersonic Streams Having Mach Numbers up to 4. R-1285-10, United Aircraft Corporation, September 1959.

244. Goethert, B. H. "Base Flow Characteristics of Missiles with Cluster-Rocket Exhausts," Aerospace Engineering, Vol. 20 (March 1961), p. 28.

245. Berman, K. and Crimp, F. W., Jr. "Performance of Plug-Type Rocket Exhaust Nozzles," ARS Journal, Vol. 31 (January 1961), pp. 18-23.

246. Krull, H. G., Beale, W. T., and Schmiedlin, R. F. Effect of Several Design Variables on Internal Performance of Convergent-Plug Exhaust Nozzles. NACA RM E56G20, October 1956.

247. Greer, H. "Rapid Method for Plug Nozzle Design," ARS Journal, Vol. 31 (April 1961), pp. 560-561.

248. Dugger, G. L., et al. Summary Report on External Ramjet Program. TG-419, Applied Physics Laboratory, The Johns Hopkins University, Octobe 1961. (Report Confidential - Title Unclassified)

249. Bankston, L. T. and Larsen, H. M. Thrust-Vectoring Experiments with Gas Injection. NAVORD Report 6548 (NOTS TP 2247), China Lake, May 1959.

250. Lingen, A. Jet-Induced Thrust-Vector Control Applied to Nozzles Having Large Expansion Ratios. U.A.C. Research Paper R-0937-33, March 1957.

251. Moog Servo Controls, Inc. Secondary Injection Thrust Vector Control Systems. East Aurora, N. Y., June 1961.

732-359 O - 64 - 29

References for Subsec. 6 (cont)

252. McCullough, F., Jr. Thrust-Vector Control by Secondary Injection. NAVWEPS Report 7780 (NOTS TP 2764), China Lake, 1962.

253. Green, L., Jr. and Nall, K. L. "Experiments on Porous-Wall Cooling and Flow Separation Control in a Supersonic Nozzle," J. Aero/Space Sci. (November 1959), pp. 689-697.

254. Rowe, P. N. Supersonic Jet Deflection, Part I - Methods of Jet Deflection and a Review of Previous Work. Ministry of Supply EMR 52-4. Imperial College JRL-24, September 1952.

255. Henning, A. B., et al. Some Data on Body and Jet Reaction Controls. NACA RM L56L17, March 1957.

256. Hunter, P. A. An Investigation of the Performance of Various Reaction Control Devices. NASA Memo 2-11-59L, March 1959.

257. Blalock, R. J., Jr. and McCracken, J. G. Design and Flight Test of a Missile Powered by a Gimbaled Solid Propellant Rocket Motor. ARS Paper 1171-60.

258. Hayes, E. J., et al. The Design of Movable Nozzles. ARS Paper 1169-60.

259. Fiedler, W. A. Jetevator Actuation. NAMTC Report 20-53, April 1953.

260. Bond, A. C. Experimental Investigation of a Flat-Plate Paddle Jet Vane Operating on a Rocket Jet. NACA RM L50I20, November 1950.

261. Carter, D. J. and Vick, A. R. Experimental Investigation of Axial and Normal Force Characteristics of Skewed Nozzles. NACA TN 4336, September 1958.

262. Moak, H. "Thrust-Vector Control Schemes for Solid Rockets. Astronautics, Vol. 7 (March 1962), pp. 28-29.

263. Dugger, G. L. and Monchick, L. External Burning Ramjets Feasibility Study. CM-948, Applied Physics Laboratory, The Johns Hopkins University, June 1959.

264. Walker, R. E., Stone, A. R., and Shandor, M. "Secondary Gas Injection in a Conical Rocket Nozzle," AIAA Journal, Vol. 1, No. 2 (February 1963).

265. Walker, R. E., Stone, A. R., and Shandor, M. Interaction Between Sonic Side-Jets and Supersonic Duct Flow. Bumblebee Report 316, Applied Physics Laboratory, The Johns Hopkins University, December 1962.

References for Subsec. 6 (cont)

266. Walker, R. E. and Shandor, M. Theoretical Performance of Selected Fluid Injectants for Thrust Vector Control. CM-1027, Applied Physics Laboratory, The Johns Hopkins University, November 1962.

Also cited in this Subsection: Refs. 6, 7, 16, 21-42 (Appendix A) 94-99 and 118.

Intentionally Blank

Appendix A

Tabulated Ranges of Parameters in Tables Relevant to Duct Flow

I. Isentropic Flow and Normal Shock Functions*

Ref. No.	γ	Mach No. Range	ΔM	Additional Information
1	1.0, 1.1, 1.2, 1.3, and 1.67 1.4	0-3 3-5 5-10 0-3 3-5 5-10	0.05 0.5 1.0 0.01 0.1 1.0	Influence coefficients. Heat addition - constant area Friction - constant area
21	7/5, 9/7, 5/3	0-5	0.01	At $\gamma = 1.4$. Properties in terms of p/p_t for p/p_t from 1 - 0.0026. Oblique-shock tables in terms of θ and M. $\Delta M = 0.01$, $\Delta\theta = 0.02°$.
22	1.4	0-10 10-20 20-50 50-100	0.01 0.02 0.2 1.0	Charts for mass flow, flow over cones and wedges and effects of caloric imperfections on all flow variables.
23	1.25, 1.3, 1.35, 1.4	1-4	--	Conical shock parameters. All in graphical form.
24	1.28-1.38 $\Delta\gamma = 0.02$	0-C	0.01	Normal shock tables give only M_2 and p_{t_2}/p_{t_1}.
25	1.10-1.28 $\Delta\gamma = 0.02$	0.02-8.0	0.02	
26	1.4	1-20	0.1	($1 \leq M \leq 5$) wedge and cone flow. (Graphical form)
27	7/5 9/7	0-5 0-2.5 2.5-5	0.001 0.001 0.01	Includes mass flow and impulse functions
28	1.2 - 1.3 ($\Delta\gamma = 0.02$) and 1.4	1-10	0.001	Gives mass flow function and impulse functions
33	4/3	0-2	0.001	Includes mass flow and velocity functions
34	1.18-1.30 ($\gamma = 0.2$) 1.15, 1.4, 1.67	0.01-10 10-20 20-50 50-100	0.01 0.02 0.2 1.0	

*All given in tabular form unless otherwise stated.

Appendix A (cont)

II. Flow with Heat and Mass Addition

Ref. No.	γ	Mach No. Range	ΔM	Description
29	1.20-1.30 ($\Delta\gamma$ = 0.02), and 1.4	1 - 10	0.001	Stagnation temperature change without friction.
30	1.20-1.30 ($\Delta\gamma$ = 0.02), and 1.4	1 - 10	0.001	Adiabatic flow with friction.
31	1.20-1.30 ($\Delta\gamma$ = 0.02), and 1.4	1 - 10	0.001	Simple gas injection with no forward velocity.
32	1.20-1.30 ($\Delta\gamma$ = 0.02), and 1.4	1 - 10	0.001	Simple gas injection with forward velocity equal to free-stream velocity.

III. Conical Flow Tables

Ref. No.	γ	Mach No. Range	Cone Semi-Angle	Description
23	1.25, 1.30 1.35, 1.60	1 - 4	0° - 58°	Graphical information only. M, T, p, and ρ ratios. Shock angles vs M_∞.
35	1.405, 4/3	1 - ∞	5° - 50° $\Delta\theta$ = 2.5°	M, T, p, and ρ between bow shock and conical surface in terms of free-stream values.
36	1.4	1.4 - 6 ΔM = 0.2	5° - 50° $\Delta\theta$ = 2.5°	Gives M and flow inclination along rays 0.2° apart.
37	1.4	2 - 5.5	20°- 45° $\Delta\theta$ = 5°	M and flow inclination in the field between nose shock and the conical surfaces. Data for the second shock front.

IV. Ramjet or Nozzle Flow Tables*

Ref. No.	γ	$\Delta\gamma$	Tabulated Information
38	1 - 1.15	0.05	Exit-to-chamber pressure ratio, p_e/p_c.
	1.15 - 1.45	0.01	Exit-to-sonic area ratio, ϵ, 1 to 1000.
	1.45 - 1.65	0.05	Thrust force coef., C_F. ΔC_F = 0.01.
	5/3	--	The product ($\epsilon \cdot p_e/p_c$).

*(References 1, 22, and 27 also contain useful information.)

Appendix A (cont)

V. Thermodynamic Properties

Ref. No.	Independent Variables	Dependent Variables
39	T: 600 - 5000°R ΔT = 100° ER: 0.25 - 4.0 Δ(ER) - varying p: 0.01 - 30 atm Δp - varying	For C_nH_{2n} - Air. Enthalpy, entropy, heat capacity (c_p), mean molecular weight (m), density, sonic velocity (equil. and frozen), $\left(\frac{\partial \ln m}{\partial \ln T}\right)$, $\left(\frac{\partial \ln m}{\partial \ln p}\right)$.
40	A compilation of 64 tables including thermodynamic properties of air and of its separate constituents as well as of the products of combustion of hydrocarbons. Compressible flow functions, Rayleigh line, Fanno line, normal-shock functions, and many other useful functions.	
41	A comprehensive tabulation of data involving heats of reaction. Perhaps the material most relevant to duct flow theory is the following: Series I - Tables of entropy and c_p. Series II - Increments in heat content, entropy and heat capacity due to transition, fusion, and vaporization.	
42	A comprehensive compilation of the heat capacity, entropy, enthalpy, and heats of formation, combustion, and reaction as a function of temperature for more than 700 elements and compounds.	

Intentionally Blank

p. 418

INDEX

acoustic analogy, 147
acoustic impedance, 147
acoustic velocity, 328
additive drag, 21, 105ff, 118, 120, 123, 132ff
additive lift, 136
air-breathing engine, thrust, 21, 118, 136
angle of attack, effect in diffusers, 106-108, 113, 118, 119, 120, 124, 125, 136, 140
area
  annular, 115, 131
  capture ratio, 22, 103ff, 115, 118, 132, 133, 137
  constant in a duct, 5
  discontinuities in, 39, 43
  throat, 108, 133, 137, 225ff, 340
    minimum running, 275
    minimum starting, 109, 122, 274, 280
  variation in a duct, 3-5, 12, 45

base pressure, 337
boundary layer
  bleed, 107, 111, 112, 119, 125, 138-142, 242, 335
  bridging, 125, 137, 138
  correction for, 14-18, 58-60, 137, 245, 248ff, 316
  development, 115, 126, 137, 238
  displacement thickness, 24, 59, 248, 316 Tables 2-1 and 4-4
  duct, in, 271
  fuselage, on, 142
  injection, 277, 278
  momentum thickness, 59, 316, Tables 2-1 and 4-4
  reflection thickness, 249
  scoop, 141, 142
  separation, 108, 120, 125, 136, 137, 139, 141, 238, 271, 275, 278
  suction, 125, 141, 241, 278-280
  thickness, 14, 58, Tables 2-1 and 4-4
  throat region, 138-141
  transition, 125, 138
buzz, 115, 125, 131, 143ff
  control of, 145, 146

calibration, of nozzles, 240, 247, 248
caloric imperfection, 13
capture-area ratio (see area)
Chapman-Jouguet detonation, 6ff
characteristic velocity, 308, 328
characteristics, method, 57, 106, 129, 132, 230, 236, 239, 243, 245, 329, 332
chemical recombination of exhaust gases, 10ff, 325, 327
choking, 108, 125, 132, 240, 338
clustered nozzles, 337
coefficient, of thrust, 308
combustion, 7, 11, 23
compatibility equations, 28
compression
  external, 114, 115, 121, 122
  internal, 108, 110, 115, 121, 122, 131
  isentropic, 108, 110, 126, 127
  maximum allowable, 126-128, 130, 132
  normal shock, 108-110
  waves, 106
contact surfaces, 34, 35, 43, 44
continuity equation, 26
contraction ratio, 112, 116, 272-276
  subsonic, 229, 230
convergence angle, wind-tunnel diffuser, 274, 275, 283, 284
cooling, nozzle, 136, 245ff
cowl
  drag, 105-107, 119
  iris type, 342
  lip, 115, 117, 124, 128-130, 133, 137, 341
critical diffuser operation, 104, 114, 137
curvature discontinuities, 232, 235

deflagration, 6-8
dependence, domain of, 31
detonation
  Chapman-Jouguet, 6-8
  Mach number, 8
  pressure, 6
  temperature, 6
diffuser, ramjet, 22, 101-223
  double-cone, 121-125, 134-137
  drag of, 102, 105-108
  efficiency of, 102, 110
  Ferri, 118
  fixed geometry, 108-110
  function of, 101
  internal compression, 108
  isentropic spike, 106, 125-135
  normal shock in, 101-102, 108-110
  oblique shock, 114-115, 132-135
  operation, critical, 104, 114, 137
  perforated, 113
  performance of, 102-108, 134-136
  probe, 120-121
  single-cone, 116-120, 134-136
  throat, 110, 118

two-dimensional, 106, 111, 136, 283
variable geometry, 110-112
diffuser, wind tunnel, 269-305
efficiency, isentropic, 270, 274-276, 278, 281-283
efficiency, polytropic, 269, 276, 281-283
hypersonic, 283-285
oblique shock, 276
with contraction, 272-276
without contraction, 108-110, 271-272
diffusion
subsonic, 101, 141-142, 269-271
supersonic, 101, 141, 269, 274
discharge correction factor, 311
displacement thickness, boundary layer, 24, 59, 248-251, Tables 2-1 and 4-4
dissociation in exhaust gases, 14, 325, 327
distortion, flow, 102-103, 112, 119, 124, 140
divergence
factor, 313, 339
wind tunnel diffuser, 271
drag
additive, 21, 105-108, 118, 120, 123, 132-133
air-breathing engine, 21
coefficient of, 9, 135, 344
cowl, 105-108, 119
diffuser, ramjet, 101-223
internal, 141
rocket jet, 20
duct
annular, 115
closed end, 33, 51
constant area, 5, 271, 272
convergent-divergent, 108, 118, 272
flow, theory, 3-100
shock, 283-285
subsonic discharge, 33, 51
supersonic discharge, 33, 51
varying area, 45

efficiency, diffuser
isentropic, 270, 274-276, 278, 281-283
kinetic, 311
nozzle throat, 318-320
polytropic, 269, 276, 281-283
ramjet diffuser, 102, 110ff
rocket nozzle, 310-313
wind tunnel, 269-283
effusor (see nozzle)
energy equation, 27
enthalpy, 7, 311, 317
entropy, specific, 26ff
equilibrium flow, 326
equivalence ratio, 11, 342
exhaust gases, 10ff, 325, 337
expansion
maximum, 231
over-, 321
processes, 325
external ramjet, 344

Ferri diffuser, 118
fixed-geometry diffuser, 108-110, 271-272
flame
fronts, 12, 37-39, 44, 54-56
temperature, 11
flange loads on free-jet nozzles, 18-19
flexible walls, 111, 141, 234, 275
flow
conical, 116-119, 121-125, 244, Appendix A
discontinuities
moving, 48
stationary, 34
distortion, 102-103, 112, 119, 124, 140
equilibrium, 326
frozen, 326-329
high-temperature, 13
hypersonic, 13, 22, 136, 243
inclination, 121, 122, 128, 133
infinite extent, 47
isentropic relations, 4
mean values, 14-18
non-adiabatic, 4-5
non-isentropic, 4-5
nozzle throat, 226-229
one-dimensional
non-steady, 24ff
non-uniform, 14ff
steady, 3ff
particle, 329
quality at exit, 102-103, 112, 119, 124, 140
radial, 63, 227, 229, 243, 248
rotational, 57, 121
separation, 108, 120, 125, 137, 229, 321
source, 63, 227, 229, 243, 248
stability, 108, 115, 131, 143ff, 272, 280
transonic, 225ff
two- and three-dimensional, 57
wake, 241
frozen flow, 326-329
fuel
addition, 8-12
specific impulse, 20, 310, 326, 342, 344, 348
velocity, 9
fuel-air ratio, 7, 8, 10, 135, 326

gas
caloric imperfections, 13

dissociation, 14, 325, 327
exhaust, 10ff, 325, 337
injection, 277, 346
interface, 25
particle flows, 329
propane, 11
real, effects, 243, 245, 250
recombination, 14, 325, 327
thermal imperfections, 13

heat
addition, 5ff, 8, 12, 26
transfer
coefficient, 316
in ducts, 23
in nozzles, 317
high-temperature flows in ducts, 13
hypersonic flow
in ducts, 13
in ramjets, 22
hypersonic nozzle design, 243
hypersonic transport, 136

ideal exhaust nozzle, 22
ideal thrust coefficient, 22
impedance, acoustic, 147
impulse, fuel specific, 20, 310, 326, 342, 344, 348
influence
coefficients, 3
range of, 31
injection
diffusers with, 277-278
velocity, 9
inlet
application to air-breathing engines, 131
engine, stability of, 146
inserts, Menard, 241
internal cowl lip angle, 115ff, 125-131, 135
isentropic
compression, 108, 110, 126
equations, 3
flow tables, Appendix A
spike diffuser, 106, 115, 125ff, 132ff, 276
surface, 115, 129, 340
wedge diffuser, 136, 276

jetavator, 346
jet
paddles, 345
vanes, 345

kinetic-energy flux correction factor, 15

lift, additive, 136, 344
load, flange, 18-19
starting, wind-tunnel, 238

Mach number, in nozzle throat, 321
mass
addition, 6, 8-12, 22, 26
control, 113
flow, 4, 9, 14, 102ff, 114, 115, 118, 121, 124, 125, 135, 144, 308
Menard inserts, 241
model, in test section, 282
momentum, equation, 26
flux correction factor, 15
momentum thickness, boundary-layer, 59, Tables 2-1 and 4-4
multi-nozzles, 233-234, 337

non-steady flow, 24ff
non-uniform flow, 14ff
normal shock
adiabatic, 12-13
at cowl lip, 133
in constant-area duct, 272, 283-285
in ramjet diffuser, 102, 106, 116, 121, 134
in throat, 110, 123, 138, 274
system, 102, 123, 131, 140, 271, 278, 279, 283
tables, Appendix A
nozzle
asymmetric, 237-240
axisymmetric, 231
calibration, 240, 247-248
characteristic length, 312
clustered, 337
conical, 245ff, 332
continuous curvature, 232-233
contoured, 331, 332
cooling, 136, 245ff
design, 331ff
divergence angle, 271
exhaust, 23, 307ff
fixed Mach number, 230-232
flexible-walled, 232, 234-236
heat transfer in, 317
hypersonic, 231, 243, 247
multi-, 233-234
over-expanded, 321
plug, 136, 331, 339
propulsion, 307
scissors-type, 236
skewed, 331, 335
sliding, 237-240
slotted, 242
swiveled, 343

temperature, 327
throat
correction, 318
flow conditions, 226ff
two-dimensional, 229, 232, 342
efficiency of, 310-313
variable Mach number, 234-242
viscous effects, 314-318
wedge, 247
wind tunnel, 225ff

oblique-shock
ramjet diffuser, 112, 114-115
wave, 121, 233
wind-tunnel diffuser, 276-277
operation, ramjet
critical, 104, 114
off-design, 118, 132-134
supercritical, 104, 114, 118
Oswatitsch diffuser, 114

particle
flow, 329
lag, 330
perforated diffuser, 113
performance
comparative, 134-136
off-design, 102, 134ff
ramjet, 102, 134ff
perturbations, small, 45-47
pipe flow, 15
pitch control, 344
plug nozzles, 136, 339
potential flow, 16, 57, 59, 225, 243
power requirements, wind tunnel, 272, 279, 282
Prandtl-Meyer expansion, 334, 341
pressure
cowl lip, 106
detonation, 7
gradient, 60-61, 137, 316
mean value, 17
ratio, critical, 337
recovery, ramjet diffuser, 23, 102ff, 110, 114-115, 117-118, 120-126, 129, 133, 135-136, 140
seal, 236-237
separation, 329
wave, 12
probe diffuser, 120-121
propulsion nozzles, 307
efficiency, 310-313
performance, 307
viscous effects, 314

quality of exit flow, 103

radial flow, 63, 227, 229, 243, 248
ramjet, diffuser, 22, 101ff
external, 344
operation, 138
critical, 114
off-design, 118, 132-134
real-gas effects, 8, 243, 245, 250
caloric imperfections, 13
dissociation, 14
recombination, 14
recombination in exhaust gases, 14, 325, 337
reflected wave, 127
reflection thickness, boundary-layer, 249
Riemann variables, 28ff
roll control, 344
rotationality, flow, 57, 121
run time, wind tunnel, 280-282

scoop, boundary-layer, 141-142
scavenger, 279, 283
seal, pressure, 236-237
second throat
fixed, 108-110, 273
variable, 110-112, 275, 280
separated flow, 108, 120, 125, 137, 229, 321
separation pressure, 322, 347
shock
conical, 106, 115-116, 121, 132
duct, 283-285
interactions, 40-44, 137
losses, 102
normal, 102, 106, 116, 121
oblique, 112, 121, 233
oblique, diffuser, 114-115, 121, 276-277
reflection, open end of duct, 40
transfer functions, 50-56
wedge, 136
shock-induced deflections, 346
side force, 346
skin friction, 23, 123, 250, 314, 332, 339
sonic
line, 226ff, 231
throat, 103, 108, 225ff, 342
source flow, 63, 227, 229, 243, 248
specific impulse, 20, 310, 326, 342, 344, 348
spike
conical, 135
isentropic, 106, 115, 125ff, 132ff, 276, 340
translation, 112, 119, 124, 132
spill-over, 105-106, 109, 113, 115, 117, 128, 132

stability, engine-inlet, 146-148
subcritical diffuser operation, 104, 114
subsonic
  contraction, 229-230
  diffusion, 101, 141-142, 269-271
suction, 125, 141, 241, 278-280
supercritical diffuser operation, 104, 114, 118
supersonic diffusion, 101, 141-142, 269, 274

temperature
  detonation, 6ff
  discontinuity, 12
  flame, 11, 327
  variation, 5ff, 327
throat
  boundary-layer in, 138-141
  curvature, 235, 243
  efficiency factor, 318-320
  height, 229, 243
  length, 110, 118
  rounded, 231, 243, Tables 4-1 to 4-3
  second, 237, 272-276
  sharp, 231, Tables 4-1 to 4-3
  sonic, 5, 103, 108, 225ff, 239, 318, 331, 340, 342
  wall curvature, 225ff
throttling plug, 103
thrust
  air-breathing engine, 21, 118, 123, 132, 136, 140
  average value in a duct, 17
  base, 338
  coefficient, 308, 333, 337
    ideal, 308
    vacuum, 309
  gross, 22, 307
  ideal, 22
  rocket jet, 19
  specific impulse, 20
  vector control, 343ff
transfer function, 50ff
transition, boundary-layer, 125, 138
translating spike, 112, 119, 124, 132
transonic flow, 225ff
two-dimensional nozzles, 342

vacuum thrust coefficient, 309
velocity
  acoustic, 328
  characteristic, 308, 328
  coefficient, 311, 337
  detonation, 7
  fuel, 9, 20
  nozzle exit, 307, 316, 318
  profile, 23
viscous effects, 23, 26, 57, 60, 101-102, 117, 272
  in duct flows, 23-24
  in propulsion nozzles, 314-318
volume flux, correction factor, 15
vortex
  flow, 17
  sheet criterion, 126, 128, 130, 132
  sheet theory, 143
  trap, 110, 140

wake flows, 233, 241, 340
wave
  centered expansion, 31
  compression, 106
  diagrams, 24ff
    boundary conditions, 32
    closed end duct, 33, 51
    subsonic discharge, 33, 51
    supersonic discharge, 33, 52
  pressure, 12, 24, 30
  simple, 31
  small amplitude, 24
  transmission, reflected, 127
wedge
  flow, 128
  nozzles, 243, 247

yaw control, 344

U. S. GOVERNMENT PRINTING OFFICE. 1964 O - 732-359